

ADVERTIMENT. La consulta d'aquesta tesi queda condicionada a l'acceptació de les següents condicions d'ús: La difusió d'aquesta tesi per mitjà del servei TDX (www.tesisenxarxa.net) ha estat autoritzada pels titulars dels drets de propietat intel·lectual únicament per a usos privats emmarcats en activitats d'investigació i docència. No s'autoritza la seva reproducció amb finalitats de lucre ni la seva difusió i posada a disposició des d'un lloc aliè al servei TDX. No s'autoritza la presentació del seu contingut en una finestra o marc aliè a TDX (framing). Aquesta reserva de drets afecta tant al resum de presentació de la tesi com als seus continguts. En la utilització o cita de parts de la tesi és obligat indicar el nom de la persona autora.

ADVERTENCIA. La consulta de esta tesis queda condicionada a la aceptación de las siguientes condiciones de uso: La difusión de esta tesis por medio del servicio TDR (www.tesisenred.net) ha sido autorizada por los titulares de los derechos de propiedad intelectual únicamente para usos privados enmarcados en actividades de investigación y docencia. No se autoriza su reproducción con finalidades de lucro ni su difusión y puesta a disposición desde un sitio ajeno al servicio TDR. No se autoriza la presentación de su contenido en una ventana o marco ajeno a TDR (framing). Esta reserva de derechos afecta tanto al resumen de presentación de la tesis como a sus contenidos. En la utilización o cita de partes de la tesis es obligado indicar el nombre de la persona autora.

WARNING. On having consulted this thesis you're accepting the following use conditions: Spreading this thesis by the TDX (www.tesisenxarxa.net) service has been authorized by the titular of the intellectual property rights only for private uses placed in investigation and teaching activities. Reproduction with lucrative aims is not authorized neither its spreading and availability from a site foreign to the TDX service. Introducing its content in a window or frame foreign to the TDX service is not authorized (framing). This rights affect to the presentation summary of the thesis as well as to its contents. In the using or citation of parts of the thesis it's obliged to indicate the name of the author



CONTRIBUTION TO THE ADVANCED ANALYSIS AND PREVENTION OF THE MECHANISMS OF NATURAL FIRE INDUCED STRUCTURAL COLLAPSE IN HIGH-RISE BUILDINGS

APORTACIÓN AL ANÁLISIS AVANZADO Y PREVENCIÓN DE LOS MECANISMOS DE COLAPSO ESTRUCTURAL DE EDIFICIOS DE GRAN ALTURA ANTE UNA SOLICITACIÓN DE INCENDIO REAL

Doctoral Thesis presented by / Tesis Doctoral presentada por

Angel Guerrero Castells *Ingeniero Industrial con Suficiencia Investigadora*

in February 2009 to obtain the degree of Doctor in Industrial Engineering

en Febrero de 2009 para obtener el grado de Doctor Ingeniero Industrial.

Thesis Directors / Directores de la Tesis:

Dr Frederic Marimon Carvajal from the / de la Universidad Politécnica de Cataluña

Dr Francesco Pesavento from the / de la Università degli Studi di Padova

PROGRAMA DE DOCTORADO DE ANÁLISIS ESTRUCTURAL

*Departamento de Resistencia de Materiales y Estructuras en la Ingeniería
Escuela Técnica Superior de Ingenieros Industriales de Barcelona*



*THIS PAGE IS INTENTIONALLY
LEFT BLANK*

ACTA DE QUALIFICACIÓ DE LA TESI DOCTORAL

Reunit el tribunal integrat pels sota signants per jutjar la tesi doctoral:

Títol de la tesi: **CONTRIBUTION TO THE ADVANCED ANALYSIS AND PREVENTION OF THE MECHANISMS OF NATURAL FIRE INDUCED STRUCTURAL COLLAPSE IN HIGH-RISE BUILDINGS**

Autor de la tesi: **ANGEL GUERRERO CASTELLS**.....

Acorda atorgar la qualificació de:

- No apte
- Aprovat
- Notable
- Excel·lent
- Excel·lent Cum Laude

Barcelona, de/d'..... de

El President

El Secretari

.....
(nom i cognoms)

.....
(nom i cognoms)

El vocal

El vocal

El vocal

.....
(nom i cognoms)

.....
(nom i cognoms)

.....
(nom i cognoms)

*THIS PAGE IS INTENTIONALLY
LEFT BLANK*

To Professor Dr Frederic Marimon – who taught me, over all, to persevere, to be infinitely patient and to know to start anew –,

Al Profesor Dr Frederic Marimon – quien me ha enseñado sobre todo a perseverar, a tener una paciencia infinita y a saber volver a empezar –,

to Professor Dr Francesco Pesavento – who has shown me the generosity, in its widest sense, from the well-deserved privilege of the most advanced knowledge –,

al Profesor Dr Francesco Pesavento – quien me ha mostrado la generosidad, en el sentido más amplio, desde el merecido privilegio del conocimiento más avanzado –,

and very especially to my sons, Anibal and Aitor, because they taught me to overcome the bad moments painting an angel smile in their little faces, being mi biggest desire to better myself,
muy especialmente a mis hijos, Aníbal y Aitor, que me han sabido hacer superar los momentos malos dibujando una sonrisa de ángel en sus caritas y siendo mi mayor afán de superación,

to my mother, Clara, with her clairvoyance and unshakeable energy, because after trying any imaginable technique to encourage me she was only left an implacable “look, I want to see you as a Doctor before I die” that was completely inexorable (do not ever change, please),
a mi madre, Clara, con su clarividencia e inquebrantable energía, porque después de probar todas las técnicas imaginables para impulsarme sólo le quedó por fin un implacable “mira que quiero verte Doctor antes de morirme” que fue del todo inexorable (no cambies nunca, por favor),

to my father, Jesus, also Doctor, because of his numerous and inexhaustible “push it forward yet and finish”,
a mi padre, Jesús, también Doctor, por sus numerosísimos e inagotables “dale un empujón ya y acábala”,

and to my sister, Eva, because I know that she always supported me in the distance.
y a mi hermana, Eva, porque sé que en la distancia siempre me apoyó.

Each of them has been a link in the chain that has allowed me to run up the anchor. Thank you!
Cada uno de ellos ha sido un eslabón de la cadena que me ha permitido izar el ancla ¡Gracias!

*THIS PAGE IS INTENTIONALLY
LEFT BLANK*

PREFACE AND ACKNOWLEDGEMENTS

I started studying my doctorate almost nine years ago because I wanted to access to an educational level which enabled me to develop global solutions to questions about basic essentials, instead of remaining applying already existing technologies to certain cases with individual repercussion within developed countries (according to the current concept of development).

I would have never expected that the path towards that starting point would be a so long, winding and non-exempt of difficulties pilgrimage with which, on the other hand, combined with personal experiences difficult to harmonize with the lucidity and serenity that were required to cover that path. However, now I think that the only thing I did was to experiment an advance of some of the difficulties that I will find in my next travel as a researcher.

It all started in the physical and temporal distance. In 2000, living in Ibiza – an island often featured with a double insularity – I began plenty of will to attend my teaching credits, which extended over two years as a result of their sharing with two jobs and a family.

Within 2002 I contacted Professor Dr Frederic Marimon, from the Department of Materials Strength and Structures in Engineering, already being a close friend with whom I had shared my career final project development, as well as many courses over several years and some research works. From the beginning, Frederic received me with all of the willingness that distinguishes him and, soon, we started to probe subjects for my doctoral thesis. As my speciality was, in that time, the advanced analysis of cold-formed steel structural profiles, the first subject we brought up – arising from incongruences that we had observed during our previous research works – consisted on the analysis of partially restrained in their movement cold-formed structural profiles and, more precisely, on the analysis of the influence of anti-sag bars on the lateral buckling of the free flange of steel purlins. With that idea settled down, and with a very precise objective, I presented my thesis proposal in September 2002 and I travelled to the Eurosteel'02 Congress held in Coimbra (Portugal) in order to expose a paper about the subject. In this paper we already

anticipated the expected solution to the subject that would be studied in my thesis since we had a clear knowledge about the actual problem involved. However, the amount of daily work lead to a delay in the thesis final development long enough to enable, in the interim, in June 2004 the official solution of the problem by a research group in the Department of Civil and Structural Engineering within the Polytechnic University of Hong Kong, Hung Hom – Kowloon (Professor Dr K. F. Chung) to whom I must acknowledge his sending of the key article – prior to its publication – so I did not have to loose any more time in this matter (at this point I had already invested some hundreds of working hours in what now unfortunately became a 'no-way' thesis).

Despite this situation, my will to continue – until I reached what had to be the starting point of my new professional career – was so strong that soon long-suffering Frederic and myself got to work and analyzed alternative aims for my thesis. A new starting point was needed between two way flights between Ibiza and Barcelona. At that moment, almost four years after having started the doctorate studies, there were many people who asked me often why I insisted so much in continuing my studies if unlikely it would be useful for me in Ibiza. Nevertheless, I always answered the same, that – first – it enriched me (wherever I were) beyond the low level managing-engineering that was developed in Ibiza in that days. On the other hand, I told them that approaching research to Ibiza was not a dream any longer thanks to the newest information technologies, and that there was only necessary the existence of people ready to assume the challenge of releasing research from geography.

Then, Frederic proposed me – from previous inquiries done by his department colleague Professor Dr Miquel Casafont, one of the few people in Spain who had introduced themselves in the subject – another idea for my thesis whose attractiveness fell not only on its related knowledge being limited to really narrow circles in the scientific world but also on its theoretical-analytical component – which had always attracted me –: the generalized beam theory. After meetings with Frederic and Miquel – to whom I acknowledge his kind introducing me in the subject

– in January 2005 I contacted the author of this theory – Mr Richard Schardt – a German scientist who sent me a personal copy of the only book in the world explaining it in depth and that was out of print ‘Verallgemeinerte technisch Biegetheorie’. My acknowledgements for him also from these lines. From the analysis of the related state-of-the-art, we concluded that it would have been extraordinarily difficult to get introduced in a subject about which the only available information out of the nucleus of the theory left me at an starting point much behind the original theorizers, becoming an almost impossible task to develop an original contribution in the subject.

After that it came a pilgrimage looking for the scientific environment to which I could make an original contribution – and where I had some previous knowledge and experience –, travelling from the Catastrophe Theory – which I do not discard to study in the future in sight of the interest that it suggested me its wide potential of application to fields so different such as engineering, economy or migratory movements) until the computational fluid dynamics and its appliance to safety in High Rise Buildings. By that moment we had already arrived at the second term of 2005, and I was beginning to despair because of not having found my starting idea.

I started reading, among the hundreds of papers and books that I have finished reading – and buying due to my difficulties to their access from the distance –, many subjects related with fire and its structural consequences. Somewhat induced by the magnitude of the tragedy occurred at the World Trade Centre at New York some years before – which had been the *raison d’être* of many research lines – I was progressively focusing in the advanced analysis and prevention of the structural collapse mechanisms of High Rise Buildings in fire. Hence, at mid 2005 I presented my second thesis proposal to the committee – with the current title – in which I opened the door of the studying chances to five wide lines among which, without any doubt, it interested me most because of the originality of its approach the analysis of the effect of the fire fighting strategies on the structural state of the load bearing elements of a High Rise Building. Once accepted the second thesis proposal, and as the proposed scope was too wide, Frederic (and his infinite patience) and me followed meeting in fleeting journeys to Barcelona in order to set the bounds of my thesis. And then was that, at the end of 2005, Frederic pronounced a single word about which I have not stopped

thinking during these three long years: spalling. The idea aroused from a simple conversation upon the conflicting points of view of fire fighting services about the convenience, or not, of cooling directly the surface of structural elements during a fire by means of the application of water jets. Up from there, and as I have learnt pretty well during this thesis one thing leads to the other, we began analyzing the different failure mechanisms of columns manufactured with High Strength Concrete until we arrived at spalling. It soon fixed my attention since I would have never imagined that the vapour pressure inside a concrete column could be high enough so that, together with its constrained elastic energy resulting from differences in temperatures of neighbouring regions, could literally explode it –at least partially–.

I started immediately to analyze the state-of-the-art and I detected severe lacks in the analytical approach of spalling. If it had not been because of an unfortunate 2006 year, with respect to personal matters, my interest in the subject would have let me see – already since that year – the aim, the methodology and the tools to fulfil my thesis. However, it was not until late 2006 – once understood the complexity of the hygro-thermo-chemo-mechanical analyses within an unsaturated porous media with multiple phase changes and chemical degradation as the High Strength Concrete – when I found the suitable tool to accomplish the research works I intended: the High TEMperature CONcrete and SPalling software (HITECOSP), a software with a very high complexity both from its formulation and from the user points of view developed mainly by the University of Padova (Italy). I do not think I fail if I say that at that time Frederic did not trust much more on my disposal to carry on with my thesis after so many years (I would have not trusted much on my success chances, in his place), and in fact this concern became deeper when I fall into serious difficulties to obtain this fundamental work tool (later I would discover that these difficulties arose because of having missed about the person to whom ask for it, as there later demonstrated me the developers of the Model of Padova, to whom I will refer later because they were finally who made possible that I am at this moment writing the closing preface of my thesis and they deserve nothing but praise).

Overcoming again the distance and my lack of renown as a researcher, Dr Franco Corsi (from the ENEA, in Italy) was who finally delivered me

the HITECOSP software in the first term of 2007 and after not few steps. From here I also acknowledge him for opening a door that, later on, the nobility of Padova people transformed into something much more immeasurable. The first half of 2007 was a strong learning period about the theoretical model hidden behind that software, and also a testing time to understand how it worked without being able to ask other experts or users about their opinion. At that moment I had already finished with one of my two jobs – more precisely, in 2006 I closed my engineering office up to this date – what not only represented me a high opportunity cost but also led to investments that were not easy for me to stand. It would have been easy that the difficult economical sustainability of my situation, together with the time past from the beginning of my doctorate studies, almost seven years before, would have made me lose the serenity and concentration that a thesis of this type demanded, but I learnt to persevere (perhaps the most valuable lesson for me outcoming from the development of my studies).

In May 2007 I had reached a deadlock in which the lack of experimental results needed to characterize suitably the materials with which I had to work, and my incapacity to assimilate by my own certain matters extremely specialized related to the calculation model implemented, made me doubt – once more – about the consecution of my objective. But because of one of the coincidences (?) that take place only a few times in a life, at short five hundred meters from my job place Dr Eugenio Oñate (from the International Center for Numerical Methods in Engineering – CIMNE – in the Polytechnic University of Catalonia) , Dr Bernhard Schrefler (director of the Istituto di Costruzioni, the Padova University department alma mater of the Model of Padova) and Dr Manolis Papadrakakis (from the Institute of Structural Analysis & Seismic Research from the National Technical University of Athens) organized the international congress called *Computational Methods for Coupled Problems in Science and Engineering II* (2007). Not only the aim of the congress, coupled problems in engineering, suited perfectly with what I was studying at that moment, but also the fact that the best world specialists in the subjected related to my thesis suddenly met at my home island. From this congress I must acknowledge, first, that Dr Oñate introduced me to Dr Schrefler who, despite being a worldwide authority, always made me feel as a true colleague. Eugenio also introduced me to

Dr Carmelo Majorana, to whom I also have to acknowledge the interesting ideas shared during the congress coffee breaks. But if in that congress I knew someone whose exquisite attention and disposal have made possible the writing of this closing preface – and only very few people really know what this means for me – was Francesco Pesavento, also from the Department of Structural and Transportation Engineering of the University of Padova. I had been reading and re-reading for some time his international papers related to the subject of my Thesis, and I did not doubt about approaching him during the congress breaks in order to explain him my situation even under the risk that, being me a complete unknown person for him, he paid me a cold and little interested deal. Nothing farther from truth! Francesco made me change deeply the concept I had about ‘that people that attends to congresses to expose their achievements and to hide their magical recipes, their knowledge’. From the very beginning he was not only an open book, where reading a page illustrated me more than a volume of other encyclopaedia, but he also immediately understood my situation and he offered to keep a narrow contact which has followed until the end of this thesis. So much so that, always with the go-ahead of my thesis director Dr Frederic Marimon to whom I followed martyring with my never ending strategic doubts (I am sorry, Frederic), Francesco became to be my thesis co-director.

In March 2008, once more, being in a really advanced state of the analysis planning and development, the distance became a problem for the continuous exchange of opinions and doubts, what led me to travel to the University of Padova (Italy), by the hand of my already close friend Francesco. Before leaving to Padova I could not imagine what that journey was going to mean both for me and for Francesco. For him, an extraordinary overload of work added to his already numerous duties as a university professor, despite of which he found some twelve hours per day to address my thesis towards an end. For me, an enriching experience and the surprising discover: the sureness that there are still persons disposed to help in an unconditional and uninterested way from the highest step of the scientific knowledge.

I came back from Padova with a renewed conceptualization of the processes involved in the hygro-thermo-chemo-mechanical behaviour of the High Strength Concrete, what allowed me to accomplish an analysis of the results much deeper

and conscious, and after having been able to work out the calculation of the cooling of a square column thanks to a supercomputer in the Department of Structural and Transportation Engineering of the University of Padova – since trying to fulfil this calculation with a personal computer would have been unviable in sight of its computational requirements –. The second half of 2008 was that what required the intellectual effort more demanding: the complexity and huge amount of results to analyze, as well as the difficulty of structuring the developed works with a simple reading morphology, bumped with the exhaustion arising from my almost nine years lasting doctoral studies, although the proximity of the goal – together with the encouraging works from my thesis directors (and others that I will mention next) and with the sight of a new professional horizon – detonated my last sprint towards this preface.

To put it all into a nut shell, I would like to acknowledge their irreplaceable professional contributions to all of those who during these nine years, either in a direct or an indirect way, helped me up to giants' shoulders to reach this end of the beginning, and very especially to Professor Dr Frederic Marimon – who taught me, over all, to persevere, to be infinitely patient and to know to start anew – and to Professor Dr Francesco Pesavento – who has shown me the generosity, in its widest sense, from the well-deserved privilege of the most advanced knowledge –. In the personal field; I would like to acknowledge very especially to my sons, Anibal and Aitor, because they taught me to overcome the bad moments painting an angel smile in their little faces and that they are my biggest desire to better myself; to my mother, Clara, with her clairvoyance and unshakeable energy, because after trying any imaginable technique to encourage me she was only left an implacable “look, I want to see you as a Doctor before I die” that was completely inexorable (do not ever change, please); to my father, Jesus, also Doctor, because of his numerous and inexhaustible “push it forward yet and finish”; and to my sister, Eva, because I know that she always supported me in the distance.

Each of them has been a link in the chain that has allowed me to run up the anchor. Thank you!

PRÓLOGO Y AGRADECIMIENTOS

Empecé a estudiar el doctorado ahora hace casi nueve años porque quería acceder a un nivel de formación que me permitiera desarrollar soluciones globales a cuestiones de primera necesidad, en lugar de aplicar tecnologías ya existentes a casos concretos y de repercusión individual en entornos ya desarrollados (según el concepto actual de desarrollo).

No había esperado, en ningún momento, que el camino hacia ese punto de partida fuera un peregrinaje tan largo, sinuoso y no exento de dificultades que, por otro lado, se combinaron con vivencias personales de escasa compatibilidad con la lucidez y serenidad que recorrer ese camino requería. De todas maneras creo que lo único que hice fue experimentar un adelanto de algunas de las dificultades con que me encontraré en mi siguiente viaje.

Todo empezó en la distancia física y temporal. En el año 2000, residiendo en Ibiza – a menudo categorizada con la doble insularidad – empecé con mucha ilusión a cursar mis créditos de docencia, alargándose éstos durante dos años como resultado de su simultaneización con dos trabajos y una familia.

En el año 2002 contacté con el profesor Dr Frederic Marimon del Departamento de Resistencia de Materiales y Estructuras en la Ingeniería, para entonces ya un buen amigo con quien había compartido un proyecto de fin de carrera, muchos cursos durante años y algún que otro trabajo de investigación. Desde el principio Frederic me recibió con toda la disposición que le caracteriza y, enseguida, comenzamos a tantear temas para mi tesis doctoral. Como quiera que mi especialidad era, para aquel entonces, el cálculo de estructura metálica, el primer tema que planteamos – a partir de incongruencias que habíamos observado durante nuestros trabajos de investigación previos – consistía en el análisis del comportamiento de perfiles metálicos conformados en frío y parcialmente restringidas en su movimiento y, con mayor precisión, en el análisis de la influencia de los tornapuntas en el pandeo lateral del ala libre de las correas de acero. Fijada esa idea, con un objetivo muy bien definido, presenté el proyecto de tesis en 2002 y viajé al congreso Eurosteel'02 celebrado en Coimbra (Portugal) para presentar una ponencia sobre el tema, en la que ya anticipaba la solución a la

cuestión que dirimiría en la Tesis dado lo claro que teníamos el origen del problema planteado. No obstante, el exceso de trabajo en el día a día hizo que el desarrollo final de la tesis se retrasara lo suficiente como para que, en el ínterin, el problema fuera oficialmente resuelto por un equipo de investigación del Department of Civil and Structural Engineering de la Polytechnic University of Hong Kong, Hung Hom – Kowloon (Professor Dr K. F. Chung) a quien debo agradecer que me enviara su artículo clave – de forma previa a su publicación – de forma que no tuve que dedicar más tiempo a esta material (en este punto había invertido ya cientos de horas de trabajo en lo que, desafortunadamente, se convirtió en una tesis sin futuro).

A pesar de ello, era tan clara mi disposición a continuar para alcanzar el punto de partida de lo que anhelo que sea mi futuro profesional, que enseguida el paciente de Frederic y yo nos pusimos a analizar temas alternativos para mi tesis. Había que empezar otra vez de cero, todo ello entre idas y venidas de Ibiza a Barcelona y sin la ayuda que supone estar integrado en un equipo de trabajo. Para aquel entonces, casi cuatro años después de haber empezado el doctorado, no era ya poca gente la que – nunca sabré si de forma constructiva – me preguntaba porqué insistía tanto en seguir con el doctorado si difícilmente me iba a servir de algo en Ibiza. Yo siempre contestaba lo mismo, que en primer lugar me enriquecía (estuviera donde estuviera yo) más allá de la ingeniería-gestora de bajo nivel que por entonces se hacía en Ibiza. Por otro lado, les decía que atraer la investigación a Ibiza había dejado de ser un sueño con las nuevas tecnologías de la información, y que sólo era necesario que existiera gente dispuesta a asumir el reto de la “desubicación” de los trabajos de investigación.

A partir de trabajos previos de un colega de su departamento, el Profesor Dr Miquel Casafont, una de las escasas personas en España que se habían introducido en la materia, Frederic me propuso otra idea para mi tesis cuyo atractivo residía no sólo en su desconocimiento excepto en círculos muy estrechos del mundo científico sino también en sus posibilidades de aplicación a los más diferentes ámbitos y en su componente teórico-analítica – que siempre me había atraído –: la teoría de la viga generalizada. Tras conversaciones con Frederic y con Miquel – a quien agradezco su desinteresada introducción a este tema – en enero de 2005 contacté con el autor de dicha teoría – Mr Richard Schardt – un

científico alemán que me facilitó un ejemplar del único libro en el mundo en que la explicaba a fondo y que se encontraba fuera de edición ‘Verallgemeinerte technisch Biegetheorie’. Mi agradecimiento también para él desde estas líneas. Del análisis del estado de la cuestión llegamos a la conclusión de que hubiera resultado de extraordinaria dificultad introducirse en un tema en el que la escasa información disponible fuera del núcleo germinal de la teoría me dejaba en un punto de arranque muy por detrás de los teorizadores originales, convirtiéndose en una tarea casi imposible desarrollar una aportación original en la materia.

Después vino una época de peregrinaje en busca del ámbito científico en que pudiera realizar una aportación original, pasando por la Teoría de Catástrofes (cuyo abordaje no descarto en el futuro dado el interés que me supuso su potencial de aplicación a campos tan diversos como la ingeniería, la economía o los movimientos migratorios) o la dinámica de fluidos computacional. Por aquel entonces era ya principios de 2005, y el hecho de no haber encontrado la idea de partida me empezaba a desesperar. Empecé a leer, entre los cientos de artículos y libros que he acabado leyendo – y comprando, dada mi dificultad de acceso a ellos desde la distancia –, todo tipo de temas relacionados con el fuego y sus consecuencias estructurales. Un poco inducido por la magnitud de la tragedia ocurrida al World Trade Centre de Nueva Cork años atrás – la cual había sido la razón de ser de muchas líneas de investigación – fui centrándome en el análisis – avanzado – y prevención de los mecanismos de colapso estructural de Edificios de Gran Altura en situaciones de incendio. Así, a mediados de 2005 presenté mi segundo proyecto de tesis – con el título actual – en que abría las posibilidades de estudio a cinco grandes líneas de entre las que, sin duda alguna, me atraía por la originalidad de su planteamiento el estudio del efecto de las estrategias de extinción de incendio sobre el estado estructural de los elementos portantes de Edificios de Gran Altura. Aprobado el segundo proyecto de tesis, y como quiera que el ámbito propuesto era demasiado amplio, Frederic (y su infinita paciencia) y yo seguimos reuniéndonos en fugaces viajes a Barcelona para ir ahorquillando el objeto de la tesis. Y he aquí que a finales de 2005 Frederic me pronunció una palabra en la que ya no he dejado de pensar durante los últimos tres largos años: el spalling. La idea surgió de una

simple conversación sobre los puntos de vista encontrados que tienen los Servicios de Bomberos sobre la conveniencia, o no, de enfriar elementos estructurales durante un incendio mediante la aplicación de chorros de agua. De ahí, y como he aprendido muy bien durante esta Tesis una cosa lleva a la otra, fuimos desgranando diferentes mecanismos de fallo de los pilares de hormigón de alta resistencia hasta llegar al spalling. En seguida me llamó la atención pues nunca habría imaginado que la presión del vapor dentro de un pilar de hormigón pudiera ser lo suficientemente alta como para que, en conjunción con la energía elástica constreñida como resultado de diferentes temperaturas en zonas adyacentes de un elemento estructural, pudiera hacer literalmente explotar – sino parcialmente – un pilar.

En seguida me puse a analizar el estado de la cuestión y detecté graves carencias en el abordaje analítico del spalling. Si no hubiera sido por un nefasto año 2006, en lo que a lo personal se refiere, el interés que me suscitaba el tema habría hecho que viera ya desde ese año el fin, el método y las herramientas. No obstante, hasta final de 2006 – una vez detectada la complejidad del análisis higro-termo-químico-mecánico de un medio poroso no saturado y con múltiples cambios de fase y degradaciones químicas como es el hormigón de alta resistencia – no encontré la herramienta adecuada para llevar a cabo la investigación que pretendía: el High Temperature Concrete and Spalling (HITECOSP), un software de gran complejidad tanto de formulación como a nivel de usuario desarrollado básicamente por la Universidad de Padua (Italia). No creo que me equivoque si digo que para entonces Frederic ya no confiaba mucho en mi disposición a llevar adelante mi tesis después de tantos años (yo, en su lugar, no habría confiado demasiado en mis posibilidades de éxito), y de hecho esta preocupación se ahondó cuando pasé por serias dificultades para conseguir esta herramienta de trabajo fundamental (más tarde descubriría que estas dificultades surgieron de no haber acertado en a quién recurrir para su consecución, tal como luego me demostraron los creadores del Modelo de Padova, a los que posteriormente me dirigí más extensamente pues fueron finalmente los que hicieron posible que ahora esté escribiendo este prólogo de remate de mi tesis).

Superando una vez más la distancia y mi escasez de renombre como investigador, el Dr Franco Corsi (del ENEA, en Italia) fue quien finalmente me facilitó el software HITECOSP en el

primer trimestre de 2007 y tras no pocas gestiones al respecto. Desde aquí le agradezco que abriera una puerta que, posteriormente, la grandeza de la gente de Padua transformó en algo mucho más inmenso. La primera mitad del 2007 fue un período de dura aprehensión del modelo teórico que se escondía tras ese software que tanto me había costado conseguir, así como de muchas pruebas para llegar a entender como funcionaba sin poder intercambiar opiniones con otros usuarios o expertos. Para entonces yo ya había dejado uno de mis dos trabajos – más concretamente en 2006 cerré mi despacho profesional hasta la actualidad –, lo cual no sólo me suponía un coste de oportunidad enorme sino que también llevaba aparejados gastos difíciles de cubrir. Hubiera sido fácil que la difícil sostenibilidad económica de la situación y el tiempo transcurrido desde el inicio del doctorado, ya casi siete años atrás, me hubieran hecho perder una vez más la serenidad y concentración que una tesis de estas características requería, pero aprendí a perseverar (tal vez la mayor lección para mí durante la realización del doctorado).

En mayo de 2007 había llegado a un punto muerto, en el que la falta de resultados experimentales para caracterizar adecuadamente los materiales con los que debía trabajar y mi incapacidad para la asimilación autodidacta de determinadas cuestiones tremendamente especializadas relacionadas con el modelo de cálculo implementado, me hicieron dudar una vez más de la consecución de mi objetivo. Pero por una de las ¿casualidades? que se dan pocas veces en la vida, a escasos quinientos metros de mi lugar de trabajo el Dr Eugenio Oñate, el Dr Bernhard Schrefler (director del Instituto di Costruzioni, el departamento de la Universidad de Padova alma mater del modelo de Padova) y el Dr Manolis Papadrakakis (del Institute of Structural Analysis & Seismic Research de la National Technical University of Athens) organizaron el congreso internacional llamado Computational Methods for Coupled Problems in Science and Engineering II (2007). No sólo la razón de ser del congreso, problemas acoplados en ingeniería, encajaba perfectamente con lo que estaba estudiando en ese momento, sino que los mayores especialistas a nivel mundial en lo referente al objeto de mi tesis iban a hacer aparición. De ese congreso tengo que agradecer, en primer lugar, que Eugenio me presentara al Dr Schrefler quien, a pesar de ser toda una autoridad, siempre me hizo sentir como un colega. Eugenio también me presentó al Dr

Carmelo Majorana, a quien también tengo que agradecer los interesantes intercambios de ideas que tuvieron lugar en los coffee breaks del congreso. Pero si en ese congreso conocí a una persona cuya atención exquisita y disposición han hecho posible que hoy esté escribiendo este prólogo – y pocas personas conocen lo que eso supone para mí – fue el Dr Francesco Pesavento, también del Departamento de Ingeniería Estructural y del Transporte de la Universidad de Padova. Había estado leyendo y releendo sus numerosas y elaboradas publicaciones en torno al tema de mi tesis, y no dudé en abordarle para explicarle mi situación aun a riesgo de que, al ser yo un completo extraño para él, me dispensara un trato distante y poco interesado. ¡Nada más lejos de la verdad!. Francesco me hizo cambiar profundamente el concepto que tenía de “esa gente que va a los congresos a exponer sus logros y a esconder sus recetas mágicas”. Desde el primer momento no sólo fue un libro abierto, en el que leer una página te ilustra más que leyendo un volumen de otras enciclopedias, sino que inmediatamente comprendió mi situación y se ofreció a mantener un contacto continuado hasta la finalización de mi tesis. Tanto es así que, con el visto bueno de Frederic al que yo seguía martirizando con numerosas dudas de estrategia y enfoque (lo siento, Frederic), Francesco pasó a ser codirector de mi tesis.

En marzo de 2008, una vez más, en un estadio ya avanzado de planteamiento de los análisis, la distancia supuso un problema para el intercambio continuado de opiniones acerca de sus definiciones, lo que me llevó a realizar una estancia en la Universidad de Padova (Italia), de la mano de mi ya entonces buen amigo Francesco. Antes de ir a Padova no me podía imaginar lo que ese viaje iba a suponer tanto para mí como para Francesco. Para él, una sobrecarga de trabajo extraordinaria y añadida a sus ya numerosísimos quehaceres como docente universitario, a pesar de lo cual dedicamos doce horas diarias a dirigir mi tesis hacia buen puerto. Para mí, una experiencia enriquecedora y un sorprendente descubrimiento: el de que todavía quedan personas dispuestas a ayudar de forma incondicional y desinteresada desde el escalón más alto del conocimiento científico. Regresé de Padova con una renovada conceptualización de los procesos involucrados en el comportamiento higró-termo-químico-mecánico del Hormigón de Alta Resistencia, lo cual me permitió acometer un análisis de los resultados mucho más profundo y concienzudo, y tras haber

podido realizar el cálculo del enfriamiento de una sección cuadrada gracias al uso de un supercomputador del Department of Structural and Transportation Engineering de la University of Padova – dado que intentar abordar dicho cálculo en un ordenador personal hubiera sido inviable a la vista de los requerimientos computacionales del mismo –. La segunda mitad de 2008 fue la que requirió de un esfuerzo mental más exigente: la complejidad y la enorme cantidad de los resultados a analizar, así como la dificultad de estructurar los trabajos realizados en una morfología redactora simple, se unieron al agotamiento resultante de llevar casi nueve años de estudios doctorales, si bien la proximidad de la meta – conjuntamente con las palabras de ánimo de mis directores de tesis (y de otros que más adelante mencionaré) y con la visión de un nuevo horizonte profesional mucho más alentador – detonaron mi último sprint hasta este prólogo.

Por todo ello, deseo agradecer su insustituible aportación profesional a todos aquéllos que durante estos nueve años, de forma directa o indirecta, me han aupado a hombros de gigante para llegar a este final del principio, y muy especialmente al Profesor Dr Frederic Marimon – quien me ha enseñado sobre todo a perseverar, a tener una paciencia infinita y a saber volver a empezar – y al Profesor Dr Francesco Pesavento – quien me ha mostrado la generosidad, en el sentido más amplio, desde el merecido privilegio del conocimiento más avanzado –. En lo personal: agradezco muy especialmente a mis hijos, Aníbal y Aitor, que me hayan sabido hacer superar los momentos malos dibujando una sonrisa de ángel en sus caritas y que sean mi mayor afán de superación; a mi madre, Clara, con su clarividencia e inquebrantable energía, porque después de probar todas las técnicas imaginables para impulsarme sólo le quedó por fin un implacable “mira que quiero verte Doctor antes de morirme” que fue del todo inexorable (no cambies nunca, por favor); a mi padre, Jesús, también Doctor, por sus numerosísimos e inagotables “dale un empujón ya y acábala”; y a mi hermana, Eva, porque sé que en la distancia siempre me apoyó.

Cada uno de ellos ha sido un eslabón de la cadena que me ha permitido izar el ancla ¡Gracias!

**Angel Guerrero Castells
Ibiza, 11th february 2009**

*THIS PAGE IS INTENTIONALLY
LEFT BLANK*

SUMMARY

The progressive gain of height of High-Rise Building has also increased the actual and potential consequences, in terms of both human and economic losses, when natural fires irrupt. In sight of these losses, the major aim of this Thesis is to contribute to the advanced analysis and prevention of the mechanisms of natural fire-induced structural collapse in High-Rise Buildings, by improving the current knowledge of both the phenomena involved in the structural failure mechanisms introduced by natural fires action and of the consequences of certain fire fighting strategies usually developed during these fires.

During heating of concrete, there take place several complex, interacting physical, chemical and mechanical phenomena resulting in significant changes of the material inner structure and properties, leading to a loss of the load bearing capacity and of other important service features of concrete structures. A significant phenomenon leading to a structural failure mechanism very specific for the High Strength Concrete used in High-Rise Buildings and of a great practical importance is the so called Thermal Spalling. This Thesis settles, first, the abovementioned major aim in the domain of the Thermal Spalling analysis – and more precisely in its computational approach, by means of the most advanced hygro-thermo-chemo-mechanical analysis software based on the so-called Model of Padova, High Temperature Concrete and Spalling software (HITECOSP) – with the particular objectives of:

- Developing a spectrum of spalling nomograms addressed to evaluate the sensitivity of the hygro-thermo-chemo-mechanical processes involved on the High-Strength concretes behaviour under a natural fire to some relevant parameters whose values may be chosen from a very early stage of High-Rise Buildings design or already known in case of existing High-Rise Buildings;
- Analyzing if spalling is energetically possible in a variety of actual cases and, hence, the spalling risk in every possible set of conditions so both Designers and Fire Fighting Services will have a valuable information in order to take decisions about design and about the expectable consequences of fire fighting

actions from a really intuitive, graphical and immediate point of view; and, finally,

- Discerning what is the energetic contribution of compressed gas to Thermal Spalling and what is that corresponding to the constrained elastic energy (namely, the two key factors leading, together, to Thermal Spalling).

To do so, there are developed more than ninety one hygro-thermo-chemo-mechanical analyses resulting from combinations of the parameters' values initially considered: the initial moisture content of concrete, its intrinsic permeability, the rate of temperature increase (fire intensity), the porosity, compressive strength, type of aggregate and, in general, the whole set of properties of concrete, and the thickness of the structural element.

Another scarcely studied matter related to the major aim of this Thesis is the analysis of the effect of the fire fighting strategies on the structural state of the High-Rise Buildings during natural fires. Thermal shock, induced by the application of water jets on the surface of structural elements, produces a significant reduction in both the flexural strength the compressive strength, whereas Post-cooling spalling may occur after the fire is over, after cooling down or maybe even during extinguishing, depending on the cooling rates of High Strength Concretes (especially those containing calcareous aggregates).

This Thesis settles, second, the major aim in the domain of the analysis of the effect of a spectrum of cooling processes on the hygro-thermo-chemo-mechanical state of a structural element, manufactured with High-Strength concrete, during the development of a natural fire in a High-Rise Building – and, again more precisely, in its computational approach with the aid of HITECOSP software – with the particular objectives of:

- Analyzing both phenomenologically and from a mechanistic point of view the effect of a spectrum of cooling processes on the hygro-thermo-chemo-mechanical state of a structural element, manufactured with High-Strength concrete, during the development of a natural fire in a High-Rise Building;

- Developing a comparative analysis to compare the final hygro-thermo-chemo-mechanical state of a structural element after the development of different types – and subtypes – of cooling processes, including comparisons about the Environment vs. Structural element’s Surface cooling attacks, among different start instants and for several velocities of the cooling processes; and, finally,
- Providing enough information to analyze the influence on the hygro-thermo-chemo-mechanical behaviour of the structural element during the cooling processes of several parameters non-related to the own cooling processes.

To do so, although there are developed more than forty five hygro-thermo-chemo-mechanical analyses resulting from combinations of the parameters’ values initially considered, two reference cases are selected where the extinguishing actions conditions are varied in order to cover the widest possible range of situations found by Fire-Fighting Services during a natural fire extinguishment: the type of cooling – either cooling the gases in the enclosure or the structural element’s surface – and the cooling start instant and its rate.

This second settling of objectives also includes the development of more than twenty Computational Fluid Dynamics simulations by means of Fire Dynamics Simulator software (FDS) in order to work out the evolution of temperature at surfaces during several extinguishing actions.

To conclude, the development of a heuristic analysis of the effect of cooling processes on the hygro-thermo-chemo-mechanical state of a square column, manufactured with High-Strength concrete, during the development of a natural fire in a High-Rise Building, is also included, being understood as an introductory extension of the abovementioned analyses to cases with bidimensional fluxes such as square columns, where Corner Thermal Spalling is often the most dangerous type.

RESUMEN

El progresivo incremento de la altura de los Edificios de Gran Altura (EGA) ha aumentado las consecuencias reales y potenciales, en términos de pérdidas humanas y económicas, cuando irrumpen en ellos los incendios naturales. A la vista de dichas pérdidas, el objeto principal de esta Tesis es la contribución al análisis avanzado y prevención de los mecanismos de colapso estructural en EGA inducidos por incendios naturales, mejorando el conocimiento actual tanto de los fenómenos involucrados en los mecanismos de fallo estructural introducidos por la acción de dichos incendios naturales como de las consecuencias de ciertas estrategias de extinción de incendios habitualmente desarrolladas durante los mismos.

Durante el calentamiento del hormigón, tienen lugar diversos fenómenos complejos, con interacciones físicas, químicas y mecánicas que resultan en cambios significativos de la estructura interior del material y de sus propiedades, comportando una pérdida de la capacidad portante y de otras características de servicio de las estructuras de hormigón. Un fenómeno significativo conducente a un mecanismo de fallo estructural muy específico de los Hormigones de Alta Resistencia usados en la construcción de Edificios de Gran Altura es el llamado Spalling Térmico. Esta Tesis fija precisamente, en primer lugar, el anteriormente citado objeto en los dominios del análisis del Spalling Térmico – y más concretamente en su vertiente computacional, por medio del software de análisis higro-termo-quimo-mecánico más avanzado y basado en el denominado Modelo de Papua, el software High Temperature Concrete and Spalling o HITECOSP – con los objetivos particulares de:

- Desarrollar un abanico de nomogramas de Spalling con el objeto de evaluar la sensibilidad de los procesos higro-termo-quimo-mecánicos involucrados en el comportamiento de los Hormigones de Alta Resistencia, bajo condiciones de incendio natural, a determinados parámetros relevantes cuyos valores pueden ser seleccionados desde una fase muy temprana del diseño de un EGA o bien ya conocidos en el caso de EGAs existentes;
- Analizar si el Spalling es energéticamente viable en un abanico de casos reales y, en consecuencia, el riesgo de Spalling en

cualquier conjunto de condiciones, de forma que tanto los *Proyectistas* como los *Servicios de Extinción de Incendios* dispongan de una valiosa información a la hora de adoptar decisiones sobre el diseño y sobre las consecuencias previsibles de las acciones de extinción, todo ello desde una óptica realmente intuitiva, gráfica y de inmediata interpretación; y, finalmente,

- Discernir cuál es la contribución energética al *Spalling Térmico* por parte del gas comprimido y cuál es la correspondiente a la energía elástica constreñida (a saber, los dos factores clave conducentes, conjuntamente, al *Spalling Térmico*).

Para ello, se han desarrollado más de noventa y un análisis *higro-termo-quimo-mecánicos*, resultantes de la combinación de los valores de los parámetros inicialmente considerados, a saber: el contenido inicial de humedad del hormigón, su permeabilidad intrínseca, la tasa de incremento de temperatura (intensidad del fuego), la porosidad, resistencia a compresión, el tipo de agregados y, en general, el conjunto completo de propiedades del hormigón, y el espesor del elemento estructural.

Una segunda materia escasamente estudiada en relación con el objeto de la Tesis señalado, consiste en el análisis del efecto de las estrategias de extinción de incendios en el estado estructural de los *EGAs* durante incendios naturales. El choque térmico inducido por la aplicación de un chorro de agua sobre la superficie de un elemento estructural, produce una reducción significativa de la resistencia a flexión y a compresión, mientras que fenómenos de *Spalling* (*Post-Spalling*) pueden tener lugar durante y después de la extinción del incendio, dependiendo de las tasas de enfriamiento de los *Hormigones de Alta Resistencia* (especialmente en aquéllos que contienen agregados calcáreos). Esta Tesis fija por tanto su objeto, en segundo lugar, en el dominio del análisis del efecto de un espectro de procesos de enfriamiento en el estado *higro-termo-quimo-mecánico* de un elemento estructural, fabricado con *Hormigón de Alta Resistencia*, durante el desarrollo de un incendio natural en un *EGA* – y, de nuevo con mayor precisión, en su vertiente computacional con la ayuda del software *HITECOSP* – con los siguientes objetivos particulares:

- Analizar, tanto desde un punto de vista fenomenológico como mecanicista, el efecto de

un espectro de procesos de enfriamiento en el estado *higro-termo-quimo-mecánico* de un elemento estructural, fabricado con *Hormigón de Alta Resistencia*, durante el desarrollo de un incendio natural en un *EGA*;

- Desarrollar un análisis comparativo con el fin de comparar el estado *higro-termo-quimo-mecánico* final de un elemento estructural después del desarrollo de diferentes tipos – y subtipos – de procesos de enfriamiento, incluyendo la comparación de enfriamientos ambientales y de superficie, así como diferentes instantes de inicio y velocidades de los procesos de enfriamiento; y, finalmente,
- Proporcionar suficiente información para analizar la influencia en el comportamiento *higro-termo-quimo-mecánico* de un elemento estructural, durante los procesos de enfriamiento, de diversos parámetros no relacionados con los propios procesos de enfriamiento.

Para ello, aunque se han desarrollado más de cuarenta y cinco análisis *higro-termo-quimo-mecánicos* resultantes de la combinación de los valores de los parámetros inicialmente considerados, dos casos de referencia han sido seleccionados y especialmente analizados en profundidad incluyendo numerosas variaciones, con el fin de abarcar la mayor variedad posible de situaciones a hallar por los *Servicios de Extinción de incendios*, de: el tipo de enfriamiento – bien enfriando los gases del escenario bien la superficie del elemento estructural –, el instante de inicio del proceso de enfriamiento y su velocidad. Este segundo encuadre de objetivos incluye, así mismo, el desarrollo de más de veinte *Simulaciones de Dinámica de Fluidos Computacional* por medio del software *Fire Dynamics Simulator (FDS)* con el objeto de extraer la evolución de la temperatura en las superficies de los elementos estructurales durante las muy diversas acciones de extinción.

Para concluir se incluye, así mismo, el desarrollo de un análisis heurístico del efecto de los procesos de enfriamiento en el estado *higro-termo-quimo-mecánico* de una columna cuadrada, fabricada con *Hormigón de Alta Resistencia*, durante el desarrollo de un incendio natural en un *EGA*, entendiéndose como una extensión – a nivel introductoria – de los análisis anteriormente mencionados a casos con flujos bidimensionales como las columnas cuadradas, en los cuales el *Spalling* de esquina es el tipo más peligroso.

*THIS PAGE IS INTENTIONALLY
LEFT BLANK*

CONTENTS

Preface and Acknowledgements – Prólogo y Agradecimientos		i
Summary – Resumen		ix
List of Symbols		xxi
CHAPTER 1: Aim, Objectives, Original Contributions and Structuring		1
<hr/>		
1.1	ABOUT THE PROBLEM	3
1.2	ABOUT THE MAJOR AIM OF THIS THESIS	5
1.3	ABOUT THE OBJECTIVES, THE ORIGINAL CONTRIBUTIONS OF THIS THESIS AND ITS STRUCTURING	11
1.3.1	About this Introductory Chapter	11
1.3.2	About the Background Studies: the State-of-the-Art	11
1.3.3	About the Modelling of Hygro-Thermal Behaviour of Concrete at High Temperature with Thermo-Chemical and Mechanical Material Degradation	11
1.3.4	About the Spalling Nomograms	12
1.3.5	About the Preliminary and Simplified Analysis of Cooling Effect on HSCs Spalling Behaviour	13
1.3.6	About the Analysis of Cooling Processes in High Strength Concretes	13
1.3.7	About the Heuristic Analysis of Cooling Processes in High Strength Concrete Square Columns	15
1.3.8	About the Conclusions of this Thesis	15
1.4	BIBLIOGRAPHY OF THE CHAPTER	15
CHAPTER 2: Background Studies: The State-of-the-Art		17
<hr/>		
2.1	THERMAL SPALLING	21
2.1.1	Definition and Nature of Thermal Spalling	21
2.1.2	Types of Thermal Spalling	22
2.1.2.1	EXPLOSIVE SPALLING	22
2.1.2.2	SURFACE SPALLING	23
2.1.2.3	AGGREGATE SPLITTING	23
2.1.2.4	CORNER SEPARATION	23
2.1.2.5	SLOUGHING OFF	23
2.1.2.6	POST-COOLING SPALLING	24
2.1.3	Significance of Thermal Spalling	24
2.1.3.1	LOAD BEARING CAPACITY FAILURE	25
2.1.3.1.1	Loss of section	25
2.1.3.1.2	Loss protection to steel reinforcement	25
2.1.3.2	SEPARATING FUNCTION	25

2.1.3.3	SAFE DESIGN	26
2.1.3.4	SPALLING IN NATURAL FIRES VS FURNACE TESTS	26
2.1.4	Assessment of the Thermal Spalling Risk: Spalling Indexes	27
2.1.4.1	HYPOTHESES CONCERNING MECHANISMS OF THERMAL SPALLING.....	28
2.1.4.1.1	<i>PRESSURE-INDUCED SHEAR MODEL</i>	29
2.1.4.1.2	<i>BUCKLING MODEL CONSIDERING GAS PRESSURE</i>	29
2.1.4.1.3	<i>SIMPLIFIED FRACTURE MECHANICS MODEL</i>	31
2.1.4.2	PRACTICAL EVALUATION OF THE THERMAL SPALLING RISK.....	32
2.1.5	Factors Affecting Thermal Spalling	36
2.1.5.1	MOISTURE CONTENT	36
2.1.5.2	WATER/CEMENT RATIO, PERMEABILITY	38
2.1.5.3	HEATING CONDITION	38
2.1.5.4	AGGREGATES	39
2.1.5.5	TEST CONDITION	39
2.1.5.6	CONCRETE STRENGTH	40
2.1.5.7	SECTION SIZE.....	41
2.1.5.8	APPLIED LOAD	41
2.1.5.9	RESTRAINT.....	42
2.1.5.10	THERMAL EXPANSION	42
2.1.5.11	REINFORCEMENT	42
2.1.5.12	COVER	43
2.1.5.13	FIBRES	43
2.1.5.14	DENSITY	44
2.1.5.15	CONDUCTIVITY	44
2.1.5.16	SPECIFIC HEAT	44
2.1.5.17	CRACKING.....	44
2.1.5.18	AIR-ENTRAINMENT	44
2.1.5.19	SUMMARY TABLES OF THE MAIN FACTORS AFFECTING SPALLING	44
2.1.6	Spalling Nomograms	46
2.1.7	Design Against Thermal Spalling	49
2.1.7.1	PREVENTIVE MEASURES	50
2.1.7.2	POLYPROPYLENE FIBRES	51
2.1.7.3	THERMAL BARRIER	52
2.2	COOLING PROCESSES IN HIGH STRENGTH CONCRETES	52
2.3	BIBLIOGRAPHY OF THE CHAPTER.....	55

CHAPTER 3: Modelling of Hygro-Thermal Behaviour of Concrete at High Temperature with Thermo-Chemical and Mechanical Material Degradation 59

3.1	INTRODUCTION.....	63
3.2	MACROSCOPIC BALANCE EQUATIONS.....	64
3.3	STATE VARIABLES	69
3.4	CONSTITUTIVE RELATIONS.....	71
3.5	THERMO-CHEMICAL AND MECHANICAL DAMAGE OF CONCRETE	75
3.6	GOVERNING EQUATIONS OF THE MODEL	78
3.7	NUMERICAL SOLUTION.....	83
3.8	CONCLUSIONS OF THE CHAPTER	86
3.9	BIBLIOGRAPHY OF THE CHAPTER.....	86
Appendix 3A.	MATRICES RESULTING FROM THE DISCRETIZATION OF MASS, ENERGY AND LINEAR MOMENTUM CONSERVATION EQUATIONS	89

CHAPTER 4: Spalling Nomograms

93

4.1	IDENTIFICATION OF THE ORIGINAL CONTRIBUTION.....	97
4.2	METHODOLOGY TO DEVELOP THE SPALLING AND ENERGETIC ANALYSIS	98
4.2.1	Definition and methodology for the evaluation of Spalling criteria	98
4.2.2	Definition and methodology for the energetic analysis.....	99
4.3	DEFINITION OF THE ANALYSIS CASE	101
4.3.1	Description of the general features of the analysis case and causes for its selection.....	101
4.3.2	Parameters with ranging values for the sensitivity analysis	104
4.3.2.1	Parameter 1. Initial Saturation Degree.....	104
4.3.2.1.1	<i>Description and Causes for its selection</i>	<i>104</i>
4.3.2.1.2	<i>Values selected for the spalling nomograms.....</i>	<i>105</i>
4.3.2.2	Parameter 2. Intrinsic Permeability.....	106
4.3.2.2.1	<i>Description and Causes for its selection</i>	<i>106</i>
4.3.2.2.2	<i>Values selected for the spalling nomograms.....</i>	<i>107</i>
4.3.2.3	Parameter 3. Thickness of the Structural Element	107
4.3.2.3.1	<i>Description and Causes for its selection</i>	<i>107</i>
4.3.2.3.2	<i>Values selected for the spalling nomograms.....</i>	<i>109</i>
4.3.2.4	Parameter 4. Heating profile	109
4.3.2.4.1	<i>Description and Causes for its selection</i>	<i>109</i>
4.3.2.4.2	<i>Values selected for the spalling nomograms.....</i>	<i>111</i>
4.3.2.5	Parameter 5. Material.....	115
4.3.2.5.1	<i>Description and Causes for its selection</i>	<i>115</i>
4.3.2.5.2	<i>First selection for the spalling nomograms: C60. Definition procedure</i>	<i>118</i>
4.3.2.5.3	<i>Second selection for the spalling nomograms: C90. Definition procedure</i>	<i>124</i>
4.4	DEFINITION OF THE RESULTING COMBINATIONS.....	131
4.5	RESULTS.....	134
4.5.1	Results to evaluate and evaluation procedure.....	134
4.5.2	Spalling index evolution for each combination	135
4.5.3	Spalling nomograms, Sensitivity and Energetic analysis for each combination	140
4.5.3.1	Nomogram TH12PAR1C60: Thickness 12 cm, ISO Curve, Material C60	154
4.5.3.2	Nomogram TH12PAR2C60: Thickness 12 cm, Slow curve, Mat. C60.....	155
4.5.3.3	Nomogram TH12PAR3C60: Thickness 12 cm, Hydroc. Curve, Mat. C60	156
4.5.3.4	Nomogram TH12PAR1C90: Thickness 12 cm, ISO Curve, Material C90	157
4.5.3.5	Nomogram TH12PAR2C90: Thickness 12 cm, Slow Curve, Mat. C90.....	158
4.5.3.6	Nomogram TH12PAR3C90: Thickness 12 cm, Hydroc. Curve, Mat. C90	159
4.5.3.7	Comparison among the six nomograms corresponding to a thickness of 12 centimetres	160
4.5.3.8	A particular analysis about the spalling velocities spectrum	161
4.5.4	Comparison for constant values of the Intrinsic Permeability	165
4.5.4.1	Thickness 12 cm – ISO Heating curve – Material C60	167
4.5.4.2	Thickness 12 cm – PAR2 Slow Heating curve – Material C60	171
4.5.4.3	Thickness 12 cm – Hydrocarbon Heating curve – Material C60.....	175
4.5.4.4	Thickness 12 cm – ISO Heating curve – Material C90	179
4.5.4.5	Thickness 12 cm – PAR2 Slow Heating curve – Material C90	183
4.5.4.6	Thickness 12 cm – Hydrocarbon Heating curve – Material C90.....	187
4.5.5	Comparison for constant values of the Initial Saturation Degree	191
4.5.6	Comparison of the Vapour Pressure and the Mechanical Damage Distribution.....	211
4.5.7	Time evolution considerations on a sample case: #5-TH12K018RH50PAR1C60.....	246
4.6	RESUME OF THE CONCLUSIONS OF THE CHAPTER.....	258
4.6.1	About the Time and Position of Main Fracture and the Sensitivity Analysis	258
4.6.2	About the Spalling Nomograms and the Energetic Analysis of Thermal Spalling	259
4.6.3	About the Evolution of each Parameter affecting the Physics of Thermal Spalling Phenomena	261
4.6.4	About extended tasks to go more deeply into Thermal Spalling Research.....	264

4.7	BIBLIOGRAPHY OF THE CHAPTER.....	266
Appendix 4A.	SPALLING INDEX EVOLUTION FOR EACH COMBINATION.....	269
Appendix 4B.	INPUT FILES FOR THE HYGRO-THERMO-CHEMO-MECHANICAL CALCULATIONS.....	319
Appendix 4C.	ACCEPTED PUBLICATIONS RELATED TO THIS CHAPTER.....	335
 CHAPTER 5: Preliminary and Simplified Analysis of Cooling Effect on HSCs Spalling Behaviour		 339

5.1	METHODOLOGY FOR THE PRELIMINARY AND SIMPLIFIED ANALYSIS OF COOLING EFFECT ON HSC SPALLING BEHAVIOUR.....	343
5.1.1	Selection and development of the case for the evaluation of the I_{s4} spalling index capabilities	344
5.1.1.1	The criteria for the selection of the case for the evaluation of the I_{s4} spalling index.....	344
5.1.1.2	The setup of the case selected for the evaluation of the I_{s4} spalling index	345
5.1.1.3	The main experimental results obtained for the case selected for the evaluation of the I_{s4} spalling index	346
5.1.1.4	The numerical simulation developed for the case selected for the evaluation of the I_{s4} spalling index	347
5.1.1.5	The results of the numerical simulation and their comparison against experimental results	348
5.1.1.6	The I_{s4} spalling index evaluation from the results of the numerical simulation and its comparison against experimental results	355
5.2	PRELIMINARY AND SIMPLIFIED ANALYSIS OF COOLING EFFECT ON HSC SPALLING BEHAVIOUR.....	358
5.2.1	Selection of the heating and “natural” cooling curves for the preliminary and simplified analysis.....	359
5.2.2	Results from the C-90 simulations.....	361
5.2.2.1	Results from the C-90 parametric Heating and “Natural” cooling simulations.....	361
5.2.2.1.1	<i>Direct results from the simulation</i>	<i>361</i>
5.2.2.1.2	<i>Evaluation of the I_{s4} spalling index</i>	<i>364</i>
5.2.2.1.3	<i>Simplified analysis to determine if concrete spalling is energetically possible.....</i>	<i>365</i>
5.2.2.2	Results from the C-90 parametric Heating and “Forced” cooling simulations (First starting point –Point A–, Slow cooling).....	366
5.2.2.2.1	<i>Direct results from the simulation</i>	<i>366</i>
5.2.2.2.2	<i>Evaluation of the I_{s4} spalling index</i>	<i>368</i>
5.2.2.2.3	<i>Simplified analysis to determine if concrete spalling is energetically possible.....</i>	<i>368</i>
5.2.2.3	Results from the C-90 parametric Heating and “Forced” cooling simulations (First starting point –Point A–, Fast cooling).....	369
5.2.2.3.1	<i>Direct results from the simulation</i>	<i>369</i>
5.2.2.3.2	<i>Evaluation of the I_{s4} spalling index</i>	<i>372</i>
5.2.2.3.3	<i>Simplified analysis to determine if concrete spalling is energetically possible.....</i>	<i>372</i>
5.2.2.4	Comparison of the I_{s4} Spalling Index values obtained for different typologies of cooling processes.....	373
5.3	BIBLIOGRAPHY OF THE CHAPTER.....	377

CHAPTER 6: Analysis of Cooling Processes in High Strength Concretes 379

6.1	IDENTIFICATION OF THE ORIGINAL CONTRIBUTION.....	385
6.2	DEFINITION AND METHODOLOGY TO DEVELOP THE PHENOMENOLOGICAL AND MECHANISTIC ANALYSIS OF THE COOLING PROCESSES.....	386
6.2.1	Definition and Methodology for the evaluation of the Spalling Criteria.....	386

6.2.2	Definition of other Parameters and Criteria required to complete the accomplishment of the Analysis	386
6.2.2.1	STATE VARIABLES AND RELATED PARAMETERS.....	387
6.2.2.2	TOTAL, MECHANICAL AND THERMO-CHEMICAL DAMAGE OF CONCRETE.....	388
6.2.2.3	VELOCITY (AVAILABLE ENERGY) OF SPALLED-OFF PIECES.....	389
6.2.2.3.1	<i>General Velocity of Spalled-Off Pieces</i>	<i>389</i>
6.2.2.3.2	<i>Velocity affected by Mechanical Damage.....</i>	<i>391</i>
6.2.2.4	MAXIMUM TEMPERATURE IN CONCRETE AND REINFORCING BARS.....	392
6.2.3	Graphical representation forms selected for the results	394
6.3	DEFINITION AND METHODOLOGY TO DEVELOP THE SUPPLY OF INFORMATION NEEDED FOR THE ANALYSIS OF THE INFLUENCE ON COOLING OF PARAMETERS NOT RELATED TO COOLING PROCESSES.....	396
6.4	DEFINITION OF THE ANALYSIS CASE	398
6.4.1	Description of the general features of the analysis case and causes for its selection.....	398
6.4.2	Description of the material selected	400
6.4.2.1	MATERIAL DESCRIPTION AND CAUSES FOR ITS SELECTION.....	400
6.4.2.2	IRREVERSIBLE DEFINITION OF MATERIAL PROPERTIES FOR COOLING PROCESSES	401
6.4.3	Definition of Temperature Profiles	402
6.4.3.1	HEATING PROFILES	402
6.4.3.1.1	<i>Value 1 (PAR1): ISO834.....</i>	<i>402</i>
6.4.3.1.2	<i>Value 2 (PAR2): Slow Heating Curve with the lowest Opening Coefficient</i>	<i>402</i>
6.4.3.1.3	<i>Value 3 (PAR4): Extremely Slow Heating Curve with an Opening Coefficient under the lowest admitted by Eurocode 1, Part 1-2.....</i>	<i>403</i>
6.4.3.1.4	<i>Collection of the Heating Profiles selected</i>	<i>403</i>
6.4.3.2	COOLING PROFILES	404
6.4.3.2.1	<i>Compartmental Fire Attack Techniques.....</i>	<i>404</i>
6.4.3.2.1.1	Mechanisms of Fire Extinction.....	404
6.4.3.2.1.2	Two Types of Structural Enclosure Fires.....	404
6.4.3.2.1.3	Methods of Fire Suppression Using Water	405
6.4.3.2.1.4	Water Spray, Fog or Mist	405
6.4.3.2.1.5	Dealing with Combustion in the Gaseous-phase.....	407
6.4.3.2.1.6	Fire-Fighting Services: their tactical flow-rates, baseline flows and extinguishing equipment.	409
6.4.3.2.2	<i>The Physics behind extinguishing with water</i>	<i>412</i>
6.4.3.2.2.1	Formation of droplet from different types of nozzles	412
6.4.3.2.2.2	Droplet size distribution.....	413
6.4.3.2.2.3	Deceleration of droplets: aerodynamic properties of the spray	414
6.4.3.2.2.4	Evaporation of water droplets.....	416
6.4.3.2.2.5	Extinguishing performance of water.....	418
6.4.3.2.2.6	Absorption of radiation in water droplets	419
6.4.3.2.3	<i>Definition of the Cooling Profiles in sight of their Physical Background and Fire Fighting Experiences.</i>	<i>421</i>
6.4.3.2.3.1	Start Time of Extinguishing Actions	421
6.4.3.2.3.2	Cooling Rate and duration of Extinguishing Actions	423
6.4.3.2.4	<i>Definition of the Cooling Profiles in sight of the results of Computational Fluid Dynamics Simulations.</i>	<i>427</i>
6.4.3.2.4.1	Introduction to the Computational Fluid Dynamics (CFD) and Fire Dynamics Simulator (FDS) Software.....	427
6.4.3.2.4.2	The case analyzed with the Fire Dynamics Simulator (FDS) Software.....	429
6.4.3.2.4.3	The main Results of the Computational Fluid Dynamics Simulations.....	436
6.4.3.2.5	<i>Final Selection of the Cooling Profiles.....</i>	<i>492</i>
6.4.3.2.5.1	Graphical Description of the Environment Cooling Profiles	493
6.4.3.2.5.2	Graphical Description of the Surface Cooling Profiles.....	493
6.4.3.2.5.3	Start Instants selected for the Cooling Processes	494
6.5	RESULTS.....	494
6.5.1	Atlas of the analyzed cases.....	494
6.5.2	Cooling Phenomenological and Mechanistic Analysis.....	496
6.5.2.1	Reference case # 05 – TH12K018RH50PAR1C60 – START OF COOLING: 600s	498
6.5.2.1.1	<i>Environmental Slow Cooling.....</i>	<i>498</i>
6.5.2.1.1.1	Phenomenological and Mechanistic analysis of the Heating Stage.....	498
6.5.2.1.1.2	Phenomenological and Mechanistic analysis of the Environment Cooling Stage.....	501
6.5.2.1.1.3	Collection of the Main Results of this Case for each Stage of the Cooling Process	505
6.5.2.1.1.4	Main Graphic Results of this Case in the Time-Space domain.	505
6.5.2.1.2	<i>Environmental Medium Cooling.....</i>	<i>509</i>

6.5.2.1.3	<i>Environmental Fast Cooling</i>	515
6.5.2.1.4	<i>Surface Cooling followed by a Heating phase</i>	519
6.5.2.1.4.1	Phenomenological and Mechanistic analysis of the Surface Cooling Stage.....	519
6.5.2.1.4.2	Phenomenological and Mechanistic analysis of the Second Heating Stage.....	521
6.5.2.1.4.3	Collection of the Main Results of this Case for each Stage of the Cooling Process.....	528
6.5.2.1.4.4	Main Graphic Results of this Case in the Time-Space Domain.....	528
6.5.2.1.5	<i>Surface Cooling followed by an imposed Constant Surface Temperature</i>	532
6.5.2.1.6	<i>Surface Cooling in Two Periods</i>	539
6.5.2.1.7	<i>Environmental Heating up to Three Hours Without any Cooling</i>	547
6.5.2.2	Reference case # 14 – TH12K018RH50PAR2C60 – START OF COOLING: 1.800s.....	551
6.5.2.2.1	<i>Environmental Slow Cooling</i>	551
6.5.2.2.2	<i>Environmental Medium Cooling</i>	555
6.5.2.2.3	<i>Environmental Fast Cooling</i>	555
6.5.2.2.4	<i>Surface Cooling followed by a Heating phase</i>	562
6.5.2.2.5	<i>Surface Cooling followed by an imposed Constant Surface Temperature</i>	562
6.5.2.2.6	<i>Surface Cooling in Two Periods</i>	562
6.5.2.3	Reference case # 14 – TH12K018RH50PAR2C60 – START OF COOLING: 2.400s.....	572
6.5.2.3.1	<i>Environmental Slow Cooling</i>	572
6.5.2.3.2	<i>Environmental Medium Cooling</i>	574
6.5.2.3.3	<i>Environmental Fast Cooling</i>	574
6.5.2.4	Reference case # 14 – TH12K018RH50PAR2C60 – START OF COOLING: 3.000s.....	577
6.5.2.4.1	<i>Environmental Slow Cooling</i>	577
6.5.2.4.2	<i>Environmental Medium Cooling</i>	579
6.5.2.4.3	<i>Environmental Fast Cooling</i>	579
6.5.2.4.4	<i>Surface Cooling followed by an imposed Constant Surface Temperature</i>	583
6.5.2.5	Reference case # 14 – TH12K018RH50PAR2C60 – START OF COOLING: 3.360s.....	583
6.5.2.5.1	<i>Environmental Slow Cooling</i>	583
6.5.2.5.1.1	Phenomenological and Mechanistic analysis of the Heating Stage.....	583
6.5.2.5.1.2	Phenomenological and Mechanistic analysis of the Environment Cooling Stage.....	586
6.5.2.5.1.3	Collection of the Main Results of this Case for each Stage of the Cooling Process.....	591
6.5.2.5.1.4	Main Graphic Results of this Case in the Time-Space domain.....	591
6.5.2.5.2	<i>Environmental Medium Cooling</i>	595
6.5.2.5.3	<i>Environmental Fast Cooling</i>	601
6.5.2.5.4	<i>Surface Cooling followed by a Heating phase</i>	605
6.5.2.5.4.1	Phenomenological and Mechanistic analysis of the Surface Cooling Stage.....	605
6.5.2.5.4.2	Phenomenological and Mechanistic analysis of the Second Heating Stage.....	606
6.5.2.5.4.3	Collection of the Main Results of this Case for each Stage of the Cooling Process.....	613
6.5.2.5.5	<i>Surface Cooling followed by an imposed Constant Surface Temperature</i>	617
6.5.2.5.6	<i>Surface Cooling in Three Periods</i>	624
6.5.2.5.7	<i>Environmental Heating up to Three hours Without any Cooling</i>	635
6.5.2.6	Reference case # 14 – TH12K018RH50PAR2C60 – START OF COOLING: 3.360s with the high cooling rates corresponding to high-pressure hose nozzles.....	639
6.5.2.6.1	<i>Surface Cooling followed by an imposed Constant Surface Temperature: Cooling Rate -136,6 K/s</i>	639
6.5.2.6.2	<i>Surface Cooling followed by an imposed Constant Surface Temperature: Cooling Rate -32,36K/s</i>	645
6.5.2.7	Reference case # 100 – TH12K019RH50PAR4C90 – START OF COOLING: 4.800s.....	649
6.5.2.7.1	<i>Surface First Cooling</i>	649
6.5.2.7.2	<i>Environmental Heating up to Three hours Without any Cooling</i>	650
6.5.2.8	Particular Phenomena and Analyses of Interest.....	657
6.5.2.8.1	<i>Compendium of Main Results</i>	657
6.5.2.8.2	<i>Environmental Humidity Infiltration</i>	659
6.5.2.8.3	<i>Introduction to the Analysis of the Effect of the Maximum Temperature and Damage reached in Concrete</i>	662
6.5.2.8.4	<i>Introduction to the Analysis of Temperature Effect on the Mechanical Properties of Steel Reinforcing Bars</i> ..	665
6.5.3	Comparative Analysis	666
6.5.3.1	Analysis of the Effect of the Type and Subtype of Cooling.....	666
6.5.3.1.1	<i>Comparison of the subtypes of Environmental Cooling</i>	667
6.5.3.1.1.1	Reference case #05 – TH12K018RH50PAR1C60.....	667
6.5.3.1.1.2	Reference case #14 – TH12K018RH50PAR2C60.....	669
6.5.3.1.2	<i>Comparison of the subtypes of Surface Cooling</i>	672
6.5.3.1.2.1	Reference case #05 – TH12K018RH50PAR1C60.....	673
6.5.3.1.2.2	Reference case #14 – TH12K018RH50PAR2C60.....	675
6.5.3.1.3	<i>Comparison of the Environmental Cooling versus the Surface Cooling and the No-Cooling case</i>	678
6.5.3.1.3.1	Comparison of the Slow Environmental Cooling versus the Natural Cooling cases.....	678
6.5.3.1.3.2	Comparison of the Surface Cooling + Heating/Repeating versus the No-Cooling cases.....	683
6.5.3.2	Analysis of the Effect of the Cooling Start Instant.....	685
6.5.3.2.1	<i>Reference case #14-TH12K018RH50PAR2C60</i>	685
6.5.3.2.1.1	Comparison of the effect of the cooling start instant on Environmental Slow Cooling cases.....	685
6.5.3.2.1.2	Comparison of the effect of the cooling start instant on Surface Cooling + Heating cases.....	688
6.5.4	Atlas of Information for the Analysis of the Influence on Cooling of Parameters not related to Cooling Process	691

6.6	RESUME OF THE CONCLUSIONS OF THE CHAPTER.....	692
6.6.1	About the Cooling Phenomenological and Mechanistic Analysis.....	692
6.6.2	About the Comparative Analysis	694
6.6.3	About the Atlas of Information for the Analysis of the Influence of Parameters not related to Cooling Processes	697
6.6.4	About the extended tasks to go more deeply into Thermal Spalling research during Cooling processes.....	698
6.7	BIBLIOGRAPHY OF THE CHAPTER	699
Appendix 6A.	ATLAS OF INFORMATION FOR THE ANALYSIS OF THE INFLUENCE ON COOLING OF PARAMETERS NOT RELATED TO COOLING PROCESS	703
Appendix 6B.	INPUT FILES FOR FIRE DYNAMICS SIMULATOR (FDS) CALCULATIONS	751

CHAPTER 7: Heuristic Analysis of Cooling Processes in High Strength Concrete Square Columns **757**

7.1	IDENTIFICATION OF THE ORIGINAL CONTRIBUTION.....	762
7.2	METHODOLOGY TO DEVELOP THE HEURISTIC ANALYSIS	762
7.3	DEFINITION OF THE ANALYSIS CASE	762
7.3.1	Description of the general features of the analysis case and causes for its selection.....	762
7.4	RESULTS.....	764
7.4.1	Heuristic Analysis of the Heating Stage.....	764
7.4.2	Heuristic Analysis of the Cooling Stage.....	768
7.4.2.1	Slow Environmental Cooling.....	768
7.4.2.2	Fast Environmental Cooling	782
7.5	RESUME OF THE CONCLUSIONS OF THE CHAPTER.....	796
7.5.1	About the Heuristic Analysis of Cooling Processes in HSC Square Columns.....	796
7.5.2	About extended tasks to go more deeply into Thermal Spalling Research in Square Columns.....	797
7.6	BIBLIOGRAPHY OF THE CHAPTER	798
Appendix 7A.	INPUT FILES FOR THE HYGRO-THERMO-CHEMO-MECHANICAL CALCULATIONS OF A SQUARE COLUMN.....	799

CHAPTER 8: Conclusions **829**

8.1	GENERAL CONCLUSIONS	833
8.1.1	General Conclusions from <i>Chapter 3 – Modelling of Hygro-Thermal Behaviour of Concrete at High Temperature with Thermo-Chemical and Mechanical Material Degradation</i>	833
8.1.2	General Conclusions from <i>Chapter 4 – Spalling Nomograms</i>	833
8.1.2.1	ABOUT THE TIME AND POSITION OF MAIN FRACTURE AND THE SENSITIVITY ANALYSIS	834
8.1.2.2	ABOUT THE SPALLING NOMOGRAMS AND THE ENERGETIC ANALYSIS OF THERMAL SPALLING.....	836
8.1.2.3	ABOUT THE EVOLUTION OF EACH PARAMETER AFFECTING THE PHYSICS OF THERMAL SPALLING PHENOMENA.....	838

8.1.3	General Conclusions from <i>Chapter 5 – Preliminary and simplified analysis of cooling effect on HSCs spalling behaviour</i>	840
8.1.4	General Conclusions from <i>Chapter 6 – Analysis of cooling processes in High Strength Concretes</i>	841
8.1.4.1	ABOUT THE COOLING PHENOMENOLOGICAL AND MECHANISTIC ANALYSIS	842
8.1.4.2	ABOUT THE COMPARATIVE ANALYSIS	844
8.1.4.3	ABOUT THE ATLAS OF INFORMATION FOR THE ANALYSIS OF THE INFLUENCE OF PARAMETERS NOT RELATED TO COOLING PROCESSES	847
8.1.5	General Conclusions from <i>Chapter 7 – Heuristic analysis of cooling processes in high strength concrete square columns</i>	848
8.2	PROPOSED EXTENDED TASKS FOR FUTURE RESEARCH WORKS	849
8.2.1	Proposed Extended tasks related to <i>Chapter 3 – Modelling of Hygro-Thermal Behaviour of Concrete at High Temperature with Thermo-Chemical and Mechanical Material Degradation</i>	849
8.2.2	Proposed Extended tasks related to <i>Chapter 4 – Spalling Nomograms</i>	849
8.2.3	Proposed Extended tasks related to <i>Chapter 6 – Analysis of cooling processes in High Strength Concretes</i>	849
8.2.4	Proposed Extended tasks related to <i>Chapter 7 – Heuristic analysis of cooling processes in high strength concrete square columns</i>	850
8.3	BIBLIOGRAPHY OF THE CHAPTER	851-852.

LIST OF SYMBOLS

C_T	tangent matrix
C_p	effective specific heat of porous medium [J kg ⁻¹ K ⁻¹]
C_p^g	specific heat of gas mixture [J kg ⁻¹ K ⁻¹]
C_p^w	specific heat of liquid phase [J kg ⁻¹ K ⁻¹]
C_s	spalling factor [-]
D_b	bound water diffusion tensor [m ² s ⁻¹]
D_{gw}	effective diffusivity tensor of water vapour in dry air [m ² s ⁻¹]
D	total damage parameter [-]
d	mechanical damage parameter [-]
d_t	component of mechanical damage (tension) [-]
d_c	component of mechanical damage (compression) [-]
E	Young's modulus [Pa]
E_0	Young's modulus of mechanically undamaged material [Pa]
e	emissivity of the interface [-]
f_c	compressive strength of concrete [MPa]
f_t	tensile strength of concrete [MPa]
f^{gws}	fugacity of water vapour (saturated) [Pa]
g	gravity acceleration [m s ⁻²]
g	correction function of damage law
G_f	specific fracture energy [J m ⁻²]
H^{gw}	specific enthalpy of water vapour [J kg ⁻¹]
H^w	specific enthalpy of liquid water [J kg ⁻¹]
H^{ws}	specific enthalpy of chemically bound water [J kg ⁻¹]
\mathbf{I}	unit tensor [-]
I_{s4}	spalling Index [-]
\mathbf{J}_d^{gw}	diffusive-dispersive flux of vapour [kg m ⁻² s ⁻¹]
\mathbf{J}_d^{ga}	diffusive-dispersive flux of dry air [kg m ⁻² s ⁻¹]
\tilde{K}_T	modified bulk modulus of the whole porous medium [Pa]
\tilde{K}_S	modified bulk modulus of the grain material [Pa]
k	absolute permeability tensor [m ²]
k	absolute permeability (scalar) [m ²]
k_o	absolute permeability (scalar) at 20°C [m ²]
$k^{r\pi}$	relative permeability of π -phase ($\pi=g,w$) [-]
L	characteristic element dimension [m]

M_w	molar mass of liquid water [kg kmol ⁻¹]
M_g	molar mass of gas phase [kg kmol ⁻¹]
M_a	molar mass of dry air [kg kmol ⁻¹]
\dot{m}_{phase}	rate of mass due to phase change [kg m ⁻³ s ⁻¹]
\dot{m}_{dehydr}	rate of mass due to dehydration [kg m ⁻³ s ⁻¹]
n	total porosity (pore volume/total volume) [-]
p_{atm}	atmospheric pressure [Pa]
p^π	pressure of π -phase ($\pi=g,w,s$) [Pa]
p_{atm}	atmospheric pressure [Pa]
p^c	capillary pressure [Pa]
p^g	pressure of gas phase [Pa]
p_o^g	initial value of pressure [Pa]
p^w	pressure of liquid water [Pa]
p^s	solid skeleton pressure [Pa]
p^{ga}	dry air partial pressure [Pa]
p^{gw}	water vapour partial pressure [Pa]
p^{gws}	water vapour saturation pressure [Pa]
$\tilde{\mathbf{q}}$	heat flux vector [W m ⁻²]
R	gas constant (8.314,41 J kmol ⁻¹ K ⁻¹)
R.H.	relative humidity [-]
S_{ssp}	solid saturation point [-]
S_w	liquid phase volumetric saturation (liquid volume/pore volume) [-]
S_g	gas phase volumetric saturation (gas volume/pore volume) [-]
S	total area [m ²]
\tilde{S}	resistant area of damaged material [m ²]
T	absolute temperature [K]
T_{crit}	critical temperature of water [K]
T_{max}	maximum temperature attained during dehydration process [K]
\mathbf{t}^s	macroscopic partial stress tensor for solid phase [Pa]
\mathbf{t}^w	macroscopic partial stress tensor for liquid phase [Pa]
\mathbf{t}^g	macroscopic partial stress tensor gas phase [Pa]
$tr\boldsymbol{\sigma}'$	trace of effective stress tensor [Pa]
t	time [s]
\mathbf{u}	displacement vector of solid matrix [m]
\mathbf{u}^π	macroscopic diffusive-dispersive velocity ($\pi = gw, ga$) [m s ⁻¹]
U	elastic energy [J m ⁻³]
V	thermo-chemical damage parameter [-]
V_r	characteristic volume [m ³]
\mathbf{v}^π	velocity vector (referred to the π -phase) in the spatial description [m s ⁻¹]
\mathbf{v}^{ga}	diffusional velocity of dry air in gaseous phase [m s ⁻¹]

$\mathbf{v}^{g,w}$	diffusional velocity of water vapour in gaseous phase [m s^{-1}]
$\mathbf{v}^{\pi s}$	relative velocity of π -phase ($\pi=g,w$) [m s^{-1}]
\mathbf{v}^{ws}	relative velocity of liquid phase [m s^{-1}]
\mathbf{v}^{gs}	relative velocity of gaseous phase [m s^{-1}]
\mathbf{v}^w	velocity of liquid phase [m s^{-1}]
\mathbf{v}^s	velocity of solid phase [m s^{-1}]
\mathbf{v}^g	velocity of gaseous phase [m s^{-1}]
Y	released energy rate [Pa]

Greek symbols

α	Biot's constant [-]
α_c	convective heat transfer coefficient [$\text{W m}^{-2} \text{K}^{-1}$]
α_t	weight coefficient (tension) [-]
α_c	weight coefficient (compression) [-]
β	shear factor [-]
β_c	convective mass transfer coefficient [m s^{-1}]
β_s	cubic thermal expansion coefficient of solid [K^{-1}]
β_{swg}	combine (solid+liquid+gas) cubic thermal expansion coefficient [K^{-1}]
β_{sw}	combine (solid+liquid) cubic thermal expansion coefficient [K^{-1}]
β_w	thermal expansion coefficient of liquid water [K^{-1}]
ΔH_{vap}	enthalpy of vaporization per unit mass [J kg^{-1}]
ΔH_{dehydr}	enthalpy of dehydration per unit mass [J kg^{-1}]
Δt	time step [s]
$\boldsymbol{\varepsilon}$	strain tensor [-]
$\boldsymbol{\varepsilon}_T$	thermal strain tensor [-]
$\boldsymbol{\varepsilon}_0$	autogeneous strain tensor [-]
$\boldsymbol{\varepsilon}^e$	elastic strain tensor [-]
$\tilde{\varepsilon}$	equivalent strain [-]
$\bar{\varepsilon}$	average equivalent strain [-]
G_{hydr}	degree of hydration (or dehydration) [-]
η^π	volume fraction of π -phase [-]
κ_0	elastic threshold [-]
κ	hardening/softening parameter [-]
μ^π	dynamic viscosity of the constituent π -phase ($\pi=g,w$) [$\mu\text{Pa s}$]
Λ_0	stiffness matrix of undamaged material
Λ	stiffness matrix of damaged material
χ_{eff}	effective thermal conductivity [$\text{W m}^{-1} \text{K}^{-1}$]
χ^s	thermal conductivity of solid skeleton [$\text{W m}^{-1} \text{K}^{-1}$]
χ^w	thermal conductivity of liquid water [$\text{W m}^{-1} \text{K}^{-1}$]

χ^g	thermal conductivity of gaseous phase [W m ⁻¹ K ⁻¹]
χ_{dry}	effective thermal conductivity of dry material [W m ⁻¹ K ⁻¹]
π	generic bulk phase (g,w,s)
ρ	apparent density of porous medium [kg m ⁻³]
ρ_π	density of π -phase [kg m ⁻³]
ρ^π	intrinsic density of π -phase ($\pi=g,w,s$) [kg m ⁻³]
ρ^g	gas phase density ($\pi=g,w,s$) [kg m ⁻³]
ρ^w	liquid phase density [kg m ⁻³]
ρ^s	solid phase density [kg m ⁻³]
ρ^{ga}	mass concentration of dry air in gas phase [kg m ⁻³]
ρ^{gw}	mass concentration of water vapour in gas phase [kg m ⁻³]
σ	Cauchy stress tensor [Pa]
σ'	effective stress tensor [Pa]
$\tilde{\sigma}$	modified effective stress tensor [Pa]
σ_0	Stefan-Boltzmann constant [W m ⁻² K ⁻¹]
Ψ_c	water potential [Pa]
Ψ_e	scalar thermodynamic potential [J kg ⁻¹]
Ψ	Jacobian matrix
ζ	distribution function for non local formulation of damage

Operators and averaged values

$\frac{D^\pi}{Dt}$	material time derivative with respect to π -phase
$\frac{\partial}{\partial t}$	partial time derivative
<i>Grad</i>	gradient operator (material description)
<i>grad</i>	gradient operator (spatial description)
<i>div</i>	divergence operator (spatial description)

Chapter 1

AIM, OBJECTIVES, ORIGINAL CONTRIBUTIONS AND STRUCTURING

1.1 ABOUT THE PROBLEM

Ancient tall structures such as the pyramids of Giza in Egypt, the Mayan temples in Tikal, Guatemala, the Kutab Minar in India or the Colossus of Rhodes are just a few examples testifying the human aspiration to build increasingly tall structures. These buildings were primarily solid structures used as monuments rather than space enclosures. By contrast, contemporary tall structures – and particularly High-Rise Buildings – are human habitats [1] where the determining factors to become progressively higher are mainly of economic and social nature.



Figure 1-1. Hong Kong skyline and its High-Rise Buildings.

The history of the development of High-Rise Buildings can be broadly classified into three periods [2]. The first period saw the erection of buildings such as the Reliance Building (Chicago, 1894) and the Carson Pirie Scott Department Store (Chicago, 1904). Most of these buildings were masonry wall bearing structures with thick and messy walls. The horizontal and lateral loads of these structures were mainly resisted solely by the load bearing masonry walls (which reached thicknesses of 2,13 metres and occupied a 15 per cent of the gross floor area).

In the second period, with the evolution of steel structures and sophisticated mechanisms such as lifts and ventilation, limitations on the height of the buildings were partially removed. The race for tallness started with a focus on Chicago and New York. Among the most famous High-Rise Buildings born during the period were the Chrysler Building (New York, 1930) and the Empire State Building (New York, 1931), measuring the latter 381 meters.

Reinforced concrete established its own identity in the 1950s into the third period. In contrast to the previous periods, where architectural emphasis was on external dressing and historical cycle, the third period placed emphasis on reasons, functional and technological facts. This new generation of High-Rise Buildings evolved from the World Trade Centre (New York, 1972), the Sears Tower (Chicago, 1974) to the Twin Towers (Kuala Lumpur, 1996). This third period saw the transition of the structural systems from rigid frame to more efficient ones. The concept of channelling the gravity and wind loads using two or more separate structural systems, giving rise to buildings with flexible exterior frames and an inner core of stiff wind-bracing frames, reduced the building weight significantly.

However, the progressive gain of height of High-Rise Building has also increased the actual and potential consequences, in terms of both human and economic losses, when natural fires erupt. Hence, the National Fire Protection Association (NFPA) has maintained an ‘international’ listing of High-Rise fires from 1911. Following is shown a synopsis of specific fires reported to the NFPA, listed chronologically with references, illustrating a spectrum of cases, outcomes and damage trends for High-Rise fires (without including recent fires caused by terrorist attacks) [3].

1. Dale's Penthouse Restaurant (mercantile/apartment complex), Montgomery, Ala., Feb. 7, 1967; 10 stories (+penthouse), penthouse origin, 25 deaths.

Largest loss in life in U.S. restaurant fire to that point since 1942. No sprinklers; combustible ceiling tiles, wall paneling, and decorations. Only one exit-a stairway.

2. Hawthorne House (apartments), Chicago, Ill., Jan. 24, 1969; 39 stories, 36th-floor origin, 4 deaths.

Possibly cigarette ignition on furniture. Elevators used by evacuating residents delayed fire fighting. Blowtorch effect in corridor.

3. Apartment building, Philadelphia, Pa., Sept. 6, 1969, 19 stories, 17th-floor origin, 1 death.

Person died from fire, believed started from cigarette, when she fell asleep smoking.

4. Conrad Hilton Hotel, Chicago, Ill., Jan. 25, 1970; 25 stories (+6 basement levels), 9th-floor origin, 2 deaths.

World's largest hotel (at the time of fire). No sprinklers nor fire-detection or automatic alarm systems for guests and fire department. Smoking materials ignited foam chairs piled in lobby (fire-code violation). Important issues raised were questions about alarm systems, fire emergency plans for guests, including those with hearing impairment or other disabilities.

5. One New York Plaza, New York, N.Y., Aug. 5, 1970; 50 stories, 33rd-floor origin, 2 deaths.

Question of whether pull boxes on each floor functioned properly; new office building. Severe, intense fire spread; fairly complete floor destruction; steel-frame damage. Air-system issues included the need to plan for venting combustion products. Deaths from elevator stopping at fire floor.

6. Office building (carpet showrooms), New York, N.Y., Dec. 4, 1970; 47 stories (+2 basement levels), 5th-floor origin, 3 deaths.

No sprinklers; fire and smoke detectors in air system (not called upon). Ignition from cutting torch sparks; prompt fire discovery and report to fire department. Issues of new (1968) New York building code construction: life-safety, venting, smoke-proof stair towers; elevators took passengers to fire floors (fire affected call buttons); (required) fire separations with 1-hour rating helped. Manual use and separation of air-conditioning systems and fans helped.

7. Pioneer International Hotel, Tucson, Ariz., Dec. 20, 1970; 11 stories, 4th-floor origin, 28 deaths.

No sprinklers, no fire-detection or evacuation alarm. Simultaneous fires due to arson; spread due to carpet, wall covering, and open stairways. Window escapes, jumping and ladder rescues. Improperly installed fire door and covered fire escape on 11th floor.

8. Motor hotel complex, New York, N.Y., July 23, 1971; 17 stories, 12th-floor origin, 6 deaths.

Management delayed reporting fire to fire department; staff mistakes allowed fire spread. Victims mistakenly tried elevators versus stairs. Arson suspected. No sprinklers; no automatic or central alarm system.

9. Tae Yon Kak Hotel, Seoul, Korea, Dec.25, 1971; 21 stories, 2nd-floor origin, 163 deaths.

Manual sprinkler in basement only; heat detectors in each room; pull stations each floor; automatic fire-evacuation alarm. LP-gas fire in coffee shop spread rapidly along interior finish through lobby, cutting off escape through one stair way (alternate stairway locked); smoke, heat, toxic gases, and fire spread through stairway (floors 1 to 5), HVAC shafts to top floors, then to middle floors. (Office/staff section of building closed for the day.) Over 100 escaped by sheet ropes, jumping (versus 38 jumping to death), and aerial fire ladders; 6 rescued from roof by helicopter (versus 2 falling during attempts).

10. Andraus building (department store and offices), Sao Paulo, Brazil, Feb. 24, 1972; 31 stories, 4th-floor origin, 16 deaths.

No sprinklers; separate air-conditioning each floor; no lighted exit signs, emergency lights, manual alarms, nor automatic detection systems. Fire started in 4th-floor light and ventilation well, spread through windows in shaft, continued spreading due to draft, winds, combustible ceiling, and finish; spread externally through windows above 7th floor; 3 nearby buildings also damaged. Emergency vehicles stuck in spectator traffic. Crush of panicked building occupants (panic jumping); rescue over ladders from adjacent building to 50th floor; ad hoc heli copter rescue of 350 from roof.

11. YMCA residence, New York, N.Y., March 22, 1972; 14 stories, 7th-floor origin, 4 deaths.

Delay in reporting of fire; incorrect address given. No sprinklers above basement level; no automatic fire-detection system; combustible acoustical tile and vinyl wall paper in central corridor.

Fire not reported by employee. Delayed alarm (nearby street box); no automatic fire-detection system; no sprinklers. Combustible wood paneling.

12. Rault Center (offices, restaurant complex), New Orleans, La., Nov.29, 1972; 16 stories (+ penthouse), 15th-floor origin, 6 deaths.

No sprinklers; no automatic alarm systems. Earlier fire same day may have obscured second, late detection (after flashover); arson possible. Vertical fire spread via 16th-floor windows; then combustible restaurant finish. Helicopter rescue from roof; frustrated and failed window rescues. Door open in stair tower (15th floor) made tower unusable; error by those trying to take elevators up to fire floor in order to help.

13. Avianca building, Bogota, Columbia, July 23, 1973; 36 stories, 13th-floor origin, 4 deaths.

Neither sprinklers, fire-detection, nor alarm systems; only one stairway. Fire started in storage room; spread due to delay in notifying fire department; interior and exterior spread; lack of water in building tanks to fight fire. 250 rescued from roof by helicopters.

14. Caiza Economica building, Rio de Janeiro, Brazil, Jan.15, 1974; 31 stories, 1st-floor origin, no deaths.

Partial sprinklers. Fire started in lobby; staff tried to fight it. Fire spread due to combustible ceiling, open stairwells with combustible finish such as carpet wall covering; stopped at 18th floor (19th story and up unfinished). Fire department called (late); then called back after leaving. Building unoccupied.

15. Joelana building, Sb Paulo, Brazil, Feb. 1, 1974; 25 stories, 12th-floor origin) 179 deaths.

No lighted exit signs, manual alarm, auto fire-detection systems, or emergency plans; water tank on roof. Electrical failure (bypassed circuit breaker) ignited window air-conditioning unit; spread by interior finish, and exterior (12th floor up). Traffic delayed fire service. Major devastation. Lack of safe exit paths (one central stairway). Elevator used heavily for rescue; occupants trapped on roof; helicopter rescues failed during fire.

16. Crival icr Beachfront Hotel. Virginia Beach, Va., Sept. 8, 1974; 11 stories, 9th-floor origin, 1 death.

No sprinklers; neither fire-detection nor automatic alarm systems (for guests and fire department alike). Delay (½ hr) reporting fire to fire department while staff tried fighting fire, only to allow its spread. Faulty stairwell door allowed heat and smoke spread.

17. Century City Office Building, Los Angeles, Calif., Nov.12, 1974; 15 stories, 8th-floor origin.

No sprinklers; no building communication or alarm systems; no evacuation or fire plans. Ignited lacquer vapors (light-switch spark) during renovation; smoke spread throughout building (partly by air-conditioning system); 2000 people evacuated (some by elevators). Helicopters used for equipment and surveys. Recessed windows helped limit vertical fire spread.

18. Esplanade apartment building, Chicago, Ill., Feb.13, 1975; 29 stories, 17th-floor origin, 1 death.

Exterior fire spread; self-closing door checked internal spread. No sprinkler or alarm system.

19. World Trade Center, New York, N.Y., Feb.13, 1975; 110 stories, 11th-floor origin.

Open files ignited; fire spread through vertical cableways (telephone) and combustible cable insulation (PVC) as far as 10th- and 16th-floor telephone closets.

20. World Trade Center (South Tower), New York, N.Y., April 17, 1975; 110 stories, 5th-floor origin.

Various extinguishing systems (such as sprinklers); smoke detectors at return-air ducts, with emergency exhaust system; evacuation plans and drills. Two-way vocal fire-alarm boxes (each floor) for sophisticated central communication system and fire department. Trash ignited (arson). Needless evacuation of floors 9 to 22 (Lathiop, 1976).

21. Squibb Building, New York, N.Y., July 11, 1975; 34 stories, 18th-floor origin.

Smoke detectors at return-air ducts; sprinklers in basement only; neither evacuation alarms nor public-address system; "stand-pipe fire alarm" pull boxes (not to fire department). Smoking material ignited temporary trash area; fire trapped 40 people on fire floor; Life Safety Code violation on length of common paths of travel.

22. Apartment complex, Dallas, Tex., Dec.23, 1975; 21 stories, 14th-floor origin, 2 deaths (fire fighters).

23. International Monetary Fund Building, Washington, D.C., May 13, 1977; 13 stories (+ penthouse), 10th-floor origin.

Sprinklers (top of atrium, not activated); HYAC air system by windows (separate system for atrium); smoke detectors at fans (optional manual control). Four of six smoke vents failed in atrium, after office fire produced smoke which banked down to all levels of atrium; building engineer's long delayed absence for smoke purging. Heavy smoke damage; need for automatic mechanical ventilation of smoke.

24. Apartment building for elderly, Charleston, W.Va., Aug. 7, 1979; 13 stories, 9th-floor origin.

Smoke detectors in apartments and hallways. Delayed alarm from staff's mistaken instructions for fire department to disregard smoke alarm.

25. Apartment building, Los Angeles, Calif., Oct.29, 1979; 19 stories, 11th-floor origin, 3 deaths.

Disconnected local alarm system (no 24-hr fire watch performed); smoke and heat at fifth-floor stairwell.

26. Westvaco office building, New York, N.Y., June 23, 1980; 42 stories, 20th-floor origin.

No sprinklers; smoke detectors had been shut down; fire drills and plans, pull alarms each floor. Smoking materials ignited fire; wide fire spread; wide smoke spread. Elevator malfunctions, a severe problem; compartmentation validated. Increased office fuel load issues; little exterior vertical fire spread.

27. Dormitory, Iowa, July 1980; 13 stories, 6th-floor origin, 1 death.

Cigarette or cigar left in upholstered chair. Student fell to death trying to escape through window.

28. MOM Grand Hotel, Las Vegas, Nev., Nov.21, 1980; 23 stories, 1st-floor origin, 85 deaths.

Partial sprinklers; evacuation alarm not activated; no smoke detectors at air vents; no use of emergency plan. Worst continental U.S. hotel fire since 1946; one of largest dollar-loss fires in 1980. Fire from short circuit (electrical ground fault) in restaurant; rapid fire spread from heavy fuel loads, building layout, lack of fire-resistant barriers, unprotected vents, and substandard stairway and tower enclosures; fire stopped at sprinklered areas. Smoke spread through air systems, stairways, and tower's elevator hoistways. Death from smoke in rooms, corridors, stairs, and elevators. Delays in notifying guests and fire department; excessive length of some escape paths; 300 evacuated from roof by helicopter (locked roof doors).

29. Las Vegas Hilton Hotel, Las Vegas, Nev., Feb.10, 1981; 30 stories, 8th- floor origin, 8 deaths.

Combination of fire-detection devices and evacuation alarms; some automatic closing (fire) doors; fire-rated elevator vestibules; smoke-proof stair towers, with smoke trap ceilings. Fire started in ea-t tower elevator lobby (arson); rapid exterior vertical spread through 22 floors. Failed to extinguish fire early, and combustible wall and ceiling carpet contributed. Fire dampers in corridor air grills helped limit spread to guests. Helicopter rescue from roof; 1500 safely evacuated from showroom.

30. Westhase Hilton Hotel, Houston, Tex., March 6, 1982; 13 stories, 4th- floor origin, 12 deaths.

Sprinklers (linen chutes only); smoke detectors ineffective or broken. Cigarette ignited furniture; wide smoke spread; deaths from toxic fumes and soot. Ineffective early fire detection; poor notification of fire department. No evacuation alarm for guests- Room door at fire origin left open and allowed smoke spread. Poor staff reaction; exits not marked clearly.

31. Alexis Nihon Plaza (apartment and office complex), Montreal, Canada, Oct.26, 1986; 15 stories, 10th-floor origin.

No sprinklers; electrical room heat detectors; smoke detectors in lobbies and air vents; stairway pull boxes. Fire started in empty rooms and went undetected for a long period. Spread (vertical and horizontal) through communication wire pathways, interim stairway, and air ducts

all the way to top floor. Remote/hidden fire annunciator panels, low water pressure (standpipes) hindered fire fighting. Building needed major reconstruction.

32. Dupont Plaza Hotel and Casino, San Juan, Puerto Rico, Dec.31, 1986; 20 stories, 1st-floor origin, 97 deaths.

No sprinklers, fire-detection system, evacuation plan, nor relevant staff training; manual evacuation alarm (broken); few exits. Arson initiated in new furniture stored in ballroom; fire spread through interior, quickly reached flashover. Smoke spread through elevators, air system, utility passageways, stairways, and building exterior. Some helicopter and ladder rescue.

33. Apartment, office, restaurant complex, New York, N.Y., Jan.11, 1988; 10 stories, 1st-floor origin, 4 deaths.

Neither central alarm system nor sprinklers. History of renovations increased fuel load, limited interior exits. Stairway doors propped open. Electrical wiring ignited couch, wood paneling.

34. Condominium, Wisconsin, 1st half of 1988; 24 stories, 16th-floor origin.

Smoke detectors in each unit and hallway Short circuit ignited wiring. Nearby combustibles.

35. First Interstate Bank building, Las Angeles, Calif., May 4, 1988; 62 stories, 12th-floor origin, 1 death.

No sprinklers; fire spread in open office settings to flashover. Exterior fire spread through floors 13 to 15 after flashover via window walls.

36. Union Bank building, Los Angeles, Calif., July 18, 1988; 39 stories, 34th-floor origin.

No sprinklers; pull boxes (evacuation bells only) each floor; smoke detectors at elevator lobbies. Spark from electrical box ignited vapors from refinishing liquids. Compartmentation limited spread; vertical fire spread quickly through windows, but damage limited due to eyebrow construction. Fire fighting hindered by lack of marked keys.

37. John Sevier Retirement Center, Johnson City, Tenn., Dec.24, 1989; 11 stories, 1st-floor origin, 16 deaths.

No sprinklers. Typifies evacuation problems in elderly housing.

38. Windsor Bulding, Madrid, Spain, Feb.12, 2005, 32 stories, 21st-floor origin, 0 deaths.

Fire not already reported to NFPA. Eight highest High-Rise in Spain. Very large fire growth rate. Building uninhabited during fire. The technical floor did not behave as designed stopping fire to move to lower floors. Arson suspected.

Next table summarizes the data accumulated from 1960. It illustrates that by far the bulk of High-Rise fires seems to occur in the United States and that, as the number of incidents increases, the distribution of fatalities per incident normalizes.

Country	Total number of fire incidents	Number of fatalities	Average number of fatalities per incident
<i>United States</i>	226	590	2.6
<i>Canada</i>	11	26	2.4
<i>Mexico</i>	2	4	2.0
<i>Puerto Rico</i>	1	96	96.0
<i>Brazil</i>	3	202	67.3
<i>Columbia</i>	1	4	4.0
<i>France</i>	1	2	2.0
<i>Philippines</i>	1	10	10.0
<i>Japan</i>	1	32	32.0
<i>Korea</i>	2	201	100.5
<i>India</i>	1	1	1.0
<i>Spain</i>	1	0	0.0

Table I-1. Fire incidents and fatalities (since 1960) [3]

In sight of the previous data it can be easily understood that the advanced analysis and prevention of the mechanisms of natural fire-induced structural collapse in High-Rise Buildings is a major concern within the current scientific environment.

1.2 ABOUT THE MAJOR AIM OF THIS THESIS

The major aim of this Thesis is, consequently, to contribute to the advanced analysis and prevention of the mechanisms of natural fire-induced structural collapse in High-Rise Buildings, by improving the current knowledge of both the phenomena involved in the structural failure mechanisms introduced by natural fires action and of the consequences of certain fire fighting strategies usually developed during these fires.

During heating of concrete, there are observed several complex, interacting physical, chemical and mechanical phenomena resulting in significant changes of the material inner structure and properties. It is commonly known that these changes can lead to a loss of load bearing capacity or other important service features of concrete structures, especially during a rapid or/and prolonged increase of environmental temperature. A significant phenomenon, constitutive of- or leading to- a structural failure mechanism very specific for concrete and of a great practical importance, is the so called Thermal Spalling which can sometimes be explosive in nature. This has been studied for many years, both experimentally and theoretically, but its physical causes are still not fully understood and their relative significance is controversial. The reason of such a situation are inherent technical difficulties associated with testing of concrete elements at high temperature, especially when changes of physical properties and several parameters are to be measured simultaneously, e.g. the temperature and pressure fields, the moisture content, the strength properties, the intrinsic permeability, etc., during experiments at controlled conditions. Usually, only fragmentary data are available from such tests and it is very difficult to deduce from their results a full picture of the analyzed phenomena. A useful tool for interpretation and better understanding of the many complex phenomena involved in Thermal Spalling, and sometimes the only possible one, can be computer simulations. However, one should remember that such an interpretation possesses all limitations and simplifications that are assumed in the mathematical model on which the simulations are based. Thus, for this purpose one should use models considering possibly the whole complexity and mutual interactions of the analyzed physical processes. Hence, in the case of concrete at high temperature, a proper choice may be models based on mechanics of multiphase porous media, taking into account chemical reactions (dehydration), phase changes, cracking and thermo-chemical material degradation, as well as their mutual couplings and influence on the hygral, thermal, chemical and mechanical properties of concrete.

Therefore, this Thesis settles, first, the abovementioned major aim in the domain of the Thermal Spalling analysis – and more precisely in its computational approach – with the particular objectives briefly exposed on paragraph 1.3 of this *Chapter* and explained in more detail in each of the following *Chapters* (especially *Chapter 4 – Spalling Nomograms*).

As already stated, Thermal Spalling is defined, in its most general form, as the violent or non-violent breaking off of layers or pieces of concrete from the surface of a structural element when it is exposed to rising temperatures as experienced in fires – particularly within the range from 200 to 300 °C –. As a result, the core concrete is exposed to these temperatures, thereby increasing the rate of heat transmission to the core part of the element and, in particular, to the reinforcement what may pose a risk for the integrity of concrete structure. Although the concepts related to Thermal Spalling are deeply described in *Chapter 2 – Background Studies: The State-of-the-Art*, figure 1-2 shows the main simultaneous phenomena leading to Thermal Spalling. It is commonly believed that the main reasons of the thermal spalling are: build-up of high pore pressure close to the heated concrete surface as a result of rapid evaporation of moisture, and the release of the stored energy due to the thermal stresses resulting from high values of restrained strains caused by temperature gradients. Nevertheless, relative importance of the two factors is not established yet and still needs further studies, both experimental and theoretical.

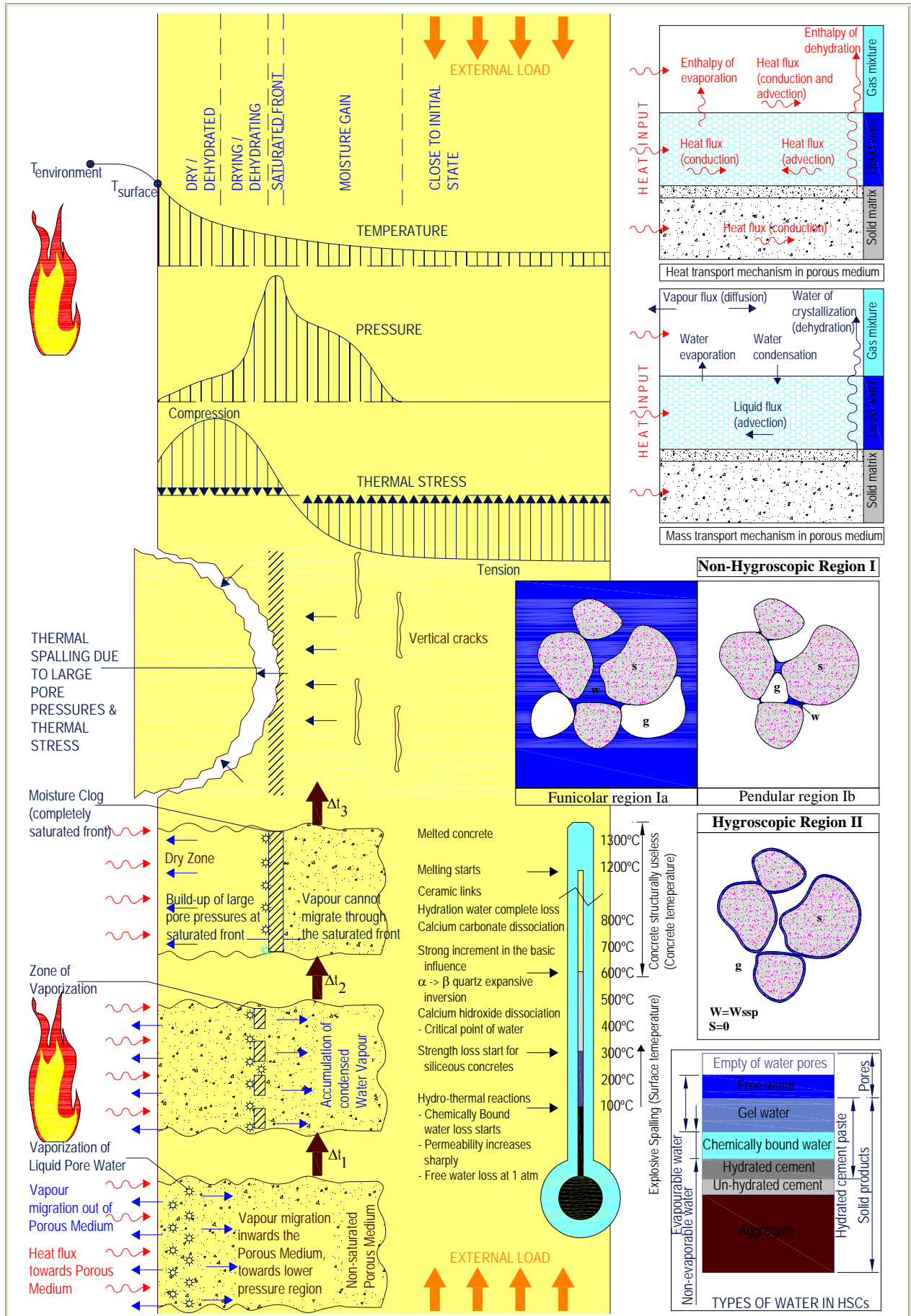


Figure 1-2. Overall main phenomena occurring in concrete during heating and spalling [4-8].



Windsor High-Rise Building natural fire
Madrid (Spain)12/02/2005

Figure 1-3. Some examples of Thermal Spalling events and their environment (I of II).

- a) HSC column after a fire endurance test [9];
- b) Spalling of a column with conventional tie configuration [10];
- c) Severe spalling in the stem of a prestressed I-beam [11];
- d) Specimen of tunnel concrete exposed to the X2000 fire curve: A spalling depth of 300 mm was observed and the reinforcement has lost its stiffness and thus hangs down [12];
- e) View of the Block No. 5 (W/C = 0,33, high-absorption coarse aggregate, no fibres) after the hydrocarbon-fire resistance test [13].

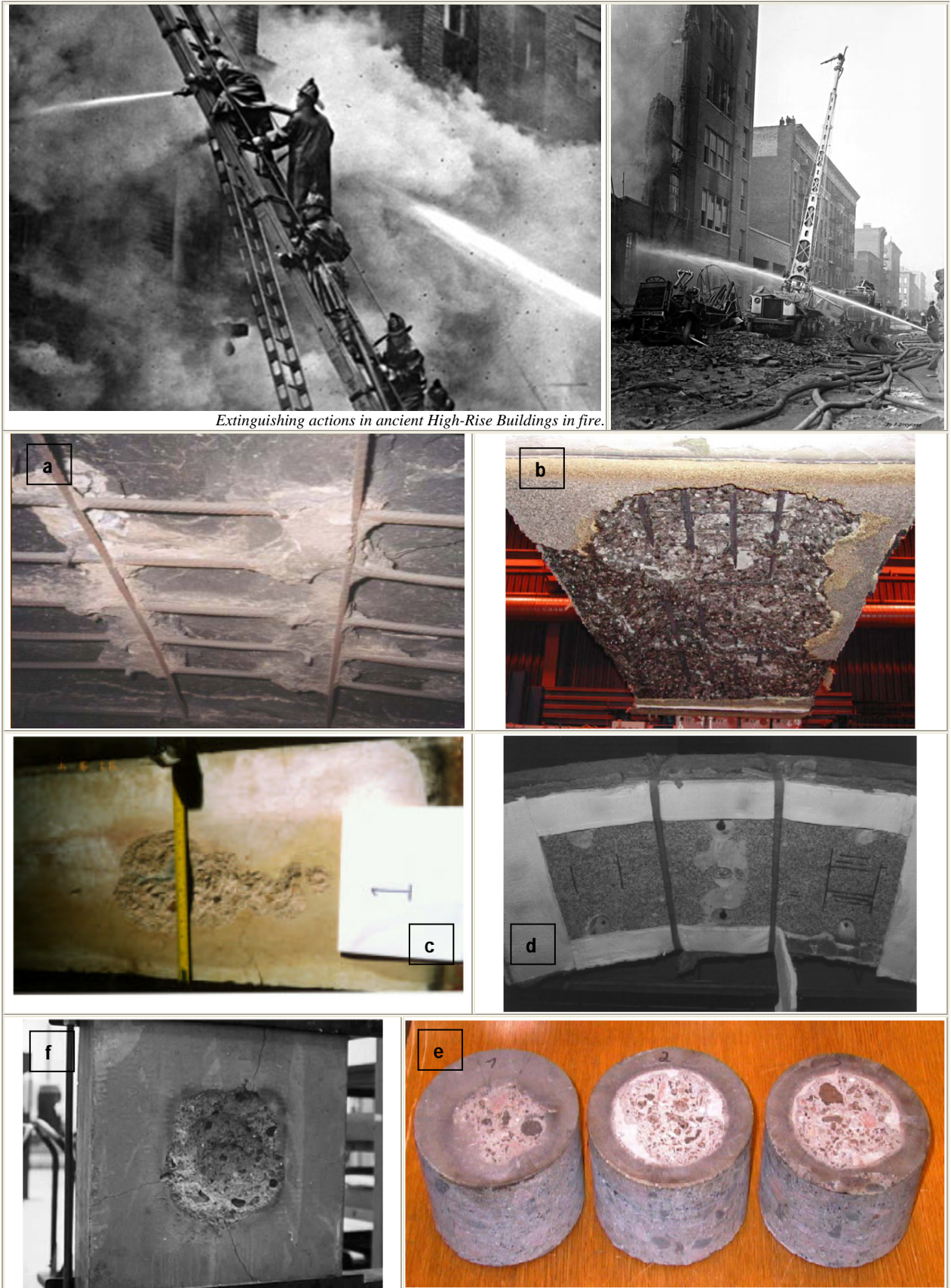


Figure 1-4. Some examples of Thermal Spalling events and their environment (II of II).

- a) Explosive spalling of the restricted unreinforced part of the section [14];
- b) Specimen where the thermal barrier fell off during a fire test. [12];
- c) Spalling of granite concrete [15];
- d) Spalled inner surface of a Great Belt Tunnel element [16];
- e) Cylinders cut out of tiles and spalled in mantle test [17];
- f) Spalling of a tile and thermal cracks causing the spalling to stop [18].

The results of the research performed up to now show, that the fire performance of concrete structures is influenced by several factors, like initial moisture content of the concrete, the rate of temperature increase (fire intensity), porosity (density) and permeability of the concrete, its compressive strength, type of aggregate, dimensions and shape of a structure, its lateral reinforcement and loading conditions. The High Strength Concrete structures are particularly affected by this phenomenon, although the extent of this influence has not already been settled. In fact, High Strength Concrete provides better structural performance, especially in terms of strength and durability, compared to traditional, normal-strength concrete (NSC). However, many studies showed that the fire performance of High Strength Concrete differs from that of Normal Strength Concrete which exhibits rather good behaviour in these conditions. Some examples of Thermal Spalling events in structural elements manufactured with High Strength Concrete are shown in previous pages – figures 1-3 and 1-4 a) to e) –.

Another scarcely studied point related to the major aim of this Thesis is the analysis of the effect of the fire fighting strategies on the structural state of the High-Rise Buildings during natural fires. Some authors [19] have reported the unquestionable benefits of combining Fire Service and Fire Science in order to increase the efficiency of the fire fighting strategies developed during the extinguishment of natural fires in High Rise Buildings. However, there is a significant lack of efforts addressed to join both disciplines and, therefore, of their synergic potential. A dramatic result of this lack happened recently in the city of Hengyang, Hunan Province, China, November 3rd, 2003, when an 8-storey reinforced concrete building collapsed catastrophically during fire extinguishing and twenty fire fighters died from the building collapse as a result of the effect of cooling regimes on the mechanical properties of concrete.

Indeed, the analysis of the cooling processes in structural elements manufactured with High Strength Concretes has only been dealt from an experimental point of view and, mostly, focused on the study of their residual mechanical properties (mainly flexural and compressive strengths of HSCs) after experimenting thermal shock during cooling. It has been repeatedly reported (see *Chapter 2 – Background Studies: The State-of-the-Art*) that thermal shock produces a significant reduction in flexural strength (and a lesser but still significant reduction in compressive strength) although thermal shock due to rapid cooling was not a primary factor causing Thermal Spalling for concrete. However, Post-cooling spalling may occur after the fire is over, after cooling down or maybe even during extinguishing, depending on the cooling rates of concretes containing calcareous aggregate: in this case occurs the rehydration of CaO to $CA(OH)_2$ after cooling, with an expansion of over 40% occurring after cooling down, when moisture is again present on the concrete surface. This expansion causes severe internal cracking on the meso-level and thus completes strength loss of the concrete. Pieces of concrete keep falling down as long as there is water to rehydrate the CaO in the dehydrated zone.

Therefore, this Thesis settles, second, the major aim mentioned in the beginning of this *Chapter* in the domain of the analysis of the effect of a spectrum of cooling processes on the hygro-thermo-chemo-mechanical state of a structural element, manufactured with High-Strength concrete, during the development of a natural fire in a High-Rise Building – and more precisely in its computational approach – with the particular objectives briefly exposed on paragraph 1.3 of this *Chapter* and explained in more detail in each of the following *Chapters* (especially *Chapter 6 – Analysis of cooling processes in High Strength Concretes*). The comparative analysis of the final hygro-thermo-chemo-mechanical state of a structural element after the development of different types – and subtypes – of cooling processes, including comparisons about the Environment vs. Structural element's Surface cooling attacks, among different start instants and for several velocities of the cooling processes, is also tackled within this second and last settling of the major aim of this Thesis.

1.3 ABOUT THE OBJECTIVES, THE ORIGINAL CONTRIBUTIONS OF THIS THESIS AND ITS STRUCTURING

1.3.1 About this Introductory Chapter

In this introductory *Chapter* is collected a brief explanation on what are the particular objectives to achieve at each of the separate parts – i.e. *Chapters* – of this Thesis, while there are summarized the original contributions of each of the tasks developed in these *Chapters* to the current State-of-the-Art corresponding to the abovementioned aim.

The reason for structuring, within this introduction, the presentation of the objectives and main original contributions of this Thesis by means of an independent paragraph per *Chapter* is, precisely, the self-sufficiency and full meaning of each related separate *Chapter*, since each *Chapter* includes:

- Its particular fully developed table of contents in order to ease the *Chapter* lecture,
- Its own definition of objectives,
- The definition of the methodology adopted to develop the tasks included in it,
- The definition of the cases analyzed therein,
- The detailed analysis of the results obtained in the *Chapter*,
- The resume of the conclusions derived from the *Chapters*' results and, finally,
- The bibliography of the *Chapter*, and its corresponding *Appendixes*.

Therefore, the only parts of this Thesis shared by all of the following Chapters, by apart from this introduction and the Nomenclature – already exposed –, are the analysis of the State-of-the-Art (*Chapter 2*) and the detailed description of the mathematical model used for the analyses of the hygro-thermo-chemo-mechanical processes involved on the High-Strength concretes behaviour (*Chapter 3*). Besides that, a final common Chapter including in a single document a collection of the general conclusions derived from each of the independent works developed in the Chapters of this Thesis is included as *Chapter 8*.

1.3.2 About the Background Studies: the State-of-the-Art

In *Chapter 2 – Background Studies: The State-of-the-Art*, there are introduced the basic concepts dealt in the subsequent *Chapters* of this Thesis, whereas there is presented a wide scope insight to the background studies currently available related to these matters – the *State-of-the-Art* –, i.e. mainly the Thermal Spalling, the Spalling Nomograms and the effect of Cooling Processes on High Strength concretes.

In the meantime, the originality of the contributions presented both herein and – respectively – in *Chapter 4 – Spalling Nomograms*, in *Chapter 6 – Analysis of Cooling Processes in High Strength Concretes* and in *Chapter 7 – Heuristic analysis of Cooling Processes in High Strength Concrete Square Columns* is also justified in *Chapter 2* in sight of the lack of any complete related references within the analyzed *State-of-the-Art*.

1.3.3 About the Modelling of Hygro-Thermal Behaviour of Concrete at High Temperature with Thermo-Chemical and Mechanical Material Degradation

The objective of *Chapter 3 – Modelling of hygro-thermal behaviour of concrete at high temperature with thermo-chemical and mechanical material degradation* is to describe in detail the mathematical model used in *Chapters 4 to 7* of this Thesis for the analysis of the hygro-thermal behaviour of concrete at high temperatures, as a multi-phase porous material, accounting for the material deterioration, in order to understand the scope and validity of the results presented herein and to justify the selection of the HITECOSP Software [20] – which is based on the Model of Padua [21]– as the most advanced software for the development of the calculations.

The complete development of the model equations, starting from the macroscopic balances of mass, energy and linear momentum of single constituents is hence presented in *Chapter 3*. The constitutive relationships for concrete at high temperature, including those concerning material damage, are also included therein. The classical isotropic non-local damage theory is presented modified to take into account the mechanical and the thermo-chemical concrete damage at high temperature. The final form of the governing equations, their discretized F.E. form, and their numerical solution are finally presented both in *Chapter 3* and within the *Appendix 3A – Matrices resulting from the discretization of mass, energy and linear momentum conservation equations*. No original contributions related to the mathematical model used in this Thesis are introduced in *Chapter 3*, since this model was completely developed and presented by D. Gawin, F. Pesavento and B.A. Schrefler [21].

1.3.4 About the Spalling Nomograms

The first objective of *Chapter 4 – Spalling Nomograms* – included in the first settling of the major aim of the Thesis, previously exposed – is to develop a spectrum of spalling nomograms addressed, as an starting point, to evaluate the sensitivity of the hygro-thermo-chemo-mechanical processes involved on the High-Strength concretes behaviour under a natural fire to some relevant parameters whose values may be chosen from a very early stage of High-Rise Buildings design or already known in case of existing High-Rise Buildings.

The second but not less important objective of the spalling nomograms to develop, and consequently of *Chapter 4*, is to analyze if spalling is energetically possible and, hence, the spalling risk in every possible set of conditions so both Designers and Fire Fighting Services will have a valuable information in order to take decisions about design and about the expectable consequences of fire fighting actions from a really intuitive, graphical and immediate point of view. An essential contribution of this work, related to this matter, is to discern what the energetic contribution of compressed gas is and what is that corresponding to the constrained elastic energy.

In this sense, some parallel and essential contributions of the work presented in this *Chapter 4* are related to the type of spalling that is expectable in each situation (either violent and explosive or slow in nature), to the extent of the spalling and, even more relevant, to the instant when spalling is expected.

Therefore, the original contributions worked out from the developments included in this *Chapter 4* are the following:

- a. The development of a spectrum of spalling nomograms addressed, as an starting point, to evaluate the sensitivity of the hygro-thermo-chemo-mechanical processes involved on the High-Strength concretes behaviour under a natural fire to some relevant parameters whose values may be chosen from a very early stage of High-Rise Buildings design or already known in case of existing High-Rise Buildings, such as the initial moisture content of concrete, its intrinsic permeability, the rate of temperature increase (fire intensity), the porosity, compressive strength, type of aggregate and, in general, the whole set of hygro-thermo-chemical properties of concrete, and the dimensions of the structural element,
- b. The analysis of the energetic viability of spalling and, hence, of the spalling risk and expectable type (either violent and explosive or slow in nature) in every possible set of conditions so both Designers and Fire Fighting Services will have a valuable information in order to take decisions about design and about the expectable consequences of fire fighting actions from a really intuitive, graphical and immediate point of view,

- c. The discerning of what is the energetic contribution of compressed gas to spalling occurrence and what is that corresponding to the constrained elastic energy since, as it has been recognised by many relevant authors [1], the relative importance of the build-up of high pore pressure close to the heated concrete surface (as a result of rapid evaporation of the moisture) and the release of the stored energy (due to the thermal stresses resulting from high values of restrained strains caused by temperature gradients) has not been already established and needs further studies.

Within the *Appendix 4A – Spalling index evolution for each combination* is included a collection of 91 figures showing the spatial distributions of the I_{s4} spalling index – selected in *Chapter 4* – at every 120 seconds and for each of the ninety one cases analyzed in *Chapter 4*, until a total simulation time of 10.800 seconds (3 hours).

Within the *Appendix 4B – Input files for the hygro-thermo-chemo-mechanical calculations* are shown the Input files developed for the calculations presented in *Chapter 4* and done by means of the HITECOSP Software [20]. The structure of these input files and the meaning of each statement included therein are also explained in this *Appendix 4B*.

Within the *Appendix 4C – Accepted publications related to this Chapter* are included the publications concerning the subjects dealt in this *Chapter* that, up to the date of this Thesis writing, have been accepted in specialized congresses related to the topics involved herein, including enclosed the brochure of the Congress, the abstract submitted for its acceptance and the confirmation of its acceptance.

1.3.5 About the Preliminary and Simplified Analysis of Cooling Effect on HSCs Spalling Behaviour

The first objective of *Chapter 5 – Preliminary and simplified analysis of cooling effect on HSCs spalling behaviour* is to establish a methodology for a preliminary and simplified analysis of the effect of a forced cooling on the spalling behaviour of High Strength (and Very High Strength) Concretes in order to evaluate if it is significant enough to justify a relevant, greater and deeper work concerning this matter.

A secondary objective of this chapter is to formulate some preliminary conclusions that may help to orientate better the analysis to be done later on models of a much higher complexity and requiring huge computational and postprocessing efforts, while testing the methodology to be used in the advanced analyses developed in *Chapter 6 – Analysis of Cooling Processes in High Strength Concretes* and *Chapter 7 – Heuristic analysis of Cooling Processes in High Strength Concrete Square Columns*.

1.3.6 About the Analysis of Cooling Processes in High Strength Concretes

The first objective of *Chapter 6 – Analysis of cooling processes in High Strength Concretes* – included in the second and last settling of the major aim of the Thesis, previously exposed – is to analyze both phenomenologically and from a mechanistic point of view the effect of a spectrum of cooling processes on the hygro-thermo-chemo-mechanical state of a structural element, manufactured with High-Strength concrete, during the development of a natural fire in a High-Rise Building. In order to ensure a practical usefulness of the results, the spectrum of cooling processes whose effect is to be analyzed in this *Chapter* must be wide enough to ensure that they are representative of all of the most expectable actions to be developed by the Fire Fighting Services during the progress of a fire. However, the precise featuring of the Fire Fighting Services cooling actions is not a purpose of this Thesis and in any case will need independent research works.

A second objective taking profit of the results arising from the first part of this Chapter is to develop a comparative analysis to compare the final hygro-thermo-chemo-mechanical state of a structural element after the development of different types – and subtypes – of cooling processes, including comparisons about the Environment vs. Structural element's Surface cooling attacks, among different start instants and for several velocities of the cooling processes.

A third objective of this *Chapter 6* is to provide – in a separate *Appendix, Appendix 6A – Atlas of information for the analysis of the influence on cooling of parameters not related to cooling process* – enough information to analyze the influence on the hygro-thermo-chemo-mechanical behaviour of the structural element during the cooling processes of several parameters non-related to the own cooling processes. This information is provided as an as an Atlas of information constituted by four Cartesian continuum representations of those variables more representative of the Thermal Spalling risk for each of the forty five cases analyzed (what has represented a total amount of 180 figures). The analysis of the influence of these parameters – such as the initial moisture content of concrete, its intrinsic permeability, the rate of temperature increase (fire intensity), the porosity, compressive strength, type of aggregate and, in general, the whole set of hygro-thermo-chemical properties of concrete – would generate an extension of the Spalling Nomograms initially obtained just for heating processes and described previously on *Chapter 4*, task not included in this Thesis but proposed as an extended task for future research works.

It must be remarked that it is not an objective of this chapter to discern a complete and definitive conclusion about the favourable or unfavourable effect of the cooling actions developed by the Fire Fighting Services during the progress of a fire, since this objective would need much more analyses than those that might be reasonable for the contents and amount of work expectable for a single Thesis. Nevertheless, some partial conclusions in this sense are included therein.

Therefore, as just stated, the main original contributions of the works presented in this *Chapter 6* are the following. Some parallel minor contributions are also identified within the text of this Chapter.

- a. The phenomenological and mechanistic analysis of the effect of a spectrum of cooling processes – representative of the most expectable actions to be developed by the Fire Fighting Services during the progress of a natural fire in a High-Rise Building – on the hygro-thermo-chemo-mechanical state of a structural element manufactured with High-Strength concrete.
- b. The development of a comparative analysis to compare the final hygro-thermo-chemo-mechanical state of a structural element after the development of different types – and subtypes – of cooling processes, including comparisons about the Environment vs. Structural element's Surface cooling attacks, among different start instants and for several velocities of the cooling processes.
- c. The supply of the information needed for the analysis of the influence on the hygro-thermo-chemo-mechanical behaviour of the structural element during the cooling processes of several parameters non-related to the own cooling processes – such as the initial moisture content of concrete, its intrinsic permeability, the rate of temperature increase (fire intensity), the porosity, compressive strength, type of aggregate and, in general, the whole set of hygro-thermo-chemical properties of concrete –, and for the generation of an extension of the Spalling Nomograms initially obtained just for heating processes and described previously on Chapter 4. Although the generation of the stated Spalling Nomograms for the cooling stage is not an objective of this Thesis and it is proposed as an extended task for future

research works, in Appendix 6A is analyzed if the variation of any of these parameters leads to an increase of the maximum value of the adopted Spalling Index I_{s4} (i.e. the risk of Thermal Spalling) during the cooling stage of the cases dealt in this Chapter.

Within the *Appendix 6B – Input files for the Fire Dynamics Simulator (FDS) calculations* are shown the Input files developed for the calculations presented in *Chapter 6* and done by means of the FIRE DYNAMICS SIMULATOR Software [22,23], adding some comments to the input files (in blue colour) in order to provide a better understanding of each statement.

1.3.7 About the Heuristic Analysis of Cooling Processes in High Strength Concrete Square Columns

The objective of this *Chapter 7 – Heuristic analysis of cooling processes in high strength concrete square columns* – also included in the second and last settling of the major aim of the Thesis, previously exposed – is to develop a heuristic analysis of the effect of cooling processes on the hygro-thermo-chemo-mechanical state of a square column, manufactured with High-Strength concrete, during the development of a natural fire in a High-Rise Building. The work presented in this *Chapter 7* must be understood as an introductory extension of the analyses already presented in *Chapter 6 – Analysis of cooling processes in High Strength Concretes* to cases with bidimensional fluxes – of both heat and mass – such as square columns, where Corner Thermal Spalling is often the most dangerous type.

The heuristic typology of the analyses presented herein is due, as it is explained in detail on *Chapter 6*, to the current lack of development of Spalling Indexes suitable for bidimensional cases and correlated against experimental data.

Therefore, as above stated, the main original contribution of the works presented in this *Chapter 7* is the heuristic analysis of the effect of cooling processes on the hygro-thermo-chemo-mechanical state of a square column manufactured with High-Strength concrete.

Finally, within the *Appendix 7A – Input files for the hygro-thermo-chemo-mechanical calculations* are shown the Input files developed for the calculations presented in *Chapter 7* and done by means of the HITECOSP Software [20]. The structure of these input files and the meaning of each statement included therein are again explained in this *Appendix 7A*.

1.3.8 About the Conclusions of this Thesis

The objective of this *Chapter 8 – Conclusions* is to collect in a single document the general conclusions derived from each of the independent works developed in the previous Chapters. Although the general conclusions derived from each of the Chapters are exposed at their last paragraphs, the author has considered necessary, in sight of the final extent of this Thesis, to include this collection of all of the conclusions in order to ease a fast review of the contributions and conclusions achieved.

Finally, in this *Chapter 8* are also collected the extended tasks proposed by the Author to go further in the analysis fields dealt herein.

1.4 BIBLIOGRAPHY OF THE CHAPTER

Bibliography of the chapter

- [1] B.S. Taranath, *Steel, concrete, & composite design of Tall Buildings*, 2nd Edition, Mc Graw-Hill, Book, 1997.
- [2] M. Chew, *Construction Technology for Tall Buildings*, 2nd Edition, Singapore University Press, Book, 2003.
- [3] Council on Tall Buildings and Urban Habitat, *Fire safety in Tall Buildings*, 1st Edition, Mc Graw-Hill, Book, 1992.

- [4] F. Pesavento, *Non-linear modelling of concrete as multiphase porous material in high temperature conditions*, Ph.D. thesis, University of Padova, Padova, 2000.
- [5] T.Z. Harmathy, *Effect of moisture on the fire endurance of building elements*, In *Moisture in Materials in Relation to Fire Tests*, ASTM Special Technical Publications 385, American Society for Testing and Materials, Philadelphia, 1965, pp.74-95.
- [6] A. Gens, S. Olivella, *THM phenomena in saturated and unsaturated porous media*, RFGC, 5(6), Environmental Geomechanics, 2001, pp. 693-717.
- [7] F. Corsi, B.A. Schrefler, C.E. Majorana, F. Pesavento, D. Gawin, *Qualified and validated procedure for spalling evaluation. Milestone M4.2*, UPTUN Upgrading of existing TUNnels report, Work Package 4, Project No.: GRD1-2001-40739 within the 5th Framework Programme of the European Union Competitive and Sustainable Growth, January 12, 2006
- [8] G.R. Consolazio, M.C. McVay, J.W. Rish III, *Measurement and prediction of pore pressures in saturated cement mortar subjected to radiant heating*, ACI Materials Journal/ September-October 1998.
- [9] V.K.R. Kodur, R. McGrath, P. Leroux, J.C. Latour, *Experimental Studies for evaluating the Fire Endurance of High Strength Concrete Columns*, Research Report No. 197 of the Fire Research Program, Institute for Research in Construction - National Research Council Canada, May 2005.
- [10] V.K.R. Kodur, *Guidelines for fire resistance design of high-strength concrete columns*, National Research Council Canada NRC-CNRC, Institute for Research in Construction, report NRCC-47729, Journal of Fire Protection Engineering, v. 15, May 2005, pp. 93-106.
- [11] K. Kordina, *Der Einfluß von Abplatzungen, Schutzschichten und des Spannsystems auf die Feuerwiderstandsdauer*, in *Fire resistance of prestressed concrete*, proceedings of a symposium held at Braunschweig Germany by the Federation Internationale de la Precontrainte, pp.51-56, 1965.
- [12] L. Boström, *Innovative Self-Compacting Concrete—Development of Test Methodology for Determination of Fire Spalling*, SP Report 2004:06, Borås, Sweden, 2004.
- [13] A. Bilodeau, V.K.R. Kodur, G.C. Hoff, *Optimization of the type and amount of polypropylene fibres for preventing the spalling of lightweight concrete subjected to hydrocarbon fire*, National Research Council Canada NRC-CNRC, Institute for Research in Construction, report NRCC-45687, Cement and Concrete Composites, v. 26, no. 2, Feb. 2004, pp. 163-174.
- [14] A. Alnajim, *Modelisation et simulation du comportement du beton sous hautes temperatures par une approche thermo-hygro-mecanique couplee. Application a des situations accidentelles*, These, Universite de Marne la Vallee U. F. R. de Sciences et Technologies, 2004.
- [15] P. Shuttleworth, *Fire performance of concrete for tunnel linings*, *Channel Tunnel*, Rail Link Technical Report, Arup, 1997.
- [16] J.O. Jersild, M. Østergaard-Nielsen, K.D. Hertz, *Rapporten. Television program with full scale fire test of an element from the Great Belt tunnel*, Danish Radio 1, June 6, 1998.
- [17] K.D. Hertz, L.S. Sørensen, *Test method for spalling of fire exposed concrete*, Fire Safety Journal, 40 (2005) 466-476.
- [18] K.D. Hertz, *Limits of spalling of fire-exposed concrete*, Fire Safety Journal, 38, 2003.
- [19] D. Madrzykowski, R.E. Sanders, *Fire Service and Fire Science: A Winning combination*, NFPA Journal Vol. 88 N° 2 (March/April 1994) pp 55-60.
- [20] Brite Euram III BRPR-CT95-0065 HITECO, *Understanding and industrial application of High Performance Concrete in High Temperature Environment – Final report*, 1999.
- [21] D. Gawin, F. Pesavento, B.A. Schrefler, *Modelling of hygro-thermal behaviour of concrete at high temperature with thermo-chemical and mechanical material degradation*, Comput. Methods Appl. Mech. Engrg . 192 (2003) 1731-1771.
- [22] K. McGrattan, S. Hostikka, J. Floyd, H. Baum, R. Rehm, W. Mell, R. McDermott, *NIST Special Publication 1018-5 – Fire Dynamics Simulator (Version 5) Technical Reference Guide, Volume 1. Mathematical Model*, NIST National Institute of Standards and Technology (US Department of Commerce) in cooperation with VTT Technical Research Centre of Finland, October 2007.
- [23] K. McGrattan, B. Klein, S. Hostikka, J. Floyd, *NIST Special Publication 1019-5 – Fire Dynamics Simulator (Version 5) User's Guide.*, NIST National Institute of Standards and Technology (US Department of Commerce) in cooperation with VTT Technical Research Centre of Finland, October 2007.

Chapter 2

BACKGROUND STUDIES: THE STATE-OF-THE-ART

2.1	THERMAL SPALLING	21
2.1.1	Definition and Nature of Thermal Spalling.....	21
2.1.2	Types of Thermal Spalling.....	22
2.1.2.1	EXPLOSIVE SPALLING	22
2.1.2.2	SURFACE SPALLING	23
2.1.2.3	AGGREGATE SPLITTING.....	23
2.1.2.4	CORNER SEPARATION	23
2.1.2.5	SLOUGHING OFF.....	23
2.1.2.6	POST-COOLING SPALLING	24
2.1.3	Significance of Thermal Spalling	24
2.1.3.1	LOAD BEARING CAPACITY FAILURE.....	25
2.1.3.1.1	<i>Loss of section.....</i>	<i>25</i>
2.1.3.1.2	<i>Loss protection to steel reinforcement.....</i>	<i>25</i>
2.1.3.2	SEPARATING FUNCTION	25
2.1.3.3	SAFE DESIGN	26
2.1.3.4	SPALLING IN NATURAL FIRES VS FURNACE TESTS.....	26
2.1.4	Assessment of the Thermal Spalling Risk: Spalling Indexes	27
2.1.4.1	HYPOTHESES CONCERNING MECHANISMS OF THERMAL SPALLING.....	28
2.1.4.1.1	<i>PRESSURE-INDUCED SHEAR MODEL</i>	<i>29</i>
2.1.4.1.2	<i>BUCKLING MODEL CONSIDERING GAS PRESSURE.....</i>	<i>29</i>
2.1.4.1.3	<i>SIMPLIFIED FRACTURE MECHANICS MODEL.....</i>	<i>31</i>
2.1.4.2	PRACTICAL EVALUATION OF THE THERMAL SPALLING RISK	32
2.1.5	Factors Affecting Thermal Spalling.....	36
2.1.5.1	MOISTURE CONTENT	36
2.1.5.2	WATER/CEMENT RATIO, PERMEABILITY	38
2.1.5.3	HEATING CONDITION	38
2.1.5.4	AGGREGATES.....	39
2.1.5.5	TEST CONDITION.....	39
2.1.5.6	CONCRETE STRENGTH	40
2.1.5.7	SECTION SIZE	41
2.1.5.8	APPLIED LOAD.....	41
2.1.5.9	RESTRAINT	42
2.1.5.10	THERMAL EXPANSION	42
2.1.5.11	REINFORCEMENT.....	42
2.1.5.12	COVER.....	43
2.1.5.13	FIBRES.....	43
2.1.5.14	DENSITY	44
2.1.5.15	CONDUCTIVITY	44
2.1.5.16	SPECIFIC HEAT.....	44
2.1.5.17	CRACKING	44
2.1.5.18	AIR-ENTRAINMENT	44
2.1.5.19	SUMMARY TABLES OF THE MAIN FACTORS AFFECTING SPALLING	44
2.1.6	Spalling Nomograms	46
2.1.7	Design Against Thermal Spalling.....	49
2.1.7.1	PREVENTIVE MEASURES	50
2.1.7.2	POLYPROPYLENE FIBRES	51
2.1.7.3	THERMAL BARRIER.....	52
2.2	COOLING PROCESSES IN HIGH STRENGTH CONCRETES.....	52
2.3	BIBLIOGRAPHY OF THE CHAPTER	55

*THIS PAGE IS INTENTIONALLY
LEFT BLANK*

Chapter 2

**BACKGROUND STUDIES:
THE STATE-OF-THE-ART**

The aim of this Chapter is to introduce the basic concepts dealt in the following *Chapters* of this Thesis, whereas there is presented a wide scope insight to the background studies currently available related to these matters – the *State-of-the-Art* –, i.e. mainly the Thermal Spalling, the Spalling Nomograms and the effect of Cooling Processes on High Strength concretes.

In the meantime, the originality of the contributions presented – respectively – in *Chapter 4 Spalling Nomograms*, *Chapter 6 Analysis of Cooling Processes in High Strength Concretes* and *Chapter 7 Heuristic analysis of Cooling Processes in High Strength Concrete Square Columns* is justified in sight of the lack of any complete references within the analyzed *State-of-the-Art*.

Finally, a general description of the available numerical models developed for the analysis of the hygro-thermo-chemo-mechanical state of a structural element at high temperature is included in a separate *Chapter* due to its extent – *Chapter 3 Modelling of hygro-thermal behaviour of concrete at high temperature with thermo-chemical and mechanical material degradation* – in order to justify the selection of the HITECOSP Software [1] – which is based on the Model of Padua [2] – as the most advanced software for the development of the calculations included in the just stated *Chapters*.

2.1 THERMAL SPALLING**2.1.1 Definition and Nature of Thermal Spalling**

Spalling, in its most general form, is defined as the violent or non-violent breaking off of layers or pieces of concrete from the surface of a structural element when it is exposed to rising temperatures as experienced in fires [3]. There are mainly five types of Thermal Spalling: Violent Spalling, Sloughing Off, Corner Spalling, Explosive Spalling and Post-Cooling Spalling, being these categories deeply exposed on next paragraph. One of the most dangerous of these is explosive spalling which occurs violently and results in serious loss of material, so in this *Chapter* it is especially addressed.

Explosive Spalling is a very violent form of Thermal Spalling characterized by the forcible separation of pieces of concrete, accompanied by a typically loud explosive noise. It normally occurs within the first 30-40 minutes of exposure to fire. It is also stochastic. For specimens from the same batch, and under identical conditions, some could spall while others do not. Under suitable environmental conditions, in terms of load and thermal attack, all concrete can display the capacity for explosive spalling.

Already in 1916, Gary [4] differentiated explosive spalling from surface spalling principally by its magnitude and he referred to it as the bursting of entire surfaces of wall slabs up to 1 m². He observed parts of slabs being ejected some 12 metres from the test building and quite reasonably classified explosive spalling as extremely dangerous.

Authors frequently refer to explosive spalling simply as “spalling”. This is because quite a number of authors regard explosive spalling as the main ‘serious’ form of Thermal Spalling. It also arises from confusion as to the different forms of spalling. Consequently, this causes some uncertainty in the reader’s mind, when it is not clear what form of spalling the author means. Furthermore, there are many contradictions in the reports from the different authors, as reported below. This could be due to the complexity of the subject, the many parameters that influence explosive spalling, and the fact that specimens and conditions vary markedly from test to test.

2.1.2 Types of Thermal Spalling

During the fire tests, the observations of Thermal Spalling of High Strength Concretes cover a wide range. These are, in a random order: observation of spalling with slow (1°C/minute) or fast (250°C/minute) heating, from gradual to explosive spalling, cracking along or through aggregate grains, spalling in the beginning of the fire or after some time, stopping after some time or progressing, stopping at the reinforcement level or continuing far beyond it, and so on. The different spalling phenomena are described below, including their relationship with their governing mechanisms (see Table 2-1) [5]:

	PORE PRESSURE DUE TO EVAPORATION OF MOISTURE	COMPRESSION OF THE HEATED SURFACE DUE TO A THERMAL GRADIENT IN THE CROSS SECTION	INTERNAL CRACKING DUE TO DIFFERENCES IN THERMAL EXPANSION BETWEEN AGGREGATE AND CEMENT PASTE	CRACKING DUE TO DIFFERENCES IN THERMAL EXPANSION / DEFORMATION BETWEEN CONCRETE AND REINFORCEMENT BARS	STRENGTH LOSS DUE TO CHEMICAL TRANSITIONS DURING HEATING/COOLING
VIOLENT SPALLING	√	√	√		
SLOUGHING OFF			√		√
CORNER SPALLING				√	
EXPLOSIVE SPALLING	√	√			
POST-COOLING SPALLING			√		√

Table 2-1. Relationships between Spalling Phenomena and their governing Mechanisms [5].

Other authors [6,7] propose a different classification of the spalling phenomena shown next, according to the description developed in next subparagraphs:

SPALLING TYPE	PROBABILISTIC TIME OF OCCURRENCE	NATURE	SOUND	INFLUENCE
EXPLOSIVE SPALLING	7 – 30 minutes	Violent	Loud Bang	Serious
SURFACE SPALLING	7 – 30 minutes	Violent	Cracking	Can be Serious
AGGREGATE SPLITTING	7 – 30 minutes	Splitting	Popping	Superficial
CORNER SEPARATION	30 – 90 mminutes	Non-Violent	None	Can be Serious
SLOUGHING OFF	When concrete weakens	Non-Violent	None	Can be Serious
POST-COOLING SPALLING	During & after cooling upon absorption of moisture	Non-Violent	None	Can be Serious

Table 2-2. Classification and main overall features of Thermal Spalling types [6].

2.1.2.1 EXPLOSIVE SPALLING

This type of spalling occurs during the early part of a fire, usually within the first thirty minutes or so of a standard furnace test. It can occur at an early stage just above 100°C. It is characterized by large or small pieces of concrete being violently expelled from the surface, accompanied by a loud noise. The pieces may be as small as 100 millimetres or as large as 300 millimetres in length and 15 – 20 millimetres deep [8].

The phenomenon can occur just once or at intervals even from the previously spalled parts. Multiple spalling layers is more likely in High Strength Concrete (HSC) than in Ordinary Strength Concrete (OSC) [9]. Occasionally, the severity of explosive spalling can lead to the

formation of holes through the thickness of the section. In many cases, this type of spalling is restricted to the unreinforced part of the section and usually does not proceed beyond a reinforcing layer [8].

Explosive spalling is the result of a combination of rising pore pressures and thermal gradients in the cross-section. At the front of heat penetration, a “moisture clog” (an area with high pore pressure) develops inside the concrete. Part of the moisture is pushed further into the colder part of the concrete due to the pressure gradient at the back of the clog. If the heated surface is under compression due to a thermal gradient, the complete heated surface may explode away with a loud bang. This type of spalling is especially likely to occur on structural members heated from more than one side, such as columns and beams. When moisture clogs are advancing into the concrete from all heated sides, at some point in time the moisture clogs will meet in the centre of the cross-section, creating a sudden rise in pore pressure which may cause large parts of the cross-section to explode. This type of spalling can also occur after a considerable duration of the fire even if the concrete surface has been protected with an insulating layer.

2.1.2.2 SURFACE SPALLING

This type of spalling is associated with local removal of surface material including, pitting and blistering. This occurs when small pieces, up to about 20 millimetres in size, fly off the surface of a concrete element during the early part of its exposure to a fire or a fire test. Surface spalling may result in exposure of the reinforcement [9].

2.1.2.3 AGGREGATE SPLITTING

This type of spalling is failure of aggregate near the surface, characterized by a popping sound. It is caused by thermal expansion of the aggregate and splitting of pieces of aggregate close to the surface because of physical or chemical changes, which occur at high temperatures in aggregates. The main causes are limonite-haemetite conversion of quartz at 570°C [8]. It has little impact on structural performance as the majority of the cover remains intact and insulates the reinforcement. In addition, because aggregate spalling only causes superficial damage to concrete, the insulation function of the structural members in fire is little affected.

2.1.2.4 CORNER SEPARATION

This type of spalling occurs during the later stages of a fire exposure when the concrete has become weak and cracks develop as a result of tensile stress along edges and corners where the reinforcement is typically located. Figures 7-1 and 7-2 in Chapter 7 show some examples.

Pieces of concrete fall off of beams and columns due to the difference in the deformation (ovalization) of the inhomogeneously heated concrete around the uniformly heated reinforcement bar, and may be followed by pieces coming away from the faces as cracks develop further. Because of the advanced stage at which such spalling occurs, the strength of the element may have already reduced significantly, and therefore this type of spalling may be of limited significance to structural stability because it has already been lost.

2.1.2.5 SLOUGHING OFF

This is a gradual progressive process which is caused by chemical deterioration of cement paste and internal cracking of concrete due to the difference in thermal expansion between the aggregate and the cement paste [5]. This type of spalling is related to the attained temperature of concrete and not the heating rate which tends to define explosive spalling.

Sloughing off is the form of spalling that is caused by strength loss due to internal cracking (meso-level) and chemical deterioration of the cement mix (micro-level). This type of spalling is

related to the attained temperature of the concrete (instead of heating rate). If the concrete is heated to a very high temperature, the strength will be too low to carry its own weight, causing small pieces of concrete to fall down without much sound. This type of spalling is likely to occur on a slab heated from below, since gravity will force the cracked pieces of concrete from the cross section.

2.1.2.6 POST-COOLING SPALLING

Post-cooling spalling occurs after the fire is over, after cooling down or maybe even during extinguishing [9]. This type of spalling was observed with concrete types containing calcareous aggregate. An explanation is the rehydration of CaO to $\text{CA}(\text{OH})_2$ after cooling, with an expansion of over 40% occurring after cooling down, when moisture is again present on the concrete surface. The expansion due to rehydration causes severe internal cracking on the meso-level and thus completes strength loss of the concrete. Pieces of concrete keep falling down as long as there is water to rehydrate the CaO in the dehydrated zone.

2.1.3 Significance of Thermal Spalling

As already explained in the previous paragraph, explosive spalling can take place as a single explosion or a series of explosions, each removing a thin layer of concrete ranging from 100 millimetres to 300 millimetres in length [10] and 15 millimetres to 20 millimetres in depth [11], capable of causing physical damage on impact. In many cases, explosive spalling is restricted to the unreinforced part of the section and usually does not proceed beyond a reinforcing layer (e.g. mesh reinforcement in a slab, or a cage of bars and links in a beam or a column [10]). Multiple spalling, as experienced recently in the Great Belt tunnel fire in Denmark [12], is more likely in high strength concrete than in normal strength concrete.



Figure 2-1. Damage of concrete and reinforcement after the Great Belt fire [3].

Explosive spalling may, however, result in a sudden and complete failure of the concrete member to sustain its load-bearing function because of significant loss of section. It can also blow holes in concrete partitions thus facilitating the spread of fire and undermining the partition's "integrity". Hence, its effect on the following three capabilities is analyzed next.

Indeed, the extent, severity and nature of occurrence of spalling are extremely varied. Spalling may be insignificant in amount and consequence, such as when surface pitting occurs. Alternatively, it can have a serious effect on the fire resistance of the structural element because of extensive removal of concrete which exposes the core of the section, and the reinforcing steel or tendons, to a more rapid rise in temperature, thus reducing the load-bearing cross-sectional area.

The consequences of spalling are also very much influenced by the application for which concrete is being used. For example, although in the majority of applications aggregate spalling may be a quite insignificant form of surface damage, it poses major problems in concrete pavements used for military aircraft [13].

All forms of spalling may reduce the period of fire resistance that a concrete structural element might achieve when tested to BS 476:Part 20:1987[14]. Spalling of concrete may cause fire resistance failure through loss of load-bearing capacity and/or loss of integrity, rendering inaccurate structural design calculations. These are discussed below.

2.1.3.1 LOAD BEARING CAPACITY FAILURE

Spalling may result in the loss of load-bearing capacity through loss of section or the protection the concrete cover provides to the steel reinforcement.

2.1.3.1.1 *Loss of section*

In some cases, the occurrence of spalling may reduce the cross-sectional area of the concrete to such an extent that it is no longer able to sustain the compressive stresses imposed upon it. The scope for such failure has been increased by current trends towards rationalization in design and the increasing likelihood for larger design stresses.

2.1.3.1.2 *Loss protection to steel reinforcement*

A second mechanism for load-bearing failure is that spalling of the concrete, which provides protective cover to the steel reinforcement, may result in the reinforcement reaching excessive temperatures. As the yield strength of steel is considerably reduced at elevated temperatures, spalling may hasten the steel towards yield, thus precipitating flexural failure of the concrete member.

With tension in the extreme fibres governing the design of most concrete elements of the structure, this form of spalling failure is quite commonly found in practice. The likelihood of flexural failure is increased by the fact that spalling and crumbling of concrete from around the reinforcement may cause loss of bond, and load-bearing failure could result from the loss of composite action.

If the reinforcement becomes exposed as a result of spalling, it is heated quickly and the resistance of the section decreases at a rapid rate. Beams and slabs are more likely to be affected in this way, narrow beams and ribs being particularly at risk [10]. The importance of spalling also depends on the form of the structure. For example, columns are more critical than continuous floors [10]. Spalling of concrete in the web of beams increases the risk of shear failure. Spalling in the compression zone may cause a compression failure [15].

2.1.3.2 SEPARATING FUNCTION

Spalling can also affect the separating function of elements by causing holes to appear in slabs or panels thus enabling the fire to spread into other compartments. Thin slabs are particularly susceptible to such “integrity” failure.

2.1.3.3 SAFE DESIGN

The unexpected damage caused to a concrete construction by spalling can render fire safety design calculations inaccurate and lead to significantly reduced levels of safety for concrete structures in the event of fire. The inability to predict the occurrence of spalling has been a limiting factor in the development of robust models of the response of concrete structures to fire.

As long as spalling remains unpredictable, fire engineering calculations and computerized simulations of fire resistance tests will not be reliable. By ignoring the effects of spalling, it is possible that current engineering models used to predict the fire resistance of concrete structural elements may produce unsafe results. This possibility has been recognised by designers who, being unable to prevent spalling, have had to adopt measures to protect against its consequences.

The crucial influence that spalling has upon the fire resistance of concrete columns was provided using analytical methods by [16]. There it was found that the amount of spalling that a column suffered was more critical in deciding its fire resistance than the patterns that heating and loading imposed. There was calculated the structural response of the column using constitutive models M1, M2 and M3 based on the work of [17-19] respectively. The relationship between the amount of spalling from a 200 millimetres square column after 15 minutes and the fire resistance time is shown in figure 2-2 as an example of his findings.

Besides this, figure 2-3 shows the effect that spalling has on the fire resistance of concrete columns. The results suggest that regardless of the size of the column, the occurrence of spalling is critical in determining fire resistance.

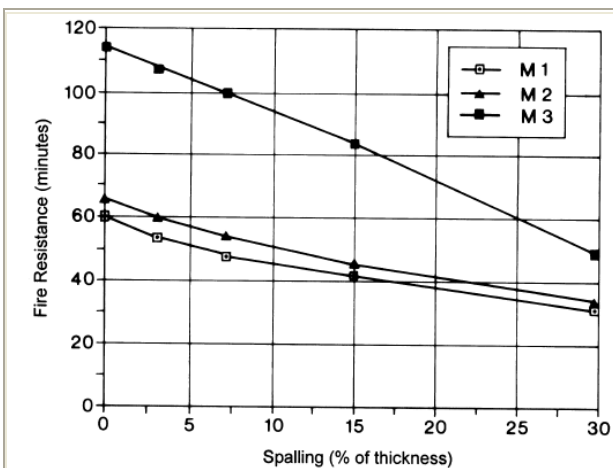


Figure 2-2. Calculated effect of spalling on fire resistance of concrete columns [16].

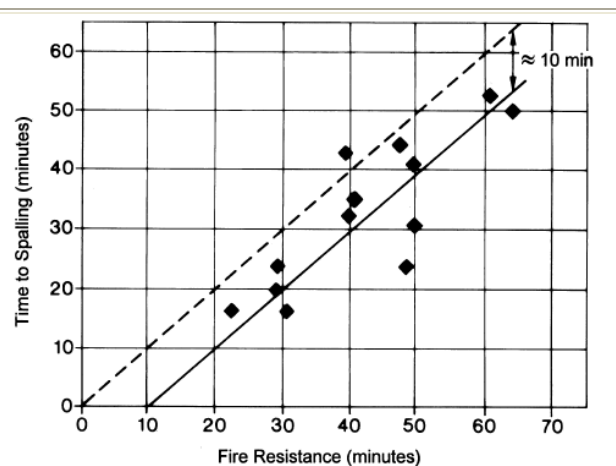


Figure 2-3. Effect of spalling on fire resistance of concrete elements [20].

2.1.3.4 SPALLING IN NATURAL FIRES VS FURNACE TESTS

Most spalling tests are performed in simulated laboratories fire conditions employing the “standard” furnace test with a heating rate in accordance with *ISO 834:1987* or *BS 476:Part 20:1987* (figure 2-4 “Fire Ramp”).

In real fires the practical consequences of spalling may be less serious than might have been anticipated from furnace tests. In real fires the exposure conditions are usually (not always) less severe and the loads (dead and live) are lower than in furnace tests. Standard furnace tests are also normally performed on individual elements. Continuous elements generally behave better than simply-supported elements [21,22]. A bigger margin of safety for concrete construction is, therefore, provided than is assumed by a grading system based on standard furnace tests. Nevertheless, the consequences of spalling cannot be ignored at all. It should be possible to take preventive measures or to compensate for the occurrence of spalling by taking into account additional structural safeguards [10].

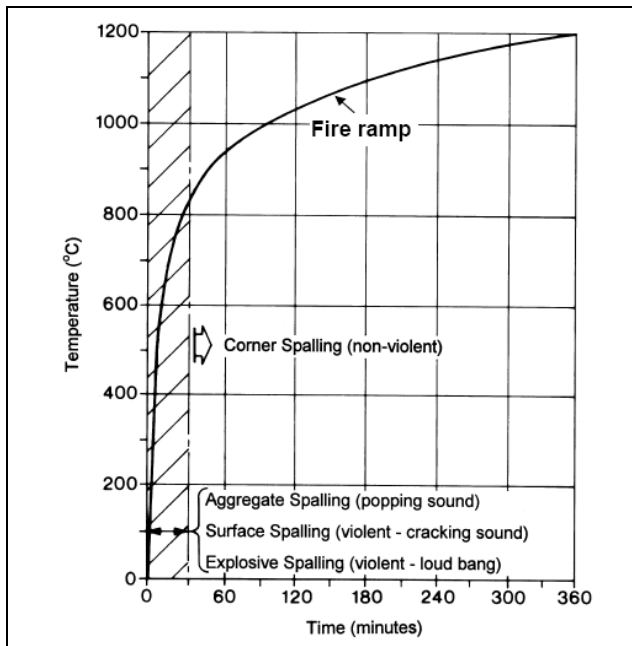


Figure 2-4. Time of occurrence of different types of spalling in fire [3]

The characterization of natural fires is deeply dealt both in *Chapter 4 Spalling Nomograms* and *Chapter 6 Analysis of Cooling Processes in High Strength Concretes* of this Thesis.

2.1.4 Assessment of the Thermal Spalling Risk: Spalling Indexes

Within this paragraph are discussed some quantitative criteria which can be useful for the assessment of the risk that Thermal Spalling of concrete layers or pieces from a heated structure occurs.

Such criteria have been already proposed in the past by several researchers [25-30,11], but most of them were formulated on an experimental basis only, often in the form of diagrams showing ‘*area of the spalling risk*’ as a function of several concrete properties like permeability or tensile strength, being their validity limited to the materials and element geometries used in the tests they were based on.

There were also formulated some analytical criteria, e.g. using limit state analysis [11,28], but they were usually based on simplified models of concrete performance during heating, by evaluating the thermally induced stresses and/or vapour pressures. Mainly, criteria presented in the past fall into three categories [31]:

1. Criteria based on pore pressure prediction, which consider the pore pressure as responsible for thermal spalling [30,21,22]. Usually, the models employed for the description of the hygral state of concrete are rather simple. For example, mass transport in concrete pores is considered as a purely diffusive phenomenon [11,32], or pore pressure is directly evaluated by using an idealized spherical model for the pores of the material [29]. In some cases the so-called “moisture clog” is indicated as the main cause of spalling [27] (see figure 2-5).
2. Criteria based on thermal stresses. These are the simplest ones and are related to the non-uniform thermal stresses that can reach the maximum compressive strength of concrete for a given temperature, e.g. [26].
3. Criteria based on combined action of thermal stresses and pore pressure. This class of spalling criteria encompasses the criteria by Zhukov [28] and Connolly [11]. The first author proposed a method for the evaluation of the strain energy density in the direction

of the heated surface W_x , taking into account the stresses due to external mechanical load, thermal field and pore pressure acting on a slab heated on one face. The spalling occurs when the strain energy density W_x in x-direction equals the rupture energy density defined on the basis of tensile strength of concrete. Connolly [11] extended Zhukov's model considering pore pressure stresses as acting simultaneously in the three directions x, y, z . The critical state for spalling was hence defined in a way similar to Zhukov's approach (see figure 2-6).

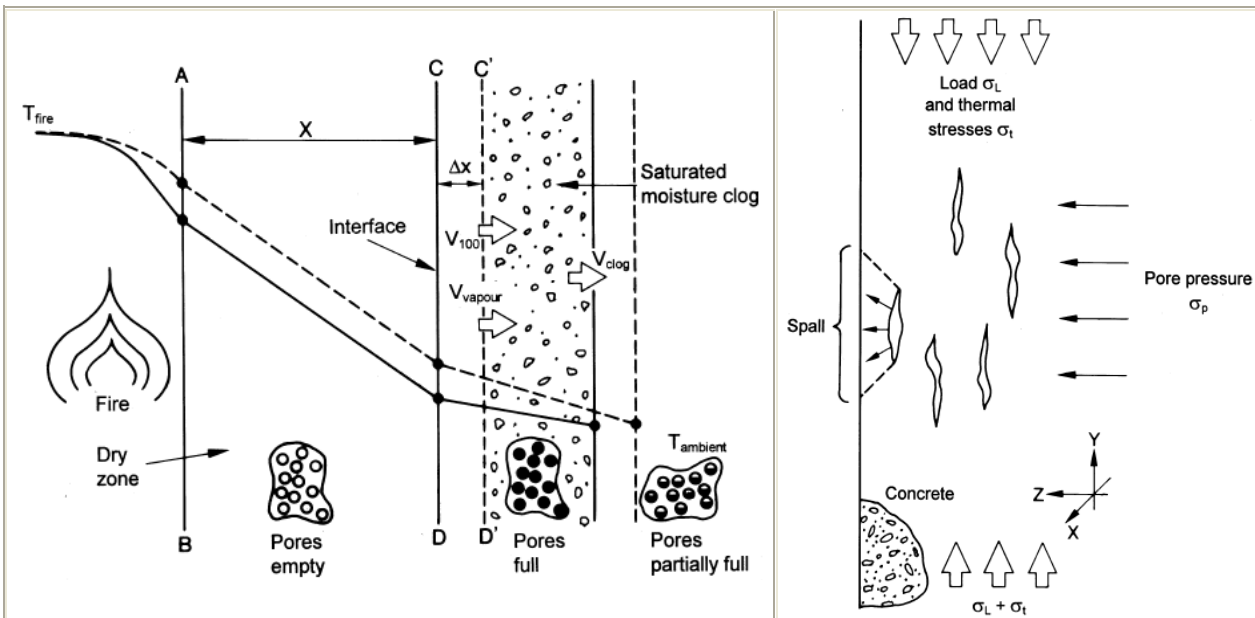


Figure 2-5. Moisture-vapour model of heated concrete [11]

Figure 2-6. Stresses acting in heated concrete [28]

In both the aforementioned methods, the mechanical behaviour of concrete is described in a simplified manner. In fact, the definition of the criterion is based on the assumption that the material behaves elastically, neglecting thermo-chemical degradation of concrete and non-linear effects, e.g. due to cracking. In the approaches presented above, the criteria omit the complexity of hygro-thermal and chemo-physical processes in concrete at high temperature so they were not able to give a realistic evaluation of the Thermal Spalling risk.

2.1.4.1 HYPOTHESES CONCERNING MECHANISMS OF THERMAL SPALLING

To assess the Thermal Spalling risk, a detailed knowledge of several local parameters describing hygro-thermal state of concrete, stresses and strains in every point of an analysed structure is necessary. However, Thermal Spalling is also a ‘‘macro’’ phenomenon, depending on several geometrical and physical parameters of the whole structure hence an analysis on this scale seems to be necessary, as well. Thus, some simplifying hypotheses concerning mechanisms leading to Thermal Spalling are assumed, based on mechanical models, which allow us to formulate some quantitative criteria [31] useful in the assessment of the risk of the phenomenon to occur, and described next. The analysis of these spalling criteria is developed in *Chapter 5*, based on the results of computer simulations performed by means of the numerical model presented in *Chapter 3*, as well as the results of the experimental tests performed at NIST [25,26,31,33]. In particular, three criteria, assuming different macromechanisms leading to concrete spalling, and one ‘intuitive’ criterion deduced from the analysis of physical processes during heating of concrete and the results of some experiments at these conditions [1,11,25-34], are exposed next. All these criteria are based on detailed data concerning the evolution in time of the variables describing material deterioration, strength properties, gas pressure and hygro-thermal state in every point of the analysed structure. Some geometrical parameters, necessary in

the ‘‘macro-mechanical’’ analysis, are deduced from the results of the experiments performed at NIST [25,26,31,33] which have been numerically modelled [31] (see *Chapter 5*).

2.1.4.1.1 PRESSURE-INDUCED SHEAR MODEL

This simple criterion is based on the pressure-induced shear model [35]. Considering a concrete slab heated on one face, it is possible to identify three zones which are of importance when analysing the progressive spalling, figure 2-7.a: the first one is a compressed concrete layer directly adjoining the heated surface, which is probably the most damaged one, the second zone is a region where the gas pressure reaches high values, and the third zone consists of partly thermo-chemically deteriorated concrete.

This simple criterion predicts the ‘‘plastic’’ failure of the material constraints for the external layer. Denoting L_r the length of the zone A (where gas pressure equal to p^g is uniformly distributed), which is delaminated from the rest of structure due to an existing continuous fracture, b the thickness of the zone B (i.e. the compressed layer), we have simply to check the following limit condition for shear:

$$\frac{p^g L_r}{b} = f_t, \quad (2.1)$$

where f_t is the tension strength of the material.

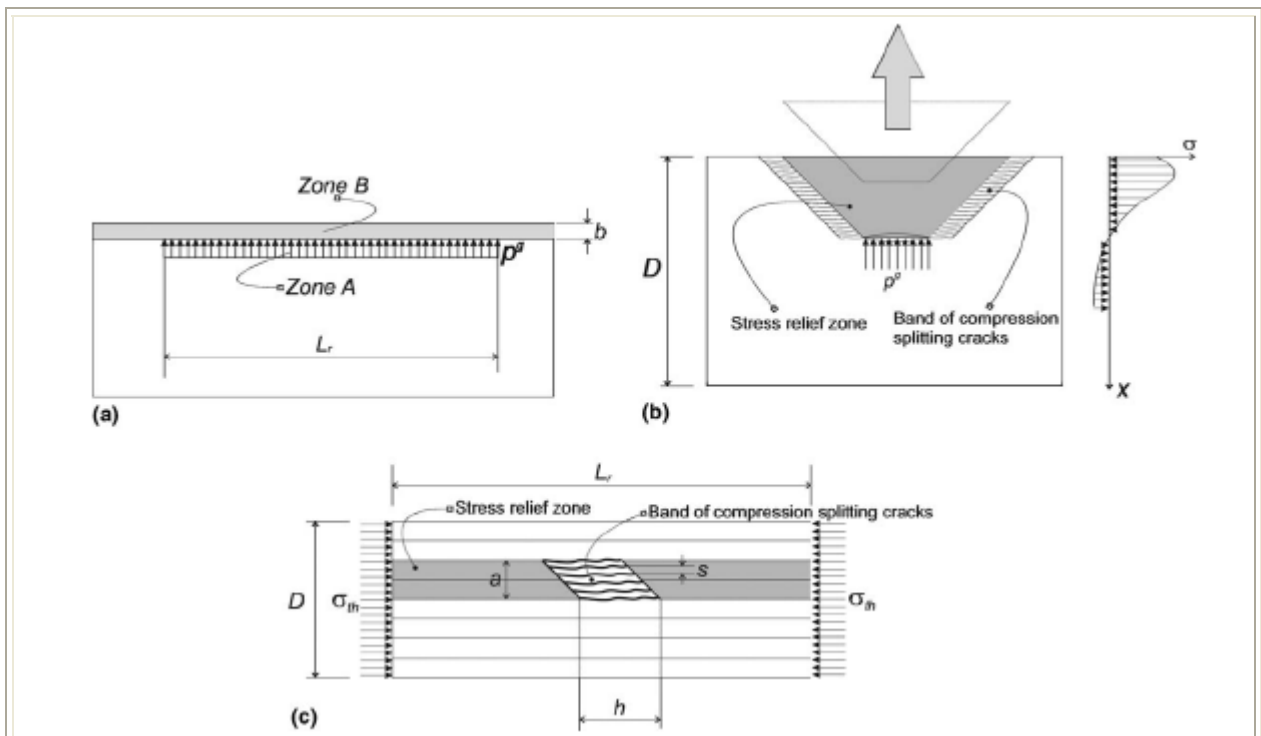


Figure 2-7. Possible mechanism of Thermal Spalling based on pressure-shear model or buckling model (a), parallel axial splitting cracks propagation model (b), band of compression splitting cracks with tensile transverse stresses model (c) [31].

It is necessary to underline that despite of its simplicity, this model presents however some intrinsic difficulties related to the definition of the characteristic parameters L_r and b , the ‘a priori’ determination of which is a non-trivial problem.

2.1.4.1.2 BUCKLING MODEL CONSIDERING GAS PRESSURE

This spalling criterion is based on the hypothesis of buckling of the zone B (see figure 2-7.a), which is initially delaminated from the rest of the structure [35]. The idea is rather simple for the 2D case. The zone B, close to the heated surface, is supposed to be a beam of length L_r and thickness b , simply supported at its ends and subjected to a compressive load due to thermal

stresses and to a lateral pressure exerted by the gas (from the zone A). This pressure causes a lateral deflection enhancing the buckling failure of the beam. Let us denote σ_{th} the mean (compressive) thermal stress in the beam and σ_E the critical buckling stress according to Euler's formula for columns.

Spalling will occur if

$$\sigma_{th} = \sigma_E = \frac{\pi^2 \cdot E}{12} \cdot \left(\frac{b}{L_r}\right)^2, \quad (2.2)$$

This equation is a rather rough approximation and does not take into account the bending contribution due to the gas pressure.

A slightly more sophisticated model can be proposed, which takes also into account the applied gas pressure. Again, the zone B (figure 2-7.a) is supposed to be a simply supported beam, but loaded by a uniform pressure p^g . The linear maximum deflection is then

$$w_0 = \frac{5}{12} \cdot \frac{p^g}{E} \cdot \left(\frac{L_r}{b}\right)^3 \cdot L_r, \quad (2.3)$$

This initial deflection will increase due to the applied compressive thermal stress, σ_{th} . The deflection produces a bending stress which adds to the compressive stress and can lead to failure on one of the beam sides. The first failure mode is a tensile failure supposed to occur if the bending stress σ_b on the tensile side is equal to compressive thermal stress σ_{th} . Another failure mode is a compressive one which occurs if the sum of the compressive bending stress and thermal stress is equal to the compressive strength of the material. The deflection due to the application of the σ_{th} stress to the beam, initially bent, is equal to

$$w = \frac{w_0}{1 - \frac{\sigma_{th}}{\sigma_E}}, \quad (2.4)$$

and the stress due to this bending displacement is given by

$$\sigma_b = 6 \cdot \sigma_{th} \cdot \frac{w}{b}, \quad (2.5)$$

In the case of tensile failure, the zero stress on the external (heated) side is obtained when $\sigma_b = \sigma_{th}$, which leads to a sort of critical value for the gas pressure given by the following relation:

$$p^g = \frac{16}{15} \cdot E \cdot \left(\frac{b}{L_r}\right)^4 \cdot \left(1 - \frac{\sigma_{th}}{\sigma_E}\right), \quad (2.6)$$

We can describe now the compressive failure. It is obtained when the compressive stress on the internal side of the compressed zone reaches the compressive strength, f_c :

$$\sigma_{th} + \sigma_b = \sigma_{th} \cdot \left(1 + 6 \cdot \frac{w}{b}\right) = f_c, \quad (2.7)$$

Using equations (2.3) and (2.4) one obtains a new definition of the 'critical' value of gas pressure:

$$p^g = \frac{64}{5\pi^2} \cdot (\sigma_E - \sigma_{th}) \cdot \left(\frac{f_c}{\sigma_{th}} - 1\right) \cdot \left(\frac{b}{L_r}\right)^2, \quad (2.8)$$

One can observe that equation (2.8) is more conservative than equation (2.6).

2.1.4.1.3 SIMPLIFIED FRACTURE MECHANICS MODEL

This hypothesis is based on fracture mechanics. The main mechanism of compressive failure is the sideways propagation of a band of parallel axial splitting cracks. Such a kind of mechanism can lead to a sudden release of the stored elastic energy and to a modification of the original stress field [36,37]. In this particular case the compressive stresses derive directly from thermal fields and the released energy is related to constrained thermal dilatation.

At a certain moment of compressive loading due to thermal stresses, axial cracks forming a band (see figure 2-7.b) appear and the micro-slabs between them behave like beams with the correlated problems of buckling.

Taking into account the initial normal stress (before any fracturing) in the cross-sections, the critical stress for the microslab buckling from Euler's equation, and finally, the energy density associated with the post-buckling deflections, it is possible to calculate the variation of strain energy density in the micro-slabs and to define an energy balance criterion of fracture mechanics by means of fracture energy.

In this context, by applying this approach to heated concrete structures, it is possible to explain why the high strength concrete exhibits a more pronounced tendency to explosive spalling than ordinary concrete. This could be due to the higher brittleness of such high performance concretes.

Observing that the tensile transverse stresses usually are not negligible, a modification of this model for compressive failure can be introduced [37]. This case is similar to that of failure under shear loading. The failure mechanism is formed by the development of two different systems of cracks: compression splitting cracks, likewise to those previously presented, and parallel cracks in the direction of compression due to the transverse tensile stresses, figure 2-7.c. The global behaviour of the concrete element at macro-scale is similar to an orthotropic material. The zone affected by the energy released due to the propagation of axial splitting micro-cracks, and consequently by a relaxation of stresses, is practically a strip between parallel tensile cracks, figure 2-7.c.

The energy released from this strip, ΔU , equals

$$\Delta U = \int_V \delta U dV; \Delta U = \frac{\sigma_{th}^2}{2 \cdot E} \cdot B \cdot a \cdot L_r, \quad (2.9)$$

where δU is the energy density, V is the volume of the stress relief zone and σ_{th} are the compressive thermal stresses.

The mechanical energy dissipated by the band of axial splitting micro-cracks is $W_f = \frac{G_f B h a}{s}$ (G_f is the fracture energy), so the energy balance during the fracture processes can be expressed as $\frac{\partial W_f}{\partial a} = -\frac{\partial \Delta U}{\partial a}$, which leads to the following criterion:

$$\frac{\sigma_{th}^2}{2 \cdot E} \cdot L_r = G_f \cdot \frac{h}{s}, \quad (2.10)$$

which clearly shows a size effect [37].

During heating of real concrete structures the situation is slightly more complex, as pointed out for example by Bazant [36]. Nevertheless, despite of some differences, it is still possible to model it, in a simplified way, by means of the model described above.

2.1.4.2 PRACTICAL EVALUATION OF THE THERMAL SPALLING RISK

In the previous subsection we have briefly presented three criteria, based on different hypotheses concerning mechanisms leading to destruction of concrete elements at high temperature. Below are described some quantitative parameters developed [31] based on them, called in the following spalling indexes, which can be useful for evaluation of the thermal spalling risk.

As mentioned previously, there are some geometrical parameters necessary to apply the spalling criteria introduced in paragraph 2.1.4.1 of this *Chapter*. Obviously, they are of crucial importance for the results of the spalling risk assessment, but unfortunately they cannot be predicted in advance, even if the material parameters and all details concerning boundary conditions are known. For this reason we shall assume these geometrical parameters in such a way that for each case the highest value of the calculated spalling index is equal to one. The indexes so introduced will give us a quantitative assessment of the spalling risk, with possible values from 0 to 1, but presumably they cannot be interpreted directly as the thermal spalling probability. The latter hypothesis would require a much vaster experimental validation.

The criterion (2.1) is based on the pressure-induced shear model with the L_r/b ratio as a geometrical parameter. The gas pressure difference between the current position and the surrounding air is $p^g - p_{atm}$. A condition necessary for the occurrence of this mode of rupture is the pre-existence of a macro-fracture at the b depth. The effect of cracks on the concrete strength properties is described in this model by the mechanical damage parameter, d , the higher value of which at a certain position favours fracturing there. Hence, the first spalling index, I_{s1} , is defined as follows:

$$I_{s1} = \frac{(p^g - p_{atm}) \cdot d}{\bar{f}_t} \cdot \left(\frac{L_r}{b} \right), \quad (2.11)$$

where \bar{f}_t is the averaged traction strength, while p^g and d are local values. In this section the over-bar means the value averaged along the distance between the current position and the heated surface, taking into account the considered geometry.

For the criterion (2.8), based on the buckling model considering gas pressure, the geometry is described by the $(L_r/b)^2$ ratio, which is also present in Euler's stress definition (2.2). Also for this rupture mode pre-existence of a macro-fracture is necessary, thus the second spalling index, I_{s2} , has the following form:

$$I_{s2} = \frac{5\pi^2}{64} \frac{(p^g - p_{atm}) \cdot d}{\left(\bar{\sigma}_E - \bar{\sigma}_{th} \right) \left(\frac{\bar{f}_c}{\bar{\sigma}_{th}} - 1 \right)} \cdot \left(\frac{L_r}{b} \right)^2, \quad (2.12)$$

where parameters $\bar{\sigma}_E$, $\bar{\sigma}_{th}$, \bar{f}_c are averaged from the heated surface to a given thickness, while p^g and d are local values at this position.

Geometry in the model (2.10), based on fracture mechanics, is characterized by the $L_r \cdot s/h$ ratio. Also for this mechanism, the pre-existence of several cracks parallel to the heated surface was assumed during the model development. The third spalling index, I_{s3} , deduced from the criterion (2.10) should consider this fact, so it is defined as:

$$I_{s3} = \left(\frac{\bar{\sigma}_{th}^2}{2E} \right) \cdot \frac{d}{G_f} \cdot \left(\frac{L_r \cdot s}{h} \right), \quad (2.13)$$

where the first term on the RHS, representing elastic energy, and \bar{G}_f are averaged over the distance from the heated surface to a given fracture position, while d is a local value of damage parameter at this position.

Finally, [31] introduced an ‘intuitive’ spalling index, I_{s4} , based on the analysis of physical phenomena during heating of concrete and leading to Thermal Spalling, as well as on the results of several experimental studies [1,11,25-33]. This criterion was formulated in such a way, that all factors favouring the material rupture were put in the numerator of a fraction defining the index, and those impeding the spalling were placed in its denominator. The developers [31] believed, that taking into account so many parameters, partly related one to another, but containing different data about the hygro-thermo-chemo-mechanical state of concrete, would generate a kind of ‘averaging’ effect and would allow us to predict thermal spalling in a reasonable way.

After analysis of the experimental data concerning the thermal spalling [1,25-33] and the discussion about its causes presented in [26], they have chosen the following factors favouring this phenomenon to be considered in the spalling index I_{s4} : high local values of gas overpressure, $p^g - p_{atm}$, and mechanical damage parameter, d , high values of averaged transversal traction stresses, $\bar{\sigma}_{th}$, and constrained elastic energy \bar{U} . The considered factors impeding thermal spalling are high average values of traction strength, \bar{f}_t , and specific fracture energy, \bar{G}_f , for the material layer between a current position and the heated surface. Additionally, to obtain a non-dimensional quantity, [31] introduced a reference pressure (assumed as equal to atmospheric pressure, p_{atm}) and a characteristic element dimension L (e.g. thickness for a wall, radius for a cylindrical specimen). In this approach, internal geometrical parameters involved are unknown and are jointly described by a scaling factor, C_s , which is a non-dimensional parameter. Therefore, the fourth spalling index selected herein, I_{s4} , is given by the following relation:

$$I_{s4} = \frac{\bar{\sigma}_{th} \cdot \bar{U} \cdot d}{\bar{f}_t \cdot \bar{G}_f} \cdot \frac{p^g - p_{atm}}{p_{atm}} \cdot L \cdot C_s, \quad (2.14)$$

where the values of $\bar{\sigma}_{th}$, d , \bar{U} , p^g and the temperatures at each position are obtained from Hitecosp software [1] and then averaged for the material layer between a current position and the heated surface.

Probably, it is possible to define a simpler form of this index, eliminating part of the physical quantities used in equation (2.14), whose effect on Thermal Spalling is similar. However, this would need much more experimental validation so here it is presented a spalling index considering possibly all factors affecting the development of this phenomenon.

Spalling indexes defined in equations (2.11) to (2.14) were tested [31] for the numerical results concerning the experiments done at NIST for a C-90 concrete exposed to the temperature of 450°C [25,26,31,33], test explained in greater detail in *Chapter 5* of this Thesis. These results were particularly suitable for this purpose because during this test all three cylindrical specimens of the concrete, called MIX 1, experienced Thermal Spalling at a thickness of about 2 cm from the heated surface.

During the test, heating rate was initially equal to 5 K/min and heating was stopped when the temperature in the centre of the specimen was within 10 K of the target temperature T , and the difference between the surface and centre temperatures of the concrete specimen was less than 10 K. For further details concerning the mix compositions and test procedures, see [25,26,31,33] and *Chapter 5*.

The evolutions of the I_{s1} and I_{s2} indexes, arisen from the calculations developed by the Hitecosp software [1,31] were very similar and they indicated the highest risk of spalling between 110 and 115 minutes of heating, and the thickness of ruptured concrete layer of 2.5–3.0 cm, figures 2-8.a and 2-8.b. Both indexes were based on the gas pressure and strength properties and they followed the changes of these quantities, indicating initially the highest risk of spalling for the specimen core and then gradually, due to cracking, also for the surface layer of about 2.0–2.5 cm thickness, where rupture actually was observed during the NIST experiments. Starting from 115 minutes the spalling risk, with regard to these criteria, was gradually decreasing.

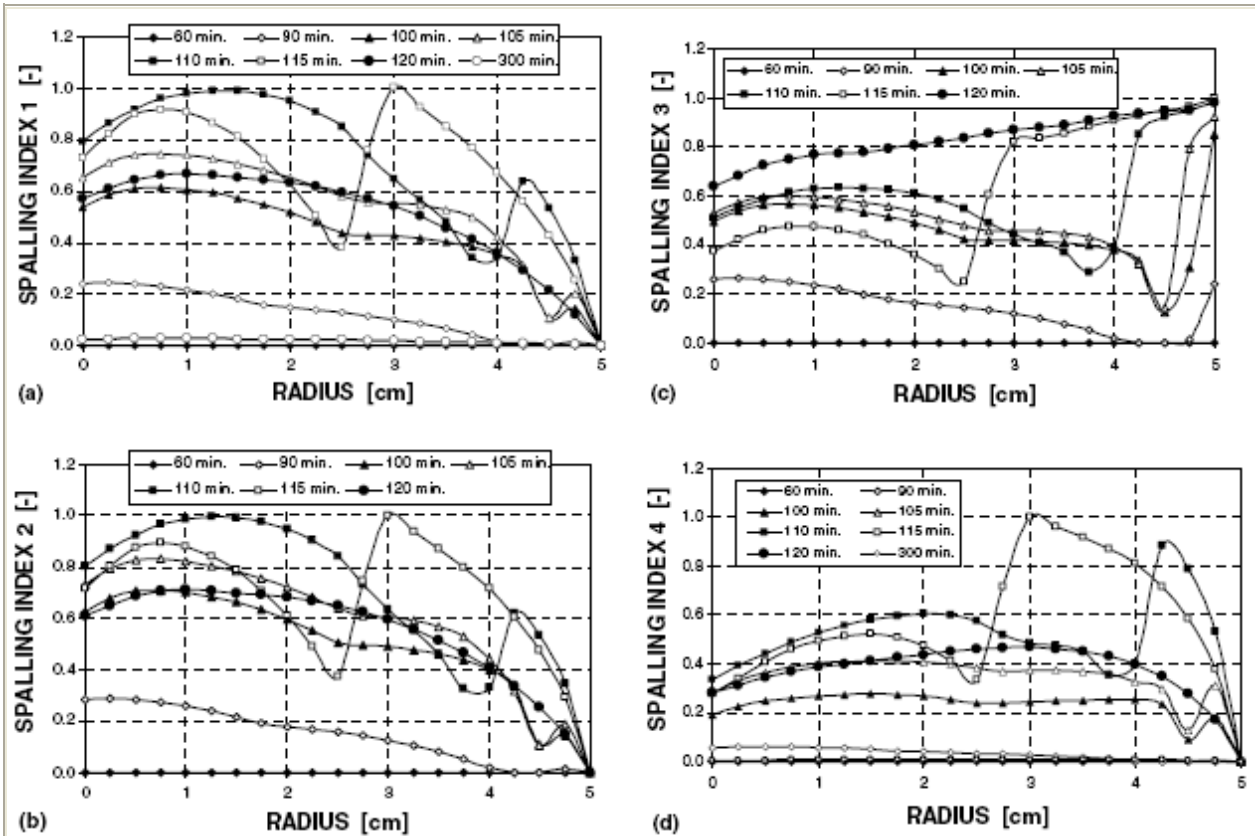


Figure 2-8. Radial distribution of spalling indexes according to: (a) eq. (2.11), (b) eq. (2.12), (c) eq. (2.13), (d) eq. (2.14) [31].

The I_{s3} index, based on fracture mechanics, had the highest values for the time interval from 100 min to 120 min, figure 2-8.c. It followed the front of mechanical damage moving from the surface towards the inner part of specimen. At time instant $t = 115$ min the higher level of the I_{s3} parameter includes the material layer of about 2-cm from the surface, i.e. the same as observed experimentally. However one should underline that in case of this index the exact position and the time instant of a possible concrete rupture are not precisely defined.

As it can be observed in figure 2-8.d, evolution of the spalling index I_{s4} indicated the highest risk of thermal spalling for the 2-cm surface layer of concrete after about 115 min of heating that was approximately at the time and position, when and where it actually occurred during the NIST tests. According to this index, based on several key factors affecting thermal spalling, including the gas pressure and specific fracture energy, only the surface zone was endangered by spalling between 110 and 120 min of heating.

A relatively good agreement of the spalling predictions with the experimental results, obtained by means of so different models of spalling mechanisms and the ‘intuitive’ criterion, based on the analysis of the physical phenomena involved, confirmed the practical usefulness of such an approach. Analyzing the results of simulations, and in particular the gas pressure, components of stresses, damages or elastic energy, it was rather difficult to deduce the exact

position of the concrete rupture. The time interval of possible spalling occurrence was more evident, taking into account the range of temperature (and corresponding time instants) when a rapid increase of mechanical damage can be observed. However, a proper combination of the simulation results, after some elaboration (e.g. calculation of the spalling indexes), allowed the spalling indexes' developers [31] to assess more precisely the Thermal Spalling risk, and first of all, an approximate thickness of concrete layer endangered by thermal spalling.

Unknown quantities, necessary for prediction of the spalling risk are geometrical parameters associated with any of the spalling mechanisms. [31] evaluated them, assuming that for each case the highest value of the spalling index equalled one and corresponded to the time instant when the material rupture had been predicted.

For the pressure induced shear criterion (2.11) it was obtained $L_r/b \cong 27,0$ and $L_r \cong 0,54\text{ m}$, what is an unrealistic value because the specimen had the height of 0,20 m only. This showed that the real rupture mechanism was rather different from that assumed by model (2.11), even if it gave reasonable predictions concerning the time interval and thickness of the layer exposed to spalling, see figure 2-8.a. This is probably due to the fact that the quantities in equation (2.11), i.e. \bar{f}_t , p^g and d , belong to key factors governing the thermal spalling.

For the criterion (2.8), based on the buckling model with considering gas pressure, the geometry is described by the $(L_r/b)^2$ ratio which appears also in the σ_E definition (2.2). Thus evaluation of the L_r/b ratio was possible only in an iterative way. Following such a procedure, the authors [31] obtained $L_r/b \cong 17,5$ and $L_r \cong 0,35\text{ m}$, and these values were used to obtain figure 2-8.b. The L_r value was greater than the specimen height and could not be considered as neither a realistic value nor the physical model which these calculations are based on. This criterion, similarly to the previous one, does not give a very precise prediction of the time instant and the position of concrete rupture.

Physical models assumed to define the indexes I_{s1} and I_{s2} take into account effect of gas pressure and degradation of strength properties, but not fracture energy. For a small specimen, as the analysed one, they can indicate high risk of spalling for the core part, where the pressure has the highest value. Such a situation corresponds to the so-called explosive spalling, when an explosion-like behaviour is observed. However, for larger elements, like for example a concrete wall analogous to that analyzed in *Chapters 4 and 6*, they will indicate an elevated spalling risk for a surface zone, where gas pressure and traction stresses perpendicular to the surface are the highest and material deteriorated, both thermo-chemically and mechanically. Such a situation corresponds to the case of the so-called surface spalling, including only a layer with thickness of 1.5–2.5 cm, but on a large area of the heated element surface.

In the model (2.10) based on fracture mechanics the geometry involved is characterized by the $L_r \cdot s/h$ ratio, which was evaluated as $L_r \cdot s/h \cong 0,0158$ (to scale the maximum I_{s3} value to 1.0). In this model one can expect that rupture length will be the same as the specimen height (as was also observed during the experimental tests [26]), i.e. $L_r = 0,2\text{ m}$. For this value, one obtains that $s/h \cong 0,079$. The physical model on which this criterion is based, not taking directly into account gas pressure, seems to correspond quite well to the so-called surface spalling, when a rupture of a surface layer, sometimes very violent, is observed. The criterion does not indicate precisely a possible position of the rupture, but rather a period of time when stored elastic energy has a particularly elevated level. This always concerns the surface layer, where thermally induced compressive stresses, parallel to heated surfaces are the highest.

The scaling factor involved in the 'intuitive criterion (2.14) was found to be equal to $C_s = 4,86$, assuming that the characteristic element dimension is $L = 0,05\text{ m}$ (i.e. the specimen radius).

This criterion is not based on any particular physical model, but on a general analysis of factors favouring and impeding thermal spalling, without associating with them any “weighting” factors (which can be also exponents), hence one can expect that it will be useful only as a general indicator of spalling risk. Surprisingly, this criterion, based on numerous key factor parameters influencing thermal spalling, including both the gas pressure and specific fracture energy, gave the most precise indications concerning the time and position of concrete rupture for the analysed case, in a good agreement with the NIST experiments. This shows that probably both the aforementioned parameters are involved in thermal spalling development, thus models omitting one of the two quantities, like for example I_{s1} , I_{s2} or I_{s3} , will not be able to give a realistic assessment of the risk of this phenomenon. This also suggests that explanations of the Thermal Spalling causes should consider rather a joint action of the pore pressure build-up and the elastic energy of constrained thermal dilatation strains, than indicate one of these factors as a decisive one.

Of course, one cannot expect that the geometrical (or scaling) parameters evaluated from the NIST tests’ results have a universal character and will be valid for any situation, because they depend on several factors, like for example the size and shape of a heated element, concrete composition, etc. Nevertheless, they can be useful as a first, rough approximation for analysis of Thermal Spalling risk in heated concrete elements, and in particular to determine the position of the main fracture, corresponding to the highest value of the spalling index. Having this value, it is also possible to perform a simplified analysis of fracture energy and stored elastic energy to determine if concrete spalling is energetically possible.

Hence, in sight of the results exposed in this paragraph related to the tests of the available spalling indexes, the fourth spalling index [31] called ‘intuitive’ or I_{s4} , based on the analysis of physical phenomena during heating of concrete and leading to Thermal Spalling, has been selected for the prediction of both the time and position of concrete rupture in the analyses developed in *Chapters 4 to 6* of this Thesis since, as just explained, it showed the best correlation against tests.

2.1.5 Factors Affecting Thermal Spalling

Spalling is influenced by a number of factors [7]: rapid heating, the heating profile, chemical composition of the cement, aggregate type, large compressive stresses, loading, restraint to thermal expansion, pore pressures as a result of moisture expanding on evaporation, and so on. The factors that affect spalling derived from the literature review carried out for this Chapter are discussed in the following sections and were all under consideration before defining the spalling nomograms presented in *Chapter 4 Spalling Nomograms*. Those factors finally selected for the latter are therefore more deeply introduced within *Chapter 4*.

2.1.5.1 MOISTURE CONTENT

Moisture content is one of the main factors influencing spalling. In the absence of moisture, the likelihood of explosive spalling is reduced [38]. However, explosive spalling due to thermal stress can still occur with no moisture in ceramic materials for instance [9]. Many researchers have shown that increasing moisture content increases the probability of spalling. Therefore, concretes in wet conditions (e.g. an external environment) will tend to spall faster and more extensively than a drier concrete. This is because the moisture increases the thermal conductivity and therefore the rate at which the concrete responds to heating and the rate of production of water vapour that builds up inside the concrete, which leads to earlier spalling [39].

It is commonly accepted that constructions of traditional concrete (normal weight, ordinary strength) with less than 3% moisture content by weight will not give rise to explosive spalling and that traditional concrete in the range of 3-4% moisture content has a limited risk of spalling

[40-43]. However, spalling has been observed in some limited instances at low moisture content (<3%) [44]. This is due, in the case of very dense High Strength Concretes, to the low porosity and permeability of such concrete, whereby even the release of chemically bound water can contribute significantly to pore pressures.

TEST REFERENCE	TEST SAMPLE	TEST CONDITIONS	SPALLING [MM]	MOISTURE CONTENT [%]	SIGNIFICANCE
Shuyttleworth (1997) [44]	C60, unstressed slab	2 hour ISO834 standard fire	5-20	2,1-2,9	Observed in 3 tests
Both (2000) [45]	C76-C86, prestressed	RWS fire curve	22-50	2,9-3	Observed in 2 tests
SINTEF (1992) [46]	HSC	Hydrocarbon fire	41	2,9	Observed in 1 test
Thomas and Webster (1953) [47]	C25-C30 columns	BS476 standard fire	Cracking and sloughing of corners	1,8-2,4	Observed in 11 tests

Table 2-3. Tests where spalling is observed in concretes with moisture contents <3% by weight [7].

The tests by [45]) and [46] were carried out on high strength concretes where the 3% rule of thumb is for normal strength concretes.

Sloughing off of concrete at the corners of the columns in the tests by [47] is caused by chemical deterioration of the cement paste and internal cracking of concrete due to the difference in thermal expansion between the aggregate and the cement paste. It is a gradual process and not thought to be as a result of moisture. The tests by [44] are significant in that spalling was observed in normal strength concrete at a moisture content of just over 2%. However, the amount of spalling during 2 hours of the standard fire was only 5-20 millimetres. From these tests there was only 1 instance where explosive spalling occurred in normal weight concrete at moisture contents below 3% by weight. The amount of spalling observed was 5-20 millimetres.

In some literature, the moisture content is expressed in terms of relative humidity of the concrete. Higher relative humidity levels lead to greater spalling. The acceptable relative humidity level of concrete to reduce the spalling risk is 75% [48].

Christiaanse et al. [49], studied the behaviour of 3 week old prestressed lightweight concrete double T-beams. Like [50], they concluded that the occurrence of spalling in heated concrete was related to a combination of compressive stresses and moisture content.

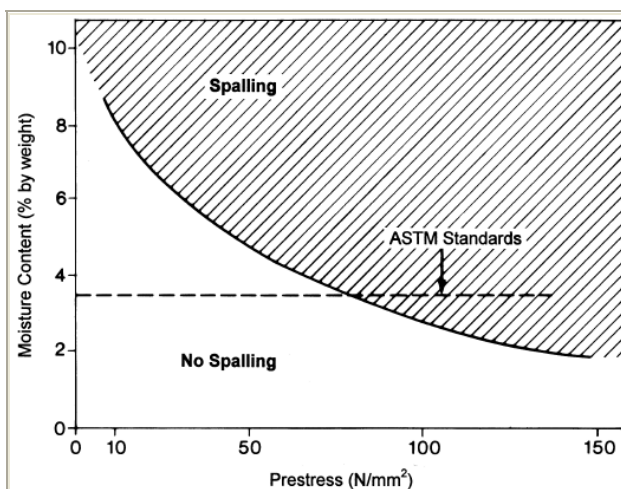


Figure 2-9. Explosive spalling envelope after [49]

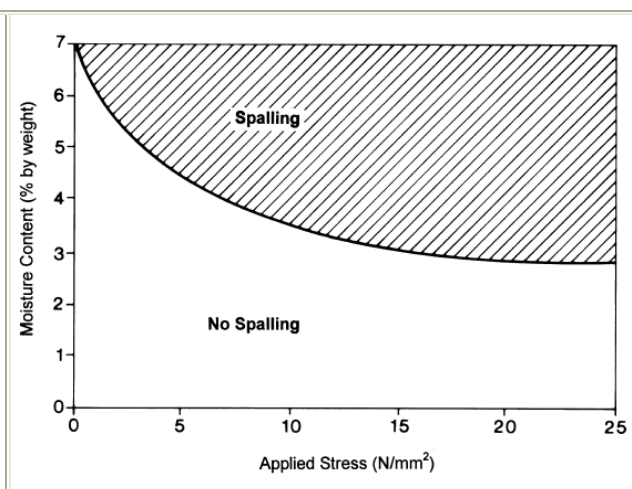


Figure 2-10. Explosive spalling envelope after [28]

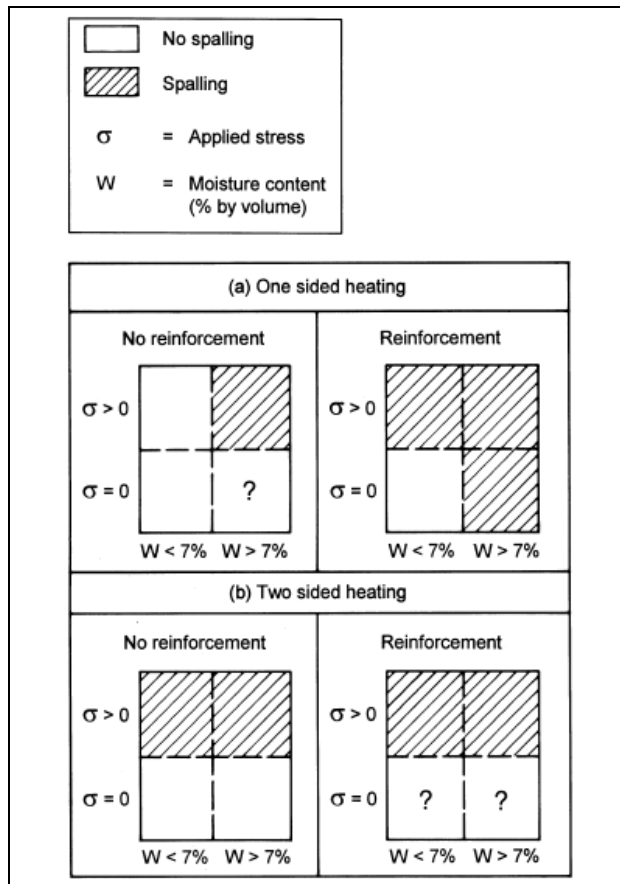


Figure 2-11. Explosive spalling envelope after [51]

They produced a chart (figure 2-9) for the design of prestressed concrete against spalling which gives the relationship between levels of prestress and moisture content and their combinations that are likely to cause spalling. [49] encountered spalling at similar moisture contents and stresses to [50] and concluded that spalling was not possible for concretes with moisture contents less than 4% by weight.

Zhukov [28] observed an increased tendency of concretes with higher moisture contents to spall. He produced a spalling envelope (figure 2-10) similar to that of [49] which indicated that spalling will not occur for moisture contents below 3% by weight.

Copier [51] concluded that moisture content is the most important factor in the determination of the likelihood of spalling. Other important factors include the presence of reinforcement and compressive stress. The actual amount of reinforcement or the magnitude of the stresses is of lesser importance (figure 2-11).

2.1.5.2 WATER/CEMENT RATIO, PERMEABILITY

Cement paste with a low water cement ratio, produces a dense almost impervious microstructure [52], which keeps the moisture vapour from escaping in a high temperature environment. This can lead to a build up of high internal pore pressure in the cement paste. Consequently the concrete is more likely to explosively spall, and to experience multiple spalling.

High strength concrete normally has a low water/cement ratio, therefore is more likely to spall when compared to normal strength concrete. Permeability is especially important in fires of high heating rate, such as hydrocarbon fires because the low permeability will trap moisture and pressure will build up rapidly under rapid heating causing spalling.

It has been suggested that spalling is unlikely to occur if the permeability of the concrete is greater than about $5 \cdot 10^{-11} \text{ cm}^2$ [27]. Concrete of higher quality generally possesses higher density and therefore offers higher resistance to flow.

A deeper introduction to the concrete intrinsic permeability is included in paragraph 4.3.2.2 of Chapter 4.

2.1.5.3 HEATING CONDITION

The heating condition is also one of the major factors influencing spalling. Spalling is much more severe in fires characterized by fast heating rates or high fire intensities due to the large temperature increase and moisture gradient in the fire-exposed parts [48]. Hydrocarbon fires pose a severe threat in this regard. Explosive spalling seems to be the dominant spalling form in a hydrocarbon type fire [53].

In addition, heating of more than one side of a concrete section (e.g. 4 sides of a column) increases the probability of spalling [38,39,54].

2.1.5.4 AGGREGATES

For normal weight concrete, there are two common aggregate groups: siliceous aggregates such as quartzite, gravel, granite and flint; calcareous aggregates such as limestone, dolomite and anorthosite. It is widely found that siliceous aggregates give the poorest resistance to spalling [41]. Flint aggregate is particularly susceptible [55]. This can be explained partly as a result of the markedly different coefficients of thermal expansion between aggregate and cement paste, particularly at higher temperatures, and partly the result of a volume increase phase transformation (at approximately 570°C) from a-quartz to b-quartz (see database). Expansion of the aggregates leads to cracks in the concrete or splitting of the aggregate which contribute to spalling.

Calcareous aggregates tend to give good fire performance [41]. There are several reasons to explain the improved resistance to spalling. First, the calcareous aggregates typically have a lower coefficient of thermal expansion than siliceous aggregates and they are closer to that of cement paste, producing lower internal stresses on heating. Secondly, there are no solid state phase changes in calcareous aggregates within fire exposure conditions.

On heating to temperatures in excess of 660°C calcium carbonates begin to break down, similarly above 740°C for magnesium carbonates. On breaking down the minerals release carbon dioxide and heat transfer is claimed to slow down despite the reaction being endothermic. The residual aggregate particles also have lower thermal conductivity, further reducing heat transfer into the concrete. During cooling the carbonates, which have broken down during heating, re-hydrate. This re-hydration reaction is believed to cause post-cooling spalling in calcareous aggregate concretes [9].

Design guidance on cover and thickness of section based on the standard BS 476 fire exposure is purely empirical and has changed at regular periods since the late 1940s as more tests were carried out. Before 1972 the beneficial effects of calcareous aggregates were represented by the code CP110. As a result of tests reported in a National Building Studies report where any benefit of calcareous aggregate was not observed the 1972 code omitted design guidance specific to calcareous aggregate. This has not changed in modern tabulated design guidance for cover and section thickness (BS 8110 Part 2).

Connolly [11] found that increasing the aggregate size promoted explosive spalling, thus supporting the earlier conclusions of Malhotra [10].

2.1.5.5 TEST CONDITION

Concrete is usually tested at high temperatures in sealed or unsealed conditions, in which the unsealed test condition is closer to reality with respect to a concrete building in a fire. In an unsealed test, vapour can escape from the concrete surface. In a sealed test, water vapour and pore pressure gradient at the fire exposed surface equal 0 [56]. Figure 2-12 illustrates the difference between sealed and unsealed test conditions. The primary difference is that moisture can escape towards the fire in an unsealed test but is forced to migrate through the concrete in a sealed test.

A sealed test is commonly carried out to test concrete pressure vessels used in the nuclear industry where there is a barrier between the concrete and the heating regime preventing moisture escaping towards the heat source.

The dominant process for unsealed concrete relates to the loss of the various forms of water (free, absorbed and chemically bound), while the dominant process in sealed concrete relates to hydrothermal chemical reactions [57].

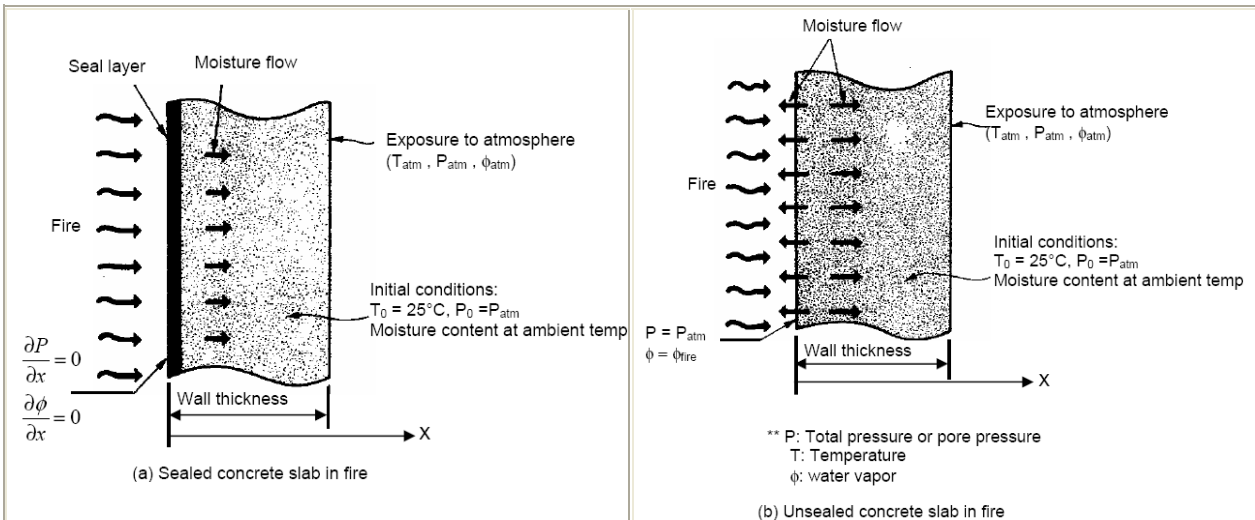


Figure 2-12. Sealed versus unsealed tests conditions [56]

A mathematical model, simulating the heat and mass transfer in concrete structures under fire [56], has shown that in both sealed and unsealed test conditions, the pore pressure builds up rapidly across the drying region of the concrete section as a result of high heat flux from the fire and low mass transport capacity of the heated concrete during the developing period of fire exposure. Consequently, spalling of concrete is expected in the early stages of the fire (typically the first 20 minutes) when the pore pressure exceeds the ultimate tensile strength of the concrete. Pore pressure then reaches a constant or dissipates during the steady state and cooling phase of the fire. Similarly spalling as a result of thermal expansion will reduce because the temperature change slows down in the steady state phase.

2.1.5.6 CONCRETE STRENGTH

Spalling in part is attributed to the build up of pore pressure during heating. High strength concrete is more susceptible to this pressure build up, because of its low permeability, which inhibits the escape of water vapour, compared to that of normal strength concrete. Available information [48] shows that concrete with strengths higher than 55MPa are more susceptible to spalling and may result in lower fire resistance.

In normal strength concrete, the vapour can be transported much more easily to the unexposed surface reducing the risk of spalling.

There can be significant variations between the design strength specified for a particular concrete and the actual strength achieved on site. Indeed 95% of the concrete samples tested on site should achieve strength greater than the design strength. The variation in strength could be up to 20% or more.

However, concrete mixed on site that has a higher strength than its design strength is not the same as high performance concrete with silica fume and very low permeability, which is very susceptible to spalling.

Ironically, poor quality concrete is superior to good concrete in spalling. Concrete that is classed as “high performance” at room temperature – because of its high strength, low permeability and consequently good durability – is in fact a “low performance” concrete at high temperature because of the increased susceptibility to spalling(62,66,63). Higher strength is achieved by reducing the water/cement ratio. In recent years, this was augmented by the use of

silica-fume which produced a dense concrete of very low permeability. Silica-fume concrete (not used in the reactors) has a high susceptibility to explosive spalling even at low heating rates. However, in general, reducing the w/c ratio would enhance pore pressure spalling (via lower permeability) but reduce thermal stress spalling (via higher strength).

2.1.5.7 SECTION SIZE

Section size is also an important factor affecting spalling – with thick members the probability of spalling decreases –. [8] concluded that beams of 200 millimetres or greater are less likely to suffer serious spalling. A design nomogram in EC2 [43] suggests spalling is unlikely for members with section size >200 millimetres.

Most variables that affect spalling are inter-related. Test results [8] show that explosive spalling is unlikely to occur if the moisture content of concrete is below 2,5% by weight and the concrete section not less than 80mm thick. For specimens about 120 millimetres in thickness, the moisture content can be as high as 4.5% before spalling occurs.

2.1.5.8 APPLIED LOAD

High compressive stresses due to external loading or prestressing in the concrete layer exposed to heating increase the probability of explosive spalling, because they induce restraint, and spalling occurs as a result of increasing stress as the concrete expands.

Normally explosive spalling is unlikely to occur for thick concrete members [38,43] with low moisture content [57] under small load and the standard fire.

The 1982 revision of the FIP/CEB recommendations [61] suggest that compressive stresses should be limited. An increase in compressive stress, either by reduction in section size or an increase in loading, encourages explosive spalling. The initial compressive stress in the exposed layer of concrete may not by itself promote spalling. However, high compressive stresses – caused by restraint to thermal expansion – develop when the rate of heating is such that the stresses cannot be relieved by creep quickly enough. Combinations of compressive stresses (above 2 N/mm²) and moisture contents (above 3,3% by weight) make the occurrence of spalling likely in a fire.

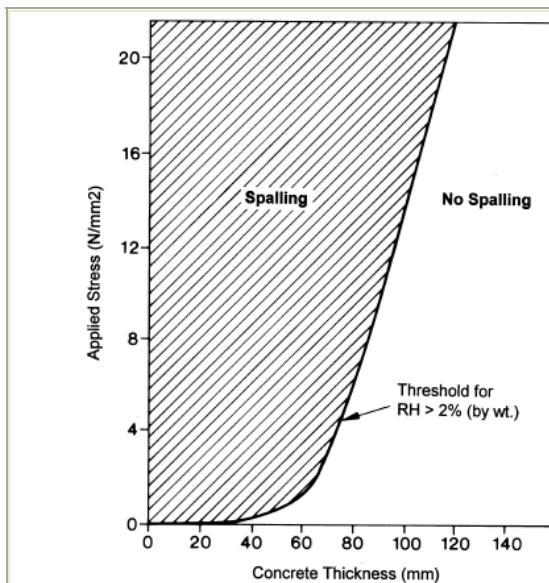


Figure 2-13. Explosive spalling nomogram by [50]

(This diagrams omits to show that spalling is significantly reduced for very small sections (few millimetres) because of rapid moisture loss)

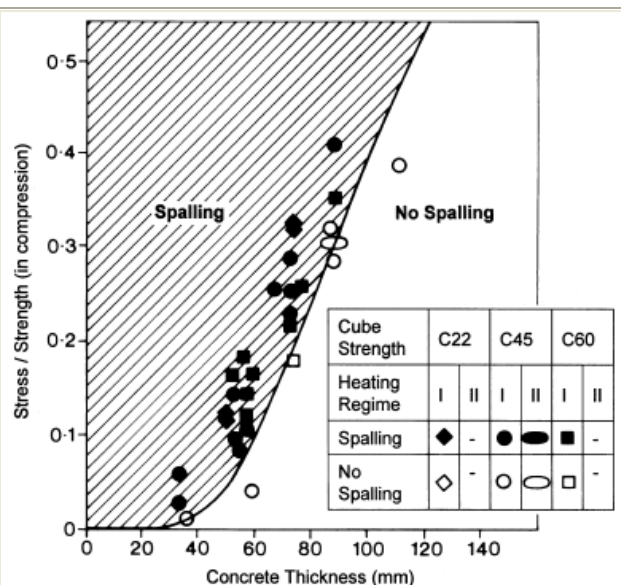


Figure 2-14. Improved explosive spalling nomogram by [62]

Meyer-Ottens [50] produced a nomogram for the prediction of spalling, which considers the member thickness and the applied compressive stress. The nomogram, shown in figure 2-13, is widely used in codes of practice for the fire design of concrete structures, e.g. [43]. Figure 2-13 was derived from tests carried out on concrete specimens with a cube strength of 45 N/mm².

Sertmehemetoglu [62] increased the applicability of figure 2-13 by plotting the spalling envelope of member thickness against the ratio of the applied compressive stresses to compressive strength, as presented in figure 2-14. The compressive stresses considered in this nomogram were generated by pre-stressing as opposed to some form of end restraint.

2.1.5.9 RESTRAINT

Restraint can hinder thermal expansion and give rise to thermal stresses [40]. Normal strength concrete showed higher levels of spalling when tested under restraint and the standard fire [63]. Restraint to structural members includes restraint to thermal expansion as well as thermal gradient. Restraint may be beneficial to a bowing beam under thermal gradient because the tension, experienced on the underside as a result of bending under imposed loading, is reduced by the beam expanding against restraints, closing any tension cracks.

A restrained column exposed on 4 sides will attract more compression as it tries to expand resulting in stress induced spalling.

A wall will generally experience fire on one side only therefore will bow towards the fire if it is restrained around its edges.

From a practical point of view, all structural members can be regarded as being restrained at some level by adjacent cold structure. A slab or beam with free ends in a standard furnace test are the only elements, which could be considered to be unrestrained.

2.1.5.10 THERMAL EXPANSION

The thermal expansion of the heated surface region is restrained by the cooler inner concrete. This imposes a compressive stresses upon the surface region. The expansion of a concrete, therefore, gives a measure of its likelihood to experience explosive spalling by thermal stress. Concrete that has its thermal expansion restrained is more likely to spall. By corollary, concrete with a low thermal expansion is less likely to spall [20].

Aggregates contribute to explosive spalling through their thermal expansion. Compressive stresses at the heated surface would be greater in concretes containing a high thermal expansion aggregate (e.g. gravel, siliceous) compared with concretes containing a low thermal expansion aggregate (e.g. basalt, lightweight).

2.1.5.11 REINFORCEMENT

The presence of reinforcement in concrete will generally improve the spalling resistance of a concrete section because it halts or delays the development of spalling at the line of the reinforcement. Meyers-Ottens [22] believes that differential expansion of reinforcement and the surrounding concrete causes cracking and contributes to spalling. There is no evidence from other work to prove this conclusion. Moreover the thermal expansion coefficient of normal weight concrete and steel is of the same order ($\sim 10 \cdot 10^{-6}$). Spalling as a result of cracking is only likely to be the case if % reinforcement is high and densely packed in which case cracks may develop in the concrete at ambient because the concrete lacks continuity around the rebar.

Copier [51], however, concluded that the actual amount of reinforcement less important than the moisture content in influencing explosive spalling (figure 2-11)

The presence or absence of reinforcement was found to be a more important factor in spalling than the quantity of reinforcement [64]. However, congestion of steel bars or tendons, with only small spaces between them is considered to induce the formation of cracks, and may therefore promote spalling.

The main reinforcement should not be located only in the corners since corners heat quicker than flat surfaces. So far as is practicable, only nominal reinforcing bars should be placed in the corners, the principal steel being located farther inwards [21,22]. Tests have shown that spalling is most severe in corners if no corner reinforcement is provided [21].

2.1.5.12 COVER

For normal strength concrete, explosive spalling can often be restricted to the unreinforced part of the section and usually does not proceed beyond a reinforcing layer. Therefore it is believed that the greater the depth of cover, the greater the risk of spalling [41]. Standard fire tests [65] have shown that spalling of limestone aggregate concrete was not observed for covers of up to 50 millimetres within 2 hours of a standard fire. Spalling in gravel aggregate concrete ribs with covers to the main reinforcement of 35 millimetres or less is not serious for up to two hours in a standard fire test. Significant spalling may occur with increased covers.

However BS 8110 Part 2 recommends that additional spalling measures should be taken for cover thickness greater than 40 millimetres for normal weight concretes exposed to the standard fire. Concrete cover thicknesses of 15 millimetres or less seem less prone to serious spalling, probably because the mass of unsupported concrete is not large [10]. Thicker covers spall more easily, and once spalling occurs and reinforcement is exposed, further behaviour is independent of the original cover.

Sanjayan and Stocks [59] varied the depth of cover (25, 50 and 75 millimetres) to the steel reinforcement over the length of 2500 x 1200 millimetres concrete T-beams exposed to standard ISO 834:1987 fire. Spalling occurred in the area of the flange with 75 millimetres cover. However, no firm conclusions may be drawn regarding the importance of cover depth, as spalling did not take place on the web, which also had 75 millimetres cover. The absence of spalling could be due to increased cracking on the lower face of the web due to deformation.

2.1.5.13 FIBRES

Tests [44,45,54] have shown that adding polypropylene fibres to the concrete mix is an effective method of reducing explosive spalling. Under relatively low temperatures, the polypropylene fibres melt, leaving a randomly orientated net of channels inside the concrete which help the high pressure vapour to escape and relieve the pressure inside the concrete, thus avoiding explosions.

Polypropylene fibres are usually used in high strength concrete to improve its permeability. For normal strength concrete, they are rarely used [44,48,57]. However this is probably because the concept of spalling is not explicitly considered as the norm in design.

Adding steel fibres in concrete has no obvious effect on improving the spalling resistance of concrete [44,58]. [58] found that the addition of a steel fibre mesh reinforcement did not eliminate the explosions in very dense (almost 2,700 kg/m³ & 60-180 N/mm²) silica-fume concrete cylinders (100 x 200 millimetres) subject to heating at a rate of 1°C per minute. In fact the increase in tensile strength produced a more violent explosion because of the sudden release of a greater amount of energy.

2.1.5.14 DENSITY

The density of a specific concrete depends upon the aggregate used and the water/cement ratio. For more details, see for instance Table 4-14 in *Chapter 4*.

High strength concrete is densified by the addition of silica fume and as a result has very low water/cement ratio and permeability, therefore this increases the risk of spalling (a deeper introduction to the concrete intrinsic permeability is included in paragraph 4.3.2.2 of *Chapter 4*).

There is no evidence in the literature to suggest that variations in the density of normal weight, ordinary strength concrete have an effect on spalling.

2.1.5.15 CONDUCTIVITY

High thermal conductivity results in higher concrete temperatures, therefore it can be assumed that it increases the spalling risk. Conductivity increases with an increase in moisture content which in turn increases the susceptibility of concrete to spalling. For more details, see for instance Table 4-25 in *Chapter 4*.

2.1.5.16 SPECIFIC HEAT

There is no information about the effect of specific heat on spalling in the published literature. For more details on specific heat at high temperatures, see for instance Table 4-26 in *Chapter 4*.

2.1.5.17 CRACKING

Internal cracking has a dual and opposite effect upon explosive spalling. While micro-cracks facilitate the escape of moisture during heating and thus relieve pore pressures, they also facilitate the process of spalling by providing a source for crack propagation.

Internal cracking in combination with pore pressure and compression in the exposed surface region (figure 2-6) is generally required to cause explosive spalling [64,10]. Cracks develop parallel to the surface when the sum of the stresses exceeds the tensile strength of the material. This is accompanied by a sudden release of energy and a violent failure of the heated surface region.

Micro-cracking is present in all concrete at ambient temperatures resulting from drying shrinkage and/or flexural loading. Additional cracking can be caused by thermal incompatibility between the concrete and steel reinforcement as well as between the aggregate and cement paste.

2.1.5.18 AIR-ENTRAINMENT

Specimens containing 10 millimetres gravel and 0,125% by weight of an air-entraining agent were completely free of spalling regardless of the heating regime [11]. The addition of the agent had the effect of reducing the moisture content and increasing the absorption value. In effect, it reduced the pore saturation thus alleviating pore pressures. It should be noted, however, that air-entrainment can reduce the strength of the concrete and, for this reason, some pre-cast concrete manufacturer who aim for high strength may prefer to use the Polypropylene fibres.

2.1.5.19 SUMMARY TABLES OF THE MAIN FACTORS AFFECTING SPALLING

Table 2-4 shows a summary (based on [7]) of what has been exposed within the previous subparagraphs related to the main factors affecting spalling, their condition to increase spalling, the evidence in literature and the conflicting evidences founding literature.

Factor	Condition to increase spalling	Evidence in literature	Conflicting evidence in literature
Moisture content	High moisture content	<3% by weight then spalling unlikely [8,40,41,57,66,67]	Spalling has been observed in some limited instants at low moisture contents [44]
Water/Cement ratio (permeability, porosity)	Low w/c	Low w/c cause spalling, but no specific value is given in the literature [41,57]	
Heating condition	Rapid heating e.g. hydrocarbon fire Fire exposure on > 1 side	Rate of heating has a significant effect on the amount of spalling [8,38,41,53,68]. Spalling is more likely if fire exposure is on more than one side [8,38,54].	
Aggregate	Calcareous – low spalling Siliceous – high spalling	Spalling less likely if a limestone aggregate is used [41,58]. Flint and river gravel increase spalling risk [38,54,57]	Limestone concretes do not always behave better. CTRL tests show no significant difference in spalling between limestone and granite concrete [45].
Test condition	Sealed (water cannot escape) – low spalling Unsealed (fire case) – high spalling	Sealed conditions limit spalling [56].	Unsealed conditions are better for spalling resistance [57].
Concrete Strength	High strength	>55 MPa can be considered high strength and therefore a higher risk for spalling [48].	Design strengths are often exceeded on site. The mean strength may be up to 20% greater. 95% of results must be greater than the design strength.
Section size	Less than 200mm thick	If section is thin then water escapes from unexposed face. If section is thick (>200mm) then spalling is less likely. Most susceptible sections are those in the mid-range between thin and thick. [8,43]	
Applied load	High compressive stress	High compressive strength in the concrete layer exposed to fire increase the probability of spalling [8,38,43,57]	Bending of a beam may improve spalling resistance because the beam is in tension on its underside and thermal expansion as a result of fire will reduce tension and associated cracking.
Restraint	Restraint	Normal strength concrete showed higher levels of spalling when tested under restraint and the standard fire [40,63].	
Thermal expansion	High expansion coefficient	High thermal expansion increases the risk of spalling.	
Reinforcement	Steel in concrete with low thermal expansion	Reinforcement will generally halt spalling or at least delay it beyond the line of rebar.	Differential expansion between steel and concrete can promote spalling [22]
Cover	>40mm in NWC. <15mm in general.	Spalling of limestone aggregate concrete was not observed for covers of up to 50 millimetres within 2 hours of a standard fire [65]. Spalling in gravel aggregate concrete ribs with covers to the main reinforcement of 35 millimetres or less is not serious for up to two hours in a standard fire test.	Spalling occurred in the area of the flange of concrete T-beams with 75 mm cover [59]. However, no firm conclusions may be drawn regarding the importance of cover depth.
Fibres	No polypropylene fibres	Polypropylene fibres (normally in HSC) significantly reduce or prevents spalling [48,53,54,57].	Steel fibre used to improve the tensile capacity of concrete has no obvious effect on spalling [45].
Density	Density is related to permeability and porosity. If these are low spalling is likely.	Silica fume used in high strength concrete decreases the permeability and increases the density. This leads to high spalling [53]. The density range of NWC does not vary greatly therefore does not influence spalling of NWC.	
Conductivity	High conductivity results in faster heating of the concrete section thus more spalling.	Conductivity is greater if moisture content is higher [39]. If moisture content is high then spalling is more likely.	
Specific heat		No information available	

Table 2-4. Main factors affecting spalling (based on [7]).

2.1.6 Spalling Nomograms

Researchers have mixed conclusions about the most critical factors which define spalling. This is to be expected given the number of variables involved and their interdependency. Table 2-5 [7] is a summary of the key factors as suggested by various researchers. Each factor is either related to moisture and pore pressures or to stress. In general there is a split in thinking between those who believe that moisture content is the dominant factor and those who consider loading and thermal stress as a result of thermal expansion to be the dominant factor, matter that is worked out within *Chapter 4 – Spalling Nomograms*, being one of the original contributions of this Thesis.

Researcher	Main factor	Secondary factor
Saito (1965) [26]	Initial load + restraint to expansion + stress caused by frictional resistance in concrete	Vapour pressure
Harmathy (1965) [27]	Moisture clog	
Meyer-Ottens (1977) [22]	Vapour pressure enhanced by frictional resistance in concrete + initial load + restraint to expansion	Initial load + restraint to expansion + frictional resistance in concrete, reinforcement expansion
Sertmehmetoglu (1977) [62]	Moisture clog + internal cracks	Initial load
Akhtaruzzaman and Sullivan (1970) [69]	Vapour pressure	
Gutaferro (1966) [70]	Vapour pressure	Aggregate expansion
Copier (1977) [71]	Vapour pressure + initial load	

Table 2-5. The key factor affecting spalling according to literature– Stress of moisture content [7].

Spalling can be modelled explicitly using state of the art thermo-hydro-mechanical modelling techniques, which aim to consider all variables that lead to spalling including the build up of pore pressures as moisture evaporates from the concrete in a fire [1,2]. The individual components of the micro structure of the concrete material are all represented in this type of modelling, so it must very detailed ([2], *Chapter 3*). This level of accuracy has been still firmly in the research domain and still requiring significant validation until very recent developments validated against experimental tests [1,2].

Precisely, due to the level of uncertainty historically associated with the explicit approach, in [7] there was proposed the development of several risk categories for spalling, based on the significant factors and available test data. Hence, in sight of the findings of the literature review described in Tables 2-4 and 2-5, [7] assigned values of risk to each variable affecting spalling and creating the following tables 2-6 and 2-7 where the analyzed concrete is assigned a risk category and associated spalling rate:

Variable affecting Spalling	Risk Factor	Variable affecting Spalling	Risk Factor
Design Strength >55 MPa	Not quantified	Calcareous aggregate	1
Design Strength ≤55 MPa	1	No. of sides exposed >1	3
Hydrocarbon fire	5	No. of sides exposed =1	1
Standard fire (BS476)	1	Section size <200 mm	3
Moisture content >3%	5	Section size ≥200 mm	1
Moisture content ≤3%	1	Restrained	3
No reinforcement	3	Unrestrained	1
Reinforcement included	1	Thermal expansion ≥10·10 ⁻⁶	3
Cover ≥40 mm	3	Thermal expansion <10·10 ⁻⁶	1
Cover <40 mm	1	Loaded in compression	3
Siliceous aggregate	3	Unloaded	1

Table 2-6. Risk factors for each variable known to affect spalling of concrete [7].

Arriving to the definition of the following spalling categories and associated spalling levels:

Category	Risk of spalling	Value of Total Risk	Key factors
A	Very low	≤ 11	Ordinary Strength, NWC, Unloaded, Unrestrained, Standard fire exposure, Reinforced, moisture <3%, one side exposure.
B	Low	12-20	Ordinary Strength, NWC, restrained, Standard fire exposure. Significant number of key variables* likely to promote spalling.
C	Medium	21-28	Ordinary Strength, NWC, restrained, Standard hydrocarbon fire exposure. Small number of key variables* likely to promote spalling.
D	High	29-37	Ordinary Strength, NWC, restrained, Standard hydrocarbon fire exposure. Significant number of key variables* likely to promote spalling.
E	Very High	>37	High Strength (Design strength >55MPa), standard hydrocarbon fire exposure.

Table 2-7. Spalling categories and associated spalling levels (*key factors = properties of the concrete of the boundary conditions that are known to promote spalling e.g. aggregate type, section thickness, etc) [7].

However, the use of these risk categories showed several limitations, since the risk factors and risk categories exposed in tables 2-6 and 2-7 should only be used in the assessment of normal weight, ordinary strength concrete enclosures. The spalling risk associated with high strength concretes needs a more detailed investigation to adapt the risk categories and associated spalling rates accordingly, taking into account additional factors influencing significantly on the spalling risk such as the concrete intrinsic permeability.

Besides what has been exposed within this and the previous subparagraph, the author of this Thesis has found a huge lack of information within the available bibliography related to spalling nomograms addressed to evaluate the sensitivity of the hygro-thermo-chemo-mechanical processes involved on the High-Strength concretes behaviour under a natural fire to parameters such as the initial moisture content of concrete, its intrinsic permeability, the rate of temperature increase (fire intensity), the porosity, compressive strength, type of aggregate and, in general, the whole set of hygro-thermo-chemical properties of concrete, and the dimensions of the structural element.

Indeed, only an additional first definition of such nomograms has been described within the 5th Framework Programme of the European Union – Competitive and Sustainable Growth 2.006 Project called ‘*Qualified and validated procedure for spalling evaluation*’ [72]. In that technical report, a procedure for the preliminary definition of an abacus of spalling was presented. For this purpose, the mathematical-numerical model described in the *Chapter 3* of this Thesis [2] was used to analyze a case dealing with a given geometry (i.e. a wall 25 centimetres thick), a given material (i.e. C60, high performance concrete) and a set of boundary conditions corresponding to a heating featured by an ISO-fire profile and mixed convective-radiative heat exchange. The variables considered within that study for the sensitivity analysis were the saturation level and the intrinsic permeability.

Its final aim was to obtain a chart in the saturation degree-absolute permeability domain, in which it were possible to define some dangerous regions with respect to the spalling occurrence (see figure 2-15):

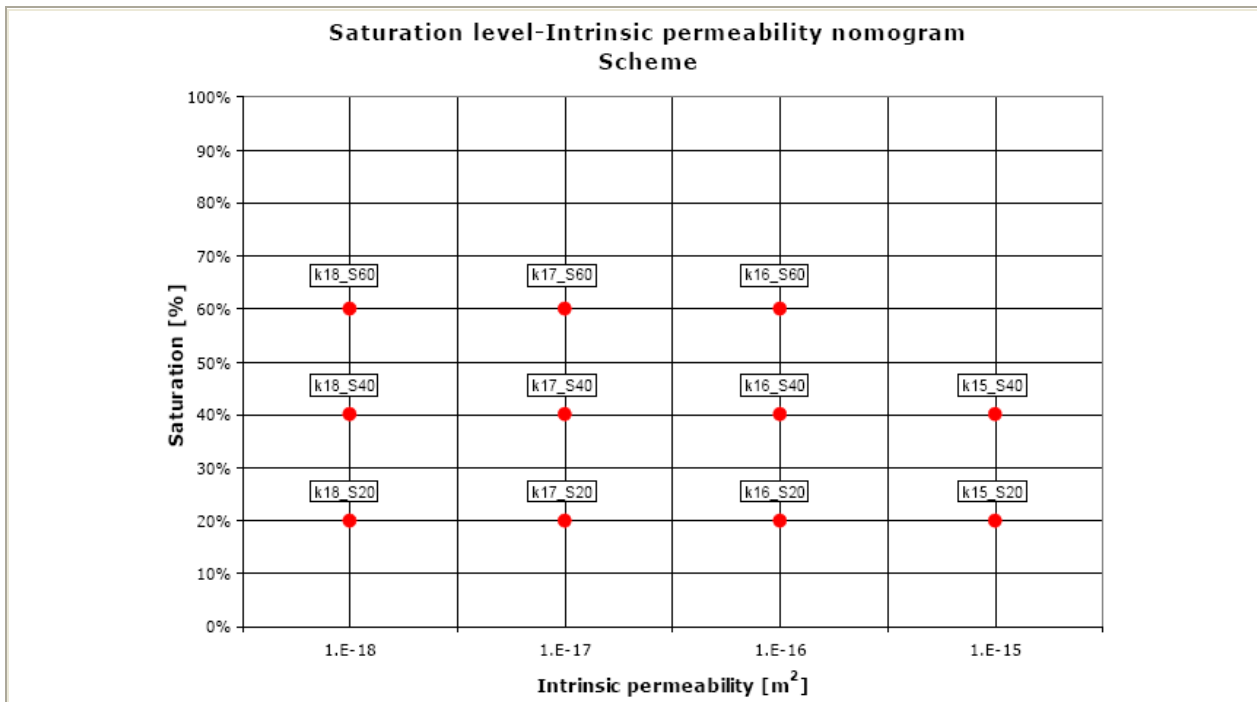


Figure 2-15. Saturation level – Intrinsic permeability scheme for the proposed abacus [72].

The spalling criterion proposed was less sophisticated than those presented in the previous paragraph, because of the lacking of any experimental data. Spalling depends on numerous factors, like geometry of structural elements, concrete properties, boundary and initial conditions, etc.. Similar criteria, for defining diagrams showing “area of the spalling risk”, have been already proposed in the past by several researchers, but most of them were formulated on an experimental basis only. The model presented in *Chapter 3*, was used for the analysis of hygro-thermochemical and mechanical behaviour of concrete at high temperature, to identify such a region of “spalling risk” in the case of a C60-concrete wall exposed to standard ISO-Fire conditions. The criterion adopted to assess spalling occurrence is rather simple: if the damage degree, temperature and vapour pressure are greater than several fixed thresholds, the material is in a critical situation and the spalling occurrence is likely. In particular we evaluate as “critical situation” in a certain point of a concrete structure if:

- ❖ Total damage level is greater than 30-50%,
- ❖ Temperature is comprised between $460 \pm 50K$,
- ❖ Vapour pressure peak is in the range 0,8-1,0 MPa.

The spalling criterion is therefore qualitative, since the previous thresholds are fixed in an empirical manner. On the base of these “limit conditions” it is possible to assess the so called “spalling time” and the thickness of the layer broken off. Both of the latter parameters (time of spalling and thickness) are of fundamental importance. A concrete structure, heated continuously for a long period, can show some sort of spalling. It is important to understand when and where. For example, it is important to assess the time at which steel bars of reinforced concrete structure can be directly exposed to the fire.

The results obtained from this analysis [72] were summarized in the nomogram of spalling whose scheme has been shown on figure 2-15. Figure 2-16 shows the final form of the abacus for spalling. There were indicated three different regions which correspond to three different level of danger with respect to spalling occurrence, by basing on the “empirical” spalling criterion proposed above.

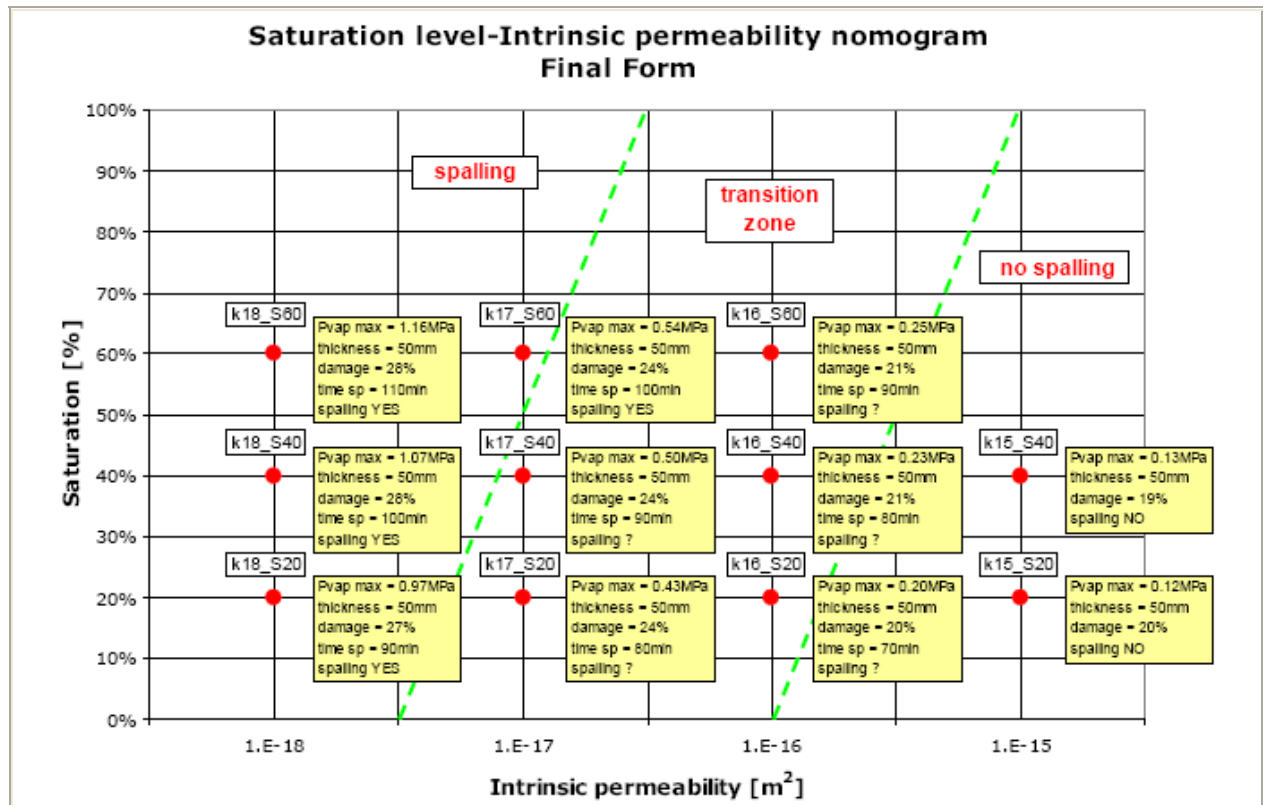


Figure 2-16. Final form of Thermal Spalling abacus [72].

However, a step forward was still needed due to the qualitative (but not quantitative) usefulness of the abacus developed, being necessary to substitute the employed empirical spalling criterion by experimentally correlated spalling indexes based on physical models.

Moreover, the analysis of the energetic viability of spalling at each instant and possible position of the main fractures and, hence, of the spalling risk and expectable type (either violent and explosive or slow in nature) in every possible set of conditions – so both Designers and Fire Fighting Services would have a valuable information in order to take decisions about design and about the expectable consequences of fire fighting actions from a really intuitive, graphical and immediate point of view – was also still needed.

In that sense, the discerning of what is the energetic contribution of compressed gas to the Thermal Spalling occurrence and what is that corresponding to the constrained elastic energy has also been recognized by many relevant authors [1] as an important lack within the current state-of-the-art, since the relative importance of the build-up of high pore pressure close to the heated concrete surface (as a result of rapid evaporation of the moisture) and the release of the stored energy (due to the thermal stresses resulting from high values of restrained strains caused by temperature gradients) has not been already established and also needs further studies.

All of these pending questions will be answered within *Chapter 4 – Spalling Nomograms* and, through an even more sophisticated methodology, in *Chapter 6 – Analysis of Cooling Processes* in High Strength Concretes of this Thesis.

2.1.7 Design Against Thermal Spalling

In order to finish up with the review of the background studies related to Thermal Spalling, and although it is not a direct aim of this Thesis, next are also explained some basic concepts to take into account for the improvement of a design against Thermal Spalling, including the evaluation of preventive measures found in the currently available literature as well as an introductory explanation of the use of polypropylene fibres [3] to avoid Thermal Spalling.

2.1.7.1 PREVENTIVE MEASURES

BS 8110 : Part 2 : 1985 [73] states that "It may be possible to show that a particular form of construction has given the required performance in a fire resistance test without any measures to avoid spalling. Alternatively, the designer may be able to demonstrate by fire engineering principles that the particular performance can be provided, even with spalling of concrete cover to the main tensile reinforcement". The standard, however, adds that "In any method of determining fire resistance where loss of cover can endanger the structural element, measures should be taken to avoid its occurrence".

The foregoing discussion [3] on the factors that influence the spalling of concrete suggests essentially nine measures can be taken to eliminate spalling or to reduce its damage (Table 2-8). These measures can be employed singly or in combinations.

Method	Effectiveness	Comments
<i>Polypropylene fibres</i>	Very effective even in high strength concrete but not so effective in ultra-high performance concrete.	May not prevent spalling in ultra- high strength concrete. More fibres needed if concrete is heated under load and for stronger concrete. Does not reduce temperatures or strength loss.
<i>Air-entraining agent</i>	Effective.	Can reduce strength. Could be problematic if concrete is water saturated.
<i>Additional thermal protection</i>	Very effective.	Increases cost but also increases fire resistance. Key potential problem is adhesion to surface. Reduces rate of heating and maximum temperatures so reduces both spalling and compressive strength loss.
<i>Moisture content control</i>	Reduces vapour pressure.	Normal moisture content is usually above the 'no spalling' limit for most buildings.
<i>Compressive stress control</i>	Reduces explosive pressure.	Not economical as section sizes increase.
<i>Choice of aggregate</i>	It is best to use low expansion and small size aggregate.	If low moisture lightweight concrete is used, additional fire resistance is possible - but in high moisture conditions violent spalling is promoted.
<i>Supplementary reinforcement</i>	Reduces spalling damage.	Difficult to use in small and narrow sections.
<i>Choice of section shape</i>	Thicker sections reduce spalling damage.	Important for I-beams and ribbed sections.

Table 2-8. Evaluation of preventive measures for the spalling of concrete [3].

The most effective methods of controlling explosive spalling are: (a) the use of Polypropylene fibres, (b) adding an air-entraining agent, and (c) the provision of a thermal barrier. The risk of explosive spalling, which can occur during the first half hour of a fire attack, is also diminished by reducing the moisture content of the concrete to less than 5% by volume (2-3% by weight), by avoiding thin sections and 'rapid' changes in shape, and by limiting the compressive stress.

Non-explosive spalling may occur after heating for 60 minutes or more. Its effects can be minimized by the provision of supplementary reinforcement in the concrete cover. Control of spalling by use of supplementary reinforcement is specified by most codes in sections where the cover to the outer bars exceeds 40 millimetres. However, supplementary reinforcement is difficult to place in thin sections, such as ribbed floors. Evidence of fires in real structures

suggests that spalling does not necessarily mean a structural failure. An important factor in improving fire behaviour is structural continuity and better detailing (e.g. by anchorage of the heat-affected bars). Nevertheless, spalling does influence the ultimate fire resistance of the element, and consequently protective measures need to be taken.

2.1.7.2 POLYPROPYLENE FIBRES

A recent development in the fight against explosive spalling of concrete has been the use of Polypropylene fibres in concrete. [3] recommended its use for the tunnels proposed for the Channel Tunnel rail Link. His recommendation was adopted as a requirement for all the tunnels of this link. Subsequent tests undertaken by [44] demonstrated the effectiveness of this method as shown in figure 2-17.



No pp fibres

Figure 2-17. Spalling of granite concrete [44].

With pp fibres in HC fire

Polypropylene fibres melt at about 160°C thus creating channels for vapour to escape and thereby release pore pressures. Monofilament fibres have been shown by tests to be more effective than fibrulated fibres. The influence of compressive load during heating is important. Tests have indicated that, for unloaded concrete, 1kg of fibres per m³ of concrete may be sufficient to eliminate spalling. For a load of 3 N/mm² the fibre content needs to be increased to 1,5-2 Kg/m³ and, for a load of 6 N/mm², a further increase to 3 Kg/m³ may be required to combat explosive spalling. Although concrete segments are lightly stressed under normal conditions [3], it should be pointed out that a circumferential compressive hoop stress will develop in the concrete during heating which is a function of the thermal expansion of the aggregate. The higher the thermal expansion of the concrete, the greater will be this thermal

stress – and limestone concrete has a relatively high thermal expansion. So it is advisable to assume a higher compressive stress level during heating in a fire when compared with the normal situation. Another factor to consider is the concrete strength. Tests conducted by [1] on ultra-high-performance concrete (180 N/mm²) indicates that a very high fibre content of 2% by volume may not be effective in eliminating spalling. In other words, the use of pp fibres is more effective in lower strength concrete.

2.1.7.3 THERMAL BARRIER

Thermal barriers reduce the rate of heating (and peak temperatures) within the concrete and thus reduce the risk of explosive spalling as well as loss of mechanical strength. They are therefore the most effective method (pp fibres do not reduce temperatures). However, there are two potential drawbacks: (a) the cost of the insulation is likely to be more than that of the fibres and (b) with some of the manufacturers there has been a problem with delamination during normal service conditions. The design criteria normally are to apply a sufficient thickness of coating so as to reduce the maximum temperature at the surface of the concrete to below about 300°C and the maximum temperature at the steel re-bar to about 250°C within 2-hours of the fire. It should be noted that experience indicates that while 25 millimetres of coating may be adequate for concrete strength up to about C60 a coating thickness of 35 millimetres may be required for higher strength concretes to avoid explosive spalling.

2.2 COOLING PROCESSES IN HIGH STRENGTH CONCRETES

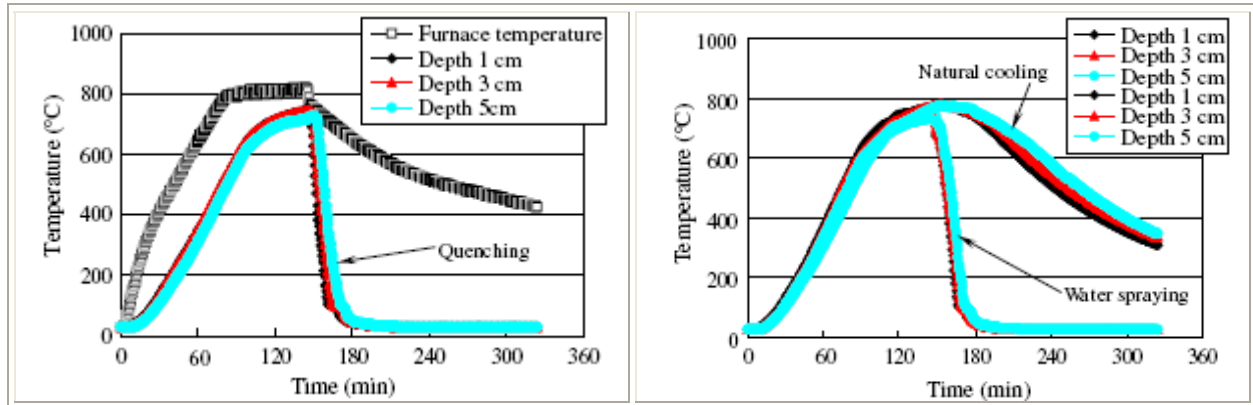
The analysis of the cooling processes in structural elements manufactured with High Strength Concretes has only been dealt from an experimental point of view and, mostly, focused on the study of their residual mechanical properties after experimenting thermal shock during cooling.

Nevertheless, most research data of residual strength after exposure to high temperature were obtained under conditions of natural cooling [74-77], which should differ obviously from cooling regimes in a real fire, where water spraying is usually used for fire extinguishing and consequently thermal shock is induced to concrete. It has been reported that water cooling caused more severe decrease in strength compared to natural cooling [78-80]. Therefore, the effect of cooling regimes on mechanical properties of concrete is of great concern, especially after a fire case was reported [81,82], which happened in the city of Hengyang, Hunan Province, China, November 3rd, 2003. In this case, an 8-storey reinforced concrete building collapsed catastrophically during fire extinguishing and twenty fire fighters died from the building collapse. Furthermore, apart from these reports on the effect of cooling on plain concrete with no fibre [78-82], there is little literature on properties of fibre concrete subjected to various cooling regimes.

As it was found in a preceding investigation by [83] that using hybrid fibre (steel fibre and polypropylene fibre) is an optimum approach for enhancing fire resistance of HSC/HPC, [83] presented a really recent experimental investigation on the effect of cooling regimes, including natural cooling, spraying water for a series of durations from 5 to 60 min, and quenching in water, on residual mechanical properties of high-performance concrete incorporating hybrid fibre after exposure to high temperatures from 200 to 800 °C [84].

Hence [84] five types of concretes were prepared, with compressive strength at 28 days ranging between 83,4 and 89,3 MPa building: cube specimens of 100 millimetres size for the strength determination, and beams of 100 millimetres height, 100 millimetres width and 400 millimetres length for fracture energy determination. The specimens were exposed to high temperatures in an electric furnace, 200, 400, 600 and 800°C respectively – after an increasing temperature branch – for 1 hour. After exposure to high temperatures, the specimens were

subjected to various cooling regimes, i.e. Natural Cooling, 5 minutes Spraying, 30 minutes Spraying, 60 minutes Spraying and, finally, Quenching by immersion in water. After the specimens cooled down to room temperature, compressive strength, tensile strength and fracture energy were measured. Figure 2-18 shows some of the temperature evolutions measured at several depths during the heating and cooling processes:



Subjected to quenching

Figure 2-18. Temperature of furnace and concrete [84].

Subjected to natural cooling and water spraying for 60 minutes.

These results [84] indicated that the inner temperature decreasing rate of a specimen during cooling, either under quenching or under water spraying for 60 minutes, was significantly higher than that of the specimen subjected to natural cooling. Hence, for the specimens subjected to quenching, temperature at 10 mm depth dropped from 754 to 103 °C within 15,5 minutes; temperature at 30 mm depth dropped from 745 to 102 °C within 17,5 min; and temperature at 50 mm depth dropped from 727 to 102 °C within 19,5 minutes. These results prove that the cooling regimes such as quenching in water, or water spraying for 30 minutes or more, caused an action of “thermal shock” to concrete under elevated temperature, characterized by a high rate of temperature decreasing ranged from 25 to 44 °C/minute.

Therefore it was concluded [84] that, in terms of thermal shock, water spraying for duration of 30 minutes or more is in consistency with quenching in water. Nevertheless, if the duration for water spraying was too short, for example 5 minutes, it was observed that temperature would drop from 743 to 681 °C at 10 millimetres depth, after which the specimens would still undergo natural cooling from 681 °C.

There was also found [84] only a slight difference between the temperature dropping rate of the specimens under quenching in water and that under water spraying for 60 minutes, i.e. quenching caused the temperature dropping rate slightly higher. Moreover, it was observed that the specimens incorporating both PP fiber and steel fiber had both a temperature rising rate during heating and a temperature dropping rate during cooling slightly higher than those of plain concrete, as steel fiber could increase thermal conductivity of hybrid fiber concrete. Related to the effect of cooling regimes on residual compressive strength, residual tensile strength and residual fracture energy, it can be resumed in figure 2-19:

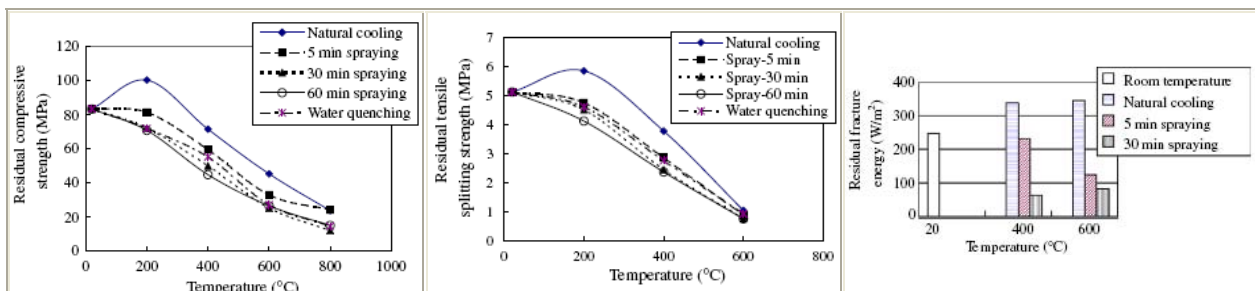


Figure 2-19. Residual properties in plain concrete [84]

Indeed, the residual compressive strength of concrete was significantly influenced by the cooling regimes [84]. For each type of concrete under an identical target temperature, among the five cooling regimes, natural cooling maintained a relatively higher value of residual compressive strength, while both quenching in water or spraying over 30 minutes caused compressive strength approximately 20 MPa lower. It was remarkable that a few specimens were severely damaged by thermal shock. On the other hand, under natural cooling after exposure to 200°C, residual compressive strength was even higher than original strength at room temperature, which might be attributed to additional hydration of residual cement in concrete activated by elevated temperature. Related to the residual tensile splitting strength, analogous conclusions arose. Finally, related to the residual fracture energy of plain concrete, for target temperatures of 400 or 600°C it increased if compared with the original value at room temperature [84]. However, under thermal shock induced by rapid cooling such as water spraying for 30 minutes, the tendency of the change in fracture energy with temperature increasing was quite different from that under natural cooling. Under water spraying for 30 minutes after exposure to 400 and 600 °C, although fracture energy of hybrid fiber concrete decreased dramatically, it was still as high as 5317 W/m². This result also confirmed that hybrid fiber (steel fiber and PP fiber) can significantly enhance fire resistance of HSC/HPC even under a condition of thermal shock caused by water spraying. The results of both mechanical strength and fracture energy in this investigation [84] revealed that fire properties of concrete might be overestimated in most previous literature, where natural cooling rather than rapid cooling was usually employed in experimental investigations. Thus, proper evaluation of fire resistance of concrete needs experimental data obtained under rapid cooling regimes such as water spraying or water quenching. On the other hand, [84] recommended from his investigation that a media other than water should be used for fire extinguishing, which will neither induce any thermal shock like the case of water spraying or quenching in water, nor cause any considerably negative effect on concrete properties.

Other authors [85] studied, experimentally, the effect of cooling condition on the flexural and compressive strengths of HSC mortar exposed after exposure to high temperature. It was observed that thermal shock produced a significant reduction in flexural strength (and a lesser but still significant reduction in compressive strength). [86] observed that thermal shock due to rapid cooling was not a primary factor causing spalling for concrete.

Wetzig et al [87] observed the importance of the cooling-off phase for the assessment of a material's resistance: a concrete element was heated for two hours up to a temperature of 1.600 °C without collapsing; although indications of sintering and melting appeared on the surface of the concrete, the concrete element itself was not destroyed. However, it was only while the element was cooling off that structural collapse occurred. As it continued to cool, glazing took place on the concrete surface and the water vapour which was forming could no longer escape. As a result, approximately 30 minutes after the end of the fire load there was an explosive destruction of the test sample. Even if the loads are not always so extreme, [86] found appropriate to include the cooling-off phase. Consistently, the test should also include the effects of extinguishing agents which lead to abrupt cooling.

In conclusion, a step forward in the understanding of the cooling effect in High Strength Concretes, justified as just explained in sight of the found lack of any complete references within the analyzed *State-of-the-Art*, will be accomplished both in *Chapter 6 Analysis of Cooling Processes in High Strength Concretes* and *Chapter 7 Heuristic analysis of Cooling Processes in High Strength Concrete Square Columns* by means of the use of the most advanced numerical models currently developed for the analysis of the hygro-thermo-chemo-mechanical state of a structural element at high temperature (HITECOSP Software [1], Model of Padua [2], see *Chapter 3*), approach not dealt at all up to this date.

2.3 BIBLIOGRAPHY OF THE CHAPTER

Bibliography of the chapter

- [1] Brite Euram III BRPR-CT95-0065 HITECO, *Understanding and industrial application of High Performance Concrete in High Temperature Environment – Final report*, 1999.
- [2] D. Gawin, F. Pesavento, B.A. Schrefler, *Modelling of hygro-thermal behaviour of concrete at high temperature with thermo-chemical and mechanical material degradation*, Comput. Methods Appl. Mech. Engrg. 192 (2003) 1731-1771.
- [3] G.A. Khoury, Y. Anderberg, *Concrete spalling review*, Fire Safety Design Report submitted to the Swedish National Road Administration, June 2000, pp 1-60.
- [4] M. Gary, *Fire tests on reinforced concrete buildings (in German)*, Verlag Wilhelm Ernst und Sohn, Heft 11, Germany, 1916.
- [5] A.J. Breunese, J.H.H. Fellingner, *Spalling of concrete and fire protection of concrete structures*, TNO Report, 2004.
- [6] G.A. Khoury, *Spalling Review*, UPTUN Project, EC, MidTermMeeting, Venice, November 2004
- [7] Arup Group Ltd, *Fire resistance of concrete enclosures, Work Package 2: Spalling categories*, report for the Nuclear Safety Directorate of the Health and Safety Executive, October 2005
- [8] CIRIA, *Spalling of concrete in fires*, Technical Note 118, 1984.
- [9] G.A. Khoury, *Course on effect of heat on concrete*, Udine, Italy, 9-13 June 2003.
- [10] H.L. Malhotra, *Spalling of concrete in fires*, Construction Industry Research and Information Association, Technical Report No. 118, London 1984, pp. 36.
- [11] R.J. Connolly, *The spalling of concrete in fires*, Ph.D. thesis, Aston University, 1995, pp. 294
- [12] J.C. Tait et. al., *Storebaelt eastern railway tunnel: Dania tunnel boring machine fire - analysis and recovery*, Proc. Institution of Civil Engineers, Stoerbaelt Eastern Railway Tunnel, ICE, 1996, ISSN 0965 089 X, pp. 40-48.
- [13] S. Austin, P. Robins and M. Richards, *Jet blast temperature resistant concrete for harrier aircraft pavements*, The Structural Engineer, 70 (23/24), 427-432, 1992.
- [14] British Standards Institution, *BS 476, Fire tests on building materials and structures, Parts 20 to 24*, BSI, London, 1987.
- [15] Federation Internationale de la Precontrainte, *Methods of assessment of the fire resistance of concrete structural members*, FIP/CEB Report, ISBN 0 7210 1107 1, 1978.
- [16] K. Mustapha, *Modelling the effects of spalling on the failure modes of concrete columns in fire*, PhD Thesis, University of Aston in Birmingham, 1994.
- [17] Y. Anderberg, *Fire exposed hyperstatic concrete structures - An experimental and theoretical study*, Bulletin 55. Division of Structural Mechanics and Concrete Construction, Lund Institute of Technology, Sweden, 1976.
- [18] U. Schneider, *Modelling of concrete behaviour at high temperatures. In Design of structures against fire*, (ed. Anchor, R.D, Malhotra, H.L. and Purkiss, J.A.), Elsevier Applied Science Publishers, London, pp 53 - 69, 1986.
- [19] T.T. Lie, *A procedure to calculate fire resistance of structural members*, Fire Technology, 14(1), 28-85, 1984.
- [20] A.W. Morris, Personal communication, 1972.
- [21] C. Meyer Ottens, *Behaviour of concrete structural members in fire conditions (in German)*, Beton, No. 4, 1974, pp. 133-136, and No. 5, 1974, pp. 175-178.
- [22] C. Meyer Ottens, *The behaviour of concrete structural elements in fires. Spalling of normal concrete elements under fire stress: causes and preventive measures*, Building Research Establishment, Translation 2058, 1977.
- [23] Institution of Structural Engineers, *Fire resistance of concrete structures*, Report of a Joint Conference of the Institution of Structural Engineers and the Concrete Society. ISE, London 1975.
- [24] Cembureau, *Concrete for fire resistant construction*, Cembureau Report, Published by the Cement and Concrete Association, 1979.
- [25] G.W. Shorter, T.Z. Harmathy, *Moisture clog spalling*, Proc. Instit. Civil Engr. 20 (1965) 75-90.
- [26] H. Saito, *Explosive spalling of prestressed concrete in fire*, Internal Report No 22, Building Research Institute, Japan, 1965.
- [27] T.Z. Harmathy, *Effect of moisture on the fire endurance of building elements*, ASTM special technical publication 385, Philadelphia, 1965.
- [28] V.V. Zhukov, *Explosive failure of concrete during a fire (in Russian)*. Translation No. DT 2124, Joint Fire Research Organization, Borehamwood, 1975.
- [29] P.J. Sullivan, A.A. Akhtaruzzaman, *Explosive spalling of concrete exposed to high temperature*, in: Proc. Of First International on Structural Mechanics in Reactor Technology, Berlin, 1971

- [30] N. Khoylou, *Modelling of moisture migration and spalling behaviour in non-uniformly heated concrete*, Ph.D. thesis, Imperial College, London, 1997, pp.1147.
- [31] D. Gawin, F. Pesavento, B.A. Schrefler, *Towards prediction of the thermal spalling risk through a multi-phase porous media model of concrete*, *Comput. Methods Appl. Mech. Engrg.* 195 (2006) 5707-5729.
- [32] Z.P. Bazant, W. Thonguthai, *Pore pressure and drying of concrete at high temperature*, *J. Engrg. Mech. ASCE* 104 (1978) 1059-1079.
- [33] R. Felicetti, P. Gambarova, M.P. Natali Sora, G. Rosati, *Caratterizzazione meccanica di calcestruzzi ad alta ed altissima resistenza esposti ad alta temperatura*, Brite Euram III report, 1999.
- [34] L.T. Phan, *High-Strength concrete at High Temperature – An overview*, Building Fire Research Laboratory Online Library, National Institute of Standards and Technology, Gaithersburg, 2002.
- [35] A. Combescure, *Reinforced concrete spalling*, UPTUN project report, 2002.
- [36] Z.P. Bazant, *Analysis of pore pressure, thermal stress and fracture in rapidly heated concrete*, in: *Proc. of Int. Workshop on Fire Performance of High-Strength Concrete*, Gaithersburg, MD, USA, February 13–14, 1997.
- [37] Z.P. Bazant, J. Planas, *Fracture and Size Effect in Concrete and other Quasi-brittle Materials*, CRC Press, New York, 1998.
- [38] U. Schneider, *Properties of materials at high temperatures – concrete*, RILEM, 1986
- [39] SINTEF, *Marine concrete structures exposed to hydrocarbon fires*, 1988
- [40] K.D. Hertz, *Limits of spalling of fire-exposed concrete*, *Fire Safety Journal*, 38, 2003
- [41] J. Newman, B.S. Choo, *Advanced concrete technology*, Elsevier Ltd, 2003
- [42] ENV 1992-1-1 (1992), *Eurocode 2 Design of concrete structures, Part 1 General rules and rules for buildings*
- [43] ENV 1992-1-2 (1996), *Eurocode 2 Design of concrete structures, Part 1.2 General rules – Structural fire design*
- [44] P. Shuttleworth, *Fire performance of concrete for tunnel linings, Channel Tunnel*, Rail Link Technical Report, Arup, 1997
- [45] R. Both, *The behaviour of unprotected loaded concrete tunnel linings subjected to RWS hydrocarbon fire*, TNO report 2000-R01360, 2000
- [46] SINTEF, *Fire testing of concrete element*, 1992
- [47] F.G. Thomas, C.T. Webster, *Investigations on building fires, Part VI – The fire resistance of reinforced concrete columns*, National Building Studies Research Paper 18, HMSO, London, 1953
- [48] V.K.R. Kodur, *Fire performance of high-strength concrete structural members*, *Construction Technology Update* No. 31, NRCC, 1999
- [49] A. Christiaanse, A. Langhorst, A. Gerriste, *Discussion of fire resistance of lightweight concrete and spalling*, Dutch Society of Engineers (STUVO), Report 12, Holland, 1972.
- [50] C. Meyer-Ottens, *The question of spalling of concrete structural elements of standard concrete under fire loading*, PhD Thesis, Technical University of Braunschweig, Germany, 1972.
- [51] W.J. Copier, *Spalling of normalweight and lightweight concrete on exposure to fire*, Report 24(2), Heron, Holland, 1979.
- [52] J. Komonen, P. Vesa, *Effects of high temperature on the pore structure and strength of plain and polypropylene fiber reinforced cement pastes*, *Fire Technology*, 39, 2003.
- [53] B. Marsh, Arup Internal Report, 2002.
- [54] T. Lennon, *Fire tests on tunnel lining segments containing polypropylene fibres*, BRE, 2000
- [55] T.D.G. Canisius, N. Waleed, S.L. Matthews, *A preliminary study of the cardington concrete building under a compartment fire*, *Structure Faults and Repair*, 2003.
- [56] C.L.D. Huang, G.N. Ahmed, D.L. Fenton, *Responses of concrete walls to fire*, *International Journal of Heat Mass Transfer*, Vol. 34, No. 3, 1991.
- [57] G.A. Houry, *Effect of fire on concrete and concrete structures*, *Progress. In Structural. Engineering and Materials*, Issue 2, pp 429-447, 2000.
- [58] K.D. Hertz, *Heat induced explosion of dense concretes*, Report no. 166, Institute of Building Design, Denmark, 1984.
- [59] G. Sanjayanan, L. Stocks, *Spalling of high strength silica fume concrete in fire*, *American Concrete Institute Materials Journal*, March/April, 170-173, 1993.
- [60] U.-M. Jumpannen, *Effect of strength on fire behaviour of concrete*, *Nordic Concrete Research*, Publication No. 8, 1989.
- [61] Federation Internationale de la Precontrainte, *Recommendations for the design of reinforced and prestressed concrete structural members for fire resistance*, FIP/CEB Guides to Good Practice, Publication 15.336, 1978.
- [62] Y. Sertmehmetoglu, *On a mechanism of spalling of concrete under fire conditions*, PhD thesis, King's College, London, 1977.

- [63] F. Ali, A. Nadjai, G. Silcock, A. Abu-Tair, *Outcomes of a major research on fire resistance of concrete columns*, Fire Safety Journal, 39, 2004.
- [64] Institution of Structural Engineers, *Fire resistance of concrete structures*, Report of a Joint Conference of the Institution of Structural Engineers and the Concrete Society. ISE, London 1975.
- [65] CIRIA, *Fire tests on ribbed concrete slabs*, Technical Note 131, 1987.
- [66] BS 8110-2 (1985), *BS 8110 Structural use of concrete, Part 2 Code of practice for special circumstances*.
- [67] T. Lennon, *Structural fire engineering design: materials behaviour – concrete*, Digest 487, BRE, 2004.
- [68] Y. Anderberg, *Spalling phenomena of HPC and OC*, NIST Special Publication 919, 1997.
- [69] A.A. Akhtaruzzaman, P.J.E. Sullivan, *Explosive spalling of concrete exposed to high temperature*, Concrete Structure and Research Report, Imperial College, 1970.
- [70] Gutaferro, *Fire resistance of prestressed concrete*, Bauverlag GmbH, Berlin, 1966.
- [71] W.J. Copier, *The spalling of normal weight and lightweight concrete on exposure to fire*, Heron (Netherlands), 1977.
- [72] F. Corsi, B.A. Schrefler, C.E. Majorana, F. Pesavento, D. Gawin, *Qualified and validated procedure for spalling evaluation. Milestone M4.2*, UPTUN Upgrading of existing TUNNELS report, Work Package 4, Project No.: GRD1-2001-40739 within the 5th Framework Programme of the European Union Competitive and Sustainable Growth, January 12, 2006
- [73] British Standards Institution *BS8110 : Part 2 : 1985, Structural use of concrete. Code of practice for special circumstances. Section four, Fire resistance*, BSI, London, 1985.
- [74] L.T. Phan, *Fire performance of high-strength concrete: a report of the state-of-the-art*, NISTIR 5934. Building and Fire Research Laboratory, National Institute of Standards and Technology, Gaithersburg, MD; 1996.
- [75] U. Schneider, *Concrete at high temperatures – a general review*. Fire Safety J 1988;13:55–68.
- [76] Y.N. Chan, G.F. Peng, M. Anson, *Residual strength and pore structure of high-strength concrete and normal strength concrete after exposure to high temperatures*, Cem Concr Comp 1999;23:23–7.
- [77] G.A. Houry, *Compressive strength of concrete at high temperatures: reassessment*, Mag Concr Res 1992; 44: 291–309.
- [78] X. Luo, W. Sun, S.Y.N. Chan, *Effect of heating and cooling on residual strength and microstructure of normal strength and high-performance concrete*, Cem Concr Res 2000;30:379–83.
- [79] S. Ishihara, T. Gshima, K. Nomura, *Crack propagation behavior of cermets and cemented carbides under repeated thermal shocks by the improved quench test*, J Mater Sci 1999;34:629–36.
- [80] A.Y. Nassif, *Postfiring stress–strain hysteresis of concrete subjected to various heating and cooling regimes*, Fire Mater 2002;26:103–9.
- [81] Anonymous, *Problems arising from the Hengyang fire case to the philosophy of fire fighting in China* (in Chinese), China News Weekly 2003; November 17.
- [82] J.Q. Chen, *Key issues in the “11-03” building fire and collapse case in the city of Hengyang* (in Chinese). Fire Science Technology (China) 2004;23:99–102.
- [83] G.F. Peng, W.W. Yang, J. Zhao, Y.F. Liu, S.H. Bian, L.H. Zhao, *Explosive spalling and residual mechanical properties of fiber-toughened highperformance concrete subjected to high temperatures*, Cem Concr Res 2006;36:723–7.
- [84] G.-F. Peng, S.H. Bian, Z.-Q. Guo, J. Zhao, X.-L. Peng, Y.-C. Jiang, *Effect of thermal shock due to rapid cooling on residual mechanical properties of fiber concrete exposed to high temperatures*, Construction and Building Materials, 2008; 22:948-955.
- [85] M. Henry, T. Nishimura, Y. Kato, T. Uomoto, *Effect of cooling conditions on residual strength of cement mortar exposed to high temperatures*, Seisan-Kenkyu 2007; 59:271-274.
- [86] W. Sun, X. Luo, Y.N. Chan, *Behaviour of high strength concrete subjected to high temperatures*, Congress - Brittle matrix composites 6: Warsaw, 9-11 October 2000.
- [87] V. Wetzig, *Destruction mechanisms in concrete material in case of fire, and protection systems*, Hagerbach Test Gallery Ltd, Switzerland, 2000

*THIS PAGE IS INTENTIONALLY
LEFT BLANK*

Chapter 3

MODELLING OF HYGRO-THERMAL BEHAVIOUR OF CONCRETE AT HIGH TEMPERATURE WITH THERMO-CHEMICAL AND MECHANICAL MATERIAL DEGRADATION

3.1	INTRODUCTION	63
3.2	MACROSCOPIC BALANCE EQUATIONS	64
3.3	STATE VARIABLES.....	69
3.4	CONSTITUTIVE RELATIONS	71
3.5	THERMO-CHEMICAL AND MECHANICAL DAMAGE OF CONCRETE.....	75
3.6	GOVERNING EQUATIONS OF THE MODEL	78
3.7	NUMERICAL SOLUTION	83
3.8	CONCLUSIONS OF THE CHAPTER.....	86
3.9	BIBLIOGRAPHY OF THE CHAPTER	86
Appendix 3A.	MATRICES RESULTING FROM THE DISCRETIZATION OF MASS, ENERGY AND LINEAR MOMENTUM CONSERVATION EQUATIONS	88

*THIS PAGE IS INTENTIONALLY
LEFT BLANK*

Chapter 3

MODELLING OF HYGRO-THERMAL BEHAVIOUR OF CONCRETE AT HIGH TEMPERATURE WITH THERMO-CHEMICAL AND MECHANICAL MATERIAL DEGRADATION

The aim of this Chapter is to describe in detail the mathematical model used in Chapters 4 to 7 of this Thesis for the analysis of the hygro-thermal behaviour of concrete at high temperatures, as a multi-phase porous material, accounting for the material deterioration. The complete development of the model equations, starting from the macroscopic balances of mass, energy and linear momentum of single constituents is presented. The constitutive relationships for concrete at high temperature, including those concerning material damage, are also included herein. The classical isotropic non-local damage theory is presented modified to take into account the mechanical and the thermo-chemical concrete damage at high temperature. The final form of the governing equations, their discretized F.E. form, and their numerical solution are finally presented.

Hence, as just stated, no original contributions related to the mathematical model used in this Thesis are introduced in this Chapter, since this model was completely developed and presented by D. Gawin, F. Pesavento and B.A. Schrefler [1].

3.1 INTRODUCTION

Since the second half of the nineties there is a renewed interest in the modelling of concrete at high and very high temperature. Introduction of new high and ultra high performance concretes required their assessment as far as spalling is concerned. The BRITE EURAM Project “HITECO” (HIGH TEMPERATURE CONCRETE), [2], was aimed at this purpose and has yielded very interesting results [3]. Further, increased recurrence of fires in Europe, often connected with losses of life, always with destruction of the concrete vaults and walls and causing heavy economical losses, have evidenced the dramatic need for an upgrading of existing buildings and tunnels and introduction of new standards. Again the need for a new modelling capacity for concretes under such extreme conditions (temperatures exceeding 1200°C for considerable time spans) has been evidenced.

The EU Project UPTUN (Cost-Effective Sustainable and Innovative Upgrading Methods for Fire Safety in Existing Tunnels), involving forty partners, is aimed at that purpose. Finally, the modelling of aging in concrete Nuclear Power Plant Structures requires also to take into account concrete under high (and cyclic) temperatures. This aspect is currently investigated within the EURATOM project MÆCENAS.

It is commonly accepted [4-7, 8-10] that all the above situations cannot satisfactorily be modelled by considering thermo-mechanical processes alone. Heat and mass transfer within the concrete body (and on its boundary) has to be taken into account, together with phase changes and dehydration. The model has, hence, to be a chemo-hygro-thermo-mechanical one. The presented model Developers [1] have been involved in all three of the above mentioned research projects. This model stems from early work of Gawin et al. [11], and Gawin & Schrefler [12] and has been further developed over the years [8]. Initially its applicability was limited by critical temperature of water. This limit has now been overcome [10]. Mechanical damage alone was initially considered.

A coupling of permeability with mechanical damage was introduced in [9]. When simulating a real experimental fire situation in, for instance, a motorway tunnel, it turned out that mechanical damage alone was not sufficient. Thermally induced deterioration due to strains at

material meso-scale and due to concrete dehydration, called thermo-chemical damage (and a modification of stress-strain curve) was also needed. This was introduced in a framework of the isotropic non-local damage theory. A full development of the model equations and their F.E. discretization are also presented. A discussion of the choice of the state variables and ensuing constitutive relations follows.

Recently, several works devoted in particular to the Thermal Spalling phenomenon in concrete at elevated temperature have been published, e.g. [13-16]. As pointed out in [15], there are two main reasons of the phenomenon: build-up of pore pressure and restrained thermal dilatation. The latter hypothesis was theoretically justified in [15] to be the most important reason of Thermal Spalling and used for analysis of the “Chunnel” fire [16]. In the model developers’ opinion [1] both of the above mentioned reasons of the phenomenon, acting together, are of importance for the Thermal Spalling occurrence, in particular for the explosive one, as shown by the experimental tests carried out by Phan et al. [14].

At this point it is worth to discuss some limitations of the recently proposed, macroscopic phenomenological theory by Ulm, Coussy and Bazant [15]. Effect of temperature on concrete strength is modelled there as chemo-plastic softening within the framework of chemo-plasticity, accounting explicitly for the dehydration of concrete and its cross-effects with deformation and temperature. In the model, most material properties are practically unique functions of temperature only, even if formally they depend on hydrate mass and plastic softening parameter. Moisture transfer and evaporation within the heated concrete are not taken into account and, hence, the effect of pore pressure cannot be considered. Effect of cracking on concrete behaviour is neglected. Most of these shortcomings are overcome by the theory presented by [1] and described in this Chapter.

3.2 MACROSCOPIC BALANCE EQUATIONS

The balance equations are written by considering concrete as a multi-phase material. The solid skeleton voids are filled partly by liquid water and partly by a gas phase.

Below the critical temperature of water, T_{cr} , the liquid phase consists of bound water, which is present in the whole range of moisture content, and capillary water, which appears when degree of water saturation exceeds the upper limit of the hygroscopic region, S_{ssp} . Above the temperature T_{cr} the liquid phase consists of bound water only. In the whole temperature range the gas phase is a mixture of dry air and water vapour (condensable gas constituent for $T < T_{cr}$).

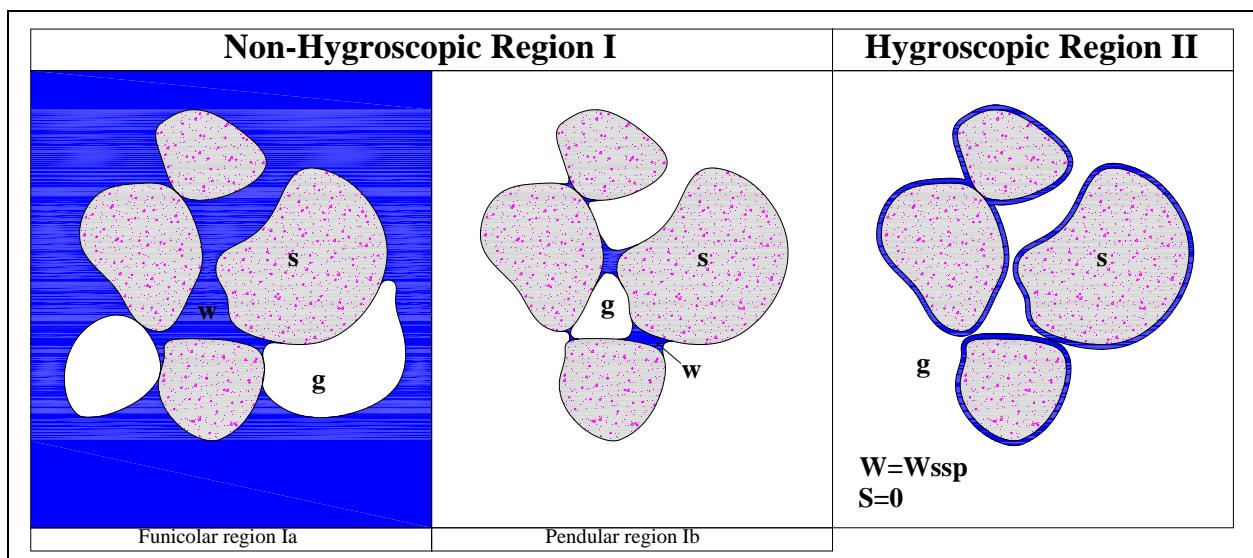


Figure 3-1. Hygroscopic region, non-hygroscopic region and solid saturation point in a porous media.

The model equations are obtained by means of the Hybrid Mixture Theory (HMT) originally proposed by Hassanizadeh and Gray [17-19] and then applied for geomaterials in general by Lewis and Schrefler [20] and Schrefler [21], and for building materials by Gawin [22]. For the sake of brevity, only the final form of the macroscopic conservation equations is given here. The full development of the model equations, starting from the local, microscopic balance equations with successive volume averaging, are presented in [20-23].

The general form of the macroscopic, volume averaged mass conservation equation of the π -phase is [20, 21]:

$$\frac{D \rho_\pi}{Dt} + \rho_\pi \operatorname{div} \mathbf{v}^\pi = \rho_\pi e^\pi(\rho), \quad (3.1)$$

where ρ_π is the apparent density (related to the whole volume of the medium), \mathbf{v}^π the velocity and $\rho_\pi e^\pi(\rho)$ the volumetric mass source, super or subscript π refers to the π -phase.

This mass balance equation has the following form for the solid skeleton [22]:

$$\frac{D \rho_s}{Dt} + \rho_s \operatorname{div} \mathbf{v}^s = -\dot{m}_{dehydr}, \quad (3.2)$$

where \dot{m}_{dehydr} is mass source of liquid water (and corresponding skeleton mass sink) related to the cement dehydration process.

After application of the relation between the phase averaged density, ρ_π , and the intrinsic phase averaged density, ρ^π , [17-20]:

$$\rho_\pi = \eta^\pi \rho^\pi, \quad (3.3)$$

with η^π being the volume fraction of the π -phase, and after some simple transformations, equation (3.2) can be rewritten as:

$$\frac{(1-n)}{\rho^s} \frac{D \rho^s}{Dt} - \frac{D n}{Dt} + (1-n) \operatorname{div} \mathbf{v}^s = -\frac{\dot{m}_{dehydr}}{\rho^s}, \quad (3.4)$$

The volume averaged mass conservation equation for liquid water (capillary and physically adsorbed) has the following form:

$$\frac{D \rho_w}{Dt} + \rho_w \operatorname{div} \mathbf{v}^w = \dot{m}_{dehydr} - \dot{m}_{vap}, \quad (3.5)$$

where \dot{m}_{vap} is the vapour mass source caused by the liquid water evaporation or desorption (for low values of the relative humidity inside the material pores). It is worth to underline that for the liquid water we have two source terms.

By introducing the water relative velocity and material derivative of water density, with respect to the skeleton, the latter equation can be written as follows:

$$\frac{D \rho_w}{Dt} + \mathbf{v}^{ws} \cdot \operatorname{grad} \rho_w + \rho_w \operatorname{div}(\mathbf{v}^s + \mathbf{v}^{ws}) = \dot{m}_{dehydr} - \dot{m}_{vap}, \quad (3.6)$$

where $\mathbf{v}^{\pi s}$ means the π -phase relative velocity with respect to the skeleton.

After some algebraic transformations and application of (3) with $\eta^w = nS_w$, we have:

$$\begin{aligned} & \frac{Dn}{Dt} + \frac{n}{\rho^w} \frac{D\rho^w}{Dt} + \frac{n}{S_w} \frac{DS_w}{Dt} + \frac{1}{S_w\rho^w} \operatorname{div}(nS_w\rho^w\mathbf{v}^{ws}) + n \operatorname{div}\mathbf{v}^s \\ & = \frac{\dot{m}_{dehydr} - \dot{m}_{vap}}{S_w\rho^w}. \end{aligned} \quad (3.7)$$

In order to eliminate the time derivative of porosity, $\frac{Dn}{Dt}$, from the latter equation, we sum it up with (3.4) and obtain the mass conservation equation of liquid water and solid skeleton as follows:

$$\begin{aligned} & \frac{(1-n)}{\rho^s} \frac{D\rho^s}{Dt} + \operatorname{div}\mathbf{v}^s + \frac{n}{\rho^w} \frac{D\rho^w}{Dt} + \frac{n}{S_w} \frac{DS_w}{Dt} + \\ & + \frac{1}{S_w\rho^w} \operatorname{div}(nS_w\rho^w\mathbf{v}^{ws}) = \frac{\dot{m}_{dehydr} - \dot{m}_{vap}}{S_w\rho^w} - \frac{\dot{m}_{dehydr}}{\rho^s} \end{aligned} \quad (3.8)$$

The macroscopic volume averaged mass conservation equation of dry air [20, 21],

$$\frac{D\rho^{ga}}{Dt} + \rho^{ga} \operatorname{div}\mathbf{v}^{ga} = 0, \quad (3.9)$$

after changing the material time derivative $\frac{D\rho^{ga}}{Dt}$ into $\frac{D\rho^{ga}}{Dt}$ and decomposition of the dry air velocity into the diffusional, $\mathbf{u}^{ga} = \mathbf{v}^{ga} - \mathbf{v}^g$, and advective (i.e. related to the centre of gravity of the whole gas phase), \mathbf{v}^g , components [20, 21], can be rewritten as:

$$\frac{D\rho^{ga}}{Dt} + \operatorname{div}\mathbf{J}_d^{ga} + \rho^{ga} \operatorname{div}\mathbf{v}^g = 0, \quad (3.10)$$

where,

$$\mathbf{J}_d^{ga} = \rho^{ga}\mathbf{u}^{ga} = nS_g\rho^{ga}\mathbf{u}^{ga}, \quad (3.11)$$

is the diffusive mass flux of dry air molecules in the gas phase.

It is reminded that there is no source term related to the dry air. Equation (3.10) is now transformed in a similar way as done for the liquid water balance, i.e. material time derivative and relative velocity with respect to the solid are introduced, relation (3.3) with $\eta^{ga} = n(1-S_w)$ is applied and the resulting equation, divided by $\rho^{ga}(1-S_w)$, is summed up with the solid skeleton mass balance (3.4). Finally, we obtain the following equation:

$$\begin{aligned} & \frac{n}{S_g} \frac{DS_g}{Dt} + \frac{n}{\rho^{ga}} \frac{D\rho^{ga}}{Dt} + \frac{1}{S_g\rho^{ga}} \operatorname{div}\mathbf{J}_d^{ga} + \frac{1}{S_g\rho^{ga}} \operatorname{div}(nS_g\rho^{ga}\mathbf{v}^{gs}) \\ & + \frac{1-n}{\rho^s} \frac{D\rho^s}{Dt} + \operatorname{div}\mathbf{v}^s = -\frac{\dot{m}_{dehydr}}{\rho^s}. \end{aligned} \quad (3.12)$$

The macroscopic mass balance of the water vapour [20-22],

$$\frac{D \rho_{gw}^{gw}}{Dt} + \rho_{gw} \operatorname{div} \mathbf{v}^{gw} = \dot{m}_{vap}, \quad (3.13)$$

can be presented, similarly to the equation for the dry air, in the following form,

$$\frac{D \rho_{gw}^g}{Dt} + \operatorname{div} \mathbf{J}_d^{gw} + \rho_{gw} \operatorname{div} \mathbf{v}^g = \dot{m}_{vap}, \quad (3.14)$$

where the diffusive mass flux of vapour molecules in the gas is defined as, [20-22],

$$\mathbf{J}_d^{gw} = \rho_{gw} \mathbf{u}^{gw} = n S_g \rho^{gw} \mathbf{u}^{gw}, \quad (3.15)$$

One should remember, that the gas phase is an ideal binary gas mixture of dry air and water vapour, hence, [20-22],

$$\mathbf{J}_d^{gw} = -\mathbf{J}_d^{ga}, \quad (3.16)$$

By applying the same transformations as for the dry air mass balance and summing (3.14) with (3.4), we obtain the following equation,

$$\begin{aligned} & \frac{n}{S_g} \frac{D S_g}{Dt} + \frac{n}{\rho^{gw}} \frac{D \rho^{gw}}{Dt} + \frac{1}{S_g \rho^{gw}} \operatorname{div} \mathbf{J}_d^{gw} + \frac{1}{S_g \rho^{gw}} \operatorname{div} (n S_g \rho^{gw} \mathbf{v}^{gs}) \\ & + \frac{1-n}{\rho^s} \frac{D \rho^s}{Dt} + \operatorname{div} \mathbf{v}^s = -\frac{\dot{m}_{dehydr}}{\rho^s} + \frac{\dot{m}_{vap}}{S_g \rho^{gw}}. \end{aligned} \quad (3.17)$$

We do not have any constitutive relationship for the mass source term, \dot{m}_{vap} , appearing in the latter equation and in (3.8), but we can use one of the two mass balance equations to eliminate this source term from the another one.

The macroscopic, volume averaged enthalpy balance equation for the π -phase, after neglecting some terms related to viscous dissipation and mechanical work, caused by density variations due to temperature changes and caused by volume fraction changes, has the following general form [20, 21]:

$$\rho_\pi C_p^\pi \frac{D T^\pi}{Dt} = \rho_\pi h^\pi - \operatorname{div} \tilde{\mathbf{q}}^\pi + \rho_\pi R_H^\pi - \rho_\pi e^\pi(\rho) H^\pi, \quad (3.18)$$

where C_p^π is the specific isobaric heat, $\tilde{\mathbf{q}}^\pi$ the heat flux, $\rho_\pi h^\pi$ the volumetric heat sources, $\rho_\pi R_H^\pi$ the term expressing energy exchange with the other phases (including mechanical interaction and excluding enthalpy exchange due to mass sources), H^π the specific enthalpy, of the π - phase. In concrete at high temperature all heat sources, except those related to phase changes and dehydration process, can be neglected.

We assume here that all phases of the material are locally in thermodynamic equilibrium, hence their temperatures are the same, $T^\pi = T$ ($\pi = s, w, g$). These temperatures may however vary throughout the domain.

Summing up the enthalpy balances for all the phases of the medium, taking into account the mass sources, specific for the particular constituents, and transforming all material time derivatives into those with respect to the solid skeleton, as well as having in mind that [30,42]:

$$\sum_{\pi} \rho_{\pi} R_H^{\pi} = 0, \quad (3.19)$$

one obtains the following enthalpy balance equation for the whole medium:

$$\begin{aligned} & (\rho C_p)_{eff} \frac{DT}{Dt} + (\rho_w C_p^w \mathbf{v}^{ws} + \rho_g C_p^g \mathbf{v}^{gs}) \cdot \text{grad } T - \text{div } \tilde{\mathbf{q}} = \\ & -\dot{m}_{vap} \Delta H_{vap} - \dot{m}_{dehydr} \Delta H_{dehydr}, \end{aligned} \quad (3.20)$$

where,

$$\begin{aligned} (\rho C_p)_{eff} &= \rho_s C_p^s + \rho_w C_p^w + \rho_g C_p^g, \\ \tilde{\mathbf{q}} &= \tilde{\mathbf{q}}^s + \tilde{\mathbf{q}}^w + \tilde{\mathbf{q}}^g, \\ \Delta H_{vap} &= H^{gw} - H^w, \\ \Delta H_{dehydr} &= H^w - H^{ws}. \end{aligned} \quad (3.21)$$

Above, H^{ws} is the specific enthalpy of the chemically bound water, ΔH_{vap} the specific enthalpy of evaporation and ΔH_{dehydr} the specific enthalpy of dehydration.

Hygro-thermal phenomena in concrete, even at high temperature, are relatively slow, hence inertial forces can be neglected. For such a case the macroscopic, volume averaged linear momentum balance equation for the π -phase has the following general form [20, 21]:

$$\text{div } \mathbf{t}^{\pi} + \rho_{\pi} \mathbf{g} + \rho_{\pi} [\mathbf{e}^{\pi} (\rho \dot{\mathbf{r}}) + \hat{\mathbf{t}}^{\pi}] = 0, \quad (3.22)$$

where \mathbf{t}^{π} is the macroscopic stress tensor in the π -phase, \mathbf{g} the acceleration of gravity, $\rho_{\pi} \hat{\mathbf{t}}^{\pi}$ the volumetric exchange term of linear momentum with other phases due to mechanical interaction, and $\rho_{\pi} \mathbf{e}^{\pi} (\rho \dot{\mathbf{r}})$ that due to phase changes or chemical reactions. These exchange terms are subject to the constraint:

$$\sum_{\pi} \rho^{\pi} [\mathbf{e}^{\pi} (\rho \dot{\mathbf{r}}) + \hat{\mathbf{t}}^{\pi}] = 0, \quad (3.23)$$

After summing up the macroscopic linear momentum balances for all the phases and introducing the total stress tensor,

$$\boldsymbol{\sigma} = \mathbf{t}^s + \mathbf{t}^w + \mathbf{t}^g, \quad (3.24)$$

taking into account condition (3.23) and assuming continuity of stresses at the fluid-solid interfaces, one obtains:

$$\text{div } \boldsymbol{\sigma} + \rho \mathbf{g} = 0, \quad (3.25)$$

where,

$$\rho = (1 - n) \rho^s + n S_w \rho^w + n (1 - S_w) \rho^g \quad (3.26)$$

is the averaged apparent density of the medium.

The volume averaged angular momentum balance equation shows, [20, 21], that for non-polar media, as moist concrete is assumed in this work, all macroscopic partial stress tensors are symmetric,

$$\mathbf{t}^\pi = (\mathbf{t}^\pi)^T, \quad (3.27)$$

From the macroscopic entropy inequalities for the medium constituents, limitations for the form of constitutive relationships can be deduced, e.g. using the Coleman-Noll procedure, as done in [24]. This assures that the constitutive relations do not violate the Second Law of Thermodynamics.

3.3 STATE VARIABLES

A proper choice of state variables for description of concrete at high temperature is of particular importance. From a practical point of view, the physical quantities used, should be possibly easy to measure during experiments, and from a theoretical point of view, they should uniquely describe the thermodynamic state of the medium [25]. They should also assure a good numerical performance of the computer code based on the resulting mathematical model. The necessary number of the state variables may be significantly reduced if existence of local thermodynamic equilibrium at each point of the medium is assumed. In such a case physical state of different phases of water can be described by use of the same variable. When fast hygro-thermal phenomena in concrete at high temperature are analyzed, the assumption is debatable, but it is almost always used in modelling. It is also applied in development of the present model.

Having in mind all the aforementioned remarks, the state variables chosen for the present model will be briefly discussed now. Use of temperature (the same for all constituents of the medium because of the assumption about the local thermodynamic equilibrium state) and solid skeleton displacement vector is rather obvious, thus it needs no further explanation. As an hygrometric state variable various physical quantities, which are thermodynamically equivalent, may be used, e.g. volumetric- or mass moisture content, vapour pressure, relative humidity, or capillary pressure. Analyzing concrete at high temperature, one must remember that at temperatures higher than the critical point of water (i.e. 647.3 K) there is no capillary (or free) water present in the pores of concrete, and there exists only the gas phase of water, i.e. vapour. Then, very different moisture contents may be encountered at the same moment in a heated concrete, ranging from full saturation with liquid water (e.g. in some nuclear vessels or in so called “moisture clog” zone in a heated concrete [26]) up to almost completely dry material. For these reasons it is not possible to use, in a direct way, one single variable for the whole range of moisture contents. Instead, an appropriate Stefan’s problem could be formulated, with different state variables in zones separated by moving interfaces. However, such an approach is numerically very costly, e.g. [27, 28], and usually avoided in practical applications, as already mentioned in [10].

For the description of the concrete moisture state, Bazant et al. used in their model [5,6] the relative humidity, but in zones fully saturated with liquid water, where pressures higher than the atmospheric one can occur, a different meaning must be given to this variable, permitting its value to be higher than one, what is physically inadmissible. Then, application of a shrinkage coefficient, relating strain changes with changes of the relative humidity, is consistent with the phenomenological approach, used in [5,6], but not with the mechanistic one, which is used in this paper. Apparently, the most natural choice for the state variable seems to be mass- or volumetric moisture content, which are well defined for the whole range of temperatures and pressures in concrete. However, these quantities are not continuous at interfaces between

different materials, and are not well adapted for numerical simulations, both in fully saturated conditions and in a range of very low moisture contents. Moreover, there is not any direct, physically sound (from the mechanistic point of view) relation between moisture content and stresses. Another possible choice for the moisture state variable is vapour pressure, which however has no physical meaning in a medium fully saturated with water and then, it creates serious numerical problems for moisture contents close to these conditions, as shown by our extensive tests.

The moisture state variable proposed by the authors in [10] is capillary pressure, which was shown to be a thermodynamic potential of the physically adsorbed water and, with an appropriate interpretation, can also be used for description of water at pressures higher than the atmospheric one [12]. The capillary pressure has been shown to assure good numerical performance of the computer code, [8-11], and is very convenient for analysis of stress state in concrete, because there is a clear relation between pressures and stresses, [24, 29]. Application of capillary pressure as a state variable was avoided in some previous models, e.g. [4-7], because of theoretical problems related to its definition at the macro-scale. However, some recent works in Thermodynamics, [24, 25], resolved these theoretical problems.

Hence, the chosen primary variables of the present model are the volume averaged values of: gas pressure, p^g , capillary pressure, p^c , temperature, T , and displacement vector of the solid matrix, \mathbf{u} .

For temperatures lower than the critical point of water, $T < T_{cr}$, and for capillary saturation range, $S > S_{ssp}(T)$ (S_{ssp} means the upper limit of the hygroscopic moisture range, being at the same time the lower limit of the capillary one), the capillary pressure is defined as

$$p^c = p^g - p^w, \quad (3.28)$$

where p^w denotes water pressure. This equation is, in reality, a constitutive relationship at thermodynamic equilibrium which can be obtained from an exploitation of the entropy inequality by means of the Coleman-Noll method, see e.g. [24, 25].

For all other situations, and in particular $T \geq T_{cr}$, when condition $S < S_{ssp}$ is always fulfilled (there is no capillary water in the pores), the capillary pressure only substitutes formally the water potential Ψ_c , defined as:

$$\Psi_c = \frac{RT}{M_w} \ln \left(\frac{p^{gw}}{f^{gws}} \right), \quad (3.29)$$

where M_w is the molar mass of water, R the universal gas constant and f^{gws} the fugacity of water vapour in thermodynamic equilibrium with saturated film of physically adsorbed water, [10]. For physically adsorbed water at lower temperatures ($S < S_{ssp}$ and $T < T_{cr}$) the fugacity f^{gws} should be substituted in the definition of the potential Ψ_c , (3.29), by the saturated vapour pressure p^{gws} . Having in mind the Kelvin equation, [30], valid for the equilibrium state of capillary water with water vapour above the curved interface (meniscus):

$$\ln \left(\frac{p^{gw}}{p^{gws}} \right) = - \frac{p^c M_w}{\rho^w RT}, \quad (3.30)$$

we can note, that in the situations, where (3.29) is valid, the capillary pressure may be treated formally as the water potential multiplied by the density of the liquid water, ρ^w , according to the relation, [10]:

$$p^c = -\Psi_c \rho^w, \quad (3.31)$$

Thanks to this similarity, it is possible to use during simulations “formally” the capillary pressure even in the low moisture content range, when the capillary water is not present in the pores. However, one should remember, that in such situations capillary pressure cannot be identified to a pressure in its normal physical meaning, [10], see for example (3.49).

3.4 CONSTITUTIVE RELATIONS

As constitutive relations may be used: equations of state for constituents of the medium, material functions describing certain physical properties of the analysed material, as well as some physical relations between fluxes of extensive thermodynamic quantities and intensive thermodynamic quantities (called sometimes thermodynamic forces) which cause them. These physical relations can be obtained directly from the entropy inequality, e.g. [24, 25], and they describe some well known laws of Physics, like Fourier’s law, Darcy’s law or Fick’s law.

In the model described herein, dry air, water vapour and their mixture are assumed to behave as perfect gases, following Dalton’s law and the Clapeyron equation of state:

$$p^g = p^{ga} + p^{gw}, \quad (3.32)$$

$$\rho^\pi = p^\pi M_\pi / TR, \quad (\pi = ga, gw, g) \quad (3.33)$$

$$\text{where } \frac{1}{M_g} = \frac{\rho^{gw}}{\rho^g} \frac{1}{M_w} + \frac{\rho^{ga}}{\rho^g} \frac{1}{M_a}, \quad (3.34)$$

The density of water vapour calculated by means of (3.33) differs significantly from the results of the laboratory tests for temperatures higher than approximately 160 °C, but as shown in [10] this difference has a small effect on the results of simulations concerning high temperature performance of concrete and (3.33) may be used for practical problems with a sufficient accuracy.

The state equation of water should take into account the considerable, non-linear decrease of water density in the temperature range close to the critical point of water, what has an important influence on hygro-thermal phenomena in concrete at these temperatures [10]. The following formula, [31], gives a reasonable accordance with experimental results and assures a good numerical performance of the code, [10]:

$$\rho_w = \left(b_0 + b_1 T + b_2 T^2 + b_3 T^3 + b_4 T^4 + b_5 T^5 \right) + (p_{wl} - p_{wr}) \left(a_0 + a_1 T + a_2 T^2 + a_3 T^3 + a_4 T^4 + a_5 T^5 \right), \quad (3.35)$$

$$\text{where: } p_{wl} = 10 \text{ MPa}, p_{wr} = 20 \text{ MPa}, a_0 = 4.89 \cdot 10^{-7}, a_1 = -1.65 \cdot 10^{-9}, a_2 = 1.86 \cdot 10^{-12}, \\ a_3 = 2.43 \cdot 10^{-13}, a_4 = -1.60 \cdot 10^{-15}, a_5 = 3.37 \cdot 10^{-18}, b_0 = 1.02 \cdot 10^{-3}, b_1 = -7.74 \cdot 10^{-1}, \\ b_2 = 8.77 \cdot 10^{-3}, b_3 = -9.21 \cdot 10^{-5}, b_4 = 3.35 \cdot 10^{-7}, b_5 = -4.40 \cdot 10^{-10}.$$

In the above formula water is assumed to be incompressible. At lower relative humidities, usually encountered at higher temperatures, most of the liquid water consists of the physically adsorbed water, which is exposed to strong interaction with the solid skeleton, resulting in an increase of the water density, [32]. At the same time one can expect a decrease of the density with an increase of the capillary pressure (decrease of the water pressure), what is the case in heated concrete. Having in mind these two opposite trends, as well as lack of sufficient experimental data, we have assumed here incompressibility of the liquid water inside the pores of concrete.

For the solid skeleton, the following form of the state equation has been assumed,

$$\rho^s = \rho^s(T, p^s, tr\boldsymbol{\sigma}', \Gamma_{dehydr}), \quad (3.36)$$

where p^s means the solid skeleton pressure [20, 21], given by (3.47), $tr\boldsymbol{\sigma}'$ the first invariant of effective stress tensor, defined by (3.48), and Γ_{dehydr} is the degree of cement dehydration at high temperature. The latter process starts at a temperature about 100°C and continues with variable intensity during increase of concrete temperature. The following relation for the rate of the first invariant of the effective stress tensor has been assumed, [20, 21],

$$\frac{D(tr\boldsymbol{\sigma}')}{Dt} = 3\tilde{K}_T \left(div \bar{\mathbf{v}}^s + \frac{1}{\tilde{K}_s} \frac{D p^s}{Dt} - \beta_s \frac{DT}{Dt} \right), \quad (3.37)$$

where β_s is thermal expansion coefficient of the solid, \tilde{K}_T and \tilde{K}_s the actual values of bulk moduli for the whole medium and the solid skeleton (grains), respectively, taking into account possible influence of both the dehydration and cracking process.

The inner structure of concrete pores is very complex and it contains both very narrow gel pores and much greater macro-pores and cracks (especially at higher temperatures), resulting sometimes in not continuous capillary pores. Nevertheless, at the macro-scale level, the volume averaged advective flux (i.e. caused by pressure gradients) of liquid water may be still described by Darcy's law, [32, 33], in the following form, [10, 20, 21],

$$n S_\pi \mathbf{v}^{\pi s} = -\frac{k^{r\pi} \mathbf{k}}{\mu^\pi} \left[grad p^\pi - \rho^\pi \mathbf{g} \right], \quad (3.38)$$

where \mathbf{k} is intrinsic permeability tensor, $k^{r\pi}$ and μ^π ($\pi=g,w$) denote relative permeability and dynamic viscosity of the gaseous phase and liquid water. The fluids' viscosities change significantly with temperature increase, what should be taken into account during analysis of concrete at high temperature. The formulae describing these changes are given in [8].

During heating of concrete, its intrinsic permeability k may increase by up to 4 orders of magnitude when compared to its initial value at ambient temperature, [7, 26]. The dehydration and cracking progress with increasing temperature (cracking may be caused also by the mechanical stress at macro-scale) and result in gradual increase of the permeability value. For description of these intrinsic permeability changes, different approaches may be followed, [9]. In the model described in this Chapter a mechanistic one is adopted, assuming that intrinsic permeability does depend not only upon temperature and moisture content, as assumed in classical phenomenological approach, e.g. [5,6], but also upon gas pressure and mechanical damage parameter, d , [8, 10]:

$$k = k_o \cdot 10^{A_T(T-T_o)} \cdot \left(\frac{p^g}{p_o^g} \right)^{A_p} \cdot 10^{A_d d}, \quad (3.39a)$$

where d is the mechanical damage parameter, A_T , A_p and A_d are material constants. The term related to mechanical damage describes the effect of concrete cracking, and the gas pressure term the effect of cracks' opening on the increase of the permeability. The influence of particular terms in (3.39a) on performance of concrete at high temperature is discussed in [9, 11]. The latter relation can be alternatively expressed in terms of total damage parameter, D , defined by eq. (3.54),

$$k = k_o \cdot 10^{f(T)} \cdot \left(\frac{p^g}{p_o^g} \right)^{A_p} \cdot 10^{A_D D}, \quad (3.39b)$$

what is more consistent with a mechanistic approach. In this formula A_D takes into account the permeability increase caused by cracking (both mechanical and thermally induced), which may be described in terms of mechanical and, in part of thermo-chemical damage parameter. Function $f(T) = A_T^2 (T - T_0)^2 + A_T^1 (T - T_0)$, with values always smaller than the parameter $A_T(T - T_0)$, takes into account the influence of the dehydration process on the permeability of concrete at high temperature.

However, as shown in [34], there are some differences between the two formulations of (3.39), when their parameters are determined experimentally, and the second one assures better numerical performance of the computer code.

Concrete is a porous material with a very well developed internal surface of solid skeleton, hence mass transport phenomena in the adsorbed water film are of importance, [32]. For description of surface diffusion of the adsorbed water, in the whole temperature range, Fick's law in the following form is used:

$$n S_w \mathbf{v}^{ws} = -\mathbf{D}_b \text{grad } S_w, \quad (3.40)$$

where $\mathbf{D}_b = f(S_w, T)$ is the bound water diffusion tensor, [8], and $S_w(\Psi_c)$ means the degree of saturation with the adsorbed water, which is assumed to be constant in the capillary moisture range (there the adsorbed water mass flux is neglected).

As a constitutive law for the diffusional flow of gas particles in the mixture of dry air and water vapour, Fick's law is applied in the following form, [20, 21],

$$\mathbf{J}_d^{gw} = -\rho^g \mathbf{D}_{g_w} \text{grad} \left(\frac{\rho^{gw}}{\rho^g} \right), \quad (3.41)$$

where $\mathbf{D}_{g_w} = f(S_w, T, p^g, n, f_s)$ is the effective diffusivity tensor of vapour in the air. In the latter relation, Knudsen effect [32] in very narrow concrete pores is taken into account, by introduction of the structure factor, f_s , see [8].

For description of heat conduction in concrete at high temperature Fourier's law is used,

$$\tilde{\mathbf{q}} = -\chi_{eff} \text{grad } T, \quad (3.42)$$

where,

$$\chi_{eff} = \chi^s + \chi^w + \chi^g, \quad (3.43)$$

is the effective thermal conductivity, dependent on the temperature and moisture content. Usually this effective value is measured experimentally and takes into account not only pure heat conduction, but also several micro-scale phenomena inside pores, like radiation and micro-convection. Often tests are performed only for the dry material at various temperatures. In such a case effective thermal conductivity of moist concrete may be evaluated from the formula [8]:

$$\chi_{eff} = \chi_{dry}(T) \left[1 + \frac{4n\rho^w S_w}{(1-n)\rho^s} \right], \quad (3.44)$$

where χ_{dry} is effective thermal conductivity of the dry material.

To describe the heat sinks, $\dot{m}_{dehydr} \Delta H_{dehydr}$, and the skeleton mass sinks, \dot{m}_{dehydr} , related to the cement dehydration process, it is necessary to know the time evolution of the degree of cement dehydration, $\Gamma_{dehydr}(t)$. It may be described by the following equation, [8]:

$$\Gamma_{dehydr}(t) = \Gamma_{dehydr}[T_{\max}(t)] \quad (3.45)$$

where $T_{\max}(t)$ is the highest temperature reached by the concrete up to the time instant t . This relation assumes irreversibility of the dehydration process.

The skeleton mass sinks may be assumed as proportional to the degree of concrete dehydration, hence,

$$\dot{m}_{dehydr} = \rho^s A_h \frac{D \Gamma_{dehydr}}{Dt}, \quad (3.46)$$

where A_h is a material parameter.

Dealing with porous media, it is convenient to use the effective stresses, $\boldsymbol{\sigma}'$, directly responsible for all deformations of the solid skeleton. Using the Coleman-Noll method, from the entropy inequality, the following relations for thermodynamic pressure of solid skeleton, p^s , and effective stress tensor, $\boldsymbol{\sigma}'$ can be obtained, [24],

$$p^s = p^w S_w + p^g (1 - S_w), \quad (3.47)$$

$$\boldsymbol{\sigma}' = \boldsymbol{\sigma} + \alpha p^s \mathbf{I}, \quad (3.48)$$

where,

$$\begin{aligned} p &= p^g - p_{atm} && \text{for } S \leq S_{ssp} \\ p &= p^g - p_{atm} - (S_w - S_{ssp}) p^c && \text{for } S > S_{ssp} \end{aligned} \quad (3.49)$$

with p_{atm} denoting atmospheric pressure, \mathbf{I} the unit tensor of the second order.

The constitutive relationship for the solid skeleton in the following form,

$$d\boldsymbol{\sigma}' = \mathbf{C}_T (d\boldsymbol{\varepsilon} - d\boldsymbol{\varepsilon}_T - d\boldsymbol{\varepsilon}_0) \quad (3.50)$$

is assumed together with the definition of the strain matrix \mathbf{B} relating strain tensor $\boldsymbol{\varepsilon}$ and displacement vector \mathbf{u} ,

$$\boldsymbol{\varepsilon} = \mathbf{B}\mathbf{u}, \quad (3.51)$$

where \mathbf{C}_T is the tangent matrix, $d\boldsymbol{\varepsilon}_T = \mathbf{I} \beta_s/3 dT$, is the strain caused by thermo-elastic expansion and $d\boldsymbol{\varepsilon}_0$ represents the autogeneous strain increment and the irreversible part of the thermal strain.

During heating of concrete at high temperature complex physical and chemical processes take place, resulting in changes of the skeleton mechanical properties, development of thermally and mechanically induced micro-cracks, as well as porosity increase, [5-7,8]. Because of this, stress – strain behaviour of concrete at high temperature is non-linear. It will be discussed in detail in paragraph 3.5.

Several physical properties of concrete at high temperature, like porosity n , density ρ^s , permeability k , Young modulus E , compressive and tensile strengths, f_c and f_t , effective thermal conductivity χ_{eff} , effective thermal capacity $(C_p \rho)_{eff}$, are dependent upon temperature, gas pressure, water saturation degree, dehydration degree and mechanical damage parameter (describing volume density of cracks). The specific form of these dependences should be determined experimentally for the concrete under consideration. Some formulae and their

parameters for several concretes, including HPC and UHPC, have been already presented [8-10] and are not given here (see Chapter 4).

For model closure we need also some thermodynamic relations, like equation (3.29) for hygroscopic moisture or Kelvin's equation (3.30) for capillary or free water, depending on the actual temperature and relative humidity value. These two equations relate the capillary pressure (or the water potential, Ψ_c) to the vapour pressure and temperature at thermodynamic equilibrium of water vapour and liquid water inside the pores. For evaluation of the water vapour saturation pressure, p^{gws} , necessary in the Kelvin equation (3.30), we use the formula of Hyland and Wexler [35] which may be applied with sufficient accuracy for practical problems, in the whole range of temperatures lower than the critical point of water, T_{cr} .

3.5 THERMO-CHEMICAL AND MECHANICAL DAMAGE OF CONCRETE

During heating, concrete at high temperature is exposed to complicated physical and chemical transformations, [3, 7], causing changes of its inner structure, what has also a sensible influence on the material properties. From a practical point of view, among the most important macroscopic consequences of these processes are concrete dehydration and crack development, resulting in a significant decrease of mechanical properties of concrete at high temperatures. The material stress – strain behaviour in such conditions is highly non-linear and depends not only on the temperature and dehydration degree, but also on the history of mechanical loading during heating [3].

All these phenomena should be accounted for during analysis of the performance of concrete structures at high temperatures. In previous research papers [8-11] the changes of concrete strength properties were expressed as functions of the mechanical damage and temperature (only heating processes were analysed), hence any information about the thermally induced material deterioration was not available directly. However, the latter one may be of importance for proper assessment of the state of concrete structure previously exposed to high temperature, e.g. after fire or nuclear accident, because thermo-chemical deterioration is irreversible.

For these reasons it was introduced in the model a parameter describing the degree of the latter process advancement, similarly as done by Gerard et al. [36] and Nechnech et al. [37]. It was called thermo-chemical damage, V , because it accounts for changes of material stiffness, both due to thermally induced micro-cracks, caused mainly by stresses at micro- and meso-level, (e.g. resulting from different thermal expansion coefficients of cement paste and aggregate, and from local increase of dehydration products' volume), and due to the decrease of concrete strength properties caused by the dehydration process (thus related to the Γ_{dehydr} value). Analysis of the experimental results for several HPC concretes showed, that the chemical effects (dehydration) cannot be distinguished with sufficient accuracy from the micro-thermo-mechanical ones [34]. An example of such an approximate damage decomposition, performed on the basis of the results of residual strength tests (i.e. for cooled specimen), to determine the total value of thermo-chemical damage, and Differential Thermal Gravimetry (DTG) tests, to determine degree of dehydration and to assess the loss of concrete strength related to it, is shown for two HPCs in [1]. The resulting thermal component of damage decreases in some points, what is physically inadmissible because damage is an irreversible physical quantity. This means that probably the chemical component was overestimated (its assessment is based on several assumptions, [34]), and the presented results could be treated only as qualitative ones. Hence these two damage components are not considered separately, even if it would be more useful from a practical point of view.

The thermo-chemical damage parameter, V , is defined in terms of the experimentally determined evolution of Young's modulus of mechanically undamaged material (i.e. heated to a given temperature, without any additional mechanical load), E_o , expressed as a function of temperature, Fig.3,

$$V = 1 - \frac{E_o(T)}{E_o(T_a)} \quad (3.52)$$

where $T_a = 20^\circ\text{C}$ is room temperature.

Mechanical damage of concrete is considered following the scalar isotropic model by Mazars [38-39]. In this model, the damaged material at given temperature, T , is supposed to behave elastically and to remain isotropic. Its Young's modulus at this temperature, $E(T)$, can be obtained from the value of mechanically undamaged material at the same temperature, $E_o(T)$, [38-39], and mechanical damage parameter, d , being a measure of cracks' volume density in the material,

$$E(T) = (1 - d) E_o(T), \quad (3.53)$$

A total effect of the mechanical and thermo-chemical damages, to which the material is exposed at the same time, is multiplicative, i.e. the total damage parameter, D , is defined by the following formula,

$$D = 1 - \frac{E(T)}{E_o(T_a)} = 1 - \frac{E(T)}{E_o(T)} \frac{E_o(T)}{E_o(T_a)} = 1 - (1 - d) \cdot (1 - V), \quad (3.54)$$

and not just by the sum of the two components of damage.

Therefore, the classical effective stress concept, [40], is modified to take into account both the mechanical and thermo-chemical damage, so a further reduction of resistant section area due to thermo-chemical degradation is added to that caused by the mechanical damage, i.e. the section reduction by cracking:

$$\tilde{\sigma} = \sigma \frac{S}{\tilde{S}} = \frac{\sigma}{(1 - d)(1 - V)}, \quad (3.55)$$

where S and \tilde{S} mean total and resistant area of the damaged material, σ is the tensor of nominal stress and $\tilde{\sigma}$ the tensor of "modified" effective stress (in the sense of Mazars [38-39]).

This definition of modified effective stress leads to the following form of elastic energy:

$$\rho\psi_e = \frac{1}{2}(1 - d)(1 - V)\Lambda_0 : \epsilon^e : \epsilon^e, \quad (3.56)$$

where the term $(\rho\psi_e)$ is the scalar thermodynamic potential, Λ_0 the initial material stiffness matrix and ϵ^e elastic strain tensor.

Hence, the stress-strain relationship, and the released energy rate, Y , are as follows:

$$\sigma = (1 - d)(1 - V)\Lambda_0 : \epsilon^e = (1 - D)\Lambda_0 : \epsilon^e, \quad (3.57)$$

$$Y = -\frac{\partial(\rho\psi_e)}{\partial D} : \epsilon^e : \epsilon^e = \frac{1}{2}\Lambda_0 : \epsilon^e : \epsilon^e, \quad (3.58)$$

In Mazars' model the damage of concrete grows with an increase of the total strain, i.e. hygro-thermal- plus mechanical one, as usual in many damage models, and cannot diminish because of restrictions imposed by the Clausius-Duhem inequality [39, 41]. The model assumes

that the extensions are responsible for crack propagation, i.e. loads allow extensions and the “mode cracking I” is predominant, [38-39, 41].

Developments concerning a possibility to take into account "unilateral effects" for considering cycling loading, inversion of the sign of the stresses and the consequent stiffness recovery, are in progress. These effects regard mainly the mechanical damage which is correlated directly to cracking due to the external loads. Thermo-chemical damage is influenced by this phenomenon only in the part related to temperature induced micro-cracks.

Taking into account different behaviour of concrete in tension and in compression, the damage parameter d , i.e. mechanical part of damage, is decomposed into two parts, d_t for tension and d_c for compression [41]. These damage variables are functions of the average equivalent strain, $\bar{\varepsilon}$, given by equation (3.61), which can be obtained from the relation, modified in comparison to [41]:

$$\sigma_i = \left\{ \frac{\kappa_0 (1 - A_i)}{\bar{\varepsilon}} + \frac{A_i}{\exp[B_i (\bar{\varepsilon} - \kappa_0) g(\varepsilon_i)]} \right\} E \varepsilon_i \quad (i = t, c) \quad (3.59)$$

where $g(\varepsilon_i)$ is a correcting function given by (3.65), κ_0 the initial value of the hardening/softening parameter $\kappa(D)$, eq. (3.66), which satisfies de Saint-Venant's criterion of maximum principal strain (loading surface):

$$f(\boldsymbol{\varepsilon}, \boldsymbol{\Lambda}, \kappa_0) = \bar{\varepsilon} - \kappa(D), \quad (3.60)$$

We follow the non-local formulation of damage theory, where the average equivalent strain over the representative volume is defined as [41],

$$\bar{\varepsilon}(x) = \frac{1}{V_r(x)} \int_V \zeta(x-s) \tilde{\varepsilon}(s) dv, \quad (3.61)$$

where ζ is a distribution function and

$$\tilde{\varepsilon} = \sqrt{\sum \langle \varepsilon_i \rangle_+^2} \quad \left(\langle x \rangle_+ = \frac{|x| + x}{2} \right) \quad (3.62)$$

are the equivalent strains (always positive) controlling the growth of damage.

The mechanical damage is obtained from its two components as their weighted sum:

$$d = \alpha_t d_t + \alpha_c d_c, \quad (3.63)$$

where α_t and α_c are weighting coefficients defined by [41]:

$$\alpha_t = \sum_{i=1}^3 \left(\frac{\varepsilon_{ti} \langle \varepsilon_i \rangle_+}{\tilde{\varepsilon}^2} \right)^\beta \quad \alpha_c = \sum_{i=1}^3 \left(\frac{\varepsilon_{ci} \langle \varepsilon_i \rangle_+}{\tilde{\varepsilon}^2} \right)^\beta \quad (3.64)$$

The temperature dependent parameters, A_b , A_c , B_b , B_c , are characteristics of the material and can be identified from the stress-strain relationships obtained during the concrete compression and traction experimental tests. The exponent β takes into account the effect of damage on the response of the material under shear.

Calibrating the model coefficients at various temperatures, it is possible to observe that, in particular for High Performance and Ultra High Performance Concrete, theoretical stress-strain curves exhibit some rapid stiffness jumps for strains exceeding the elastic threshold (see [1]), leading to an unphysical behaviour can be corrected by introducing in (3.59) a especial correction function $g(\varepsilon)$. It may be found from an additional condition concerning continuity of

the first derivative of the curve, i.e. equality of the left and right curve tangents at the elastic threshold [1]. Physically this means a modification of the material response, as compared to the original formulation of damage theory, [38, 39, 41].

In fact, in classical Mazar's model the σ - ε curve for a given temperature (in a case of uniaxial compression) has to pass through the two points corresponding to the elastic threshold and to the maximum concrete strength, and at the latter point the first derivative of the curve must be equal to zero (stationarity condition).

This additional condition physically means that the first derivative of the stress-strain curve has to be equal to the material Young's modulus at the elastic threshold.

As far as the function $g(\varepsilon)$ is concerned, one can assume for it various mathematical forms, but the following exponential form was found most convenient [1]:

$$g(\varepsilon_c) = \left(\frac{\kappa_0 - \varepsilon_c}{\kappa_0 - \varepsilon_{c_{\max}}} \right)^\gamma, \quad (3.65)$$

where $\varepsilon_{c_{\max}}$ is the strain corresponding to the stress equal to the compression strength and parameter γ is function of B_c and $\varepsilon_{c_{\max}}$. Such an approach assures a good accordance between the model and the experimental data.

Moreover, in Mazars' model $\kappa_o(T)$ is the tensile strain, at which damage is initiated at a given temperature T , i.e. when the maximum tensile stress $f_t(T)$ is reached in an uniaxial test. It can be calculated from the formula:

$$\kappa_o(T) = \frac{f_t(T)}{E_o(T)}, \quad (3.66)$$

3.6 GOVERNING EQUATIONS OF THE MODEL

The macroscopic conservation equations, in their general form, have been formulated in paragraph 3.2 of this Chapter. Here we introduce into them the constitutive relations (paragraph 3.4) to obtain the governing equations of the present model.

Material time derivative of the solid density, appearing in several equations of paragraph 3.2, taking into account (3.36), (3.37) and (3.48), can be written as, [20, 21]:

$$\begin{aligned} \frac{1}{\rho^s} \frac{D \rho^s}{Dt} = & -\beta_s \frac{DT}{Dt} + \frac{1}{\tilde{K}_s} \frac{D p^s}{Dt} - \frac{1}{3(1-n)\tilde{K}_s} \frac{D \text{tr} \boldsymbol{\sigma}'}{Dt} \\ & + \frac{1}{\rho^s} \frac{\partial \rho^s}{\partial \Gamma_{dehydr}} \frac{D \Gamma_{dehydr}}{Dt}, \end{aligned} \quad (3.67)$$

where,

$$\frac{1}{\rho^s} \frac{\partial \rho^s}{\partial p^s} = \frac{1}{\tilde{K}_s}, \quad \frac{1}{\rho^s} \frac{\partial \rho^s}{\partial \text{tr} \boldsymbol{\sigma}'} = -\frac{1}{3(n-1)\tilde{K}_s}, \quad (3.68)$$

$$\frac{1}{\rho^s} \frac{\partial \rho^s}{\partial T} = -\beta_s, \quad \frac{1}{\rho^w} \frac{\partial \rho^w}{\partial T} = -\beta_w, \quad (3.69)$$

$$\alpha = 1 - \frac{\tilde{K}_T}{\tilde{K}_s}, \quad (3.70)$$

Introducing (3.67) into the mass conservation equation (3.8), the latter may be presented in the following form:

$$\begin{aligned} & \frac{\alpha - n}{\tilde{K}_s} \frac{D}{Dt} \left[S_w p^w + (1 - S_w) p^g \right] - \beta_s (\alpha - n) \frac{DT}{Dt} \\ & + \alpha \operatorname{div} \mathbf{v}^s + \frac{n}{S_w} \frac{D S_w}{Dt} - n \beta_w \frac{DT}{Dt} + \frac{1}{S_w \rho^w} \operatorname{div} (n S_w \rho^w \mathbf{v}^{ws}), \\ & + \frac{(1 - n)}{\rho^s} \frac{\partial \rho^s}{\partial \Gamma_{dehydr}} \frac{D \Gamma_{dehydr}}{Dt} = \frac{\dot{m}_{dehydr} - \dot{m}_{vap}}{S_w \rho^w} - \frac{\dot{m}_{dehydr}}{\rho^s}. \end{aligned} \quad (3.71)$$

After grouping together terms connected to time derivatives of specific variables and multiplying by S_w , we obtain:

$$\begin{aligned} & \frac{\alpha - n}{\tilde{K}_s} S_w^2 \frac{D p^w}{Dt} + \frac{\alpha - n}{\tilde{K}_s} S_w (1 - S_w) \frac{D p^g}{Dt} + \alpha S_w \operatorname{div} \mathbf{v}^s \\ & - \beta_{sw} \frac{DT}{Dt} + \left(\frac{\alpha - n}{\tilde{K}_s} S_w (p^w - p^g) + n \right) \frac{D S_w}{Dt} + \frac{1}{\rho^w} \operatorname{div} (n S_w \rho^w \mathbf{v}^{ws}), \\ & + \frac{(1 - n) S_w}{\rho^s} \frac{\partial \rho^s}{\partial \Gamma_{dehydr}} \frac{D \Gamma_{dehydr}}{Dt} = \frac{\dot{m}_{dehydr} - \dot{m}_{vap}}{\rho^w} - \frac{\dot{m}_{dehydr}}{\rho^s} S_w \end{aligned} \quad (3.72)$$

$$\text{where } \beta_{sw} = S_w [(\alpha - n) \beta_s + n \beta_w], \quad (3.73)$$

Usually in practical problems the concrete skeleton can be assumed to be incompressible, hence:

$$\alpha = 1, \quad 1/\tilde{K}_s = 0, \quad (3.74)$$

and equation (3.72) is reduced to its simplified form:

$$\begin{aligned} & S_w \operatorname{div} \mathbf{v}^s - \beta_{sw}^* \frac{DT}{Dt} + n \frac{D S_w}{Dt} + \frac{(1 - n) S_w}{\rho^s} \frac{\partial \rho^s}{\partial \Gamma_{dehydr}} \frac{D \Gamma_{dehydr}}{Dt}, \\ & + \frac{1}{\rho^w} \operatorname{div} (n S_w \rho^w \mathbf{v}^{ws}) = \frac{\dot{m}_{dehydr} - \dot{m}_{vap}}{\rho^w} - \frac{\dot{m}_{dehydr}}{\rho^s} S_w \end{aligned} \quad (3.75)$$

$$\text{with, } \beta_{sw}^* = S_w [(1 - n) \beta_s + n \beta_w], \quad (3.76)$$

Performing similar transformations, as done above, for the dry air mass balance equation (3.12), one obtains:

$$\begin{aligned} & \frac{\alpha - n}{\tilde{K}_s} S_g S_w \frac{D p^w}{Dt} + \frac{\alpha - n}{\tilde{K}_s} S_g^2 \frac{D p^g}{Dt} - \left(n - \frac{\alpha - n}{\tilde{K}_s} S_g p^c \right) \frac{D S_w}{Dt} \\ & - \beta_s (\alpha - n) S_g \frac{DT}{Dt} + S_g \alpha \operatorname{div} \mathbf{v}^s + \frac{S_g n}{\rho^{ga}} \frac{D \rho^{ga}}{Dt} + \frac{1}{\rho^{ga}} \operatorname{div} \mathbf{J}_d^{ga} \\ & + \frac{1}{\rho^{ga}} \operatorname{div} (n S_g \rho^{ga} \mathbf{v}^{gs}) + \frac{(1 - n) S_g}{\rho^s} \frac{\partial \rho^s}{\partial \Gamma_{dehydr}} \frac{D \Gamma_{dehydr}}{Dt} = - \frac{\dot{m}_{dehydr}}{\rho^s} S_g, \end{aligned} \quad (3.77)$$

For the case of incompressible solid skeleton, i.e. $\alpha=1$ and $1/\tilde{K}_s = 0$, we obtain the following simplified form of equation (3.77):

$$\begin{aligned}
 & -n \frac{D S_w}{Dt} - \beta_s (1-n) S_g \frac{DT}{Dt} + S_g \operatorname{div} \mathbf{v}^s + \frac{S_g n}{\rho^{ga}} \frac{D \rho^{ga}}{Dt} + \frac{1}{\rho^{ga}} \operatorname{div} \mathbf{J}_g^{ga} + \\
 & + \frac{1}{\rho^{ga}} \operatorname{div} (n S_g \rho^{ga} \mathbf{v}^{gs}) + \frac{(1-n) S_g}{\rho^s} \frac{\partial \rho^s}{\partial \Gamma_{hydr}} \frac{D \Gamma_{hydr}}{Dt} = -\frac{\dot{m}_{dehydr}}{\rho^s} S_g
 \end{aligned} \quad (3.78)$$

Similar transformations, done for the vapour mass balance equation (3.17), result in:

$$\begin{aligned}
 & \frac{\alpha-n}{\tilde{K}_s} S_g S_w \frac{D p^w}{Dt} + \frac{\alpha-n}{\tilde{K}_s} S_g^2 \frac{D p^g}{Dt} - \left(n - \frac{\alpha-n}{\tilde{K}_s} S_g p^c \right) \frac{D S_w}{Dt} \\
 & - \beta_s (\alpha-n) S_g \frac{DT}{Dt} + S_g \alpha \operatorname{div} \mathbf{v}^s + \frac{n S_g}{\rho^{gw}} \frac{D \rho^{gw}}{Dt} + \frac{1}{\rho^{gw}} \operatorname{div} \mathbf{J}_d^{gw} + \\
 & + \frac{1}{\rho^{gw}} \operatorname{div} (n S_g \rho^{gw} \mathbf{v}^{gs}) + \frac{(1-n) S_g}{\rho^s} \frac{\partial \rho^s}{\partial \Gamma_{dehydr}} \frac{D \Gamma_{dehydr}}{Dt} = -\frac{\dot{m}_{dehydr}}{\rho^s} S_g + \frac{\dot{m}_{vap}}{\rho^{gw}}
 \end{aligned} \quad (3.79)$$

and its simplified form (i.e. for $\alpha=1$ and $1/\tilde{K}_s = 0$):

$$\begin{aligned}
 & -n \frac{D S_w}{Dt} - \beta_s (1-n) S_g \frac{DT}{Dt} + S_g \operatorname{div} \mathbf{v}^s + \frac{n S_g}{\rho^{gw}} \frac{D \rho^{gw}}{Dt} + \frac{1}{\rho^{gw}} \operatorname{div} \mathbf{J}_d^{gw} \\
 & + \frac{1}{\rho^{gw}} \operatorname{div} (n S_g \rho^{gw} \mathbf{v}^{gs}) + \frac{(1-n) S_g}{\rho^s} \frac{\partial \rho^s}{\partial \Gamma_{dehydr}} \frac{D \Gamma_{dehydr}}{Dt} = -\frac{\dot{m}_{dehydr}}{\rho^s} S_g + \frac{\dot{m}_{vap}}{\rho^{gw}}
 \end{aligned} \quad (3.80)$$

The two latter mass balance equations for water vapour may be used to eliminate from equations (3.72) or (3.75) the vapour mass source term \dot{m}_{vap} , for which we do not have any constitutive relation (its evolution is however controlled by the enthalpy conservation equation). Hence, the simplified mass balance equations for the liquid water and vapour are summed together, the first one multiplied by ρ^w and the second one by ρ^{gw} , resulting in the following mass balance equation for water species:

$$\begin{aligned}
 & n (\rho^w - \rho^{gw}) \frac{D S_w}{Dt} - \beta_{swg} \frac{DT}{Dt} + (\rho^{gw} S_g + \rho^w S_w) \operatorname{div} \mathbf{v}^s + \\
 & - \operatorname{div} \mathbf{J}_d^{gw} + S_g n \frac{D \rho^{gw}}{Dt} + \operatorname{div} (n S_g \rho^{gw} \mathbf{v}^{gs}) + \operatorname{div} (n S_w \rho^w \mathbf{v}^{ws}) + \\
 & + \frac{(1-n) (S_g \rho^{gw} + \rho^w S_w)}{\rho^s} \frac{\partial \rho^s}{\partial \Gamma_{dehydr}} \frac{D \Gamma_{dehydr}}{Dt} = -\frac{\rho^{gw} S_g + \rho^w S_w - \rho^s}{\rho^s} \dot{m}_{dehydr}
 \end{aligned} \quad (3.81)$$

$$\text{where} \quad \beta_{swg} = \beta_s (1-n) (S_g \rho^{gw} + S_w \rho^w) + n \beta_w S_w \rho^w, \quad (3.82)$$

The enthalpy balance equation (3.20), after accounting for (3.43), can be written as:

$$\begin{aligned}
 & (\rho C_p)_{eff} \frac{DT}{Dt} + (\rho_w C_p^w \mathbf{v}^{ws} + \rho_g C_p^g \mathbf{v}^{gs}) \cdot \operatorname{grad} T \\
 & + \operatorname{div} (\chi_{eff} \operatorname{grad} T) = -\dot{m}_{vap} \Delta H_{vap} - \dot{m}_{dehydr} \Delta H_{dehydr},
 \end{aligned} \quad (3.83)$$

where the vapour mass source term \dot{m}_{vap} can be eliminated by use of the vapour mass balance equation multiplied by ρ^{gw} .

Considering the effective stress definition (3.48) together with (3.49), the macroscopic linear momentum balance equation for the whole medium (3.25), may be expressed in the following form:

$$\text{div}(\boldsymbol{\sigma}' - p \mathbf{I}) + \rho \mathbf{g} = 0, \quad (3.84)$$

If the partial derivatives of the displacements with respect to the material coordinates \mathbf{X} are small compared to unity, their squares and products may be neglected in comparison to the linear terms. The remaining terms give the small strain tensor which is used in the classical linearized theory of small strains and rotations.

In these conditions, the Eulerian strain tensor also reduces to the form of the small-strain tensor, except that the derivatives are with respect to the spatial coordinates instead of the material coordinates. When displacements and displacements gradients are sufficiently small, the distinction between the two small-strain definitions is usually ignored and the deformed configuration is virtually indistinguishable from the undeformed configuration. Hence, assuming small displacements for the solid phase, we can neglect the convective terms in the balance equations.

To describe uniquely the state of concrete at high temperature, we need 4 primary state variables, i.e. gas pressure, p^g , capillary pressure, p^c , temperature, T , and displacement vector, \mathbf{u} , as well as 3 variables describing advancement of the dehydration and deterioration processes, i.e. degree of dehydration, Γ_{dehydr} , chemical damage parameter, V , and mechanical damage parameter, d . All other physical quantities characterizing the moist concrete and its constituents can be found by means of the state equations and thermodynamic relations presented in paragraph 3.3.

Thus totally, the present model consists of 7 equations: 2 mass balances (continuity equations), enthalpy (energy) balance, linear momentum balance (mechanical equilibrium equation) and 3 evolution equations. The model equations for the case of incompressible skeleton ($\alpha=1$), expressed in terms of the primary state variables, after introducing the constitutive relations, have the following final form:

- *Mass balance equation of the dry air (involving the solid skeleton mass balance):*

$$\begin{aligned} & -n\rho^{ga} \left(\frac{\partial S_w}{\partial T} \frac{\partial T}{\partial t} + \frac{\partial S_w}{\partial p^c} \frac{\partial p^c}{\partial t} \right) - \beta_s \rho^{ga} (1-n)(1-S_w) \frac{\partial T}{\partial t} \\ & + (1-S_w) \rho^{ga} \text{div} \frac{\partial \mathbf{u}}{\partial t} + (1-S_w) n \left(\frac{\partial \rho^{ga}}{\partial T} \frac{\partial T}{\partial t} + \frac{\partial \rho^{ga}}{\partial p^c} \frac{\partial p^c}{\partial t} + \frac{\partial \rho^{ga}}{\partial p^g} \frac{\partial p^g}{\partial t} \right) \\ & - \text{div} \left[\rho^g \frac{M_a M_w}{M_g^2} \mathbf{D}_b^{ga} \text{grad} \left(\frac{p^{ga}}{p^g} \right) \right] + \text{div} \left\{ \rho^{ga} \frac{\mathbf{k}k^{rg}}{\mu^g} [-\text{grad} p^g + \rho^g \mathbf{g}] \right\} \\ & = \frac{\rho^{ga}}{\rho^s} (1-S_w) \left[\dot{m}_{dehydr} + (1-n) \frac{\partial \rho^s}{\partial \Gamma_{dehydr}} \frac{\partial \Gamma_{dehydr}}{\partial t} \right] \end{aligned} \quad (3.85)$$

- Mass balance equation of the water species (involving the solid skeleton mass balance):

$$\begin{aligned}
 & n(\rho^w - \rho^{gw}) \left(\frac{\partial S_w}{\partial T} \frac{\partial T}{\partial t} + \frac{\partial S_w}{\partial p^c} \frac{\partial p^c}{\partial t} \right) + [\rho^w S_w + \rho^{gw} (1 - S_w)] \operatorname{div} \frac{\partial \mathbf{u}}{\partial t} \\
 & + (1 - S_w) n \left(\frac{\partial \rho^{gw}}{\partial T} \frac{\partial T}{\partial t} + \frac{\partial \rho^{gw}}{\partial p^c} \frac{\partial p^c}{\partial t} \right) - \operatorname{div} \left[\rho^g \frac{M_a M_w}{M_g^2} \mathbf{D}_d^{gw} \operatorname{grad} \left(\frac{p^{gw}}{p^g} \right) \right] \\
 & + \operatorname{div} \left\{ \rho^{gw} \frac{\mathbf{k}k^{rg}}{\mu^g} [-\operatorname{grad} p^g + \rho^g \mathbf{g}] \right\} - \beta_{swg} \frac{\partial T}{\partial t} \\
 & + \operatorname{div} \left\{ \rho^w \frac{\mathbf{k}k^{rw}}{\mu^w} [-\operatorname{grad} p^g + \operatorname{grad} p^c + \rho^w \mathbf{g}] \right\} = \\
 & + \frac{\rho^w S_w + \rho^{gw} (1 - S_w)}{\rho^s} \left[(1 - n) \frac{\partial \rho^s}{\partial \Gamma_{dehydr}} \frac{\partial \Gamma_{dehydr}}{\partial t} + \dot{m}_{dehydr} \right] - \dot{m}_{dehydr},
 \end{aligned} \tag{3.86}$$

with β_{swg} defined by (3.82).

- Enthalpy balance equation of the multi-phase medium:

$$\begin{aligned}
 & (\rho C_p)_{eff} \frac{\partial T}{\partial t} + \rho^w C_p^w \left\{ \frac{\mathbf{k}k^{rw}}{\mu^w} [-\operatorname{grad} p^g + \operatorname{grad} p^c + \rho^w \mathbf{g}] \right\} \cdot \operatorname{grad} T \\
 & + \rho^g C_p^g \left\{ \frac{\mathbf{k}k^{rg}}{\mu^g} [-\operatorname{grad} p^g + \rho^g \mathbf{g}] \right\} \cdot \operatorname{grad} T - \operatorname{div} (\chi_{eff} \operatorname{grad} T) \\
 & = -\dot{m}_{vap} \Delta H_{vap} - \dot{m}_{dehydr} \Delta H_{dehydr}
 \end{aligned} \tag{3.87}$$

where the water vapour source term is given by:

$$\begin{aligned}
 \dot{m}_{vap} = & -\rho^w S_w \operatorname{div} \frac{\partial \mathbf{u}}{\partial t} + \beta_{sw}^* \rho^w \frac{\partial T}{\partial t} - \rho^w n \left(\frac{\partial S_w}{\partial T} \frac{\partial T}{\partial t} + \frac{\partial S_w}{\partial p^c} \frac{\partial p^c}{\partial t} \right) \\
 & - \operatorname{div} \left[\rho^w \frac{\mathbf{k}k^{rw}}{\mu^w} (-\operatorname{grad} p^g + \operatorname{grad} p^c + \rho^w \mathbf{g}) \right] + \\
 & - \left(\dot{m}_{dehydr} + (1 - n) \frac{\partial \rho^s}{\partial \Gamma_{dehydr}} \frac{\partial \Gamma_{dehydr}}{\partial t} \right) \frac{\rho^w S_w}{\rho^s} + \dot{m}_{dehydr}
 \end{aligned} \tag{3.88}$$

with β_{sw}^* defined by (3.76);

- Linear momentum conservation equation of the multi-phase medium:

$$\operatorname{div} (\boldsymbol{\sigma}' - p \mathbf{I}) + [(1 - n) \rho^s + n S_w \rho^w + n (1 - S_w) \rho^g] \mathbf{g} = 0, \tag{3.89}$$

with p defined by (3.49);

- Dehydration process evolution equation, $\Gamma_{dehydr}(t)$ – given by (3.45);

- Thermo-chemical damage evolution equation, $V(t)$ – obtained from the experimental results by means of (3.52);

- Mechanical damage evolution equation, $d(t)$ – given by (3.63), (3.64) and (3.59);

For the model closure the initial and boundary conditions are needed. The initial conditions specify the full fields of primary state variables at time instant $t=0$, in the whole analysed domain Ω and on its boundary Γ , ($\Gamma = \Gamma_\pi \cup \Gamma_\pi^q$, $\pi=g, c, t, u$):

$$p^g = p_o^g, p^c = p_o^c, T = T_o, \mathbf{u} = \mathbf{u}_o, \quad \text{on } (\Omega \cup \Gamma), \quad (3.90)$$

The boundary conditions (BCs) can be of Dirichlet's type on Γ_π :

$$\begin{aligned} p^g(t) &= \hat{p}^g(t) \quad \text{on } \Gamma_g, \\ p^c(t) &= \hat{p}^c(t) \quad \text{on } \Gamma_c, \\ T(t) &= \hat{T}(t) \quad \text{on } \Gamma_t, \\ \mathbf{u}(t) &= \hat{\mathbf{u}}(t) \quad \text{on } \Gamma_u, \end{aligned} \quad (3.91)$$

or of Cauchy's type (the mixed BCs) on Γ_π^q :

$$\begin{aligned} (n S_g \rho^{ga} \mathbf{v}^{gs} + \mathbf{J}_d^{ga}) \cdot \mathbf{n} &= q^{ga}, & \text{on } \Gamma_g^q \\ (n S_w \rho^w \mathbf{v}^{ws} + n S_g \rho^{gw} \mathbf{v}^{gs} + \mathbf{J}_d^{gw}) \cdot \mathbf{n} &= q^{gw} + q^w + \beta_c (\rho^{gw} - \rho_\infty^{gw}), & \text{on } \Gamma_c^q \\ (n S_w \rho^w \mathbf{v}^{ws} \Delta H_{vap} - \chi_{eff} grad T) \cdot \mathbf{n} &= & , \quad (3.92) \\ &= q^T + \alpha_c (T - T_\infty) + e \sigma_o (T^4 - T_\infty^4), & \text{on } \Gamma_t^q \\ \boldsymbol{\sigma}' \cdot \mathbf{n} &= \bar{\mathbf{t}}, & \text{on } \Gamma_u^q \end{aligned}$$

where \mathbf{n} is the unit normal vector, pointing toward the surrounding gas, q^{ga} , q^{gw} , q^w and q^T are respectively the imposed fluxes of dry air, vapour, liquid water and the imposed heat flux, and $\bar{\mathbf{t}}$ is the imposed traction, ρ_∞^{gw} and T_∞ are the mass concentration of water vapour and the temperature in the far field of undisturbed gas phase, e is emissivity of the interface, σ_o the Stefan-Boltzmann constant, while α_c and β_c are convective heat and mass exchange coefficients. The boundary conditions, with only imposed fluxes given, are called Neumann's BCs. The purely convective boundary conditions for heat and moisture exchange are also called Robin's BCs.

3.7 NUMERICAL SOLUTION

The governing equations of the model are discretized in space by means of the finite element method, [42, 43]. The unknown variables are expressed in terms of their nodal values as,

$$\begin{aligned} p^g(t) &= \mathbf{N}_p \bar{\mathbf{p}}^g(t), & p^c(t) &= \mathbf{N}_p \bar{\mathbf{p}}^c(t), \\ T(t) &= \mathbf{N}_t \bar{\mathbf{T}}(t), & \mathbf{u}(t) &= \mathbf{N}_u \bar{\mathbf{u}}(t). \end{aligned} \quad (3.93)$$

The variational or weak form of the model equations, applying also the other ones required to complete the model, was obtained in [22, 23] by means of Galerkin's method (weighted residuals), and can be written in the following concise discretized matrix form,

$$\mathbf{C}_{ij}(\mathbf{x}) \frac{\partial \mathbf{x}}{\partial t} + \mathbf{K}_{ij}(\mathbf{x}) \mathbf{x} = \mathbf{f}_i(\mathbf{x}), \quad (3.94)$$

with,

$$\mathbf{K}_{ij} = \begin{bmatrix} \mathbf{K}_{gg} & \mathbf{K}_{gc} & \mathbf{K}_{gt} & \mathbf{0} \\ \mathbf{K}_{cg} & \mathbf{K}_{cc} & \mathbf{K}_{ct} & \mathbf{0} \\ \mathbf{K}_{tg} & \mathbf{K}_{tc} & \mathbf{K}_{tt} & \mathbf{0} \\ \mathbf{K}_{ug} & \mathbf{K}_{uc} & \mathbf{K}_{ut} & \mathbf{K}_{uu} \end{bmatrix}, \quad \mathbf{C}_{ij} = \begin{bmatrix} \mathbf{C}_{gg} & \mathbf{C}_{gc} & \mathbf{C}_{gt} & \mathbf{C}_{gu} \\ \mathbf{0} & \mathbf{C}_{cc} & \mathbf{C}_{ct} & \mathbf{C}_{cu} \\ \mathbf{0} & \mathbf{C}_{tc} & \mathbf{C}_{tt} & \mathbf{C}_{tu} \\ \mathbf{0} & \mathbf{0} & \mathbf{0} & \mathbf{0} \end{bmatrix}, \quad \mathbf{f}_i = \begin{Bmatrix} \mathbf{f}_g \\ \mathbf{f}_c \\ \mathbf{f}_t \\ \mathbf{f}_u \end{Bmatrix}, \quad (3.95)$$

where $\mathbf{x}^T = \{\bar{\mathbf{p}}^g, \bar{\mathbf{p}}^c, \bar{\mathbf{T}}, \bar{\mathbf{u}}\}$ and the non-linear matrix coefficients $\mathbf{C}_{ij}(\mathbf{x})$, $\mathbf{K}_{ij}(\mathbf{x})$ and $\mathbf{f}_i(\mathbf{x})$ are defined in detail in Appendix 3A.

The time discretization is accomplished through a fully implicit finite difference scheme (backward difference),

$$\Psi^i(\mathbf{x}_{n+1}) = \mathbf{C}_{ij}(\mathbf{x}_{n+1}) \frac{\mathbf{x}_{n+1} - \mathbf{x}_n}{\Delta t} + \mathbf{K}_{ij}(\mathbf{x}_{n+1}) \mathbf{x}_{n+1} - \mathbf{f}_i(\mathbf{x}_{n+1}) = \mathbf{0}, \quad (3.96)$$

where superscript i ($i = g, c, t, u$) denotes the state variable, n is the time step number and Δt the time step length.

The equation set (3.96) is solved by means of a monolithic Newton-Raphson type iterative procedure [12, 20]:

$$\Psi^i(\mathbf{x}_{n+1}^k) = - \frac{\partial \Psi^i}{\partial \mathbf{x}} \bigg|_{\mathbf{x}_{n+1}^k} \Delta \mathbf{x}_{n+1}^k, \quad \mathbf{x}_{n+1}^{k+1} = \mathbf{x}_{n+1}^k + \Delta \mathbf{x}_{n+1}^k, \quad (3.97)$$

where k is the iteration index and the Jacobian matrix is defined by:

$$\frac{\partial \Psi^i}{\partial \mathbf{x}} \bigg|_{\mathbf{x}_{n+1}^k} = \begin{bmatrix} \frac{\partial \Psi^g}{\partial \bar{\mathbf{p}}^g} & \frac{\partial \Psi^g}{\partial \bar{\mathbf{p}}^c} & \frac{\partial \Psi^g}{\partial \bar{\mathbf{T}}} & \frac{\partial \Psi^g}{\partial \bar{\mathbf{u}}} \\ \frac{\partial \Psi^c}{\partial \bar{\mathbf{p}}^g} & \frac{\partial \Psi^c}{\partial \bar{\mathbf{p}}^c} & \frac{\partial \Psi^c}{\partial \bar{\mathbf{T}}} & \frac{\partial \Psi^c}{\partial \bar{\mathbf{u}}} \\ \frac{\partial \Psi^t}{\partial \bar{\mathbf{p}}^g} & \frac{\partial \Psi^t}{\partial \bar{\mathbf{p}}^c} & \frac{\partial \Psi^t}{\partial \bar{\mathbf{T}}} & \frac{\partial \Psi^t}{\partial \bar{\mathbf{u}}} \\ \frac{\partial \Psi^u}{\partial \bar{\mathbf{p}}^g} & \frac{\partial \Psi^u}{\partial \bar{\mathbf{p}}^c} & \frac{\partial \Psi^u}{\partial \bar{\mathbf{T}}} & \frac{\partial \Psi^u}{\partial \bar{\mathbf{u}}} \end{bmatrix} \bigg|_{\mathbf{x}=\mathbf{x}_{n+1}^k} \quad (3.98)$$

A two-stage solution strategy has been applied at every time step to take into account damage of concrete. First an intermediate problem, keeping the mechanical damage value constant and equal to that obtained at the previous time step, is solved. Then, the ‘‘final’’ solution is obtained, for all state variables and total damage parameter, by means of the modified Newton-Raphson method, using the tangential or Jacobian matrix from the last iteration of the first stage. This allowed the model developers to avoid differentiation with respect to the damage and to obtain a converging solution, [8-11].

Because of different physical meaning of the capillary pressure p^c and different nature of the physical phenomena above the temperature T_{cr} (paragraph 3.3), a special ‘switching’ procedure was introduced, [10] When in an element part of its nodes have temperature above T_{cr} , the capillary pressure is blocked at the previous value, until the temperature in all the nodes passes the critical point of water. Then equations valid for temperature range $T > T_{cr}$ are applied in all nodes of this element.

Finally, the scheme in the next page shows the general procedure and main features of the theoretical model and the postprocessing works developed for this Thesis:

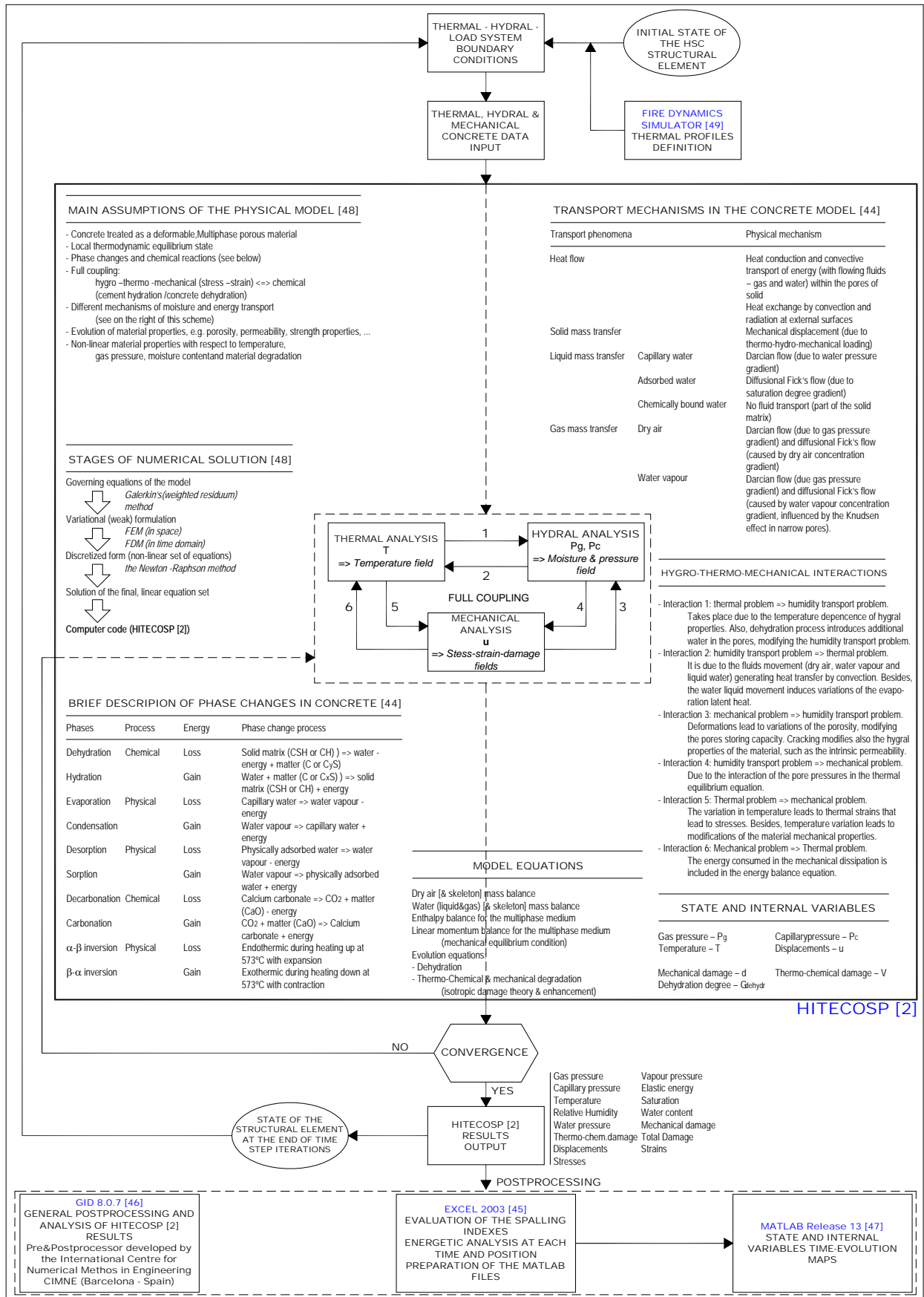


Figure 3-2. General procedure and main features of the theoretical model and the postprocessing works developed for this Thesis.

3.8 CONCLUSIONS OF THE CHAPTER

A mathematical model for the analysis of hygro-thermal behaviour of concrete as a multi-phase porous material at high temperatures, including the range above the critical point of water and taking into account material deterioration, has been presented [1]. A full development of the model equations, starting from the macroscopic balances of mass, energy and linear momentum, obtained elsewhere by means of the Hybrid Mixture Theory, for all constituents of the medium, has been presented. Constitutive relations for concrete at high temperature, and in particular those concerning material damage, have been discussed. The classical isotropic non-local damage theory appropriate modification to take into account both the mechanical damage and the thermo-chemical material deterioration at high temperature has been described. The final form of the model governing equations, their discretization by means of the F.E.M., and a method of their numerical solution have been presented.

3.9 BIBLIOGRAPHY OF THE CHAPTER

Bibliography of the chapter

- [1] D. Gawin, F. Pesavento, B.A. Schrefler, *Modelling of hygro-thermal behaviour of concrete at high temperature with thermo-chemical and mechanical material degradation*, Comput. Methods Appl. Mech. Engrg. 192 (2003) 1731-1771.
- [2] Brite Euram III BRPR-CT95-0065 HITECO, *Understanding and industrial application of High Performance Concrete in High Temperature Environment – Final report*, 1999.
- [3] G.A. Khoury, C.E. Majorana, F. Pesavento, B.A. Schrefler, *Modelling of Heated Concrete*, Mag. Concr. Res. 54 (2002) 1-25.
- [4] Z.P. Bazant, L.J. Najjar, *Nonlinear Water Diffusion in Nonsaturated Concrete*, Matériaux et Constructions (Paris) 5 (1972) 3-20.
- [5] Z.P. Bazant, W. Thonguthai, *Pore Pressure and Drying of Concrete at High Temperature*, J. Engng. Mech. Div. ASCE. 104 (1978) 1059-1079.
- [6] Z.P. Bazant, W. Thonguthai, *Pore Pressure in Heated Concrete Walls: Theoretical Prediction*, Mag. Concr. Res. 31 (1979) 67-76.
- [7] Z.P. Bazant, M.F. Kaplan, *Concrete at High Temperatures: Material Properties and Mathematical Models*, (Longman, Harlow, 1996).
- [8] D. Gawin, C.E. Majorana, B.A. Schrefler, *Numerical Analysis of Hygro-Thermic Behaviour and Damage of Concrete at High Temperature*, Mech. Cohes.-Frict. Mater. 4 (1999) 37-74.
- [9] D. Gawin, F. Pesavento, B.A. Schrefler, *Simulation of Damage – Permeability Coupling in Hygro-Thermo-Mechanical Analysis of Concrete at High Temperature*, Commun. Numer. Meth. Engrg. 18 (2002) 113-119.
- [10] D. Gawin, F. Pesavento, B.A. Schrefler, *Modelling of Hygro-Thermal Behaviour and Damage of Concrete at Temperature Above the Critical Point of Water*, Int. J. Numer. Anal. Meth. Geomech. 26 (2002) 537-562.
- [11] D. Gawin, P. Baggio, B.A. Schrefler, *Modelling heat and moisture transfer in deformable porous building materials*, Arch. of Civil Engrg. 42 (1996) 325-349.
- [12] D. Gawin, B.A. Schrefler, *Thermo- Hydro- Mechanical Analysis of Partially Saturated Porous Materials*, Eng. Comput. 13 (1996) 113-143.
- [13] L.T. Phan, N.J. Carino, D. Duthinh, E. Garboczi, eds, *Proc. Int. Workshop on Fire Performance of High-Strength Concrete*, (NIST, Gaithersburg, 1997)
- [14] L.T. Phan, J.R. Lawson, F.L. Davis, *Effects of elevated temperature exposure on heating characteristics, spalling, and residual properties of high performance concrete*, Materials and Structures. 34 (March 2001) 83-91
- [15] F.-J. Ulm, P. Acker, M. Levy, *The “Chunnel” fire. II. Analysis of concrete damage*, J. Eng. Mech. ASCE, 125(3) (1999) 283-289.
- [16] F.-J. Ulm, O. Coussy, Z. Bazant, *The “Chunnel” fire. I. Chemoplastic softening in rapidly heated concrete*, J. Eng. Mech. ASCE, 125(3) (1999) 272-282.
- [17] S.M. Hassanizadeh, W.G. Gray, *General Conservation Equations for Multi-Phase Systems: 1. Averaging Procedure*, Adv. Water Resources 2 (1979) 131-144.
- [18] S.M. Hassanizadeh, W.G. Gray, *General Conservation Equations for Multi-Phase Systems: 2. Mass, Momenta, Energy and Entropy Equations*, Adv. Water Resources 2 (1979) 191-203.
- [19] S. M. Hassanizadeh, W.G. Gray, *General Conservation Equations for Multi-Phase Systems: 3. Constitutive Theory for Porous Media Flow*, Adv. Water Resources 3 (1980) 25-40.

- [20] R.W. Lewis, B.A. Schrefler, *The Finite Element Method in the Static and Dynamic Deformation and Consolidation of Porous Media* (Wiley & Sons, Chichester, 1998).
- [21] B.A. Schrefler, *Mechanics and Thermodynamics of Saturated-Unsaturated Porous Materials and Quantitative Solutions*, Applied Mechanics Review (ASME Intern., New York, in print).
- [22] D. Gawin, *Modelling of Coupled Hygro-Thermal Phenomena in Building Materials and Building Components* (in Polish) (Publ. of Łódź Technical University No. 853, Editions of Łódź Technical University, Łódź, 2000).
- [23] F. Pesavento, *Non-linear modelling of concrete as multiphase porous material in high temperature conditions*, Ph.D. thesis, University of Padova, Padova, 2000.
- [24] W.G. Gray, B.A. Schrefler, *Thermodynamic Approach to Effective Stress in Partially Saturated Porous Media*, Eur. J. Mech. A/Solids, 20 (2001) 521-538.
- [25] W.G. Gray, *Macroscale Equilibrium Conditions for Two-Phase Flow in Porous Media*, Int. J. Multiphase Flow, 26 (2000) 467-50.
- [26] G.L. England, N. Khoylou, *Moisture Flow in Concrete Under Steady State Non-Uniform Temperature States: Experimental Observations and Theoretical Modelling*, Nucl. Eng. Des. 156 (1995) 83-107.
- [27] R.H. Nochetto, M. Paolini, C. Verdi, *An Adaptive Finite Element Method for Two-Phase Stefan Problems in Two Space Variables*, Math. Comput. (1991) 78-108.
- [28] M. Picasso, *An Adaptive Finite Element Algorithm for a Two-Dimensional Stationary Stefan-Like Problem*, Comput. Methods Appl. Mech. Engng. 124 (1995) 213-230.
- [29] B.A. Schrefler, D. Gawin, *The Effective Stress Principle: Incremental or Finite Form?*, Int. J. Numer. Anal. Meth. Geomech. 20 (1996) 785-815.
- [30] S.J. Gregg, K.S.W. Sing, *Adsorption, Surface Area and Porosity* (Academic Press, London, 1982).
- [31] D.J. Furbish, *Fluid Physics in Geology: An Introduction to Fluid Motions on Earth's Surface and Within Its Crust*, (Oxford University Press, Oxford, 1997).
- [32] N.V. Churaev, *Liquid and Vapour Flows in Porous Bodies: Surface Phenomena. Topics in Chemical Engineering*, vol.13 (Gordon and Breach Science Publishers, Australia, 2000).
- [33] A.E. Scheidegger, *The Physics of Flow through Porous Media* (Univ. of Toronto Press, Toronto, 1960).
- [34] D. Gawin, C. Alonso, C. Andrade, C.E. Majorana, F. Pesavento, *Effect of damage on permeability and hygro-thermal behaviour of high performance concretes at elevated temperatures*, (in preparation).
- [35] *ASHRAE Handbook Fundamentals* (ASHRAE, Atlanta, 1993).
- [36] B. Gerard, J. Pijaudier-Cabot, C. Laborderie, *Coupled Diffusion-Damage Modelling and the Implications on Failure Due to Strain Localisation*, Int. J. Solids Structures 35 (1998) 4107-4120.
- [37] W. Nechnech, J.M. Reynouard, F. Meftah, *On modelling of thermo-mechanical concrete for the finite element analysis of structures submitted to elevated temperatures*, in: Proc. Fracture Mechanics of Concrete Structures, R. de Borst, J. Mazars, G. Pijaudier-Cabot, J.G.M. van Mier, eds, (Swets & Zeitlinger, Lisse, 2001), 271-278.
- [38] J. Mazars, *Application de la mecanique de l' endommagement au comportement non lineaire et la rupture du beton de structure*, Thèse de Doctorat d' Etat, L.M.T., Universite de Paris, France, 1984.
- [39] J. Mazars, *Description of the behaviour of composite concretes under complex loadings through continuum damage mechanics*, in: Proc. Tenth U.S. National Congress of Applied Mechanics, (ed. by J.P. Lamb, ASME, 1989).
- [40] M.D. Kachanov, *Time of Rupture Process under Creep Conditions*, Izvestia akademii nauk, (in Russian) 8 (1958) 26-31.
- [41] J. Pijaudier – Cabot, *Non Local Damage*, in: *Continuum models for materials with microstructure, chapter 4*, H.B. Mühlhaus, ed, (Wiley & Sons, Chichester, 1995) 105-143.
- [42] O.C. Zienkiewicz, R.L. Taylor, *The Finite Element Method*, vol. 1: The Basis (Butterworth-Heinemann, Oxford, 2000).
- [43] O.C. Zienkiewicz, R.L. Taylor, *The Finite Element Method*, vol. 2: Solid Mechanics (Butterworth-Heinemann, Oxford, 2000).
- [44] B.A. Schrefler, G.A. Houry, D. Gawin, C.E. Majorana, *Thermo-hydro-mechanical modelling of high performance concrete at high temperatures*, Engineering Computations, Vol. 19 No. 7, 2002, pp. 787-819.
- [45] Microsoft Corporation, *Microsoft Excel 2003 Windows XP Home Edition*.
- [46] International Centre for Numerical Methods in Engineering CIMNE (Barcelona – Spain), *GID Pre&Post Processor*, Release 8.0.7.
- [47] Matlab, *The Language of Technical Computing*, Release 13, June 2002, The MathWorks, Inc.
- [48] C.E. Majorana, *Incontro Tecnico promosso da Gruppo EFFE2 e Summania Beton, Progettazione di Strutture Prefabbricate Civili e Industriali Resistenti al Fuoco*, Vicenza, 21 Giugno 2006.
- [49] K. McGrattan, S. Hostikka, J. Floyd, H. Baum, R. Rehm, W. Mell, R. McDermott, *NIST Special Publication 1018-5 – Fire Dynamics Simulator (Version 5) Technical Reference Guide, Volume 1. Mathematical Model*,

NIST National Institute of Standards and Technology (US Department of Commerce) in cooperation with VTT Technical Research Centre of Finland, October 2007.

K. McGrattan, B. Klein, S. Hostikka, J. Floyd, *NIST Special Publication 1019-5 – Fire Dynamics Simulator (Version 5) User's Guide.*, NIST National Institute of Standards and Technology (US Department of Commerce) in cooperation with VTT Technical Research Centre of Finland, October 2007.

Bibliography of the annexes

[A.1] D. Gawin, F. Pesavento, B.A. Schrefler, *Modelling of hygro-thermal behaviour of concrete at high temperature with thermo-chemical and mechanical material degradation*, *Comput. Methods Appl. Mech. Engrg.* 192 (2003) 1731-1771.

Appendix 3A. MATRICES RESULTING FROM THE DISCRETIZATION OF MASS, ENERGY AND LINEAR MOMENTUM CONSERVATION EQUATIONS

(See next pages)

Appendix 3A

Appendix 3A.1 MATRICES RESULTING FROM THE DISCRETIZATION OF MASS, ENERGY AND LINEAR MOMENTUM CONSERVATION EQUATIONS

In this Appendix is included the discretization, by means of the F.E.M., of the final form of the model governing equations exposed in *Chapter 3*, [A.1]. Hence, the matrices occurring in the discretized form of mass, energy and linear momentum conservation equations (3.89) - (3.90) are defined as follows:

$$\mathbf{C}_{gg} = \int_{\Omega} \mathbf{N}_p^T \left[(1 - S_w) n \frac{M_a}{RT} \mathbf{N}_p \right] d\Omega \quad (3A.1)$$

$$\mathbf{C}_{gc} = \int_{\Omega} \mathbf{N}_p^T \left[n \rho^{ga} \frac{\partial S_w}{\partial p^c} \mathbf{N}_p + (1 - S_w) n \frac{M_w}{RT} \frac{\partial p^{gw}}{\partial p^c} \mathbf{N}_p \right] d\Omega \quad (3A.2)$$

$$\begin{aligned} \mathbf{C}_{gt} = & \int_{\Omega} \mathbf{N}_p^T \left[n \rho^{ga} \frac{\partial S_w}{\partial T} \mathbf{N}_t - \rho^{ga} \beta_s (1 - n) (1 - S_w)_t \mathbf{N}_t \right] d\Omega + \\ & + \int_{\Omega} \mathbf{N}_p^T \left[(1 - S_w) n \left[-\frac{M_w}{RT} \left(\frac{\partial p^{gw}}{\partial T} - \frac{p^{gw}}{T} \right) - \frac{M_a}{T^2 R} \right] \mathbf{N}_t \right] d\Omega \\ & - \int_{\Omega} \mathbf{N}_p^T \left[\left(\frac{\partial m_{dehydr}}{\partial T} + (1 - n) \frac{\partial \rho^s}{\partial \Gamma_{dehydr}} \frac{\partial \Gamma_{dehydr}}{\partial T} \right) \frac{\rho^{ga}}{\rho^s} (1 - S_w) \mathbf{N}_t \right] d\Omega \end{aligned} \quad (3A.3)$$

$$\mathbf{C}_{gu} = \int_{\Omega} \mathbf{N}_p^T \left[(1 - S_w) \rho^{ga} \mathbf{m}^T \mathbf{L} \mathbf{N}_u \right] d\Omega \quad (3A.4)$$

$$\begin{aligned} \mathbf{K}_{gg} = & - \int_{\Omega} (\nabla \mathbf{N}_p)^T \left[\rho^{ga} \frac{\mathbf{k} k^{rg}}{\mu^g} (-\nabla \mathbf{N}_p) \right] d\Omega + \\ & - \int_{\Omega} (\nabla \mathbf{N}_p)^T \left[\rho^g \frac{M_a M_w}{M_g^2} \mathbf{D}_g^{gw} \left(-\frac{p^{gw}}{(p^g)^2} \nabla \mathbf{N}_p \right) \right] d\Omega \end{aligned} \quad (3A.5)$$

$$\mathbf{K}_{gc} = - \int_{\Omega} (\nabla \mathbf{N}_p)^T \left[\rho^g \frac{M_a M_w}{M_g^2} \mathbf{D}_g^{gw} \frac{1}{p^g} \frac{\partial p^{gw}}{\partial p^c} \nabla \mathbf{N}_p \right] d\Omega \quad (3A.6)$$

$$\mathbf{K}_{gt} = - \int_{\Omega} (\nabla \mathbf{N}_p)^T \left[\rho^g \frac{M_a M_w}{M_g^2} \mathbf{D}_g^{gw} \frac{1}{p^g} \frac{\partial p^{gw}}{\partial T} \nabla \mathbf{N}_t \right] d\Omega \quad (3A.7)$$

$$\mathbf{K}_{gu} = \mathbf{0} \quad (3A.8)$$

$$\mathbf{f}_g = \int_{\Omega} (\nabla \mathbf{N}_p)^T \left[\rho^{ga} \frac{\mathbf{k} k^{rg}}{\mu^g} \rho^g \mathbf{g} \right] d\Omega \quad (3A.9)$$

$$\mathbf{C}_{cg} = \mathbf{0} \quad (3A.10)$$

$$\mathbf{C}_{cc} = \int_{\Omega} \mathbf{N}_p^T \left[(1 - S_w) n \frac{M_w}{RT} \frac{\partial p^{gw}}{\partial p^c} \mathbf{N}_p + n (\rho^w - \rho^{gw}) \frac{\partial S_w}{\partial p^c} \mathbf{N}_p \right] d\Omega \quad (3A.11)$$

$$\begin{aligned} \mathbf{C}_{ct} = & \int_{\Omega} \mathbf{N}_p^T \left[-\beta_{swg}^* \mathbf{N}_t + (1 - S_w) n \frac{M_w}{RT} \left(\frac{\partial p^{gw}}{\partial T} - \frac{p^{gw}}{T} \right) \mathbf{N}_t \right] d\Omega + \\ & + \int_{\Omega} \mathbf{N}_p^T \left[n (\rho^w - \rho^{gw}) \frac{\partial S_w}{\partial T} \mathbf{N}_t \right] d\Omega \\ & - \int_{\Omega} \mathbf{N}_p^T \left[\left(\frac{\partial m_{dehydr}}{\partial T} + (1 - n) \frac{\partial \rho^s}{\partial \Gamma_{dehydr}} \frac{\partial \Gamma_{dehydr}}{\partial T} \right) \frac{\rho^{gw} (1 - S_w) + \rho^w S_w}{\rho^s} \mathbf{N}_t \right] d\Omega \\ & - \int_{\Omega} \mathbf{N}_p^T \left[-\frac{\partial m_{dehydr}}{\partial T} \mathbf{N}_t \right] d\Omega \end{aligned} \quad (3A.12)$$

$$\mathbf{C}_{cu} = \int_{\Omega} \mathbf{N}_p^T \left\{ \left[\rho^{gw} (1 - S_w) + \rho^w S_w \right] \mathbf{m}^T \mathbf{B} \right\} d\Omega \quad (3A.13)$$

$$\begin{aligned} \mathbf{K}_{cg} = & - \int_{\Omega} (\nabla \mathbf{N}_p)^T \left[-\rho^g \frac{M_a M_w}{M_g^2} \mathbf{D}_g^v \left(-\frac{p^{gw}}{(p^g)^2} \nabla \mathbf{N}_p \right) \right] d\Omega + \\ & - \int_{\Omega} (\nabla \mathbf{N}_p)^T \left[\rho^{gw} \frac{\mathbf{k} k^{rg}}{\mu^g} (-\nabla \mathbf{N}_p) + \rho^w \frac{\mathbf{k} k^{rw}}{\mu^w} (-\nabla \mathbf{N}_p) \right] d\Omega \end{aligned} \quad (3A.14)$$

$$\begin{aligned} \mathbf{K}_{cc} = & \int_{\Omega} (\nabla \mathbf{N}_p)^T \left[\rho^g \frac{M_a M_w}{M_g^2} \mathbf{D}_g^{gw} \left(\frac{1}{p^g} \frac{\partial p^{gw}}{\partial p^c} \nabla \mathbf{N}_p \right) \right] d\Omega + \\ & - \int_{\Omega} (\nabla \mathbf{N}_p)^T \left[\rho^w \frac{\mathbf{k} k^{rw}}{\mu^w} \nabla \mathbf{N}_p \right] d\Omega \end{aligned} \quad (3A.15)$$

$$\mathbf{K}_{ct} = - \int_{\Omega} (\nabla \mathbf{N}_p)^T \left[-\rho^g \frac{M_a M_w}{M_g^2} \mathbf{D}_g^{gw} \left(\frac{1}{p^g} \frac{\partial p^{gw}}{\partial T} \nabla \mathbf{N}_t \right) \right] d\Omega \quad (3A.16)$$

$$\mathbf{K}_{cu} = \mathbf{0} \quad (3A.17)$$

$$\mathbf{f}_c = \int_{\Omega} (\nabla \mathbf{N}_p)^T \left[\rho^{gw} \frac{\mathbf{k}k^{rg}}{\mu^g} (\rho^g \mathbf{g}) + \rho^w \frac{\mathbf{k}k^{rw}}{\mu^w} (\rho^w \mathbf{g}) \right] d\Omega + \int_{\Gamma_c^q} \mathbf{N}_p^T [q^w + q^{gw} + \beta_c (\rho^{gw} - \rho_{\infty}^{gw})] d\Gamma \quad (3A.18)$$

$$\mathbf{C}_{tg} = \mathbf{0} \quad (3A.19)$$

$$\mathbf{C}_{tc} = \int_{\Omega} \mathbf{N}_t^T \Delta H_{vap} \left(-\rho^w n \frac{\partial S_w}{\partial p^c} \mathbf{N}_p \right) d\Omega \quad (3A.20)$$

$$\begin{aligned} \mathbf{C}_{tt} = & \int_{\Omega} \mathbf{N}_t^T \Delta H_{vap} \left\{ (\rho C_p)_{eff} + \beta_{sw}^* \rho^w \mathbf{N}_t - \rho^w n \frac{\partial S_w}{\partial T} \mathbf{N}_t \right\} d\Omega + \\ & - \int_{\Omega} \mathbf{N}_t^T \left(\Delta H_{dehydr} \frac{\partial m_{dehydr}}{\partial T} \mathbf{N}_t \right) d\Omega + \\ & - \int_{\Omega} \mathbf{N}_t^T \Delta H_{vap} \left[\left(\frac{\partial m_{dehydr}}{\partial T} + (1-n) \frac{\partial \rho^s}{\partial \Gamma_{dehydr}} \frac{\partial \Gamma_{dehydr}}{\partial T} \right) \frac{\rho^w S_w}{\rho^s} \right] \mathbf{N}_t d\Omega + \\ & + \int_{\Omega} \mathbf{N}_t^T \Delta H_{vap} \frac{\partial m_{dehydr}}{\partial T} \mathbf{N}_t d\Omega \end{aligned} \quad (3A.21)$$

$$\mathbf{C}_{tu} = \int_{\Omega} \mathbf{N}_t^T \Delta H_{vap} \left\{ -\rho^w S_w \mathbf{m}^T \mathbf{L} \mathbf{N}_u \right\} d\Omega \quad (3A.22)$$

$$\begin{aligned} \mathbf{K}_{tg} = & \int_{\Omega} \mathbf{N}_t^T \left\{ \left[\rho^w C_p^w \frac{\mathbf{k}k^{rw}}{\mu^w} (-\nabla \mathbf{N}_p) \right] \cdot \nabla T \right\} d\Omega + \\ & + \int_{\Omega} \mathbf{N}_t^T \left\{ \left[\rho^g C_p^g \frac{\mathbf{k}k^{rg}}{\mu^g} (-\nabla \mathbf{N}_p) \right] \cdot \nabla T \right\} d\Omega + \\ & + \int_{\Omega} (\nabla \mathbf{N}_t)^T \Delta H_{vap} \left[\rho^w \frac{\mathbf{k}k^{rw}}{\mu^w} (-\nabla \mathbf{N}_p) \right] d\Omega \end{aligned} \quad (3A.23)$$

$$\begin{aligned} \mathbf{K}_{tc} = & \int_{\Omega} \mathbf{N}_t^T \left\{ \left[\rho^w C_p^w \frac{\mathbf{k}k^{rw}}{\mu^w} (\nabla \mathbf{N}_p) \right] \cdot \nabla T \right\} d\Omega + \\ & + \int_{\Omega} (\nabla \mathbf{N}_t)^T \Delta H_{vap} \left[\rho^w \frac{\mathbf{k}k^{rw}}{\mu^w} (\nabla \mathbf{N}_p) \right] d\Omega \end{aligned} \quad (3A.24)$$

$$\begin{aligned}
 \mathbf{K}_{tt} = & \int_{\Omega} (\nabla \mathbf{N}_t)^T \chi_{eff} \nabla \mathbf{N}_t d\Omega + \\
 & + \int_{\Omega} \mathbf{N}_t^T \left\{ \left[\rho^w C_p^w \frac{\mathbf{k}k^{rw}}{\mu^w} (-\nabla p^g + \nabla p^c + \rho^w \mathbf{g}) \right] \cdot \nabla \mathbf{N}_t \right\} d\Omega + \\
 & + \int_{\Omega} \mathbf{N}_t^T \left\{ \left[\rho^g C_p^g \frac{\mathbf{k}k^{rg}}{\mu^g} (-\nabla p^g + \rho^g \mathbf{g}) \right] \cdot \nabla \mathbf{N}_t \right\} d\Omega
 \end{aligned} \tag{3A.25}$$

$$\mathbf{K}_{tu} = \mathbf{0} \tag{3A.26}$$

$$\begin{aligned}
 \mathbf{f}_t = & - \int_{\Omega} \mathbf{N}_t^T \left\{ \left[\rho^w C_p^w \frac{\mathbf{k}k^{rw}}{\mu^w} (\rho^w \mathbf{g}) \right] \cdot \nabla T \right\} d\Omega + \\
 & - \int_{\Omega} \mathbf{N}_t^T \left\{ \left[\rho^g C_p^g \frac{\mathbf{k}k^{rg}}{\mu^g} (\rho^g \mathbf{g}) \right] \cdot \nabla T \right\} d\Omega + \\
 & - \int_{\Omega} (\nabla \mathbf{N}_t)^T \Delta H_{vap} \left[\rho^w \frac{\mathbf{k}k^{rw}}{\mu^w} (\rho^w \mathbf{g}) \right] d\Omega + \\
 & - \int_{\Gamma_t^q} \mathbf{N}_t^T [q^T + \alpha_c (T - T_{\infty}) + \epsilon \sigma_o (T^4 - T_{\infty}^4)] d\Gamma
 \end{aligned} \tag{3A.27}$$

$$\mathbf{C}_{ug} = \mathbf{C}_{uc} = \mathbf{C}_{ut} = \mathbf{C}_{uu} = \mathbf{0} \tag{3A.28}$$

$$\mathbf{K}_{ug} = \int_{\Omega} \mathbf{B}^T (\mathbf{m}^T \mathbf{N}_p) d\Omega \tag{3A.29}$$

$$\mathbf{K}_{uc} = - \int_{\Omega} \mathbf{B}^T (\mathbf{m}^T S_w \mathbf{N}_p) d\Omega \tag{3A.30}$$

$$\mathbf{K}_{ut} = \int_{\Omega} \mathbf{B}^T [\mathbf{Dm}^T (\beta_s / 3) \mathbf{N}_t] d\Omega \tag{3A.31}$$

$$\mathbf{K}_{uu} = - \int_{\Omega} \mathbf{B}^T \mathbf{D} \mathbf{B} d\Omega \tag{3A.32}$$

$$\begin{aligned}
 \mathbf{f}_u = & \int_{\Omega} \mathbf{B}^T [\mathbf{Dm}^T (\beta_s / 3) T_o] d\Omega - \int_{\Gamma_u^q} \mathbf{N}_u^T \mathbf{t} d\Gamma \\
 & - \int_{\Omega} \mathbf{N}_u^T [(1-n)\rho^s + nS_w \rho^w + n(1-S_w)\rho^g] \mathbf{g} d\Omega
 \end{aligned} \tag{3A.33}$$

Chapter 4

SPALLING NOMOGRAMS

4.1	IDENTIFICATION OF THE ORIGINAL CONTRIBUTION	97
4.2	METHODOLOGY TO DEVELOP THE SPALLING AND ENERGETIC ANALYSIS	98
4.2.1	Definition and methodology for the evaluation of Spalling criteria	98
4.2.2	Definition and methodology for the energetic analysis	99
4.3	DEFINITION OF THE ANALYSIS CASE	101
4.3.1	Description of the general features of the analysis case and causes for its selection	101
4.3.2	Parameters with ranging values for the sensitivity analysis	104
4.3.2.1	Parameter 1. Initial Saturation Degree.....	104
4.3.2.1.1	<i>Description and Causes for its selection</i>	<i>104</i>
4.3.2.1.2	<i>Values selected for the spalling nomograms</i>	<i>105</i>
4.3.2.2	Parameter 2. Intrinsic Permeability.....	106
4.3.2.2.1	<i>Description and Causes for its selection</i>	<i>106</i>
4.3.2.2.2	<i>Values selected for the spalling nomograms</i>	<i>107</i>
4.3.2.3	Parameter 3. Thickness of the Structural Element	107
4.3.2.3.1	<i>Description and Causes for its selection</i>	<i>107</i>
4.3.2.3.2	<i>Values selected for the spalling nomograms</i>	<i>109</i>
4.3.2.4	Parameter 4. Heating profile	109
4.3.2.4.1	<i>Description and Causes for its selection</i>	<i>109</i>
4.3.2.4.2	<i>Values selected for the spalling nomograms</i>	<i>111</i>
4.3.2.5	Parameter 5. Material.....	115
4.3.2.5.1	<i>Description and Causes for its selection</i>	<i>115</i>
4.3.2.5.2	<i>First selection for the spalling nomograms: C60. Definition procedure</i>	<i>118</i>
4.3.2.5.3	<i>Second selection for the spalling nomograms: C90. Definition procedure</i>	<i>124</i>
4.4	DEFINITION OF THE RESULTING COMBINATIONS	131
4.5	RESULTS	134
4.5.1	Results to evaluate and evaluation procedure	134
4.5.2	Spalling index evolution for each combination	135
4.5.3	Spalling nomograms, Sensitivity and Energetic analysis for each combination	140
4.5.3.1	Nomogram TH12PAR1C60: Thickness 12 cm, ISO Curve, Material C60	154
4.5.3.2	Nomogram TH12PAR2C60: Thickness 12 cm, Slow curve, Mat. C60.....	155
4.5.3.3	Nomogram TH12PAR3C60: Thickness 12 cm, Hydroc. Curve, Mat. C60	156
4.5.3.4	Nomogram TH12PAR1C90: Thickness 12 cm, ISO Curve, Material C90	157
4.5.3.5	Nomogram TH12PAR2C90: Thickness 12 cm, Slow Curve, Mat. C90.....	158
4.5.3.6	Nomogram TH12PAR3C90: Thickness 12 cm, Hydroc. Curve, Mat. C90	159
4.5.3.7	Comparison among the six nomograms corresponding to a thickness of 12 centimetres	160
4.5.3.8	A particular analysis about the spalling velocities spectrum	161
4.5.4	Comparison for constant values of the Intrinsic Permeability	165
4.5.4.1	Thickness 12 cm – ISO Heating curve – Material C60	167
4.5.4.2	Thickness 12 cm – PAR2 Slow Heating curve – Material C60.....	171
4.5.4.3	Thickness 12 cm – Hydrocarbon Heating curve – Material C60.....	175
4.5.4.4	Thickness 12 cm – ISO Heating curve – Material C90	179
4.5.4.5	Thickness 12 cm – PAR2 Slow Heating curve – Material C90.....	183
4.5.4.6	Thickness 12 cm – Hydrocarbon Heating curve – Material C90.....	187
4.5.5	Comparison for constant values of the Initial Saturation Degree	191
4.5.6	Comparison of the Vapour Pressure and the Mechanical Damage Distribution	211
4.5.7	Time evolution considerations on a sample case: #5-TH12K018RH50PAR1C60	246
4.6	RESUME OF THE CONCLUSIONS OF THE CHAPTER	258
4.6.1	About the Time and Position of Main Fracture and the Sensitivity Analysis	258

4.6.2	About the Spalling Nomograms and the Energetic Analysis of Thermal Spalling.....	259
4.6.3	About the Evolution of each Parameter affecting the Physics of Thermal Spalling Phenomena.....	261
4.6.4	About extended tasks to go more deeply into Thermal Spalling Research	264
4.7	BIBLIOGRAPHY OF THE CHAPTER.....	266
Appendix 4A.	SPALLING INDEX EVOLUTION FOR EACH COMBINATION.....	267
Appendix 4B.	INPUT FILES FOR THE HYGRO-THERMO-CHEMO-MECHANICAL CALCULATIONS.....	267
Appendix 4C.	ACCEPTED PUBLICATIONS RELATED TO THIS CHAPTER.....	267

*Chapter 4***SPALLING NOMOGRAMS**

The first aim of this chapter is to develop a spectrum of spalling nomograms addressed, as an starting point, to evaluate the sensitivity of the hygro-thermo-chemo-mechanical processes involved on the High-Strength concretes behaviour under a natural fire to some relevant parameters whose values may be chosen from a very early stage of High-Rise Buildings design or already known in case of existing High-Rise Buildings.

The second but not less important aim of the spalling nomograms to develop, and consequently of this chapter, is to analyse if spalling is energetically possible and, hence, the spalling risk in every possible set of conditions so both Designers and Fire Fighting Services will have a valuable information in order to take decisions about design and about the expectable consequences of fire fighting actions from a really intuitive, graphical and immediate point of view. An essential contribution of this work, related to this matter, is to discern what is the energetic contribution of compressed gas and what is that corresponding to the constrained elastic energy.

In this sense, some parallel and essential contributions of the work presented in this chapter are related to the type of spalling that is expectable in each situation (either violent and explosive or slow in nature), to the extent of the spalling and, even more relevant, to the instant when spalling is expected.

4.1 IDENTIFICATION OF THE ORIGINAL CONTRIBUTION

As just stated, the main original contributions of the works presented in this chapter are the following:

- a. The development of a spectrum of spalling nomograms addressed, as an starting point, to evaluate the sensitivity of the hygro-thermo-chemo-mechanical processes involved on the High-Strength concretes behaviour under a natural fire to some relevant parameters whose values may be chosen from a very early stage of High-Rise Buildings design or already known in case of existing High-Rise Buildings, such as the initial moisture content of concrete, its intrinsic permeability, the rate of temperature increase (fire intensity), the porosity, compressive strength, type of aggregate and, in general, the whole set of hygro-thermo-chemical properties of concrete, and the dimensions of the structural element,
- b. The analysis of the energetic viability of spalling and, hence, of the spalling risk and expectable type (either violent and explosive or slow in nature) in every possible set of conditions so both Designers and Fire Fighting Services will have a valuable information in order to take decisions about design and about the expectable consequences of fire fighting actions from a really intuitive, graphical and immediate point of view,
- c. The discerning of what is the energetic contribution of compressed gas to spalling occurrence and what is that corresponding to the constrained elastic energy since, as it has been recognised by many relevant authors [1], the relative importance of the build-up of high pore pressure close to the heated concrete surface (as a result of rapid evaporation of the moisture) and the release of the stored energy (due to the thermal stresses resulting from high values of restrained strains caused by temperature gradients) has not been already established and needs further studies.

4.2 METHODOLOGY TO DEVELOP THE SPALLING AND ENERGETIC ANALYSIS

In order to achieve the contributions presented on the previous paragraph, the methodologies described on the following subparagraphs will be applied at each stage of this work to the analysis case defined on next paragraphs.

4.2.1 Definition and methodology for the evaluation of Spalling criteria

As explained in the chapter concerning the historical evolution of spalling evaluation methodologies, to assess the thermal spalling risk several authors [2-8] have discussed some quantitative criteria based on different physical phenomena leading to thermal spalling of concrete layers of pieces from a heated surface.

However, most of these criteria were based on an experimental basis only, often in the form of diagrams showing ‘area of the spalling risk’ as a function of several concrete properties like permeability or tensile strength, being their validity limited to the materials and element geometries used in the tests they were based on. There were also formulated some analytical criteria, using limit state analysis [5,7], but they were usually based on simplified models of concrete performance during heating, by evaluating the thermally induced stress and/or vapour pressures. Mainly, criteria presented in the past fall into three categories [9]:

1. Criteria based on pore pressure prediction, which consider the pore pressure as responsible for thermal spalling [8]. Usually, the models employed for the description of the hygral state of concrete are rather simple. For example, mass transport in concrete pores is considered as a purely diffusive phenomenon [7,10], or pore pressure is directly evaluated by using an idealized spherical model for the pores of the material [6]. In some cases the so-called “moisture clog” is indicated as the main cause of spalling [4].
2. Criteria based on thermal stresses. These are the simplest ones and are related to the non-uniform thermal stresses that can reach the maximum compressive strength of concrete for a given temperature, e.g. [3].
3. Criteria based on combined action of thermal stresses and pore pressure. This class of spalling criteria encompasses the criteria by Zhukov [5] and Connelly [7]. The first author proposed a method for the evaluation of the strain energy density in the direction of the heated surface W_x , taking into account the stresses due to external mechanical load, thermal field and pore pressure acting on a slab heated on one face. The spalling occurs when the strain energy density W_x in x-direction equals the rupture energy density defined on the basis of tensile strength of concrete. Connelly [7] extended Zhukov’s model considering pore pressure stresses as acting simultaneously in the three directions x, y, z. The critical state for spalling was hence defined in a way similar to Zhukov’s approach.

These criteria omitted the complexity of hygro-thermal and chemo-physical processes in concrete at high temperature so they were not able to give a realistic evaluation of the thermal spalling risk.

Gawin, Pesavento and Schrefler [9] have recently developed simplified models of thermal spalling used to define special indexes aiming for quantitative assessment of its risk, considering both effects of pore pressure build-up and the accumulated strain energy, together with thermo-chemical material degradation and cracking, namely:

1. Pressure-induced shear model, which predicts the ‘plastic’ failure of the material constraints for the external layer, leading to a spalling index called I_{s1} .

2. Buckling model considering gas pressure, involving the hypothesis of buckling of a zone which is initially delaminated from the rest of the structure, leading to a spalling index called I_{s2} .
3. And, finally, a simplified fracture mechanics model, where the main mechanism considered for the compressive failure is the sideways propagation of a band of parallel axial splitting cracks, leading to a spalling index called I_{s3} .

Although these three models have been tested for the results of numerical simulations based on an experimental test described in the following paragraphs, showing their usefulness in the prediction of both the time and position of concrete rupture, a fourth spalling index [9] called 'intuitive' or I_{s4} , based on the analysis of physical phenomena during heating of concrete and leading to thermal spalling, will be selected for the prediction of both the time and position of concrete rupture since, as it will be explained later, it showed the best correlation against tests.

The selected spalling index [9] is obtained choosing the following factors favouring thermal spalling: high local values of gas overpressure, $p^g - p_{atm}$, and mechanical damage parameter, d , high values of averaged transversal traction stresses, $\bar{\sigma}_{th}$, and constrained elastic energy \bar{U} . The considered factors impeding thermal spalling are high average values of traction strength, \bar{f}_t , and specific fracture energy, \bar{G}_f , for the material layer between a current position and the heated surface. Additionally, to obtain a non-dimensional quantity, [9] introduced a reference pressure (assumed as equal to atmospheric pressure, p_{atm}) and a characteristic element dimension L (e.g. thickness for a wall, radius for a cylindrical specimen). Finally, internal geometrical parameters involved are unknown and are jointly described by a scaling factor, C_s , which is a non-dimensional parameter. Therefore, the fourth spalling index selected herein, I_{s4} , is given by the following relation:

$$I_{s4} = \frac{\bar{\sigma}_{th} \cdot \bar{U} \cdot d}{\bar{f}_t \cdot \bar{G}_f} \cdot \frac{p^g - p_{atm}}{p_{atm}} \cdot L \cdot C_s \quad (4.1)$$

Herein,

- The values of $\bar{\sigma}_{th}$, d , \bar{U} , p^g and the temperatures at each position are obtained from Hitecosp software [1] and then averaged for the material layer between a current position and the heated surface.
- The values of the specific fracture energy are obtained from experimental tests [11].
- The value of \bar{f}_t is obtained from the material tensile strength equation for the temperature at each temperature and then averaged as described.

4.2.2 Definition and methodology for the energetic analysis

Once determined the time and position of the main fracture it must be analysed, at least through a simplified methodology, if concrete spalling is energetically possible through the comparison of the fracture energy and the stored energy similarly as it was already done in [9].

Beyond this result, there will be estimated the energetic contributions to spalling occurrence of both the compressed gas and the constrained elastic energy since the relative importance of the build-up of high pore pressure closed to the heated concrete surface (as a result of rapid evaporation of the moisture) and the release of the stored energy (due to the thermal stresses resulting from high values of restrained strains caused by temperature gradients), has not been already established. The expectable type of spalling, either violent and explosive or slow in

nature, in every possible set of conditions will also be determined through the calculation of the velocity of the spalled pieces.

The steps to develop for each set of conditions to work out the parameters just described are explained on next table for the concrete pieces spalled from one square metre:

Parameter	Source / equation
Possible thickness of the ruptured layer of concrete, Δx [m]	From numerical calculations and evaluation of the Spalling Index, fixed by the position and instant corresponding to the maximum valued of the Spalling Index I_{s4} .
Released elastic energy, ΔU [J]	Integrating the curve of the elastic energy density at the instant showing the highest value of the spalling index and in the range of the coordinates corresponding to the ruptured layer (and for a total surface of 1 m^2).
Total mass of spalled concrete, Δm [Kg]	$\rho_0 [\text{Kg}/\text{m}^3] \cdot \Delta x [\text{m}] \cdot 1 \text{ m}^2$, where ρ is the density at ambient temperature for each kind of material
Total Area of rupture, ΔA_{fr} [m^2]	Assuming certain average dimensions of the spalled pieces of concrete: calculated for 1 m^2 of total surface considering that the average piece of concrete has dimensions $\Delta x \cdot \Delta x \cdot \Delta x$ (for a smaller value of the total surface of all cracks created during concrete fracturing, i.e. for larger dimensions of the spalled material pieces, their kinetic energy would be higher).
Energy consumed for fracturing, ΔE_{fr} [J]	$\Delta E_{fr} = \Delta A_{fr} \cdot G_f$ Where G_f is the specific fracture energy obtained from experimental tests [11], $200 \text{ J}/\text{m}^2$
Kinetic energy E_{k0} [J] taking into account only the released elastic energy ΔU [J]	$E_{k0} = \Delta U - \Delta E_{fr}$
Contribution to the concrete fracturing done by the compressed gas, W [J]	Initial assumptions and data: <ul style="list-style-type: none"> - Initial pressure: p_1 corresponding to the position of the main fracture at the instant showing the maximum value of the spalling index, - It is assumed that during spalling the gas expands adiabatically (good approximation for very quick processes) to the atmospheric pressure $p_2 \approx 0,1 \text{ MPa}$, - Initial width of the crack: $0,5 \text{ mm}$ (the higher the initial crack width, the higher would be the value of the work performed by gas), Then, the work performed by compressed gas can be estimated from: $W = \frac{p_1 \cdot V_1 - p_2 \cdot V_2}{k - 1}$ $p_2 \cdot (V_2)^k = p_1 \cdot (V_1)^k, \text{ where } k = c_p / c_v$ <p>k is the specific heat ratio characteristic for a given gas, c_p and c_v are the isobaric and isochoric specific heats of a gas, and V_1 and V_2 are the initial and final gas volumes.</p>
Estimation for the total kinetic energy ΔE_k [J], taking into account both the released elastic energy and the work performed by compressed gas during its expansion to the atmospheric pressure	$\Delta E_k = \Delta E_{k0} + W$
Average velocity of the concrete spalled pieces, v [m/s]	$v = \sqrt{\frac{2 \cdot \Delta E_k}{\rho_0 \cdot \Delta x \cdot 1 \text{ m}^2}}$

Table 4-1. Scheme for the energetic analysis

Whenever the total kinetic energy value is positive (i.e. the sum of the stored elastic energy and the work performed by compress gas during its expansion to the atmospheric pressure is greater than the energy needed for the rupture) and, consequently, the average velocity of the concrete spalled pieces is greater than zero, the concrete spalling will be energetically possible (either explosive or progressive spalling depending on ΔE_k value, the mass of spalled concrete and the gas pressure).

4.3 DEFINITION OF THE ANALYSIS CASE

4.3.1 Description of the general features of the analysis case and causes for its selection

The structural element selected for the analyses to develop in this chapter must be as more versatile as possible in order to achieve results applicable to most of the High Strength Concrete structural elements usually found in High-Rise Buildings.

For this reason, it has been decided to deal with a numerical model representing a slice of any High Strength Concrete structural element which may work in plain strain conditions and under one-dimensional fluxes of both heat and mass. A wide sample of these type of structural elements is described on paragraph 4.3.2.3.1 of this chapter (excluding columns, corners of cores and similar)

Hence, the general layout and model selected for these analyses are shown on next figures, corresponding to a situation where the structural element is exposed to fire at only one face:

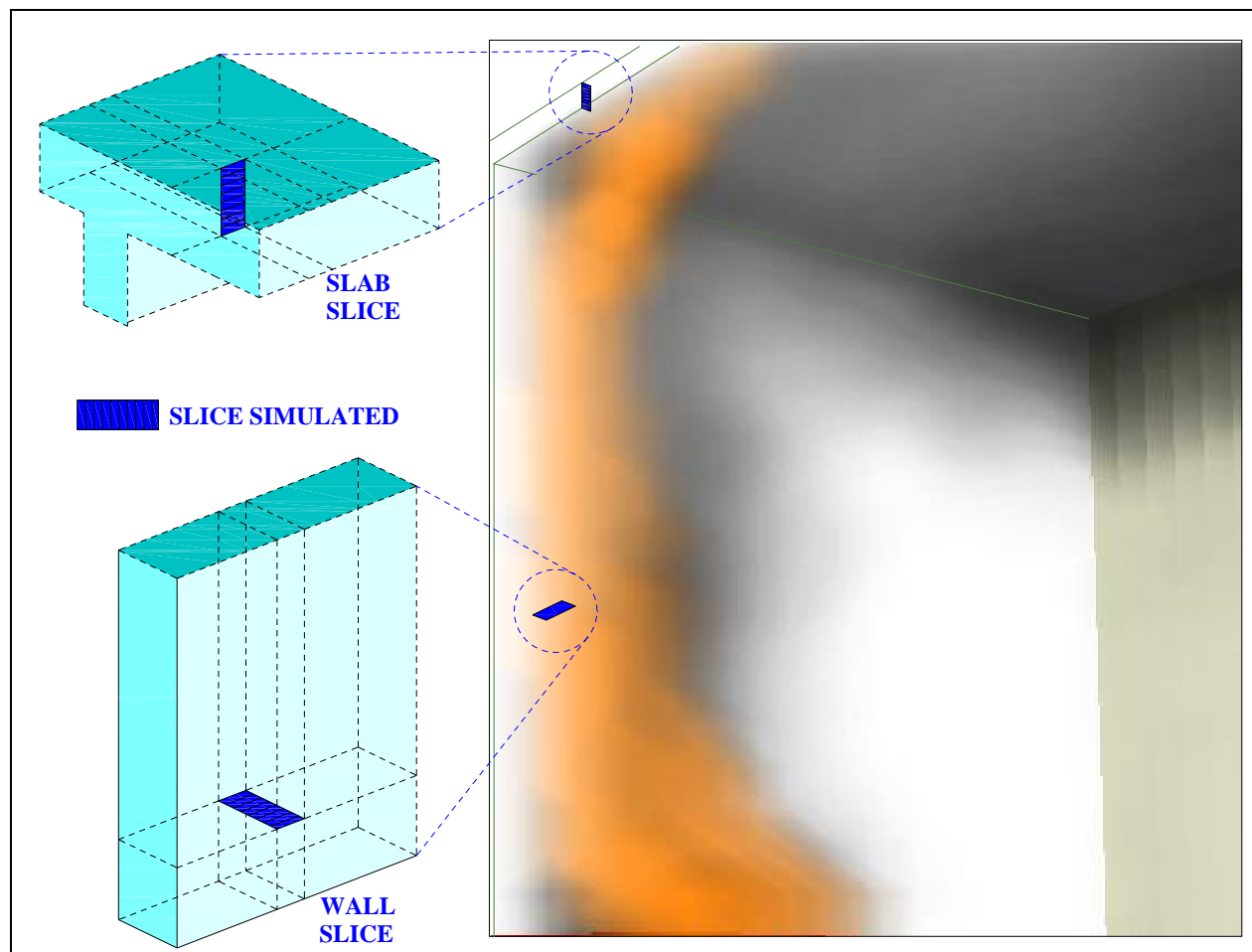


Figure 4-1. Some examples of the general layout selected for the analyses.



Figure 4-3. Thermal cracks and moisture movement in a fire-exposed concrete slab (excerpt from [12])

Some samples of the structural elements involved in the analyses.

Figure 4-2. Thermal cracks in a test wall element of dense concrete (excerpt from [12]).

The general features and the mesh needed for the numerical simulation of the analysis case described herein must be defined with enough refinement to show the sharp gradients of parameters such as gas pressure mostly in the zone close to the heated surface. On next figure, a brief description of the model used in the simulations is observed:

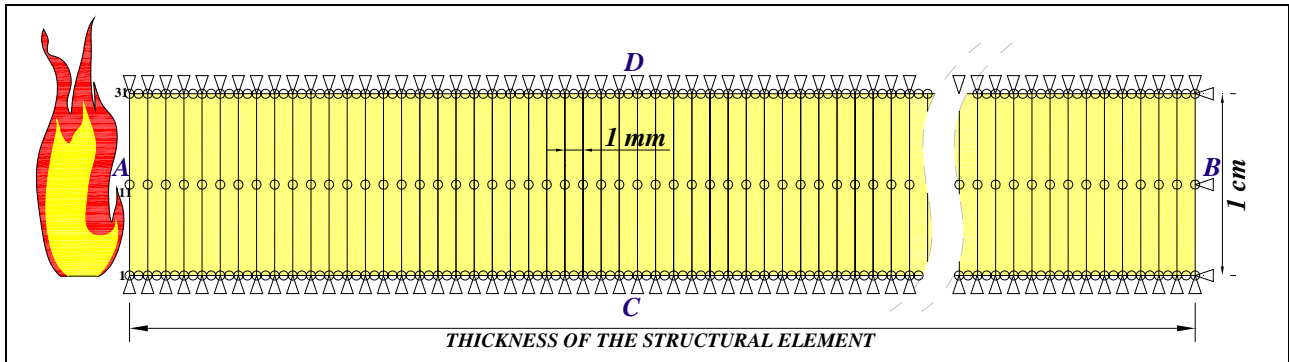


Figure 4-3. Plane strain finite element model of the Structural Concrete element slice.

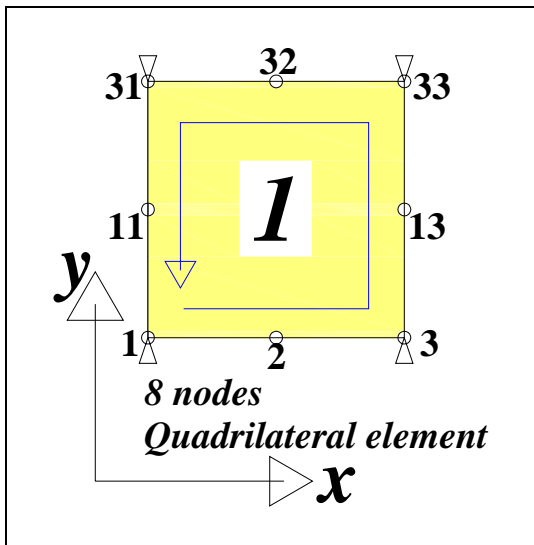


Figure 4-4. Finite Element detail.

Side	Variables	Values and coefficients
A	p^g	$p^g = 101.325 \text{ Pa}$
	p^c	$p^v = 1.300 \text{ Pa}, \beta_c = 0,02 \text{ m/s}$
	T: convective	T = See Parameter 4 in paragraph 4.2.3.4
	T: radiative	$e\sigma_0 = 5,1 \times 10^{-8} \text{ W m}^{-2} \text{ K}^{-1}$
B	u_x	$u_x = 0$
	p^g	$p^g = 101.325 \text{ Pa}$
	p^c	Environm. Relative Humidity=50%, $\beta_c=0,005\text{m/s}$
C,D	T: convective	Constant environment temperature: 298,15K
	u_y	$u_y = 0$

Table 4-2. Boundary conditions used in the numerical simulation.

The Cauchy's type boundary conditions (mixed radiative-convective) described on table 4-2 represent, in the case of the heated face, a constant in time value of the environment water vapour pressure – equal to 1.300 Pa –. This means that initially, at ambient temperature, the air relative humidity is around the 50 %, decreasing this value with time as the environment temperature increases (and vice versa if the environment temperature decreased). This type of condition is much more real, during the development of a natural fire, than keeping constant the relative humidity of the environment because during the fire evolution water vapour will be produced and eliminated. On the contrary on the opposite face, face B, the relative humidity value is fixed constant at a 50% during all the simulation because it is not expectable that it might vary significantly (since it is not expectable that water vapour from inside concrete may transfer significantly to the environment not exposed to fire). In both cases, a constant gas pressure value equal to the atmospheric pressure has been considered.

The heating profiles applied to face A are one of the ranging parameters (Parameter 4) taken into account for the sensitivity analysis dealt in this chapter. Their definition is extensively described on paragraph 4.3.2.4 and they are always related to the evolution of the environment temperature (and not to the evolution of the heated surface temperature). The heat exchange coefficients are derived from prestigious bibliography [13] taken into account the physics and phenomena occurring at each of the environments:

Fluid Condition	α_c [W/m ² ·K]
Buoyant flows in air	5-10
Laminar match flame	≈ 30
Turbulent liquid pool fire surface	≈ 20
Fire plume impinging on a ceiling	5-50
2 m/s wind speed in air	≈ 10
35 m/s wind speed in air	≈ 75

Table 4-3. Typical values for convective coefficients, α_c .

Since the structural element dealt in these analyses may appear in different positions (vertical / horizontal) and distances to the flames, the following average values of the heat exchange coefficients have been selected:

- For the Heated Environment – Surface A exchange:

$$\alpha_c = 20 \text{ W/m}^2\cdot\text{K}, \text{ since forced convection is expected,} \\ \text{(emissivity coefficient is equal to 0,85),}$$

- For the non-Heated Environment – Surface B exchange:

$$\alpha_c = 5 \text{ W/m}^2\cdot\text{K}, \text{ since natural convection is expected.}$$

Finally, the mass exchange coefficients β_c between the environment and each surface are convective-type exchanges and have been taken as a thousandth of each heat exchange coefficients α_c , appearing their values on table 4-2.

Consequently, a model with a total number of 120, 240 or 500 eight-nodes quadrilateral elements (depending on each value of Parameter 3 Thickness of the wall – see paragraph 4.3.2.3), with 40 degrees of freedom and a 3x3 order of integration, and 603, 1.203 or 2.503 nodes respectively, and the boundary conditions exposed on the table 4-2 has been implemented and calculated for each possible combination of the ranging parameters detailed in paragraph 4.3.2.

According to the different stages of each heating curve defined by Parameter 4, curves that are shown on paragraph 4.3.4., simulations have been divided into the following ten stages described by different time steps and frequency of results recording:

Input file name	Initial time (s)	Time step (s)	Number of time steps	Frequency of results record (in time steps)	Final time (s)
<i>Remark: The notation of the Input files is explained on paragraph 4.4.</i>					
TH**K0**RH**PAR*C**_01	0	1E-6	10	10	1E-5
TH**K0**RH**PAR*C**_02	1E-5	3,0	400	40	1.200
TH**K0**RH**PAR*C**_03	1.200	3,0	400	40	2.400
TH**K0**RH**PAR*C**_04	2.400	3,0	400	40	3.600
TH**K0**RH**PAR*C**_05	3.600	3,0	400	40	4.800
TH**K0**RH**PAR*C**_06	4.800	3,0	400	40	6.000
TH**K0**RH**PAR*C**_07	6.000	3,0	400	40	7.200
TH**K0**RH**PAR*C**_08	7.200	3,0	400	40	8.400
TH**K0**RH**PAR*C**_09	8.400	3,0	400	40	9.600
TH**K0**RH**PAR*C**_10	9.600	3,0	400	40	10.800

Table 4-4. Time history of the simulation stages.

4.3.2 Parameters with ranging values for the sensitivity analysis

4.3.2.1 PARAMETER 1. INITIAL SATURATION DEGREE

4.3.2.1.1 Description and Causes for its selection

The numerical model described on Chapter 3 to predict the hygral-thermal-structural state of High Strength Concrete elements under natural fire conditions considers concrete as a multiphase material consisting of a solid phase, two gas phases and three water phases. Hence, concrete is treated as a multiphase system [14] where the voids of the skeleton are filled partly with liquid and partly with a gas-phase. The liquid phase consists of bound water (or adsorbed water) – which is present in the whole range of water contents of the medium, and capillary water (or free water), which appears when water content exceeds the so-called solid saturation point S_{ssp} (the upper limit of the hygroscopic region of moisture content – see figure 4-5 –).

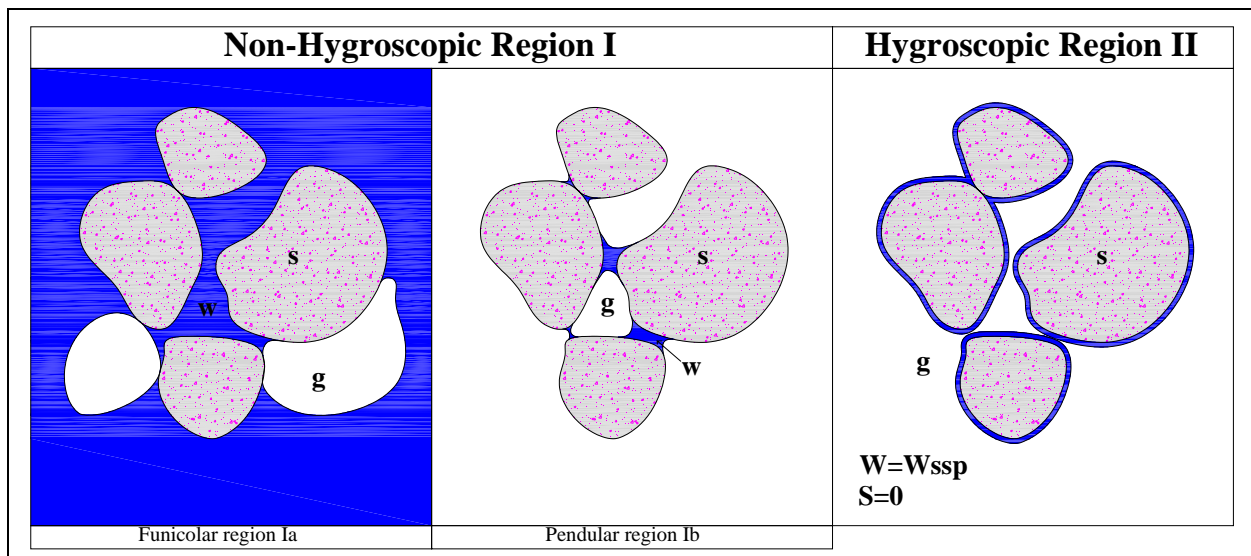


Figure 4-5. Hygroscopic region, non-hygroscopic region and solid saturation point in a porous media.

As it is observed on figure 4-5, there are two clearly differenced regions depending on the state of the water present in the representative elementary volume:

- The Non-hygroscopic region (I), where free water exists within the representative elementary volume ($0 < \text{Saturation} < 1$), retained by capillary forces, and the solid phase is fully saturated with bound water physically adsorbed on the walls of the solid structure by Van der Waals or electrostatic forces under the form of multimolecular layers [15].

This region is also divided by some authors into two parts – the Funicular region and the Pendular region – by using the concept of the irreducible saturation point ($S=S_{irr}$ or $W=W_{irr}$), above which the liquid phase is continuous (region Ia or Funicular) and discontinuous below it (region Ib called Pendular). In the Funicular region, saturation is higher than S_{irr} and free water transfer is described by the generalized Darcy's law, while in the Pendular region saturation is lower than S_{irr} . Some authors prefer to assume that free water exists in only Funicular state above the solid saturation point, especially for hygroscopic media like concretes.

- The hygroscopic region (II), where only bound water remains in the representative elementary volume.

The transition point between the region I and the region II is reached when all free water has been removed from the pores and the solid phase remains saturated with bound water. This point is known as the solid saturation point (Saturation = 0, or $W = W_{ssp}$).

Therefore, to estimate the water content present in the medium, one usually uses the dry based moisture content, W , defined as the ratio of the mass of water to the mass of dry product, or the water saturation, S , which locally represents the free water volume to the pore volume ratio. During drying, free water is first eliminated thanks to the action of the capillary forces until the local saturation falls to zero. At this point, the solid saturation point, no more free water locally exists but the solid structure is still saturated with bound water. As previously stated, the bound water content is actually to its maximum value, W_{ssp} , corresponding to the saturation point of the solid matrix. Below this saturation point, bound water removal starts.

Since the water content present in the medium is strictly related to the build-up of high pore pressure close to the heated concrete surface (as a result of rapid evaporation of the moisture), the initial degree of saturation is the first parameter selected for the spalling nomograms, being useful both from the concrete design point of view and since it may be possible to estimate (through comparison against experimental results) the water content present in the High Strength Concrete elements of existing High-Rise Buildings knowing its water content when it was manufactured, the age of the concrete and the environmental conditions under which it has lived before the fire.

4.3.2.1.2 Values selected for the spalling nomograms

In previously unheated concrete, the application of non-uniform temperatures elevates the pore vapour pressures and causes initial migration towards lower temperature zones. Initially, for concrete in *as cast* conditions, the internal pores are not physically saturated. Typically they contain an unfilled pore volume of 2-4% for normal concrete [14]. However, the corresponding value for High Strength Concrete is likely to be much less, particularly when superplasticisers are used to produce a flowing mix. Taking this into account, the values selected for the Initial Saturation Degree parameter are those exposed on next table:

PARAMETER 1	VALUE 1	VALUE 2	VALUE 3
Initial Saturation Degree	40%	50%	60%

Table 4-5. Values selected for the Initial Saturation Degree.

4.3.2.2 PARAMETER 2. INTRINSIC PERMEABILITY

4.3.2.2.1 Description and Causes for its selection

The intrinsic permeability, also called absolute permeability, is a material feature describing the penetration of gases or liquids through a porous material due to pressure head and it is generally determined by means of experimental tests performed using gas or water. Typical gases employed in these measurements are molecular oxygen and nitrogen. Theoretically, the intrinsic permeability coefficient of a given concrete should be the same regardless of whether a gas or a liquid is used in the tests, depending only on the microstructure of the concrete.

However, there are large differences between values obtained using water or gases. The gas values are consistently higher, the difference being greater at lower permeability coefficients, even if the material is almost dried. The difference may be explained by the theory of the slip in the flow of gas, whereby the gas close to a wall has a finite velocity. As a consequence, the quantity of gas flowing through a capillary is larger than would be predicted from Poiseuille's formula, i.e. supposing a laminar flow.

The problem concerning the measure of absolute permeability is decisively more complex if the temperature is not constant, in particular at high temperature, i.e. above 100°C. In such a case, many factors can influence the results. Usually, the measure is the result of a "residual" water or gas permeability test conducted at ambient temperature after a heat treatment.

Heating concrete from ambient temperature to 120 °C increases k by up to 2 orders of magnitude. Moreover, drying (e.g. in the range 120-600 °C) causes internal structural damage and dehydration of the cement, resulting in (a) an increase in k value, and (b) k values which are time dependent initially on re-wetting. In fact, the dehydration caused by drying at high temperature is partially reversed on exposure to moisture, resulting in a reduction of the k values by 1 or 2 orders of magnitude. However, the resulting values of k remain high when compared to a material which has not been heated, e.g. up to 6 orders of magnitude. The damage increases with increase of temperature, thus resulting in progressively increasing of k with temperature increase. The curing treatments are of importance, too. In fact, with particular curing during heating of concrete it is possible to minimize damage degree, resulting in lower k increase.

Hence, damage plays a really important role and should be taken into account. As above mentioned, a significant increase of concrete intrinsic permeability at high temperature is mainly generated by arising micro-cracks and by changes of material inner structure, as well as by crack-opening due to high gas pressure values. As a result, it depends not only upon temperature, moisture content and gas pressure but also upon a degree of cracks development, which may be describe by use of damage parameter D . There is still a lack of sufficient experimental research to form a bases of a mathematical model of the complex phenomena occurring in concrete at high temperature, although some authors [14] have proposed, taking into account the joint effect of temperature, gas pressure and material damaging (crack development) on the intrinsic permeability, k , the following description:

$$k = k_0 \cdot 10^{f(T)} \cdot \left(\frac{P_g}{P_0} \right)^{A_p} \cdot 10^{A_D \cdot D_{tot}}$$

where A_p and A_D are material constants. Parameter A_p has a clear physical interpretation because it describes the effect on the material permeability increase of crack opening caused by pressure rise. The value of parameter A_D is dependent on the type and dimensions of the cracks developed in concrete matrix, as it will be explained on next paragraph.

4.3.2.2.2 Values selected for the spalling nomograms

As described by [14] and explained on last paragraph, for typical structural concrete, the most likely values of intrinsic permeability are in the range from 10^{-19} to 10^{-17} m², with large increases of these values with increasing temperature. In order to cover the complete range of values of the intrinsic permeability of High Strength concretes at the whole range of temperatures, the equation described on last paragraph will be used:

$$k = k_0 \cdot 10^{f(T)} \cdot \left(\frac{p_g}{p_0} \right)^{A_p} \cdot 10^{A_{Dtot} \cdot D_{tot}} \quad (4.2)$$

with the following considerations and values [1]:

k_0 is the intrinsic permeability at reference conditions. This has been the parameter selected to range for the sensitivity analysis, remaining the intrinsic permeability dependency with temperature and damage according to the same equation for all of the analyzed cases.

$f(T)$ takes into account the influence of dehydration process and follows the following equation:

$$f(T) = A_T^2 \cdot (T - T_0)^2 + A_T^1 \cdot (T - T_0),$$

where,

$$A_T^1 \text{ is an empirical factor } (2,26 \cdot 10^{-3})$$

$$A_T^2 \text{ is an empirical factor } (-1,136 \cdot 10^{-6})$$
(4.3)

A_{Dtot} is an empirical exponent and equals 4

A_p is an empirical exponent and equals $\ln(5/3)/\ln(4)$

D_{tot} is the Total Damage parameter calculated through the expression $1 - (1-d) \cdot (1-V)$ where d and V are the mechanical damage parameter and the thermo-chemical damage parameter respectively.

Therefore, the values selected for the intrinsic permeability parameter (at reference conditions, k_0) are those exposed on next table:

PARAMETER 2 – Intrinsic permeability at reference conditions	VALUE 1	VALUE 2	VALUE 3
	10^{-19} m ²	10^{-18} m ²	10^{-17} m ²

Table 4-6. Values selected for the Intrinsic permeability at reference conditions.

4.3.2.3 PARAMETER 3. THICKNESS OF THE STRUCTURAL ELEMENT

4.3.2.3.1 Description and Causes for its selection

The thickness of structural elements is a geometry-defining basic parameter which may be easily evaluated both from the project drawings of a High-Rise building and from a direct insight during a fire. Its influence on the hygro-thermo-chemo-mechanical behaviour of a High Strength concrete element during a natural fire will depend on the rate of heat release of the fire and on the total time that the fire lasts.

On table 4-7, there is a survey of concrete structural elements present in real High-Rise buildings and classified, from their structural function point of view, in core and/or shear walls, slabs, beams and/or girders and columns. Furthermore, some general data of the buildings where they were built are included (overall structural description, concrete strength – which will be useful to select the values of Parameter 5, Material – number of stories and total height of the High-Rise building).

HIGH-RISE BUILDING. OVERALL STRUCTURAL DESCRIPTION	CONCRETE STRENGTH	# STORIES HEIGHT (m)	CORE AND/OR SHEAR-WALLS	SLABS	BEAMS AND/OR GIRDERS	COLUMNS
The Museum Tower, Los Angeles. Tubular ductile concrete frame with perimeter columns.	N/A	22 stories 73 m	N/A	0,203 m	N/A	N/A
The Miglin-Beitler Tower, Chicago, Illinois (PROJECT). Concrete core, steel composite floor system, concrete fin columns, link beams interconnecting the four corners of the core to the eight fin columns.	N/A	107 stories 483 m	Maximum 0,91 m Minimum 0,46 m	74 mm deep corrugated metal deck and 89 mm normal weight concrete topping	N/A	Maximum 2x10m Minimum 1,38x4m
The NCNB Tower, North Carolina. Reinforced concrete perimeter tube with normal-weight concrete. Post-tensioned beams	55 MPa (base) to 41 MPa (top)	60 stories 265,12 m	Core columns: 0,61x0,92m	0,118 m	0,458 m (slab) 1,01 m (columns connecting spandrel beams)	Maximum 0,61x0,97m Minimum 0,61x0,61m
The South Walker Tower, Chicago. Core shear walls with shear wall-frame interaction, perimeter columns and perimeter spandrel beams through girders that span from core to the perimeter.	55 MPa (base) to 28 MPa (upper levels)	65 stories 288,4 m	N/A	0,114 m	1,0 m (girders) 0,92 m (spandrels)	Maximum 1,53x1,53m
Metro-Dade Administration Building, Miami, Florida. Concrete columns and shear walls located at the two narrow sides. Thick Slabs supported on haunch girders.	N/A	33 stories 152,4 m	N/A	0,152 m	0,61 m (girders)	N/A
Jin Mao Tower, Shanghai, China. Steel and reinforced concrete mixed structure. Central reinforced concrete core linked to exterior composite megacolumns by outrigger trusses.	52 MPa (base) to 35 MPa	88 stories 421 m	Maximum 0,84 m Minimum 0,46 m	76 mm deep metal deck and 82,5 mm normal weight concrete topping	N/A	Maximum 1,5x4,88m Minimum 0,91x3,53m (composite)
Petronas Towers, Malaysia. Central reinforced concrete core, perimeter columns and ring beams	80 MPa to 40 MPa	95 stories 452 m	0,35 m (core walls) 0,75 to 0,35 (outer walls)	53 mm deep metal deck and 110 mm to 200 mm normal weight concrete topping	0,775 m (ring beams, at midspan) 0,737 m (bustles, at midspan)	Maximum diam. 2,4m Minimum diam. 1,2m
Hong Kong Central Plaza. Triangular design with 10% lateral load carrying core shear walls external façade frames acting as a tube above the transfer girder.	N/A	78 stories 368 m	N/A	1,0 m (thick slab at the wind shears transfer level)	1,1 m (spandrel beams) 2,8 m (transfer girder)	1,5x1,5 m
MTA Headquarters, Los Angeles. Composite beams spanning from the core to the exterior. Lateral system: perimeter tube with widely spaced columns tied together with spandrel beams.	N/A	28 stories 122 m	N/A	76 mm deep metal deck and 83 mm lightweight concrete topping	0,54 m (composite beams)	0,87x0,40m (box columns) 0,61x0,61m (box columns at corners)

Table 4-7. Main data corresponding to some existing High-Rise Buildings around the world (excerpt and resumed from [16])

4.3.2.3.2 Values selected for the spalling nomograms

From the analysis of the values appearing on table 4-7, the following values have been selected for the thickness of the structural element since they cover most of their real range of values:

PARAMETER 3	VALUE 1	VALUE 2	VALUE 3
Thickness of the structural element	12 centimetres	24 centimetres	50 centimetres

Table 4-8. Values selected for the Thickness of the structural elements.

However, as it might be expectable that the third value of the thickness, 50 centimetres, is beyond a threshold value of the thickness above which there is no influence on the hygro-thermo-chemo-mechanical behaviour of the analyzed element (especially for high rates of heat release of the fire), initially a unique sample calculation with this thickness is programmed and, if necessary, other cases with this third value will be added. The sample selected for this evaluation is that corresponding to the medium considered values of both the Initial Saturation Degree (50%) and the Intrinsic Permeability at reference conditions (10^{-18} m^2) (see combination number 73 in the list of total combinations included in paragraph 4.4).

4.3.2.4 PARAMETER 4. HEATING PROFILE

4.3.2.4.1 Description and Causes for its selection

Since the temperature evolution in a High Strength Concrete element has an essential influence on the thermal spalling risk [17], the heating profiles selected for the nomograms development need to be chosen covering the complete range of possible realistic fires that may arise in High-Rise Buildings rooms and/or offices.

Therefore, the adopted heating profiles will be obtained from the time-temperature parametric curves defined in the Eurocode 1, Part 1-2 [18], since this is an European regulation widely spread and prestigious document where parametric curves have been defined on an experimental bases, definition that will be briefly described and applied next:

The time-temperature parametric curves defined in the Annex A of the Eurocode 1, Part 1-2 [18] are, on the contrary than the nominal curves, dependent on certain physic parameters such as the following:

- The fire load density (the higher fire load density the longer the fire is),
- The ventilation conditions, depending mainly on the geometry, size and distribution of the compartment openings (big ventilation openings lead to fast fires but less severe),
- The properties of the closing walls of the fire compartment (walls gain energy and limit the fire temperature).

These curves also differ from the nominal curves in the sense that after a heating stage they present a cooling one (as it will be explained in detail on next chapter), and they are valid for fire sectors with a built surface not higher than 500 square meters, without holes at the roof and with a maximum height of 4 meters, assuming a complete combustion of the fire load.

They are defined in the *heating* stage (in the *cooling* stage there is a different definition that will be explained on next chapter) by:

$$\Theta_g = 20 + 1.325 \cdot (1 - 0.324 \cdot e^{-0.2 \cdot t^*} - 0.204 \cdot e^{-1.7 \cdot t^*} - 0.472 \cdot e^{-19 \cdot t^*}) \quad (4.4)$$

Where,

Θ_g is the air temperature within the fire sector [°C]

t^*	$= t \cdot \Gamma$	[h]
Γ	$= [O/b]^2 / (0,04 / 1.160)^2$	[-]
b	$= \sqrt{\rho \cdot c \cdot \lambda}$ with the following limits: $100 \leq b \leq 2.200$	[J/m ³ s ^{1/2} K]
ρ	is the density of the element closing the fire sector (At ambient temperature)	[Kg/m ³]
c	is the specific heat of the element closing the fire sector (At ambient temperature)	[J/KgK]
λ	is the thermal conductivity of the element closing the fire sector (At ambient temperature)	[W/mK]
O	is the opening coefficient: $A_v \cdot \sqrt{h_{eq}} / A_t$ with the following limits: $0,02 \leq O \leq 0,20$	[m ^{1/2}]
A_v	is the total surface of the vertical openings at all of the walls	[m ²]
h_{eq}	is the averaged height of the windows at all of the walls	[m]
A_t	is the total surface closing the fire sector, including openings	[m ²]

The maximum temperature Θ_{max} in the heating stage takes place at $t^* = t^*_{max}$

$$t^*_{max} = t_{max} \cdot \Gamma \quad [h]$$

$$t_{max} = \max \left[\frac{0,2 \cdot 10^{-3} \cdot q_{t,d}}{O}; t_{lim} \right] \quad [h] \quad (4.5)$$

where,

- $q_{t,d}$ is the fire load density referred to the total surface A_t of the envolvent
 $q_{t,d} = q_{f,d} \cdot A_f / A_t$ [MJ/m²], with the following limits: $50 \leq q_{t,d} \leq 1.000$ [MJ/m²];
- $q_{f,d}$ is the calculation value of the fire load density referred to the built floor surface A_f [MJ/m²], deducted from the Annex E of the Eurocode 1, Part 1-2 [18]
- t_{lim} takes the following values [h]:
 $t_{lim} = 25$ min, for fires of slow development,
 $t_{lim} = 20$ min, for fires of medium-speed development,
 $t_{lim} = 15$ min, for fires of fast development,

so, whenever fire is controlled by the fire load, the time t_{max} corresponding to the maximum temperature is determined by t_{lim} , while t_{max} is determined by $(0,2 \cdot 10^{-3} \cdot q_{t,d} / O)$ if the fire is controlled by ventilation.

In order to illustrate the type of parametric curves that may be obtained, it is next included a graphic obtained for a calculation value of the fire load density of $q_{f,d} = 600$ MJ/m², a thermal inertia of the walls of $b = 1.500$ J/m²s^{1/2}K, a total area of the surrounding surface of $A_t = 360$ m², a pavement area of $A_f = 100$ m², a t_{lim} equal to 25 minutes (what corresponds to a slow development fire) and an opening coefficient O with ranging values from $0,02$ m^{1/2} to $0,20$ m^{1/2}.

Figure 4-6 shows that when fire is controlled by the ventilation conditions the increase of the opening coefficient leads to shorter but more severe fires, until fires are controlled by the fire load, where the influence of the opening coefficient is especially observed on the cooling rate of the environment.

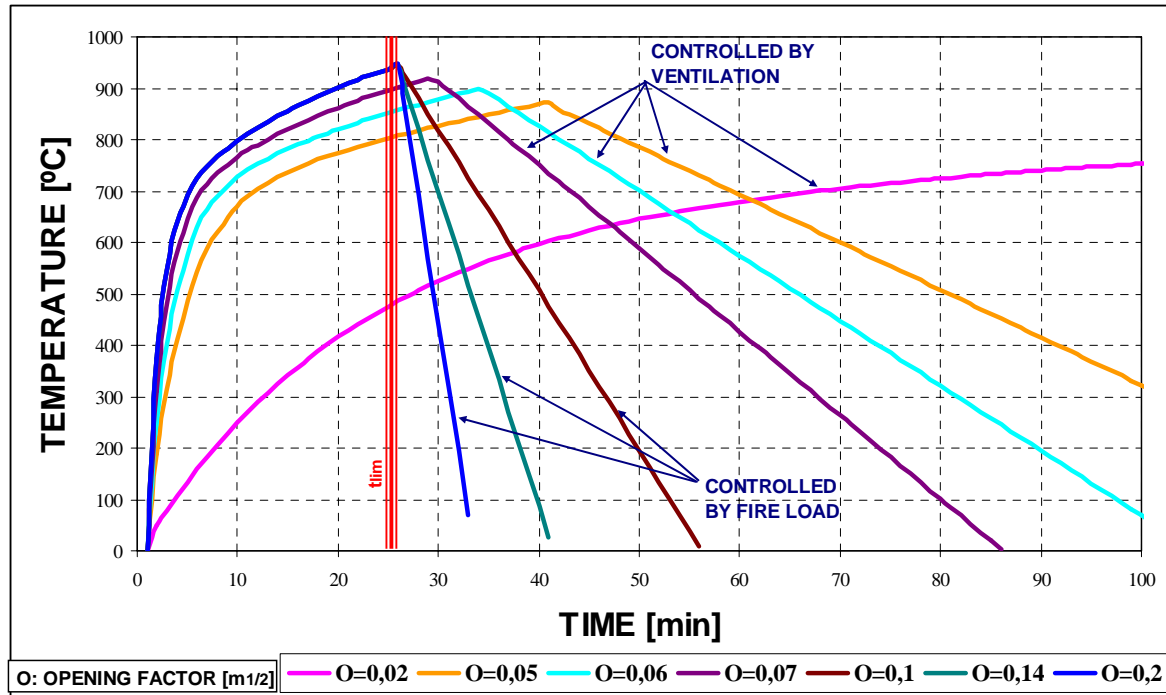


Figure 4-6. Family of parametric curves as a function of the opening coefficient, O .

The heating profiles selected for the spalling nomograms must cover this wide range of possibilities, from the longest but less severe fires up to the shortest but more severe ones. This selection, exposed on paragraph 4.3.2.4.2, will start from some common values of the intervening parameters defined by the analyzed case:

- b will present a common value of $b=2.016 \text{ J/m}^2\text{s}^{1/2}\text{K}$, value obtained through the ambient values of the C60 material density, specific heat and thermal conductivity,
- $q_{f,d}$ will present a common value of $q_{f,d}=1.145 \text{ MJ/m}^2$ resulting from applying to the characteristic value of the fire load density corresponding to a hotel office the coefficients described on the Annex E of the Eurocode 1, Part 1-2 [18]. This value will only have influence on the start time of the cooling stage, which is not included in these calculations so it is not especially influencing the results.
- t_{lim} will present a common value of $t_{lim}=20$ minutes, corresponding to a medium speed development fire as it is prescribed for hotel offices and rooms on the table E.5 of the Annex E of the Eurocode 1, Part 1-2 [18].

Taking these common values into account, each selected value will be adopted by varying the opening coefficient, as it is explained on next paragraph.

4.3.2.4.2 Values selected for the spalling nomograms

4.3.2.4.2.1 Value 1. Reasons for its selection and definition procedure

The first value to adopt results from applying to the equation used in Eurocode 1, Part 1-2 [18] to define parametric curves in heating stage,

$$\Theta_g = 20 + 1.325 \cdot (1 - 0.324 \cdot e^{-0.2 \cdot t^*} - 0.204 \cdot e^{-1.7 \cdot t^*} - 0.472 \cdot e^{-19 \cdot t^*}) \quad (4.6)$$

a value of $\Gamma = [O/b]^2 / (0.04 / 1.160)^2 = 1$ (where $t^* = t \cdot \Gamma$) which in this case represents an opening coefficient of about $O = 0.07 \text{ m}^{1/2}$.

In such a way, the curve obtained matches the normalized time-temperature curve (ISO 834) defined in the regulation project prEN 13501-2 to represent a fire model completely developed in a fire sector. This selection has many advantages since this curve is widely spread and adopted to classify or to verify the fire resistance, both from the experimental and from the analytical points of view, so it enables an easier comparison of the results obtained with any source of comparable experimental results.

This curve represents a set of heating conditions more severe than most of the conditions that may appear during a natural fire in a High-Rise building. Its final form is the following:

PARAMETER 4 Heating profile PARI	VALUE 1 (Θ_g [°C] ,t [min])
	$\Theta_g = 20 + 345 \cdot \log_{10}(8 \cdot t + 1)$

Table 4-9. First Value selected for the Heating profile.

Figure 4-7 shows the graphical representation of the heating parametric curve obtained with $\Gamma=1$ and its comparison against the normalized time-temperature ISO 834 curve (the curve selected for this first value is exactly the ISO 834 curve, since its mathematical definition is easier to deal from the numerical point of view):

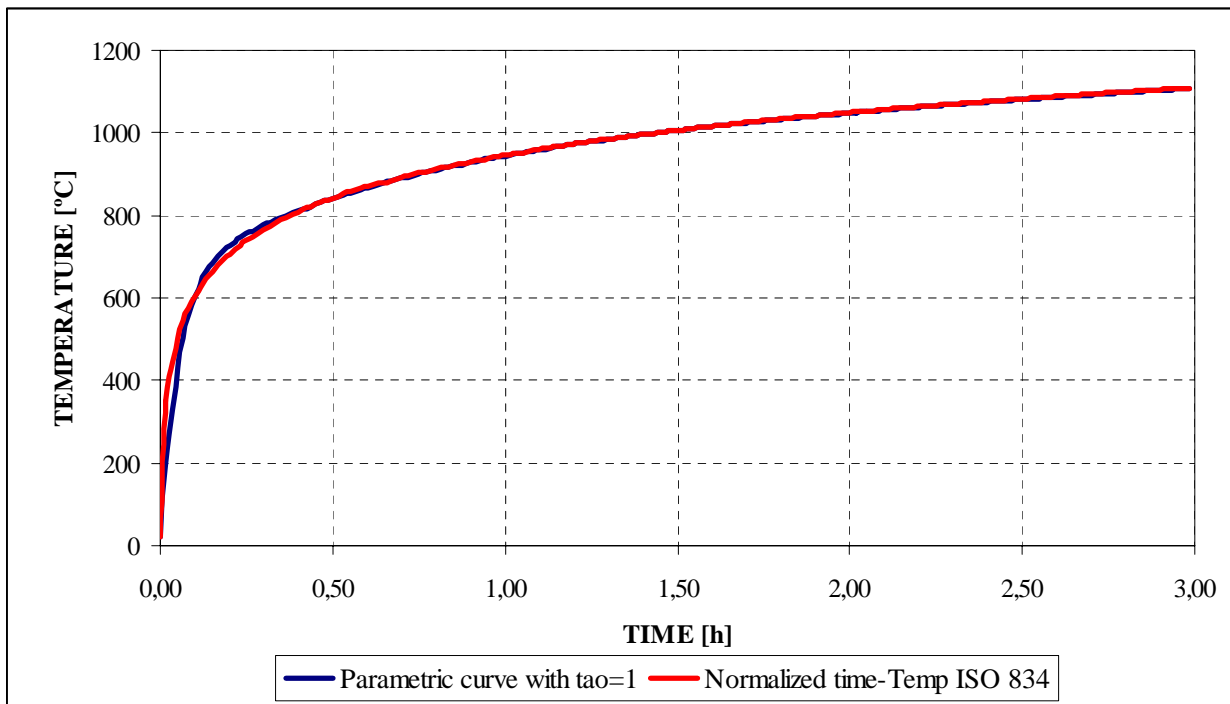


Figure 4-7. Comparison of the normalized time-temperature ISO 834 curve against the parametric curve obtained with $\Gamma=1$.

4.3.2.4.2.2 Value 2. Reasons for its selection and definition procedure

The second value to adopt results from applying to the equation used in Eurocode 1, Part 1-2 [18] to define parametric curves in heating stage,

$$\Theta_g = 20 + 1.325 \cdot (1 - 0.324 \cdot e^{-0.2 \cdot t^*} - 0.204 \cdot e^{-1.7 \cdot t^*} - 0.472 \cdot e^{-19 \cdot t^*}) \quad (4.7)$$

the lowest value of the opening coefficient allowed in the Eurocode $O = 0,02 \text{ m}^{1/2}$ (and the rest of common values described on paragraph 4.3.2.4.1).

In such a way, the curve obtained is one of the slowest and less severe curves that may be obtained from the family of heating curves defined by parametric curves. It clearly represents a

slow development fire that reaches its maximum temperature at a total time of three hours, time that is being considered within the simulations.

This curve represents a set of heating conditions less severe than most of the conditions that may appear during a natural fire in a High-Rise building. Its final form is the following:

PARAMETER 4 Heating profile PAR2	VALUE 2 (Θ_g [°C] ,t [h])
	$\Theta_g = 20 + 1.325 \cdot (1 - 0,324 \cdot e^{-0,0152t} - 0,204 \cdot e^{-0,1292t} - 0,472 \cdot e^{-1,444t})$

Table 4-10. Second Value selected for the Heating profile.

Figure 4-8 shows the graphical representation of this heating parametric curve and its comparison against the normalized time-temperature ISO 834 curve:

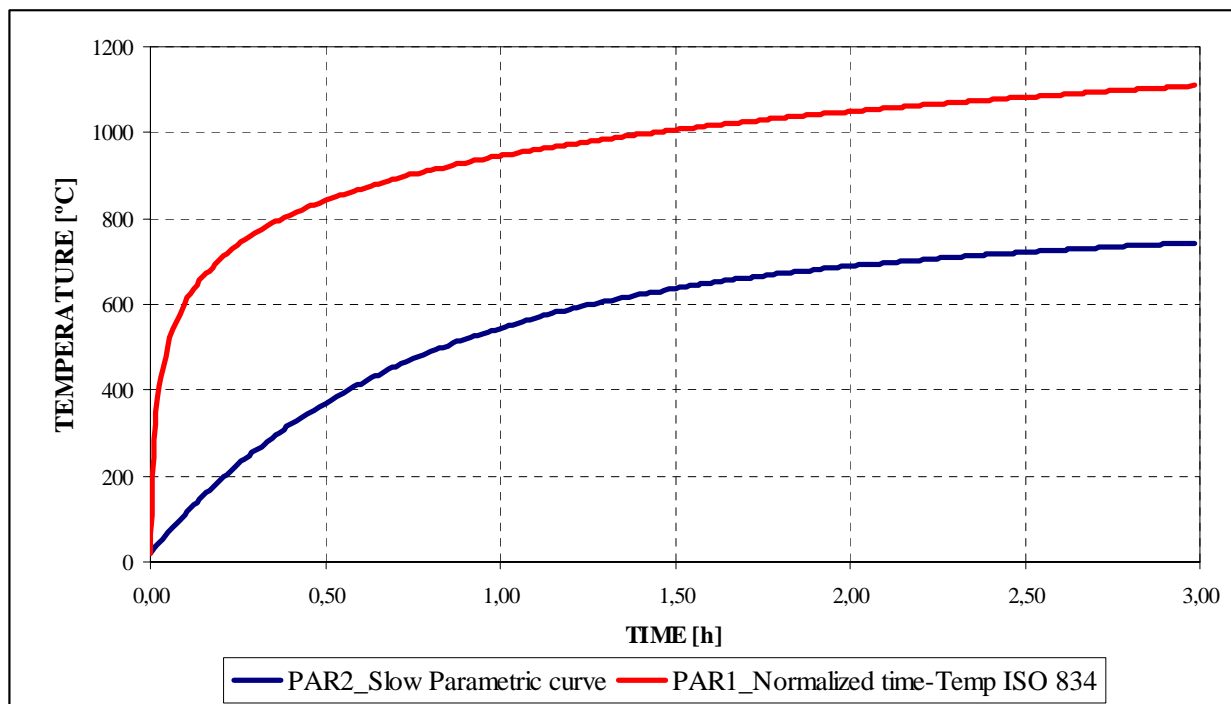


Figure 4-8. Comparison of the normalized time-temperature ISO 834 curve against the slow parametric described on table 4-10.

4.3.2.4.2.3 Value 3. Reasons for its selection and definition procedure

The third and last value to adopt does not result from applying any particular value to the equation used in Eurocode 1, Part 1-2 [18] to define parametric curves in heating stage.

On the contrary it has been selected another nominal time-temperature curve referred to in Eurocode 1, Part 1-2 [18] as the Hydrocarbon fire curve, which represents the fire conditions where hydrocarbon products are present. This curve has been selected because it is the most fast and severe heating curve which is expectable (mainly, during blasts or vehicles crashes). Since it is also widely spread and adopted to classify or to verify the fire resistance, both from the experimental and from the analytical points of view, it will also enable an easier comparison of the results obtained with any source of comparable experimental results covering the whole range of possible natural fires in High-Rise Buildings.

The Eurocode 1, Part 1-2 [18] defines the Hydrocarbon heating curve in the following form:

PARAMETER 4 Heating profile PAR3	VALUE 3 (Θ_g [°C] ,t [min])
	$\Theta_g = 20 + 1.080 \cdot (1 - 0,325 \cdot e^{-0,167t} - 0,675 \cdot e^{-2,5t})$

Table 4-11. Third Value selected for the Heating profile.

Figure 4-9 shows the graphical representation of this third parametric heating curve (PAR3_Hydrocarbon) and its comparison against the slow parametric curve (PAR2) and the normalized time-temperature ISO 834 curve (PAR1):

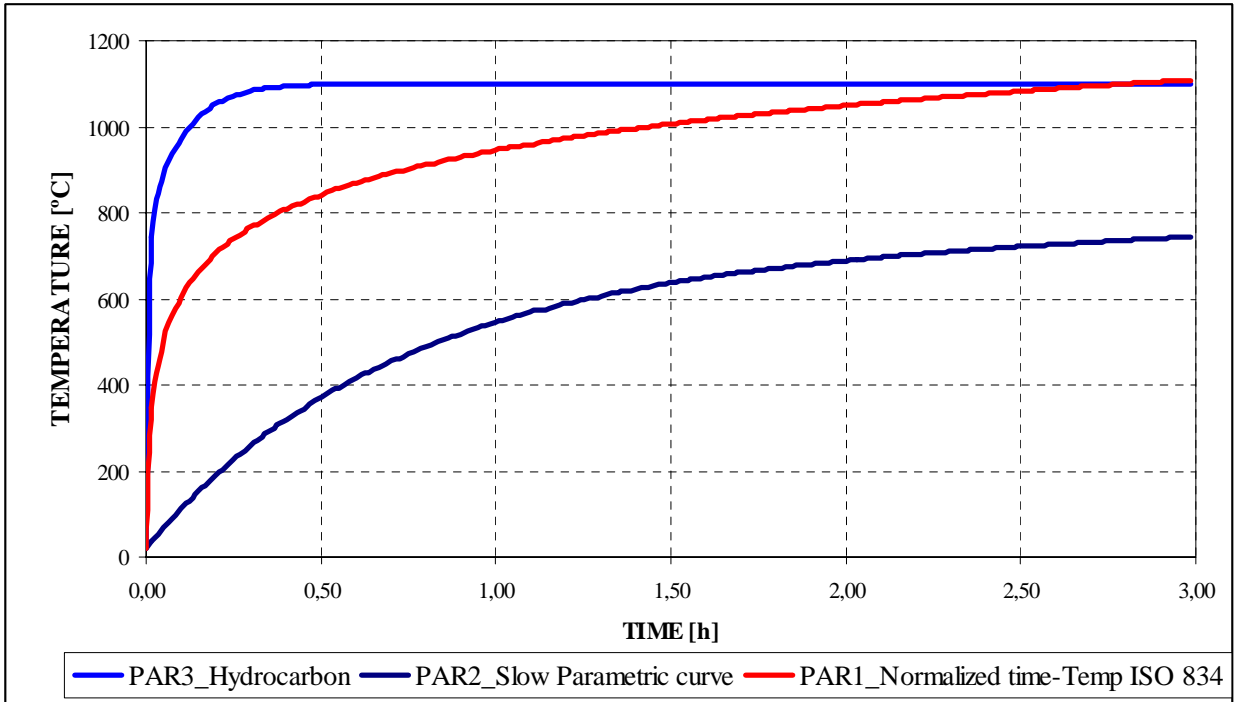


Figure 4-9. Comparison of the Hydrocarbon curve against the normalized time-temperature ISO 834 curve (PAR1) and the slow parametric (PAR2).

Finally, in figure 4-10 if we compare the three heating profiles selected against the whole range of possible parametric curves obtainable with the common values described on paragraph 4.3.2.4.1, it will be shown that there are none possible heating profiles outside the range of analysis:

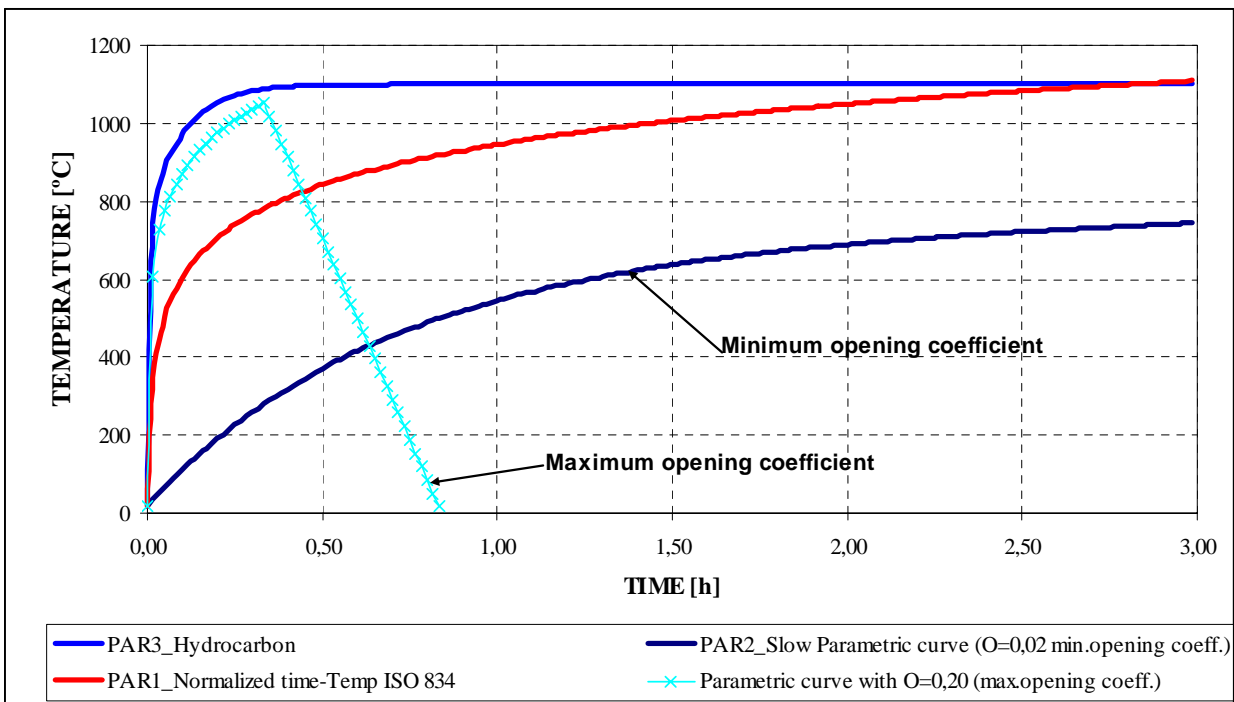


Figure 4-10. Comparison of the possible heating profiles and the range defined by the selected curves PAR1, PAR2 and PAR3.

4.3.2.5 PARAMETER 5. MATERIAL

4.3.2.5.1 *Description and Causes for its selection*

Heat transfer in concrete cannot be predicted just from the traditional thermal properties: thermal conductivity, volumetric specific heat and thermal diffusivity. Movement of air, water and possibly carbon dioxide through the concrete is accompanied by significant energy transfer, particularly associated with the latent heat of water and the heats of hydration and dehydration. Forced convection and diffusion are also necessary to consider due to the high pore pressures that result when high-strength concrete is exposed to fire [14]. Furthermore, the extent of hydration and free moisture content may also vary throughout the concrete because of the heat released during initial curing and drying and if the different surfaces have been exposed to different humidities.

When exposing concrete to fire free moisture, both liquid and vapour, will migrate toward the colder regions. Initially, this moisture movement occurs by diffusion processes, where the driving force may be considered to be the gradient in moisture content (commonly expressed as partial pressure, humidity, molar or mass fraction, or molar or mass density). As the temperature increases, any free liquid water will boil off and migrate toward the colder regions where some of it will condense. The latent heat required to boil the liquid water will retard the rate of temperature increase at that location. When water vapour is transported into a colder region, some of it is absorbed into the concrete, with a heat of sorption that is approximately equal to the latent heat associated with condensation of free water vapour into liquid, so that significant heat is released.

As moisture moves inwards and the inner temperature increases towards 100 °C, portions of the concrete element will experience additional hydration (conversion of free water to chemically bound water), with the corresponding release of heat. When the temperature of any portion of the concrete element exceeds the boiling point of water at the local pressure, some dehydration (release of chemically bound water) will begin to take place, with a simultaneous release of heat. Dehydration reactions continue up to temperatures in excess of 800 °C, with the most pronounced reaction being the dehydration of calcium hydroxide between 400 and 600 °C (see figure 4-11 at the temperature of 500 °C). The free water introduced into the concrete tries to diffuse toward the cold side. However, high-strength concrete is not very permeable to water vapour and is even less permeable to liquid water.

For concrete with carbonate aggregates, between 660 and 980 °C, calcium carbonate breaks down into calcium oxide with the release of carbon dioxide. Magnesium carbonate is similarly decomposed between 740 and 840 °C. Both reactions are endothermic, absorbing heat and delaying temperature rise in the concrete. Quartz undergoes a pronounced phase transformation, with an accompanying volume increase, at about 573 °C.

During temperature exposure of the concrete, its transport properties for both heat and mass can change quite significantly due to differential thermal expansion opening up microcracks and changes in the solid structure associated with chemical decomposition of the cement paste (dehydration) and of any carbonate aggregates (conversion to oxides), both processes leading to less dense material and thus lower thermal conductivity (and thermal diffusivity) and higher mass transport properties.

With respect to mass transport, diffusion and forced convection have to be considered. The mass flux due to a unitary gradient in the density/pressure of the transported fluid is simply the mass flux and, in the case of diffusion processes, it is called mass diffusivity. It is often expressed in terms of partial pressures and in both cases it is replaced with a coefficient usually named 'permeability'.

On table 4-12 are resumed the main physical-chemical reactions that experiences concrete when subjected to high temperature.

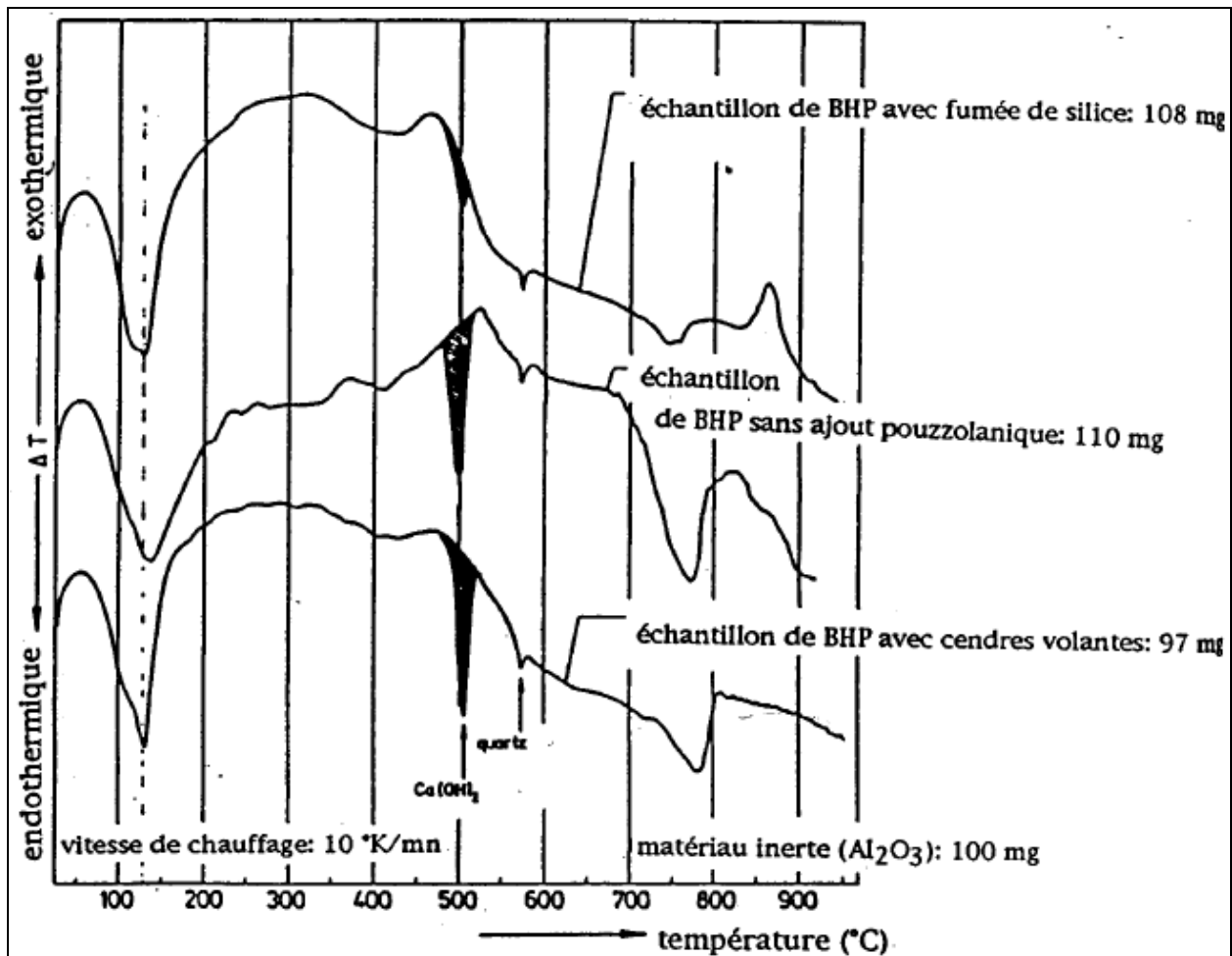


Figure 4-11. Curves obtained by means of thermal differential analysis for three types of concretes [30].

Temperature interval	Reaction observed
30 °C – 120 °C	Free water and a fraction of the absorbed water migrate both out of concrete and towards colder regions. Free water is completely eliminated at about 120 °C.
130 °C – 170 °C	A double endothermic reaction may take place corresponding the decomposition of $\text{CaSO}_4 \cdot 2\text{H}_2\text{O}$.
180 °C – 300 °C	The first stage of dehydration. There is a rupture of the cement gel. Heat breaks the cement gel and eliminates water molecules from the hydrated silicates.
250 °C – 370 °C	Small endothermic peaks may arise as an effect of the decomposition and oxidation of metal elements (ferric).
400 °C – 600 °C	Dehydration of calcium hydroxide: $\text{Ca}(\text{OH})_2 \rightarrow \text{CaO} + \text{H}_2\text{O}$
573 °C	Quartz undergoes a pronounced phase transformation (α -quartz \rightarrow β -quartz), with an accompanying volume increase.
600 °C- 700 °C	There is a decomposition of the phases of C-S-H and formation of β -C ₂ S. It is the second stage of dehydration of the hydrated calcium silicates that produces a new form of bicalcique silicates.
660 °C – 980 °C	For concrete with carbonate aggregates, calcium carbonate breaks down into calcium oxide with the release of carbon dioxide: $\text{CaCO}_3 \rightarrow \text{CaO} + \text{CO}_2$, reaction which is strongly endothermic.
Above 1.300 °C – 1.400 °C	Concrete moves to a 'mud' state.

Table 4-12. Main physico-chemical reactions that experiences concrete when subjected to high temperature.

The energy transport (heat flux) associated with a mass flux is simply the enthalpy multiplied by time derivative of mass, and an additional term that has to be taken into account in the energy equation.

Also phenomena of absorption and desorption by the concrete cannot be neglected. For moisture transfer at temperature below the boiling point of water, absorption effects are quite important and the mass storage of water, and the associated enthalpy storage, need to be considered. Absorption/desorption of water vapour is usually described in terms of sorption isotherms, curves which relate the equilibrium absorbed moisture content of a medium, at a specific temperature, to the moisture content (usually expressed as vapour pressure or humidity) to which it is exposed. At low humidities, absorption is mainly by adsorption, first in monomolecular layers and then in multimolecular layers. Above about 40 percent relative humidity, capillary condensation begins in the smallest micropores of the material and then, as the humidity increases, there is condensation in larger pores and cracks, due to the depression of vapour pressure over the curved menisci of the water-filled capillaries. Beyond that, porous materials exhibit hysteresis, so that absorption isotherms differ from desorption isotherms. The moisture capacity of a material is defined as the slope of the sorption isotherm (analogous to the heat capacity being the slope of the enthalpy-versus-temperature curve). The moisture capacity increases markedly as the water vapour pressure increases toward the saturation vapour pressure. Above a relative humidity of about 97 percent it is customary to treat the moisture as being a liquid. Here the moisture capacity of a material is related to the capillary suction pressure by what is known as a suction curve, which also exhibits hysteresis, being the mass flux and moisture capacity considered in a differential equation expressed with density of the water vapour as driving potential, partial pressure or relative humidity.

As it is expectable, the consideration of all of these physical-chemical processes within a numerical model needs the previous definition of a sophisticated extent of thermal, chemical and mechanical properties of concrete (beyond those needed for the suitable characterization of water in both liquid and gas phases), extremely complicated to find in literature from existing experimental tests, properties that are enounced next:

- Cubic thermal expansion coefficient of solid β_s ,
- Skeleton density ρ_s ,
- Young's modulus E_c for compression,
- Young's modulus E_t for tension,
- Compressive strength f_c ,
- Tensile strength f_t ,
- Poisson's ratio ν ,
- Characteristic length l ,
- Degree of saturation S (isotherms of desorption),
- Stechiometric factor,
- Porosity ϕ ,
- Intrinsic permeability,
- Thermal conductivity of dry concrete λ_{dry} , and
- Specific apparent heat C_{ps}

Furthermore these are not constant values but varying with temperature, so their temperature evolution is also needed. On the next paragraphs are shown the values adopted in the available literature for two of the materials more widely used in High-Rise Buildings (see table 4-7), being a High-Strength Concrete named C60 with a compressive strength of about 60 MPa at 20 °C and a Very-High-Strength Concrete named C90 with a compressive strength above 80 MPa at ambient temperature.

4.3.2.5.2 First selection for the spalling nomograms: C60. Definition procedure

Cubic thermal expansion coefficient of solid β_s (excerpt from [1])					
Symbol	Units	Meaning	Expansion	Values	Ref.
β_{lin}	$^{\circ}\text{C}^{-1}$	Linear thermal expansion coefficient of solid	-	$6,02 \cdot 10^{-6}$	[19]
β_s	$^{\circ}\text{C}^{-1}$	Cubic thermal expansion coefficient of solid	$3 \cdot \beta_{lin}$	$18,06 \cdot 10^{-6}$	-

Comments:

1. Data have been measured with dilatometri during Hiteco project [20]. β_s is the slope of curves. In order to simplify calculations, a constant value equal to mean slope is assumed.
2. The factor 3 is used to pass from linear coefficient to cubic coefficient.

Table 4-13. Cubic thermal expansion coefficient of solid.

Skeleton density ρ_s (excerpt from [1])					
$\rho_s = r + s \cdot (T - T_0)$					
Symbol	Units	Meaning	Expansion	Values	Ref.
ρ_s	kg/m^3	Solid phase density	Previous equation	-	-
r	kg/m^3	Empirical coefficient	-	2.627,4	-
s	$\text{kg}/(\text{m}^3\text{K})$	Empirical coefficient	-	0,3422	-
T	K	Temperature at current point and time	-	Calculated with F.E.M.	-
T_0	K	Reference Temperature	-	273,15	-

Comments:

1. Solid density of dry material ρ_{dry} has been measured by [21] during HITECO project. Heat treatment induces a mass loss (which results in a decrease in density) as well as a slight shrinkage during dehydration (which results in a slight increase in density).
2. Then, choosing an average value for it (in fact the density of dry material is almost constant between 105°C and 600 °C), the solid phase density ρ_s has been calculated using the relationship $\bar{\rho}_{dry} = (1 - \phi) \cdot \rho_s$. As a consequence, ρ_s follows a linear relationship due to the porosity and increase with temperature.

Table 4-14. Skeleton density.

Young's modulus E_c for compression (excerpt from [1])					
$E_c = a + b \cdot T$, for $T \leq 500^{\circ}\text{C}$; $E_c = a \cdot e^{b \cdot (T - 500)}$, for $T > 500^{\circ}\text{C}$					
Symbol	Units	Meaning	Expansion	Values	Ref.
E_c	Pa	Young's modulus for compression	Previous equations	-	-
a	Pa	Empirical parameter	-	$3,5604 \cdot 10^{10}$ for $T \leq 500^{\circ}\text{C}$ $0,8576 \cdot 10^{10}$ for $T > 500^{\circ}\text{C}$	-
b	$\text{Pa}/^{\circ}\text{C}$	Empirical parameter	-	$-54,089 \cdot 10^6$ for $T \leq 500^{\circ}\text{C}$ $-54,089/8.576$ for $T > 500^{\circ}\text{C}$	-

T	°C	Temperature at current point and time	-	Calculated with F.E.M.	-
<p><i>Comments:</i></p> <p>1. The equation of Young's modulus for compression is deduced from experimental data of Hiteco project ([22]). Values have been measured after cooling to ambient temperature.</p> <p>2. The value of Young's modulus at 20°C is $3,3634 \cdot 10^{10}$ Pa.</p>					

Table 4-15. Young's modulus for compression.

Young's modulus E_t for tension (excerpt from [1])					
$E_t = E_c$					
Symbol	Units	Meaning	Expansion	Values	Ref.
E_t	Pa	Young's modulus for tension	Previous equation	-	-
<p><i>Comments:</i></p> <p>1. Due to the lack of experimental data and in order to simplify the problem, it has been assumed that the Young's modulus for tension is equal to the one for compression.</p>					

Table 4-16. Young's modulus for tension.

Compressive strength f_c (excerpt from [1])					
$f_c = c + d \cdot T$					
Symbol	Units	Meaning	Expansion	Values	Ref.
f_c	Pa	Compressive strength	Previous equation	-	-
c	Pa	Empirical parameter	-	If $T \leq 200^\circ\text{C}$: $-55,556 \cdot 10^6$ Else if $T < 600^\circ\text{C}$: $-80,46 \cdot 10^6$ Else: $-33,88 \cdot 10^6$	-
d	Pa/°C	Empirical parameter	-	If $T \leq 200^\circ\text{C}$: $-0,0222 \cdot 10^6$ Else if $T < 600^\circ\text{C}$: $0,1024 \cdot 10^6$ Else: $0,0248 \cdot 10^6$	-
T	°C	Temperature at current point and time	-	Calculated with F.E.M.	-

Comments:

1. The equation of compressive strength is deduced from experimental data of Hiteco project ([22]). Values have been measured after cooling to ambient temperature (see figure 4-12).

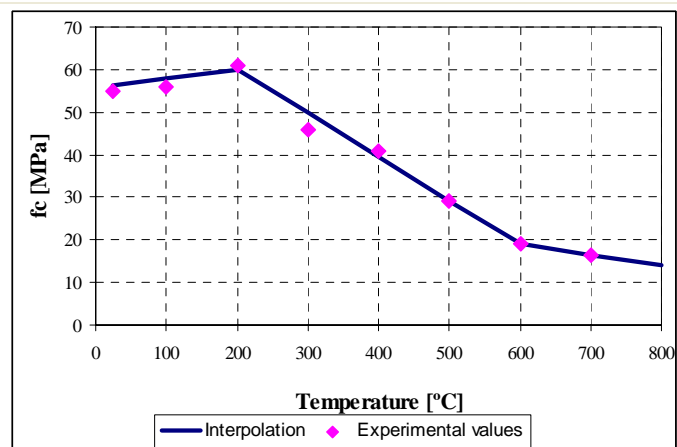


Figure 4-12. Comparison of the experimental data against interpolation.

Table 4-17. Compressive strength.

Tensile strength f_t (excerpt from [1])					
$f_t = e + f \cdot T$					
Symbol	Units	Meaning	Expansion	Values	Ref.
f_t	Pa	Tensile strength	Previous equation	-	-
e	Pa	Empirical parameter	-	If $T \leq 600^\circ\text{C}$: $6 \cdot 10^6$ Else: $0,864 \cdot 10^6$	-
f	$\text{Pa}/^\circ\text{C}$	Empirical parameter	-	If $T \leq 600^\circ\text{C}$: $-8,56 \cdot 10^3$ Else: 0	-
T	$^\circ\text{C}$	Temperature at current point and time	-	Calculated with F.E.M.	-

Comments:

1. The equation of tensile strength is deduced from experimental data on generic high performance concretes elaborated by [11] (see figure 4-13).

Figure 4-13. Comparison of the experimental data against interpolation.

Table 4-18. Tensile strength.

Poisson's ratio ν (excerpt from [1])					
Symbol	Units	Meaning	Expansion	Values	Ref.
ν	-	Poisson's ratio	-	0,18	-

Comments:

- Experimental data on Poisson's ratio have been performed by [19] during Hiteco project; wire resistance strain gauges were used for the full loading curve.
- Calculations have been done using a constant value.

Table 4-19. Poisson's ratio.

Characteristic length l (excerpt from [1])					
Symbol	Units	Meaning	Expansion	Values	Ref.
l	m	Characteristic length	-	$8 \cdot 10^{-2}$	-

Comments:

- This parameter is important in order to define the representative elementary volume and area correctly. In this way, it's possible to perform operations of averaging which are consistent.
- There is no possibility to get this parameter from direct experimental tests.
- The characteristic length depends on the type of material, especially on the diameter ϕ of aggregates; in fact Bazant suggests to use a value equal to $2-3 \cdot \phi_{max}$. Anyway, for high performance concretes, a different approach has been used: l comes from the energy of fracture estimated at ambient temperature.
- l is considered constant at any temperature.

Table 4-20. Characteristic length.

Degree of saturation S (isotherms of desorption) (excerpt from [1])					
$S = (G+1)^{\frac{1}{b}}$					
Symbol	Units	Meaning	Expansion	Values	Ref.
S	-	Degree of saturation	Previous equation	-	-
G	-	Function of temperature and of capillary pressure	$\left[\frac{E}{a} \cdot p_c \right]^{\frac{b}{b-1}}$	-	-
E	-	Function of temperature	$\left[\frac{T_{crit} - T_0}{T_{crit} - T} \right]^N$ if $T \leq T_{crit}$ $\frac{N}{z} \cdot E_0 \cdot T + \left[E_0 - \frac{N}{z} \cdot E_0 \cdot (T_{crit} - z) \right]$ if $T > T_{crit}$	-	-
N	-	Empirical parameter	-	1,2	-
z	-	Parameter that governs the transition through the critical temperature of water	-	0,5	-
E ₀	-	Function of temperature E when T=T _{crit}	$\left(\frac{T_{crit} - T_0}{z} \right)^N$	-	-
T	K	Temperature at current position and time	-	Calculated with F.E.M.	-
T _{crit}	K	Critical temperature of water	-	Calculated with F.E.M.	-
T ₀	K	Ambient temperature	-	293,15	-
a	Pa	Parameter function of temperature	Polynomial case: Q ₃ if T ≤ 373,15 K Q ₀ +Q ₂ if T > 373,15 K Exponential case: Q ₀ +Q ₂ for all T	-	-
Q ₃	Pa	Empirical constant	-	18,62·10 ⁶	-
Q ₂	Pa	Empirical constant	-	7·10 ⁶	-
Q ₁	K ⁻¹	Empirical constant to govern	-	0,01	-

		exponential relationship			
Q_0	Pa	Function of Temperature	Polynomial case: $(Q_3-Q_2) \cdot [2 \cdot T^3 - 3 \cdot T^2 + 1]$; Exponential case: $(Q_3-Q_2) \cdot \exp[Q_1 \cdot (T_0-T)]$	-	-
T'	-	Adimensional temperature	$\frac{T - 373,15}{T_{crit} - 373,15}$	-	-
p_c	Pa	Capillary pressure	-	Calculated with F.E.M.	-
b	-	Constant parameter	-	2,27	-

Comments:

1. This formulation for desorption isotherms is due to [23] who proposed this relationship: $p_c(S) = a \cdot (S^b - 1)^{1-1/b}$ which fits experimental data at ambient temperature. This relationship has been subjected to some changes to take into account high temperature effects: b has been kept the same under 100 °C and related with temperature above 100 °C (see Q_0). New formulation is represented on figures 4-14 and 4-15, which are an example excerpt from [1].

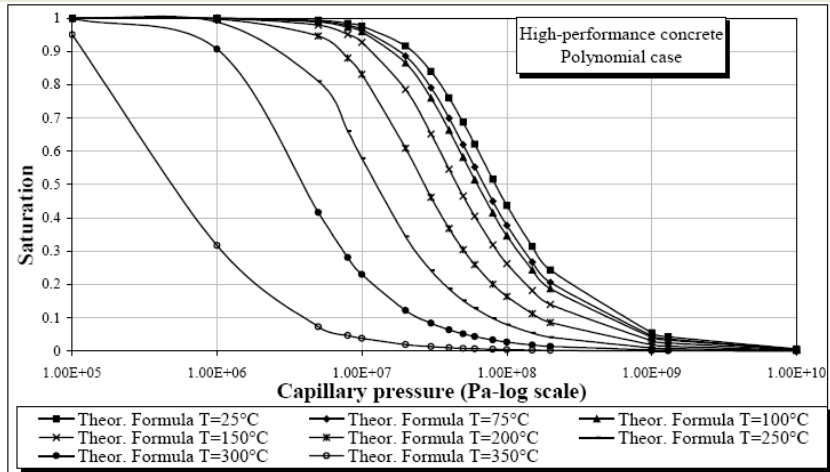


Figure 4-14. Isotherms of desorption in the polynomial case.

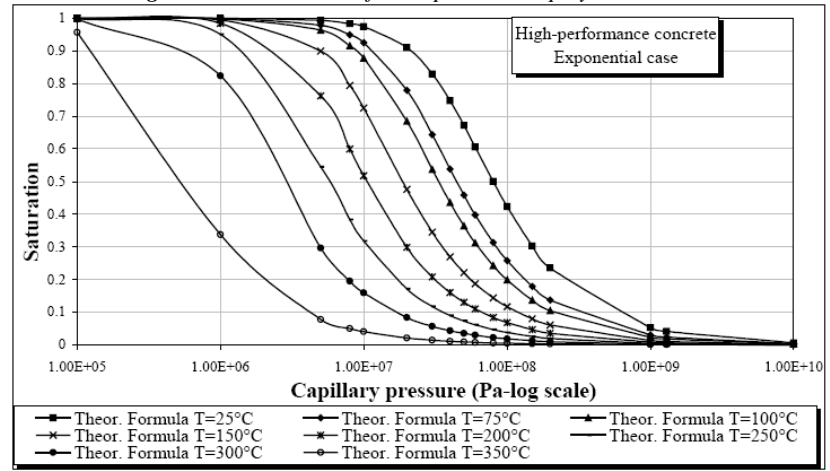


Figure 4-15. Isotherms of desorption in the exponential case.

Table 4-21. Degree of saturation S (isotherms of desorption).

Stoichiometric factor (excerpt from [1])					
$f_s = \frac{w}{c}$					
Symbol	Units	Meaning	Expansion	Values	Ref.
f_s	-	Stoichiometric factor	Previous equation	0,36	-
w	kg/m ³	Water content	-	162	[24]

c	kg/m ³	Cement content	-	450	[24]
<p>Comments:</p> <p>1. w and c refer to the mixes selected for Hiteco project.</p>					

Table 4-22. Stechiometric factor.

Porosity ϕ (excerpt from [1])					
$\phi = \phi_0 + A_n \cdot (T - T_0)$					
Symbol	Units	Meaning	Expansion	Values	Ref.
ϕ	-	Porosity	Previous equation	-	-
ϕ_0	-	Porosity at T=T ₀	-	0,10385	-
A _n	K ⁻¹	Empirical coefficient	-	0,000109	-
T	K	Temperature at current point and time	-	Calculated with F.E.M.	-
T ₀	K	Reference temperature	-	273,15	-

Comments:

1. The changes of porosity with increase of temperature were investigated by [25]. The previous equation is a result of a linear interpolation of experimental data obtained by [21] and [26] during Hiteco project. [21] calculated porosity from mass measurements, while [26] used mercury porosimetry (see figure 4-16).

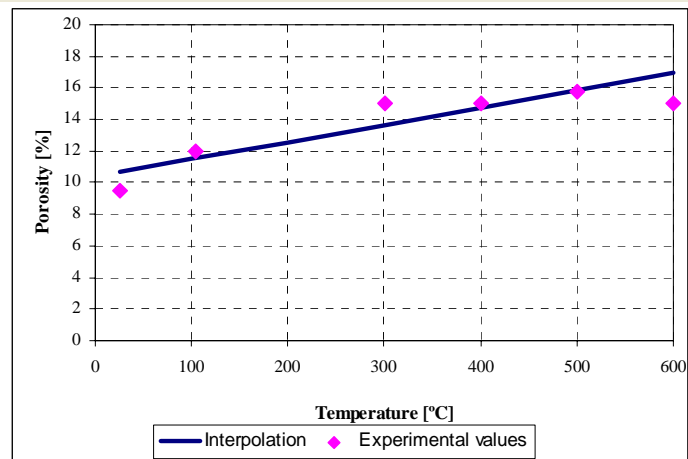


Figure 4-16. Comparison of the experimental data against interpolation.

Table 4-23 Porosity.

Intrinsic permeability (excerpt from [1])	
$k = k_0 \cdot 10^{f(T)} \cdot \left(\frac{p_g}{p_0} \right)^{A_p} \cdot 10^{A_{D_{tot}} \cdot D_{tot}}$	
<p>Comments:</p> <p>1. This parameter is one of the ranging parameters taken into account for the sensitivity analysis (Parameter 2). Its formulation and adopted values are explained in depth in paragraph 4.3.2.2.2.</p> <p>2. The usual value of the intrinsic permeability at reference conditions k_0 for the C60 material is $2 \cdot 10^{-18} \text{ m}^2$.</p>	

Table 4-24. Intrinsic permeability.

Thermal conductivity of dry concrete λ_{dry} (excerpt from [1])					
$\lambda_{dry}(T) = u + v \cdot T$					
Symbol	Units	Meaning	Expansion	Values	Ref.
λ_{dry}	W/mK	Thermal conductivity of	Previous equation	-	[27]

		dry concrete			
u	W/mK	Empirical parameter	-	1,8079	-
v	W/mK	Empirical parameter	-	-0,0013	-
T	°C	Temperature at current point and time	-	Calculated with F.E.M. (if $T \geq 600^\circ\text{C}$ then $T=600^\circ\text{C}$)	-

Comments:

1. The equation for the thermal conductivity of a dry material has been deduced from experimental data of Hiteco Project [21]. Unfortunately tests have been performed in non thermodynamic equilibrium which means that specimens were heated and then kept at reached temperature for a short period, not sufficient to achieve a steady state. As a consequence, concrete didn't lose the whole quantity of water. Anyway, data at 105°C (real presence of dry steady state) and 600°C (non steady state, but high enough to consider a quasi-dry condition) give two points to determine the linear relationship for λ_{dry} (see figure 4-17).

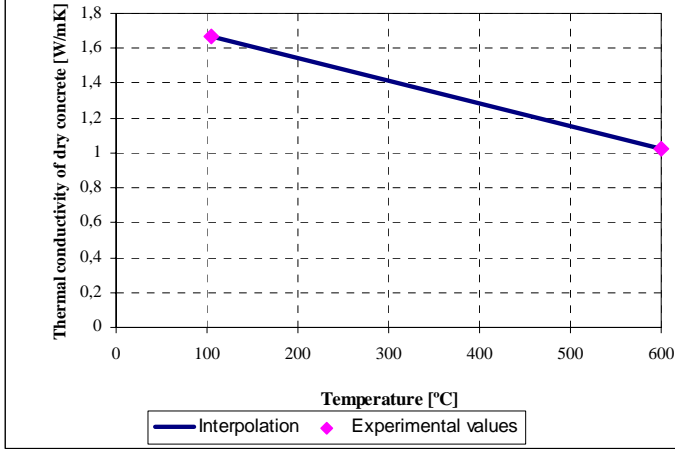


Figure 4-17. Comparison of the experimental data against interpolation.

Table 4-25 Thermal conductivity of dry concrete.

Specific apparent heat C_{ps} (excerpt from [1])					
$C_{ps} = i + q \cdot T$					
Symbol	Units	Meaning	Expansion	Values	Ref.
C_{ps}	J/(Kkg)	Specific heat of the solid skeleton	Previous equation	-	-
i	J/(Kkg)	Empirical parameter	-	855,25758	-
q	J/(Kkg°C)	Empirical parameter	-	-0,22626263	-
T	°C	Temperature at current point and time	-	Calculated with F.E.M. (if $T \geq 600^\circ\text{C}$ then $T=600^\circ\text{C}$)	-

Comments:

1. Specific heat of solid skeleton has been obtained from an elaboration of experimental data measured by [21].

Table 4-26. Specific apparent heat.

4.3.2.5.3 Second selection for the spalling nomograms: C90. Definition procedure

Cubic thermal expansion coefficient of solid β_s (excerpt from [1])					
Symbol	Units	Meaning	Expansion	Values	Ref.
β_{lin}	°C ⁻¹	Linear thermal expansion coefficient of solid	-	$5,38 \cdot 10^{-6}$	[19]
β_s	°C ⁻¹	Cubic thermal expansion	$3 \cdot \beta_{lin}$	$16,14 \cdot 10^{-6}$	-

		coefficient of solid		
<i>Comments:</i>				
1. Data have been measured with dilatometri during Hiteco project [20]. β_s is the slope of curves. In order to simplify calculations, a constant value equal to mean slope is assumed.				
2. The factor 3 is used to pass from linear coefficient to cubic coefficient.				

Table 4-27. Cubic thermal expansion coefficient of solid.

Skeleton density ρ_s (excerpt from [1])					
$\rho_s = r + s \cdot (T - T_0)$					
Symbol	Units	Meaning	Expansion	Values	Ref.
ρ_s	kg/m ³	Solid phase density	Previous equation	-	-
r	kg/m ³	Empirical coefficient	-	2.620,6	-
s	kg/(m ³ K)	Empirical coefficient	-	0,6252	-
T	K	Temperature at current point and time	-	Calculated with F.E.M.	-
T ₀	K	Reference Temperature	-	273,15	-
<i>Comments:</i>					
1. Solid density of dry material ρ_{dry} has been measured by [21] during HITECO project. Heat treatment induces a mass loss (which results in a decrease in density) as well as a slight shrinkage during dehydration (which results in a slight increase in density).					
2. Then, choosing an average value for it (in fact the density of dry material is almost constant between 105°C and 600 °C), the solid phase density ρ_s has been calculated using the relationship $\bar{\rho}_{dry} = (1 - \phi) \cdot \rho_s$. As a consequence, ρ_s follows a linear relationship due to the porosity and increase with temperature.					

Table 4-28. Skeleton density.

Young's modulus E_c for compression (excerpt from [1])					
$E_c = a + b \cdot T$					
Symbol	Units	Meaning	Expansion	Values	Ref.
E_c	Pa	Young's modulus for compression	Previous equations	-	-
a	Pa	Empirical parameter	-	3,9281·10 ¹⁰ for T≤120°C 2,9967·10 ¹⁰ for T≤400°C 1,440·10 ¹⁰ for T>400°C	-
b	Pa/°C	Empirical parameter	-	-129,03·10 ⁶ for T≤120°C -51,418·10 ⁶ for T≤400°C -12,5·10 ⁶ for T>400°C	-
T	°C	Temperature at current point and time	-	Calculated with F.E.M.	-
<i>Comments:</i>					
1. The equation of Young's modulus for compression is deduced from experimental data of Hiteco project ([28]) measured at the chosen temperature ("hot" values).					
2. The value of Young's modulus at 20°C is 3,67·10 ¹⁰ Pa.					

Table 4-29. Young's modulus for compression.

Young's modulus E_t for tension (excerpt from [1])					
$E_t = E_c$					
Symbol	Units	Meaning	Expansion	Values	Ref.
E_t	Pa	Young's modulus for tension	Previous equation	-	-
<p><i>Comments:</i></p> <p>1. Due to the lack of experimental data and in order to simplify the problem, it has been assumed that the Young's modulus for tension is equal to the one for compression.</p>					

Table 4-30. Young's modulus for tension.

Compressive strength f_c (excerpt from [1])					
$f_c = c + d \cdot T$					
Symbol	Units	Meaning	Expansion	Values	Ref.
f_c	Pa	Compressive strength	Previous equation	-	-
c	Pa	Empirical parameter	-	If $T \leq 120^\circ\text{C}$: $-82,48 \cdot 10^6$ Else if $T \leq 200^\circ\text{C}$: $-42,55 \cdot 10^6$ Else if $T \leq 500^\circ\text{C}$: $-85,50 \cdot 10^6$ Else: $-47,10 \cdot 10^6$	-
d	Pa/°C	Empirical parameter	-	If $T \leq 120^\circ\text{C}$: $-0,2440 \cdot 10^6$ Else if $T \leq 200^\circ\text{C}$: $-0,0888 \cdot 10^6$ Else if $T \leq 500^\circ\text{C}$: $0,1260 \cdot 10^6$ Else: $0,0490 \cdot 10^6$	-
T	°C	Temperature at current point and time	-	Calculated with F.E.M. (if $T \geq 600^\circ\text{C}$ then $T = 600^\circ\text{C}$)	-

Comments:

1. The equation of compressive strength is deduced from experimental data of Hiteco project ([28]).

2. If $T > 600^\circ\text{C}$ then T assumes constant value equal to 600°C (see figure 4-18).

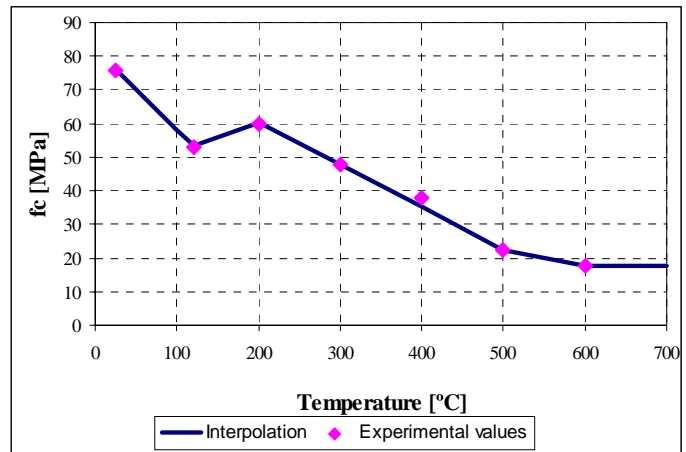


Figure 4-18. Comparison of the experimental data against interpolation.

Table 4-31. Compressive strength.

Tensile strength f_t (excerpt from [1])					
$f_t = e + f \cdot T$					
Symbol	Units	Meaning	Expansion	Values	Ref.
f_t	Pa	Tensile strength	Previous	-	-

			equation		
e	Pa	Empirical parameter	-	If $T \leq 600^\circ\text{C}$: $6 \cdot 10^6$ Else: $0,864 \cdot 10^6$	-
f	Pa/°C	Empirical parameter	-	If $T \leq 600^\circ\text{C}$: $-8,56 \cdot 10^3$ Else: 0	-
T	°C	Temperature at current point and time	-	Calculated with F.E.M.	

Comments:

1. The equation of tensile strength is deduced from experimental data on generic high performance concretes elaborated by [11] (see figure 4-19).

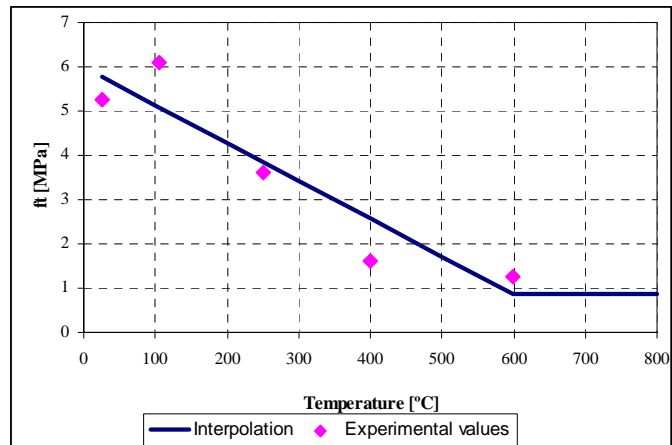


Figure 4-19. Comparison of the experimental data against interpolation.

Table 4-32. Tensile strength.

Poisson's ratio ν (excerpt from [1])					
Symbol	Units	Meaning	Expansion	Values	Ref.
ν	-	Poisson's ratio	-	0,18	-

Comments:

1. Experimental data on Poisson's ratio have been performed by [29] during Hiteco project.
2. The experimental value has been observed to be above the expected level of literature.
3. Calculations have been done using a constant value.

Table 4-33. Poisson's ratio.

Characteristic length l (excerpt from [1])					
Symbol	Units	Meaning	Expansion	Values	Ref.
l	m	Characteristic length	-	$8 \cdot 10^{-2}$	-

Comments:

1. This parameter is important in order to define the representative elementary volume and area correctly. In this way, it's possible to perform operations of averaging which are consistent.
2. There is no possibility to get this parameter from direct experimental tests.
3. The characteristic length depends on the type of material, especially on the diameter ϕ of aggregates; in fact Bazant suggests to use a value equal to $2-3 \cdot \phi_{max}$. Anyway, for high performance concretes, a different approach has been used: l comes from the energy of fracture estimated at ambient temperature.
4. l is considered constant at any temperature.

Table 4-34. Characteristic length.

Degree of saturation S (isotherms of desorption) (excerpt from [1])					
$S = (G + 1)^{\frac{1}{b}}$					
Symbol	Units	Meaning	Expansion	Values	Ref.
S	-	Degree of saturation	Previous equation	-	-
G	-	Function of temperature and of capillary pressure	$\left[\frac{E}{a} \cdot p_c \right]^{\frac{b}{b-1}}$	-	-
E	-	Function of temperature	$\left[\frac{T_{crit} - T_0}{T_{crit} - T} \right]^N$ if $T \leq T_{crit}$ $\frac{N}{z} \cdot E_0 \cdot T + \left[E_0 - \frac{N}{z} \cdot E_0 \cdot (T_{crit} - z) \right]$ if $T > T_{crit}$	-	-
N	-	Empirical parameter	-	1,2	-
z	-	Parameter that governs the transition through the critical temperature of water	-	0,5	-
E ₀	-	Function of temperature E when T=T _{crit}	$\left(\frac{T_{crit} - T_0}{z} \right)^N$	-	-
T	K	Temperature at current position and time	-	Calculated with F.E.M.	-
T _{crit}	K	Critical temperature of water	-	Calculated with F.E.M.	-
T ₀	K	Ambient temperature	-	293,15	-
a	Pa	Parameter function of temperature	Polynomial case: Q ₃ if T ≤ 373,15 K Q ₀ +Q ₂ if T > 373,15 K Exponential case: Q ₀ +Q ₂ for all T	-	-
Q ₃	Pa	Empirical constant	-	46,9364·10 ⁶	-
Q ₂	Pa	Empirical constant	-	7·10 ⁶	-
Q ₁	K ⁻¹	Empirical constant to govern	-	0,01	-

		exponential relationship			
Q_0	Pa	Function of Temperature	Polynomial case: $(Q_3-Q_2) \cdot [2 \cdot T^3 - 3 \cdot T^2 + 1]$; Exponential case: $(Q_3-Q_2) \cdot \exp[Q_1 \cdot (T_0-T)]$	-	-
T'	-	Adimensional temperature	$\frac{T - 373,15}{T_{crit} - 373,15}$	-	-
p_c	Pa	Capillary pressure	-	Calculated with F.E.M.	-
b	-	Constant parameter	-	2,0601	-

Comments:

1. This formulation for desorption isotherms is due to [23] who proposed this relationship: $p_c(S) = a \cdot (S^b - 1)^{1-1/b}$ which fits experimental data at ambient temperature. This relationship has been subjected to some changes to take into account high temperature effects: b has been kept the same under 100 °C and related with temperature above 100 °C (see Q_0). New formulation is represented on figures 4-20 and 4-21, which are an example excerpt from [1].

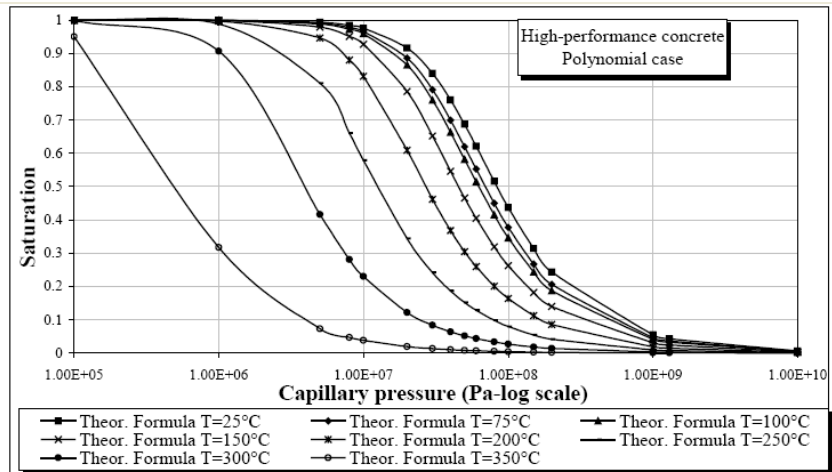


Figure 4-20. Isotherms of desorption in the polynomial case.

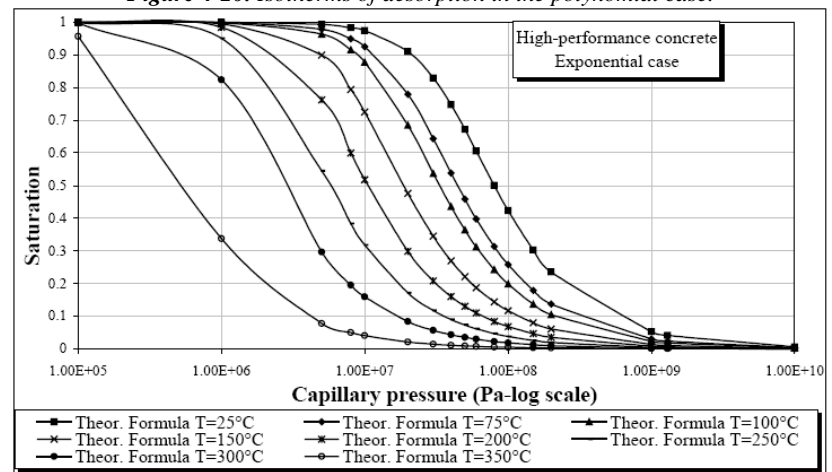


Figure 4-21. Isotherms of desorption in the exponential case.

Table 4-35. Degree of saturation S (isotherms of desorption).

Stoichiometric factor (excerpt from [1])					
$f_s = \frac{w}{c}$					
Symbol	Units	Meaning	Expansion	Values	Ref.
f_s	-	Stoichiometric factor	Previous equation	0,32	-
w	kg/m ³	Water content	-	163	[24]

c	kg/m ³	Cement content	-	510	[24]
<p><i>Comments:</i></p> <p>1. <i>w and c refer to the mixes selected for Hiteco project.</i></p>					

Table 4-36. Stechiometric factor.

Porosity ϕ (excerpt from [1])					
$\phi = \phi_0 + A_n \cdot (T - T_0)$					
Symbol	Units	Meaning	Expansion	Values	Ref.
ϕ	-	Porosity	Previous equation	-	-
ϕ_0	-	Porosity at T=T ₀	-	0,0512581	-
A _n	K ⁻¹	Empirical coefficient	-	0,0001967	-
T	K	Temperature at current point and time	-	Calculated with F.E.M.	-
T ₀	K	Reference temperature	-	273,15	-

Comments:

1. *The changes of porosity with increase of temperature were investigated by [25]. The previous equation is a result of a linear interpolation of experimental data obtained by [21] and [26] during Hiteco project. [21] calculated porosity from mass measurements, while [26] used mercury porosimetry (see figure 4-22).*

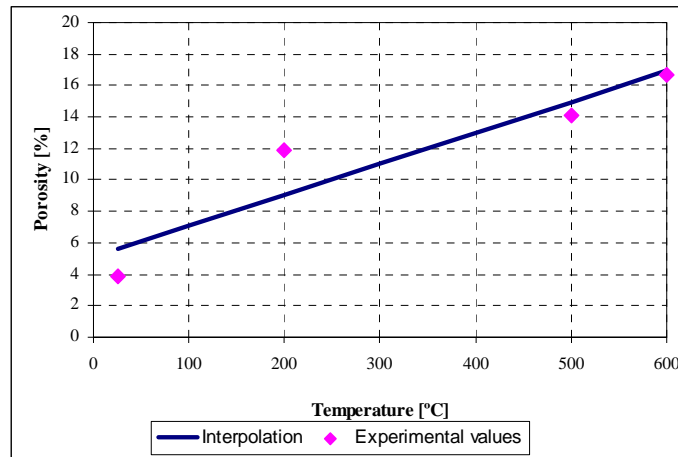


Figure 4-22. Comparison of the experimental data against interpolation.

Table 4-37 Porosity.

Intrinsic permeability (excerpt from [1])	
$k = k_0 \cdot 10^{f(T)} \cdot \left(\frac{P_g}{P_0} \right)^{A_p} \cdot 10^{A_{D_{tot}} \cdot D_{tot}}$	
<p><i>Comments:</i></p> <p>1. <i>This parameter is one of the ranging parameters taken into account for the sensitivity analysis (Parameter 2). Its formulation and adopted values are explained in depth in paragraph 4.3.2.2.2.</i></p> <p>2. <i>The usual value of the intrinsic permeability at reference conditions k₀ for the C60 material is 2 · 10⁻¹⁸ m².</i></p>	

Table 4-38. Intrinsic permeability.

Thermal conductivity of dry concrete λ_{dry} (excerpt from [1])					
$\lambda_{dry}(T) = u + v \cdot T$					
Symbol	Units	Meaning	Expansion	Values	Ref.
λ_{dry}	W/mK	Thermal conductivity of	Previous equation	-	[27]

dry concrete					
u	W/mK	Empirical parameter	-	1,386363636	-
v	W/mK	Empirical parameter	-	-0,000727273	-
T	°C	Temperature at current point and time	-	Calculated with F.E.M. (if $T \geq 600^\circ\text{C}$ then $T=600^\circ\text{C}$)	-
<p><i>Comments:</i></p> <p>1. The equation for the thermal conductivity of a dry material has been deduced from experimental data of Hiteco Project [21]. Unfortunately tests have been performed in non thermodynamic equilibrium which means that specimens were heated and then kept at reached temperature for a short period, not sufficient to achieve a steady state. As a consequence, concrete didn't lose the whole quantity of water. Anyway, data at 105°C (real presence of dry steady state) and 600°C (non steady state, but high enough to consider a quasi-dry condition) give two points to determine the linear relationship for λ_{dry} (see figure 4-23).</p>					

Table 4-39 Thermal conductivity of dry concrete.

Specific apparent heat C_{ps} (excerpt from [1])					
$C_{ps} = i + q \cdot T$					
Symbol	Units	Meaning	Expansion	Values	Ref.
C_{ps}	J/(Kkg)	Specific heat of the solid skeleton	Previous equation	-	-
i	J/(Kkg)	Empirical parameter	-	940,15	-
q	J/(Kkg°C)	Empirical parameter	-	-0,2586	-
T	°C	Temperature at current point and time	-	Calculated with F.E.M. (if $T \geq 600^\circ\text{C}$ then $T=600^\circ\text{C}$)	-
<p><i>Comments:</i></p> <p>1. Specific heat of solid skeleton has been obtained from an elaboration of experimental data measured by [21].</p>					

Table 4-40. Specific apparent heat.

4.4 DEFINITION OF THE RESULTING COMBINATIONS

The values shown on paragraph 4.3.2, adopted for each of the ranging parameters considered in the spalling nomograms, must be combined with all of the others. The whole set of the ninety one resulting combinations of the parameters' values initially considered is described in table 4-41.

For a better and faster understanding and identification of the values characterizing each combination, the type of notation used to describe each of these ninety one combinations is the following one:

TH**K***RH**PAR*C**, where,

TH** indicates the value of the thickness of the model (in cm) used in the computation
 – Parameter 3 –

K*** indicates the value of the intrinsic permeability (in m²) – Parameter 2 –,

RH** indicates the value of the initial saturation degree (in %) – Parameter 1 –,

PAR* indicates the parametric heating curve taken into account in the computation,
 – Parameter 4 –

C** indicates the material considered in the computation – Parameter 5 –.

Hence, for example, the combination TH12K018RH50PAR1C60 stands for a case characterised by a *thickness*=12 cm, $k=10^{-18}$ m², $S_{init}=50\%$, *Parametric curve*=ISO Curve (Par1) and C60 material.

#	Combination	PC1 (RH) [%]			PC2 (K) [m ²]			PC3 (TH) [cm]			PC4 (Heating curve)			PC5 (Mat)	
		40	50	60	10 ⁻¹⁹	10 ⁻¹⁸	10 ⁻¹⁷	12	24	50	PAR1	PAR2	PAR3	C60	C90
1	TH12K017RH40PAR1C60	X					X	X			X			X	
2	TH12K018RH40PAR1C60	X				X		X			X			X	
3	TH12K019RH40PAR1C60	X			X			X			X			X	
4	TH12K017RH50PAR1C60		X				X	X			X			X	
5	TH12K018RH50PAR1C60		X			X		X			X			X	
6	TH12K019RH50PAR1C60		X		X			X			X			X	
7	TH12K017RH60PAR1C60			X			X	X			X			X	
8	TH12K018RH60PAR1C60			X		X		X			X			X	
9	TH12K019RH60PAR1C60			X	X			X			X			X	
10	TH12K017RH40PAR2C60	X					X	X				X		X	
11	TH12K018RH40PAR2C60	X				X		X				X		X	
12	TH12K019RH40PAR2C60	X			X			X				X		X	
13	TH12K017RH50PAR2C60		X				X	X				X		X	
14	TH12K018RH50PAR2C60		X			X		X				X		X	
15	TH12K019RH50PAR2C60		X		X			X				X		X	
16	TH12K017RH60PAR2C60			X			X	X				X		X	
17	TH12K018RH60PAR2C60			X		X		X				X		X	
18	TH12K019RH60PAR2C60			X	X			X				X		X	
19	TH24K017RH40PAR1C60	X					X		X		X			X	
20	TH24K018RH40PAR1C60	X				X			X		X			X	
21	TH24K019RH40PAR1C60	X			X				X		X			X	
22	TH24K017RH50PAR1C60		X				X		X		X			X	
23	TH24K018RH50PAR1C60		X			X			X		X			X	
24	TH24K019RH50PAR1C60		X		X				X		X			X	
25	TH24K017RH60PAR1C60			X			X		X		X			X	
26	TH24K018RH60PAR1C60			X		X			X		X			X	
27	TH24K019RH60PAR1C60			X	X				X		X			X	
28	TH24K017RH40PAR2C60	X					X		X			X		X	
29	TH24K018RH40PAR2C60	X				X			X			X		X	
30	TH24K019RH40PAR2C60	X			X				X			X		X	
31	TH24K017RH50PAR2C60		X				X		X			X		X	
32	TH24K018RH50PAR2C60		X			X			X			X		X	
33	TH24K019RH50PAR2C60		X		X				X			X		X	
34	TH24K017RH60PAR2C60			X			X		X			X		X	

Table 4-41. Set of combinations analysed for the development of the Spalling Nomograms

<i>(continued)</i>		PC1 (RH) [%]			PC2 (K) [m ²]			PC3 (TH) [cm]			PC4 (Heating curve)			PC5 (Mat)	
#	Combination	40	50	60	10 ⁻¹⁹	10 ⁻¹⁸	10 ⁻¹⁷	12	24	50	PAR1	PAR2	PAR3	C60	C90
35	TH24K018RH60PAR2C60			X		X			X			X		X	
36	TH24K019RH60PAR2C60			X	X				X			X		X	
37	TH12K017RH40PAR1C90	X					X	X			X				X
38	TH12K018RH40PAR1C90	X				X		X			X				X
39	TH12K019RH40PAR1C90	X			X			X			X				X
40	TH12K017RH50PAR1C90		X				X	X			X				X
41	TH12K018RH50PAR1C90		X			X		X			X				X
42	TH12K019RH50PAR1C90		X		X			X			X				X
43	TH12K017RH60PAR1C90			X			X	X			X				X
44	TH12K018RH60PAR1C90			X		X		X			X				X
45	TH12K019RH60PAR1C90			X	X			X			X				X
46	TH12K017RH40PAR2C90	X					X	X				X			X
47	TH12K018RH40PAR2C90	X				X		X				X			X
48	TH12K019RH40PAR2C90	X			X			X				X			X
49	TH12K017RH50PAR2C90		X				X	X				X			X
50	TH12K018RH50PAR2C90		X			X		X				X			X
51	TH12K019RH50PAR2C90		X		X			X				X			X
52	TH12K017RH60PAR2C90			X			X	X				X			X
53	TH12K018RH60PAR2C90			X		X		X				X			X
54	TH12K019RH60PAR2C90			X	X			X				X			X
55	TH24K017RH40PAR1C90	X					X		X		X				X
56	TH24K018RH40PAR1C90	X				X			X		X				X
57	TH24K019RH40PAR1C90	X			X				X		X				X
58	TH24K017RH50PAR1C90		X				X		X		X				X
59	TH24K018RH50PAR1C90		X			X			X		X				X
60	TH24K019RH50PAR1C90		X		X				X		X				X
61	TH24K017RH60PAR1C90			X			X		X		X				X
62	TH24K018RH60PAR1C90			X		X			X		X				X
63	TH24K019RH60PAR1C90			X	X				X		X				X
64	TH24K017RH40PAR2C90	X					X		X			X			X
65	TH24K018RH40PAR2C90	X				X			X			X			X
66	TH24K019RH40PAR2C90	X			X				X			X			X
67	TH24K017RH50PAR2C90		X				X		X			X			X
68	TH24K018RH50PAR2C90		X			X			X			X			X
69	TH24K019RH50PAR2C90		X		X				X			X			X
70	TH24K017RH60PAR2C90			X			X		X			X			X
71	TH24K018RH60PAR2C90			X		X			X			X			X
72	TH24K019RH60PAR2C90			X	X				X			X			X
73	TH50K018RH50PAR1C60		X			X				X	X			X	
74	TH12K017RH40PAR3C60	X					X	X					X	X	
75	TH12K018RH40PAR3C60	X				X		X					X	X	
76	TH12K019RH40PAR3C60	X			X			X					X	X	
77	TH12K017RH50PAR3C60		X				X	X					X	X	
78	TH12K018RH50PAR3C60		X			X		X					X	X	
79	TH12K019RH50PAR3C60		X		X			X					X	X	
80	TH12K017RH60PAR3C60			X			X	X					X	X	
81	TH12K018RH60PAR3C60			X		X		X					X	X	
82	TH12K019RH60PAR3C60			X	X			X					X	X	

Table 4-41. Set of combinations analysed for the development of the Spalling Nomograms (continued)

(continued)

#	Combination	PC1 (RH) [%]			PC2 (K) [m ²]			PC3 (TH) [cm]			PC4 (Heating curve)			PC5 (Mat)	
		40	50	60	10 ⁻¹⁹	10 ⁻¹⁸	10 ⁻¹⁷	12	24	50	PAR1	PAR2	PAR3	C60	C90
83	TH12K017RH40PAR3C90	X					X	X					X		X
84	TH12K018RH40PAR3C90	X				X		X					X		X
85	TH12K019RH40PAR3C90	X			X			X					X		X
86	TH12K017RH50PAR3C90		X				X	X					X		X
87	TH12K018RH50PAR3C90		X			X		X					X		X
88	TH12K019RH50PAR3C90		X		X			X					X		X
89	TH12K017RH60PAR3C90			X			X	X					X		X
90	TH12K018RH60PAR3C90			X		X		X					X		X
91	TH12K019RH60PAR3C90			X	X			X					X		X

Table 4-41. Set of combinations analysed for the development of the Spalling Nomograms (continued)

4.5 RESULTS

4.5.1 Results to evaluate and evaluation procedure

The main results to analyze in the following paragraphs are the following:

Type of Result	Objective of its analysis	Figures numbers
Spalling Index Evolution	1. Evaluate, through a comparative methodology, the spalling risk corresponding to each case and the main features of the expected spalling phenomena (mainly the position of the main fracture in the HSC, the spalling risk evolution with time and the instant corresponding to its maximum value).	4-24 to 4-25 and Appendix 4A
Spalling nomograms and energetic analysis	1. Evaluate the sensitivity of the hygro-thermo-chemo-mechanical processes involved on the High-Strength concretes behaviour under a natural fire to some relevant parameters. 2. Analysis of the energetic viability of spalling and, hence, of the spalling risk and expectable type (either violent and explosive or slow in nature). 3. Discern the energetic contribution of compressed gas to spalling occurrence and what is that corresponding to the constrained elastic energy.	4-26 to 4-38
Comparison for constant values of the Intrinsic Permeability	1. Direct comparison of the cases characterized by the same value of the intrinsic permeability, by means of the comparison of the gas pressure, the vapour pressure and the Total Damage.	4-39 to 4-56
Comparison for constant values of the Initial Saturation Degree	1. Direct comparison of the cases characterized by the same value of the Initial Saturation Degree, by means of the comparison of the gas pressure, the vapour pressure and the Mechanical Damage.	4-57 to 4-74
Comparison of the Vapour Pressure and the Mechanical Damage Distribution	1. Direct comparison of some of the most relevant cases in the space domain, at different time stages, by means of the comparison of vapour pressure and Mechanical Damage.	4-75 to 4-108
Time evolution considerations on a sample case	1. Graphical description of a sample case in the time and space domain, by means of the drawing of the time evolution of several parameters directly involved in the thermal-spalling phenomena.	4-109 to 4-118

Table 4-42. Main results analyzed in the following paragraphs.

4.5.2 Spalling index evolution for each combination

As it has been explained on paragraph 4.2.1, to predict both the time and position of concrete rupture a spalling index developed by [9] and called 'intuitive' or I_{s4} has been selected. This spalling index is obtained choosing factors favouring thermal spalling and factors impeding thermal spalling. Additionally, internal geometrical parameters involved are unknown and are jointly described by a scaling factor, C_s , which is a non-dimensional parameter. Therefore, the spalling index selected herein, I_{s4} , is given by the following relation:

$$I_{s4} = \frac{\overline{\sigma}_{th} \cdot \overline{U} \cdot d}{\overline{f}_t \cdot \overline{G}_f} \cdot \frac{p^g - p_{atm}}{p_{atm}} \cdot L \cdot C_s \quad (4.8)$$

Herein, the meaning of each parameter has been already explained on paragraph 4.2.1. The scaling factor, C_s , has been chosen in such a way that its maximum value corresponding to cases 1 to 73 (heating curves PAR1 or ISO and PAR2 or slow) equals 1,0. The reason for not including cases 74 to 91 (heating curve PAR3 or Hydrocarbon) in the definition of the scaling factor is that the high values obtained for these cases would have made it really difficult to compare the values corresponding to cases 1 to 73 because, once scaled, they would have been very low.

Hence, the value of the scaling factor obtained for the I_{s4} spalling index through such a methodology is 0,00066347, being the maximum value among cases 1 to 73 corresponding to combination #27–TH24K019RH60PAR1C60. In this way, the values of obtained for the analyzed cases range among the following values:

Cases 1 to 73:	Minimum:	0,0079	corresponding to #46–TH12K017RH40PAR2C90,
	Maximum:	1,0000	corresponding to #27–TH24K019RH60PAR1C60,
Cases 74 to 91:	Minimum:	0,3414	corresponding to #83–TH12K017RH40PAR3C90,
	Maximum:	16,2964	corresponding to #82–TH12K019RH60PAR3C60

These scaled values do not determine if spalling is occurring in each case, answer that will be given by means of the energetic analysis described on next paragraphs, but it is useful for comparative purposes.

The complete set of results concerning the value of the I_{s4} spalling index, the time at which it appears and the position of the main fracture are shown on Table 4-45, deduced from the following figures 4-24 and 4-25.

On figures 4-24 and 4-25 are shown the spatial distributions of the values of the I_{s4} spalling index at the instants where the maximum of these values are found for each case. They are organized into two figures: figure 4-24 showing the results obtained from cases featured by C60 material and figure 4-25 showing the results obtained from cases featured by C90. As really different values are shown, each figure includes three levels of detail to easy the comparison.

On Appendix 4A, figures 4A-1 to 4A-91 show the spatial distributions of the I_{s4} spalling index at every 120 seconds and for each of the ninety one cases analyzed, until a total simulation time of 10.800 seconds (3 hours). However, there have been the following exceptions related to the cases where the PAR3 Hydrocarbon heating curve has been considered:

- Cases number 83, 84, 86, 87, 89 and 90 have been run up to a total simulation time of 2.400 seconds (instead of the general simulation time of 10.800 seconds) because the high rate of heating induces a value of the Total Damage at 2.400 seconds of 0,99, which means that the material is completely destroyed, so it is not worthy to carry on simulations beyond this point.
- Cases included on next list have had lack of convergence at certain instants because of the combination of extreme conditions, i.e. high rate of heating joint to the lowest limit

value of intrinsic permeability (10^{-19} m^2), so results are represented up to the converged simulation time, resumed next:

<i>Combination</i>	74	75	76	77	78	79	80	81	82	85	88	91
<i>Final time [s]</i>	1.050	1.020	150	1.065	285	148	1.080	1.080	180	150	150	150

From the analysis of figure 4-24 – C60 material – it can be concluded that for this material the worst case, from the spalling point of view, is clearly #82–TH12K019RH60PAR3C60. This is an expectable result because it combines the lowest value of the intrinsic permeability at ambient temperature, the highest value of the initial saturation degree and the fastest heating profile, so in only 180 seconds the value of the I_{s4} spalling index is really high and really close to the heated surface. Despite this conclusion is not definite since this case has only converged up to 180 seconds, definitive analogous conclusions can be derived for cases 1 to 73, as it will be explained next.

For the same C60 material, if we analyze only the cases not referred to the PAR3-Hydrocarbon heating curves (cases among 1 and 73) – see the maximum detail level at the upper-right corner of figure 4-24 –, we observe that the worst case is #27–TH24K019RH60PAR1C60, again characterized by the lowest value of the intrinsic permeability at ambient temperature, the highest value of the initial saturation degree and the fastest heating profile among PAR1-ISO and PAR2-Slow values, being the position of the main fracture expected farther from the heated surface than if considering the PAR3-Hydrocarbon heating curve. Here we can see that both the value of the intrinsic permeability and the heating profiles have a determinant role in the spalling phenomena since we observe a huge difference on the values corresponding to the lowest value of the intrinsic permeability combined with the fastest heating curve – cases 3, 6 and 9 –, independently of the initial saturation degree, with respect to the rest of the cases. In fact, for these combinations it is observed a really low sensitivity to the initial saturation degree. It can also be observed that faster heating profiles are more unfavourable, from the spalling point of view, than the slower ones.

From the analysis of figure 4-25 – C90 material – again it can be concluded that for this material the worst case, from the spalling point of view, is the case defined by #85–TH12K019RH40PAR3C60. In this case, temperature value at the instant showing the maximum I_{s4} spalling index is higher than those corresponding to higher initial saturation degrees – cases 88 and 91 – as well as the gas pressure, and the mechanical damage (but not the restrained elastic energy). This fact makes that the explosive nature of the expected spalling phenomena is similar energetically, as it will be shown on the energetic analysis of next paragraph, between the cases corresponding to low and high initial saturation degrees. Once more it must be remarked that this conclusions are again partial, since cases 85, 88 and 91 have short in time simulation results available.

For the same C90 material, if we analyze only the cases not referred to the PAR3-Hydrocarbon heating curves (cases among 1 and 73) – see the maximum detail level at the upper-right corner of figure 4-25 –, we observe that the worst case is #45–TH12K019RH60PAR1C90, again characterized by the lowest value of the intrinsic permeability at ambient temperature, the highest value of the initial saturation degree and the fastest heating profile among PAR1-ISO and PAR2-Slow values. Here, the sensitivity of results to the intrinsic permeability and the heating profile is still much higher – but not as much as in the case of C60 material – than the sensitivity to the initial saturation degree.

Comparing the values of the I_{s4} spalling index corresponding to C60 (figure 4-24) and C90 (figure 4-25) materials, it is observed both that in general the position of main fracture is closer to the heated surface in the C90 cases and that the values of the I_{s4} spalling index are lower in this latter cases. This is mainly due to two factors: the much higher gas pressure values in the

#9–TH12K019RH60PAR1C60 than in the #45–TH12K019RH60PAR1C90 ($p_{\text{CASE } 9 \text{ (C60)}}^g = 2,03 \cdot 10^6 \text{ Pa}$ while $p_{\text{CASE } 45 \text{ (C90)}}^g = 1,15 \cdot 10^6 \text{ Pa}$), due to a lower cracking level of C60 case at the instant corresponding to the maximum value of the I_{s4} spalling index ($d_{\text{CASE } 9 \text{ (C60)}} = 0,44$ while $d_{\text{CASE } 45 \text{ (C90)}} = 0,57$), and the lower restrained elastic energy in the #45–TH12K019RH60PAR1C90 ($U_{\text{CASE } 9 \text{ (C60)}} = 562 \text{ J}$ while $U_{\text{CASE } 45 \text{ (C90)}} = 327 \text{ J}$) due in part to the lower distance of the main fracture to the heated surface in the #45–TH12K019RH60PAR1C90 case ($x_{\text{CASE } 9 \text{ (C60)}} = 0,5 \text{ cm}$ while $x_{\text{CASE } 45 \text{ (C90)}} = 0,4 \text{ cm}$) surely due, in the meantime, to the lower porosity of C90 material. To understand, for instance in this particular case, what is the material more prone to experiment spalling, let's show the following evolutions of the total kinetic energy ΔE_k [J], taking into account both the released elastic energy and the work performed by compressed gas during its expansion to the atmospheric pressure, and the mechanical damage d [-] for each of both cases:

#9–TH12K019RH60PAR1C60							$\frac{\Delta E_k [J]}{d [-]}$
t [s]	120	240	360	480	600	720	
x [m]							
0,001	10	1.561	625	625	191	-64	
	0,000	0,006	0,298	0,338	0,402	0,468	
0,002	-177	1.426	1.050	1.093	568	248	
	0,000	0,000	0,299	0,357	0,411	0,473	
0,003	-333	1.205	1.435	1.405	845	495	
	0,000	0,000	0,237	0,372	0,422	0,476	
0,004	-438	980	1.305	1.629	1.189	700	
	0,000	0,000	0,230	0,386	0,433	0,478	
0,005	-495	750	1.180	1.794	1.447	873	
	0,000	0,000	0,224	0,381	0,442	0,479	
0,010	-559	-177	926	1.382	2.198	1.888	
	0,000	0,000	0,172	0,270	0,362	0,510	

#45–TH12K019RH60PAR1C90							$\frac{\Delta E_k [J]}{d [-]}$
t [s]	120	240	360	480	600	720	
x [m]							
0,001	-170	1.457	116	73	-190	-281	
	0,000	0,000	0,425	0,480	0,513	0,550	
0,002	-275	1.299	392	342	20	-85	
	0,000	0,000	0,429	0,503	0,530	0,562	
0,003	-372	1.158	684	518	269	66	
	0,000	0,000	0,312	0,525	0,548	0,573	
0,004	-456	1.021	697	638	457	186	
	0,000	0,000	0,235	0,551	0,565	0,582	
0,005	-514	883	578	725	593	373	
	0,000	0,000	0,205	0,542	0,582	0,594	
0,010	-569	157	562	589	1.023	873	
	0,000	0,000	0,124	0,199	0,317	0,660	

Table 4-43. Time and spatial evolution of the total kinetic energy ΔE_k and the mechanical damage d , for C60 and C90 materials

Remark: In green letters are represented the cases where spalling is not possible either because the total kinetic energy is not positive and/or because the level of cracking is not enough. In orange letters are represented the cases where spalling is energetically possible but the level of cracking may still be insufficient. Finally, in red letters are represented the cases where thermal spalling is energetically possible and the level of cracking is high enough to ensure its viability. Highlighted in yellow colour are the instants and depths corresponding to the time and position where the maximum value of the I_{s4} spalling index has been obtained.

From the comparison of these values it is observed that in the C90 case the total kinetic energy of the spalled pieces is lower than in the C60 case mainly due to the fact that, in the meantime, the mechanical damage (standing for the level of cracking of the material) is higher (especially for the layers closer to the heated surface) so the gas pressure is lower and so it is the contribution to the concrete fracturing of the compressed gas.

These results show that in the C90 case spalling will occur before than in the C60 case (in this particular case until 240 seconds before) but it will be less violent (as it will be shown on next paragraph, the velocity of spalled pieces is estimated to be 14,8 m/s for the C60 case and 9,3 m/s for the C90 case – although both of explosive type –).

A final remark about figures 4-24 and 4-25 is that there are not included the cases corresponding to thicknesses of 24 centimetres and 50 centimetres (cases 19 to 36 and 55 to 73) since their corresponding results are not significantly different than those obtained for a thickness of 12 centimetres, as it will be shown on next paragraph.

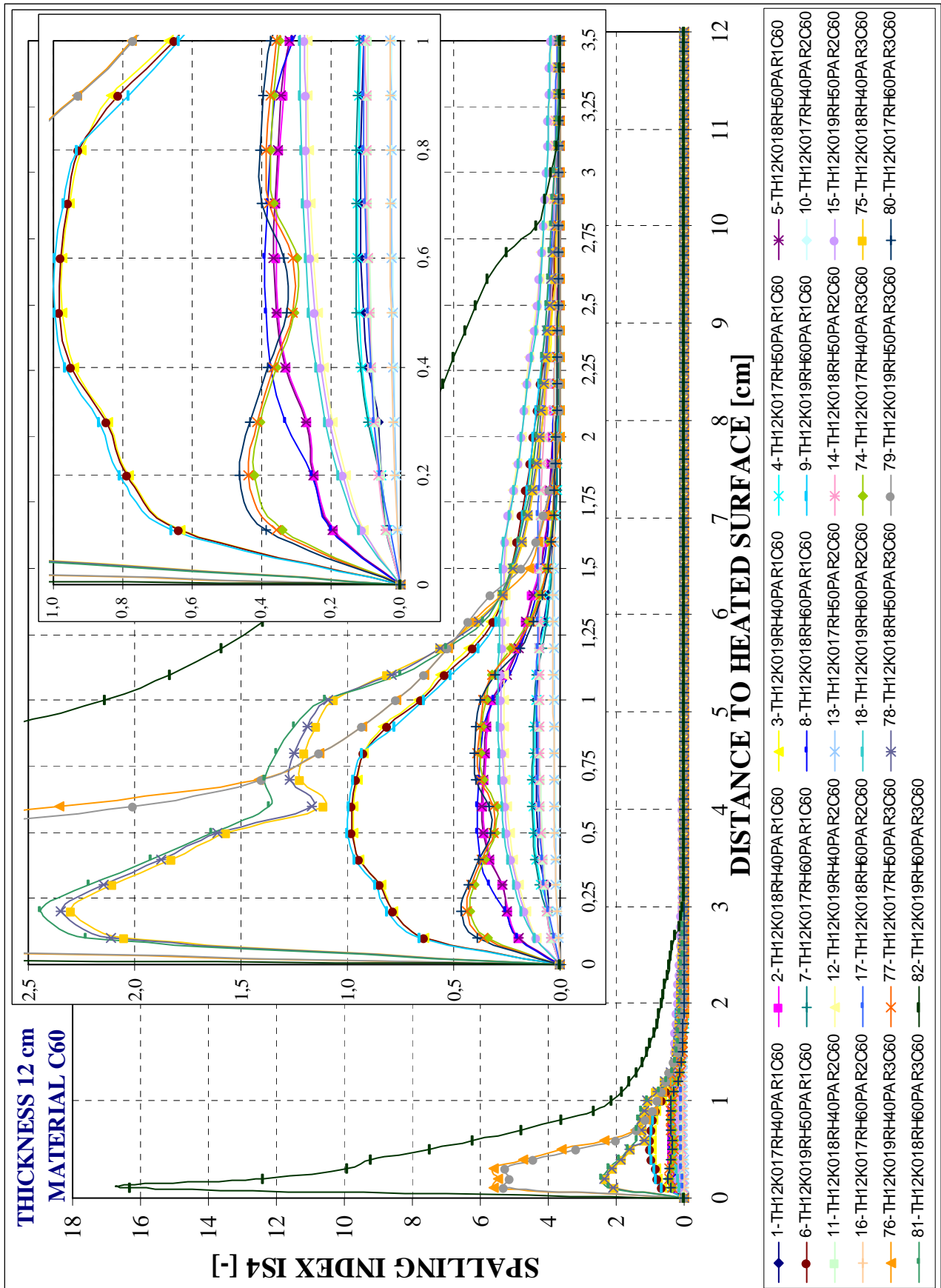


Figure 4-24. Spalling Index IS4 spatial distribution at the instant corresponding to the maximum risk of spalling for each of the combinations corresponding to: Thickness: 12 centimetres, Material C60

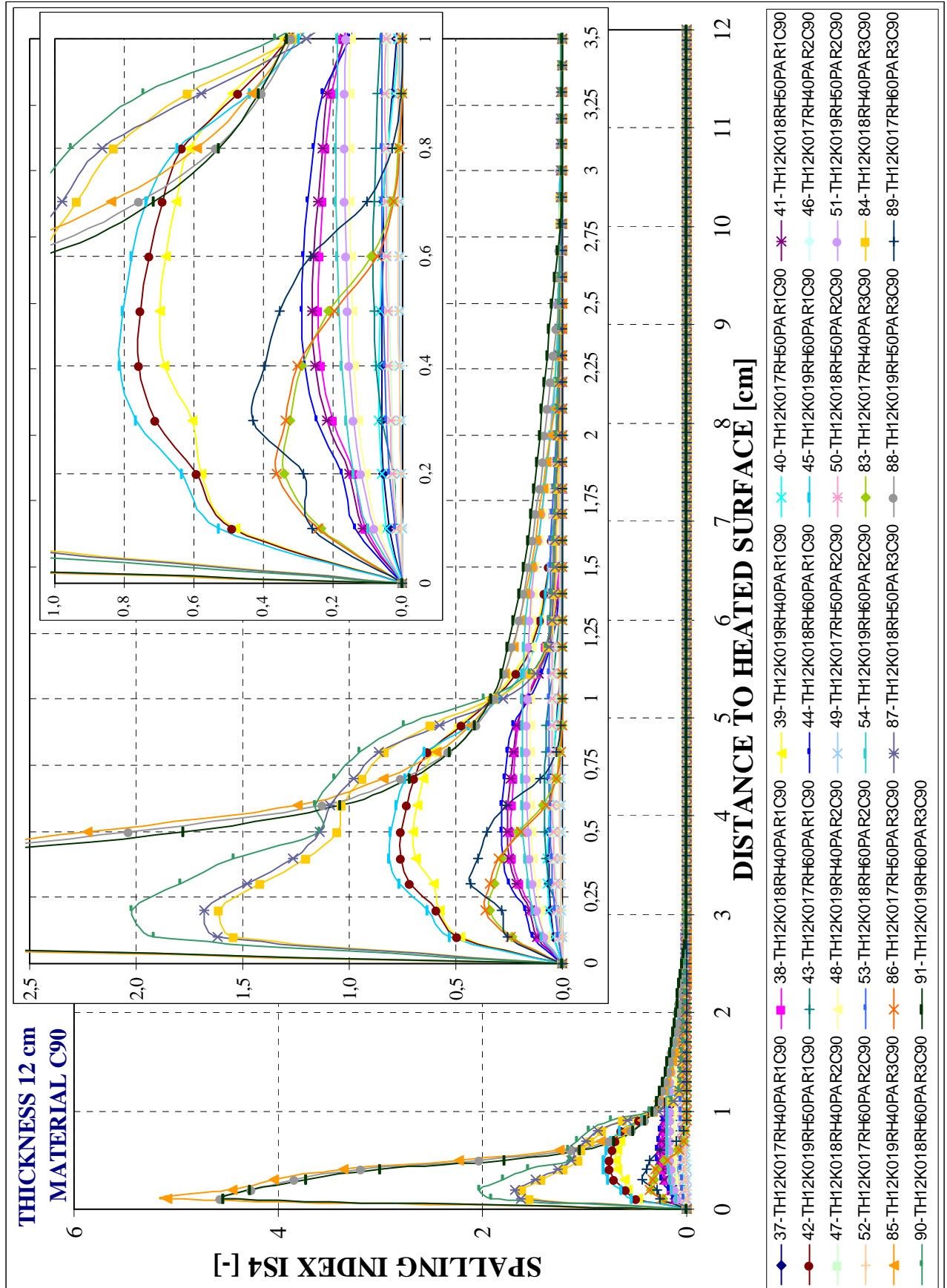


Figure 4-25. Spalling Index IS4 spatial distribution at the instant corresponding to the maximum risk of spalling for each of the combinations corresponding to: Thickness: 12 centimetres, Material C90

4.5.3 Spalling nomograms, Sensitivity and Energetic analysis for each combination

Once determined the time and position of the main fracture, a set of thermal spalling nomograms is developed in this paragraph in order to achieve the following goals:

1. Evaluate the sensitivity of the hygro-thermo-chemo-mechanical processes involved on the High-Strength concretes behaviour under a natural fire to some relevant parameters.
2. Analysis of the energetic viability of spalling and, hence, of the spalling risk and expectable type (either violent and explosive or slow in nature).
3. Discern the energetic contribution of compressed gas to spalling occurrence and what is that corresponding to the constrained elastic energy.

The variables considered for the development of these spalling nomograms have been organized according to the following methodology:

- They are organized as a set of charts in the initial saturation degree – intrinsic permeability domain (Parameter 1 vs. Parameter 2), so it is possible to define some dangerous regions with respect to the spalling occurrence. In this way, nine of the analyzed cases are represented at each chart, featured each by a particular value of the thickness of the structural element (Parameter 3), of the heating profile (Parameter 4) and of the type of material (Parameter 5), resulting the following spalling nomograms:

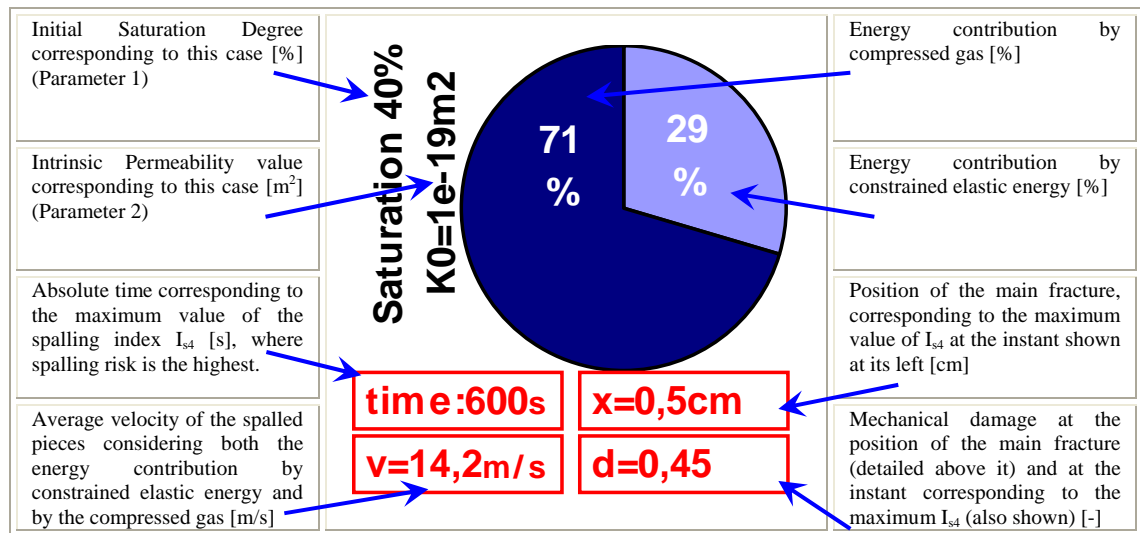
Figure number	Cases numbers shown in each nomogram (at the same position as shown)			Thickness (Parameter 3)	Heat profile (Parameter 4)	Material (Parameter 5)
4-26	3	6	9	12	PAR1 – ISO	C60 (H.S.C.)
	2	5	8			
	1	4	7			
4-27	12	15	18	12	PAR2 – SLOW	C60 (H.S.C.)
	11	14	17			
	10	13	16			
4-28	76	79	82	12	PAR3 – HYD	C60 (H.S.C.)
	75	78	81			
	74	77	80			
4-29	39	42	45	12	PAR1 – ISO	C90 (VHSC)
	38	41	44			
	37	40	43			
4-30	48	51	54	12	PAR2 – SLOW	C90 (VHSC)
	47	50	53			
	46	49	52			
4-31	85	88	91	12	PAR3 – HYD	C90 (VHSC)
	84	87	90			
	83	86	89			
4-32	21	24	27	24	PAR1 – ISO	C60 (H.S.C.)
	20	23	26			
	19	22	25			
4-33	30	33	36	24	PAR2 – SLOW	C60 (H.S.C.)
	29	32	35			
	28	31	34			

Table 4-44. Overall description of the family of nomograms developed.

Figure number	Cases numbers shown in each nomogram (at the same position as shown)			Thickness (Parameter 3)	Heat profile (Parameter 4)	Material (Parameter 5)
4-34	57	60	63	24	PAR1 – ISO	C90 (VHSC)
	56	59	62			
	55	58	61			
Nomogram Name: TH24PAR1C90						
4-35	66	69	72	24	PAR2 – SLOW	C90 (VHSC)
	65	68	71			
	64	67	70			
Nomogram Name: TH24PAR2C90						

Table 4-44 (continued). Overall description of the family of nomograms developed.

- In every spalling nomogram it is represented the value of the I_{s4} spalling index already described, indicating its value for each combination, and coloured in red whenever spalling is energetically possible and in green colour whenever available energy is not enough for the thermal spalling occurrence.
- At the right side of the nomograms it is presented the energetic analysis corresponding to each of the nine cases represented therein. Hence, for each combination of the Initial Saturation Degree versus the Intrinsic Permeability, it is included a graphic where the following considerations may be observed:



Besides the graphical representation of both the thermal spalling nomograms and the results of the energetic analysis, on table 4-45 are described the complete set of results corresponding to both analyses. In that table appear several parameters whose meanings are explained next and in Table 4-1:

I_{s4}	is the spalling index selected for this thesis and already described,
X_{IS4max}	is the position [cm] corresponding to the maximum value of I_{s4} ,
t_{IS4max}	is the absolute time [s] corresponding to the maximum value of I_{s4} ,
$P_{g,max,abs}$	is the maximum value of the gas pressure [Pa] achieved at any position and time,
$P_{g,Xis4,tis4}$	is the gas pressure value [Pa] achieved at the X_{IS4max} position at the t_{IS4max} instant,
$T_{Xis4,tis4}$	is the temperature [K] at the X_{IS4max} position at the t_{IS4max} instant,
ΔU	is the elastic strain energy [J] (area under the graph of elastic energy between $x=0$ and $x= X_{IS4max}$ at the instant t_{IS4max} ,
E_{k0}	is the energy contributed to spalling by elastic strain energy [J] (ΔU – Energy consumed for fracturing ΔE_{fr} assuming that the average piece of spalled concrete has dimensions $X_{IS4max} \cdot X_{IS4max} \cdot X_{IS4max}$),
W	is the work performed by gas [J] to expand adiabatically from $P_{g,Xis4,tis4}$ to the atmospheric pressure,

ΔE_k is the sum of E_{k0} and W [J] (when it is negative spalling is not energetically possible),
 v is the average velocity of spalled pieces considering both the energy contribution by the elastic strain energy and by the compressed gas [m/s] (it appears as a zero value when ΔE_k is negative and spalling is not possible; it appears in red letters whenever ΔE_k and thermal spalling is energetically possible),
 $d_{t_{IS4max}, X_{IS4max}}$ is the mechanical damage at the X_{IS4max} position at the t_{IS4max} instant.

#	Combination	$IS4_{max}$ [-]	X_{IS4max} [cm]	t_{IS4max} [s]	$P_{g,max,abs}$ [Pa]	$P_{g,XIS4,tIS4}$ [Pa]	$T_{XIS4,tIS4}$ [K]	ΔU [J]	E_{k0} [J]	W [J]	ΔE_k [J]	v [m/s]	$d_{t_{IS4max}, X_{IS4max}}$ [-]
1	TH12K017RH40PAR1C60	0,1144	0,7	600	615580	400689	555	747	144	164	309	5,8	0,40
2	TH12K018RH40PAR1C60	0,3588	0,6	600	1284320	910375	576	672	70	537	606	8,8	0,41
3	TH12K019RH40PAR1C60	0,9748	0,5	600	2627450	1897770	599	569	-33	1364	1330	14,2	0,45
4	TH12K017RH50PAR1C60	0,1230	0,6	600	624901	407813	570	676	73	169	242	5,5	0,38
5	TH12K018RH50PAR1C60	0,3653	0,6	600	1310120	944196	574	667	65	563	628	8,9	0,41
6	TH12K019RH50PAR1C60	0,9810	0,5	600	2641720	1942880	596	565	-37	1403	1366	14,4	0,45
7	TH12K017RH60PAR1C60	0,1293	0,6	600	652052	442558	566	674	71	192	264	5,8	0,37
8	TH12K018RH60PAR1C60	0,3903	0,6	600	1393860	1039510	570	665	62	639	701	9,4	0,40
9	TH12K019RH60PAR1C60	0,9973	0,5	600	2735450	2037830	594	562	-40	1487	1447	14,8	0,44
10	TH12K017RH40PAR2C60	0,0262	1,2	3360	342357	239716	536	730	125	66	191	3,5	0,52
11	TH12K018RH40PAR2C60	0,0954	1,0	3360	786846	547331	553	642	38	265	303	4,8	0,53
12	TH12K019RH40PAR2C60	0,2669	1,0	3480	1647170	1203440	566	647	43	772	815	7,9	0,57
13	TH12K017RH50PAR2C60	0,0283	1,2	3360	366671	252032	534	732	127	73	200	3,6	0,52
14	TH12K018RH50PAR2C60	0,1002	1,0	3360	827567	573889	551	643	39	283	322	5,0	0,52
15	TH12K019RH50PAR2C60	0,2752	1,0	3480	1700650	1246700	564	646	42	808	850	8,0	0,56
16	TH12K017RH60PAR2C60	0,0318	1,2	3360	404745	274049	530	742	137	86	223	3,8	0,50
17	TH12K018RH60PAR2C60	0,1079	1,1	3480	890978	602930	551	731	126	304	431	5,5	0,52
18	TH12K019RH60PAR2C60	0,2897	1,0	3480	1791080	1325960	561	651	47	874	920	8,4	0,56
19	TH24K017RH40PAR1C60	0,1144	0,7	600	615582	400681	555	747	144	164	309	5,8	0,40
20	TH24K018RH40PAR1C60	0,3583	0,6	600	1288180	908284	576	673	70	535	605	8,8	0,41
21	TH24K019RH40PAR1C60	0,9746	0,5	600	2627310	1897000	598	569	-33	1363	1330	14,2	0,45
22	TH24K017RH50PAR1C60	0,1229	0,7	600	624418	431740	552	741	138	185	323	5,9	0,39
23	TH24K018RH50PAR1C60	0,3653	0,6	600	1310490	944017	574	667	65	563	628	8,9	0,41
24	TH24K019RH50PAR1C60	0,9802	0,5	600	2641730	1940550	596	565	-37	1401	1364	14,4	0,45
25	TH24K017RH60PAR1C60	0,1293	0,6	600	652062	442590	566	674	71	192	264	5,8	0,37
26	TH24K018RH60PAR1C60	0,3901	0,6	600	1393900	1039250	570	665	62	639	701	9,4	0,40
27	TH24K019RH60PAR1C60	1,0000	0,5	600	2736820	2042240	594	561	-41	1491	1450	14,9	0,44
28	TH24K017RH40PAR2C60	0,0271	1,3	3360	346482	245908	529	771	166	69	236	3,7	0,53
29	TH24K018RH40PAR2C60	0,0986	1,0	3360	797911	550058	553	644	40	266	306	4,8	0,54
30	TH24K019RH40PAR2C60	0,2744	1,0	3480	1664310	1205430	566	646	42	774	816	7,9	0,58
31	TH24K017RH50PAR2C60	0,0292	1,2	3360	370953	252876	534	734	130	73	203	3,6	0,53
32	TH24K018RH50PAR2C60	0,1036	1,0	3360	836964	576862	551	644	40	286	326	5,0	0,53
33	TH24K019RH50PAR2C60	0,2831	1,0	3480	1716440	1249160	564	646	42	810	852	8,1	0,58
34	TH24K017RH60PAR2C60	0,0328	1,2	3360	408598	274876	530	745	140	86	226	3,8	0,51
35	TH24K018RH60PAR2C60	0,1116	1,1	3480	900374	605182	551	732	128	306	434	5,5	0,53
36	TH24K019RH60PAR2C60	0,2992	1,0	3480	1806440	1331220	561	650	46	878	924	8,4	0,57
37	TH12K017RH40PAR1C90	0,0608	0,4	480	517085	231971	544	242	-360	62	-298	0,0	0,53
38	TH12K018RH40PAR1C90	0,2424	0,5	600	1043220	448425	583	384	-218	196	-22	0,0	0,57
39	TH12K019RH40PAR1C90	0,6983	0,5	600	2428360	1063780	584	370	-232	659	427	8,1	0,60
40	TH12K017RH50PAR1C90	0,0663	0,4	480	521201	247622	539	241	-360	70	-290	0,0	0,52
41	TH12K018RH50PAR1C90	0,2578	0,5	600	1083000	476109	580	386	-216	215	-1	0,0	0,56
42	TH12K019RH50PAR1C90	0,7594	0,4	600	2522630	1056570	606	321	-281	653	372	8,4	0,58
43	TH12K017RH60PAR1C90	0,0831	0,6	600	506429	243962	548	445	-158	68	-89	0,0	0,53

Table 4-45. Main results obtained from the Spalling risk analysis and from the energetic analysis for each of the ninety one combinations calculated.

(continued)

#	Combination	IS4max [-]	XIS4max [cm]	tIS4max [s]	Pg,max,abs [Pa]	Pg,XIS4,tIS4 [Pa]	TXIS4,tIS4 [K]	DU [J]	Ek0 [J]	W [J]	DEk [J]	v [m/s]	dtIS4max,XIS4m ax [-]
44	TH12K018RH60PAR1C90	0,2882	0,5	600	1192500	532995	575	396	-206	254	49	2,7	0,54
45	TH12K019RH60PAR1C90	0,8125	0,4	600	2623520	1153280	602	327	-275	731	457	9,3	0,57
46	TH12K017RH40PAR2C90	0,0079	1,1	3240	286742	142054	522	362	-243	16	-226	0,0	0,70
47	TH12K018RH40PAR2C90	0,0437	0,9	3360	602455	283416	552	341	-263	91	-172	0,0	0,70
48	TH12K019RH40PAR2C90	0,1533	0,8	3360	1225280	680625	562	311	-292	361	69	2,6	0,71
49	TH12K017RH50PAR2C90	0,0095	1,2	3360	320135	148067	521	413	-192	19	-173	0,0	0,70
50	TH12K018RH50PAR2C90	0,0490	0,9	3360	618959	301060	549	349	-254	102	-153	0,0	0,69
51	TH12K019RH50PAR2C90	0,1654	0,8	3360	1260140	719491	560	316	-287	390	103	3,1	0,70
52	TH12K017RH60PAR2C90	0,0133	1,1	3360	411763	160547	526	421	-184	25	-159	0,0	0,67
53	TH12K018RH60PAR2C90	0,0603	0,9	3360	736636	336945	547	371	-233	124	-109	0,0	0,66
54	TH12K019RH60PAR2C90	0,1902	0,7	3360	1341740	760556	567	301	-302	421	119	3,6	0,68
55	TH24K017RH40PAR1C90	0,0608	0,4	480	517216	231971	544	242	-360	62	-298	0,0	0,53
56	TH24K018RH40PAR1C90	0,2420	0,5	600	1042880	448164	583	384	-218	196	-23	0,0	0,57
57	TH24K019RH40PAR1C90	0,6911	0,5	600	2428690	1054200	584	371	-231	651	420	8,0	0,60
58	TH24K017RH50PAR1C90	0,0663	0,4	480	521028	247650	539	241	-360	70	-290	0,0	0,52
59	TH24K018RH50PAR1C90	0,2578	0,5	600	1083360	476171	580	386	-216	215	-1	0,0	0,56
60	TH24K019RH50PAR1C90	0,7584	0,4	600	2522780	1055670	606	321	-281	652	371	8,4	0,58
61	TH24K017RH60PAR1C90	0,0829	0,6	600	506343	243671	548	444	-158	68	-90	0,0	0,54
62	TH24K018RH60PAR1C90	0,2882	0,5	600	1189860	532942	575	396	-206	254	49	2,7	0,54
63	TH24K019RH60PAR1C90	0,8131	0,4	600	2623270	1154030	602	327	-275	732	457	9,3	0,57
64	TH24K017RH40PAR2C90	0,0082	1,1	3240	286949	142707	522	366	-239	17	-222	0,0	0,70
65	TH24K018RH40PAR2C90	0,0459	0,9	3360	602932	286473	552	345	-258	93	-165	0,0	0,70
66	TH24K019RH40PAR2C90	0,1603	0,8	3360	1226130	688425	562	315	-288	367	79	2,7	0,71
67	TH24K017RH50PAR2C90	0,0099	1,2	3360	320236	148751	521	418	-187	19	-167	0,0	0,70
68	TH24K018RH50PAR2C90	0,0513	0,9	3360	619464	304067	550	354	-250	103	-146	0,0	0,69
69	TH24K019RH50PAR2C90	0,1729	0,8	3360	1261240	727546	560	320	-283	396	113	3,3	0,70
70	TH24K017RH60PAR2C90	0,0140	1,1	3360	411848	162090	526	425	-180	26	-154	0,0	0,67
71	TH24K018RH60PAR2C90	0,0626	0,9	3360	736652	339746	547	375	-229	125	-103	0,0	0,67
72	TH24K019RH60PAR2C90	0,1980	0,7	3360	1341750	768021	567	304	-299	427	128	3,7	0,68
73	TH50K018RH50PAR1C60	0,3654	0,6	600	1310490	944223	574	667	65	563	628	8,9	0,41
74	TH12K017RH40PAR3C60	0,4231	0,2	240	1187060	220545	828	713	113	55	168	8,0	0,33
75	TH12K018RH40PAR3C60	2,3004	0,2	240	2672970	643907	833	680	80	334	414	12,5	0,37
76	TH12K019RH40PAR3C60	5,6010	0,1	150	4761910	3328220	725	219	-382	2665	2283	41,7	0,33
77	TH12K017RH50PAR3C60	0,4365	0,2	240	1197220	227865	825	713	112	59	172	8,1	0,32
78	TH12K018RH50PAR3C60	2,3503	0,2	240	2715320	664573	831	679	78	349	428	12,8	0,37
79	TH12K019RH50PAR3C60	5,2916	0,1	148	4903010	3391090	718	213	-387	2724	2337	42,2	0,33
80	TH12K017RH60PAR3C60	0,4624	0,2	240	1191880	243906	820	717	116	68	184	8,4	0,31
81	TH12K018RH60PAR3C60	2,4441	0,2	240	2717250	707048	828	680	79	381	460	13,2	0,36
82	TH12K019RH60PAR3C60	16,2964	0,1	180	5692340	4448860	781	193	-407	3730	3323	50,3	0,57
83	TH12K017RH40PAR3C90	0,3414	0,2	135	923231	407847	614	244	-357	169	-188	0,0	0,38
84	TH12K018RH40PAR3C90	1,6091	0,2	225	2096000	407756	795	473	-128	169	41	3,9	0,44
85	TH12K019RH40PAR3C90	5,0857	0,1	150	4458350	2142750	719	145	-455	1580	1125	29,3	0,50
86	TH12K017RH50PAR3C90	0,3630	0,2	135	956361	449162	608	241	-360	197	-163	0,0	0,37
87	TH12K018RH50PAR3C90	1,6803	0,2	225	2051550	432855	791	477	-124	186	62	4,8	0,43
88	TH12K019RH50PAR3C90	4,5656	0,1	150	4582870	2009560	716	148	-453	1462	1009	27,7	0,48
89	TH12K017RH60PAR3C90	0,4278	0,3	165	1000040	414813	610	420	-181	174	-7	0,0	0,40
90	TH12K018RH60PAR3C90	2,0232	0,2	240	2091430	460414	809	516	-85	204	119	6,7	0,42
91	TH12K019RH60PAR3C90	4,5297	0,1	150	4826320	2130450	711	149	-452	1569	1118	29,2	0,46

Table 4-45 (continued). Main results obtained from the Spalling risk analysis and from the energetic analysis for each of the ninety one combinations calculated.

Remark: In red letters are highlighted the cases where thermal spalling is energetically possible (velocity of spalled pieces higher than zero) and the level of cracking is high enough to ensure its viability.

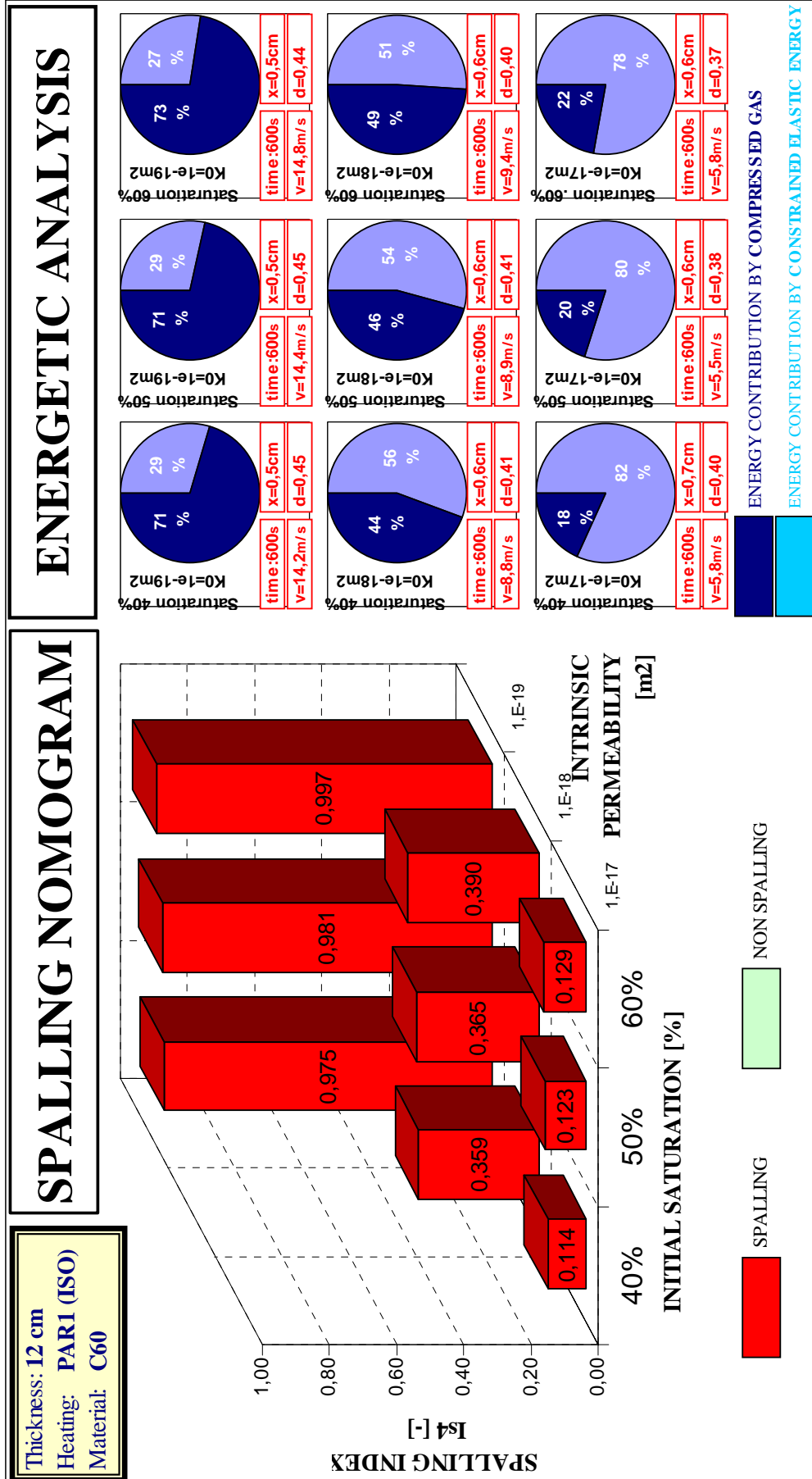


Figure 4-26. Spalling Nomogram and resume of the Energetic Analysis corresponding to:
 Thickness: 12 centimetres, Material: C60 Heating curve: PARI (ISO 834 heating curve)

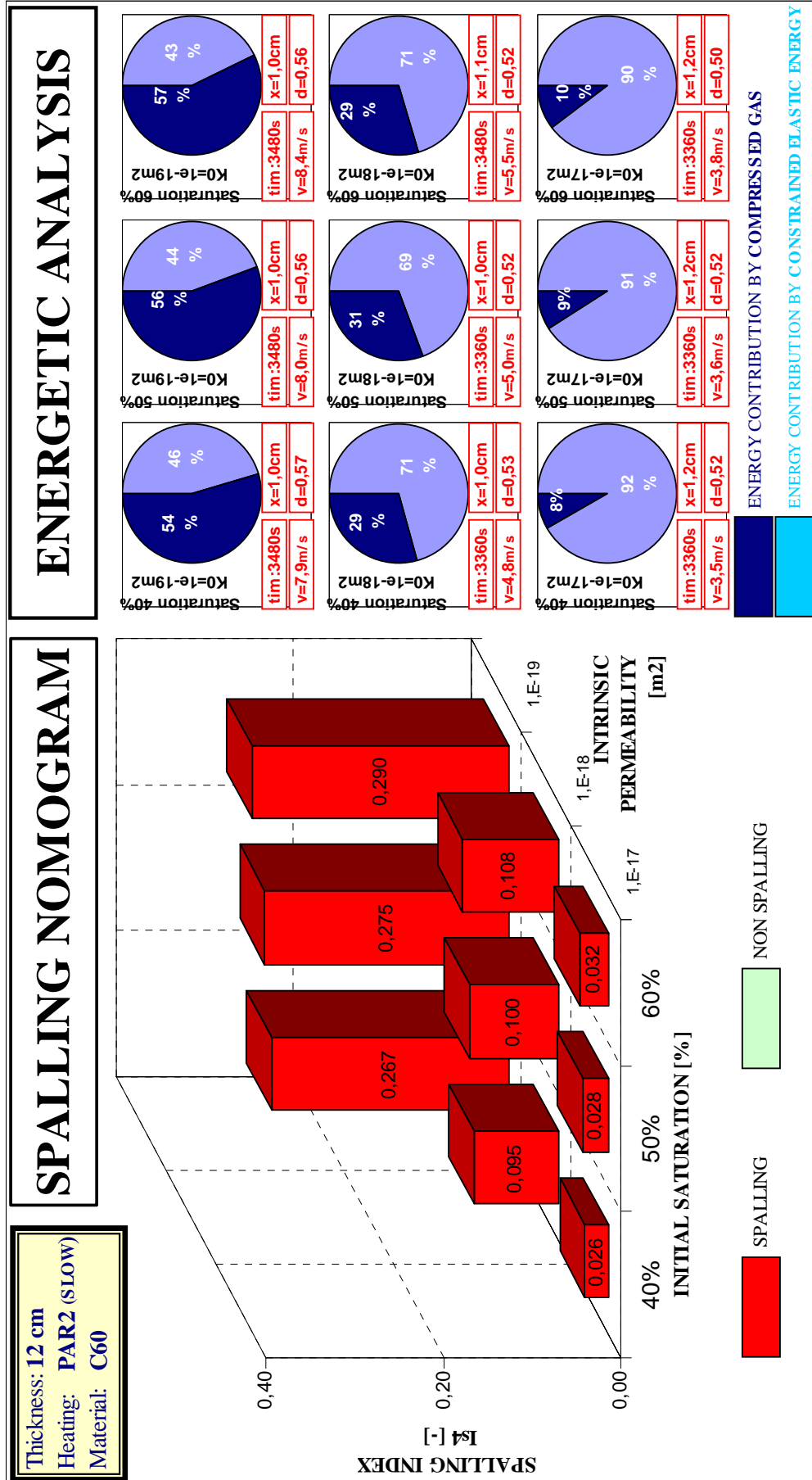


Figure 4-27. Spalling Nomogram and resume of the Energetic Analysis corresponding to:
 Heating curve: PAR2 (SLOW parametric heating curve)
 Thickness: 12 centimetres, Material: C60

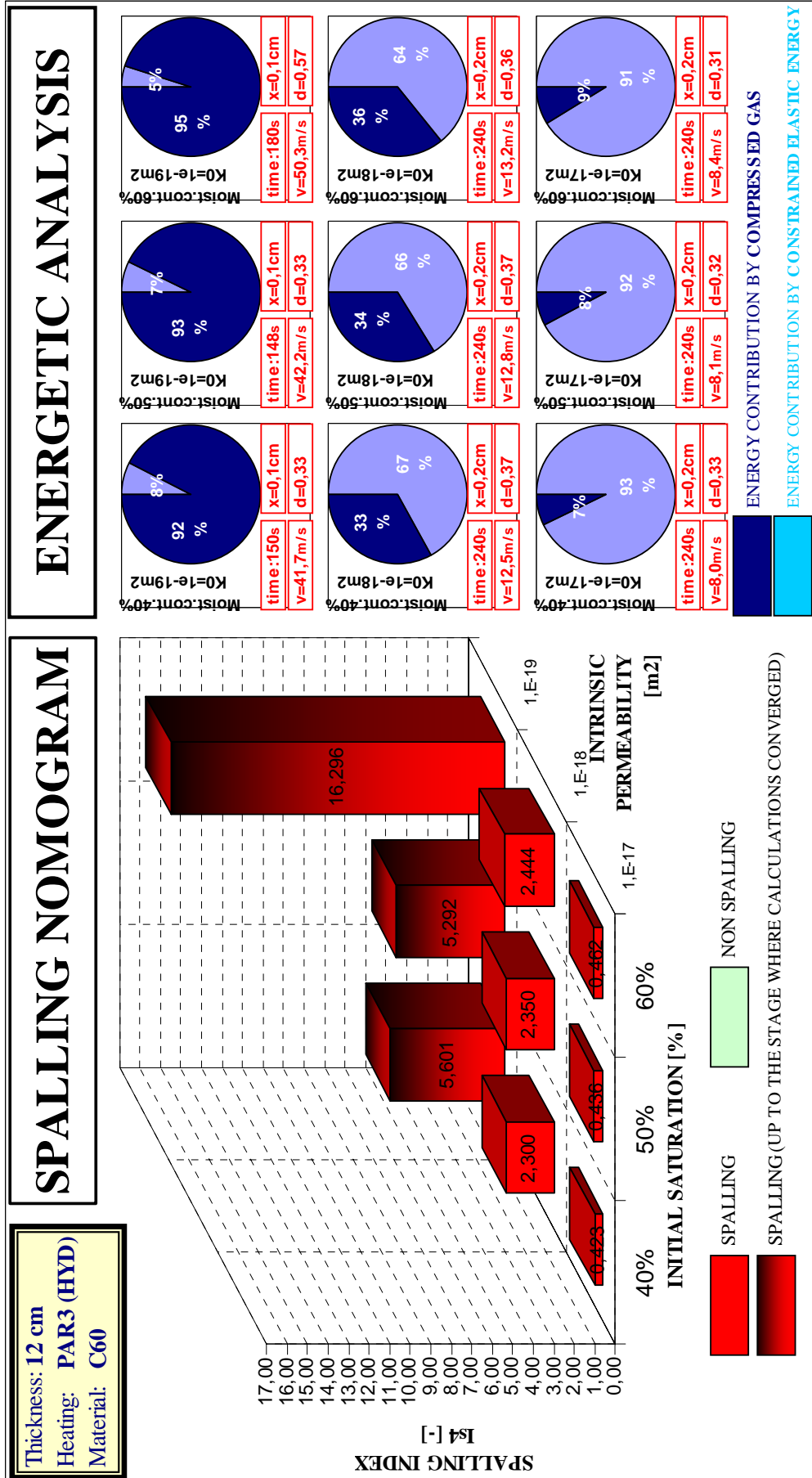


Figure 4-28. Spalling Nomogram and resume of the Energetic Analysis corresponding to:
Thickness: 12 centimetres, Material: C60 Heating curve: PAR3 (HYDROCARBON heating curve)

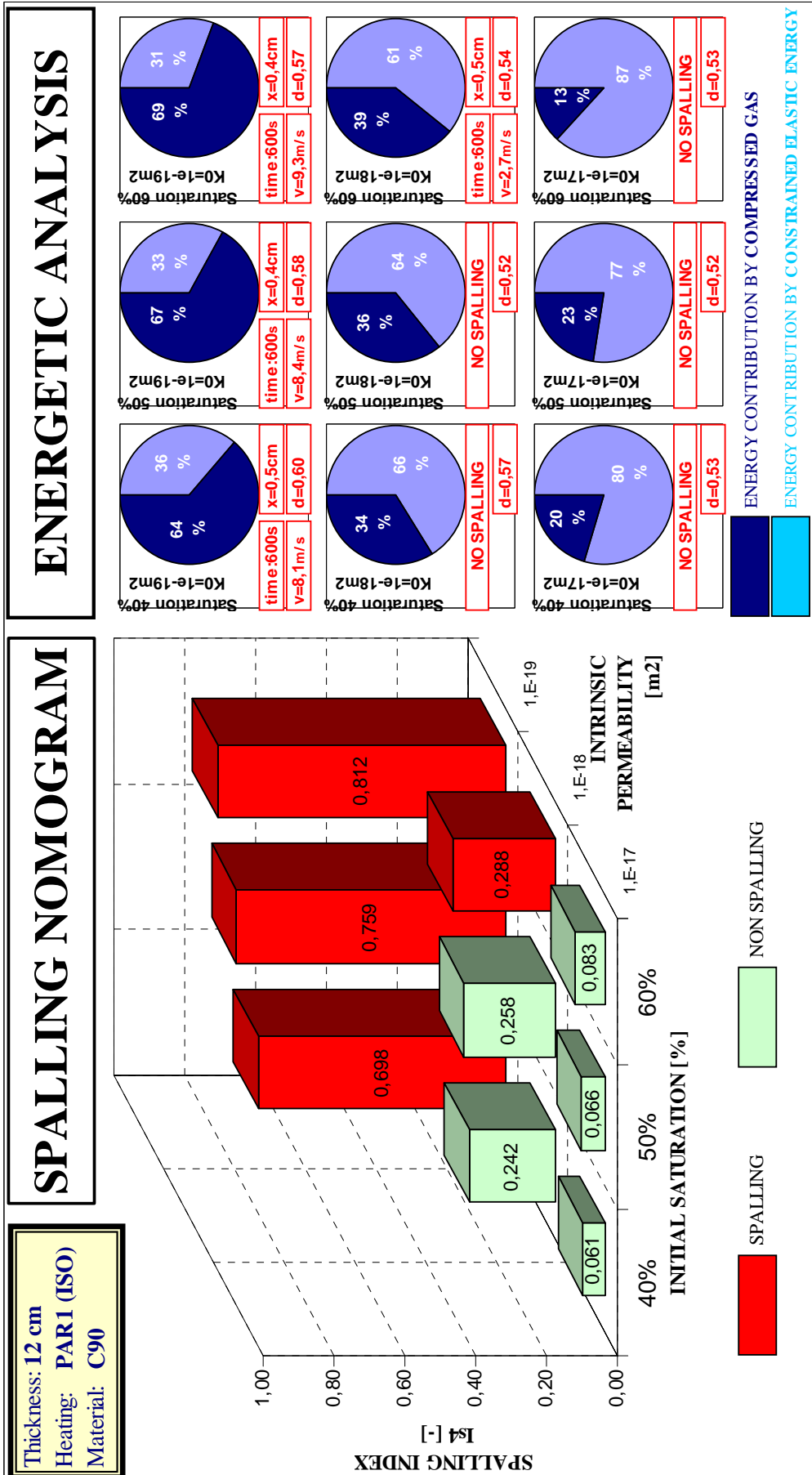


Figure 4-29 Spalling Nomogram and resume of the Energetic Analysis corresponding to:
 Thickness: 12 centimetres, Material: C60 Heating curve: PARI (ISO834 heating curve)

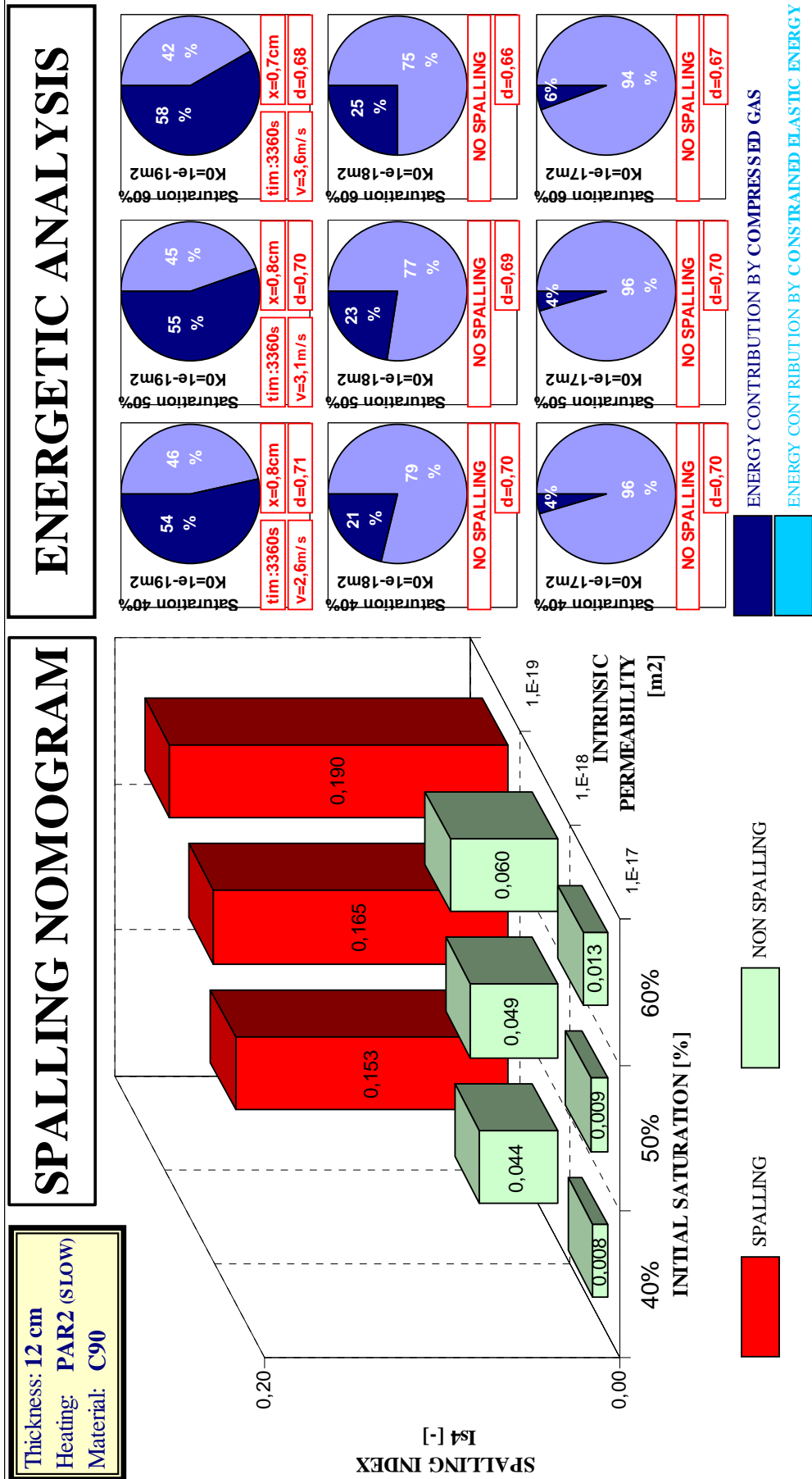


Figure 4-30. Spalling Nomogram and resume of the Energetic Analysis corresponding to:
 Thickness: 12 centimetres, Material: C90 Heating curve: PAR2 (SLOW Parametric heating curve)

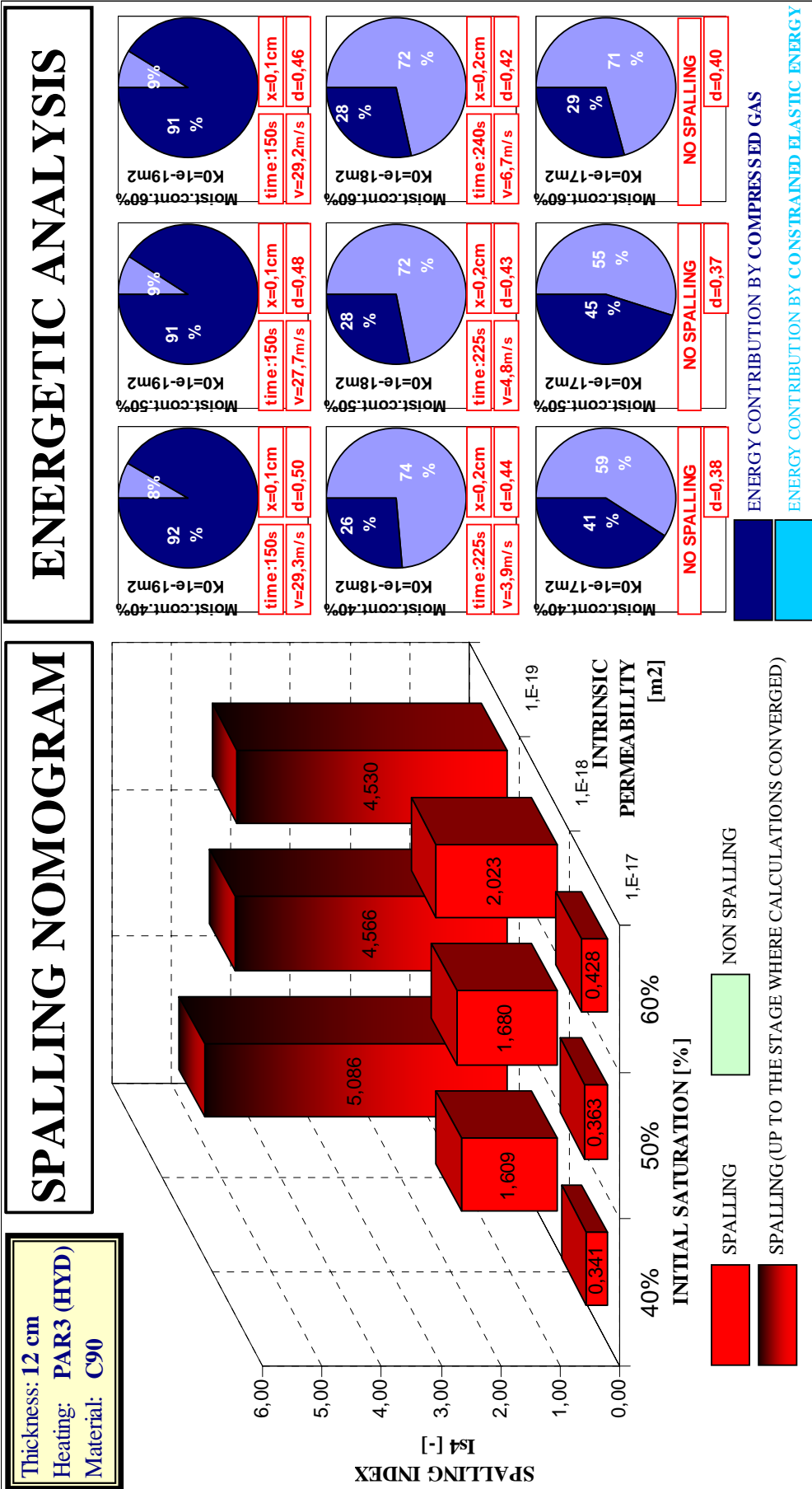


Figure 4-31. Spalling Nomogram and resume of the Energetic Analysis corresponding to:
 Thickness: 12 centimetres, Material: C90 Heating curve: PAR3 (HYDROCARBON heating curve)

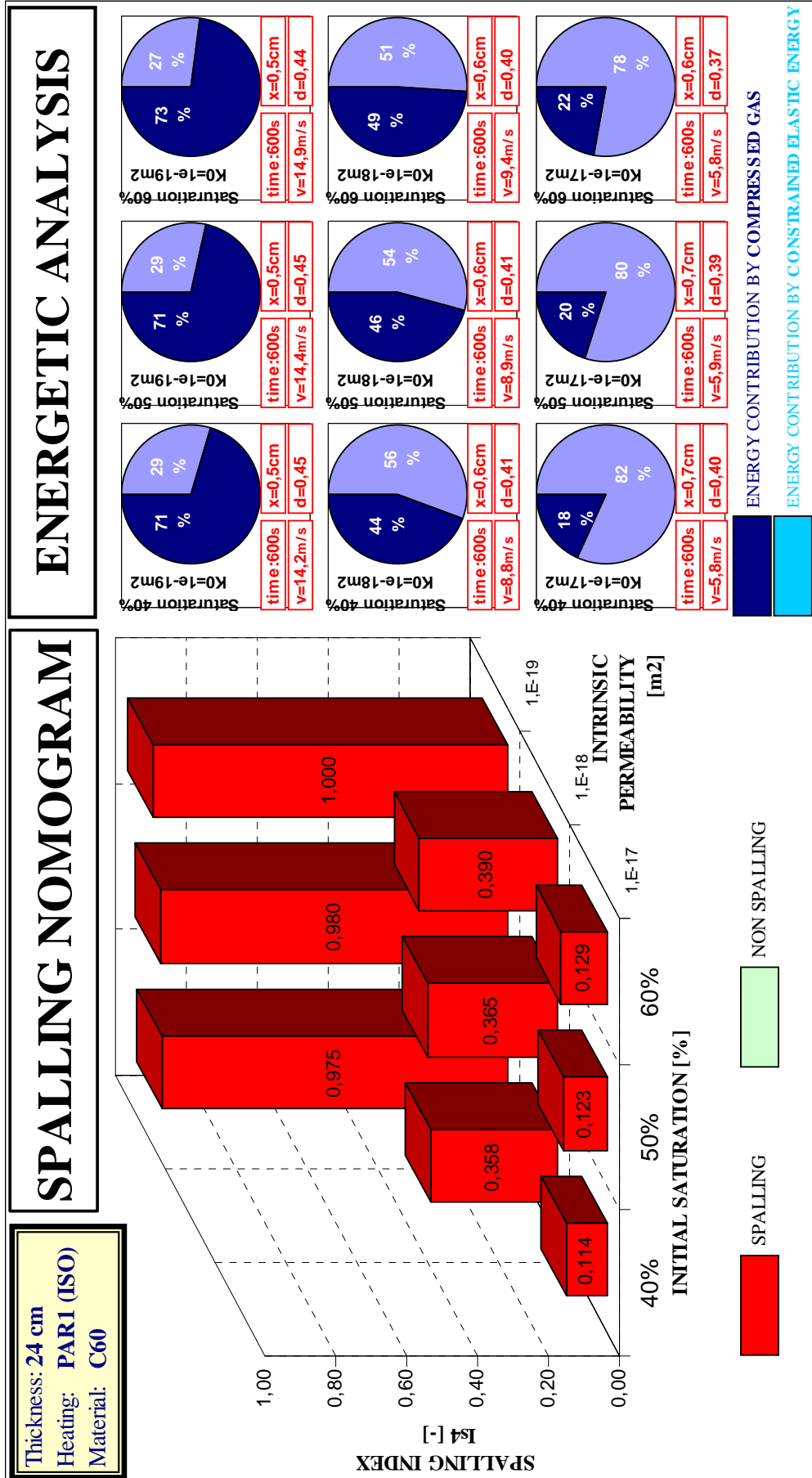


Figure 4-32. Spalling Nomogram and resume of the Energetic Analysis corresponding to:
Thickness: 24 centimetres, Material: C60 Heating curve: PARI (ISO 834 heating curve)

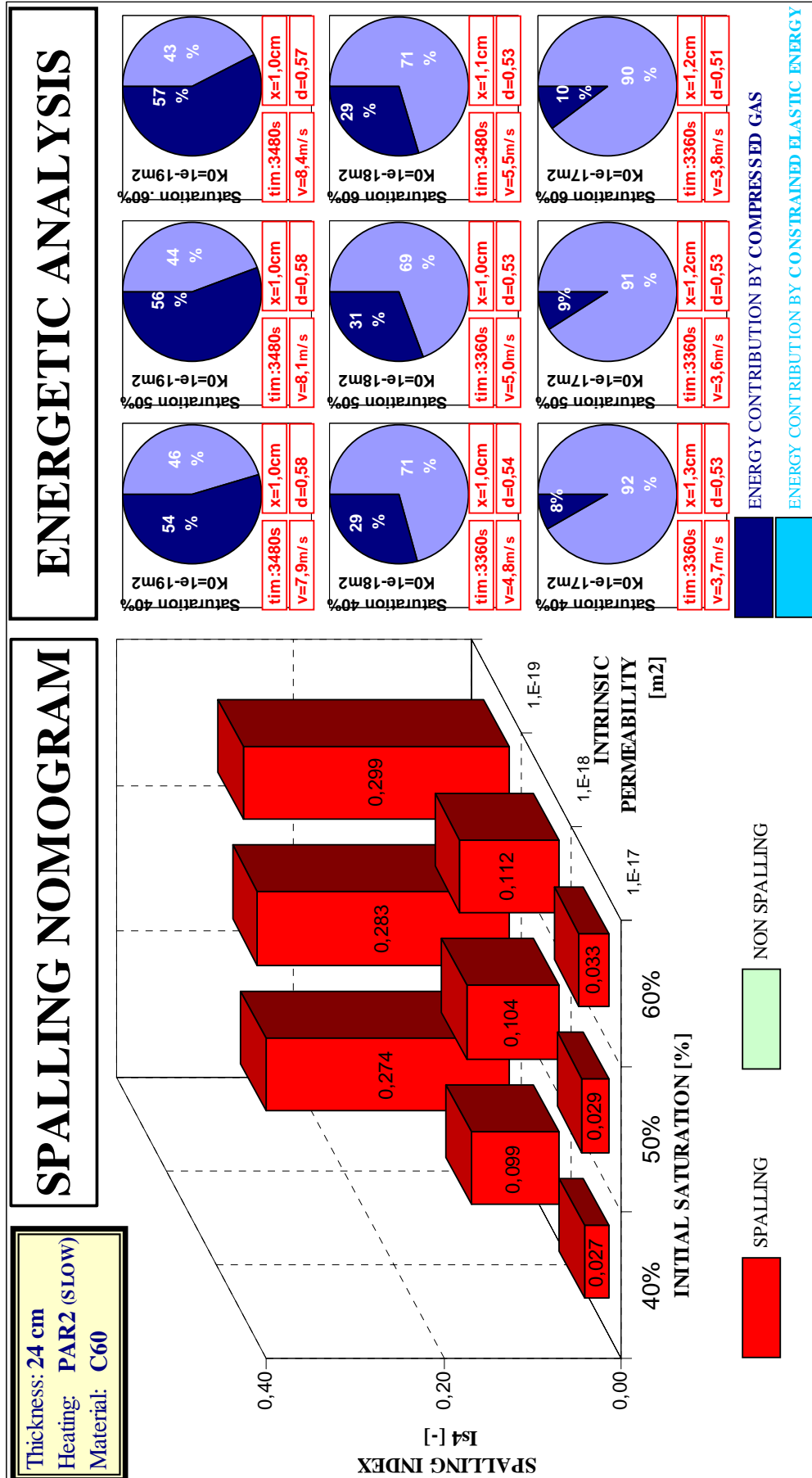


Figure 4-33. Spalling Nomogram and resume of the Energetic Analysis corresponding to:
 Thickness: 24 centimetres, Material: C60 Heating curve: PAR2 (SLOW parametric heating curve)

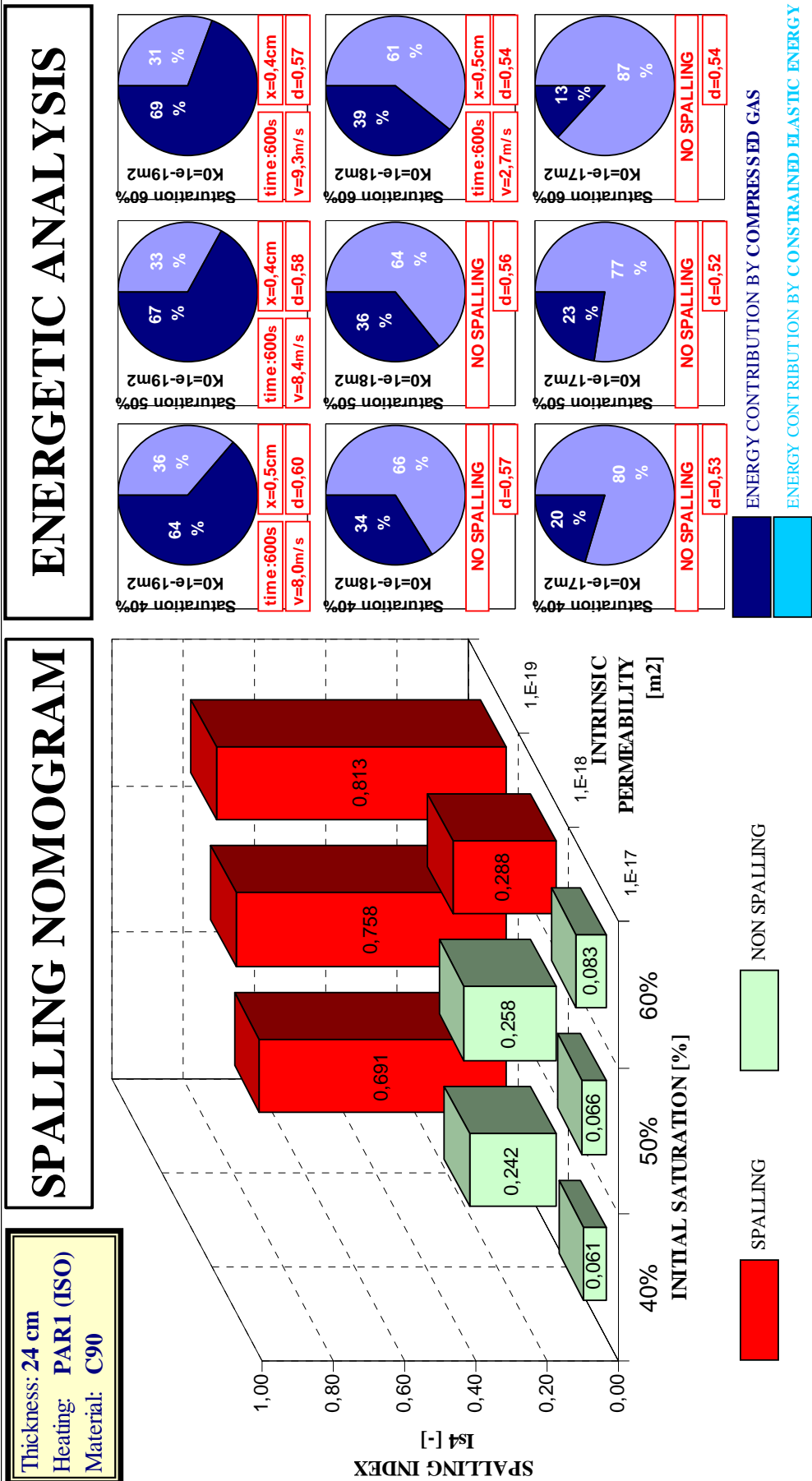


Figure 4-34. Spalling Nomogram and resume of the Energetic Analysis corresponding to:
Thickness: 24 centimetres, Material: C90 Heating curve: PARI (ISO 834 heating curve)

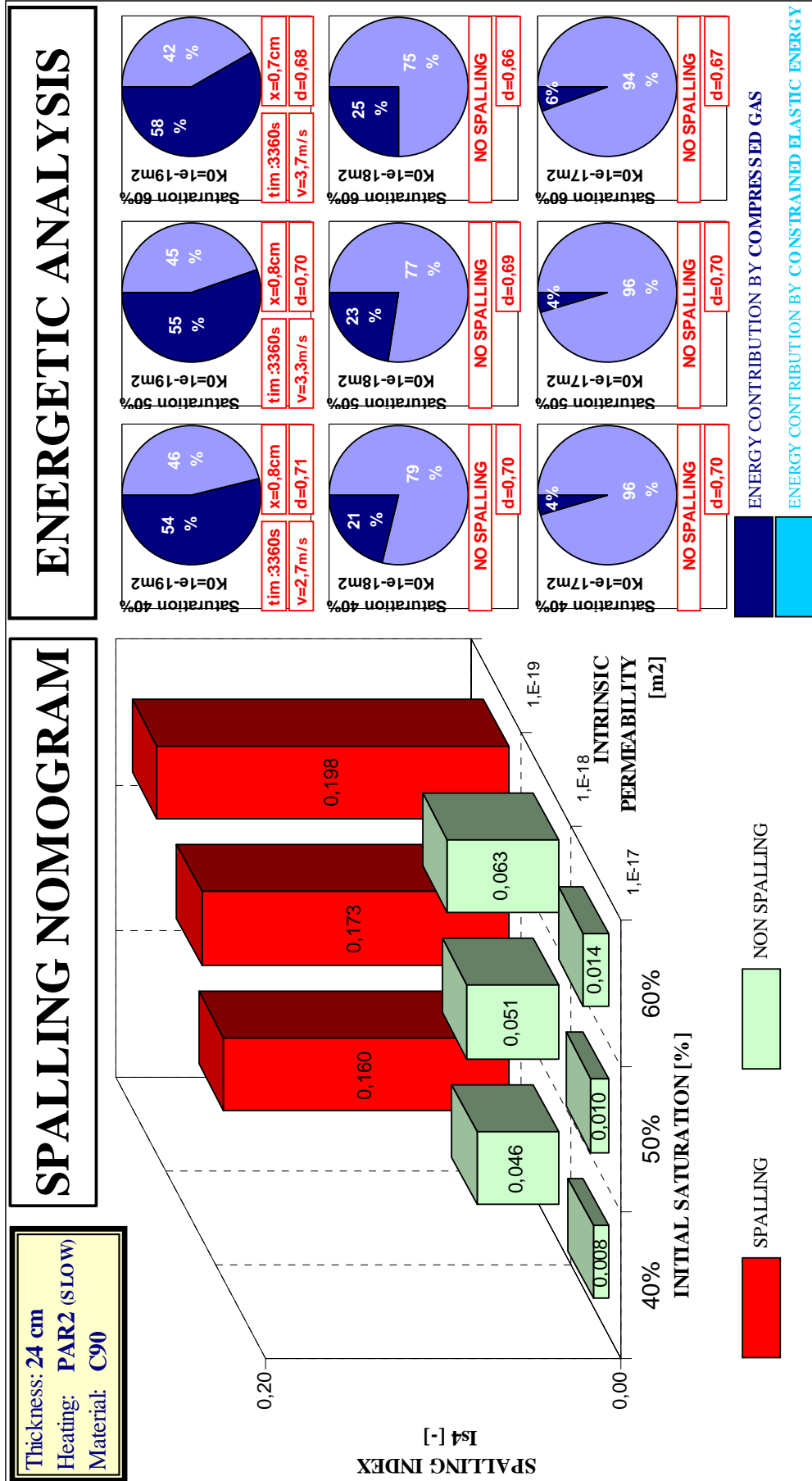


Figure 4-35. Spalling Nomogram and resume of the Energetic Analysis corresponding to:
Heating curve: PAR2 (SLOW parametric heating curve)
Thickness: 24 centimetres, Material: C90

4.5.3.1 NOMOGRAM TH12PAR1C60: THICKNESS 12 CM, ISO CURVE, MATERIAL C60

Figure number	Cases numbers shown in each nomogram (at the same position as shown)			Thickness (Parameter 3)	Heat profile (Parameter 4)	Material (Parameter 5)
4-26	3	6	9	12	PAR1 – ISO	C60 (H.S.C.)
	2	5	8			
	1	4	7			
Nomogram Name: TH12PAR1C60						

This nomogram is presented in figure 4-26, and represents the results characterized by a thickness of 12 centimeters, a PAR1-ISO heating curve and a C60 Material, as it was explained on Table 4-44. The main conclusions that may be derived from this nomogram are the following:

- The worst combination of the Initial Saturation Degree and the Intrinsic Permeability, from the point of view of thermal spalling risk, is featured by $S = 60\%$ and $k_0 = 10^{-19} \text{ m}^2$ (case #9). In this case, spalling is energetically possible, the mechanical damage level is high enough to allow it and the velocity of the spalled pieces, 14,8 m/s, describes an explosive spalling process.
- The best combination of the Initial Saturation Degree and the Intrinsic Permeability, from the point of view of thermal spalling risk, is featured by $S = 40\%$ and $k_0 = 10^{-17} \text{ m}^2$ (case #1). However, in this case spalling is still energetically possible, the mechanical damage level is high enough to allow it and the velocity of the spalled pieces, 5,8 m/s, describes a much less but still explosive spalling process.
- It is observed a very little sensitivity of the I_{s4} spalling index values to the Initial Saturation Degree. On the contrary, it is observed a very pronounced sensitivity of the I_{s4} spalling index values to the Intrinsic Permeability level, increasing its value a 678% when Intrinsic Permeability decreases two orders of magnitude. The larger increase of the I_{s4} spalling index value is found when changing the Intrinsic Permeability from $k_0 = 10^{-18} \text{ m}^2$ to $k_0 = 10^{-19} \text{ m}^2$, so this last value seems to be an upper limit for Intrinsic Permeability from the point of view of thermal spalling.
- Within this nomogram, all of the cases analyzed experiment thermal spalling. In all of them spalling occurs at a really early stage, only 10 minutes away from the start of the fire, and at really superficial layers (only 5 to 6 millimeters away from the heated surface). The level of mechanical damage is medium (0,38 to 0,45) and the velocity of spalled pieces indicates, in all of the cases, explosive spalling processes.
- About the relative energetic contribution of compressed gas and the constrained elastic energy to spalling occurrence, it is observed that:
 - ❖ For the highest levels of the Intrinsic Permeability, the main contributor is the constrained elastic energy ΔU (approximately the 80% of the total energy).
 - ❖ For the lowest levels of the Intrinsic Permeability, the main contributor is the compressed gas W (approximately the 72% of the total energy).
 - ❖ The Initial Saturation Degree does not affect significantly to the relative energetic contribution of both factors.

Highest spalling risk	#9: $S = 60\%$ and $k_0 = 10^{-19} \text{ m}^2$	Mechanical damage level	Medium (0,38 to 0,45); Depth: 5-6 mm.
Lowest spalling risk	#8: $S = 40\%$ and $k_0 = 10^{-17} \text{ m}^2$	Velocity range	5,8 - 14,8 m/s
Sensitivity to S	Non significant	Type of spalling expected	Explosive spalling. 10 minutes from start.
Sensitivity to k	High	Main energetic contributor	Depending mainly on k: ΔU for the highest k; W for the lowest.
%cases suffering spalling	100%		

Table 4-46. Resume of the main conclusions of nomogram TH12PAR1C60.

4.5.3.2 NOMOGRAM TH12PAR2C60: THICKNESS 12 CM, SLOW CURVE, MAT. C60

Figure number	Cases numbers shown in each nomogram (at the same position as shown)			Thickness (Parameter 3)	Heat profile (Parameter 4)	Material (Parameter 5)
4-27	12	15	18	12	PAR2 – SLOW	C60 (H.S.C.)
	11	14	17			
	10	13	16			
Nomogram Name: TH12PAR2C60						

This nomogram is presented in figure 4-29, and represents the results characterized by a thickness of 12 centimeters, a PAR2-Slow heating curve and a C60 Material, as it was explained on Table 4-44. The main conclusions that may be derived from this nomogram are the following:

- The worst combination of the Initial Saturation Degree and the Intrinsic Permeability, from the point of view of thermal spalling risk, is featured by $S = 60\%$ and $k_0 = 10^{-19} \text{ m}^2$ (case #18). In this case, spalling is energetically possible, the mechanical damage level is high enough to allow it and the velocity of the spalled pieces, 8,4 m/s, describes an explosive spalling process.
- The best combination of the Initial Saturation Degree and the Intrinsic Permeability, from the point of view of thermal spalling risk, is featured by $S = 40\%$ and $k_0 = 10^{-17} \text{ m}^2$ (case #10). However, in this case spalling is still energetically possible, the mechanical damage level is high enough to allow it and the velocity of the spalled pieces, 3,5 m/s, describes an spalling process between progressive and explosive.
- It is observed a very little sensitivity of the I_{s4} spalling index values to the Initial Saturation Degree. On the contrary, it is observed a very pronounced sensitivity of the I_{s4} spalling index values to the Intrinsic Permeability level, increasing its value an 806% when Intrinsic Permeability decreases two orders of magnitude. The larger increase of the I_{s4} spalling index value is found when changing the Intrinsic Permeability from $k_0 = 10^{-18} \text{ m}^2$ to $k_0 = 10^{-19} \text{ m}^2$, so this last value seems to be an upper limit for Intrinsic Permeability from the point of view of thermal spalling.
- Within this nomogram, all of the cases analyzed experiment thermal spalling. In all of them spalling occurs at a late stage, 56 to 58 minutes away from the start of the fire, and at somewhat superficial layers (10 to 12 millimeters away from the heated surface). The level of mechanical damage is medium (0,52 to 0,57) and the velocity of spalled pieces indicates, in most of the cases, explosive spalling processes.
- About the relative energetic contribution of compressed gas and the constrained elastic energy to spalling occurrence, it is observed that:
 - ❖ For the highest levels of the Intrinsic Permeability, the main contributor is the constrained elastic energy ΔU (approximately the 90% of the total energy).
 - ❖ For the lowest levels of the Intrinsic Permeability, the main contributor is the compressed gas W (approximately the 55% of the total energy).
 - ❖ The Initial Saturation Degree does not affect significantly to the relative energetic contribution of both factors (at least much less than k).

Highest spalling risk	#18: $S = 60\%$ and $k_0 = 10^{-19} \text{ m}^2$	Mechanical damage level	Medium (0,52 to 0,57); Depth: 10-12 mm.
Lowest spalling risk	#10: $S = 40\%$ and $k_0 = 10^{-17} \text{ m}^2$	Velocity range	3,5 – 8,4 m/s
Sensitivity to S	Non significant	Type of spalling expected	Explosive spalling. 56 minutes from start.
Sensitivity to k	High	Main energetic contributor	Depending mainly on k: ΔU for the highest k; W for the lowest.
%cases suffering spalling	100%		

Table 4-47. Resume of the main conclusions of nomogram TH12PAR2C60.

4.5.3.3 NOMOGRAM TH12PAR3C60: THICKNESS 12 CM, HYDROC. CURVE, MAT. C60

Figure number	Cases numbers shown in each nomogram (at the same position as shown)			Thickness (Parameter 3)	Heat profile (Parameter 4)	Material (Parameter 5)
4-28	76	79	82	12	PAR3 – HYD	C60 (H.S.C.)
	75	78	81			
	74	77	80			
Nomogram Name: TH12PAR3C60						

This nomogram is presented in figure 4-28, and represents the results characterized by a thickness of 12 centimeters, a PAR3-Hydrocarbon heating curve and a C60 Material, as it was explained on Table 4-44. The main conclusions that may be derived from this nomogram are the following taking always into account that, due to the lack of numerical convergence experimented in the cases with the lowest value of the Intrinsic Permeability, the conclusions included herein will always be partial (and one must remember that, for the cases with $k_0 = 10^{-19} \text{ m}^2$, the results shown correspond to the instant when calculations have diverged and not to the instant with the maximum I_{s4} value, which was increasing in the instant of divergence):

- The worst combination of the Initial Saturation Degree and the Intrinsic Permeability, from the point of view of thermal spalling risk, is featured by $S = 60\%$ and $k_0 = 10^{-19} \text{ m}^2$ (case #82). In this case, despite the really early stage of the evolution of the fire – only 3 minutes away from the start of the fire, spalling is energetically possible, the mechanical damage level is high enough to allow it and the velocity of the spalled pieces, 50,3 m/s, describes a dramatically explosive spalling process of the most superficial layers.
- The best combination of the Initial Saturation Degree and the Intrinsic Permeability, from the point of view of thermal spalling risk, is featured by $S = 40\%$ and $k_0 = 10^{-17} \text{ m}^2$ (case #74). However, in this case spalling is still energetically possible, the mechanical damage level is high enough to allow it and the velocity of the spalled pieces, 8,0 m/s, describes a much less but still explosive spalling process.
- It is observed a very little sensitivity of the I_{s4} spalling index values to the Initial Saturation Degree. It must not be mistaken the understanding of the high differences among the I_{s4} values corresponding to a $k_0 = 10^{-19} \text{ m}^2$ with a sensitivity to the Initial Saturation Degree: instead, these differences are due to the fact that in the case of an Initial Saturation Degree of a 60%, calculations converged 30 seconds later than in the rest of the cases, and this time gap is really significant when considering an ultra-fast heating profile as Hydrocarbon curve. On the contrary, it is observed a very pronounced sensitivity of the I_{s4} spalling index values to the Intrinsic Permeability level, increasing its value a 678% when Intrinsic Permeability decreases two orders of magnitude. The larger increase of the I_{s4} spalling index value is found when changing the Intrinsic Permeability from $k_0 = 10^{-18} \text{ m}^2$ to $k_0 = 10^{-19} \text{ m}^2$.
- Within this nomogram, all of the cases analyzed experiment thermal spalling. In all of them spalling occurs at a really early stage, only 2 to 4 minutes away from the start of the fire, and at really superficial layers (only 1 to 2 millimeters away from the heated surface). The level of mechanical damage is medium (0,33 to 0,57) and the velocity of spalled pieces indicates, in all of the cases, explosive spalling processes.
- About the relative energetic contribution of compressed gas and the constrained elastic energy to spalling occurrence, it is observed that:

- ❖ For the highest levels of the Intrinsic Permeability, the main contributor is the constrained elastic energy ΔU (approximately the 92% of the total energy).
- ❖ For the lowest levels of the Intrinsic Permeability, the main contributor is the compressed gas W (approximately the 93% of the total energy).
- ❖ The Initial Saturation Degree does not affect significantly to the relative energetic contribution of both factors.

Highest spalling risk	#82:S = 60% and $k_0 = 10^{-19} \text{ m}^2$	Mechanical damage level	Medium (0,33 to 0,57); Depth: 1-2 mm
Lowest spalling risk	#74:S = 40% and $k_0 = 10^{-17} \text{ m}^2$	Velocity range	8,0 - 50,3 m/s
Sensitivity to S	Non significant	Type of spalling expected	Explosive spalling. 2-4 minutes from start.
Sensitivity to k	High	Main energetic contributor	Depending mainly on k: ΔU for the highest k; W for the lowest.
% cases suffering spalling	100%		

Table 4-48. Resume of the main conclusions of nomogram TH12PAR3C60.

4.5.3.4 NOMOGRAM TH12PAR1C90: THICKNESS 12 CM, ISO CURVE, MATERIAL C90

Figure number	Cases numbers shown in each nomogram (at the same position as shown)			Thickness (Parameter 3)	Heat profile (Parameter 4)	Material (Parameter 5)
4-29	39	42	45	12	PAR1 – ISO	C90 (VHSC)
	38	41	44			
	37	40	43			
Nomogram Name: TH12PAR1C90						

This nomogram is presented in figure 4-29, and represents the results characterized by a thickness of 12 centimeters, a PAR1-ISO heating curve and a C90 Material, as it was explained on Table 4-44. The main conclusions that may be derived from this nomogram are the following:

- The worst combination of the Initial Saturation Degree and the Intrinsic Permeability, from the point of view of thermal spalling risk, is featured by $S = 60\%$ and $k_0 = 10^{-19} \text{ m}^2$ (case #45). In this case, spalling is energetically possible, the mechanical damage level is high enough to allow it and the velocity of the spalled pieces, 9,3 m/s, describes an explosive spalling process.
- The best combination of the Initial Saturation Degree and the Intrinsic Permeability, from the point of view of thermal spalling risk, is featured by $S = 40\%$ and $k_0 = 10^{-17} \text{ m}^2$ (case #37). In this case spalling is not energetically possible although the mechanical damage level is medium.
- It is observed a very little sensitivity of the I_{s4} spalling index values to the Initial Saturation Degree except at cases with an Intrinsic Permeability of $k_0 = 10^{-19} \text{ m}^2$. On the contrary, it is observed a very pronounced sensitivity of the I_{s4} spalling index values to the Intrinsic Permeability level, increasing its value an 878% when Intrinsic Permeability decreases two orders of magnitude. The larger increase of the I_{s4} spalling index value is again found when changing the Intrinsic Permeability from $k_0 = 10^{-18} \text{ m}^2$ to $k_0 = 10^{-19} \text{ m}^2$, so this last value seems to be an upper limit for Intrinsic Permeability from the point of view of thermal spalling.
- Within this nomogram, only 4 of the cases analyzed experiment thermal spalling. In all of them spalling occurs at a really early stage, only 10 minutes away from the start of the fire, and at really superficial layers (only 4 to 5 millimeters away from the heated surface). The level of mechanical damage is medium-high (0,53 to 0,60) and the velocity of spalled pieces indicates, in all of the cases where spalling is energetically possible, explosive spalling processes.

- About the relative energetic contribution of compressed gas and the constrained elastic energy to spalling occurrence, it is observed that:
 - ❖ For the highest levels of the Intrinsic Permeability, the main contributor is the constrained elastic energy ΔU (approximately the 82% of the total energy).
 - ❖ For the lowest levels of the Intrinsic Permeability, the main contributor is the compressed gas W (approximately the 67% of the total energy).
 - ❖ The Initial Saturation Degree does not affect significantly to the relative energetic contribution of both factors but decreasing slightly the contribution of the constrained elastic energy as the Initial Saturation Degree increases.

Highest spalling risk	#45: $S = 60\%$ and $k_0 = 10^{-19} \text{ m}^2$	Mechanical damage level	Medium (0,53 to 0,60); Depth: 4-5mm.
Lowest spalling risk	#37: $S = 40\%$ and $k_0 = 10^{-17} \text{ m}^2$	Velocity range	8,1 - 9,3 m/s
Sensitivity to S	Non significant except for cases with $k_0 = 10^{-19} \text{ m}^2$	Type of spalling expected	Explosive spalling. 10 minutes from start.
Sensitivity to k	High	Main energetic contributor	Depending mainly on k: ΔU for the highest k; W for the lowest.
%cases suffering spalling	44%		

Table 4-49. Resume of the main conclusions of nomogram TH12PAR1C90.

4.5.3.5 NOMOGRAM TH12PAR2C90: THICKNESS 12 CM, SLOW CURVE, MAT. C90

Figure number	Cases numbers shown in each nomogram (at the same position as shown)			Thickness (Parameter 3)	Heat profile (Parameter 4)	Material (Parameter 5)
4-30	48	51	54	12	PAR2 – SLOW	C90 (VHSC)
	47	50	53			
	46	49	52			
Nomogram Name: TH12PAR2C90						

This nomogram is presented in figure 4-30, and represents the results characterized by a thickness of 12 centimeters, a PAR2-Slow heating curve and a C90 Material, as it was explained on Table 4-44. The main conclusions that may be derived from this nomogram are the following:

- The worst combination of the Initial Saturation Degree and the Intrinsic Permeability, from the point of view of thermal spalling risk, is featured by $S = 60\%$ and $k_0 = 10^{-19} \text{ m}^2$ (case #54). In this case, spalling is energetically possible, the mechanical damage level is high enough to allow it and the velocity of the spalled pieces, 3,6 m/s, describes an intermediate progressive to explosive spalling process.
- The best combination of the Initial Saturation Degree and the Intrinsic Permeability, from the point of view of thermal spalling risk, is featured by $S = 40\%$ and $k_0 = 10^{-17} \text{ m}^2$ (case #46). In this case spalling is not energetically possible although the mechanical damage level is high. It is precisely this high level of damaging, 0,70, what leads to a decrease in gas pressure and, consequently, to a low value of the I_{s4} and of the contribution of compressed gas.
- It is observed a little sensitivity of the I_{s4} spalling index values to the Initial Saturation Degree. On the contrary, it is observed a very pronounced sensitivity of the I_{s4} spalling index values to the Intrinsic Permeability level, increasing its value a 1361% when Intrinsic Permeability decreases two orders of magnitude. The larger increase of the I_{s4} spalling index value is found when changing the Intrinsic Permeability from $k_0 = 10^{-18} \text{ m}^2$ to $k_0 = 10^{-19} \text{ m}^2$, so this last value seems to be again an upper limit for Intrinsic Permeability from the point of view of thermal spalling.
- Within this nomogram, only three of the cases analyzed experiment thermal spalling. In all of them spalling occurs at a late stage, 56 minutes away from the start of the fire, and

at really superficial layers (only 7 to 8 millimeters away from the heated surface). The level of mechanical damage is high (0,66 to 0,71) and the velocity of spalled pieces indicates, in all of the spalling cases, intermediate progressive to explosive spalling processes.

- About the relative energetic contribution of compressed gas and the constrained elastic energy to spalling occurrence, it is observed that:
 - ❖ For the highest levels of the Intrinsic Permeability, the main contributor is the constrained elastic energy ΔU (approximately the 95% of the total energy).
 - ❖ For the lowest levels of the Intrinsic Permeability, the main contributor is the compressed gas W (approximately the 56% of the total energy).
 - ❖ The Initial Saturation Degree does not affect significantly to the relative energetic contribution of both factors.

Highest spalling risk	#54: S = 60% and $k_0 = 10^{-19} \text{ m}^2$	Mechanical damage level	Medium (0,66 to 0,71) ; Depth: 7-8mm.
Lowest spalling risk	#46: S = 40% and $k_0 = 10^{-17} \text{ m}^2$	Velocity range	2,6 - 3,6 m/s
Sensitivity to S	Non significant	Type of spalling expected	Intermediate Progressive to Explosive spalling. 56 minutes away from start.
Sensitivity to k	High	Main energetic contributor	Depending mainly on k: ΔU for the highest k; W for the lowest.
%cases suffering spalling	33,3%		

Table 4-50. Resume of the main conclusions of nomogram TH12PAR2C90.

4.5.3.6 NOMOGRAM TH12PAR3C90: THICKNESS 12 CM, HYDROC. CURVE, MAT. C90

Figure number	Cases numbers shown in each nomogram (at the same position as shown)			Thickness (Parameter 3)	Heat profile (Parameter 4)	Material (Parameter 5)
4-31	85	88	91	12	PAR3 – HYD	C90 (VHSC)
	84	87	90			
	83	86	89			
Nomogram Name: TH12PAR3C90						

This nomogram is presented in figure 4-31, and represents the results characterized by a thickness of 12 centimeters, a PAR3-Hydrocarbon heating curve and a C90 Material, as it was explained on Table 4-44. The main conclusions that may be derived from this nomogram are the following taking always into account that, due to the lack of numerical convergence experimented in the cases with the lowest value of the Intrinsic Permeability, the conclusions included herein will always be partial (and one must remember that, for the cases with $k_0 = 10^{-19} \text{ m}^2$, the results shown correspond to the instant when calculations have diverged and not to the instant with the maximum I_{s4} value, which was increasing in the instant of divergence):

- The worst combination of the Initial Saturation Degree and the Intrinsic Permeability, from the point of view of thermal spalling risk, is featured by S = 40% and $k_0 = 10^{-19} \text{ m}^2$ (case #85). In this case, despite the really early stage of the evolution of the fire – only 5 minutes away from the start of the fire, spalling is energetically possible, the mechanical damage level is high enough to allow it and the velocity of the spalled pieces, 29,3 m/s, describes a dramatically explosive spalling process of the most superficial layers.
- The best combination of the Initial Saturation Degree and the Intrinsic Permeability, from the point of view of thermal spalling risk, is featured by S = 40% and $k_0 = 10^{-17} \text{ m}^2$ (case #83). In this case spalling is not energetically possible although the mechanical damage level is medium.

- It is observed a very little sensitivity of the I_{s4} spalling index values to the Initial Saturation Degree except at cases with an Intrinsic Permeability of $k_0 = 10^{-19} \text{ m}^2$. On the contrary, it is observed a very pronounced sensitivity of the I_{s4} spalling index values to the Intrinsic Permeability level, increasing its value an 958% when Intrinsic Permeability decreases two orders of magnitude. The larger increase of the I_{s4} spalling index value is again found when changing the Intrinsic Permeability from $k_0 = 10^{-18} \text{ m}^2$ to $k_0 = 10^{-19} \text{ m}^2$, so this last value seems to be an upper limit for Intrinsic Permeability from the point of view of thermal spalling.
- Within this nomogram, six of the cases analyzed experiment thermal spalling. In all of them spalling occurs at a really early stage, only 2 to 4 minutes away from the start of the fire, and at really superficial layers (only 1 to 2 millimeters away from the heated surface). The level of mechanical damage is medium (0,42 to 0,50) and the velocity of spalled pieces indicates, in all of the cases, explosive spalling processes.
- About the relative energetic contribution of compressed gas and the constrained elastic energy to spalling occurrence, it is observed that:
 - ❖ For the highest levels of the Intrinsic Permeability, the main contributor is the constrained elastic energy ΔU (approximately the 62% of the total energy).
 - ❖ For the lowest levels of the Intrinsic Permeability, the main contributor is the compressed gas W (approximately the 91% of the total energy).
 - ❖ The Initial Saturation Degree does not affect significantly to the relative energetic contribution of both factors (the higher contribution of constrained elastic energy shown in case #89 with respect to cases #83 and #86 is due to a finishing time of #89 numerical calculation 30 seconds later, what represents a quite important time gap with an ultra-fast heating curve as Hydrocarbon curve).

Highest spalling risk	#85:S = 40% and $k_0 = 10^{-19} \text{ m}^2$	Mechanical damage level	Medium (0,42 to 0,50); Depth: 1-2 mm
Lowest spalling risk	#83:S = 40% and $k_0 = 10^{-17} \text{ m}^2$	Velocity range	3,9 - 29,3 m/s
Sensitivity to S	Non significant	Type of spalling expected	Explosive spalling. 2-4 minutes from start.
Sensitivity to k	High	Main energetic contributor	Depending mainly on k: ΔU for the highest k; W for the lowest.
%cases suffering spalling	66,6%		

Table 4-51. Resume of the main conclusions of nomogram TH12PAR3C90.

4.5.3.7 COMPARISON AMONG THE SIX NOMOGRAMS CORRESPONDING TO A THICKNESS OF 12 CENTIMETRES

A final comparison will be done among the six nomograms corresponding to a thickness of 12 centimetres. The reason for not including the nomograms corresponding to a thickness of 24 centimetres both in this comparison and in the previous paragraphs is that, as it can be observed in figures 4-32 to 4-35, the results related to Thermal Spalling of these cases are not significantly different from those obtained for a thickness of 12 centimetres (analogously happens, as it was already stated in previous paragraphs, for the case with a thickness of 50 centimetres).

At table 4-52 are collected together the resumed data of each nomogram in order to easy their comparison.

In general, it is observed that the influence of the heating profile is as follows: as the heating profile considered is faster and more severe (Slow → ISO → Hydrocarbon), independently of the material considered, the following trends arise for all the combinations of the Initial Saturation Degree and the Intrinsic Permeability:

- The I_{s4} spalling index values increase,

- The average velocity of the spalled pieces increases,
- The number of combinations of the Initial Saturation Degree and the Intrinsic Permeability where spalling occurs increases,
- The time at which it is found the maximum risk of spalling (maximum value of the I_{s4} spalling index) decreases,
- The position of the main fracture is closer to the heated surface.
- There is not a definite trend with respect to mechanical damage, increasing in some of the combinations of the Initial Saturation Degree and the Intrinsic Permeability and decreasing in the others.
- About the energetic analysis comparison, the following conclusions are only referred to heating curves ISO and Slow, since the lack of convergence of Hydrocarbon cases may lead to deceptive conclusions about this particular matter:
 - ❖ The relative contribution of the constrained elastic energy decreases as the heating profile increases its speed and severity. On the other hand, the relative contribution of the work done by compressed gas increases. This might be due to higher gas pressures arising with faster heating profiles.

It is also observed that the influence of the material is as follows: independently of the heating curve considered, the following trends arise for all the combinations of the Initial Saturation Degree and the Intrinsic Permeability:

- The I_{s4} spalling index values are higher for C60 (H.S.C.) than for C90 (U.H.S.C.),
- The average velocity of the spalled pieces is higher for C60 material,
- The number of combinations of the Initial Saturation Degree and the Intrinsic Permeability where spalling occurs is higher for C60 material,
- The time at which it is found the maximum risk of spalling (maximum value of the I_{s4} spalling index) is higher for C60 material,
- The position of the main fracture is closer to the heated surface for C90 material just in some cases (mainly for the Slow Heating curve). In the rest of cases, there are no significant differences between the position of the main fracture between C60 and C90.
- There is a well-defined trend with the mechanical damage values, being significantly higher in the cases corresponding to C90 material.
- About the energetic analysis comparison, the following conclusions are only referred to heating curves ISO and Slow, since the lack of convergence of Hydrocarbon cases may lead to deceptive conclusions about this particular matter:
 - ❖ The relative contribution of the constrained elastic energy is higher for the C90 material than for the C60 material. This trend is more pronounced for high values of the Intrinsic Permeability (10^{-17} and 10^{-18} m^2) than for 10^{-19} .

4.5.3.8 A PARTICULAR ANALYSIS ABOUT THE SPALLING VELOCITIES SPECTRUM

Figure 4-36 collects the average velocities of the spalled-off concrete pieces for each of the ninety one combinations analyzed. Since velocities corresponding to the cases with Hydrocarbon heating profile are much higher than the rest, two detail levels are included in this figure (the higher detailed level corresponds to cases with Slow and ISO heating profiles).

Resume of the main conclusions of nomogram TH12PAR1C60			
Highest spalling risk	#9: S = 60% and $k_0 = 10^{-19} \text{ m}^2$	Mechanical damage level	Medium (0,38 to 0,45); Depth: 5-6 mm.
Lowest spalling risk	#8: S = 40% and $k_0 = 10^{-17} \text{ m}^2$	Velocity range	5,8 - 14,8 m/s
Sensitivity to S	Non significant	Type of spalling expected	Explosive spalling. 10 minutes from start.
Sensitivity to k	High	Main energetic contributor	Depending mainly on k: ΔU for the highest k; W for the lowest.
%cases suffering spalling	100%		

Resume of the main conclusions of nomogram TH12PAR2C60			
Highest spalling risk	#18:S = 60% and $k_0 = 10^{-19} \text{ m}^2$	Mechanical damage level	Medium (0,52 to 0,57); Depth: 10-12 mm.
Lowest spalling risk	#10:S = 40% and $k_0 = 10^{-17} \text{ m}^2$	Velocity range	3,5 - 8,4 m/s
Sensitivity to S	Non significant	Type of spalling expected	Explosive spalling. 56 minutes from start.
Sensitivity to k	High	Main energetic contributor	Depending mainly on k: ΔU for the highest k; W for the lowest.
%cases suffering spalling	100%		

Resume of the main conclusions of nomogram TH12PAR3C60			
Highest spalling risk	#82:S = 60% and $k_0 = 10^{-19} \text{ m}^2$	Mechanical damage level	Medium (0,33 to 0,57); Depth: 1-2 mm
Lowest spalling risk	#74:S = 40% and $k_0 = 10^{-17} \text{ m}^2$	Velocity range	8,0 - 50,3 m/s
Sensitivity to S	Non significant	Type of spalling expected	Explosive spalling. 2-4 minutes from start.
Sensitivity to k	High	Main energetic contributor	Depending mainly on k: ΔU for the highest k; W for the lowest.
%cases suffering spalling	100%		

Resume of the main conclusions of nomogram TH12PAR1C90			
Highest spalling risk	#45:S = 60% and $k_0 = 10^{-19} \text{ m}^2$	Mechanical damage level	Medium (0,53 to 0,60); Depth: 4-5mm.
Lowest spalling risk	#37:S = 40% and $k_0 = 10^{-17} \text{ m}^2$	Velocity range	8,1 - 9,3 m/s
Sensitivity to S	Non significant except for cases with $k_0 = 10^{-19} \text{ m}^2$	Type of spalling expected	Explosive spalling. 10 minutes from start.
Sensitivity to k	High	Main energetic contributor	Depending mainly on k: ΔU for the highest k; W for the lowest.
%cases suffering spalling	44%		

Resume of the main conclusions of nomogram TH12PAR2C90			
Highest spalling risk	#54:S = 60% and $k_0 = 10^{-19} \text{ m}^2$	Mechanical damage level	Medium (0,66 to 0,71) ; Depth: 7-8mm.
Lowest spalling risk	#46:S = 40% and $k_0 = 10^{-17} \text{ m}^2$	Velocity range	2,6 - 3,6 m/s
Sensitivity to S	Non significant	Type of spalling expected	Intermediate Progressive to Explosive spalling. 56 minutes away from start.
Sensitivity to k	High	Main energetic contributor	Depending mainly on k: ΔU for the highest k; W for the lowest.
%cases suffering spalling	33,3%		

Resume of the main conclusions of nomogram TH12PAR3C90			
Highest spalling risk	#85:S = 40% and $k_0 = 10^{-19} \text{ m}^2$	Mechanical damage level	Medium (0,42 to 0,50); Depth: 1-2 mm
Lowest spalling risk	#83:S = 40% and $k_0 = 10^{-17} \text{ m}^2$	Velocity range	3,9 - 29,3 m/s
Sensitivity to S	Non significant	Type of spalling expected	Explosive spalling. 2-4 minutes from start.
Sensitivity to k	High	Main energetic contributor	Depending mainly on k: ΔU for the highest k; W for the lowest.
%cases suffering spalling	66,6%		

Table 4-52. Collection of the resumed data of each nomogram corresponding to a thickness of 12 centimetres.

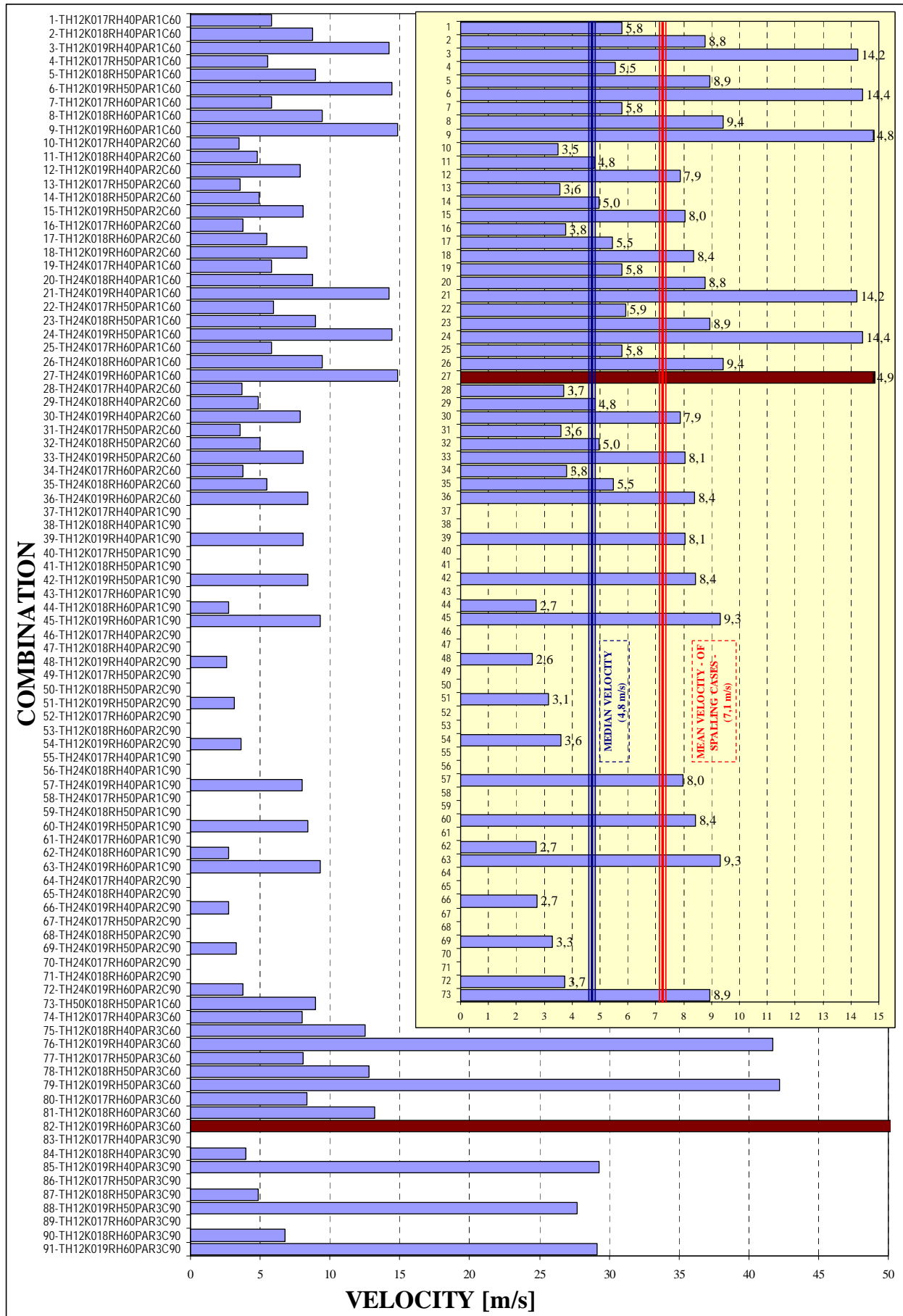


Figure 4-36. Velocities of spalled-off pieces for each of the ninety one combinations.

Hence, in figure 4-36 may be observed that the cases with the highest average velocity of the spalled-off pieces, among all of the cases analyzed, is case #82 corresponding precisely to the Hydrocarbon heating curve and C60 material.

On the other hand, referring only to cases with Slow and ISO Heating curves, the case with the highest average velocity of the spalled-off pieces is case #27, corresponding to an Initial Saturation Degree at 60%, an Intrinsic Permeability value of 10^{-19} m^2 , an ISO heating curve and C60 material. The mean velocity of the spalled-off pieces considering only the spalling cases not related to Hydrocarbon heating curve is 7,1 m/s and its median value is 4,8 m/s (considering zero values for the cases where spalling is not occurring).

Figure 4-37 shows the distribution of average velocities of spalled pieces evaluated for each combination. It indicates the existence of two peaks, lying with the range of $4,5 < v \leq 6,0 \text{ m/s}$ and of $7,5 < v \leq 9,0 \text{ m/s}$. As an example of the experimental observations, on figure 4-38 are shown the minimum and maximum velocity of distinct pieces spalled-off during a set of experimental tests developed by [32], in which were recorded spalling events by means of a high-speed camera, giving insight into the size/shape and velocity of the spalled pieces. These experimental results are *not* to be compared against the results obtained in this *Chapter* since they were obtained using different materials (C60/C30), different water/cement ratios and different heating profiles.

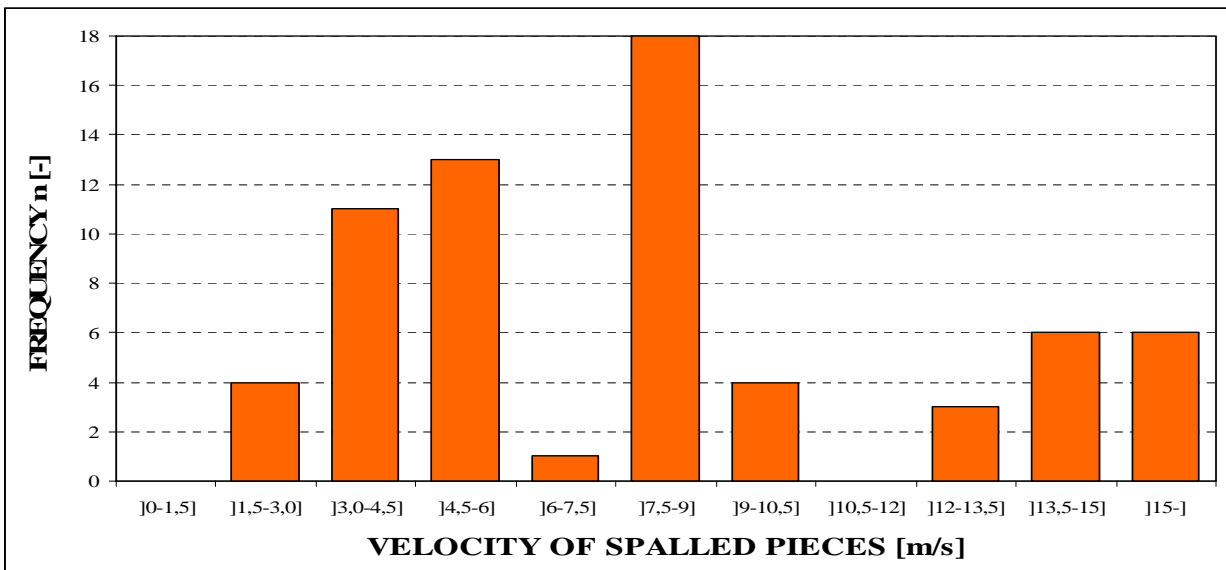


Figure 4-37. Distribution of Velocities of spalled-off pieces evaluated for each of the ninety one combinations.

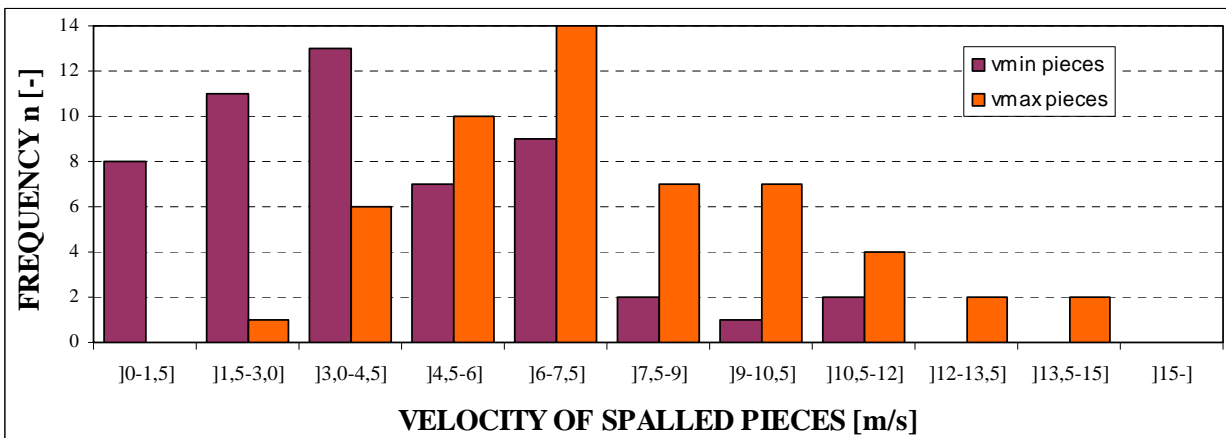


Figure 4-38. Distribution of minimum and maximum velocity of distinct spalled-off pieces evaluated for each spalling event in experimental tests [32].

4.5.4 Comparison for constant values of the Intrinsic Permeability

Within this paragraph a direct comparison of the results of the cases characterized by the same value of intrinsic permeability is shown.

The graphics are presented in Figures 4.39 to 4.56 for values of intrinsic permeability ranging from 10^{-19} to 10^{-17} m^2 and for five different depths from the heated surface detailed in the following table:

	<i>Combinations with PAR1 (ISO) and PAR2 (Slow-parametric) heating curves</i>	<i>Combinations with PAR3 (Hydrocarbon) heating curve and intrinsic permeability from 10^{-17} to 10^{-18} m^2</i>	<i>Combinations with PAR3 (Hydrocarbon) heating curve and intrinsic permeability 10^{-19} m^2</i>
<i>(a) First depth</i>	0,6 centimetres	0,3 centimetres	0,3 centimetres
<i>(b) Second depth</i>	1,2 centimetres	0,5 centimetres	0,5 centimetres
<i>(c) Third depth</i>	2,5 centimetres	1,5 centimetres	1,5 centimetres
<i>(d) Fourth depth</i>	5,0 centimetres	2,0 centimetres	2,0 centimetres
<i>(e) Fifth depth</i>	10,0 centimetres	5,0 centimetres	2,5 centimetres

Table 4-53. Depths of representation for each type of combination.

The reason for choosing different representation depths for combinations characterised by PAR1 and PAR2 heating curves from those corresponding to PAR3 heating curve is the highest gradients of the represented data in the proximity of the heated surface in the case of the fastest heating (PAR3 Hydrocarbon heating curve).

Furthermore, the fifth depth chosen for the combinations with PAR3 heating curve and an intrinsic permeability of 10^{-19} m^2 has been selected smaller than that corresponding to smaller intrinsic permeability values because, otherwise, no representative results would have been possible to show within the converged simulation time.

The graphics represent the time history of gas pressure, vapour pressure and total damage for each set of three combinations characterised by the same intrinsic permeability (this means that within each graphic, combinations characterised by an initial saturation degree of 40%, 50% and 60% are compared). Taking into account development of temperature T in time, it has been possible to show the distribution of the mentioned variables in the domain of temperature.

It must be remarked that, in order to avoid complicating in excess the interpretation of the graphic results, the total damage represented in each graphic is that corresponding to an initial saturation degree of 50%, which is the average value of the considered range for this parameter.

The values of gas pressure differ from those of vapour pressure because of dry air pressure. Close to critical point of water vapour and gas pressure tend to be equal. This is due to the vapour molar fraction which increase with temperature and close T_{crit} is practically equal to one, i.e. only vapour is represent in the pores of the material. This effect has been confirmed experimentally and is in accordance with the Physics of water in porous media at high temperature [31].

Such a kind of analysis confirms also that the “limit case”, characterized by an intrinsic permeability of 10^{-18} m^2 (and of course 10^{-19} m^2) and an initial value of saturation degree equal to 60%, is a case for which the spalling is likely, as it will be explained later in detail.

The graphics are organized according to the following table:

Figure number	Thickness [cm]	Material	Heating curve	Intrinsic permeability [m ²]	Combination numbers for each initial saturation degree		
					S=40%	S=50%	S=60%
4-39	12	C60 (High Strength Concrete)	PAR 1 (ISO 834)	10 ⁻¹⁹	3	6	9
4-40				10 ⁻¹⁸	2	5	8
4-41				10 ⁻¹⁷	1	4	7
4-42			PAR 2 (Slow parametric)	10 ⁻¹⁹	12	15	18
4-43				10 ⁻¹⁸	11	14	17
4-44				10 ⁻¹⁷	10	13	16
4-45			PAR 3 (Hydrocarbon)	10 ⁻¹⁹	76**	79**	82**
4-46				10 ⁻¹⁸	75**	78**	81**
4-47				10 ⁻¹⁷	74**	77**	80**
4-48		C90 (Ultra-High Strength Concrete)	PAR 1 (ISO 834)	10 ⁻¹⁹	39	42	45
4-49				10 ⁻¹⁸	38	41	44
4-50				10 ⁻¹⁷	37	40	43
4-51			PAR 2 (Slow parametric)	10 ⁻¹⁹	48	51	54
4-52				10 ⁻¹⁸	47	50	53
4-53				10 ⁻¹⁷	46	49	52
4-54			PAR 3 (Hydrocarbon)	10 ⁻¹⁹	85**	88**	91**
4-55				10 ⁻¹⁸	84*	87*	90*
4-56				10 ⁻¹⁷	83*	86*	89*

Table 4-54. List of graphics included in the comparison for constant values of Intrinsic Permeability.

Remark *: As it was previously explained, these combinations have been run up to a total simulation time of 2.400 seconds (instead of the general simulation time of 10.800 seconds) because the high rate of heating induces a value of the Total Damage at 2.400 seconds of 0.99, which means that the material is completely destroyed, so it is not worthy to carry on simulations beyond this point.

Remark **: As it was also previously explained, these combinations have had lack of convergence at certain instants because of the combination of extreme conditions, i.e. high rate of heating joint to the lower limit value of intrinsic permeability (10⁻¹⁹ m²), so results are represented up to the converged simulation time, resumed in the next table:

Combination	74	75	76	77	78	79	80	81	82	85	88	91
Final time [s]	1.050	1.020	150	1.065	285	148	1.080	1.080	180	150	150	150

It must be also remarked, as it has been explained in previous paragraphs, that combinations corresponding to thicknesses of 24 and 50 centimetres have been discarded for this type of results representation because the showed no significant deviations with respect to those results obtained for the cases of 12 centimetres.

4.5.4.1 THICKNESS 12 CM – ISO HEATING CURVE – MATERIAL C60

Figure number	Thickness [cm]	Material	Heating curve	Intrinsic permeability [m ²]	Combination numbers for each initial saturation degree		
					S=40%	S=50%	S=60%
4-39	12	C60 (High Strength Concrete)	PAR 1 (ISO 834)	10 ⁻¹⁹	3	6	9
4-40				10 ⁻¹⁸	2	5	8
4-41				10 ⁻¹⁷	1	4	7

For all of these three figures featured by increasing values of Intrinsic Permeability, and independently of the Initial Saturation Degree, the following trends are observed:

- In these cases, the lower depth at which results are graphed, 0,6 centimetres, show the highest gas and vapour pressure values. However, the lower depth does not necessarily mean higher Total Damage levels at the same temperature; for instance, in the cases of an Intrinsic Permeability of 10⁻¹⁹ m², the Total Damage at a depth of 0,6 centimetres and a temperature of about 500 K is 0,32 while this value rises up to 0,80 at a depth of 10 centimetres (where this temperature is reached much later).
- The maximum absolute gas pressure reached during the three hours of simulations is always found, for all of the depths considered, within the temperature range of 473 ±50 K, being this the temperature at which spalling is usually observed. This fact suggests that despite the I_{s4} maximum values are achieved at higher temperatures, within the range of 573 ±25 K, spalling may be occurring before the instants corresponding to these maxima, as it was explained on table 4-43.
- It is observed a slight increase of the maximum absolute gas and vapour pressures as the Initial Saturation Degree increases, but the temperature at which these maxima appear is not affected. The maximum absolute vapour pressure values matches in time with the maximum of gas pressure.
- On the contrary, comparing these three figures it is clearly observed a pronounced sensitivity of both the maximum absolute gas pressure and the pressure corresponding to the maximum I_{s4} spalling index with the values of the Intrinsic Permeability, increasing all of these pressures as the latter decreases. The temperature at which these maxima are found decreases when increasing Intrinsic Permeability, so it can be easily concluded that low values of Intrinsic Permeability may lead to spalling phenomena more violent but not necessarily occurring earlier.
- Analogously, as Intrinsic Permeability increases the Total Damage level at the temperatures showing both the maximum absolute gas pressure and the pressure corresponding to the maximum I_{s4} spalling index decrease. At the inner layers, among 5 and 10 centimetres away from the heated surface, it is observed that the material is not completely cracked at the end of the simulation and that the final Total Damage level also decreases as Intrinsic Permeability increases.
- It is worthy to remark that the evolution curve of Total Damage at all of the depths considered present a singularity – in the form of a sudden reduction of its slope – at the temperatures where gas and vapour pressure maxima are reached. This fact suggests that the compressed gas contribution to material damaging is significant.

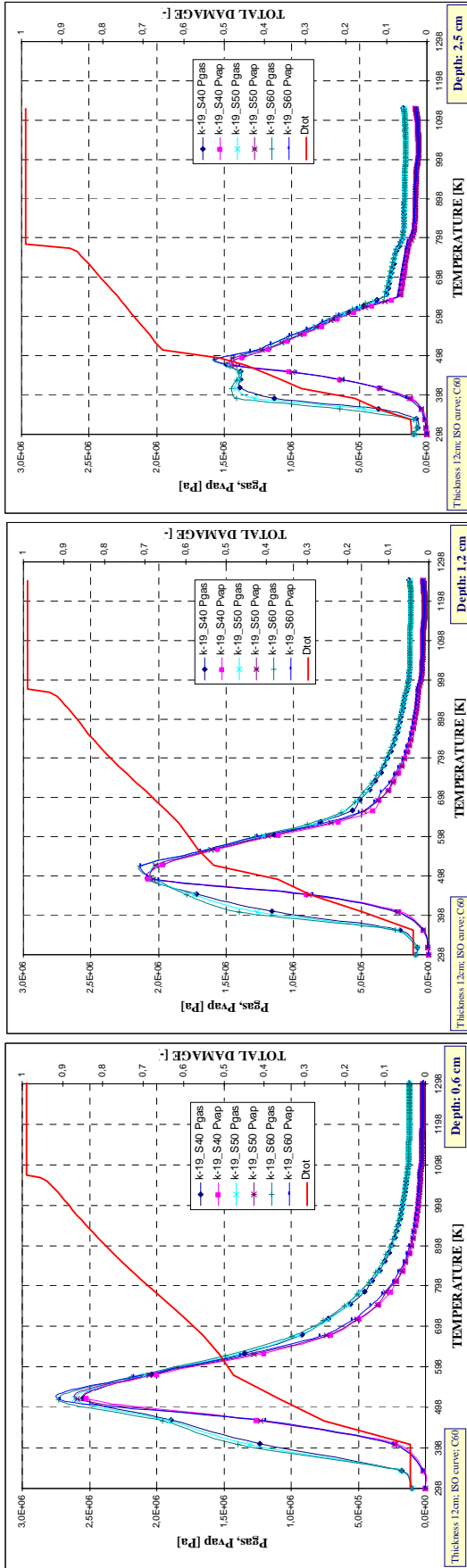
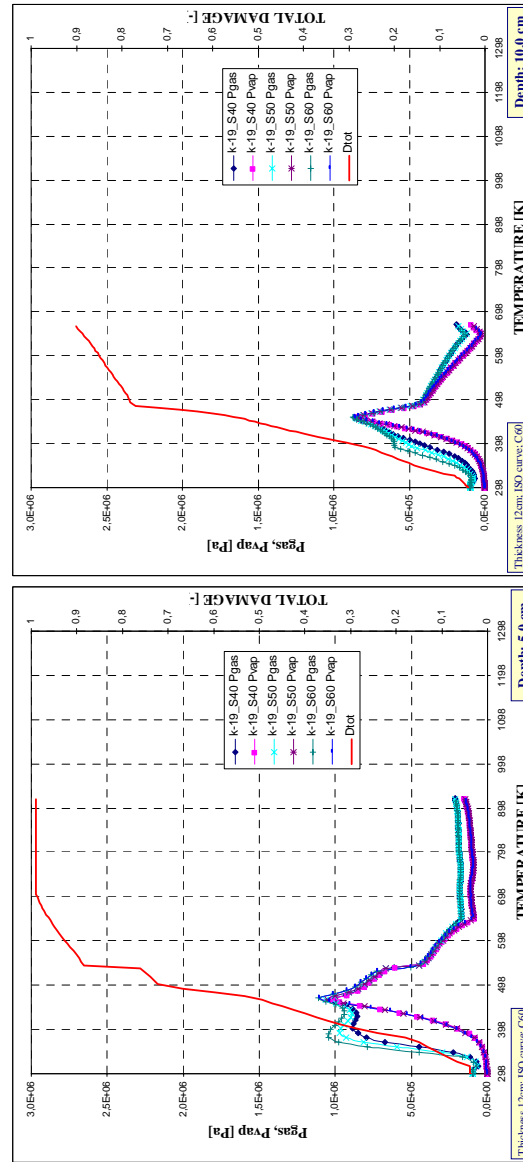


Figure 4-39. Total damage, vapour and gas pressure development for three values of initial saturation degree (40%, 50%, 60%) in case of $k=10^{-19} \text{ m}^2$.

Thickness = 12 centimetres
ISO 834 Heating curve
Material C60

- (a) Depth 0,6 cm,
- (b) Depth 1,2 cm,
- (c) Depth 2,5 cm,
- (d) Depth 5,0 cm,
- (e) Depth 10 cm



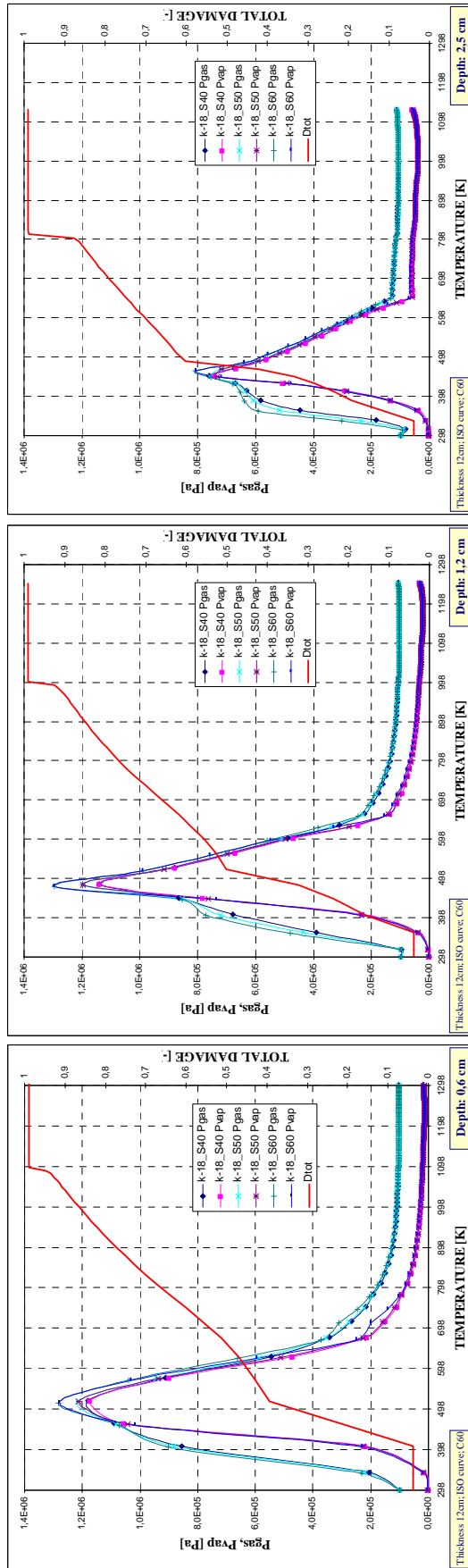
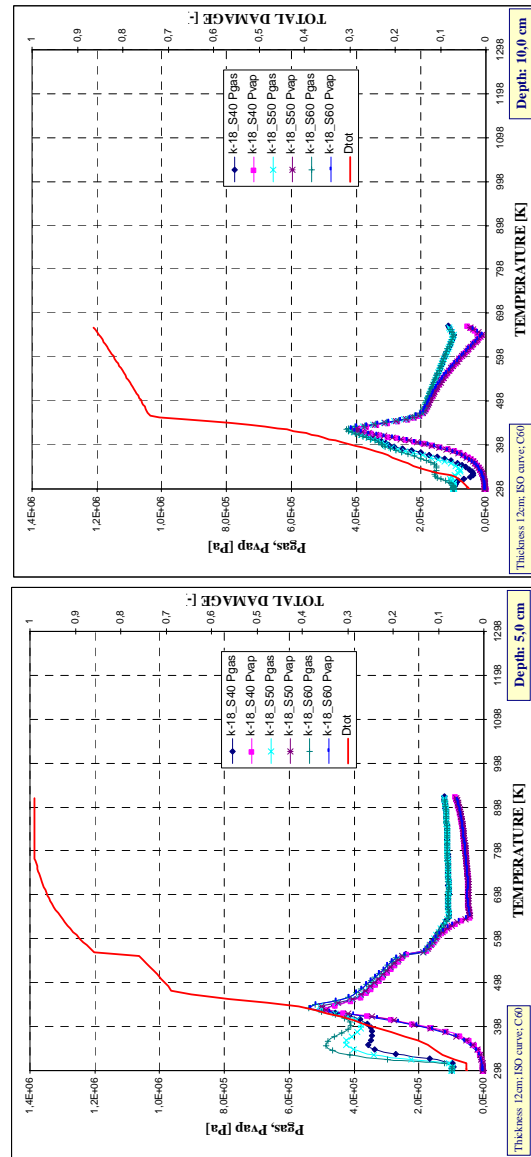


Figure 4-40. Total damage, vapour and gas pressure development for three values of initial saturation degree (40%, 50%, 60%) in case of $k=10^{18} m^2$.

Thickness = 12 centimetres
 ISO 834 Heating curve
 Material C60

- (a) Depth 0,6 cm,
- (b) Depth 1,2 cm,
- (c) Depth 2,5 cm,
- (d) Depth 5,0 cm,
- (e) Depth 10 cm



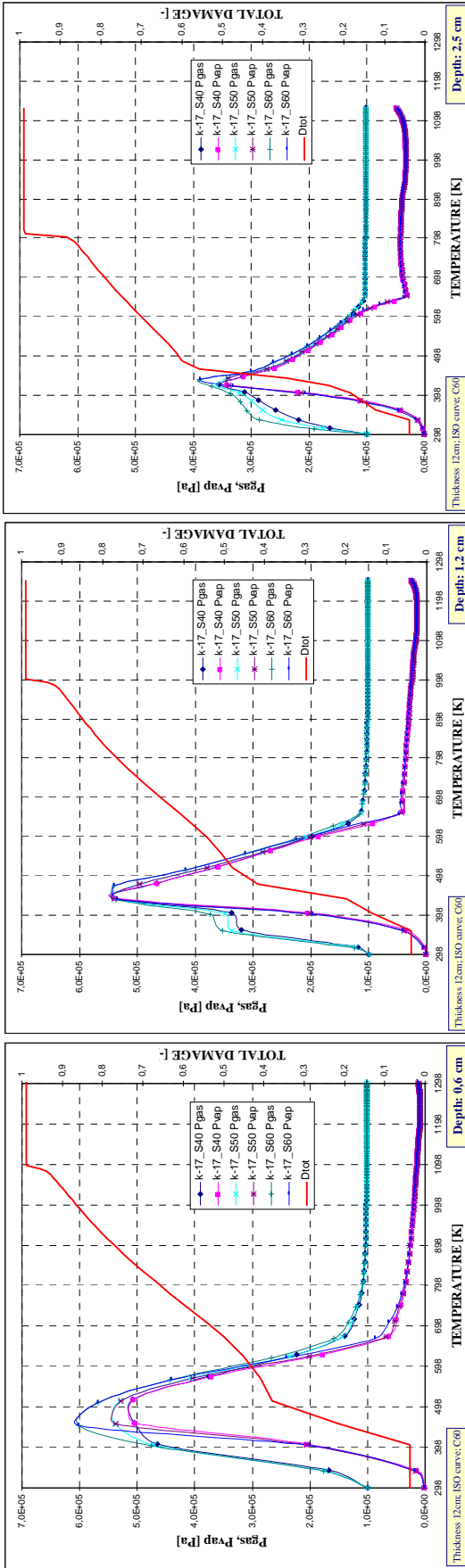
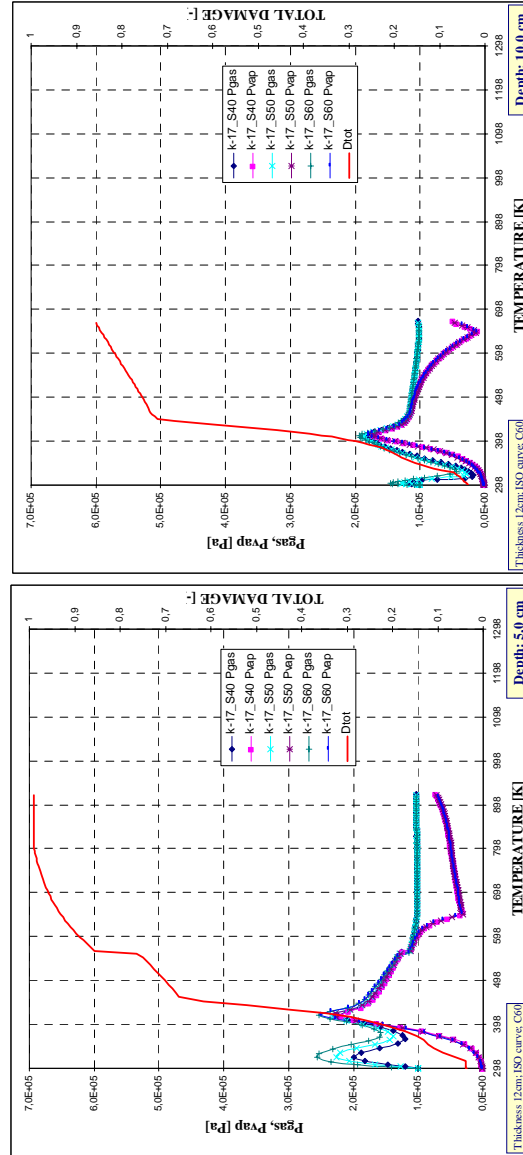


Figure 4-41. Total damage, vapour and gas pressure development for three values of initial saturation degree (40%, 50%, 60%) in case of $k=10^{-17} m^2$.

Thickness = 12 centimetres
ISO 834 Heating curve
Material C60

- (a) Depth 0,6 cm,
- (b) Depth 1,2 cm,
- (c) Depth 2,5 cm,
- (d) Depth 5,0 cm,
- (e) Depth 10 cm



4.5.4.2 THICKNESS 12 CM – PAR2 SLOW HEATING CURVE – MATERIAL C60

Figure number	Thickness [cm]	Material	Heating curve	Intrinsic permeability [m ²]	Combination numbers for each initial saturation degree		
					S=40%	S=50%	S=60%
4-42	12	C60 (High Strength Concrete)	PAR 2 (Slow parametric)	10 ⁻¹⁹	12	15	18
4-43				10 ⁻¹⁸	11	14	17
4-44				10 ⁻¹⁷	10	13	16

For all of these three figures featured by increasing values of Intrinsic Permeability, and independently of the Initial Saturation Degree, the following trends are observed:

- In these cases, the lower depth at which results are graphed, 0,6 centimetres, does not show either the highest gas and vapour pressure values or the highest Total Damage. On the contrary, the depth at which these maxima appear increases with Intrinsic Permeability, being at 1,2 centimetres for 10⁻¹⁹ and 10⁻¹⁸ m² and 2,5 centimetres for 10⁻¹⁷ m². Again, the lower depth does not necessarily mean higher Total Damage levels at the same temperature; for instance, in the cases of an Intrinsic Permeability of 10⁻¹⁹ m², the Total Damage at a depth of 0,6 centimetres and a temperature of about 500 K is 0,40 while this value rises beyond 0,70 at a depth of 10 centimetres (where this temperature is reached much later).
- The maximum absolute gas pressure reached during the three hours of simulations, considerably lower than in the cases featured by the ISO heating curve, is always found for all of the depths considered within the temperature range of 473 ±50 K, being this the temperature at which spalling is usually observed. This fact suggests that despite the I_{s4} maximum values are achieved at higher temperatures, within the range of 550 ±25 K, spalling may be occurring before the instants corresponding to these maxima.
- In this case, where the heating curve is much slower than that considered in the previous paragraph, it is observed a slight but higher increase of the maximum absolute gas and vapour pressures as the Initial Saturation Degree increases, although the temperature at which these maxima appear is still not affected by the Initial Saturation Degree. The maximum absolute vapour pressure values matches in time with the maximum of gas pressure. The difference between gas and vapour pressure is, in general and for all the cases, higher than in the previous case featured by an ISO heating curve.
- On the other hand, comparing these three figures it is again clearly observed a pronounced sensitivity of both the maximum absolute gas pressure and the pressure corresponding to the maximum I_{s4} spalling index with the values of the Intrinsic Permeability, increasing all of these pressures as the latter decreases. The temperature at which these maxima are found decreases when increasing Intrinsic Permeability, so it can be easily concluded that low values of Intrinsic Permeability may lead to spalling phenomena more violent but not necessarily occurring earlier.
- Analogously, as Intrinsic Permeability increases the Total Damage level at the temperatures showing both the maximum absolute gas pressure and the pressure corresponding to the maximum I_{s4} spalling index decrease. At the inner layers, among 5 and 10 centimetres away from the heated surface, it is observed that the material is not completely cracked at the end of the simulation and that the final Total Damage level here increases as Intrinsic Permeability increases.

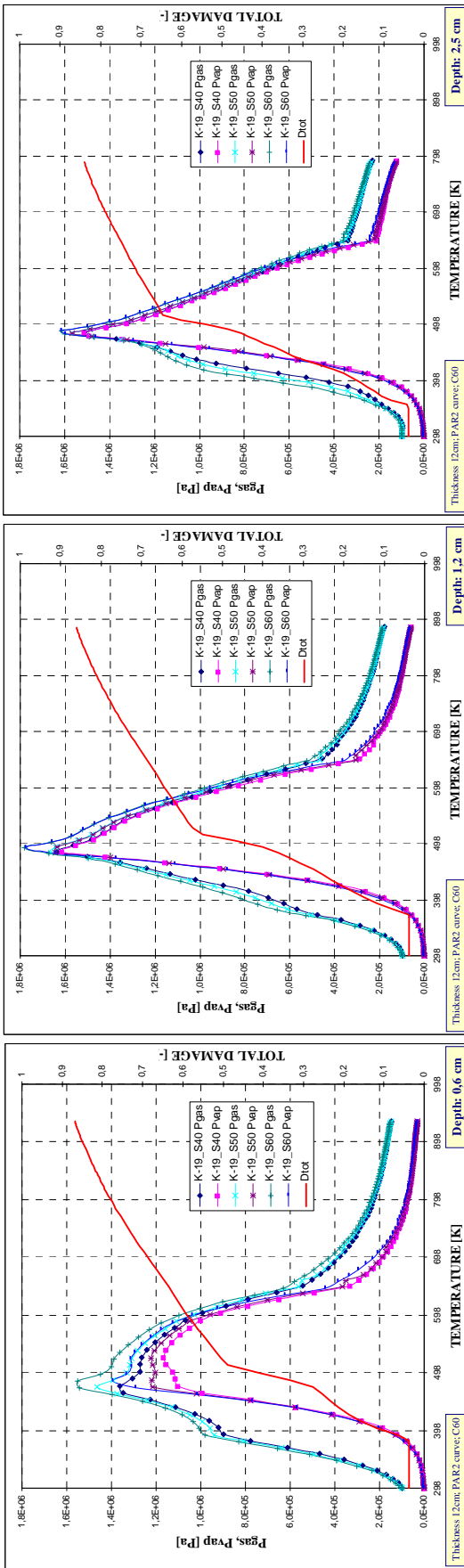
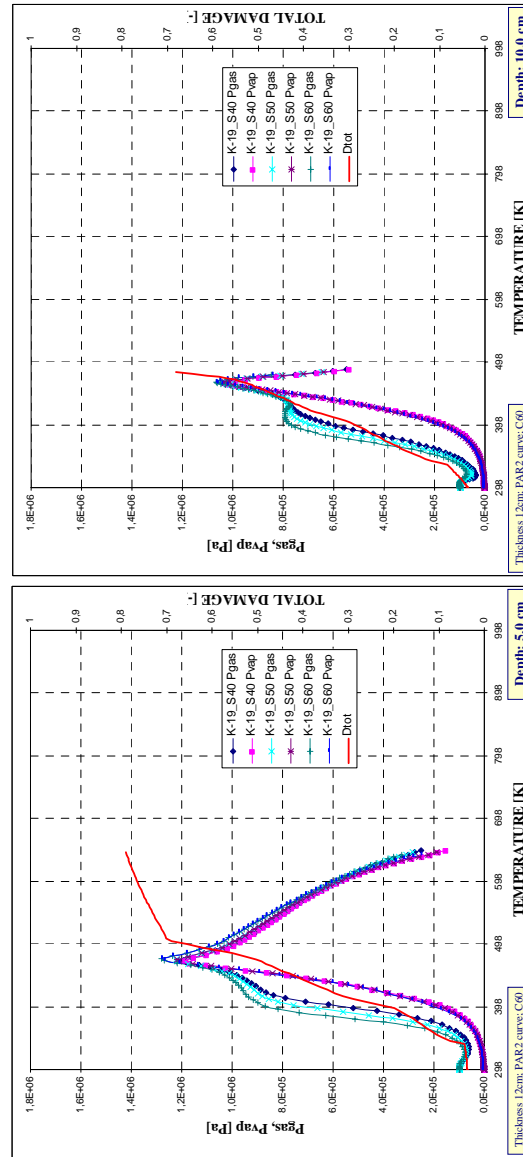


Figure 4-42. Total damage, vapour and gas pressure development for three values of initial saturation degree (40%, 50%, 60%) in case of $k=10^{-19} m^2$.

Thickness = 12 centimetres
 PAR2 Slow Parametric Heating curve
 Material C60

- (a) Depth 0,6 cm,
- (b) Depth 1,2 cm,
- (c) Depth 2,5 cm,
- (d) Depth 5,0 cm,
- (e) Depth 10 cm



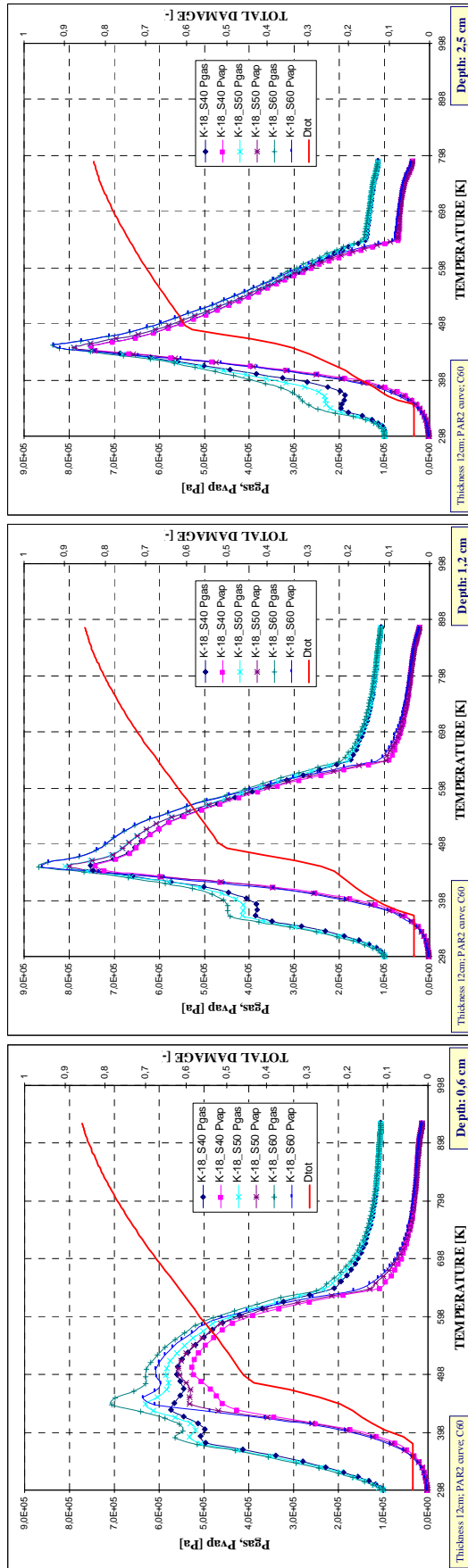
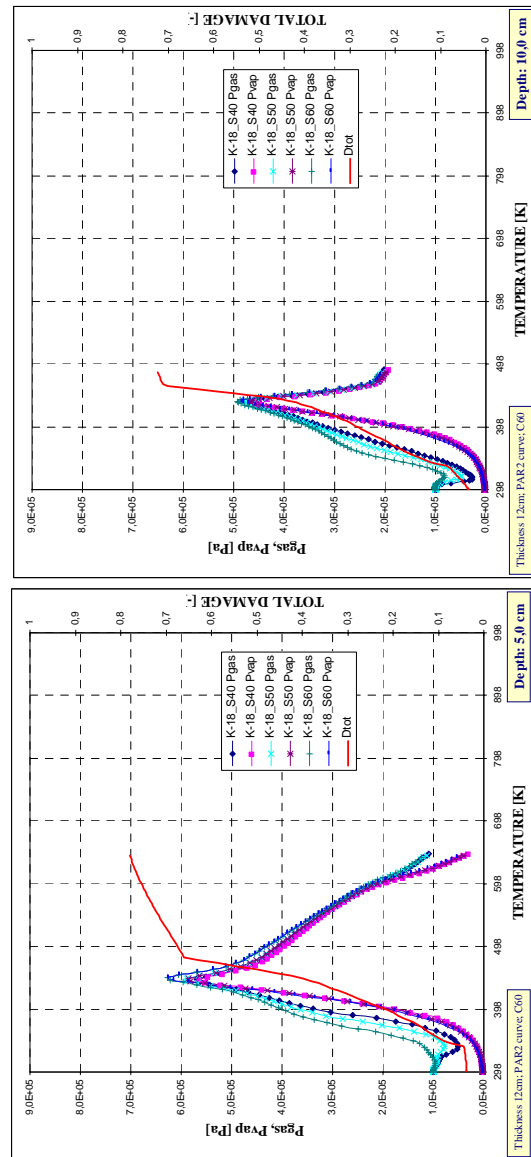


Figure 4-43. Total damage, vapour and gas pressure development for three values of initial saturation degree (40%, 50%, 60%) in case of $k=10^{-18} m^2$.

Thickness = 12 centimetres
 PAR2 Slow Parametric Heating curve
 Material C60

- (a) Depth 0,6 cm,
- (b) Depth 1,2 cm,
- (c) Depth 2,5 cm,
- (d) Depth 5,0 cm,
- (e) Depth 10 cm



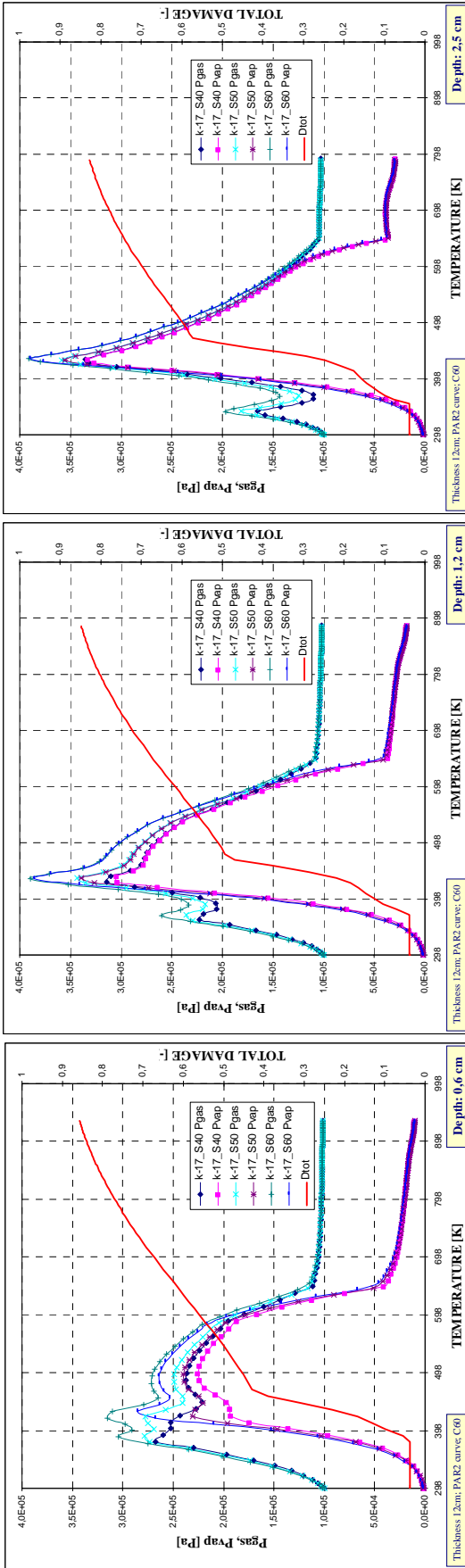
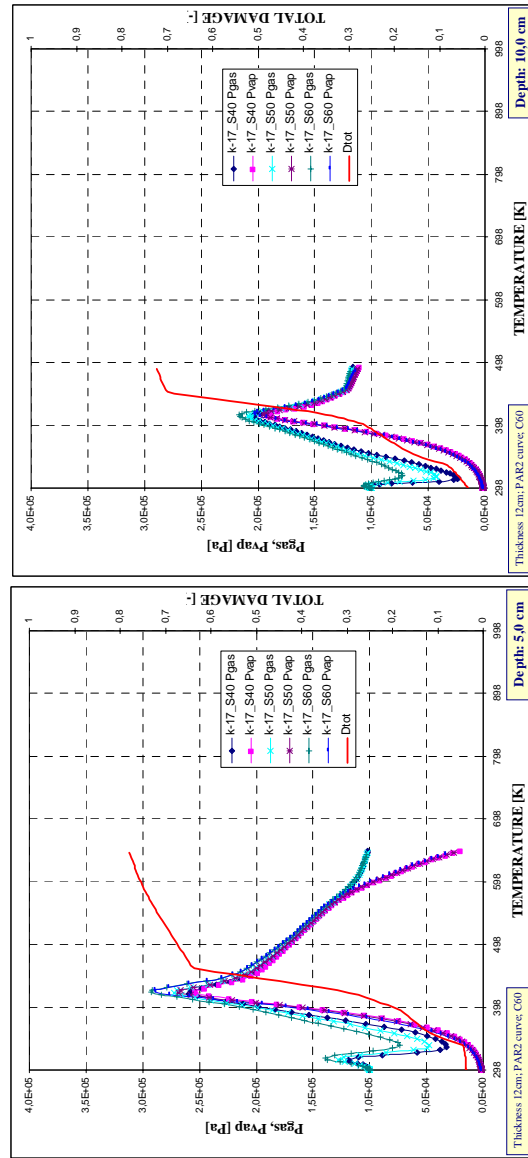


Figure 4-44. Total damage, vapour and gas pressure development for three values of initial saturation degree (40%, 50%, 60%) in case of $k=10^{-17} m^2$.

Thickness = 12 centimetres
 PAR2 Slow Parametric Heating curve
 Material C60

- (a) Depth 0,6 cm,
- (b) Depth 1,2 cm,
- (c) Depth 2,5 cm,
- (d) Depth 5,0 cm,
- (e) Depth 10 cm



4.5.4.3 THICKNESS 12 CM – HYDROCARBON HEATING CURVE – MATERIAL C60

Figure number	Thickness [cm]	Material	Heating curve	Intrinsic permeability [m ²]	Combination numbers for each initial saturation degree		
					S=40%	S=50%	S=60%
4-45	12	C60 (High Strength Concrete)	PAR 3 (Hydrocarbon)	10 ⁻¹⁹	76**	79**	82**
4-46				10 ⁻¹⁸	75**	78**	81**
4-47				10 ⁻¹⁷	74**	77**	80**

Remark **: As it was also previously explained, these combinations have had lack of convergence at certain instants because of the combination of extreme conditions, i.e. high rate of heating joint to the lower limit value of intrinsic permeability (10⁻¹⁹ m²), so results are represented up to the converged simulation time, resumed in the next table:

Combination	74	75	76	77	78	79	80	81	82	85	88	91
Final time [s]	1.050	1.020	150	1.065	285	148	1.080	1.080	180	150	150	150

For all of these three figures featured by increasing values of Intrinsic Permeability, conclusions must be derived with extreme caution since, as it was previously stated, some of these calculations have had lack of numerical convergence at stages earlier than the others. Taking this relevant fact into account, the following trends are observed:

- In these cases, due to the very high heating rate, the lower depth at which results are graphed, 0,3 centimetres, show the highest gas and vapour pressure values. However, the lower depth does not necessarily mean higher Total Damage levels at the same temperature; for instance, in the cases of an Intrinsic Permeability of 10⁻¹⁸ m², the Total Damage at a depth of 0,3 centimetres and a temperature of about 500 K is 0,12 while this value rises up to 0,25 at a depth of only 0,5 centimetres (where this temperature is reached later).
- The maximum absolute gas pressure reached during the simulation time is always found, for all of the depths considered, within the temperature range of 473 ±50 K, being this the temperature at which spalling is usually observed. However, the I_{s4} maximum values are achieved at much higher temperatures, within the range of 825 ±25 K mainly due to the fact that the Total Damage level at the 473 ±50 K is still low.
- It is observed an increase of the maximum absolute gas and vapour pressures as the Initial Saturation Degree increases, but the temperature at which these maxima appear is not affected. The maximum absolute vapour pressure values matches in time with the maximum of gas pressure. The difference between gas and vapour pressure is, in general and for all the cases, much lower than in the case featured by a Slow heating curve.
- On the contrary, comparing figures 4-46 and 4-47 it is clearly observed a pronounced sensitivity of both the maximum absolute gas pressure and the pressure corresponding to the maximum I_{s4} spalling index with the values of the Intrinsic Permeability, increasing all of these pressures as the latter decreases. With respect to figure 4-45, corresponding to the lowest Intrinsic Permeability, despite the early stage where calculations diverged there are observed really high values of gas pressure (up to 5-6 MPa), much higher than in the cases with higher values of the Intrinsic Permeability.
- Analogously, as Intrinsic Permeability increases the Total Damage level at the temperatures showing both the maximum absolute gas pressure and the pressure corresponding to the maximum I_{s4} spalling index decrease.
- It is worthy to remark that the evolution curve of Total Damage at all of the depths considered present a singularity – in the form of a sudden reduction of its slope almost to zero – at the temperatures where gas and vapour pressure maxima are reached. This fact suggests that the compressed gas is the main contribution to material damaging at the stages analyzed.

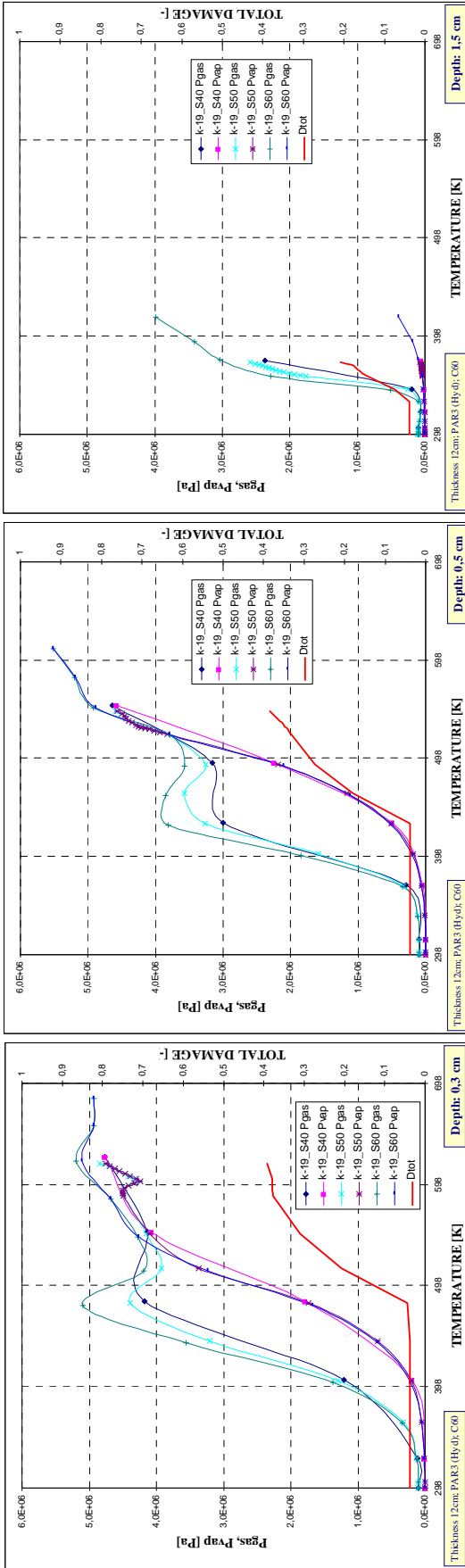
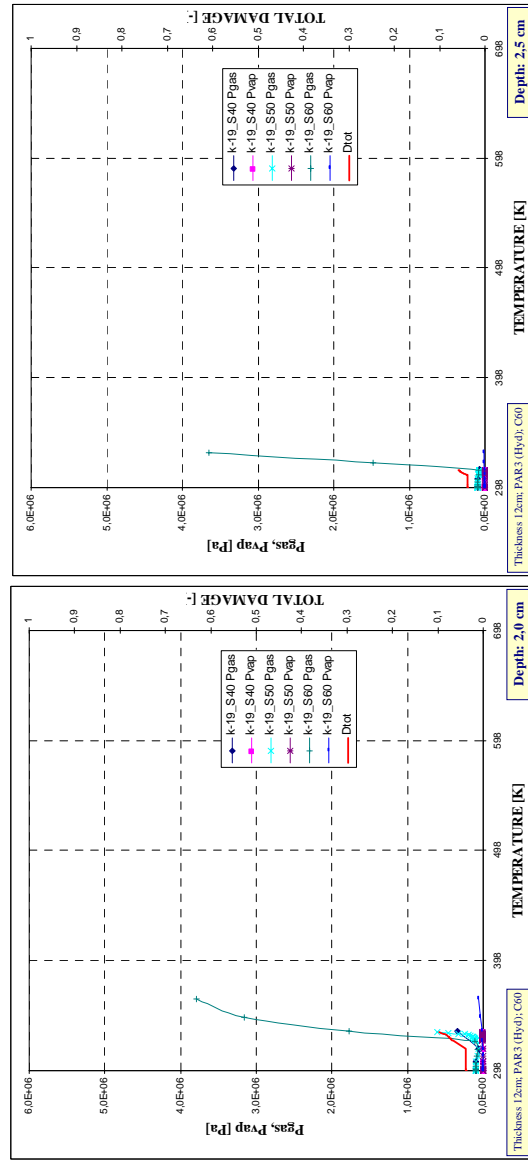


Figure 4-45. Total damage, vapour and gas pressure development for three values of initial saturation degree (40%, 50%, 60%) in case of $k=10^{-19} m^2$.

Thickness = 12 centimetres
 PAR3 Hydrocarbon Heating curve
 Material C60

- (a) Depth 0,3 cm,
- (b) Depth 0,5 cm,
- (c) Depth 1,5 cm,
- (d) Depth 2,0 cm,
- (e) Depth 2,5 cm



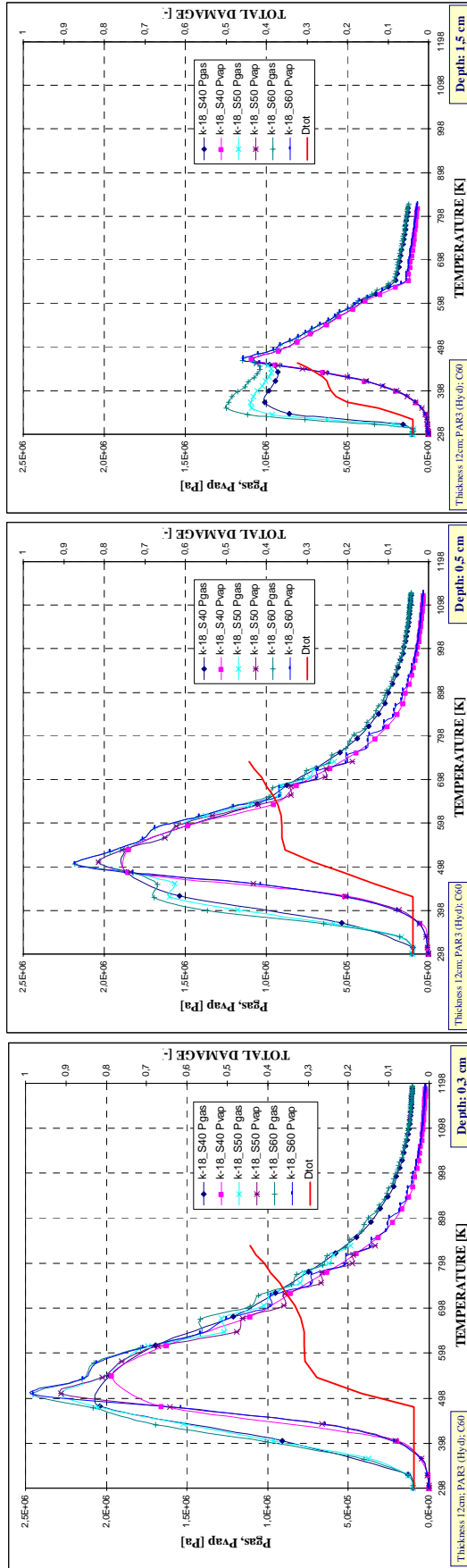
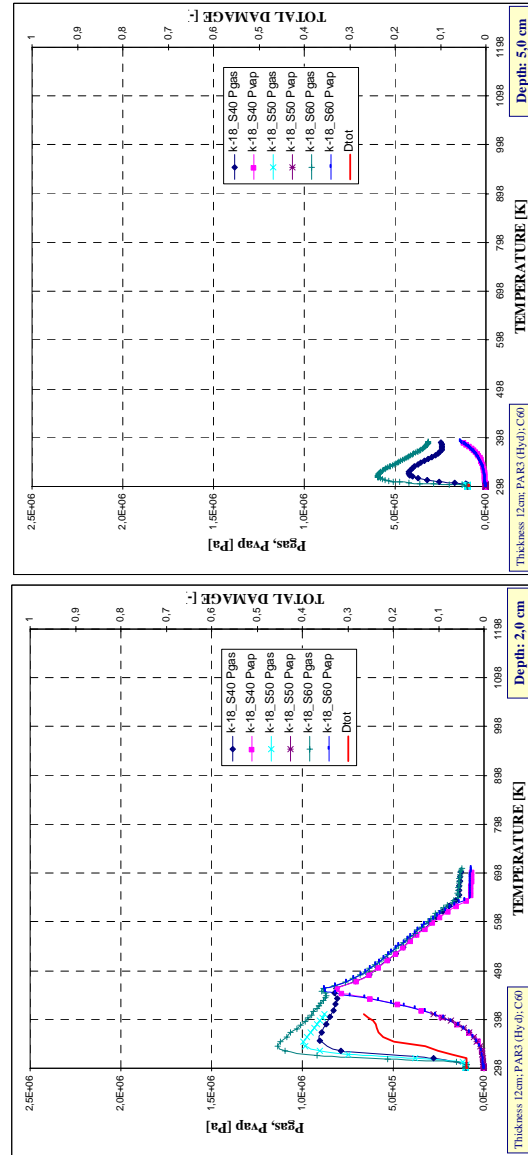


Figure 4-46. Total damage, vapour and gas pressure development for three values of initial saturation degree (40%, 50%, 60%) in case of $k=10^{-18} m^2$.

Thickness = 12 centimetres
 PAR3 Hydrocarbon heating curve
 Material C60

- (a) Depth 0,3 cm,
- (b) Depth 0,5 cm,
- (c) Depth 1,5 cm,
- (d) Depth 2,0 cm,
- (e) Depth 5,0 cm



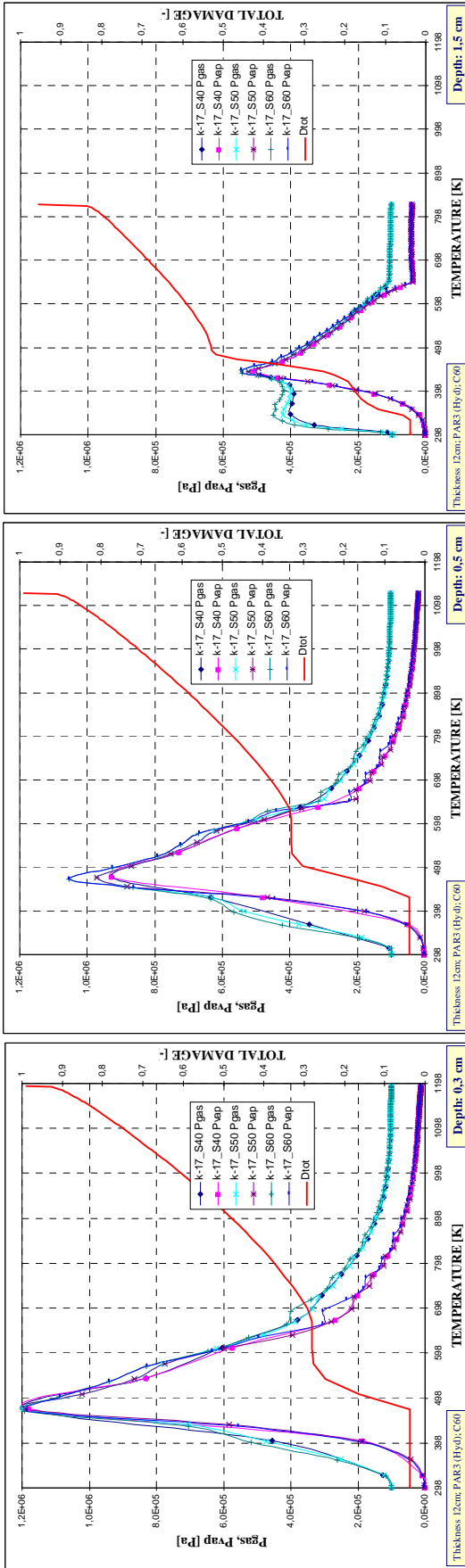
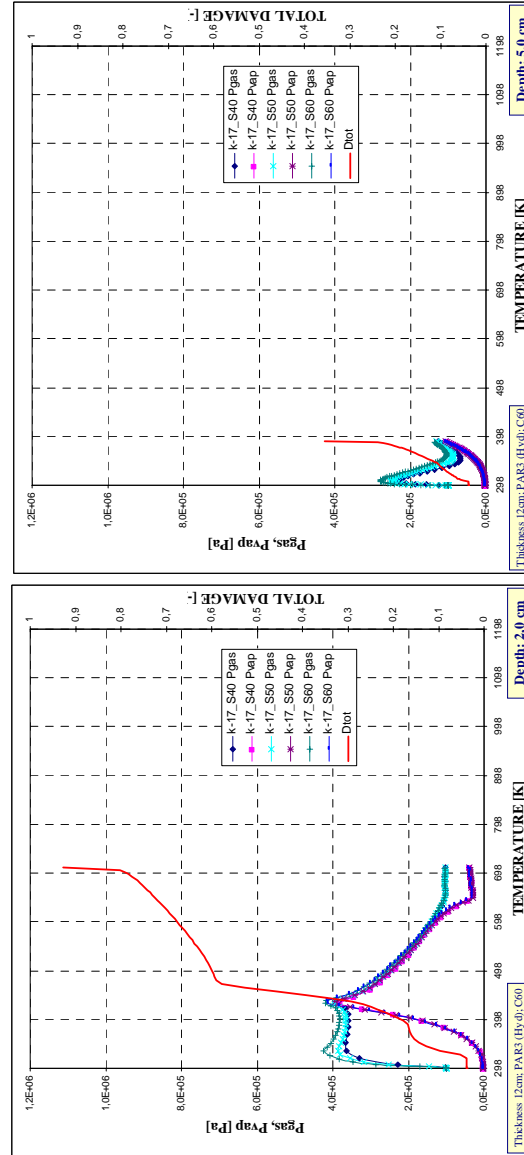


Figure 4-47. Total damage, vapour and gas pressure development for three values of initial saturation degree (40%, 50%, 60%) in case of $k=10^{-17} m^2$.

Thickness = 12 centimetres
 PAR3 Hydrocarbon Heating curve
 Material C60

- (a) Depth 0,3 cm,
- (b) Depth 0,5 cm,
- (c) Depth 1,5 cm,
- (d) Depth 2,0 cm,
- (e) Depth 5,0 cm



4.5.4.4 THICKNESS 12 CM – ISO HEATING CURVE – MATERIAL C90

Figure number	Thickness [cm]	Material	Heating curve	Intrinsic permeability [m^2]	Combination numbers for each initial saturation degree		
					S=40%	S=50%	S=60%
4-48	12	C90 (Ultra-High Strength Concrete)	PAR 1 (ISO 834)	10^{-19}	39	42	45
4-49				10^{-18}	38	41	44
4-50				10^{-17}	37	40	43

For all of these three figures featured by increasing values of Intrinsic Permeability, the following trends are observed:

- In these cases, the lower depth at which results are graphed, 0,6 centimetres, show the highest gas and vapour pressure values. However, the lower depth does not necessarily mean higher Total Damage levels at the same temperature. A double peak of gas pressure in the case with the lowest Intrinsic Permeability is first caused by an increase of the dry air pressure and, afterwards, of the vapour pressure.
- The maximum absolute gas pressure reached during the three hours of simulations is always found, for all of the depths considered, within the temperature range of 448 ± 50 K, being this somewhat lower than the temperature at which spalling is usually observed. This fact suggests that despite the I_{s4} maximum values are achieved at higher temperatures, within the range of 595 ± 25 K, spalling may be occurring before the instants corresponding to these maxima, as it was explained on table 4-43.
- It is observed an increase of the maximum absolute gas and vapour pressures as the Initial Saturation Degree increases, but the temperature at which these maxima appear is not affected by the Initial Saturation Degree. The maximum absolute vapour pressure values matches in time with the maximum of gas pressure (in particular, with the second maximum in the case of the lowest Intrinsic Permeability).
- Comparing these three figures it is clearly observed a pronounced sensitivity of both the maximum absolute gas pressure and the pressure corresponding to the maximum I_{s4} spalling index with the values of the Intrinsic Permeability, increasing all of these pressures as the latter decreases. The evolution of the temperature at which these maxima are found with Intrinsic Permeability does not present a clear trend so again, in these cases, it is not possible to conclude – from these graphs – that low values of Intrinsic Permeability may lead to spalling phenomena occurring earlier.
- As Intrinsic Permeability increases the Total Damage level at the temperatures showing both the maximum absolute gas pressure and the pressure corresponding to the maximum I_{s4} spalling index decrease slightly. At the inner layers, 10 centimetres away from the heated surface, it is observed that the material is not completely cracked at the end of the simulation and that the final Total Damage level also decreases slightly as Intrinsic Permeability increases.
- It is worthy to remark that the evolution curve of Total Damage at all of the depths considered present a singularity – in the form of a sudden reduction of its slope – at temperatures slightly higher where gas and vapour pressure maxima have been reached. This fact suggests that the compressed gas contribution to material damaging is significant but there is a delay in its effect on Total Damage.

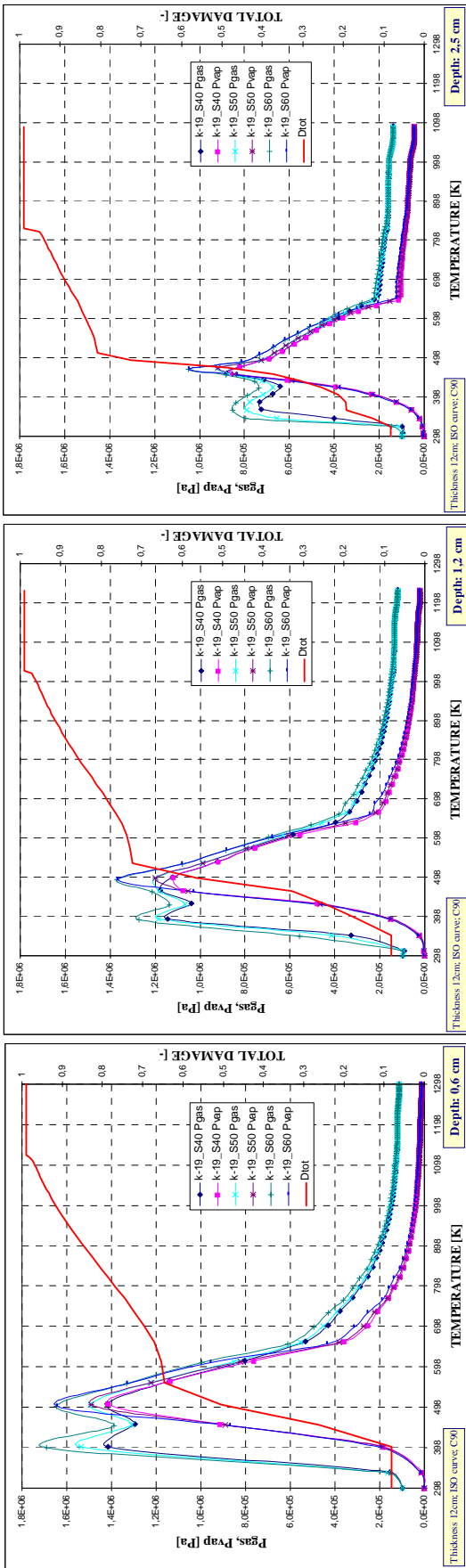
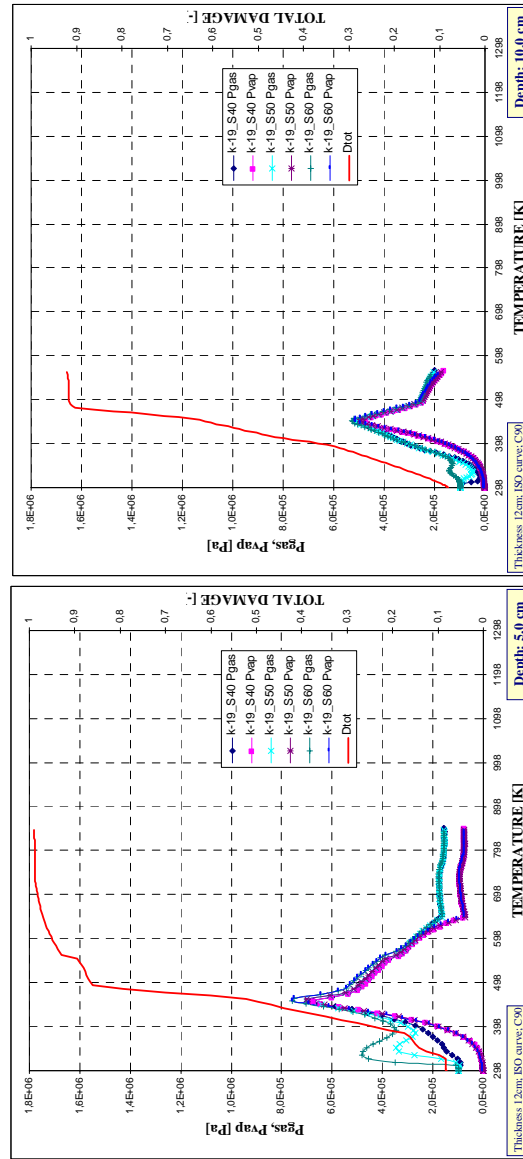


Figure 4-48. Total damage, vapour and gas pressure development for three values of initial saturation degree (40%, 50%, 60%) in case of $k=10^{-19} m^2$.

Thickness = 12 centimetres
ISO 834 Heating curve
Material C90

- (a) Depth 0,6 cm,
- (b) Depth 1,2 cm,
- (c) Depth 2,5 cm,
- (d) Depth 5,0 cm,
- (e) Depth 10 cm



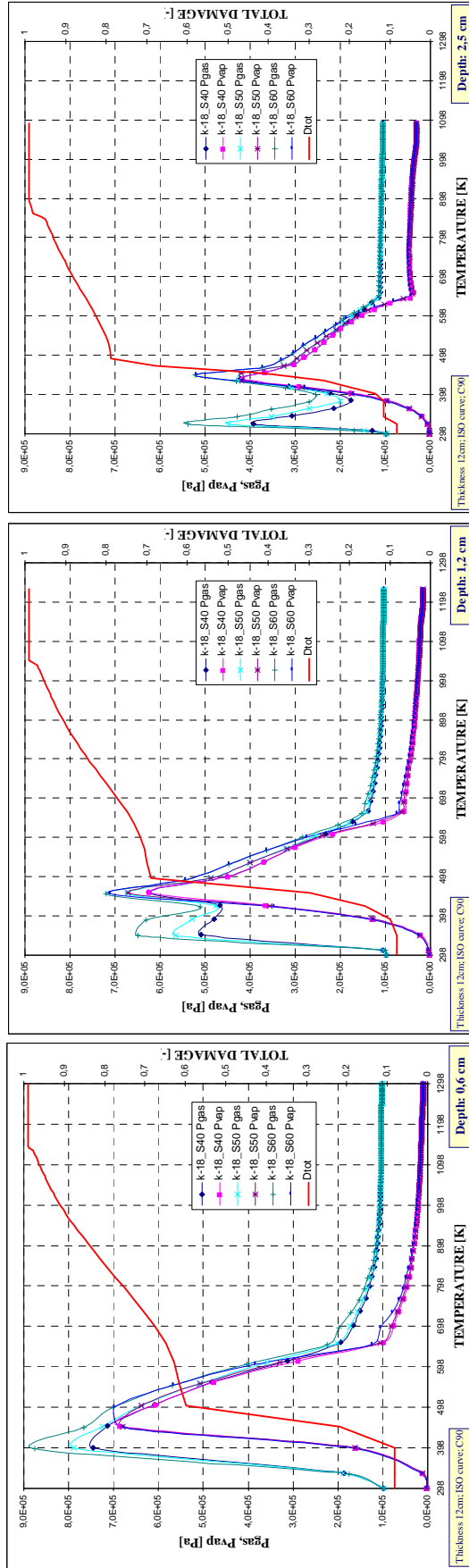
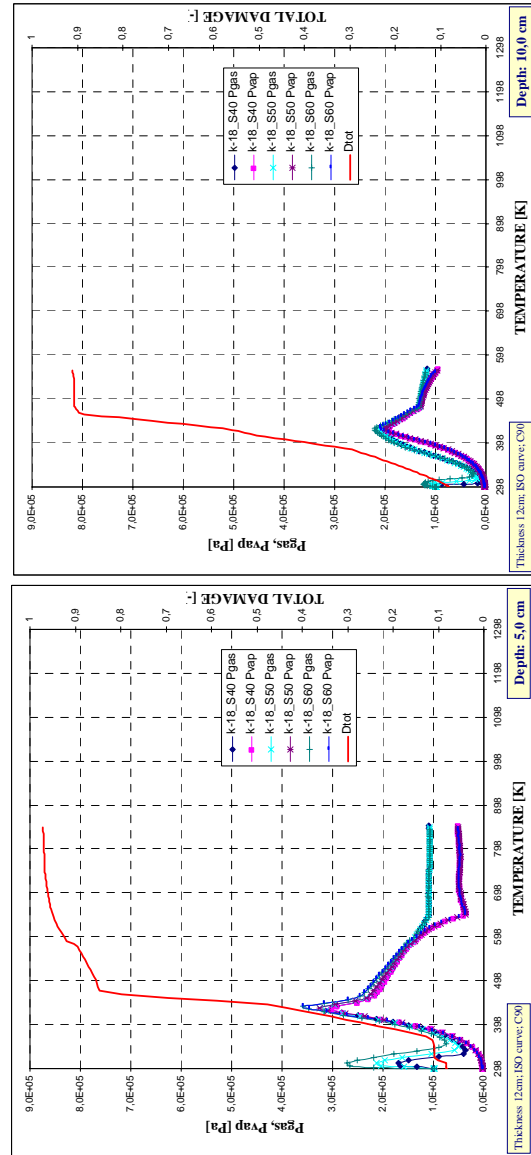


Figure 4-49. Total damage, vapour and gas pressure development for three values of initial saturation degree (40%, 50%, 60%) in case of $k=10^{-18} m^2$.

Thickness = 12 centimetres
ISO 834 Heating curve
Material C90

- (a) Depth 0,6 cm,
- (b) Depth 1,2 cm,
- (c) Depth 2,5 cm,
- (d) Depth 5,0 cm,
- (e) Depth 10 cm



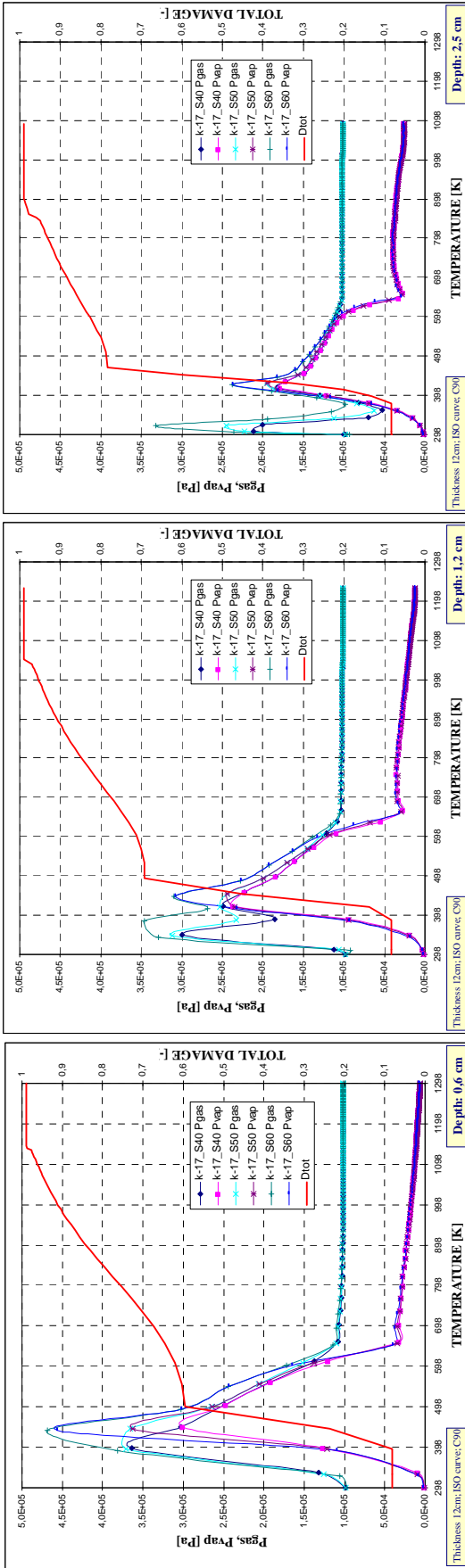
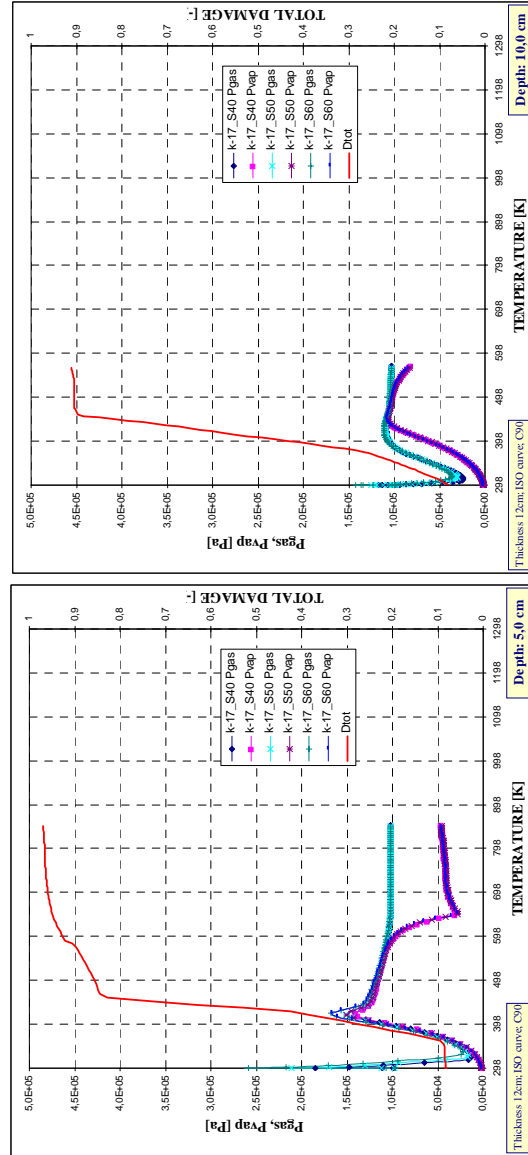


Figure 4-50. Total damage, vapour and gas pressure development for three values of initial saturation degree (40%, 50%, 60%) in case of $k=10^{-17} \text{ m}^2$.

Thickness = 12 centimetres
ISO 834 Heating curve
Material C90

- (a) Depth 0,6 cm,
- (b) Depth 1,2 cm,
- (c) Depth 2,5 cm,
- (d) Depth 5,0 cm,
- (e) Depth 10 cm



4.5.4.5 THICKNESS 12 CM – PAR2 SLOW HEATING CURVE – MATERIAL C90

Figure number	Thickness [cm]	Material	Heating curve	Intrinsic permeability [m ²]	Combination numbers for each initial saturation degree		
					S=40%	S=50%	S=60%
4-51	12	C90 (Ultra-High Strength Concrete)	PAR 2 (Slow parametric)	10 ⁻¹⁹	48	51	54
4-52				10 ⁻¹⁸	47	50	53
4-53				10 ⁻¹⁷	46	49	52

For all of these three figures featured by increasing values of Intrinsic Permeability, the following trends are observed:

- In these cases, the lower depth at which results are graphed, 0,6 centimetres, does not show either the highest gas and vapour pressure values or the highest Total Damage. On the contrary, the depth at which these maxima appear increases with Intrinsic Permeability, being at 1,2 centimetres for 10⁻¹⁹ and 10⁻¹⁸ m², and then it decreases again to 0,6 centimetres for 10⁻¹⁷ m². The lower depth does not necessarily mean higher Total Damage levels at the same temperature; for instance, in the cases of an Intrinsic Permeability of 10⁻¹⁹ m², the Total Damage at a depth of 0,6 centimetres and a temperature of about 400 K is about zero while this value rises to 0,35 at a depth of 10 centimetres (where this temperature is reached much later).
- The maximum absolute gas pressure reached during the three hours of simulations, lower than in the cases featured by the ISO heating curve, is always found for all of the depths considered within the temperature range of 473 ±50 K, being this the temperature at which spalling is usually observed. This fact suggests that despite the I_{s4} maximum values are achieved at higher temperatures, within the range of 540 ±25 K, spalling may be occurring before the instants corresponding to these maxima.
- In this case, where the heating curve is much slower than that considered in the previous paragraph, it is observed a higher increase of the maximum absolute gas and vapour pressures as the Initial Saturation Degree increases, although the temperature at which these maxima appear is still not affected by the Initial Saturation Degree. The maximum absolute vapour pressure values matches in time with the maximum of gas pressure.
- On the other hand, comparing these three figures it is again clearly observed a pronounced sensitivity of both the maximum absolute gas pressure and the pressure corresponding to the maximum I_{s4} spalling index with the values of the Intrinsic Permeability, increasing all of these pressures as the latter decreases.
- As Intrinsic Permeability increases the Total Damage level at the temperatures showing both the maximum absolute gas pressure and the pressure corresponding to the maximum I_{s4} spalling index decrease. However, at the inner layers, among 5 and 10 centimetres away from the heated surface, it is observed that the material is not completely cracked at the end of the simulation and that the final Total Damage level here increases as Intrinsic Permeability increases.
- It is worthy to remark that the evolution curve of Total Damage at all of the depths considered present a singularity – in the form of a sudden reduction of its slope – at temperatures where gas and vapour pressure evolutions present inflection points. This fact might be related to high gradients – increases – in capillary pressure.

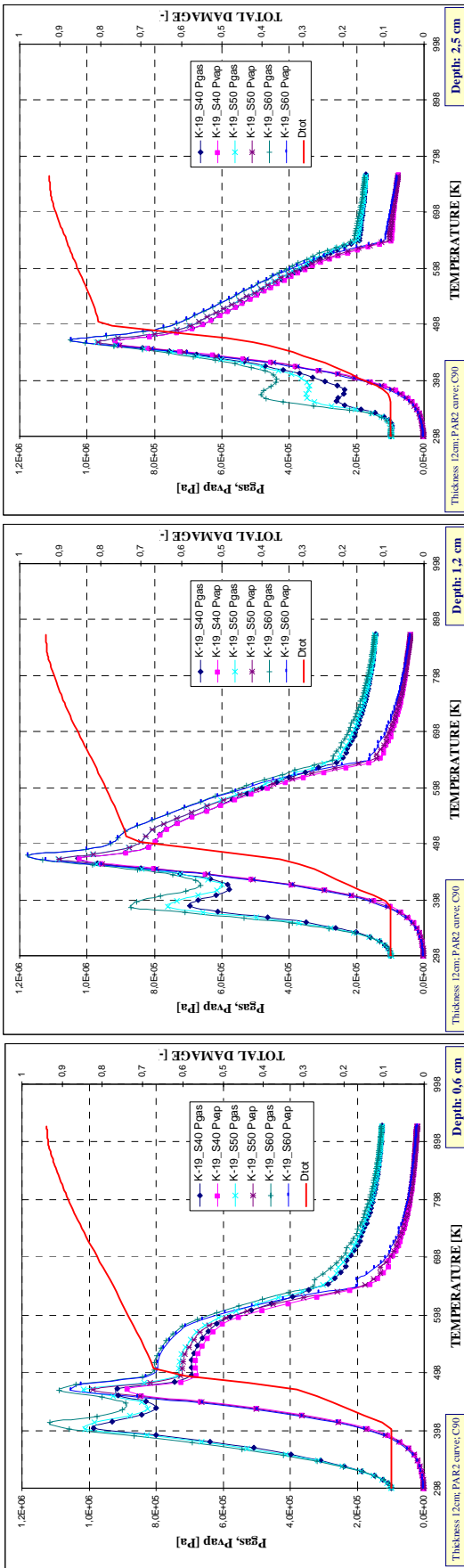
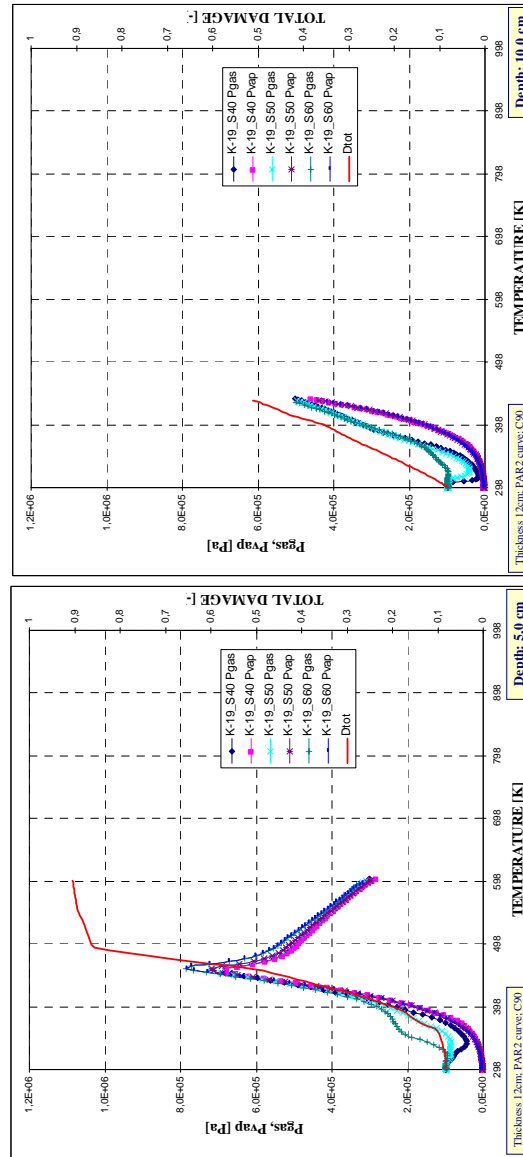


Figure 4-51. Total damage, vapour and gas pressure development for three values of initial saturation degree (40%, 50%, 60%) in case of $k=10^{-19} m^2$.

Thickness = 12 centimetres
 PAR2 Slow Parametric Heating curve
 Material C90

- (a) Depth 0,6 cm,
- (b) Depth 1,2 cm,
- (c) Depth 2,5 cm,
- (d) Depth 5,0 cm,
- (e) Depth 10 cm



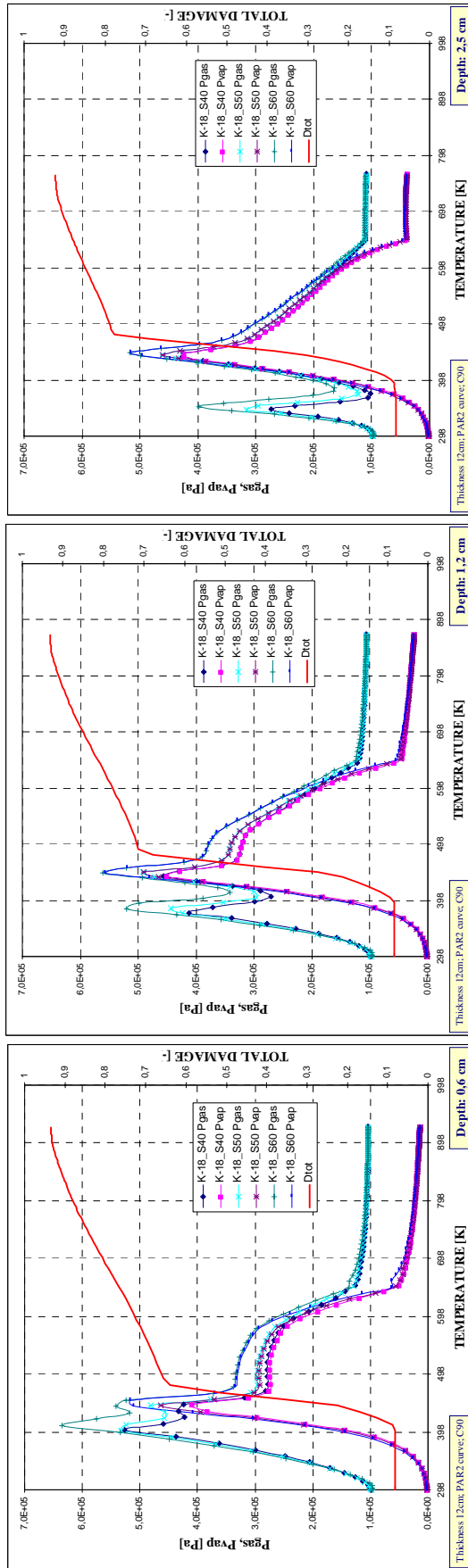
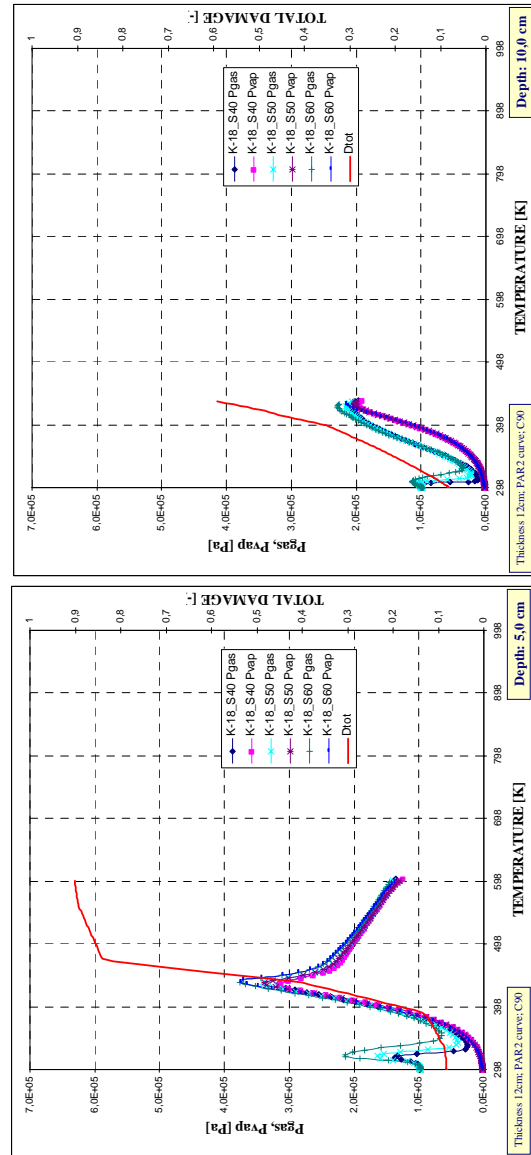


Figure 4-52. Total damage, vapour and gas pressure development for three values of initial saturation degree (40%, 50%, 60%) in case of $k=10^{-18} m^2$.

Thickness = 12 centimetres
 PAR2 Slow Parametric Heating curve
 Material C90

- (a) Depth 0,6 cm,
- (b) Depth 1,2 cm,
- (c) Depth 2,5 cm,
- (d) Depth 5,0 cm,
- (e) Depth 10 cm



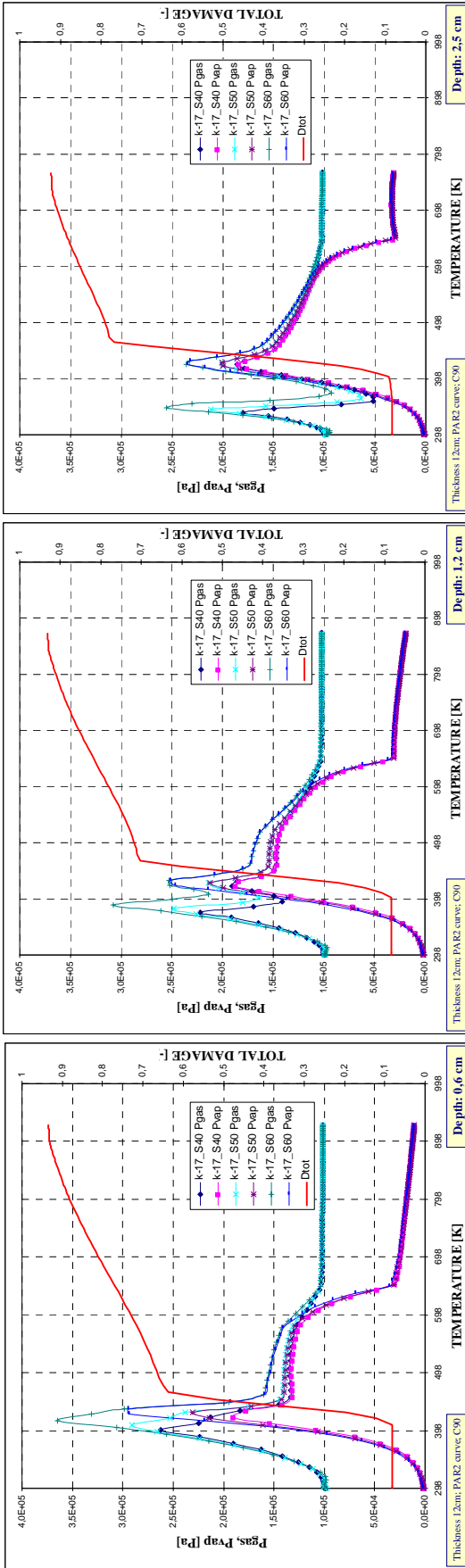
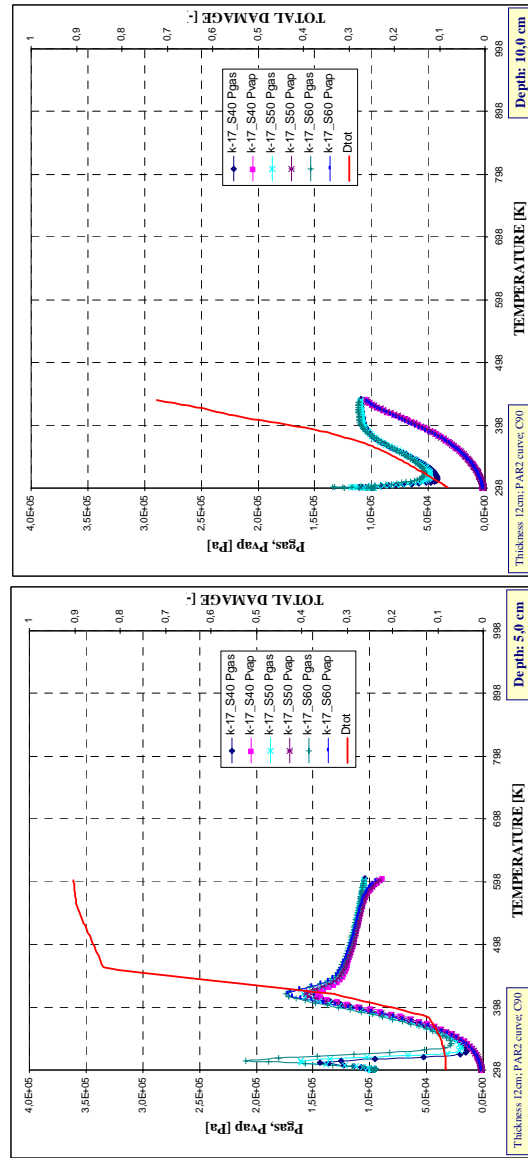


Figure 4-53. Total damage, vapour and gas pressure development for three values of initial saturation degree (40%, 50%, 60%) in case of $k=10^{-17} m^2$.

Thickness = 12 centimetres
 PAR2 Slow Parametric Heating curve
 Material C90

- (a) Depth 0,6 cm,
- (b) Depth 1,2 cm,
- (c) Depth 2,5 cm,
- (d) Depth 5,0 cm,
- (e) Depth 10 cm



4.5.4.6 THICKNESS 12 CM – HYDROCARBON HEATING CURVE – MATERIAL C90

Figure number	Thickness [cm]	Material	Heating curve	Intrinsic permeability [m ²]	Combination numbers for each initial saturation degree		
					S=40%	S=50%	S=60%
4-54	12	C90 (Ultra-High Strength Concrete)	PAR 3 (Hydrocarbon)	10 ⁻¹⁹	85**	88**	91**
4-55				10 ⁻¹⁸	84*	87*	90*
4-56				10 ⁻¹⁷	83*	86*	89*

Remark *: As it was previously explained, these combinations have been run up to a total simulation time of 2.400 seconds (instead of the general simulation time of 10.800 seconds) because the high rate of heating induces a value of the Total Damage at 2.400 seconds of 0.99, which means that the material is completely destroyed, so it is not worthy to carry on simulations beyond this point.

Remark **: As it was also previously explained, these combinations have had lack of convergence at certain instants because of the combination of extreme conditions, i.e. high rate of heating joint to the lower limit value of intrinsic permeability (10⁻¹⁹ m²), so results are represented up to the converged simulation time, resumed in the next table:

Combination	74	75	76	77	78	79	80	81	82	85	88	91
Final time [s]	1.050	1.020	150	1.065	285	148	1.080	1.080	180	150	150	150

For all of these three figures featured by increasing values of Intrinsic Permeability, conclusions must be derived with extreme caution since, as it was previously stated, some of these calculations have had lack of numerical convergence at stages earlier than the others. Taking this relevant fact into account, the following trends are observed:

- In these cases, due to the very high heating rate, the lower depth at which results are graphed, 0,3 centimetres, show the highest gas and vapour pressure values. However, the lower depth does not necessarily mean higher Total Damage levels at the same temperature.
- The maximum absolute gas pressure reached during the simulation time is always found, for all of the depths considered, within the temperature range of 473 ±50 K, being this the temperature at which spalling is usually observed. However, the I_{s4} maximum values are achieved at much higher temperatures, within the range of 795 ±25 K in the case of an Intrinsic Permeability of 10⁻¹⁸ m² and 610 ±25 K in the case of an Intrinsic Permeability of 10⁻¹⁷ m², mainly due to the fact that the Total Damage level at the 473 ±50 K is still low.
- It is observed a very slight increase of the maximum absolute gas and vapour pressures as the Initial Saturation Degree increases, and the temperature at which these maxima appear is neither affected significantly by the Initial Saturation Degree. The maximum absolute vapour pressure values appear later than the maxima of gas pressure. The difference between gas and vapour pressure is, in general and for all the cases, much lower than in the case featured by a Slow heating curve.
- On the contrary, comparing figures 4-55 and 4-56 it is clearly observed a pronounced sensitivity of both the maximum absolute gas pressure and the pressure corresponding to the maximum I_{s4} spalling index with the values of the Intrinsic Permeability, increasing all of these pressures as the latter decreases. With respect to figure 4-54, corresponding to the lowest Intrinsic Permeability, despite the early stage where calculations diverged there are observed really high values of gas pressure (up to 4 MPa), twice and ever four times those corresponding to the cases with 10⁻¹⁸ m² and 10⁻¹⁷ m² values of the Intrinsic Permeability respectively.
- Analogously, as Intrinsic Permeability increases the Total Damage level at the temperatures showing both the maximum absolute gas pressure and the pressure corresponding to the maximum I_{s4} spalling index decrease, being remarkable the high levels of Total Damage obtained for the lowest Intrinsic Permeability at only 2,5 minutes from the start of the fire (about 0,60 in the outer layers).

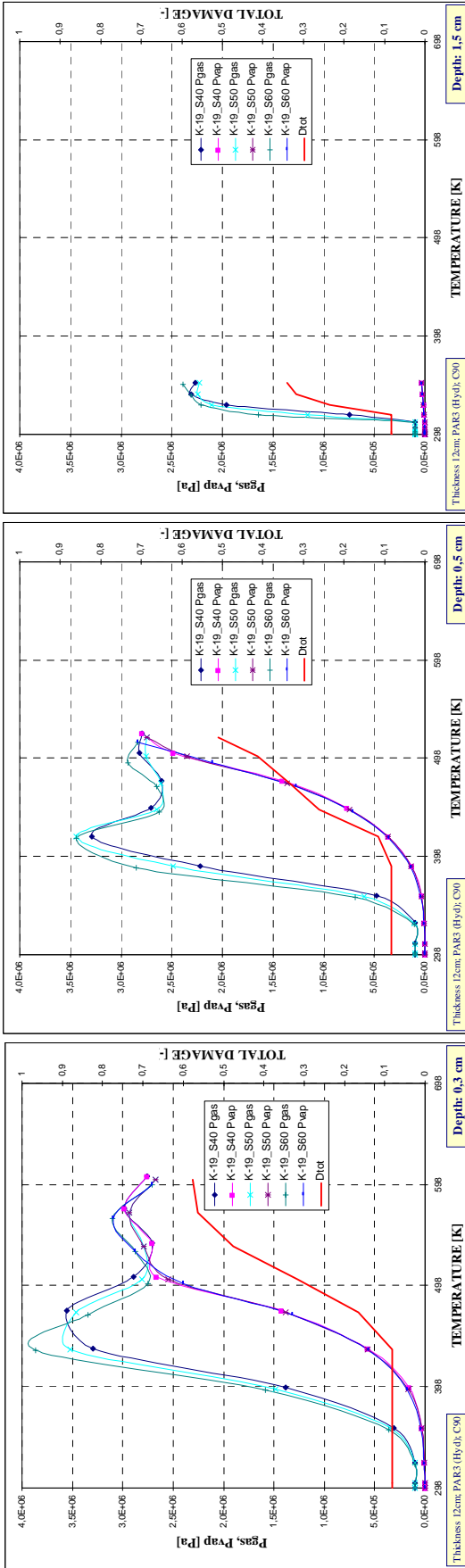
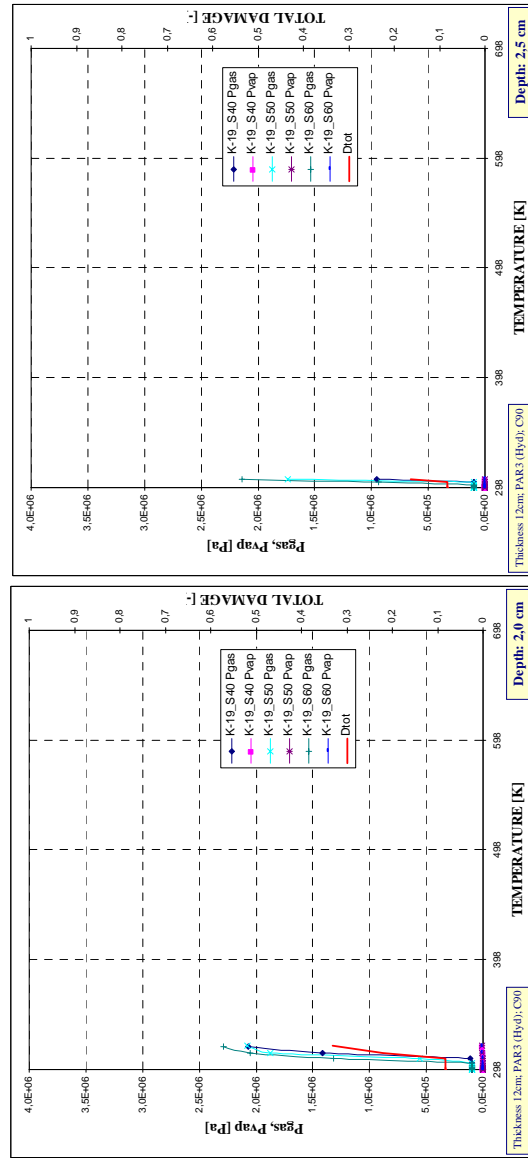


Figure 4-54. Total damage, vapour and gas pressure development for three values of initial saturation degree (40%, 50%, 60%) in case of $k=10^{-19} m^2$.

Thickness = 12 centimetres
 PAR3 Hydrocarbon Heating curve
 Material C90

- (a) Depth 0,3 cm,
- (b) Depth 0,5 cm,
- (c) Depth 1,5 cm,
- (d) Depth 2,0 cm,
- (e) Depth 2,5 cm



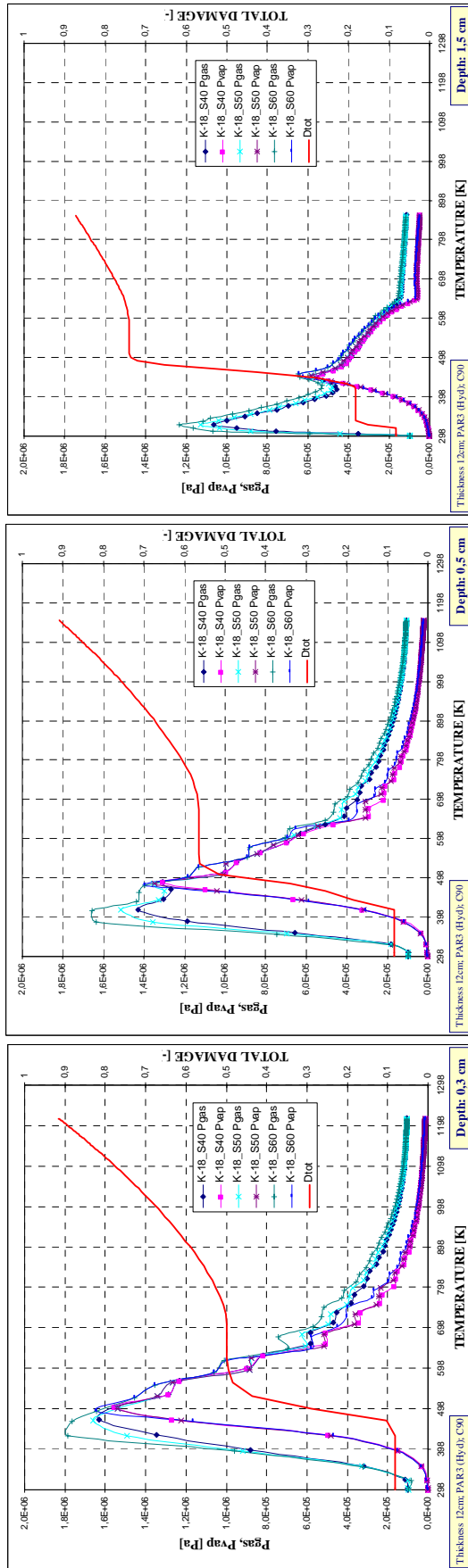
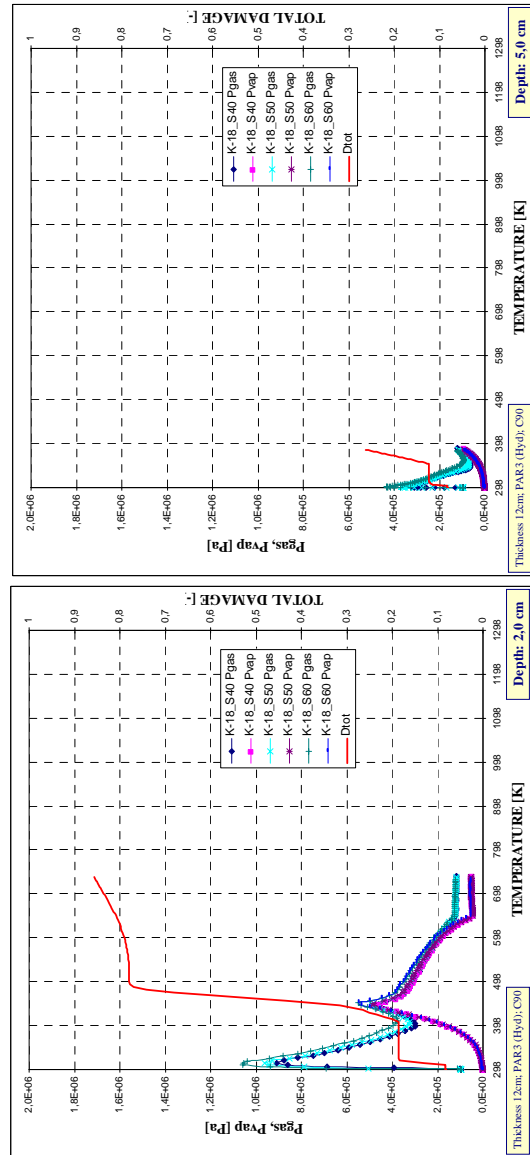


Figure 4-55. Total damage, vapour and gas pressure development for three values of initial saturation degree (40%, 50%, 60%) in case of $k=10^{-18} m^2$.

Thickness = 12 centimetres
 PAR3 Hydrocarbon heating curve
 Material C90

- (a) Depth 0,3 cm,
- (b) Depth 0,5 cm,
- (c) Depth 1,5 cm,
- (d) Depth 2,0 cm,
- (e) Depth 5,0 cm



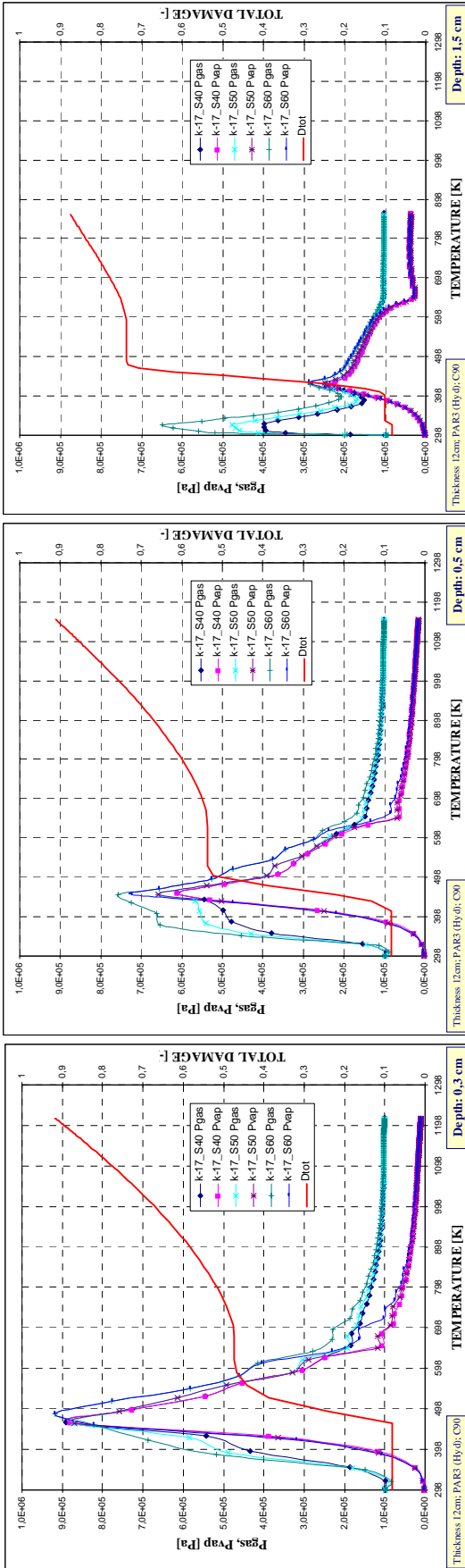
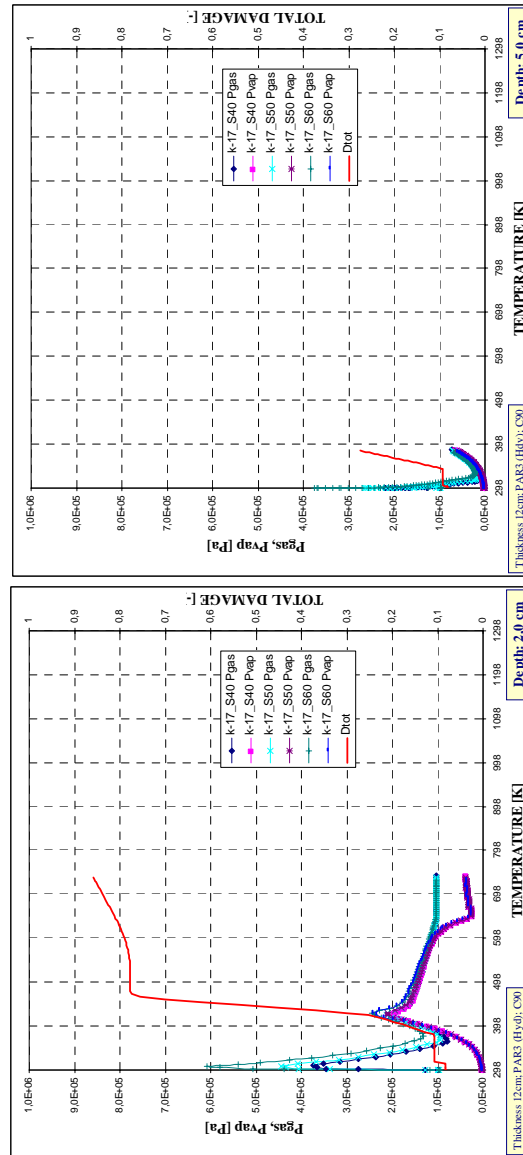


Figure 4-56. Total damage, vapour and gas pressure development for three values of initial saturation degree (40%, 50%, 60%) in case of $k=10^{-17} m^2$.

Thickness = 12 centimetres
 PAR3 Hydrocarbon Heating curve
 Material C90

- (a) Depth 0,3 cm,
- (b) Depth 0,5 cm,
- (c) Depth 1,5 cm,
- (d) Depth 2,0 cm,
- (e) Depth 5,0 cm



4.5.5 Comparison for constant values of the Initial Saturation Degree

Analogously to what done previously with intrinsic permeability, in this paragraph a direct comparison of the results of the cases characterized by the same value of the initial saturation degree is shown.

The graphics are presented in Figures 4.57 to 4.74 for values of the initial saturation degree ranging from 40% to 60% and for five different depths from the heated surface detailed in the following table:

	<i>Combinations with PAR1 (ISO) and PAR2 (Slow-parametric) heating curves</i>	<i>Combinations with PAR3 (Hydrocarbon) heating curve and intrinsic permeability from 10^{-17} to 10^{-18} m²</i>	<i>Combinations with PAR3 (Hydrocarbon) heating curve and intrinsic permeability 10^{-19} m²</i>
<i>(a) First depth</i>	0,6 centimetres	0,3 centimetres	0,3 centimetres
<i>(b) Second depth</i>	1,2 centimetres	0,5 centimetres	0,5 centimetres
<i>(c) Third depth</i>	2,5 centimetres	1,5 centimetres	1,5 centimetres
<i>(d) Fourth depth</i>	5,0 centimetres	2,0 centimetres	2,0 centimetres
<i>(e) Fifth depth</i>	10,0 centimetres	5,0 centimetres	2,5 centimetres

Table 4-55. Depths of representation for each type of combination.

Again, the reason for choosing different representation depths for combinations characterised by PAR1 and PAR2 heating curves from those corresponding to PAR3 heating curve is the highest gradients of the represented data in the proximity of the heated surface in the case of the fastest heating (PAR3 Hydrocarbon heating curve).

Furthermore, the fifth depth chosen for the combinations with PAR3 heating curve and an intrinsic permeability of 10^{-19} m² has been selected smaller than that corresponding to smaller intrinsic permeability values because, otherwise, no representative results would have been possible to show within the converged simulation time.

The graphics represent the time history of gas pressure, vapour pressure and Mechanical Damage for each set of three combinations characterised by the same initial saturation degree (this means that within each graphic, combinations characterised by an intrinsic permeability of 10^{-17} , 10^{-18} and 10^{-19} m² are compared).

For this case, the Mechanical Damage, *d*, has been chosen instead of the Total Damage, *D*, in order to show some more information about the contribution of Mechanical and Thermo-Chemical damages to the Total Damage.

Taking into account development of temperature *T* in time it has been possible to show the distribution of the mentioned variables in the domain of temperature.

It must be remarked that, in order to avoid complicating in excess the interpretation of the graphic results, the Mechanical Damage represented in each graphic is that corresponding to an intrinsic permeability of 10^{-18} m² which is the average value of the considered range for this parameter.

The graphics are organised according to the following table.

It must be also remarked that, as it has been explained in previous paragraphs, combinations corresponding to thicknesses of 24 and 50 centimetres have been discarded for this type of results representation because they showed no significant deviations with respect to those results obtained for the cases of 12 centimetres.

Figure number	Thickness [cm]	Material	Heating curve	Initial Saturation Degree	Combination numbers for each intrinsic permeability value [m ²]		
					10 ⁻¹⁷	10 ⁻¹⁸	10 ⁻¹⁹
4-57	12	C60 (High Strength Concrete)	PAR 1 (ISO 834)	40%	1	2	3
4-58				50%	4	5	6
4-59				60%	7	8	9
4-60			PAR 2 (Slow parametric)	40%	10	11	12
4-61				50%	13	14	15
4-62				60%	16	17	18
4-63			PAR 3 (Hydrocarbon)	40%	74**	75**	76**
4-64				50%	77**	78**	79**
4-65				60%	80**	81**	82**
4-66		C90 (Ultra-High Strength Concrete)	PAR 1 (ISO 834)	40%	37	38	39
4-67				50%	40	41	42
4-68				60%	43	44	45
4-69			PAR 2 (Slow parametric)	40%	46	47	48
4-70				50%	49	50	51
4-71				60%	52	53	54
4-72			PAR 3 (Hydrocarbon)	40%	83*	84*	85**
4-73				50%	86*	87*	88**
4-74				60%	89*	90*	91**

Table 4-56. List of graphics included in the comparison for constant values of Intrinsic Permeability.

Remark *: As it was previously explained, these combinations have been run up to a total simulation time of 2.400 seconds (instead of the general simulation time of 10.800 seconds) because the high rate of heating induces a value of the Total Damage at 2.400 seconds of 0.99, which means that the material is completely destroyed, so it is not worthy to carry on simulations beyond this point.

Remark **: As it was also previously explained, these combinations have had lack of convergence at certain instants because of the combination of extreme conditions, i.e. high rate of heating joint to the lower limit value of intrinsic permeability (10⁻¹⁹ m²), so results are represented up to the converged simulation time, resumed in the next table:

Combination	74	75	76	77	78	79	80	81	82	85	88	91
Final time [s]	1.050	1.020	150	1.065	285	148	1.080	1.080	180	150	150	150

As it will be explained later on, the cases with an intrinsic permeability value of 10⁻¹⁹ m² and an initial saturation degree of 60% are the most dangerous (for each set of the rest of conditions), while for the cases with a value of the intrinsic permeability greater than 10⁻¹⁸ m², and C90 material, the probability of spalling occurrence seems sufficiently low with regard to the integrity of the structure (this is not the case with C60, where intrinsic permeability values greater than 10⁻¹⁸ m² also lead to spalling occurrence). This conclusion is not valid for the cases where the Hydrocarbon heating curve is considered, since in all of these cases spalling occurs independently on the value of the intrinsic permeability.

Analogous conclusions to those excerpted from the analysis of the comparison for constant values of the Intrinsic Permeability may be excerpted from next graphics. The following graphics are extremely useful to confirm what it has been already concluded about the cases where results show sensitivity to the Initial Saturation Degree and where not, addressing to the previous paragraphs for their study.

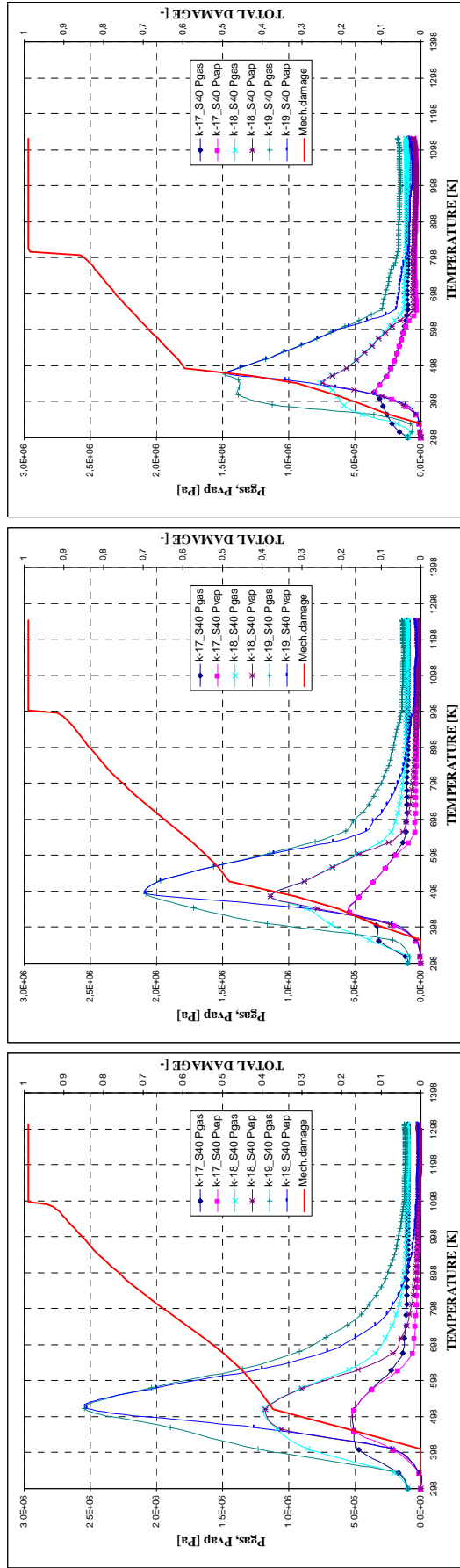
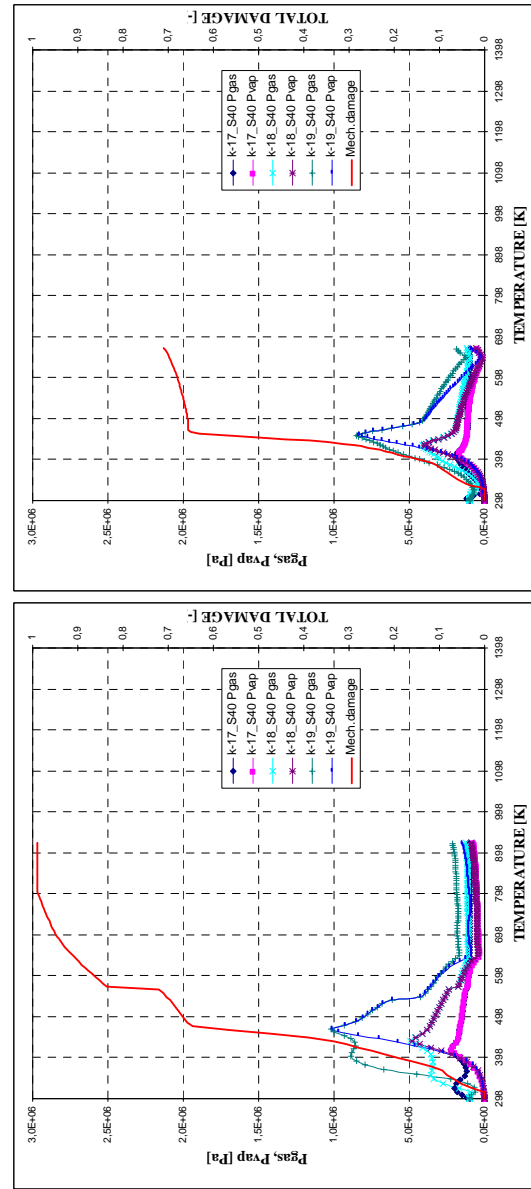


Figure 4-57 Total damage, vapour and gas pressure development for three values of intrinsic permeability ($10^{-17}, 10^{-18}, 10^{-19}$) in case of $s=40\%$.

Thickness = 12 centimetres
ISO 834 Heating curve
Material C60

- (a) Depth 0,6 cm,
- (b) Depth 1,2 cm,
- (c) Depth 2,5 cm,
- (d) Depth 5,0 cm,
- (e) Depth 10 cm



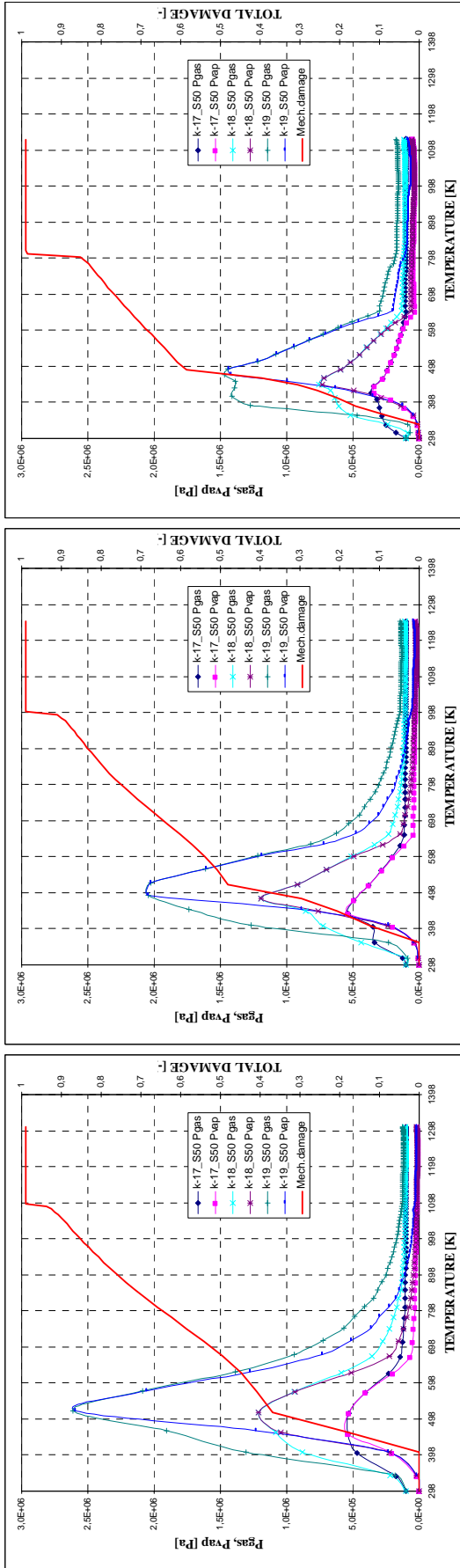
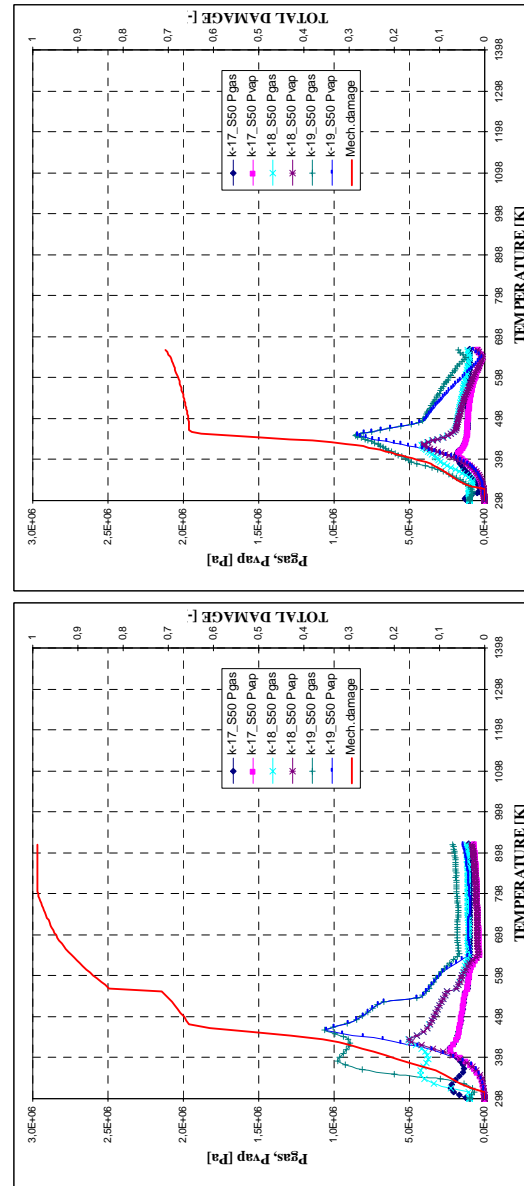


Figure 4-58. Total damage, vapour and gas pressure development for three values of intrinsic permeability ($10^{-17}, 10^{-18}, 10^{-19}$) in case of $s=50\%$.

Thickness = 12 centimetres
ISO 834 Heating curve
Material C60

(a) Depth 0,6 cm, (b) Depth 1,2 cm, (c) Depth 2,5 cm,
(d) Depth 5,0 cm, (e) Depth 10 cm



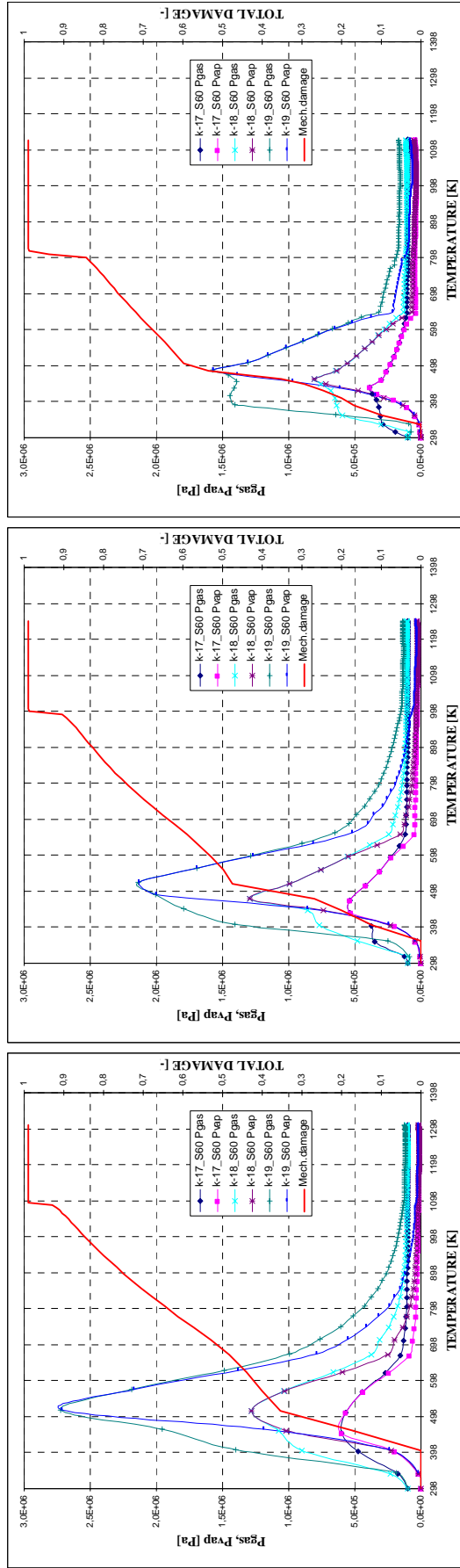
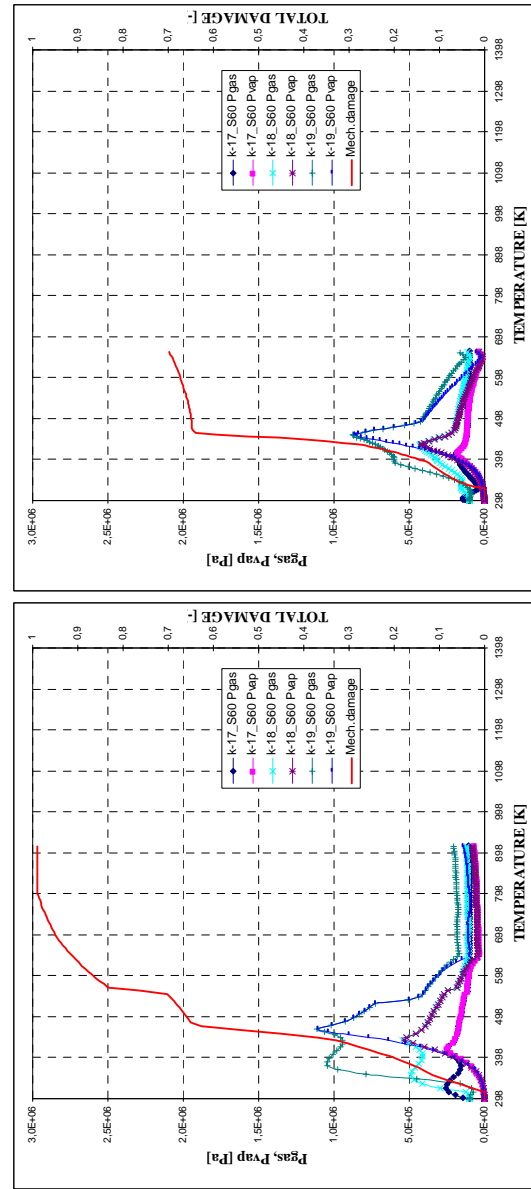


Figure 4-59. Total damage, vapour and gas pressure development for three values of intrinsic permeability (10⁻¹⁷, 10⁻¹⁸, 10⁻¹⁹) in case of s=60%.

Thickness = 12 centimetres
ISO 834 Heating curve
Material C60

(a) Depth 0,6 cm, (b) Depth 1,2 cm, (c) Depth 2,5 cm,
(d) Depth 5,0 cm, (e) Depth 10 cm



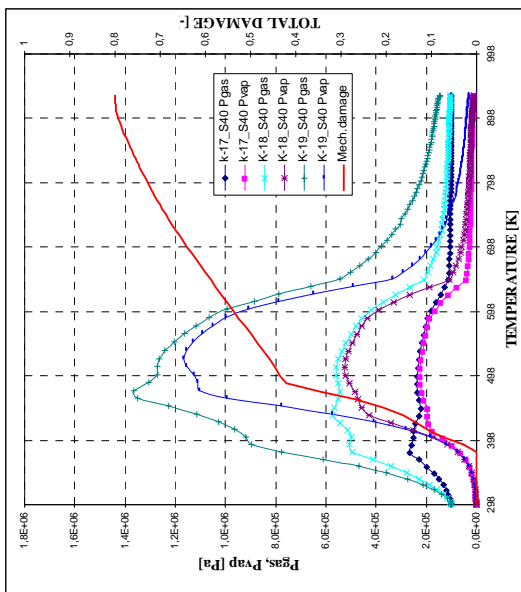
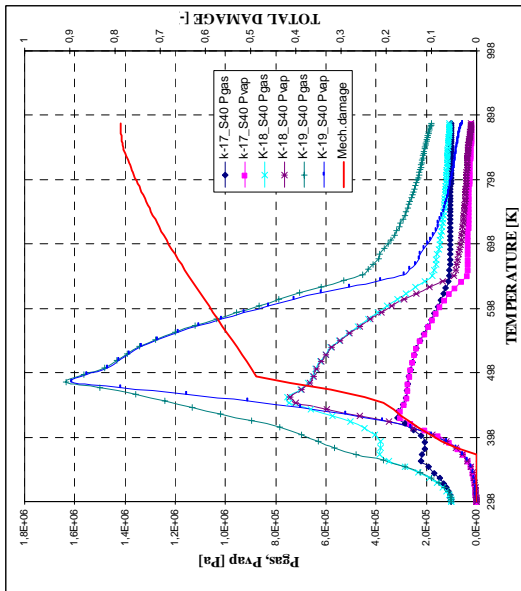
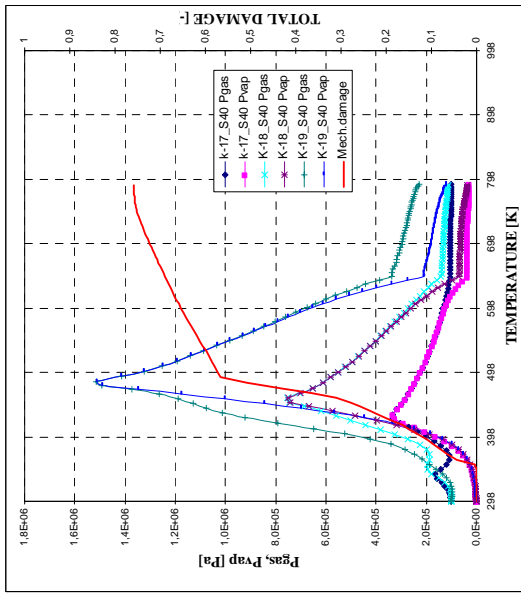
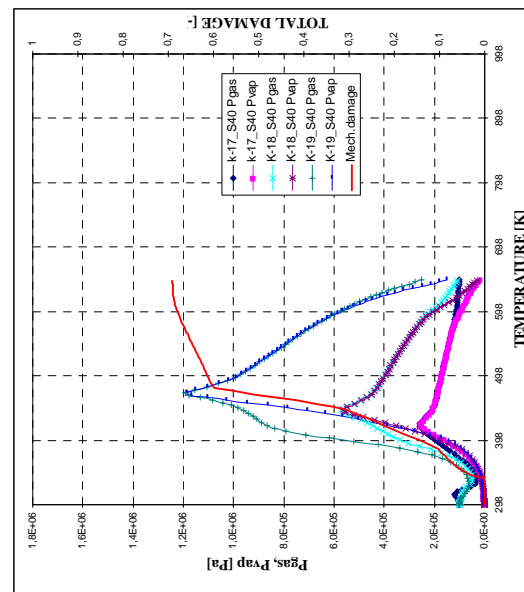
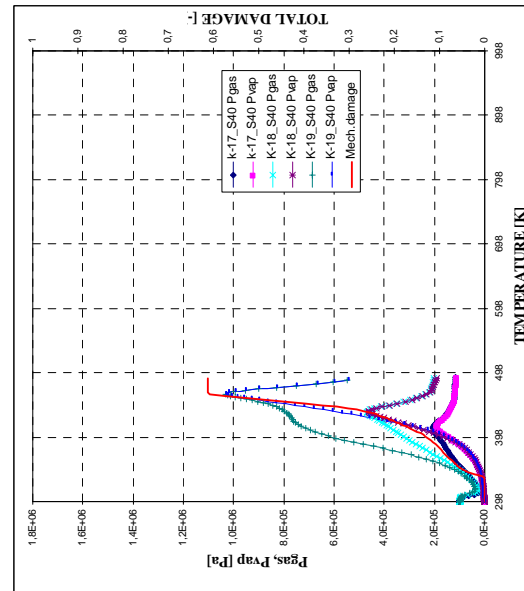


Figure 4-60. Total damage, vapour and gas pressure development for three values of intrinsic permeability ($10^{-17}, 10^{-18}, 10^{-19}$) in case of $s=40\%$.

Thickness = 12 centimetres
 PAR2 Slow Parametric Heating curve
 Material C60

(a) Depth 0,6 cm, (b) Depth 1,2 cm, (c) Depth 2,5 cm,
 (d) Depth 5,0 cm, (e) Depth 10 cm



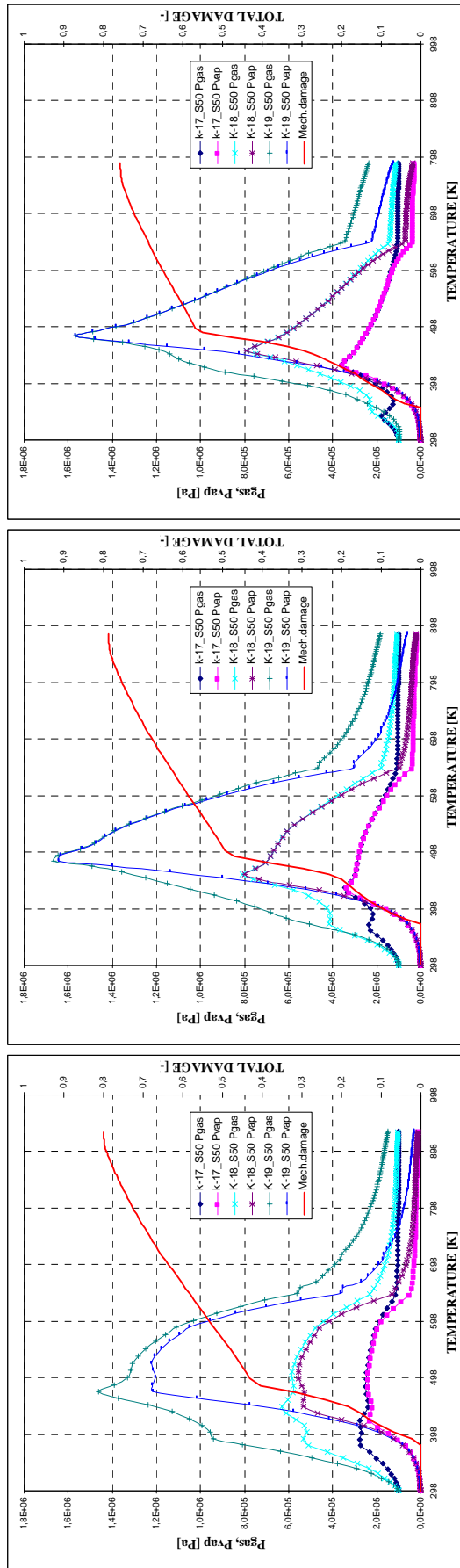
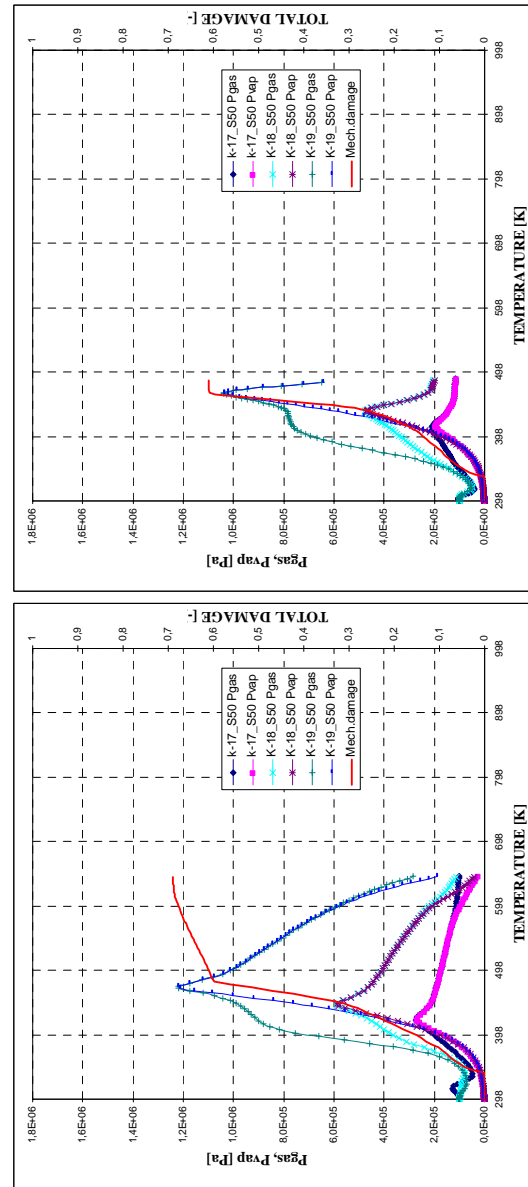


Figure 4-61. Total damage, vapour and gas pressure development for three values of intrinsic permeability (10^{-17} , 10^{-18} , 10^{-19}) in case of $s=50\%$.

Thickness = 12 centimetres
 PAR2 Slow Parametric Heating curve
 Material C60

- (a) Depth 0,6 cm, (b) Depth 1,2 cm, (c) Depth 2,5 cm,
- (d) Depth 5,0 cm, (e) Depth 10 cm



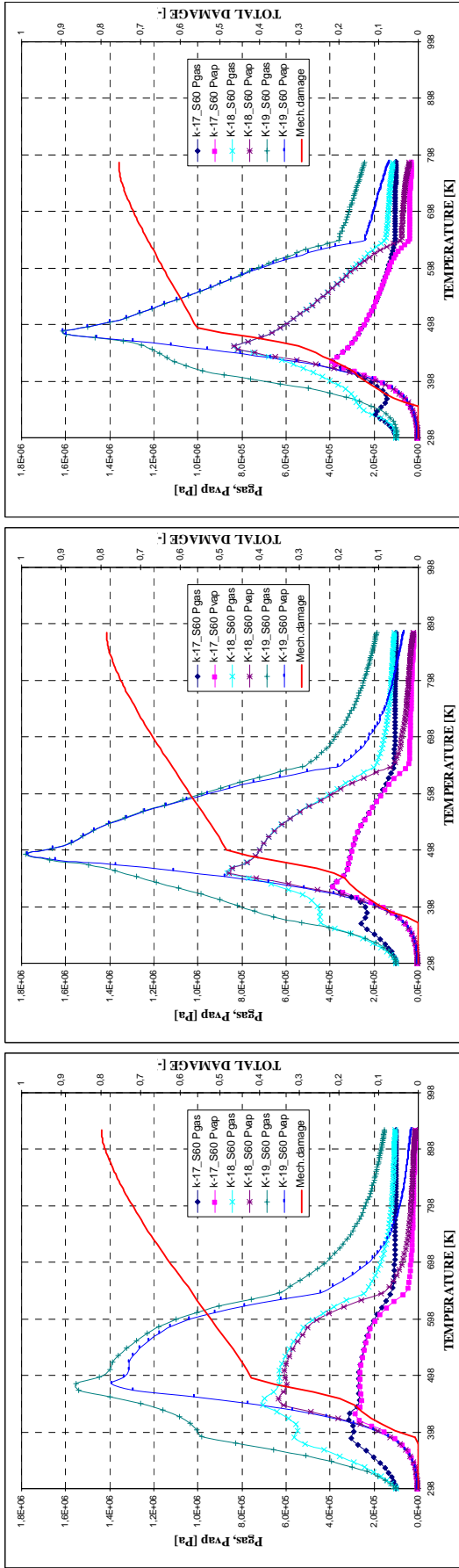
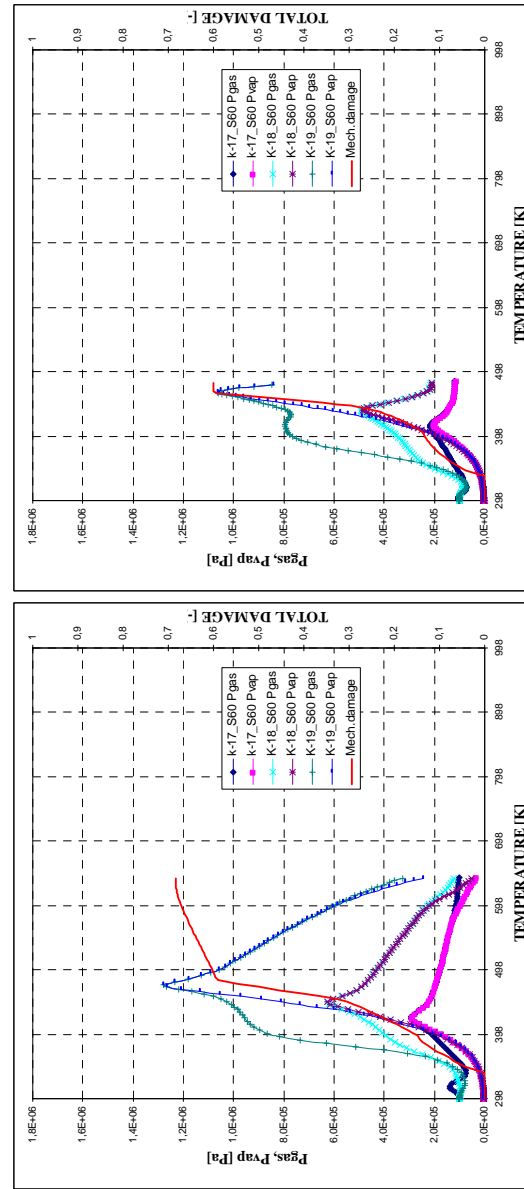


Figure 4-62. Total damage, vapour and gas pressure development for three values of intrinsic permeability ($10^{-17}, 10^{-18}, 10^{-19}$) in case of $s=60\%$.

Thickness = 12 centimetres
 PAR2 Slow Parametric Heating curve
 Material C60

(a) Depth 0,6 cm, (b) Depth 1,2 cm, (c) Depth 2,5 cm,
 (d) Depth 5,0 cm, (e) Depth 10 cm



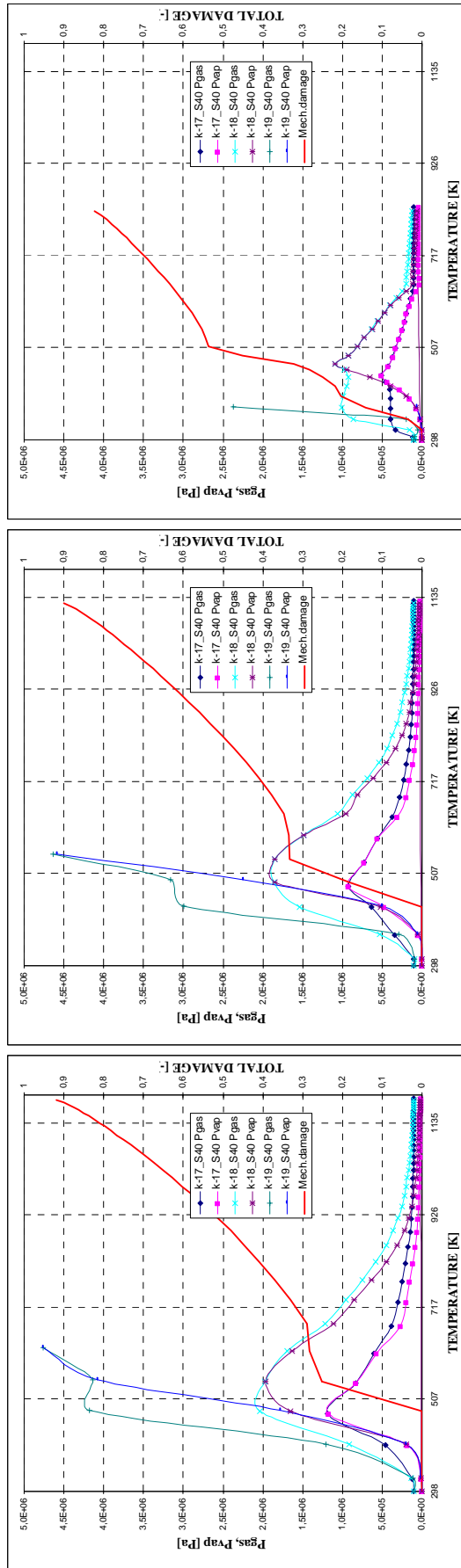
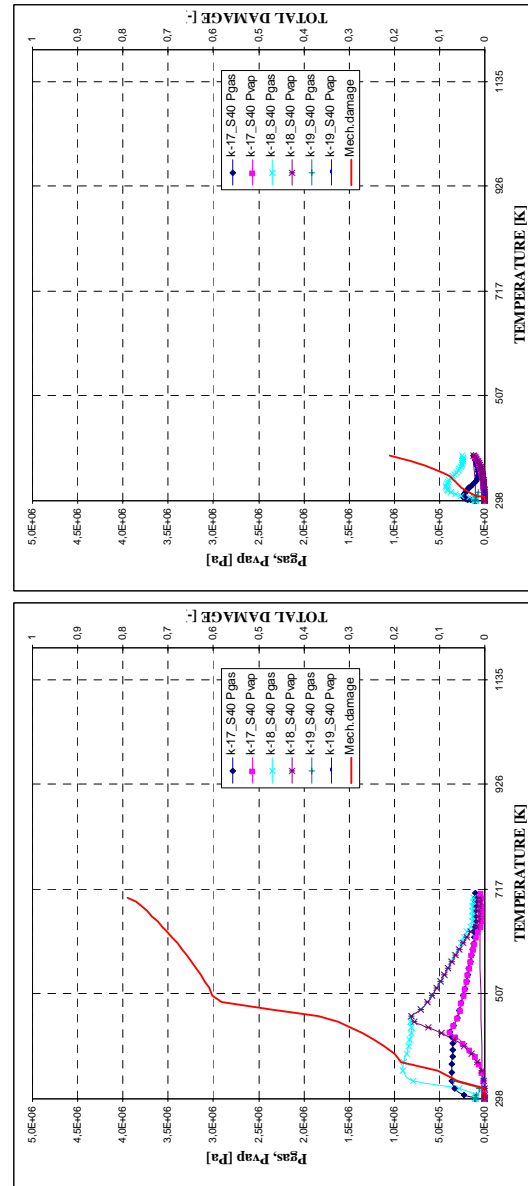


Figure 4-63. Total damage, vapour and gas pressure development for three values of intrinsic permeability ($10^{-17}, 10^{-18}, 10^{-19}$) in case of $s=40\%$.

Thickness = 12 centimetres
 PAR3 Hydrocarbon Heating curve
 Material C60

- (a) Depth 0,3 cm,
- (b) Depth 0,5 cm,
- (c) Depth 1,5 cm,
- (d) Depth 2,0 cm,
- (e) Depth 2,5 cm



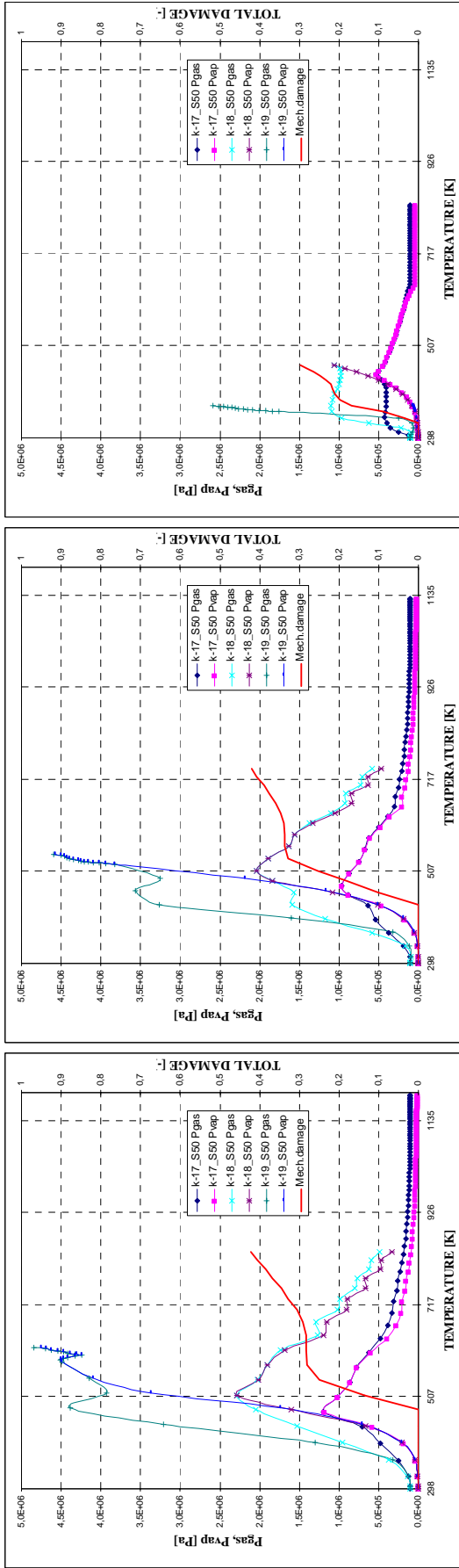
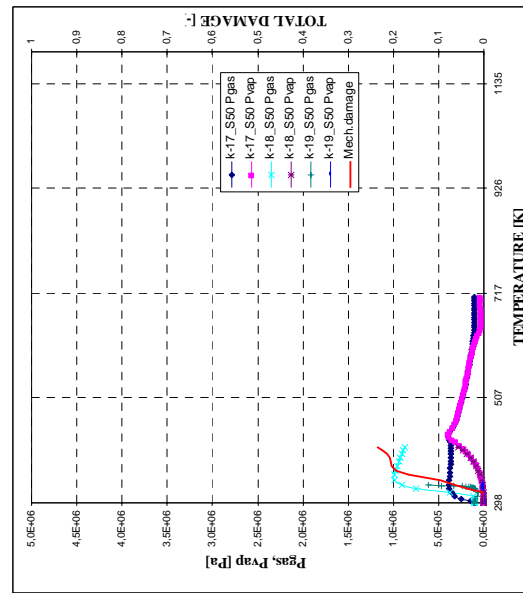


Figure 4-64. Total damage, vapour and gas pressure development for three values of intrinsic permeability ($10^{17}, 10^{18}, 10^{19}$) in case of $\nu=50\%$.

Thickness = 12 centimetres
 PAR3 Hydrocarbon heating curve
 Material C60

- (a) Depth 0,3 cm,
- (b) Depth 0,5 cm,
- (c) Depth 1,5 cm,
- (d) Depth 2,0 cm,
- (e) Depth 5,0 cm

No significant/visible effect for the available simulation time at a depth of 5 centimeters.



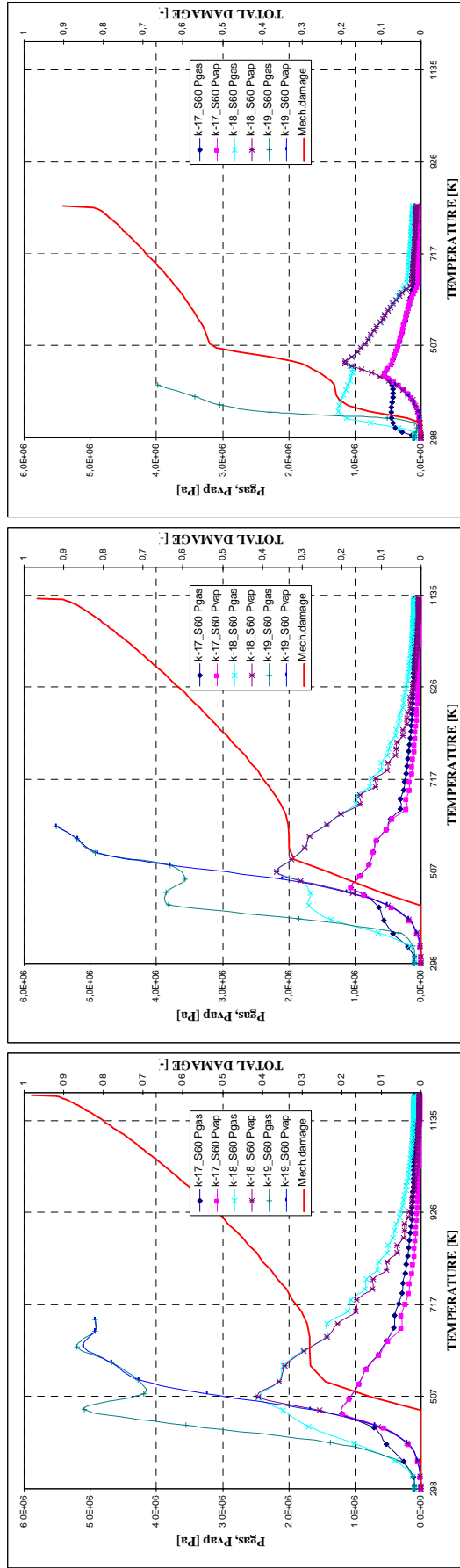
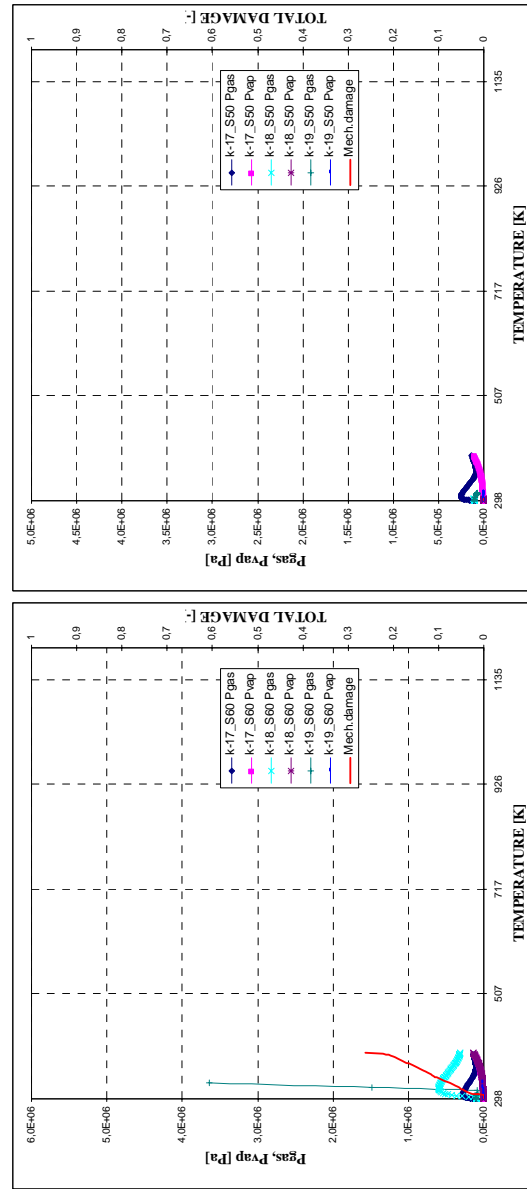


Figure 4-65. Total damage, vapour and gas pressure development for three values of intrinsic permeability ($10^{-17}, 10^{-18}, 10^{-19}$) in case of $s=60\%$.

Thickness = 12 centimetres
 PAR3 Hydrocarbon Heating curve
 Material C60

- (a) Depth 0,3 cm,
- (b) Depth 0,5 cm,
- (c) Depth 1,5 cm,
- (d) Depth 2,0 cm,
- (e) Depth 5,0 cm



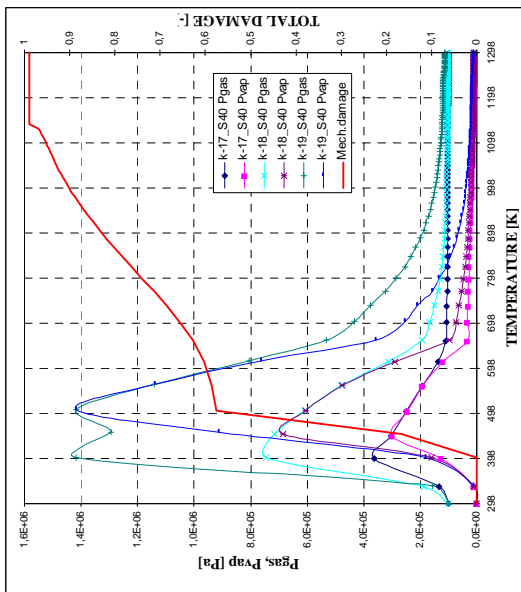
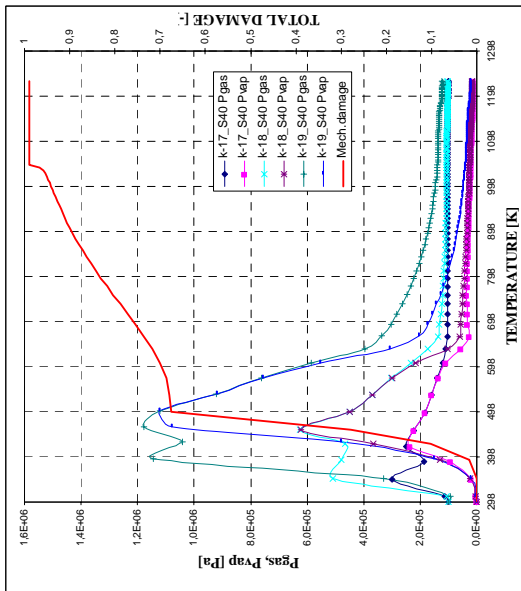
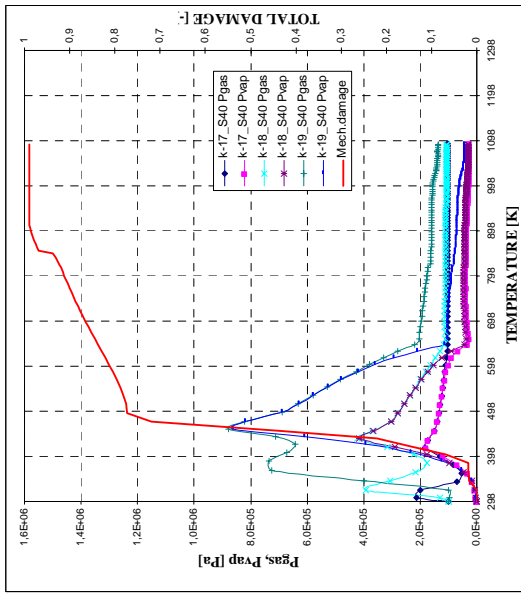
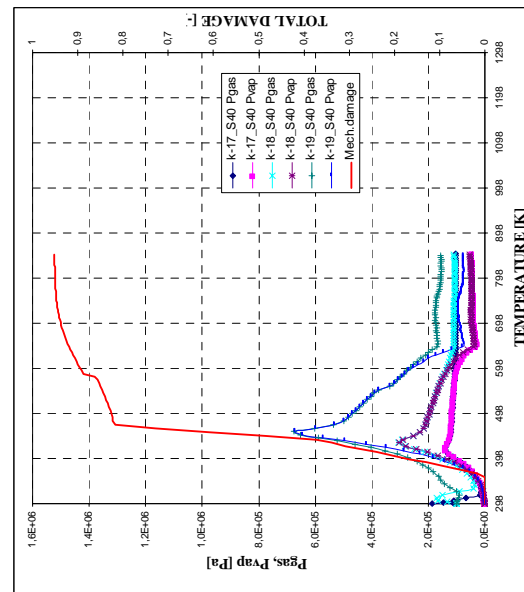
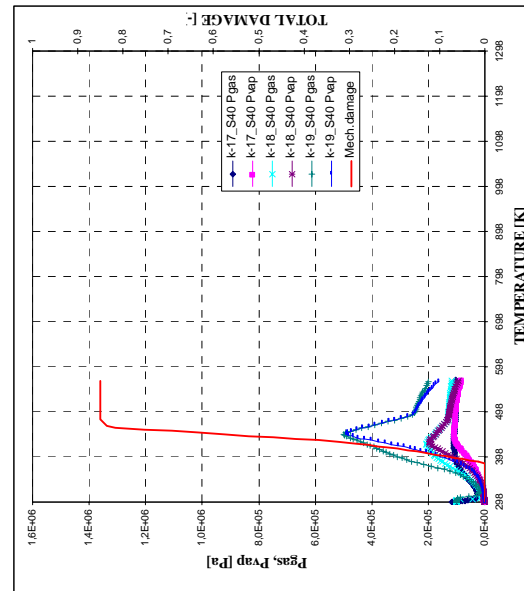


Figure 4-66. Total damage, vapour and gas pressure development for three values of intrinsic permeability ($10^{-17}, 10^{-18}, 10^{-19}$) in case of $s=40\%$.

Thickness = 12 centimetres
ISO 834 Heating curve
Material C90

(a) Depth 0,6 cm, (b) Depth 1,2 cm, (c) Depth 2,5 cm,
(d) Depth 5,0 cm, (e) Depth 10 cm



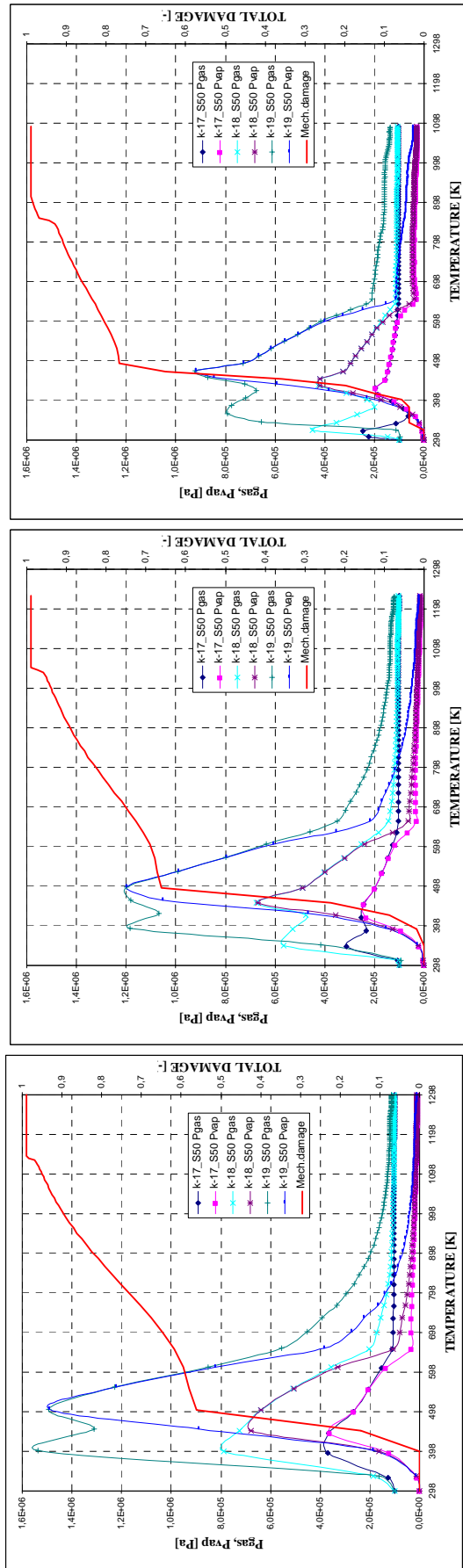
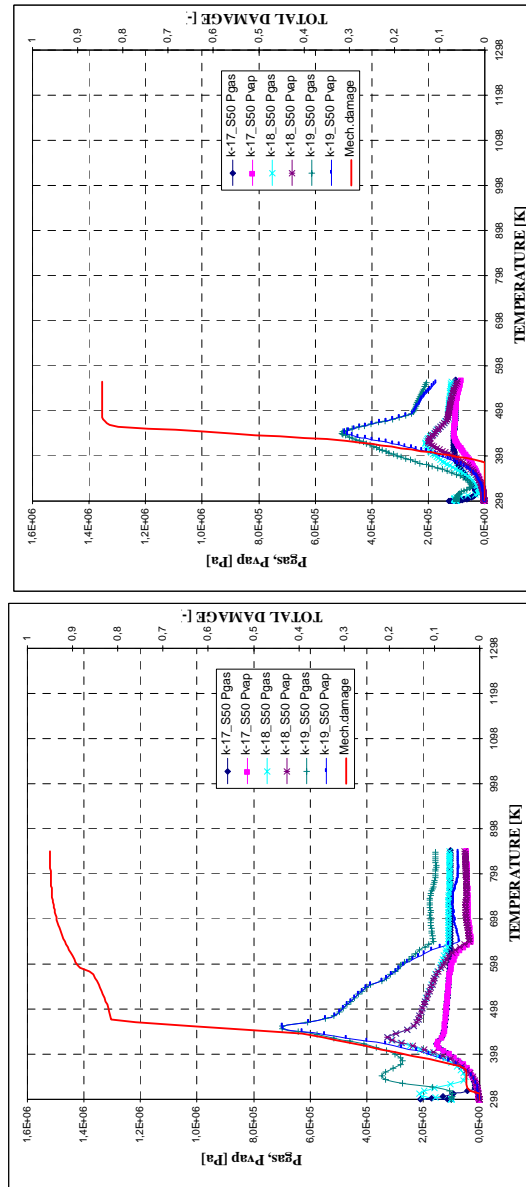


Figure 4-67. Total damage, vapour and gas pressure development for three values of intrinsic permeability (10^{-17} , 10^{-18} , 10^{-19}) in case of $s=50\%$.

Thickness = 12 centimetres
ISO 834 Heating curve
Material C90

(a) Depth 0,6 cm, (b) Depth 1,2 cm, (c) Depth 2,5 cm,
(d) Depth 5,0 cm, (e) Depth 10 cm



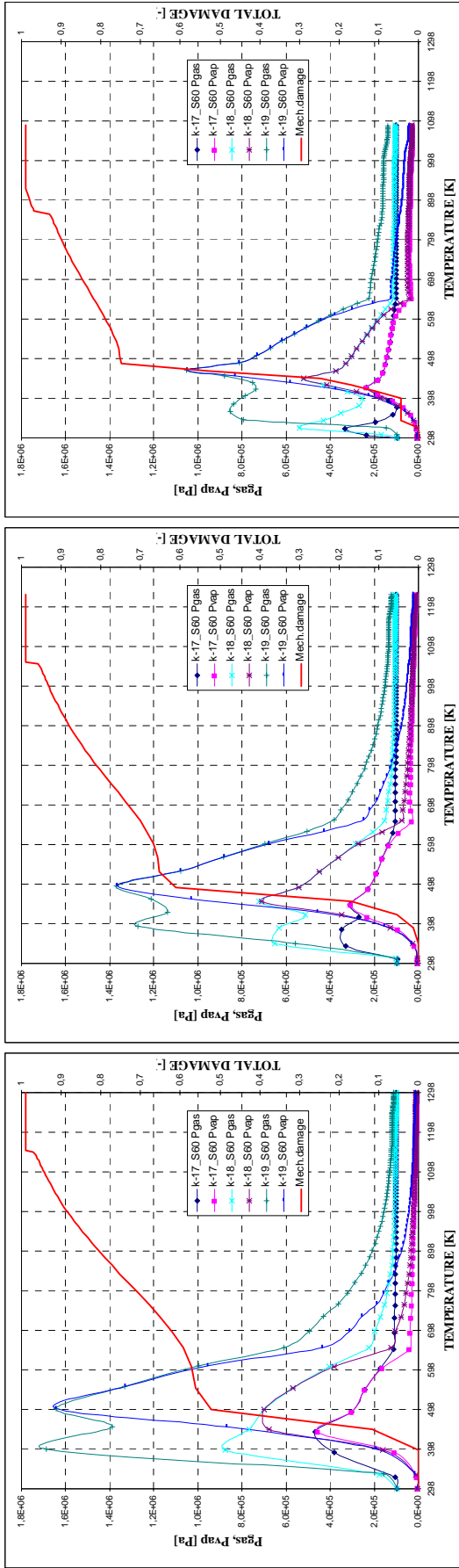
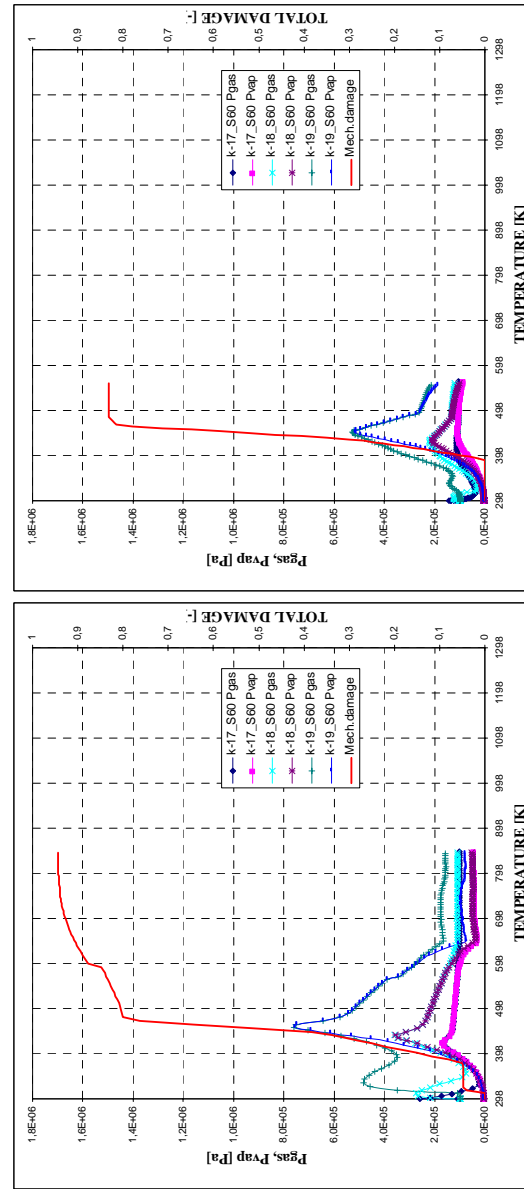


Figure 4-68. Total damage, vapour and gas pressure development for three values of intrinsic permeability ($10^{-17}, 10^{-18}, 10^{-19}$) in case of $s=60\%$.

Thickness = 12 centimetres
ISO 834 Heating curve
Material C90

(a) Depth 0,6 cm, (b) Depth 1,2 cm, (c) Depth 2,5 cm,
(d) Depth 5,0 cm, (e) Depth 10 cm



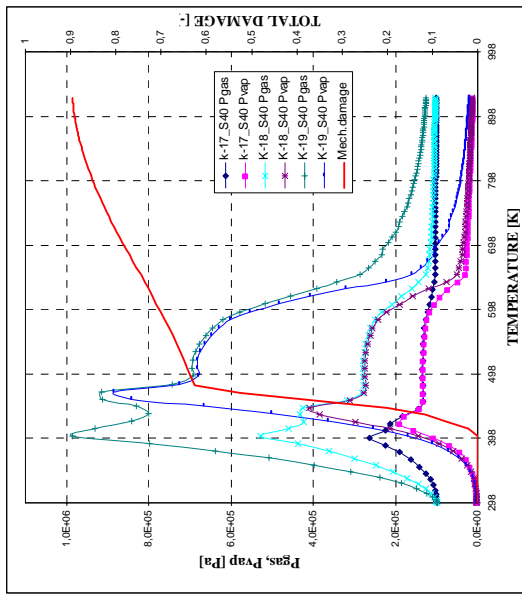
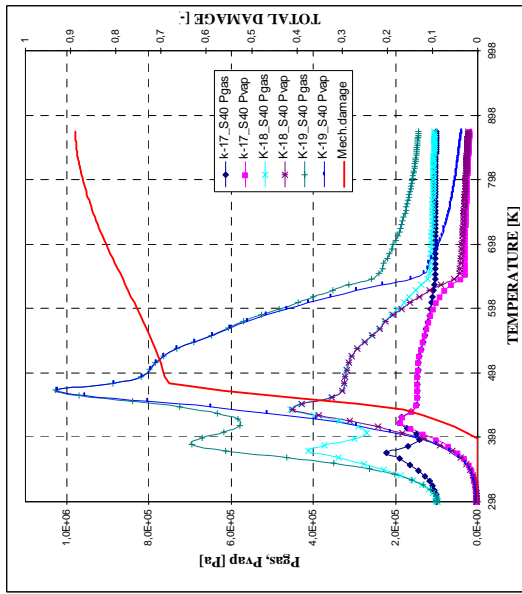
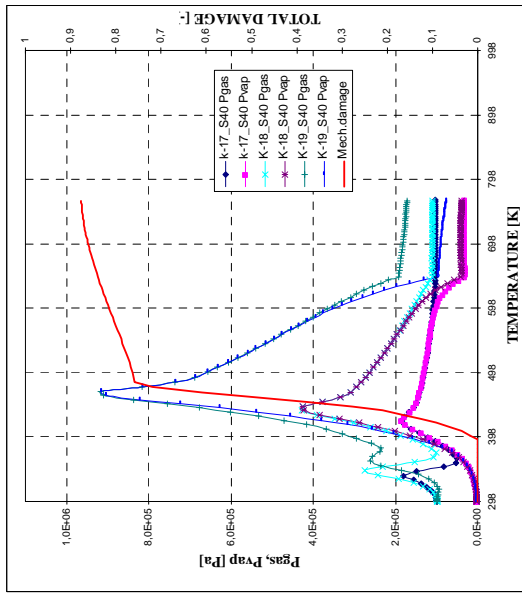
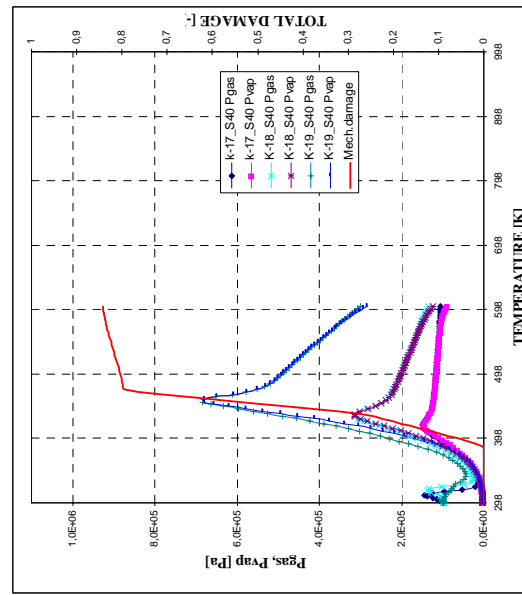
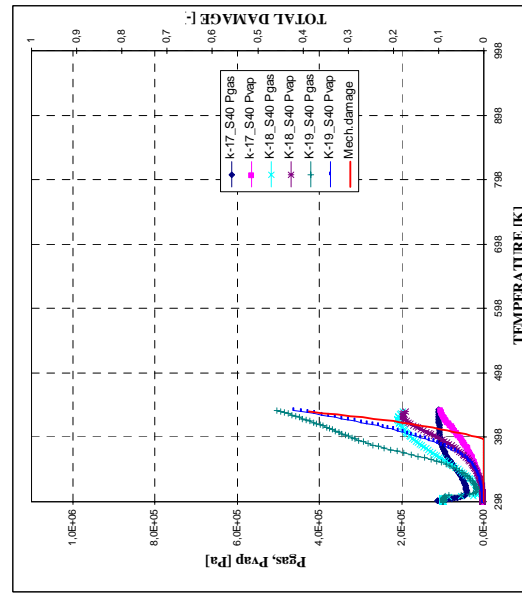


Figure 4-69. Total damage, vapour and gas pressure development for three values of intrinsic permeability ($10^{-17}, 10^{-18}, 10^{-19}$) in case of $s=40\%$.

Thickness = 12 centimetres
PAR2 Slow Parametric Heating curve
Material C90

(a) Depth 0,6 cm, (b) Depth 1,2 cm, (c) Depth 2,5 cm,
(d) Depth 5,0 cm, (e) Depth 10 cm



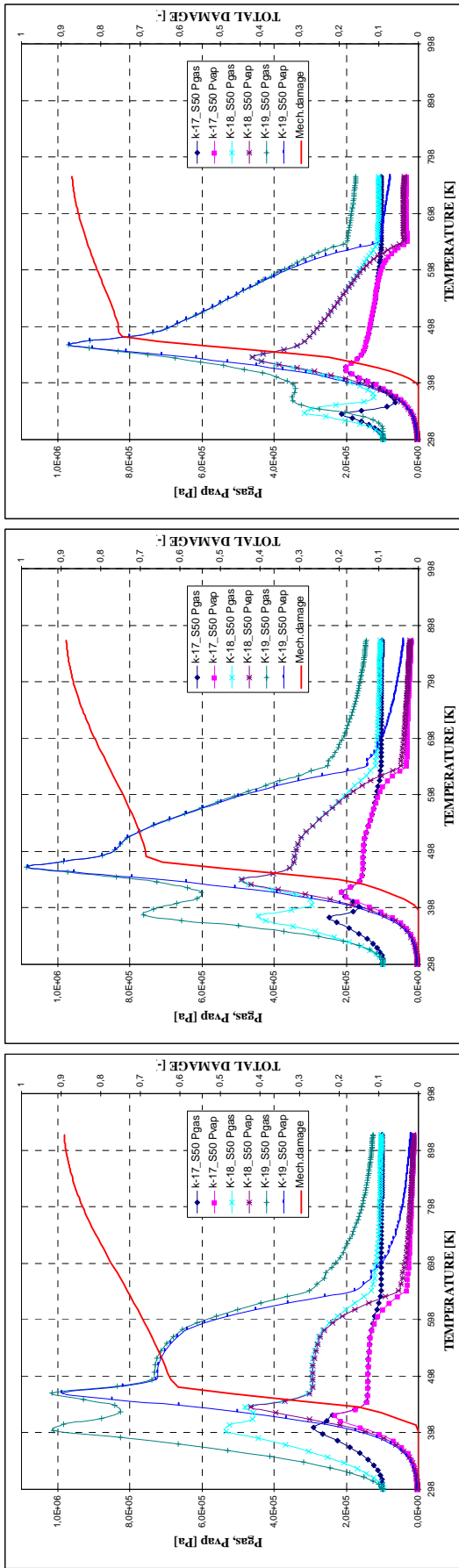
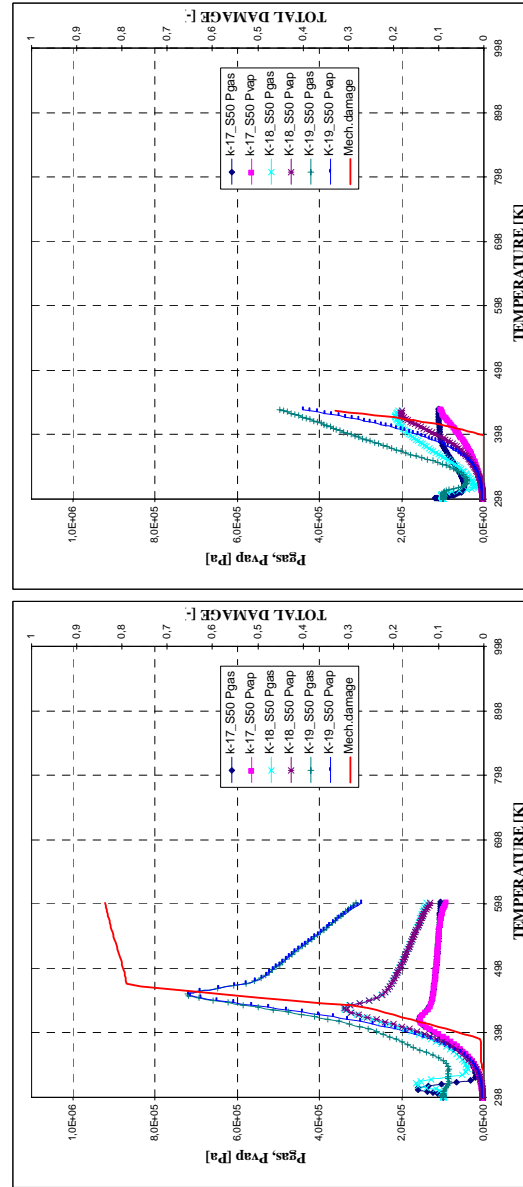


Figure 4-70. Total damage, vapour and gas pressure development for three values of intrinsic permeability (10^{-17} , 10^{-18} , 10^{-19}) in case of $s=50\%$.

Thickness = 12 centimetres
 PAR2 Slow Parametric Heating curve
 Material C90

(a) Depth 0,6 cm, (b) Depth 1,2 cm, (c) Depth 2,5 cm,
 (d) Depth 5,0 cm, (e) Depth 10 cm



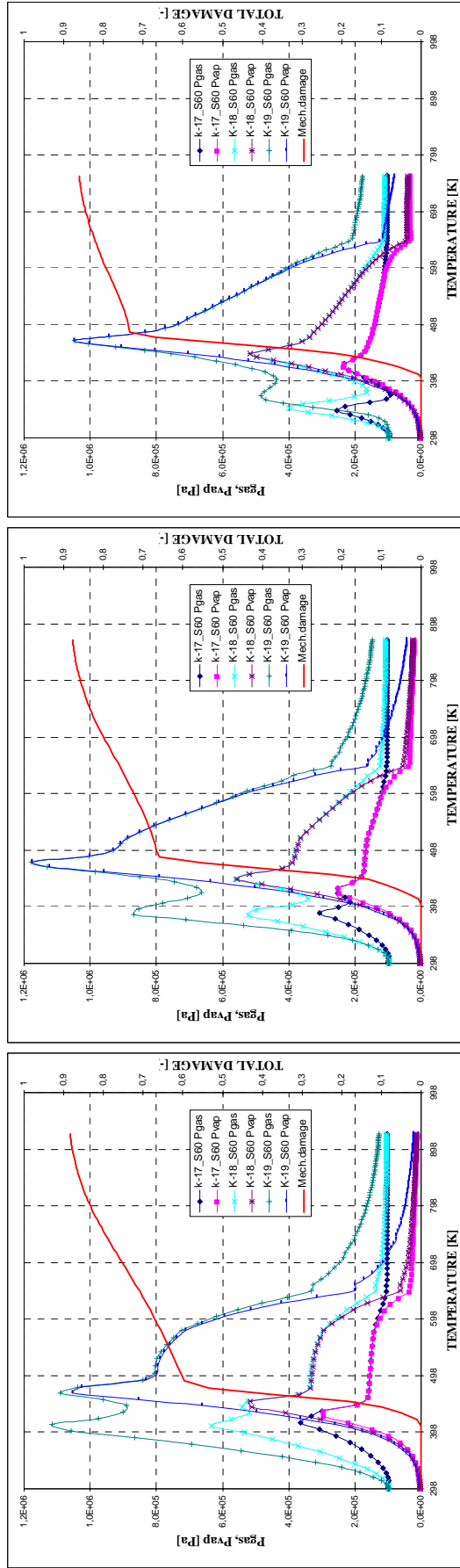
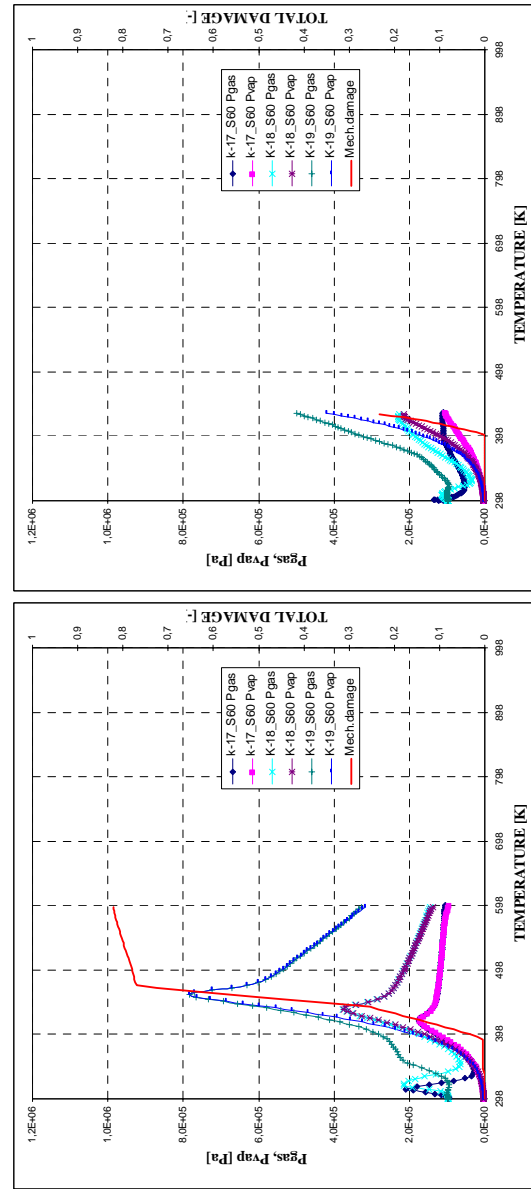


Figure 4-71. Total damage, vapour and gas pressure development for three values of intrinsic permeability ($10^{-17}, 10^{-18}, 10^{-19}$) in case of $s=60\%$.

Thickness = 12 centimetres
 PAR2 Slow Parametric Heating curve
 Material C90

(a) Depth 0,6 cm, (b) Depth 1,2 cm, (c) Depth 2,5 cm,
 (d) Depth 5,0 cm, (e) Depth 10 cm



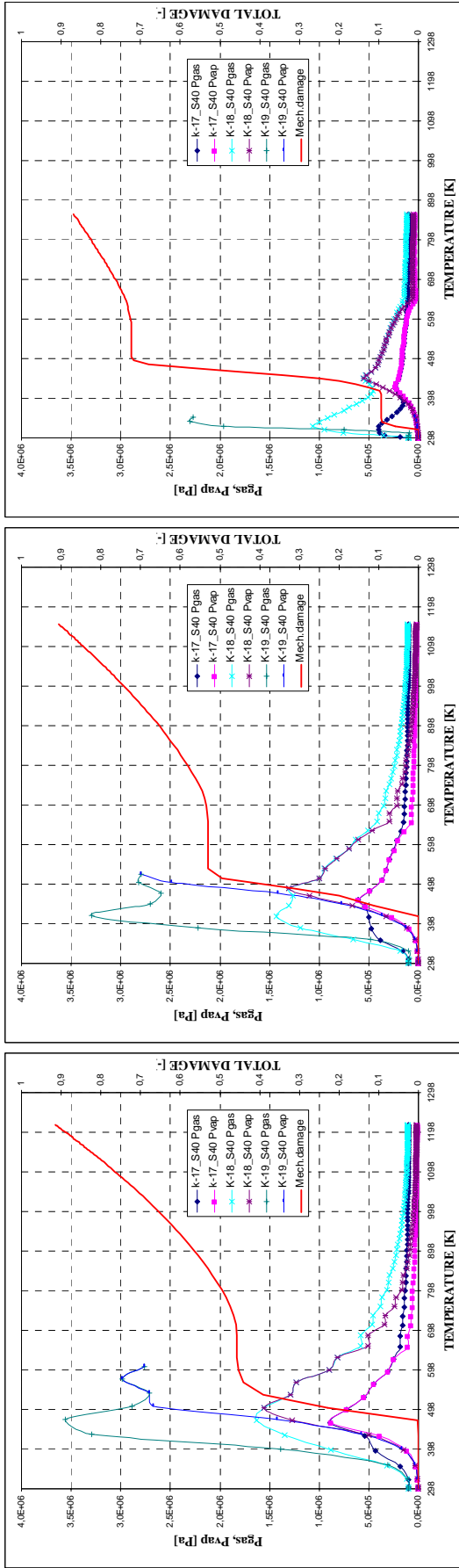
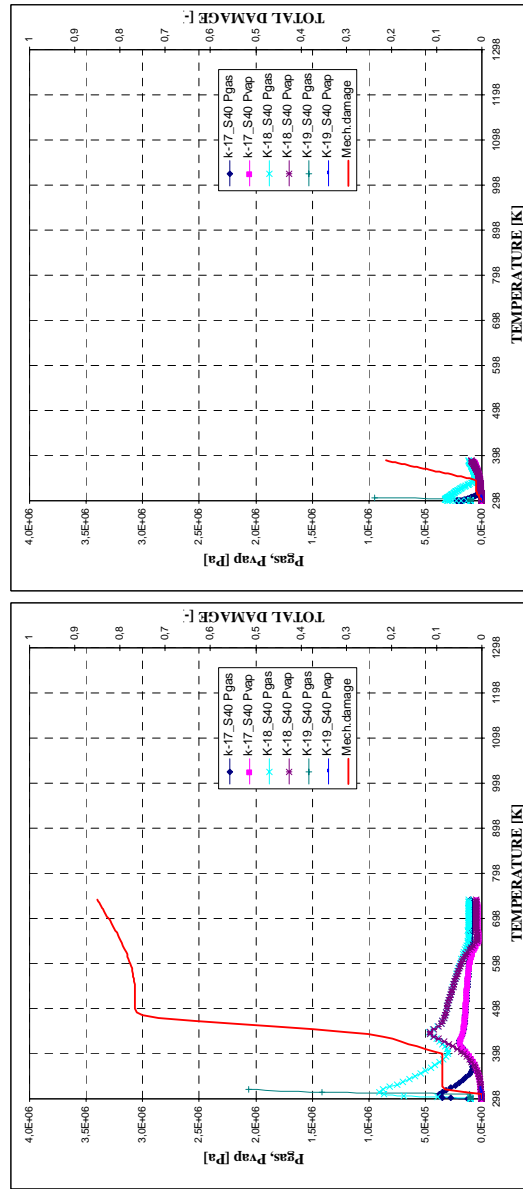


Figure 4-72. Total damage, vapour and gas pressure development for three values of intrinsic permeability ($10^{17}, 10^{18}, 10^{19}$) in case of $s=40\%$.

Thickness = 12 centimetres
 PAR3 Hydrocarbon Heating curve
 Material C90

(a) Depth 0,3 cm, (b) Depth 0,5 cm, (c) Depth 1,5 cm,
 (d) Depth 2,0 cm, (e) Depth 5,0 cm for $k=10^{17}, 10^{18}, 10^{19}$ m²
 (e') Depth 2,5 cm for $k=10^{19}$ m²



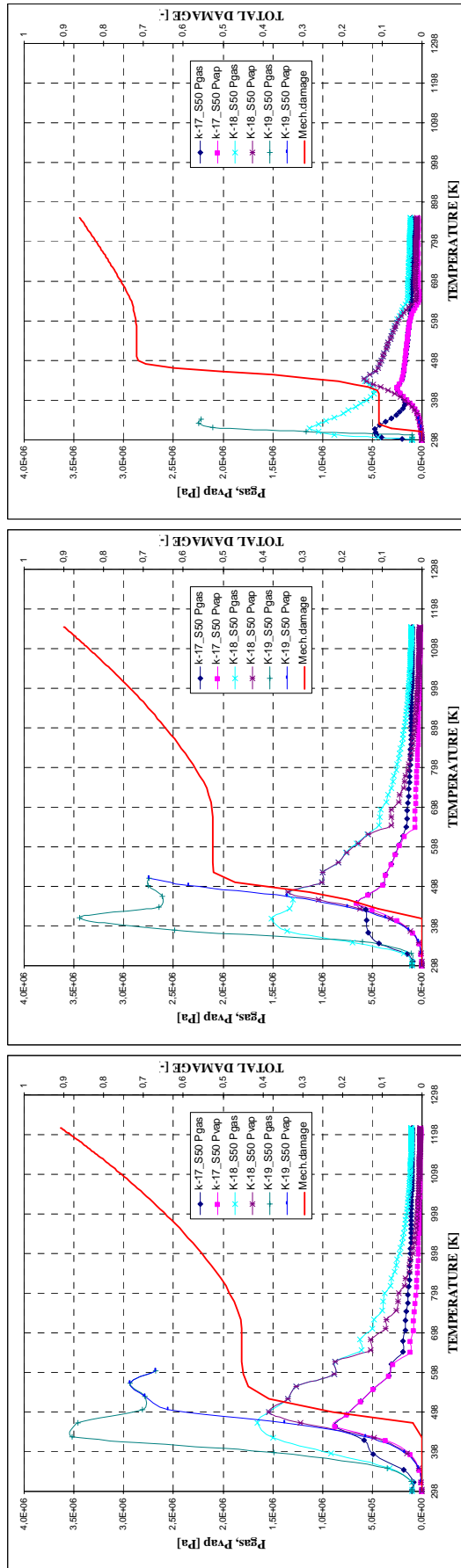
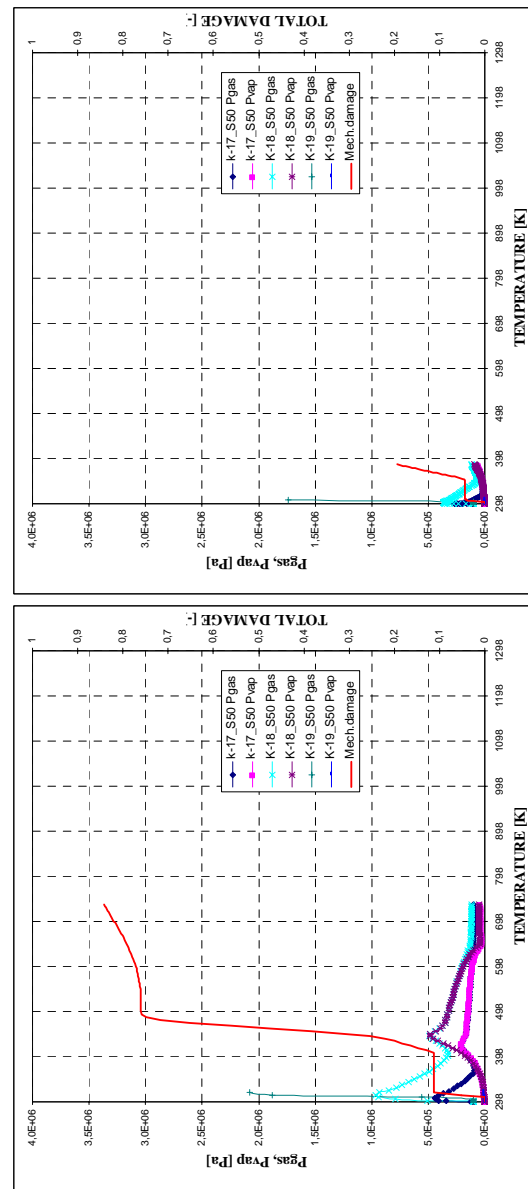


Figure 4-73. Total damage, vapour and gas pressure development for three values of intrinsic permeability (10^{-17} , 10^{-18} , 10^{-19}) in case of $s=50\%$.

Thickness = 12 centimetres
 PAR3 Hydrocarbon heating curve
 Material C90

- (a) Depth 0,3 cm,
- (b) Depth 0,5 cm,
- (c) Depth 1,5 cm,
- (d) Depth 2,0 cm,
- (e) Depth 5,0 cm for $k=10^{-17}$, 10^{-18} m²
- (e') Depth 2,5 cm for $k=10^{-19}$ m²



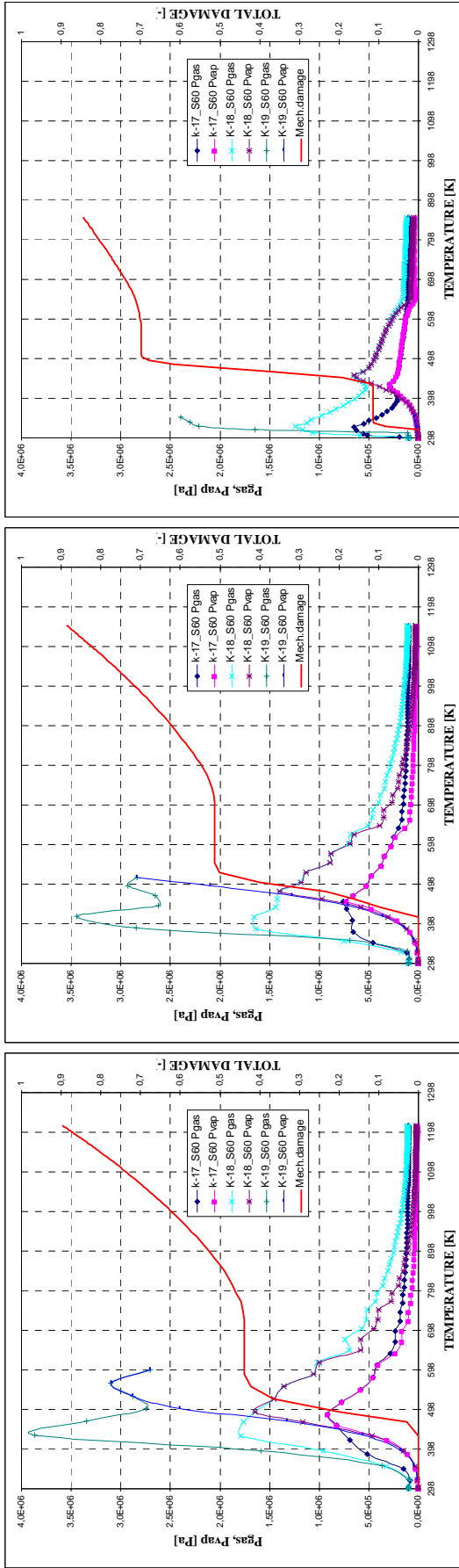
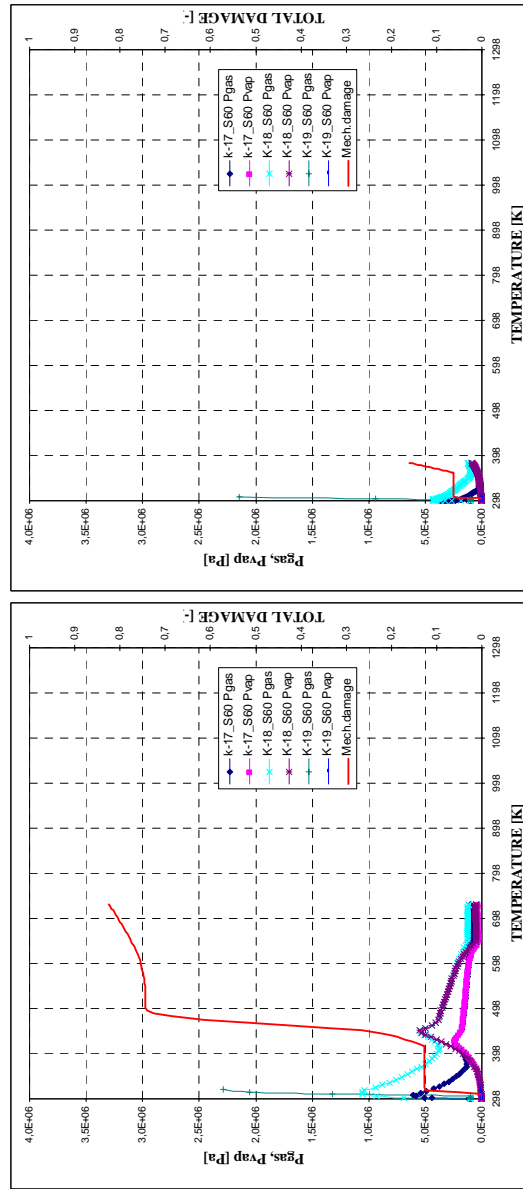


Figure 4-74. Total damage, vapour and gas pressure development for three values of intrinsic permeability ($10^{17}, 10^{18}, 10^{19}$) in case of $s=60\%$.

Thickness = 12 centimetres
 PAR3 Hydrocarbon Heating curve
 Material C90

(a) Depth 0,3 cm, (b) Depth 0,5 cm, (c) Depth 1,5 cm,
 (d) Depth 2,0 cm, (e) Depth 5,0 cm for $k=10^{17}, 10^{18}, 10^{19} m^2$
 (e') Depth 2,5 cm for $k=10^{19} m^2$



4.5.6 Comparison of the Vapour Pressure and the Mechanical Damage Distribution

In this paragraph it is developed a direct comparison of some of the most relevant cases in the space domain, at different time stages, by means of the comparison of vapour pressure and mechanical damage values.

Figure number	Thickness [cm]	Material	Heating curve	Initial Saturation Degree	Combination numbers for each intrinsic permeability value [m^2]			
					10^{-17}	10^{-18}	10^{-19}	
4-75	12	C60 (High Strength Concrete)	PAR 1 (ISO 834)	40%	1	2	3	
4-76				50%	4	5	6	
4-77				60%	7	8	9	
4-78			PAR 2 (Slow parametric)	40%	10	11	12	
4-79				50%	13	14	15	
4-80				60%	16	17	18	
4-100			PAR 3 (Hydrocarbon)	40%	74**	75**	N/A	
4-101				50%	77**	78**	N/A	
4-102				60%	80**	81**	N/A	
4-88		C90 (Ultra-High Strength Concrete)	PAR 1 (ISO 834)	40%	37	38	39	
4-89				50%	40	41	42	
4-90				60%	43	44	45	
4-91			PAR 2 (Slow parametric)	40%	46	47	48	
4-92				50%	49	50	51	
4-93				60%	52	53	54	
4-103			PAR 3 (Hydrocarbon)	40%	83*	84*	N/A	
4-104				50%	86*	87*	N/A	
4-105				60%	89*	90*	N/A	
4-81		24	C60 (High Strength Concrete)	PAR 1 (ISO 834)	40%	19	20	21
4-82					50%	22	23	24
4-83	60%				25	26	27	
4-84	PAR 2 (Slow parametric)			40%	28	29	30	
4-85				50%	31	32	33	
4-86				60%	34	35	36	
4-94	C90 (Ultra-High Strength Concrete)		PAR 1 (ISO 834)	40%	55	56	57	
4-95				50%	58	59	60	
4-96				60%	61	62	63	
4-97			PAR 2 (Slow parametric)	40%	64	65	66	
4-98				50%	67	68	69	
4-99				60%	70	71	72	
4-87	50	C60 (H.S.C.)	PAR 1 (ISO 834)	50%	---	73	---	

Table 4-57. List of graphics included in the comparison for constant values of Intrinsic Permeability.

Remark *: As it was previously explained, these combinations have been run up to a total simulation time of 2.400 seconds (instead of the general simulation time of 10.800 seconds) because the high rate of heating induces a value of the Total Damage at 2.400 seconds of 0.99, which means that the material is completely destroyed, so it is not worthy to carry on simulations beyond this point.

Remark **: As it was also previously explained, these combinations have had lack of convergence at certain instants because of the combination of extreme conditions, i.e. high rate of heating joint to the lower limit value of intrinsic permeability ($10^{-19} m^2$), so results are represented up to the converged simulation time, resumed in the next table:

Combination	74	75	76	77	78	79	80	81	82	85	88	91
Final time [s]	1.050	1.020	150	1.065	285	148	1.080	1.080	180	150	150	150

The graphics corresponding to this comparison are presented in Figures 4.75 to 4.105 for values of the initial saturation degree ranging from 40% to 60% and for three different instants during the fire evolution, i.e. one hour, two hours and three hours after the fire start (in the cases featured by Hydrocarbon heating curve, since simulations have only been worked out until 2.400 seconds due to the extreme values of the Total damage, the comparing instants have been set at 300, 600 and 2.400 seconds – where available –). The description of these figures is detailed in the table 4-57. (*Remark: In figures 4.75 to 4.105 mechanical damage is represented according to the Y-axis shown in the right of each figure*).

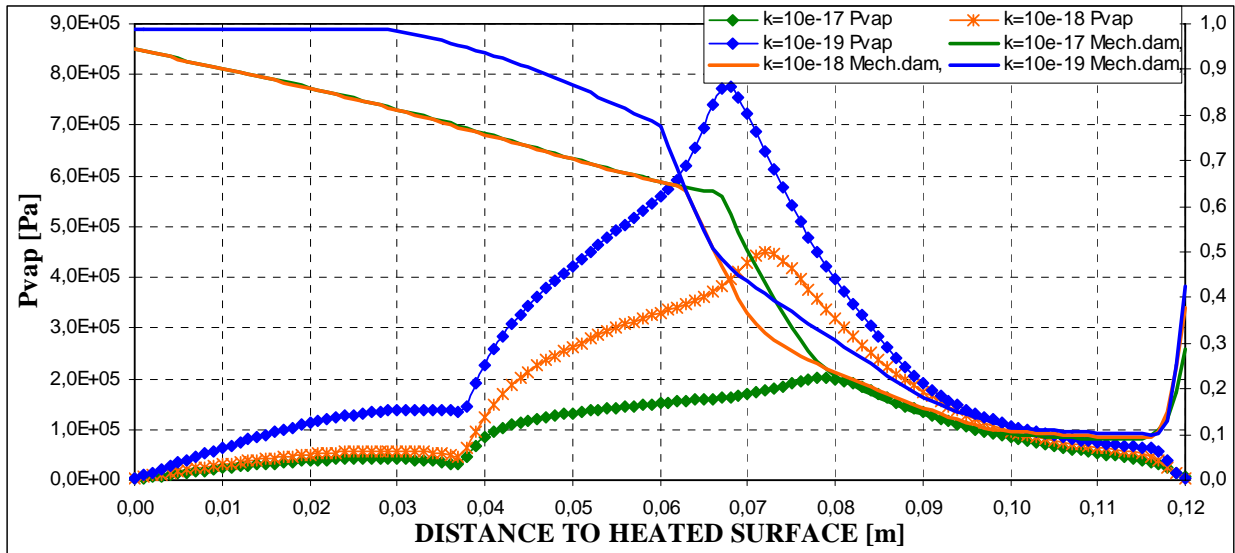
First, it will be analyzed a set of cases that will be taken as a reference set to compare the rest of them. This set of cases is the one shown below, featured by a 12 cm thick structural element of C60 material and with an ISO heating curve applied (cases 1 to 9).

Figure number	Thickness [cm]	Material	Heating curve	Initial Saturation Degree	Combination numbers for each intrinsic permeability value [m^2]		
					10^{-17}	10^{-18}	10^{-19}
4-75	12	C60 (High Strength Concrete)	PAR 1 (ISO 834)	40%	1	2	3
4-76				50%	4	5	6
4-77				60%	7	8	9

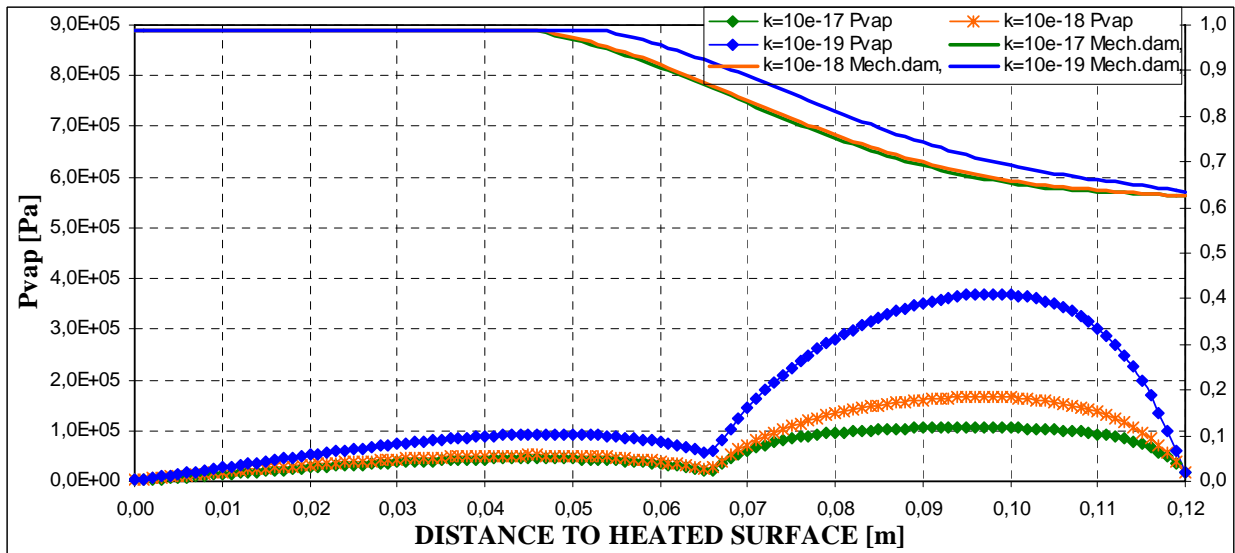
Table 4-58. Definition of the reference set used for the comparison of the rest of cases.

Analyzing this set of nine cases it is observed, mainly, what it was already explained on paragraph 4.5.4.1 plus the following considerations:

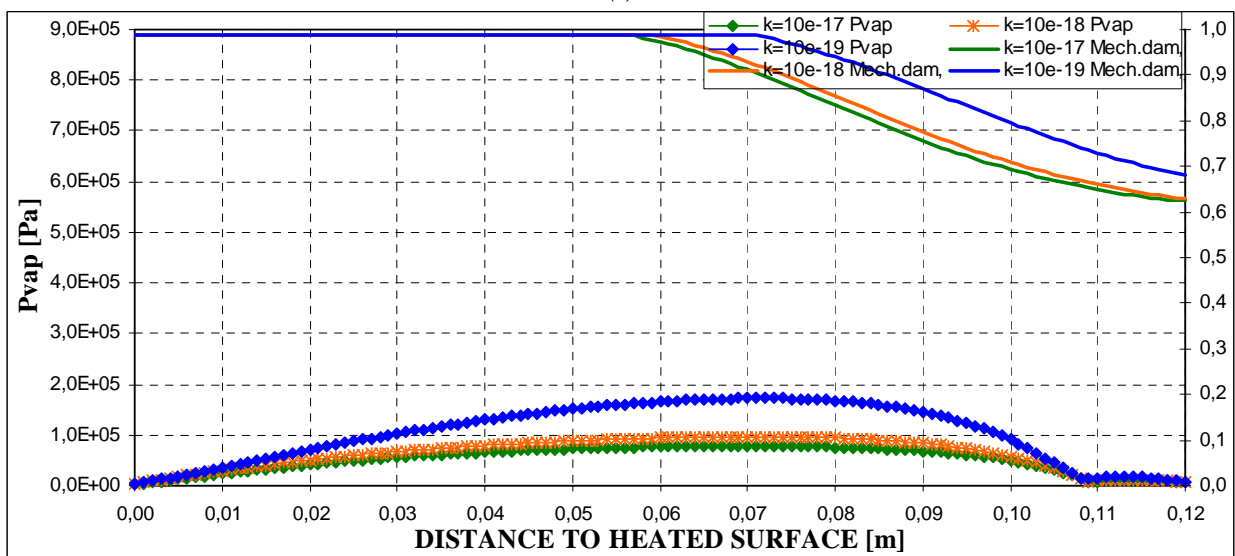
- The depth where the vapour pressure shows its maximum values increases with time (until 10 centimetres away from the heated surface) up to an absolute heating time of 9.600 seconds, instant at which the maximum value (much lower than in the previous stages) appears at 7 centimetres from the heated surface. Again, the maximum absolute vapour pressure reached at each instant matches the gas pressure maximum (in depth and absolute time) and is always found within the temperature range of 473 ± 50 K, being this the temperature at which spalling is usually observed. This fact suggests that despite the I_{s4} maximum values are achieved at higher temperatures, within the range of 573 ± 25 K, spalling may be occurring before the instants corresponding to these maxima, as it was explained on table 4-43.
- The regions where mechanical damage values are maxima at any certain instant are those most exposed to temperature rising (close to the heated surface). However, as previously stated, one must remember that a lower depth does not necessarily mean higher Total/Mechanical Damage levels at the same temperature.
- It is observed a slight increase of the maximum value of the vapour pressure and a decrease of its corresponding depth as the Initial Saturation Degree increases. This increase in the maximum vapour pressure value is more pronounced when increasing the Initial Saturation Degree from the 50% to the 60%.
- Also comparing these three figures it is clearly observed a pronounced sensitivity of the maximum absolute vapour pressure with the values of the Intrinsic Permeability, increasing this pressure as the latter decreases. The depth at which these maxima are found increases with Intrinsic Permeability. The highest difference of the value and position of the maximum vapour pressure appears between an Intrinsic Permeability of $10^{-19} m^2$ and $10^{-18} m^2$.



(a)

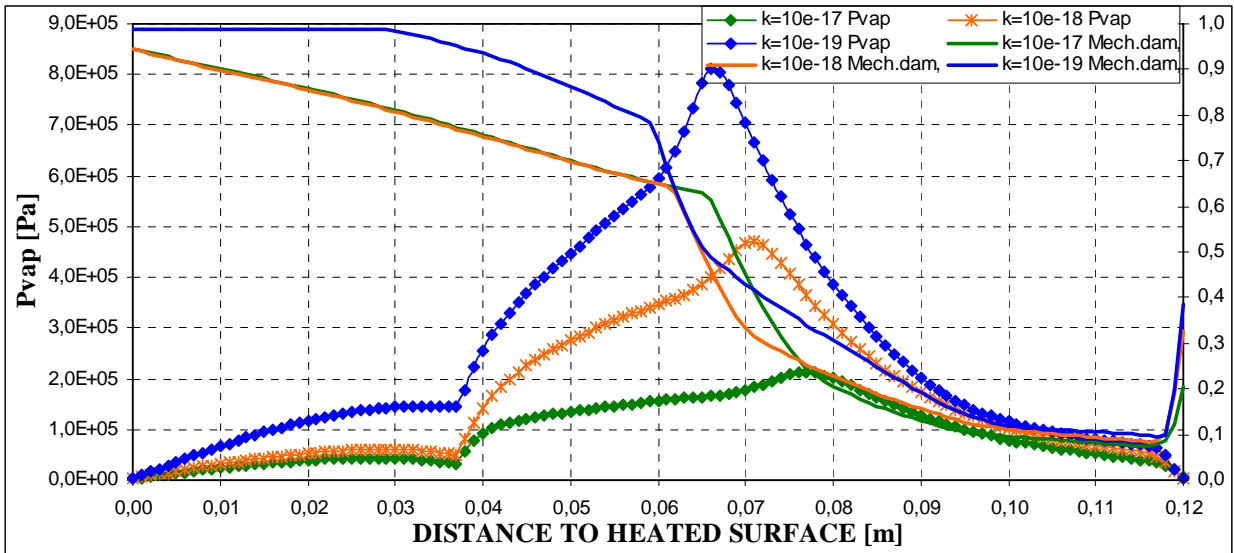


(b)

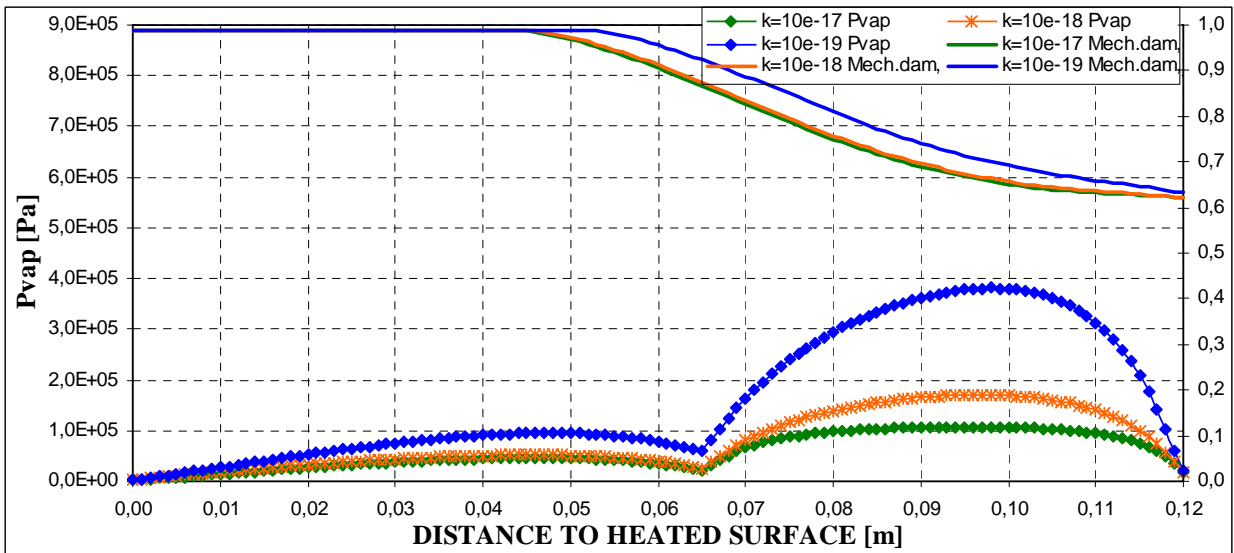


(c)

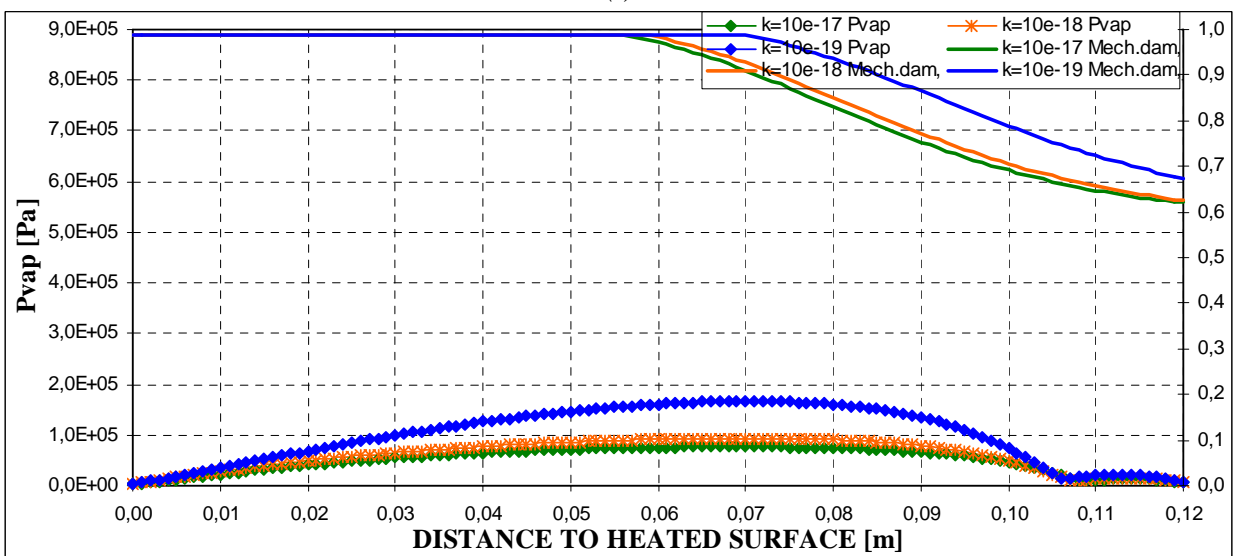
Figure 4-75. Mechanical damage and vapour pressure space distribution for three values of intrinsic permeability (10^{-17} , 10^{-18} , 10^{-19}) in case of $s=40\%$, Thickness = 12 centimetres, PARI ISO Heating curve, Material C60
(a) 1 hour; (b) 2 hours; (c) 3 hours



(a)

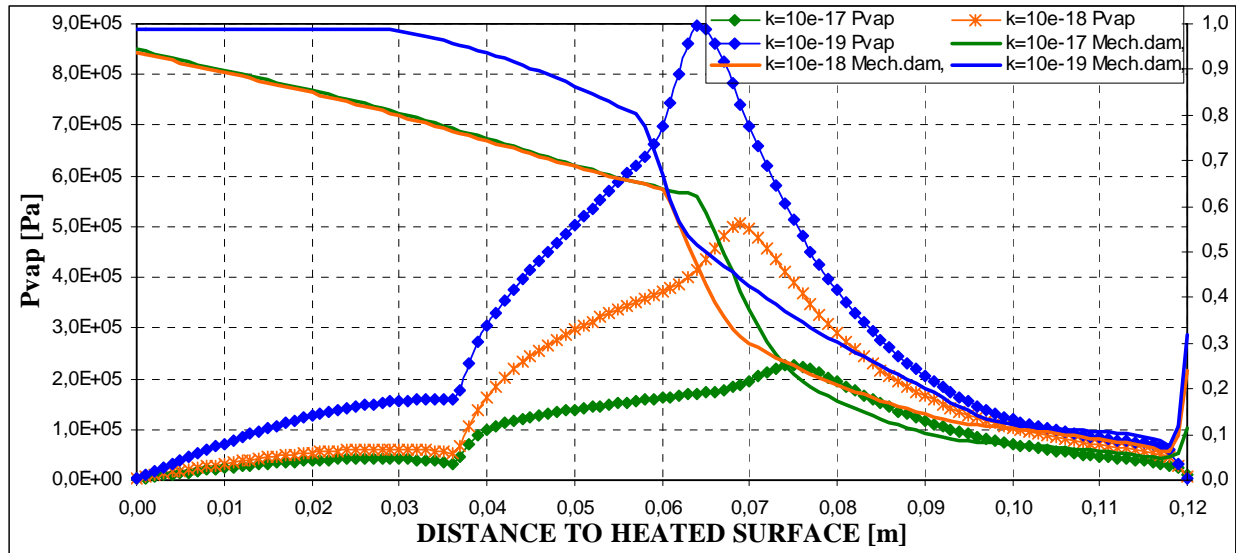


(b)

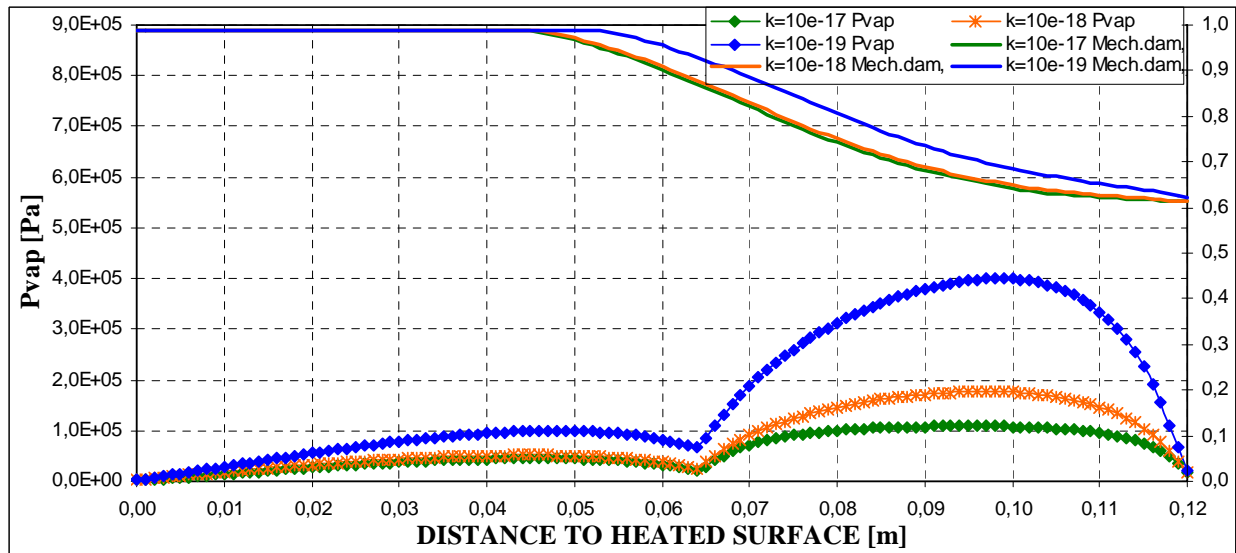


(c)

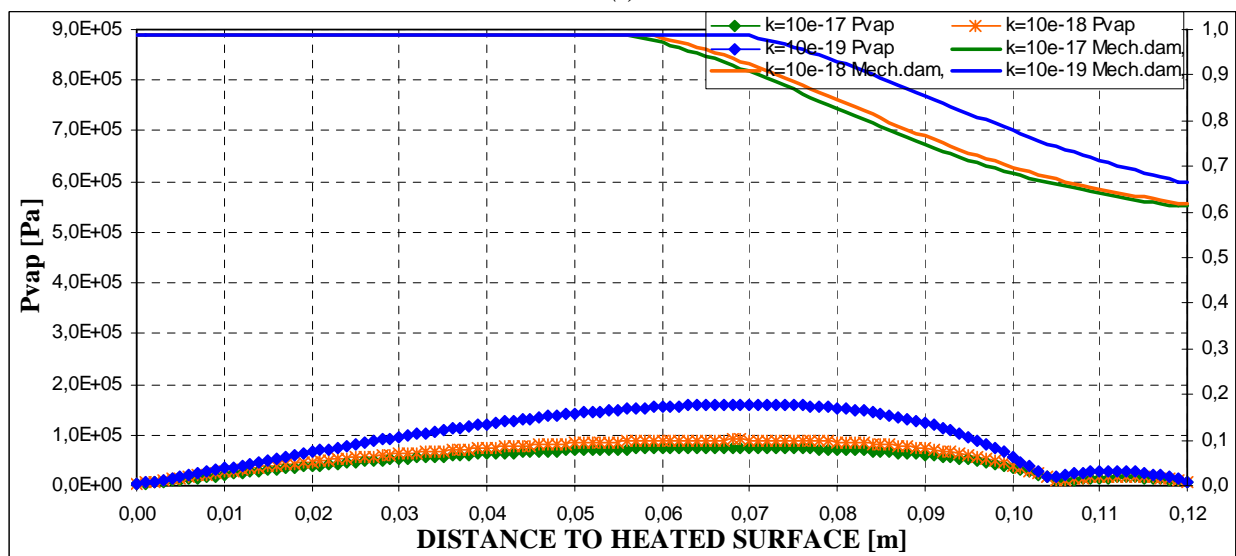
Figure 4-76. Mechanical damage and vapour pressure space distribution for three values of intrinsic permeability ($10^{-17}, 10^{-18}, 10^{-19}$) in case of $s=50\%$, Thickness = 12 centimetres, PAR1 ISO Heating curve, Material C60
(a) 1 hour; (b) 2 hours; (c) 3 hours



(a)

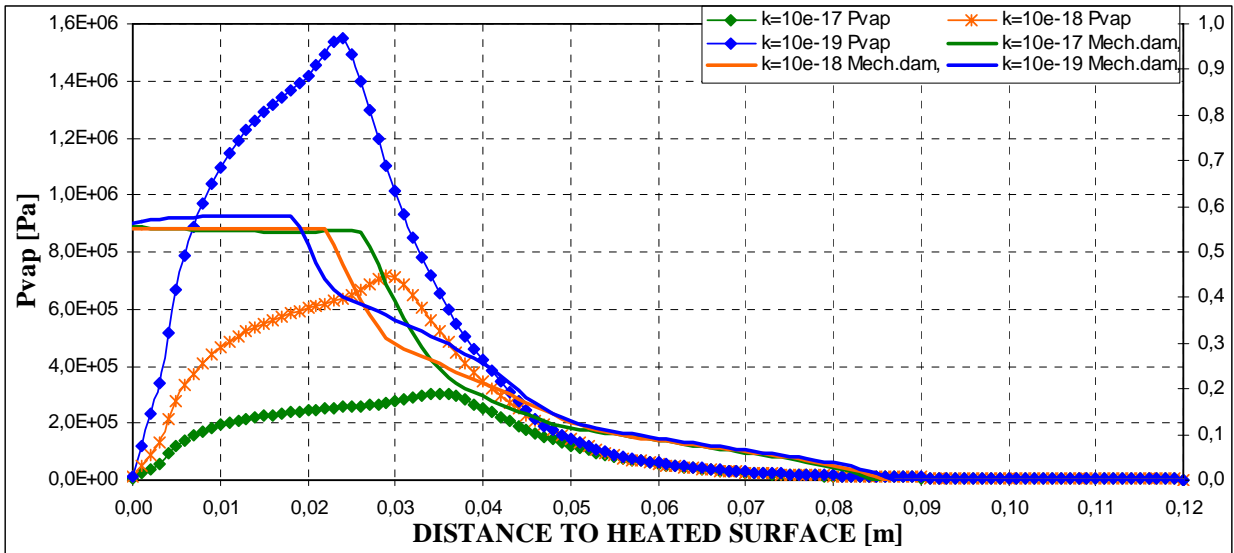


(b)

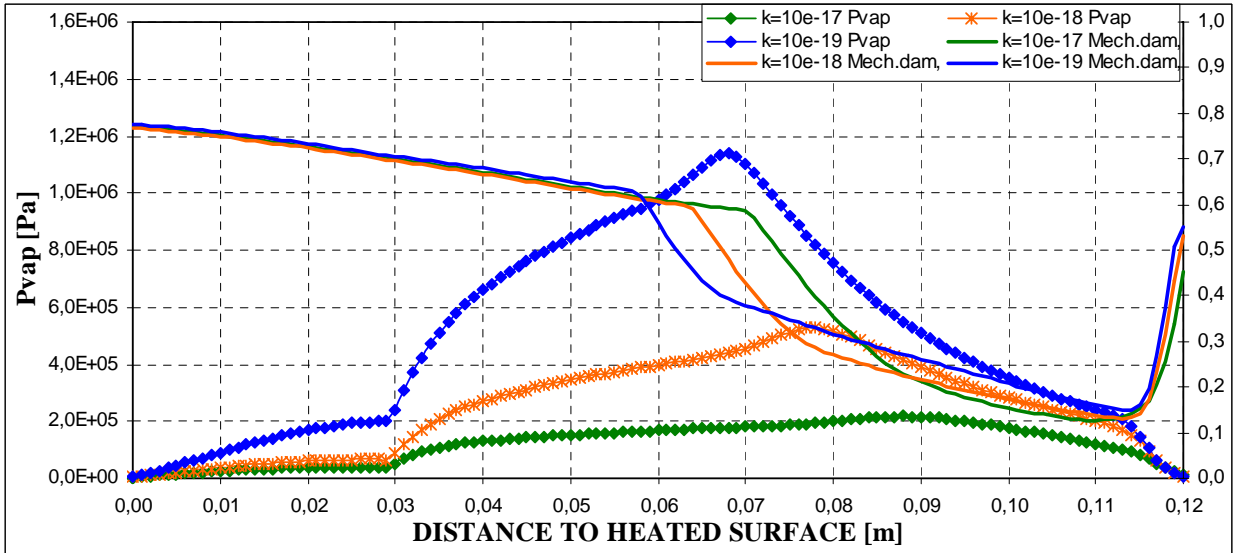


(c)

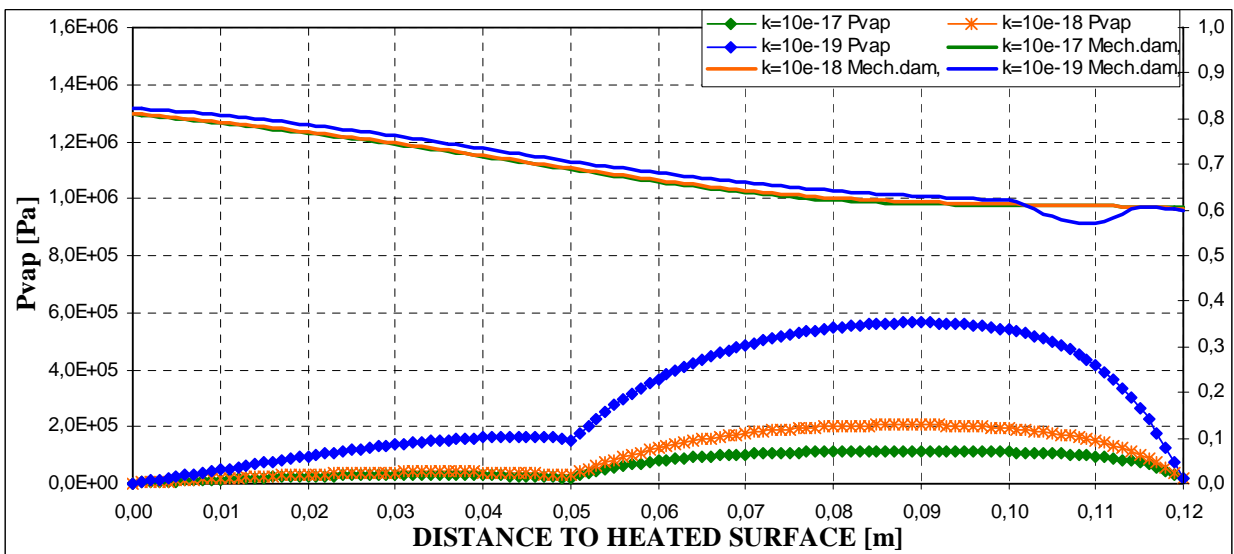
Figure 4-77. Mechanical damage and vapour pressure space distribution for three values of intrinsic permeability (10^{-17} , 10^{-18} , 10^{-19}) in case of $s=60\%$, Thickness = 12 centimetres, PARI ISO Heating curve, Material C60
(a) 1 hour; (b) 2 hours; (c) 3 hours



(a)

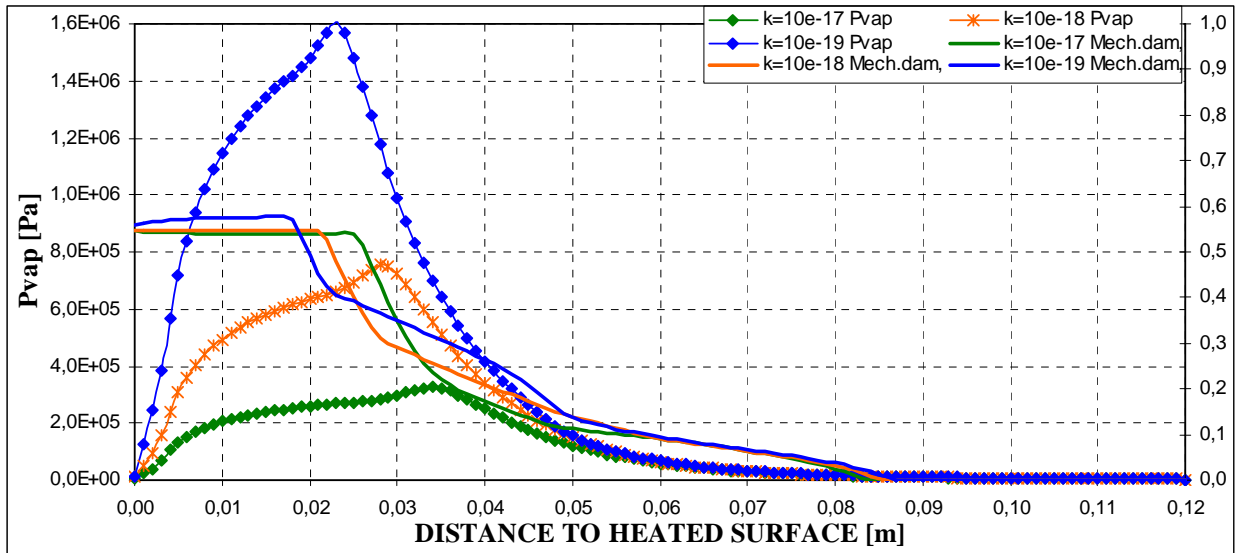


(b)

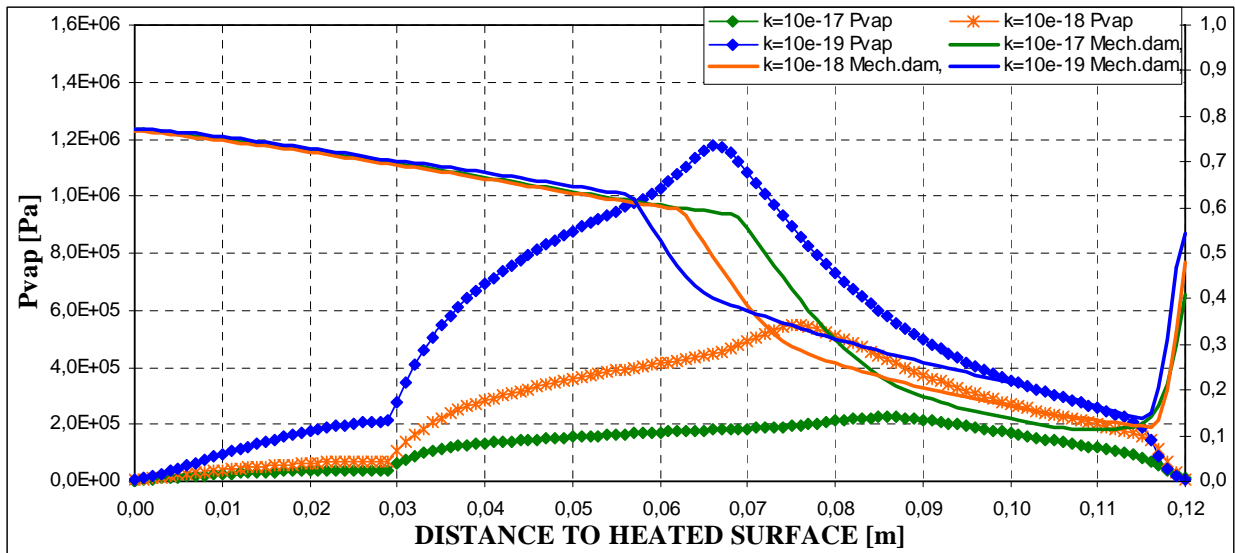


(c)

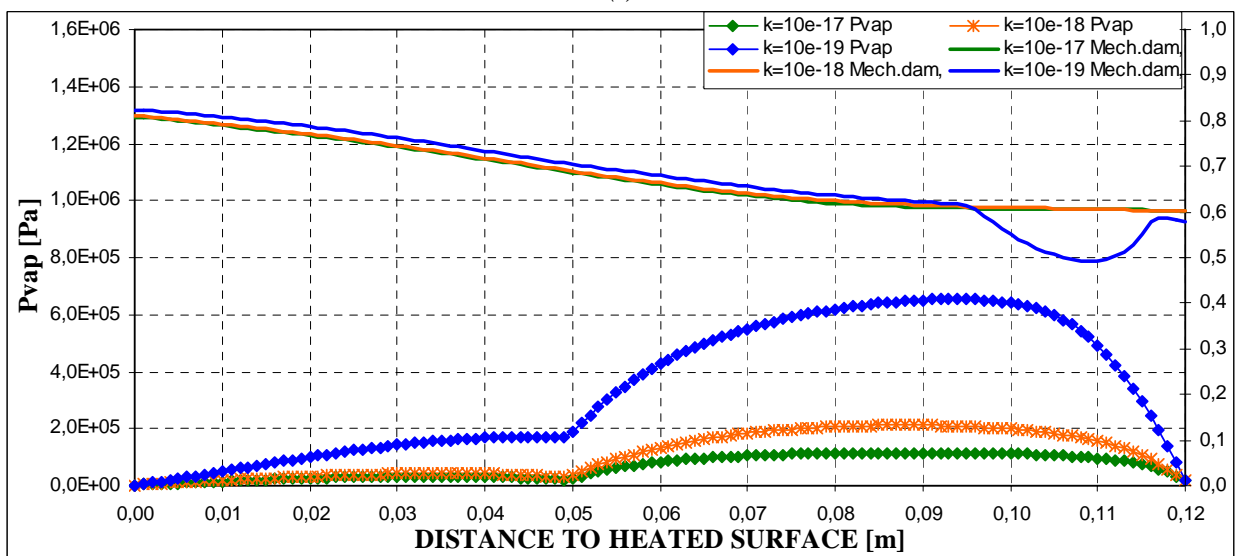
Figure 4-78. Mechanical damage and vapour pressure space distribution for three values of intrinsic permeability ($10^{-17}, 10^{-18}, 10^{-19}$) in case of $s=40\%$, Thickness = 12 centimetres, PAR2 SLOW Heating curve, Material C60
(a) 1 hour; (b) 2 hours; (c) 3 hours



(a)

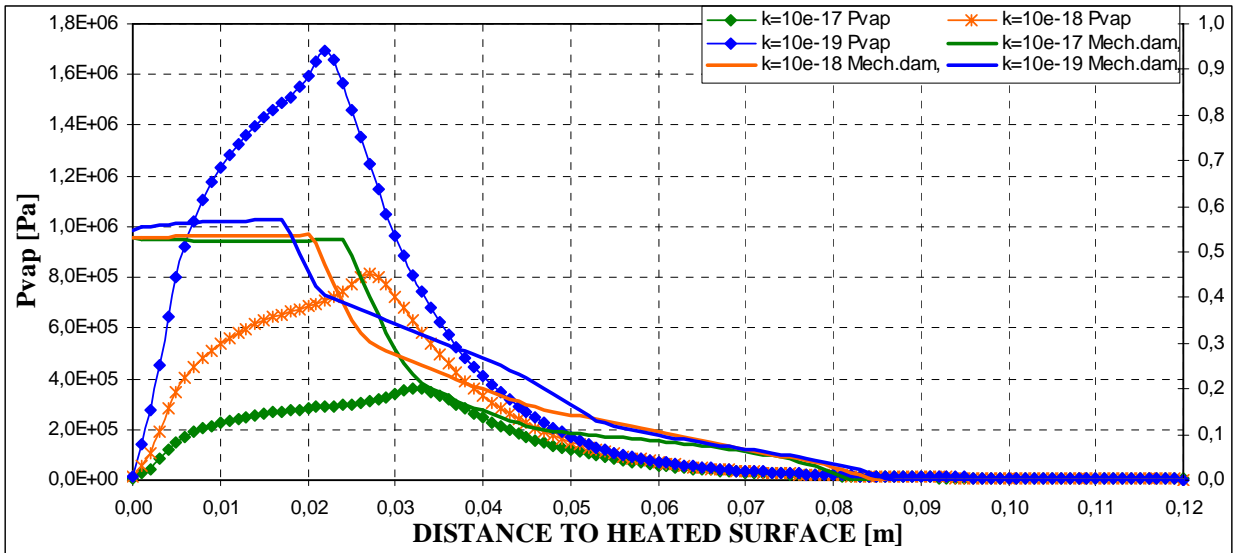


(b)

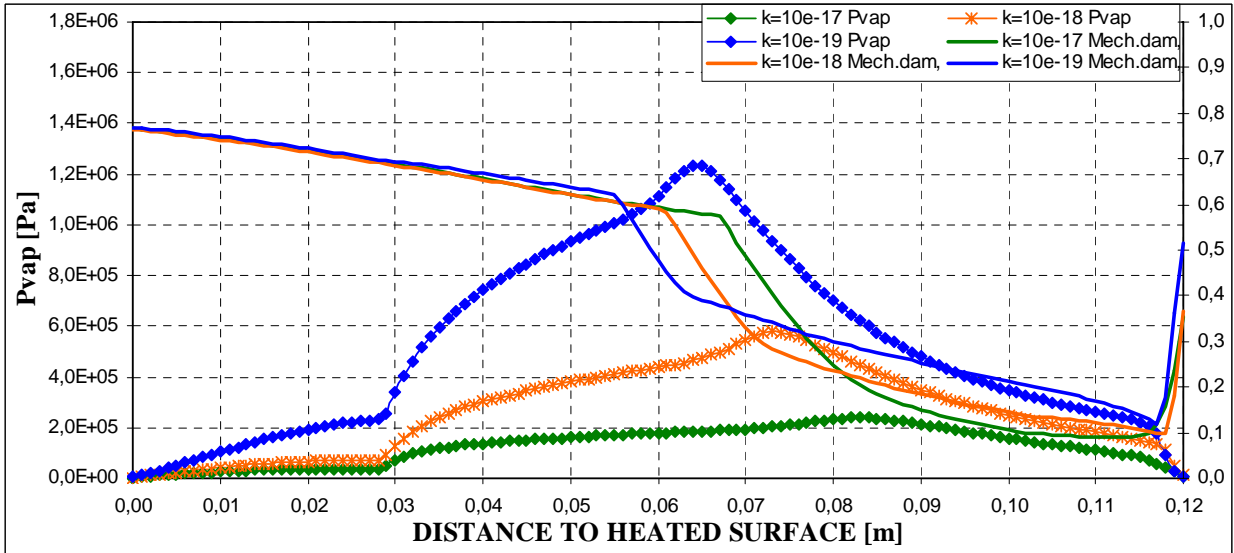


(c)

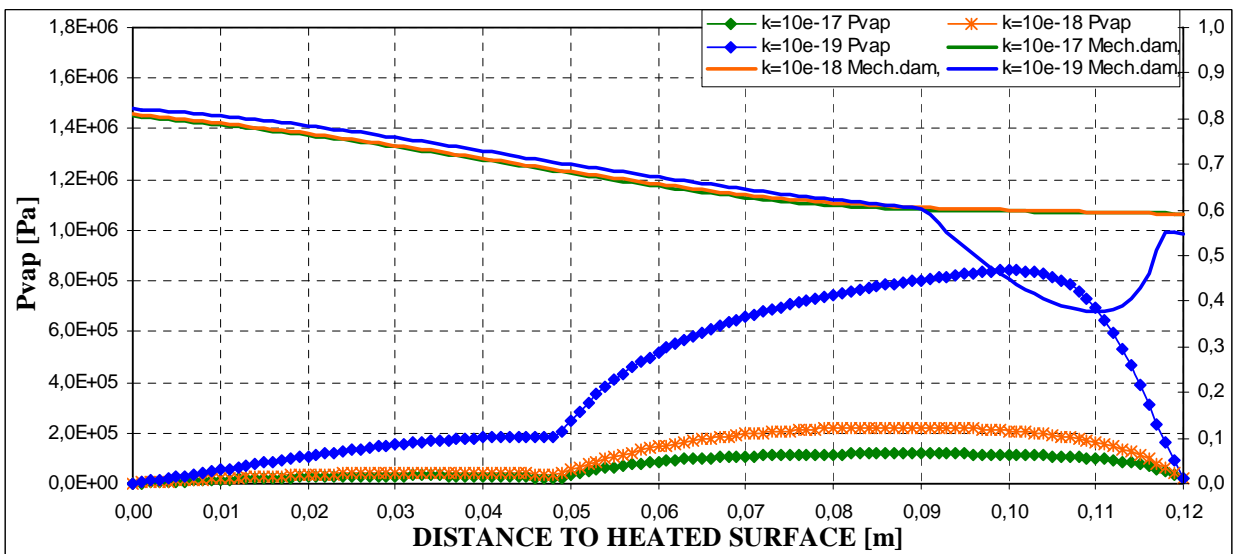
Figure 4-79. Mechanical damage and vapour pressure space distribution for three values of intrinsic permeability ($10^{-17}, 10^{-18}, 10^{-19}$) in case of $s=50\%$, Thickness = 12 centimetres, PAR2 SLOW Heating curve, Material C60
(a) 1 hour; (b) 2 hours; (c) 3 hours



(a)

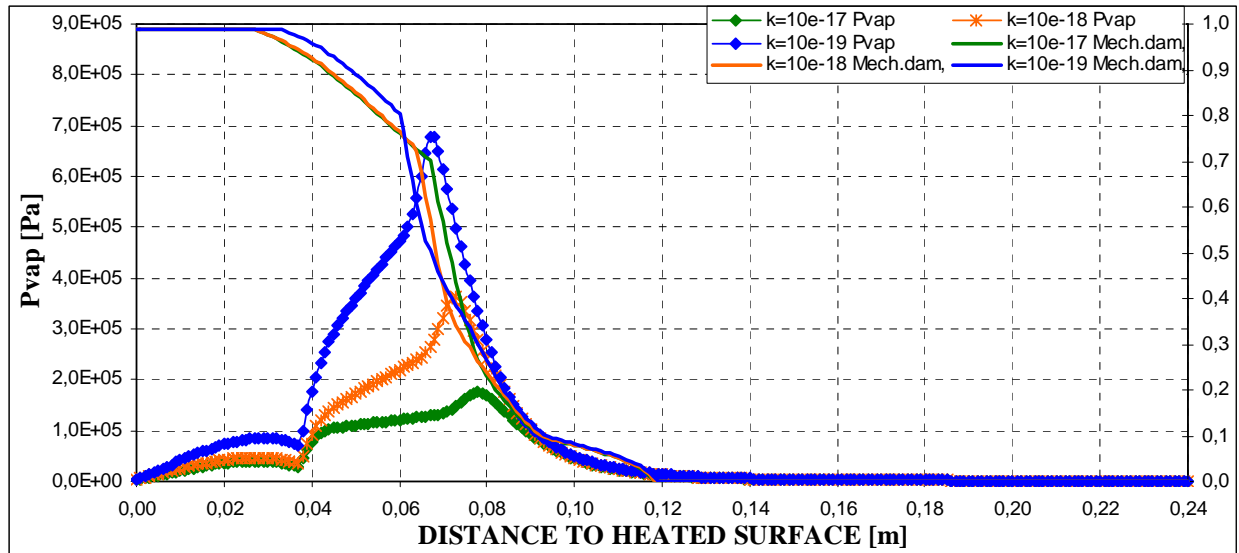


(b)

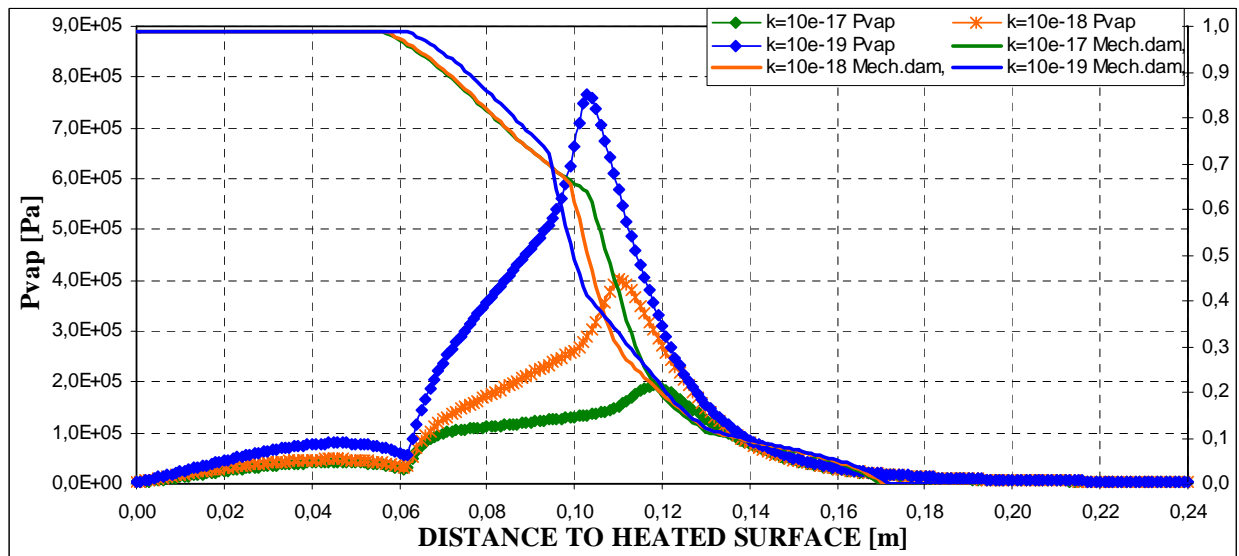


(c)

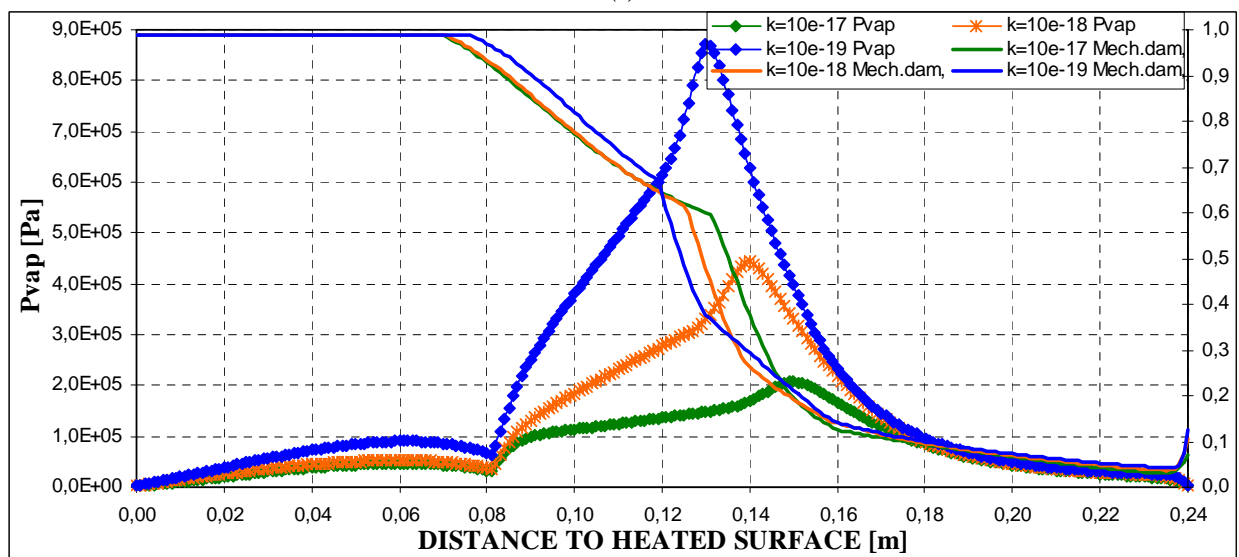
Figure 4-80. Mechanical damage and vapour pressure distribution for three values of intrinsic permeability ($10^{-17}, 10^{-18}, 10^{-19}$) in case of $s=60\%$, Thickness = 12 centimetres, PAR2 SLOW Heating curve, Material C60
(a) 1 hour; (b) 2 hours; (c) 3 hours



(a)

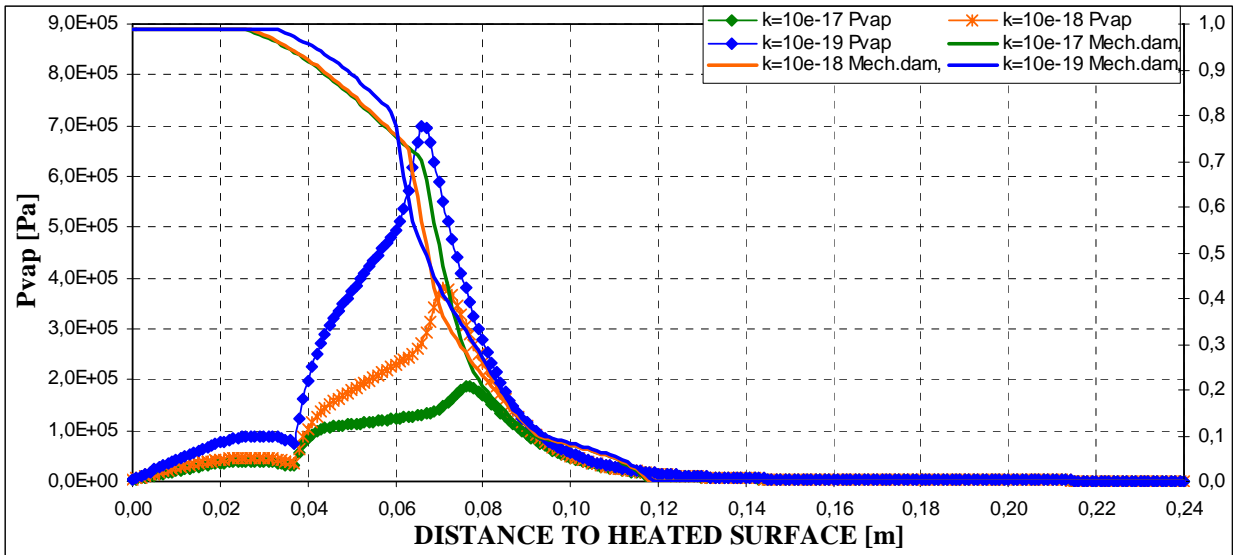


(b)

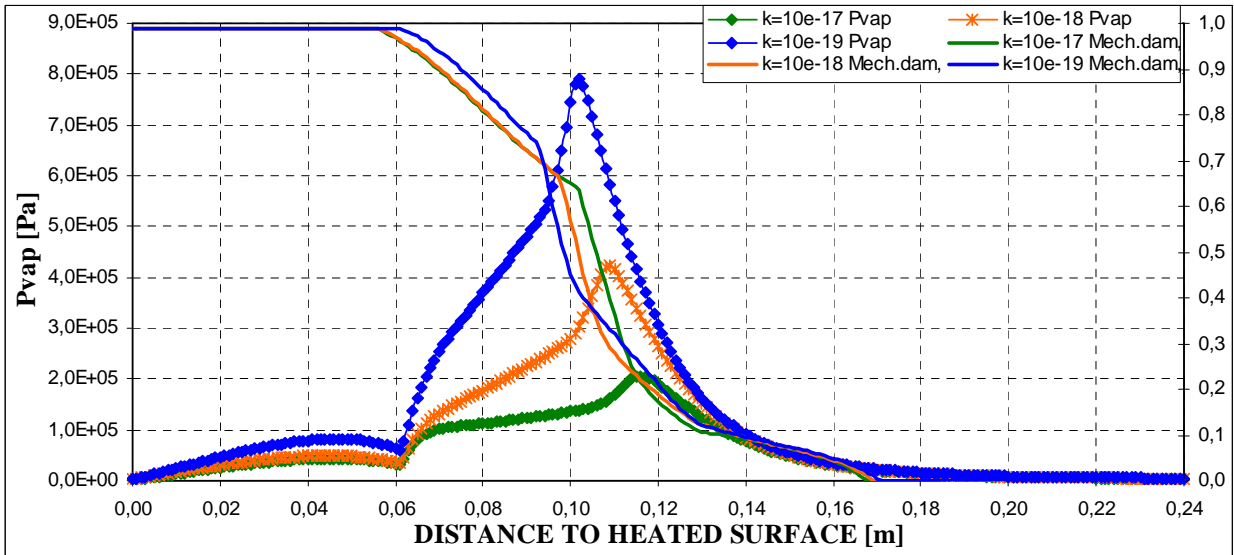


(c)

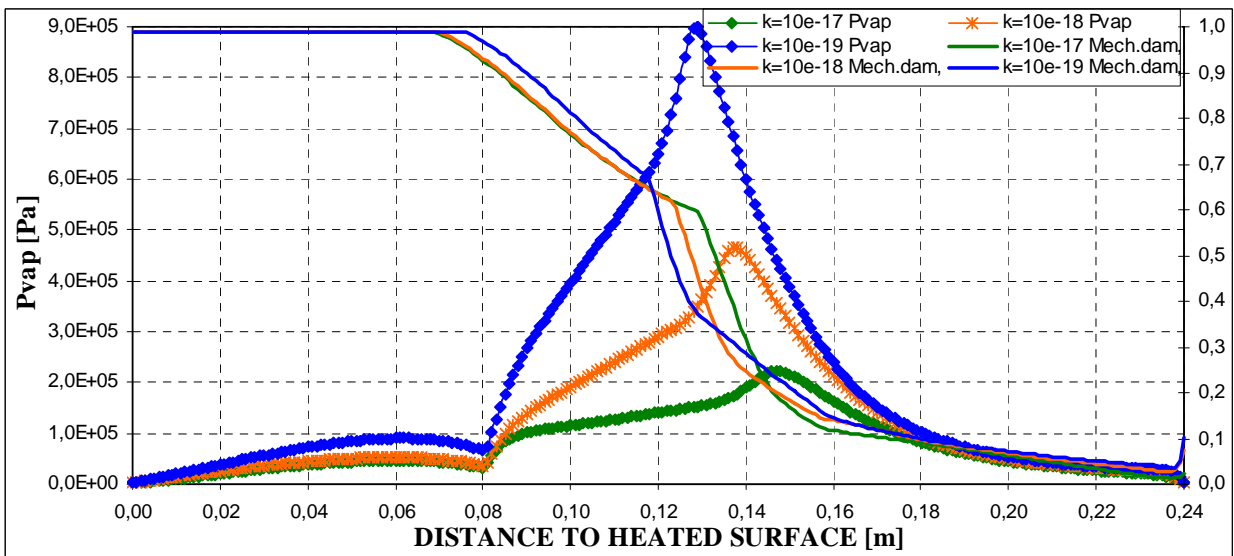
Figure 4-81. Mechanical damage and vapour pressure distribution for three values of intrinsic permeability ($10^{-17}, 10^{-18}, 10^{-19}$) in case of $s=40\%$, Thickness = 24 centimetres, PAR1 ISO Heating curve, Material C60
(a) 1 hour; (b) 2 hours; (c) 3 hours



(a)

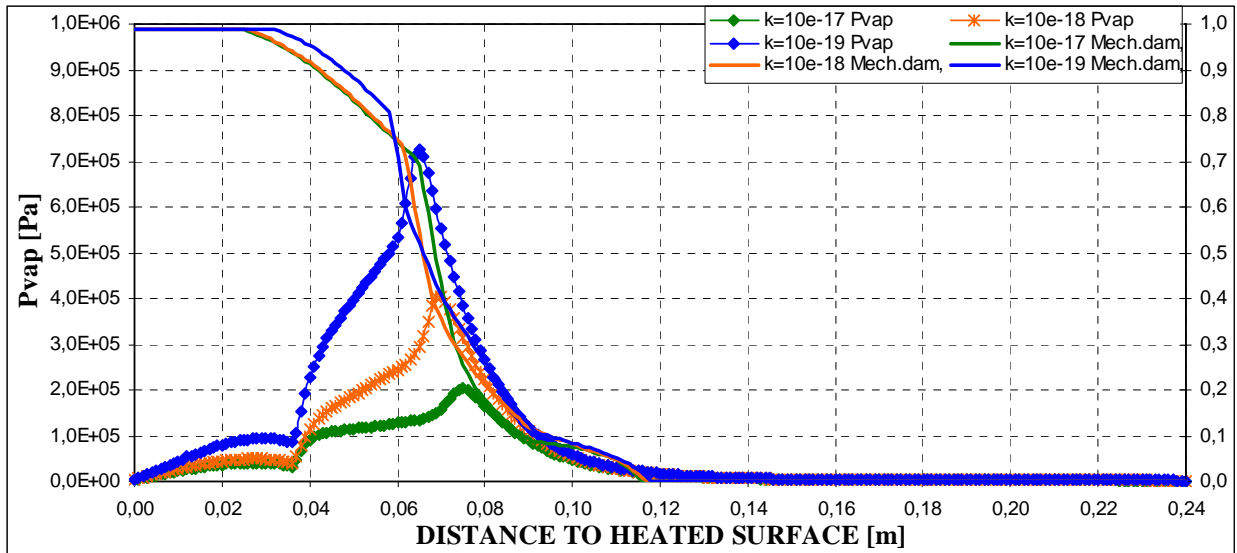


(b)

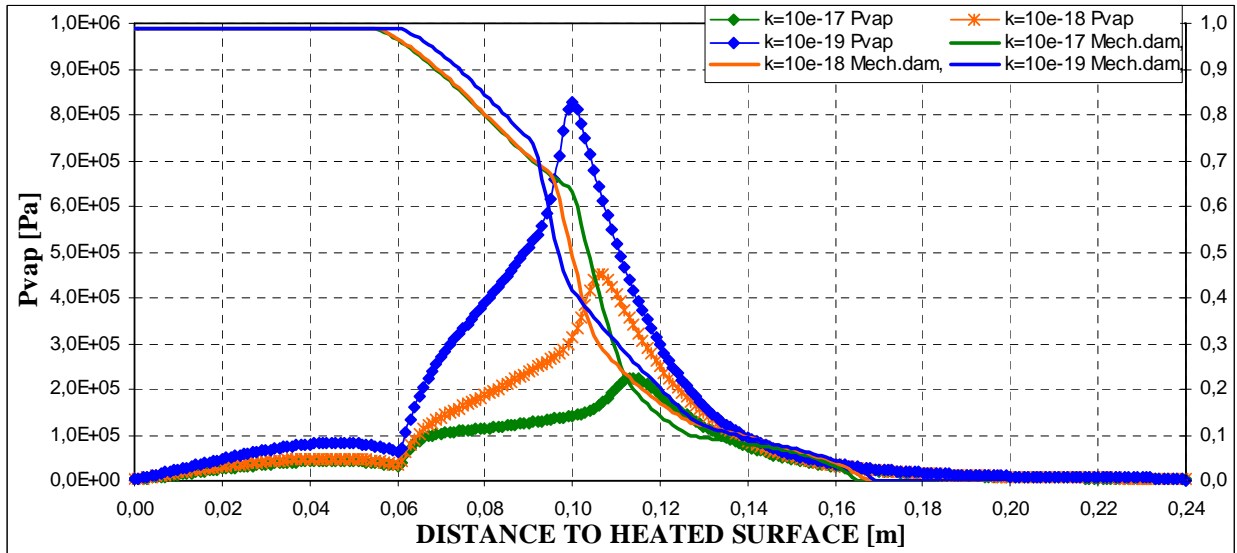


(c)

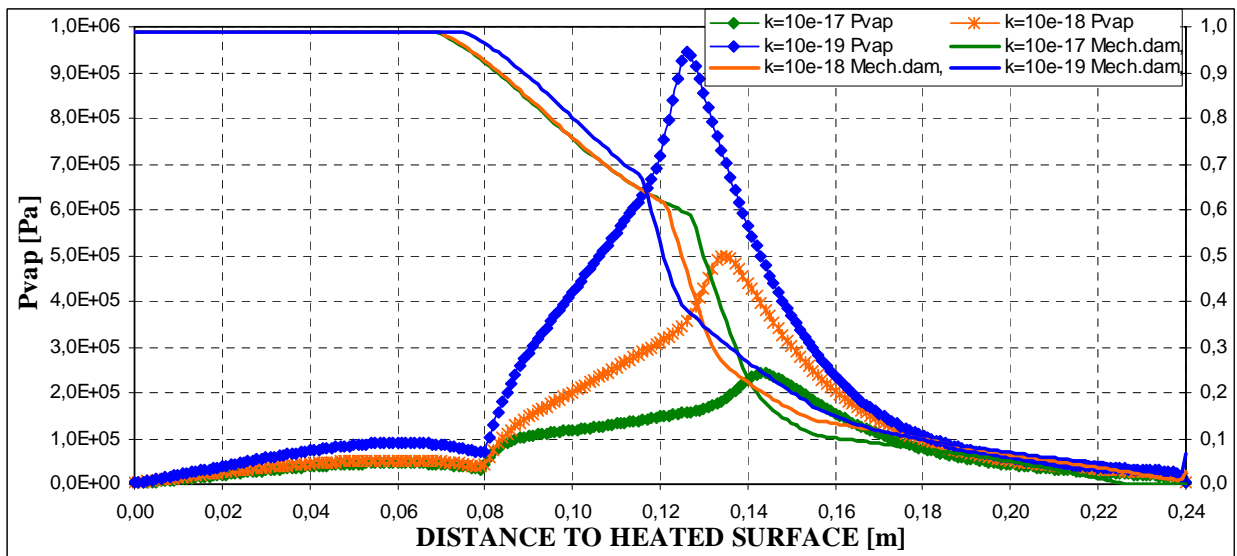
Figure 4-82. Mechanical damage and vapour pressure space distribution for three values of intrinsic permeability ($10^{-17}, 10^{-18}, 10^{-19}$) in case of $s=50\%$, Thickness = 24 centimetres, PAR1 ISO Heating curve, Material C60
(a) 1 hour; (b) 2 hours; (c) 3 hours



(a)

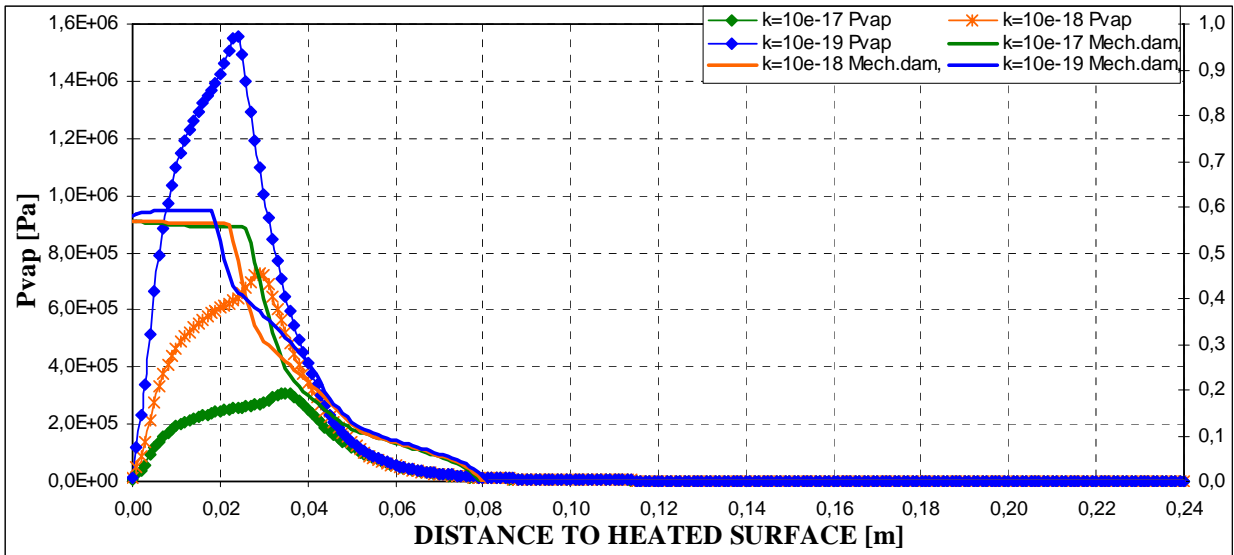


(b)

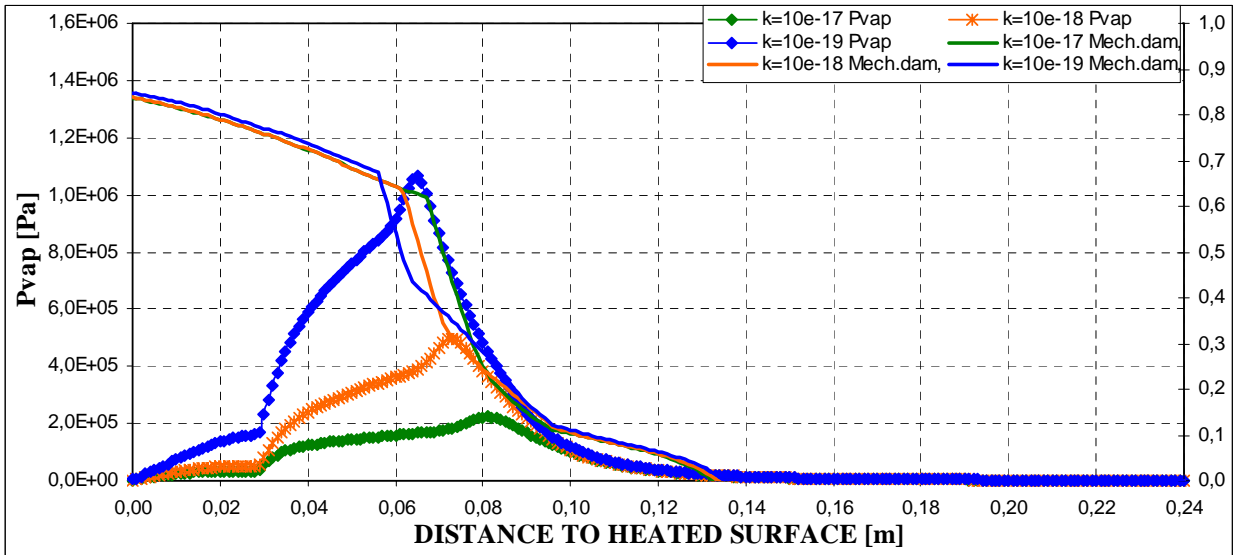


(c)

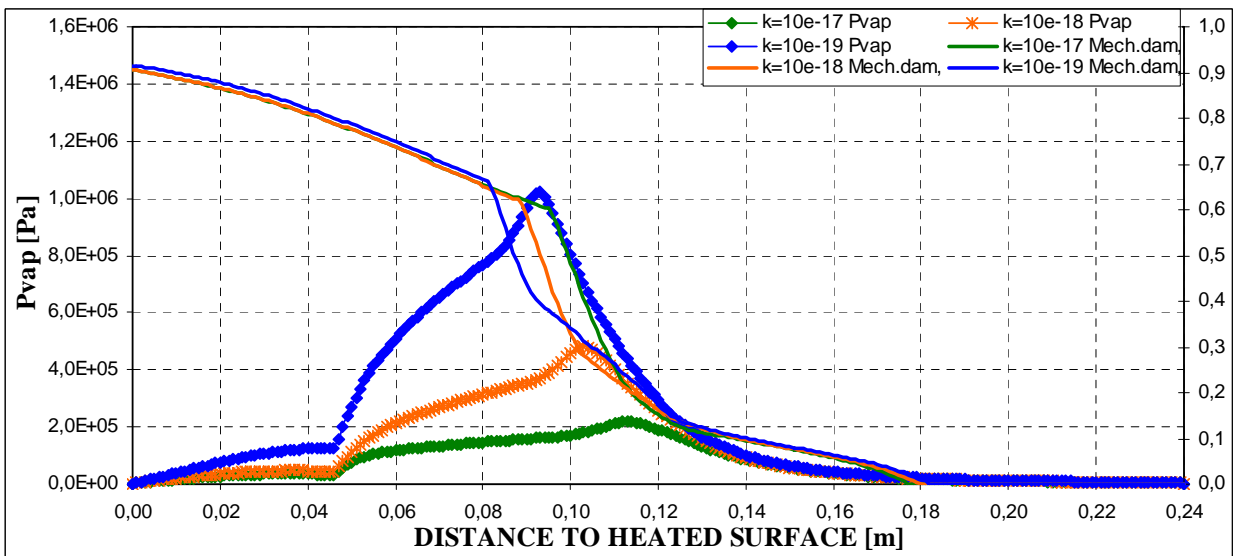
Figure 4-83. Mechanical damage and vapour pressure space distribution for three values of intrinsic permeability ($10^{-17}, 10^{-18}, 10^{-19}$) in case of $s=60\%$, Thickness = 24 centimetres, PAR1 ISO Heating curve, Material C60
(a) 1 hour; (b) 2 hours; (c) 3 hours



(a)

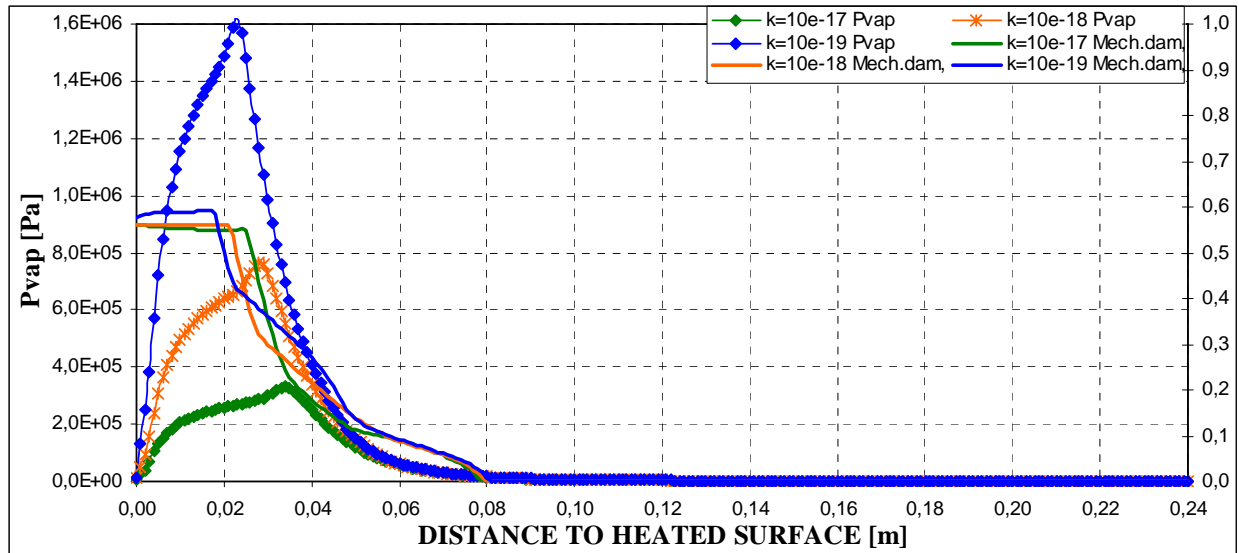


(b)

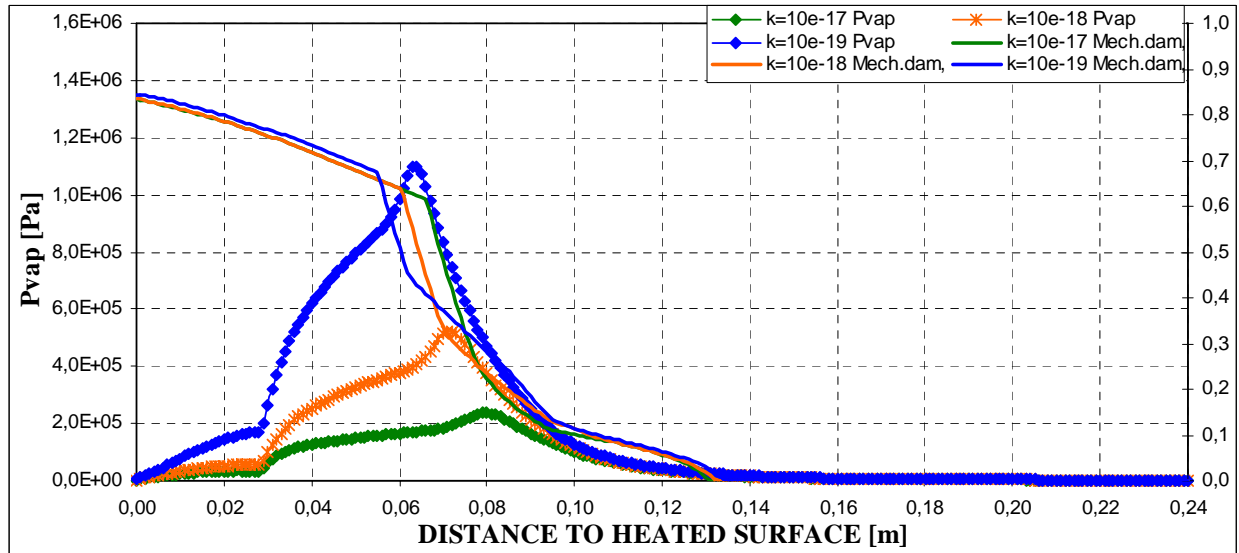


(c)

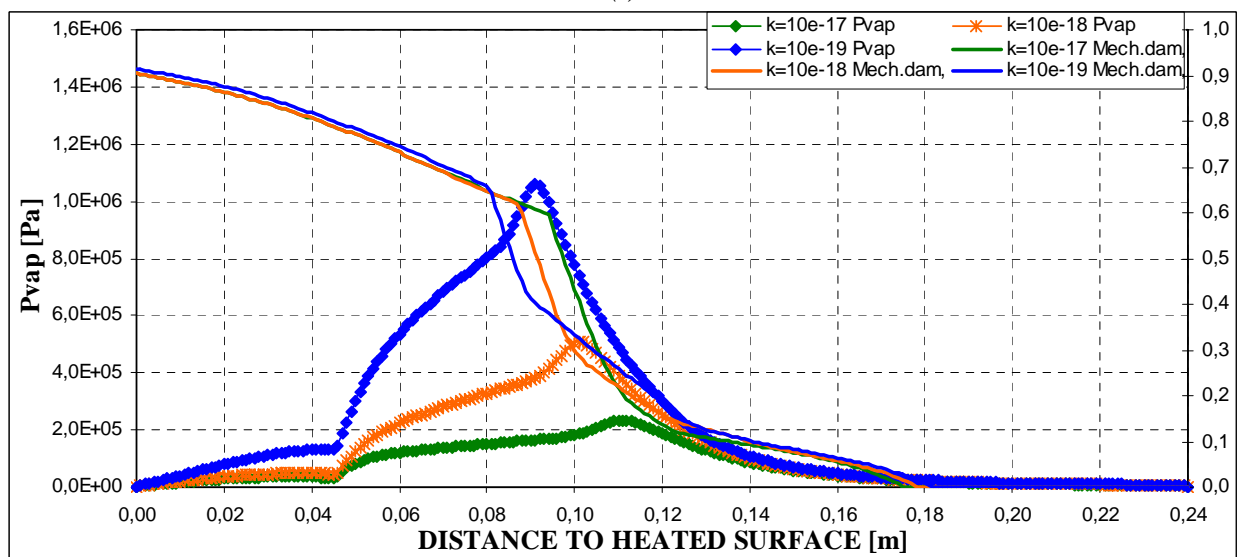
Figure 4-84. Mechanical damage and vapour pressure space distribution for three values of intrinsic permeability ($10^{-17}, 10^{-18}, 10^{-19}$) in case of $s=40\%$, Thickness = 24 centimetres, PAR2 SLOW Heating curve, Material C60
(a) 1 hour; (b) 2 hours; (c) 3 hours



(a)

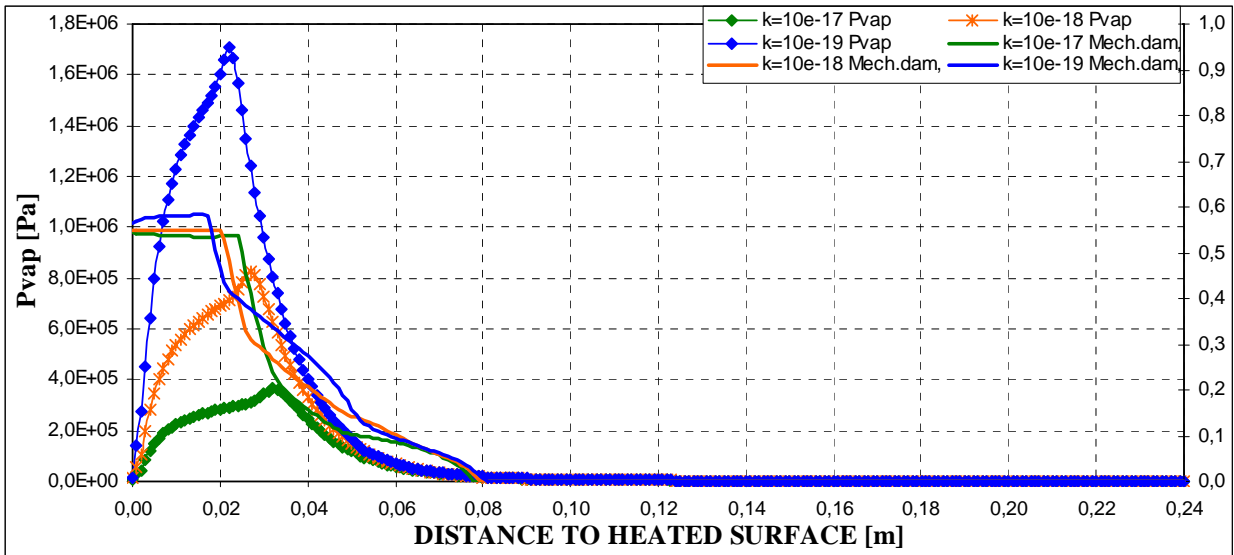


(b)

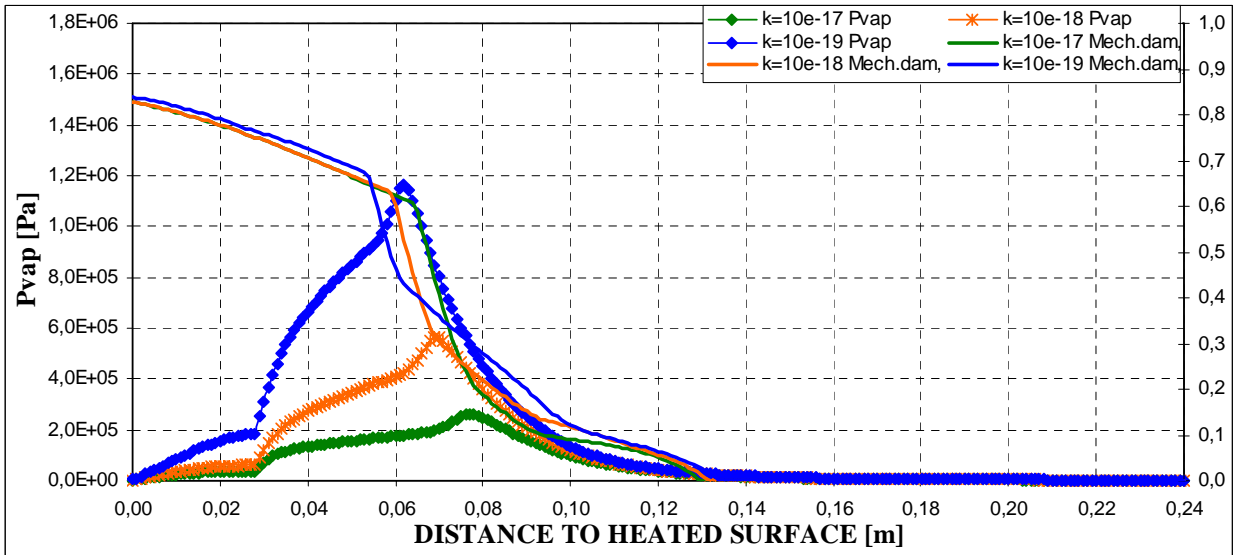


(c)

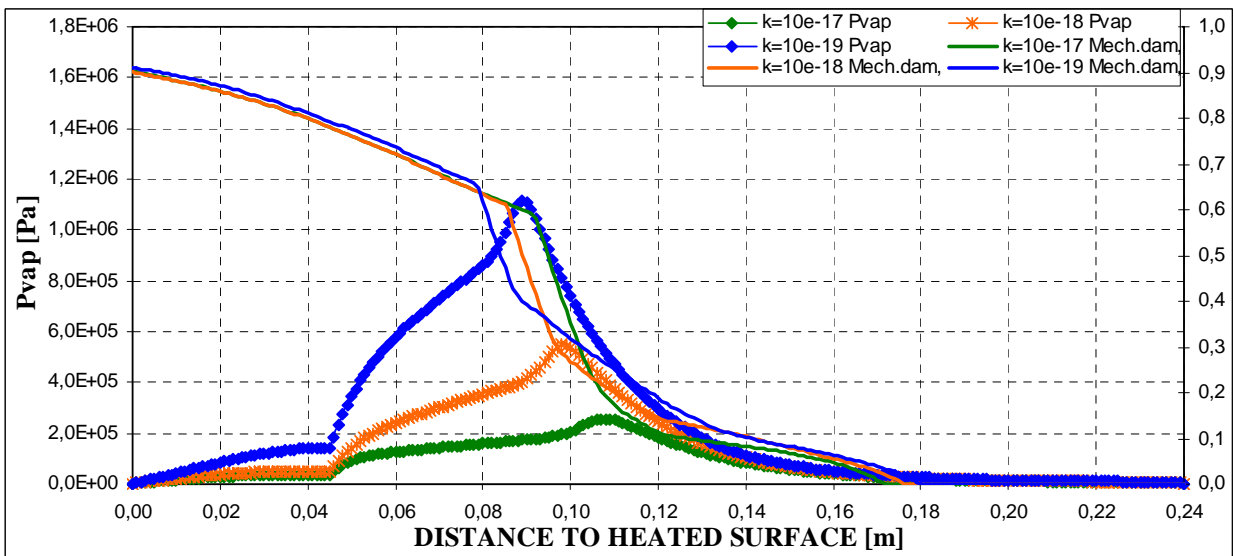
Figure 4-85. Mechanical damage and vapour pressure distribution for three values of intrinsic permeability (10^{-17} , 10^{-18} , 10^{-19}) in case of $s=50\%$, Thickness = 24 centimetres, PAR2 SLOW Heating curve, Material C60
(a) 1 hour; (b) 2 hours; (c) 3 hours



(a)

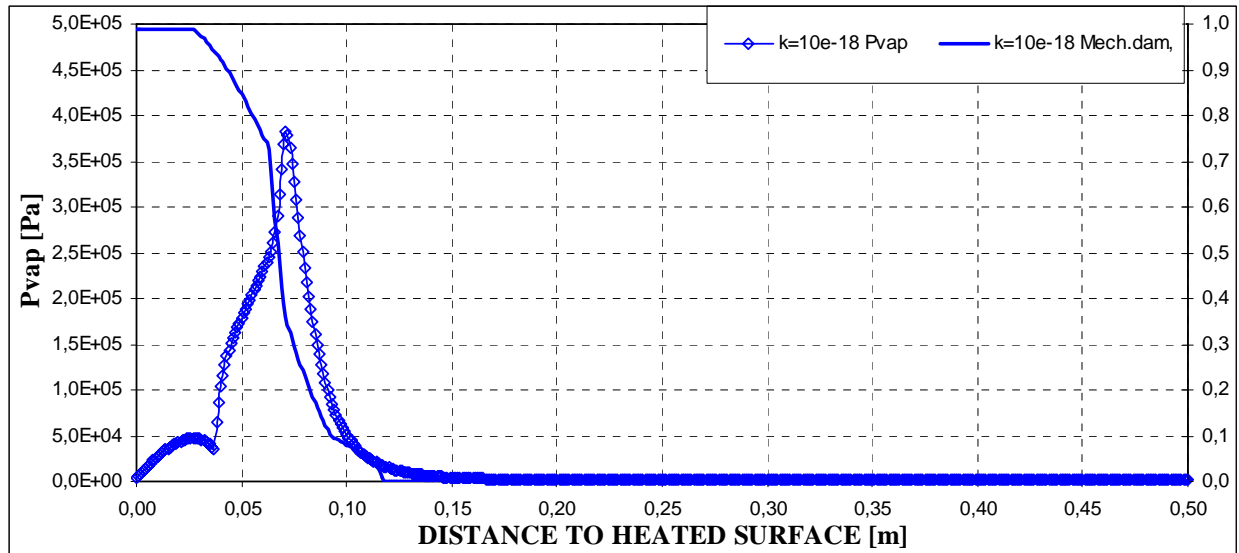


(b)

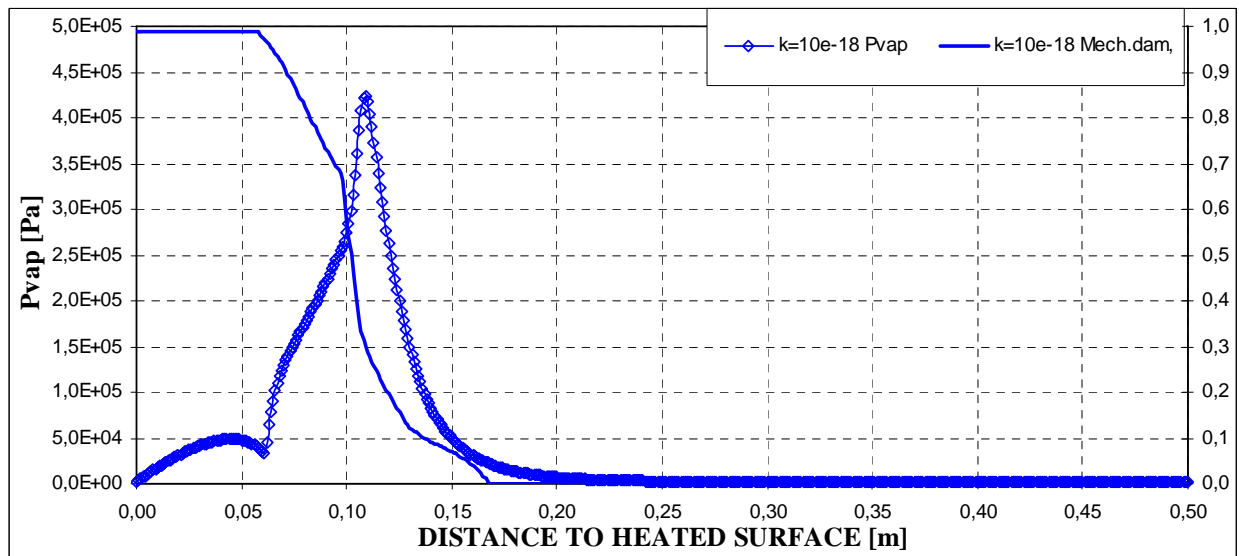


(c)

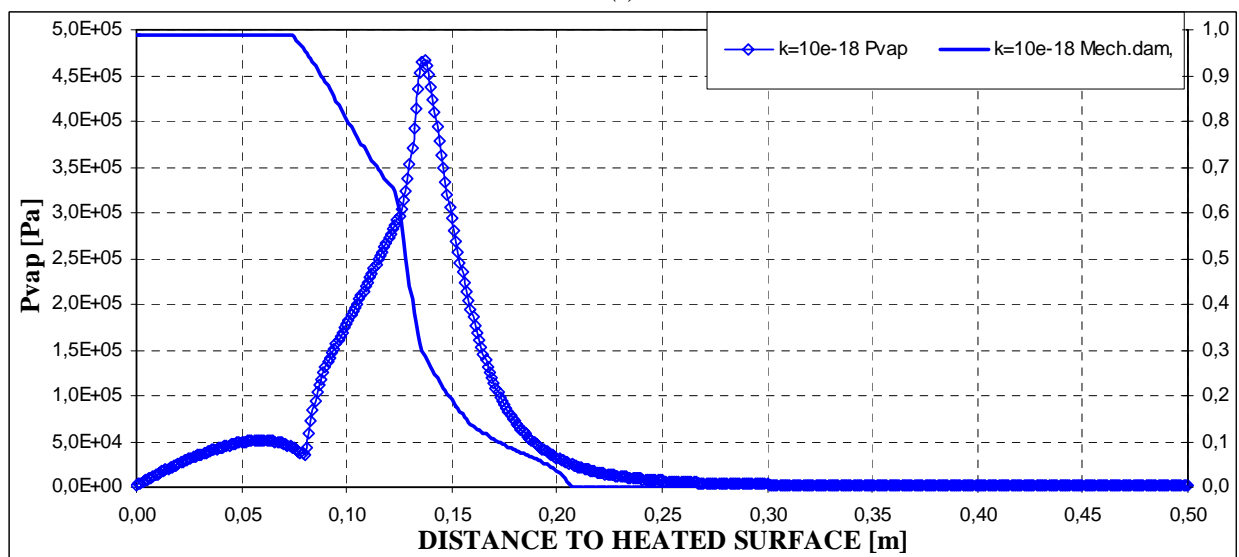
Figure 4-86. Mechanical damage and vapour pressure space distribution for three values of intrinsic permeability ($10^{-17}, 10^{-18}, 10^{-19}$) in case of $s=60\%$, Thickness = 24 centimetres, PAR2 SLOW Heating curve, Material C60
(a) 1 hour; (b) 2 hours; (c) 3 hours



(a)

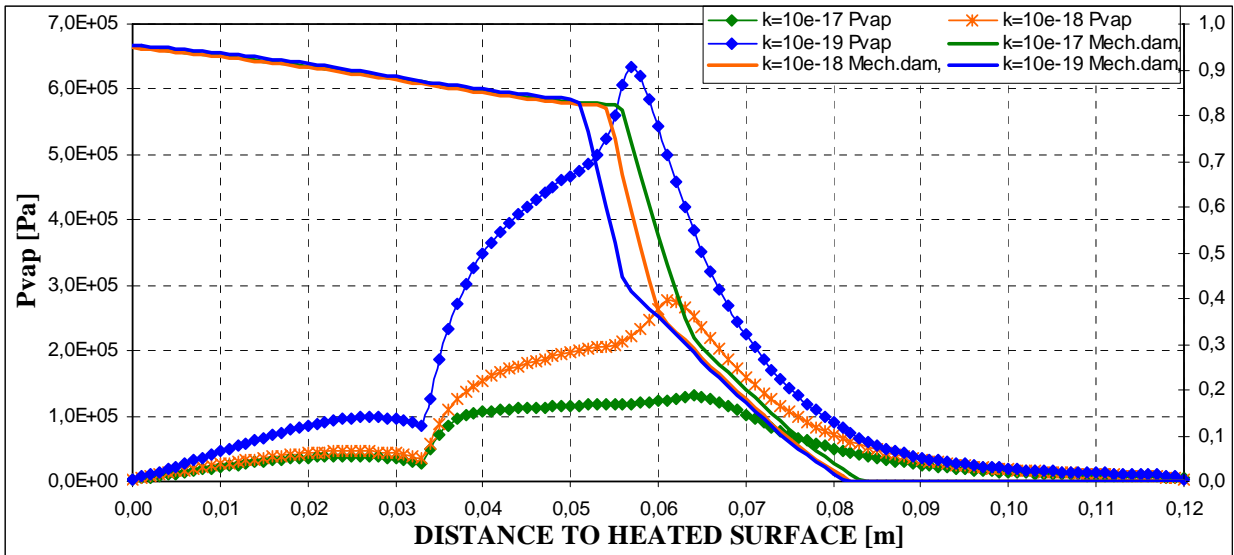


(b)

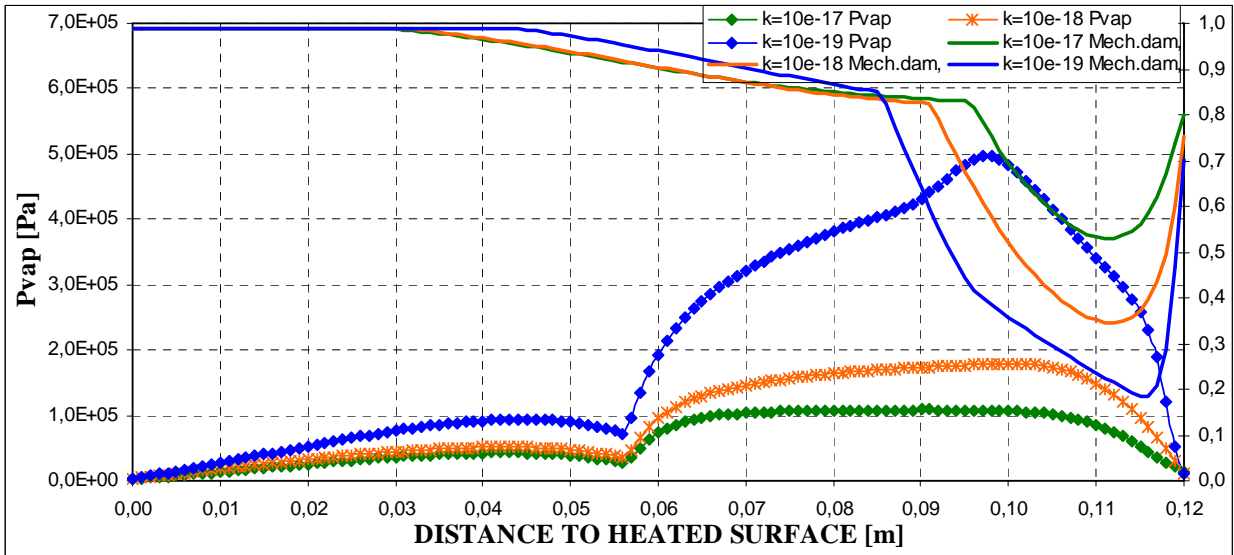


(c)

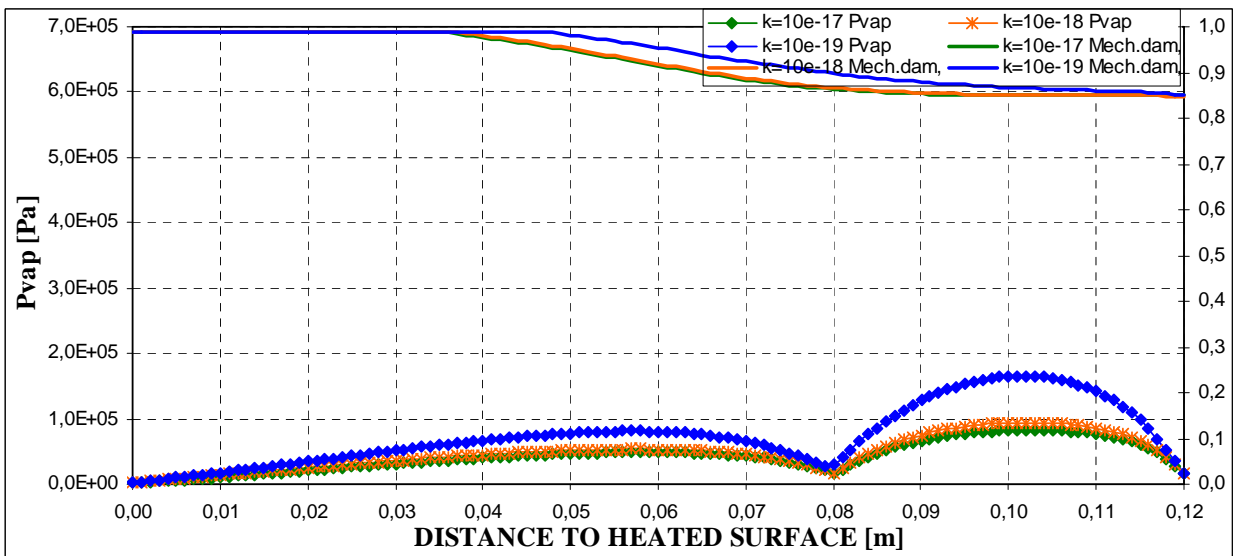
Figure 4-87. Mechanical damage and vapour pressure distribution for three values of intrinsic permeability ($10^{-17}, 10^{-18}, 10^{-19}$) in case of $s=50\%$, Thickness = 50 centimetres, PAR1 ISO Heating curve, Material C60
(a) 1 hour; (b) 2 hours; (c) 3 hours



(a)

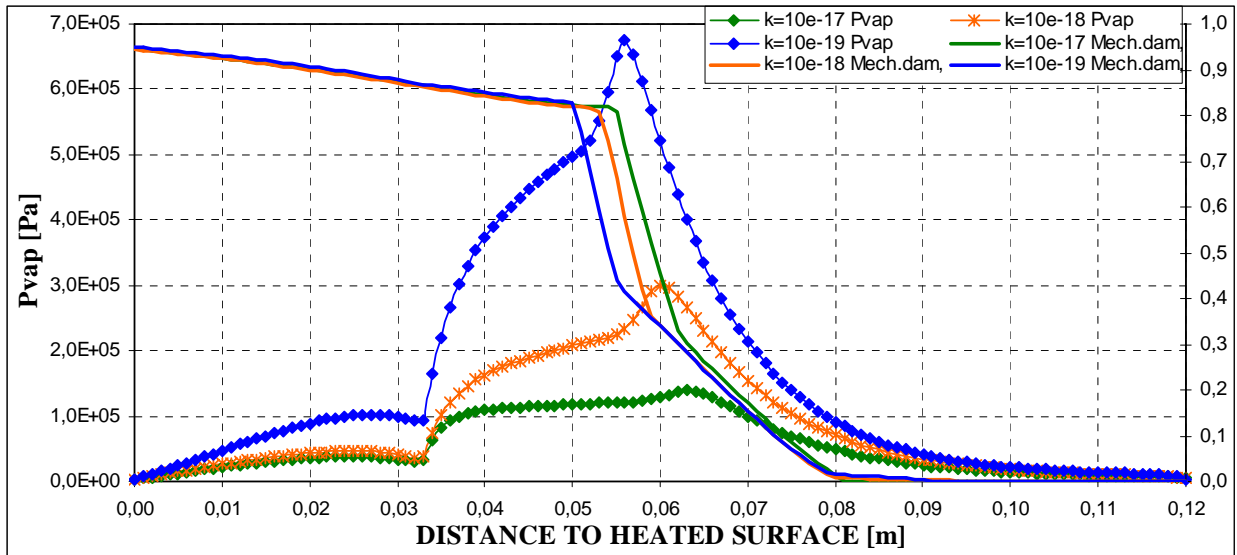


(b)

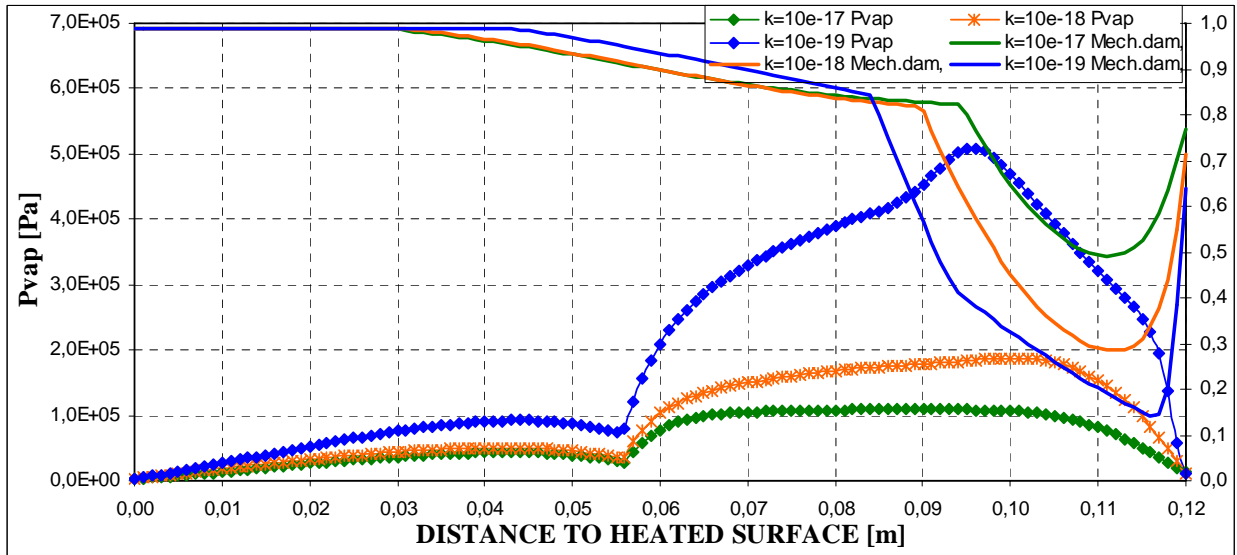


(c)

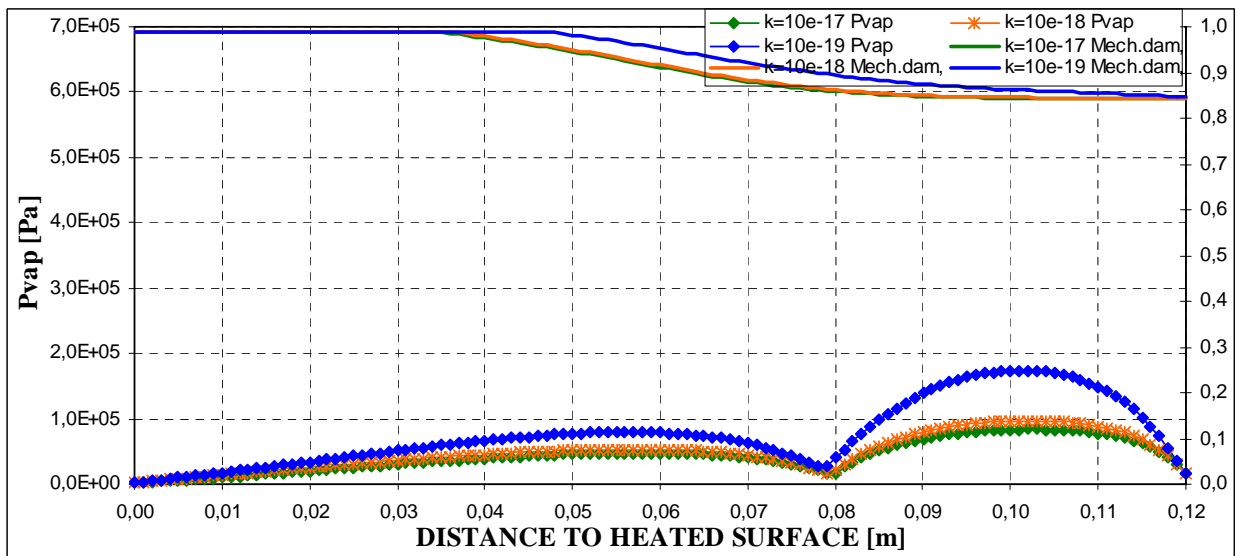
Figure 4-88. Mechanical damage and vapour pressure space distribution for three values of intrinsic permeability ($10^{-17}, 10^{-18}, 10^{-19}$) in case of $s=40\%$, Thickness = 12 centimetres, PAR1 ISO Heating curve, Material C90
 (a) 1 hour; (b) 2 hours; (c) 3 hours



(a)

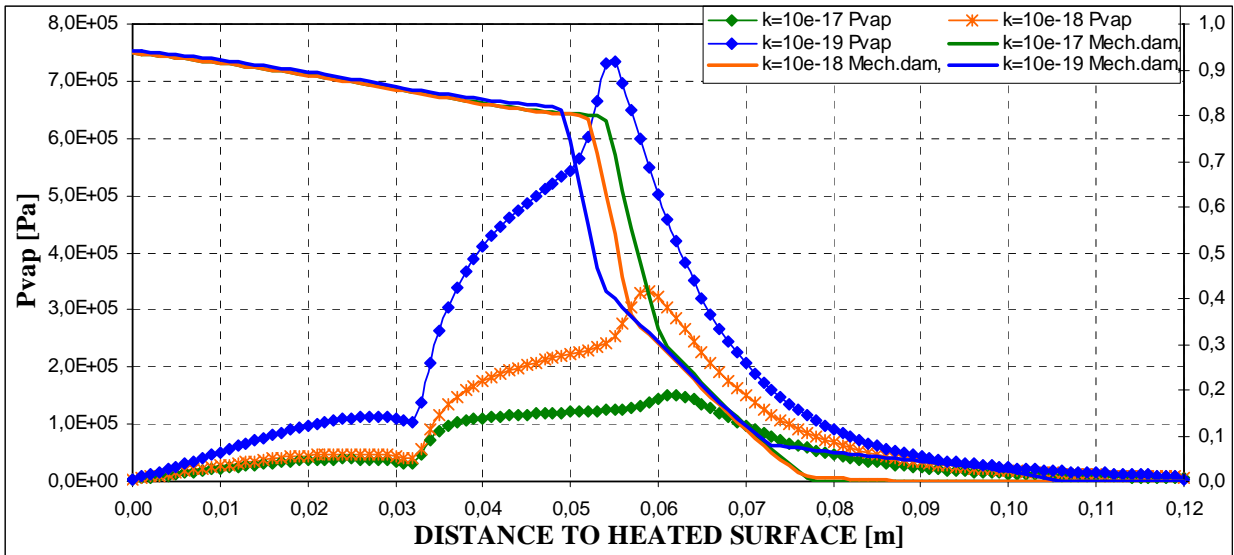


(b)

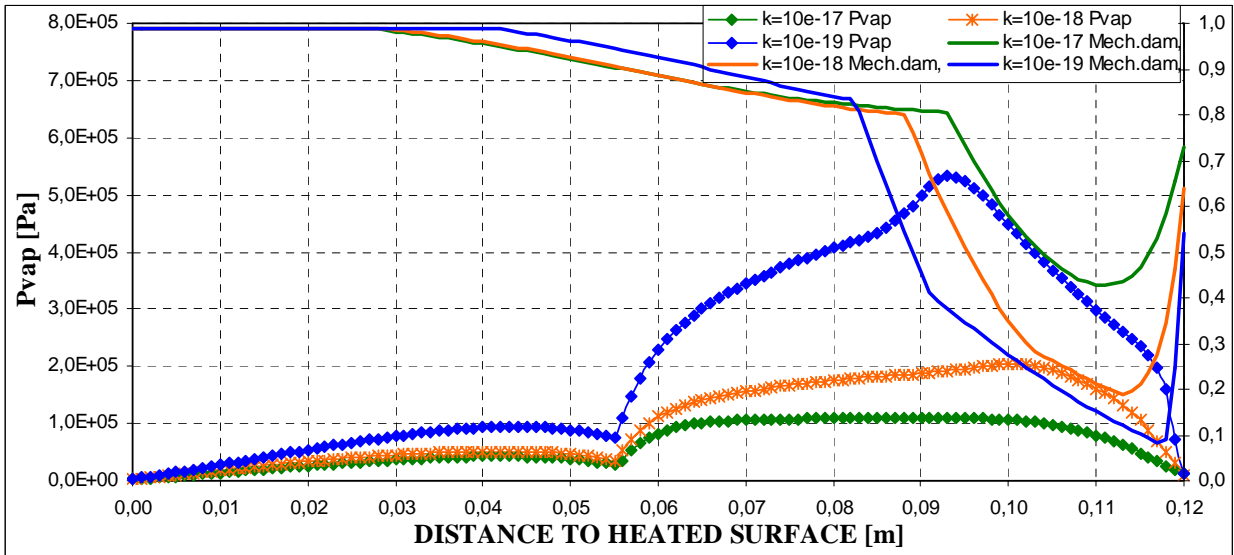


(c)

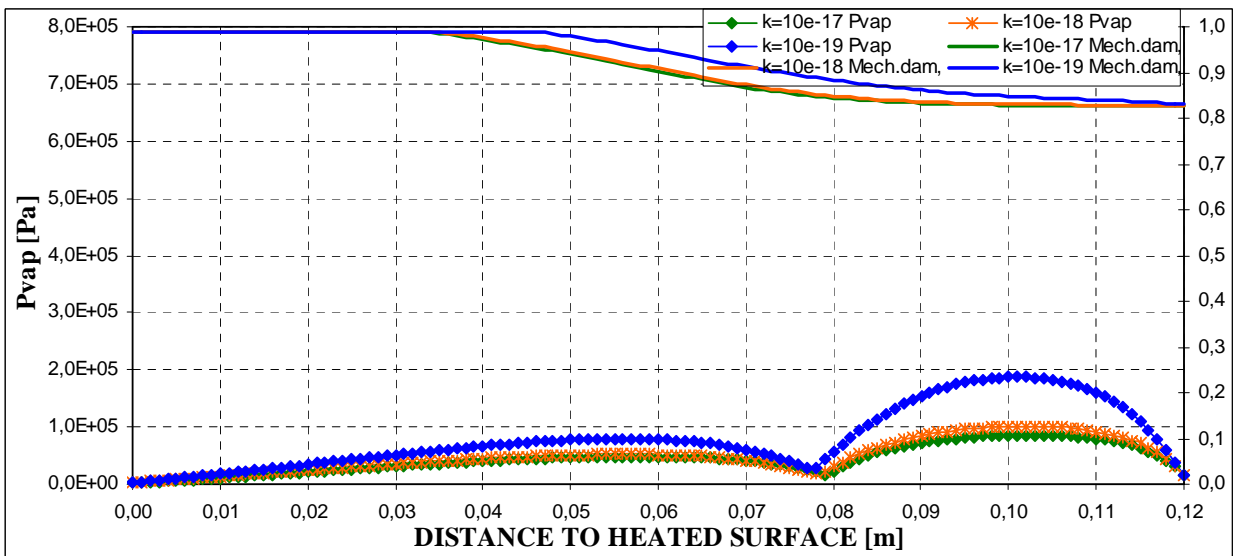
Figure 4-89. Mechanical damage and vapour pressure distribution for three values of intrinsic permeability ($10^{-17}, 10^{-18}, 10^{-19}$) in case of $s=50\%$, Thickness = 12 centimetres, PAR1 ISO Heating curve, Material C90
(a) 1 hour; (b) 2 hours; (c) 3 hours



(a)

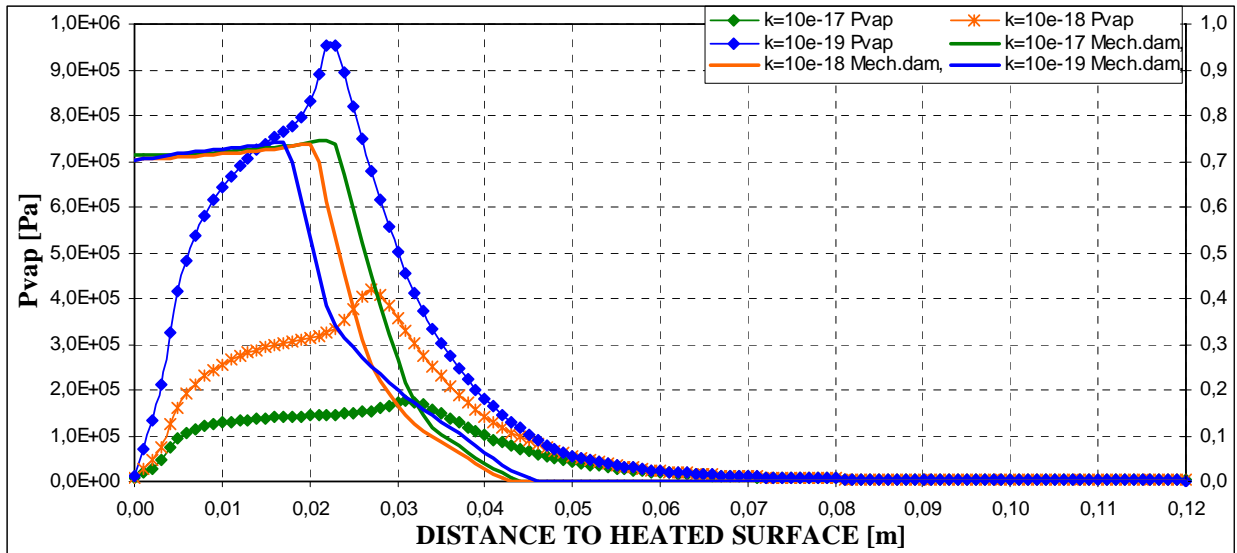


(b)

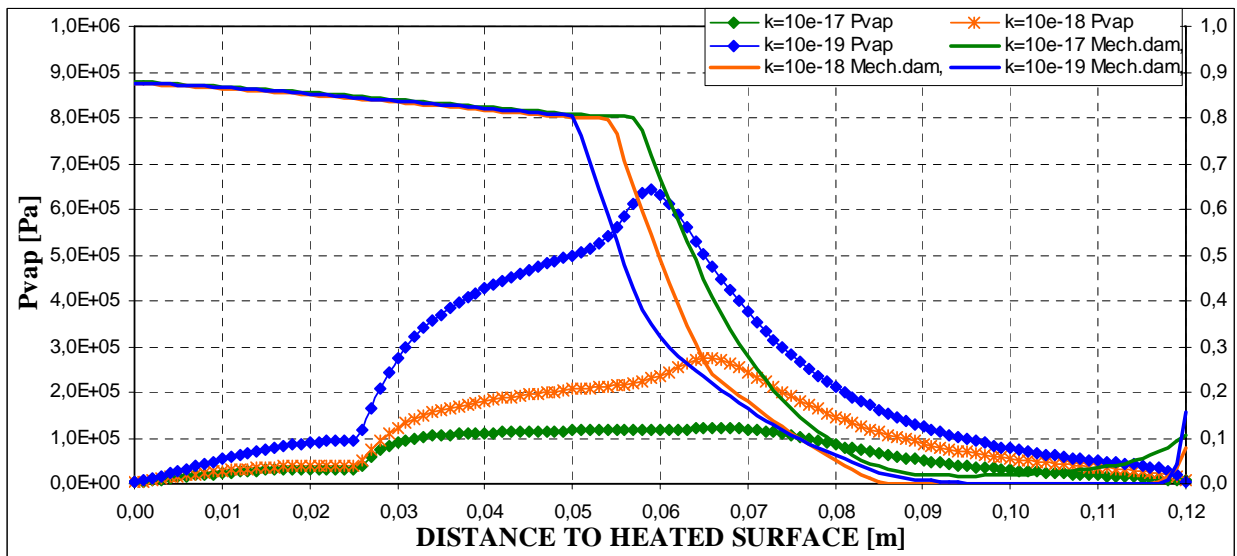


(c)

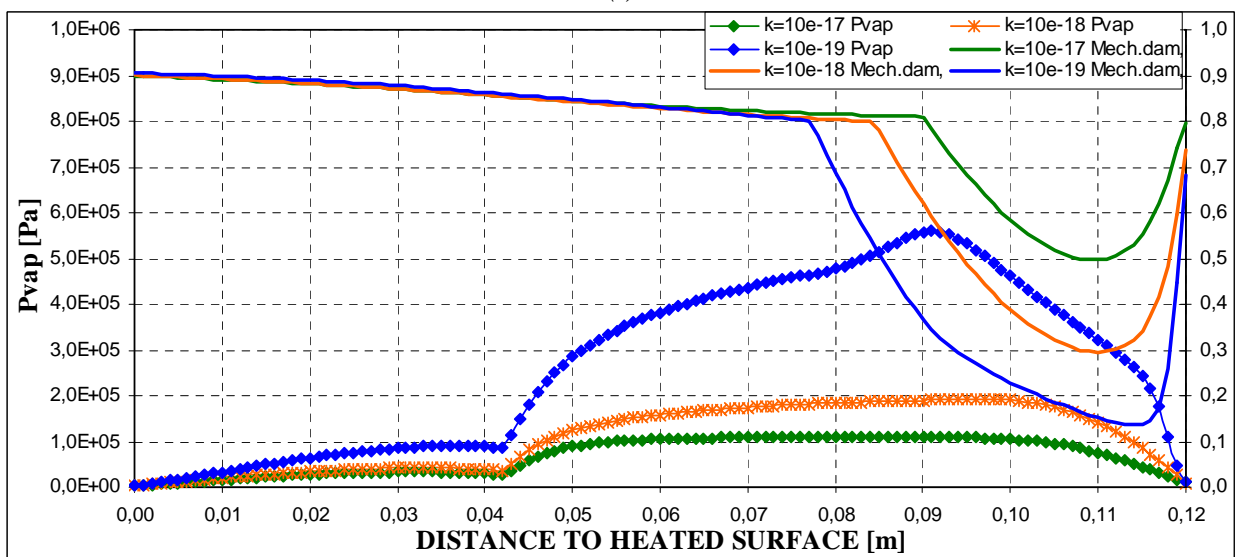
Figure 4-90. Mechanical damage and vapour pressure space distribution for three values of intrinsic permeability ($10^{-17}, 10^{-18}, 10^{-19}$) in case of $s=60\%$, Thickness = 12 centimetres, PAR1 ISO Heating curve, Material C90
(a) 1 hour; (b) 2 hours; (c) 3 hours



(a)

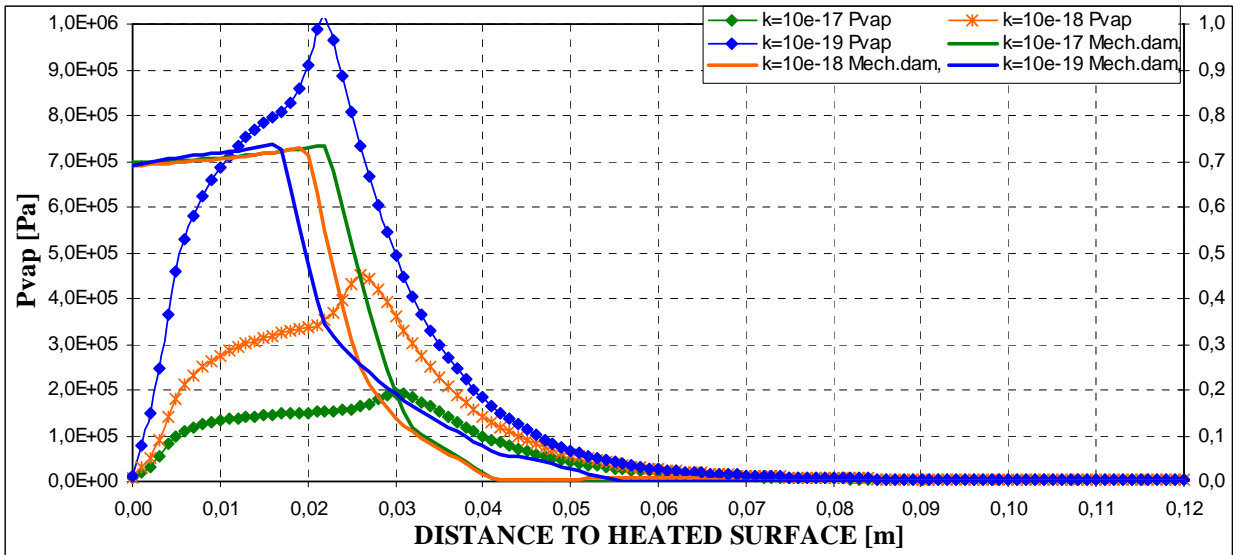


(b)

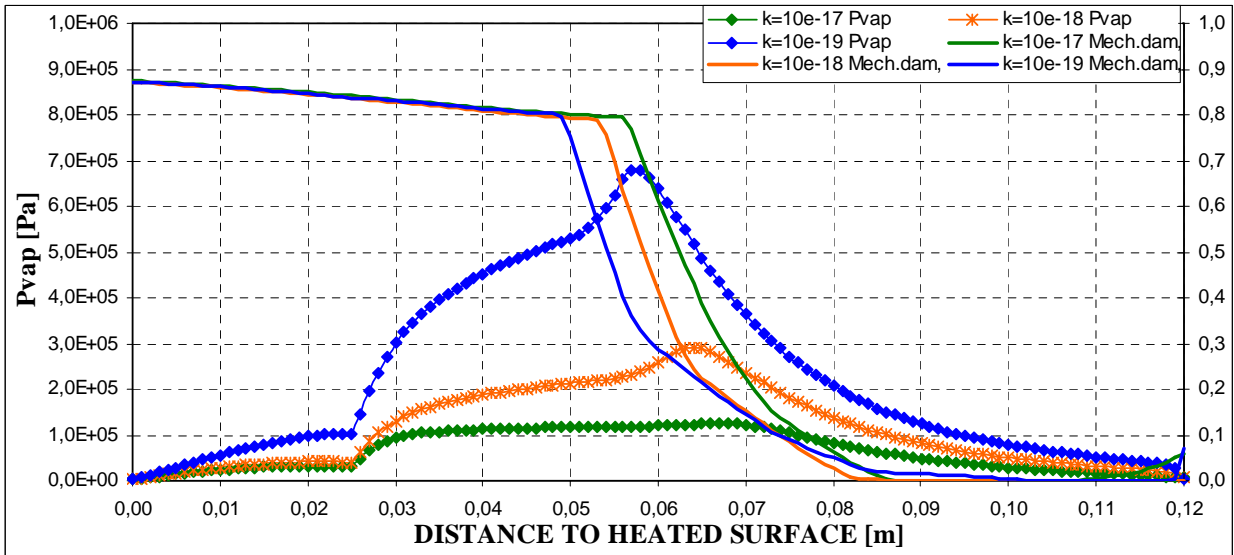


(c)

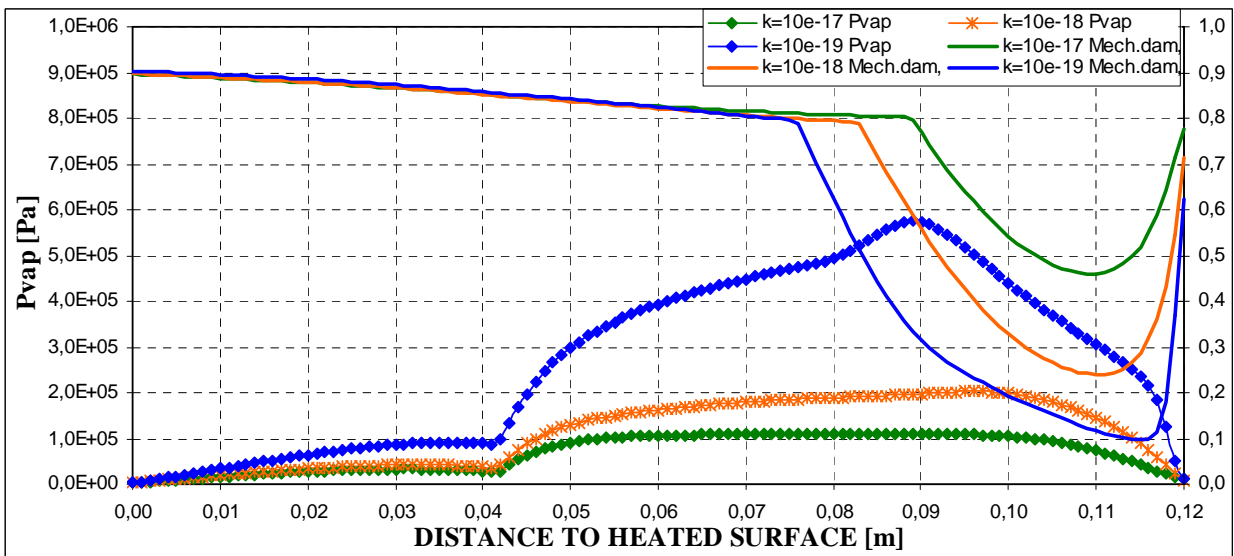
Figure 4-91. Mechanical damage and vapour pressure space distribution for three values of intrinsic permeability ($10^{-17}, 10^{-18}, 10^{-19}$) in case of $s=40\%$, Thickness = 12 centimetres, PAR2 SLOW Heating curve, Material C90
(a) 1 hour; (b) 2 hours; (c) 3 hours



(a)

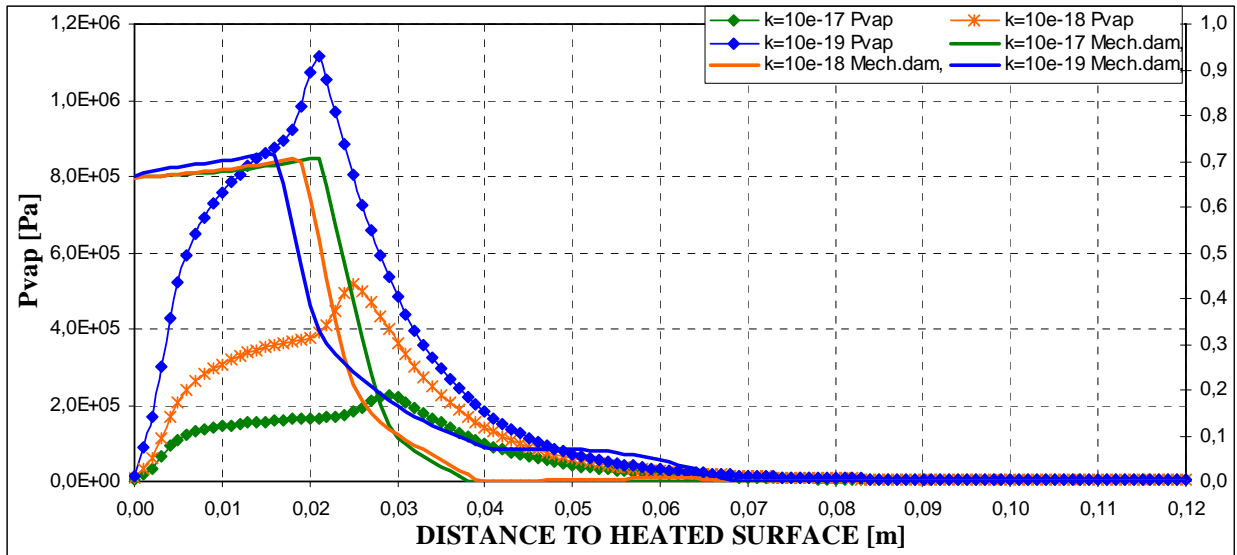


(b)

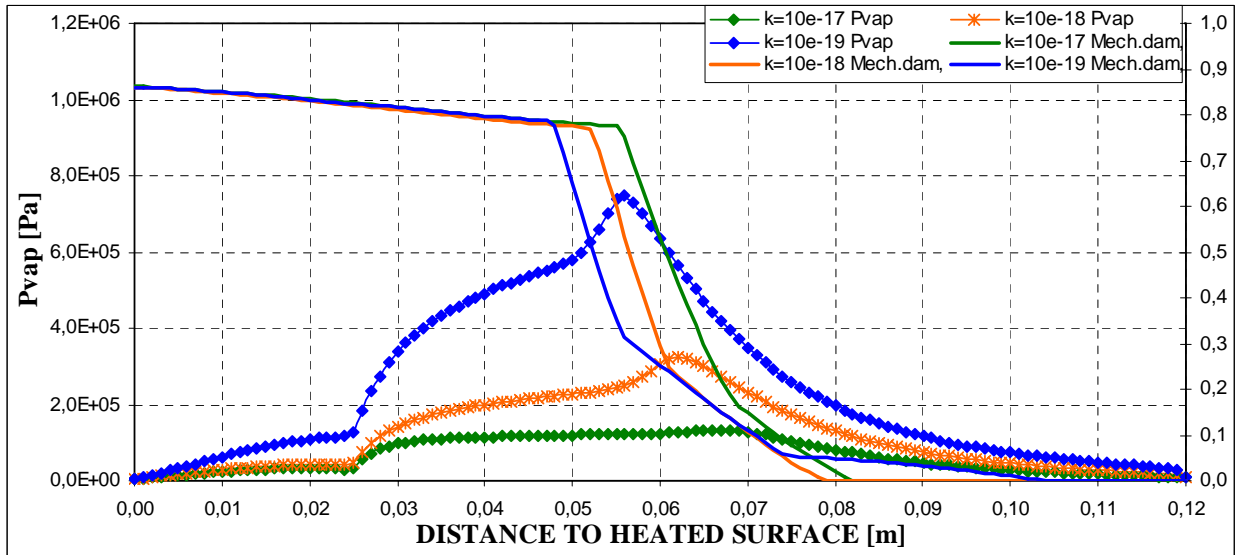


(c)

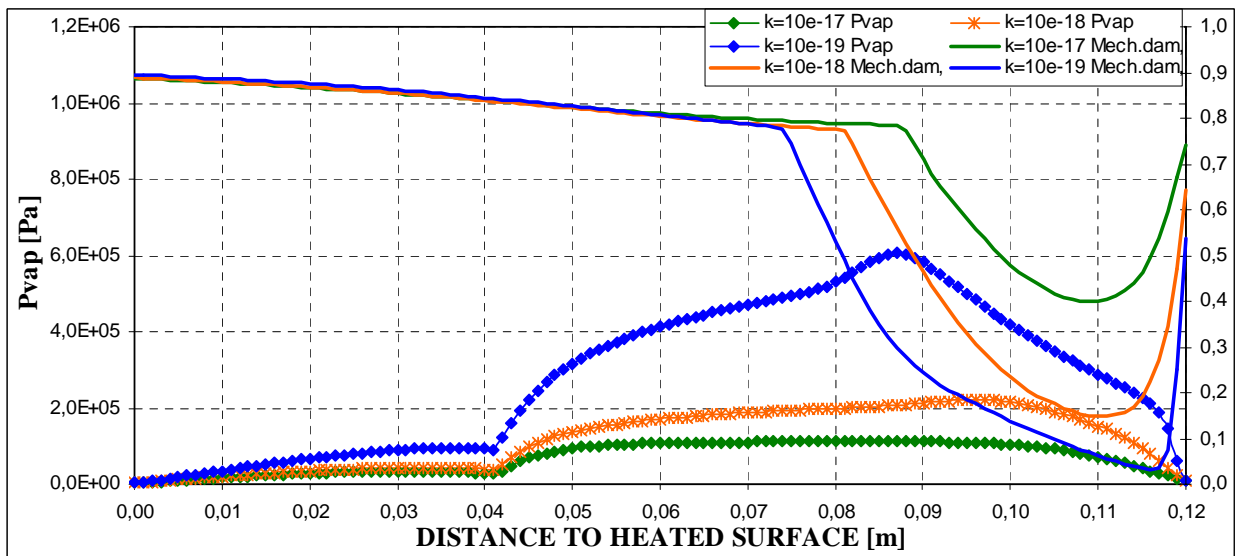
Figure 4-92. Mechanical damage and vapour pressure distribution for three values of intrinsic permeability ($10^{-17}, 10^{-18}, 10^{-19}$) in case of $s=50\%$, Thickness = 12 centimetres, PAR2 SLOW Heating curve, Material C90
 (a) 1 hour; (b) 2 hours; (c) 3 hours



(a)

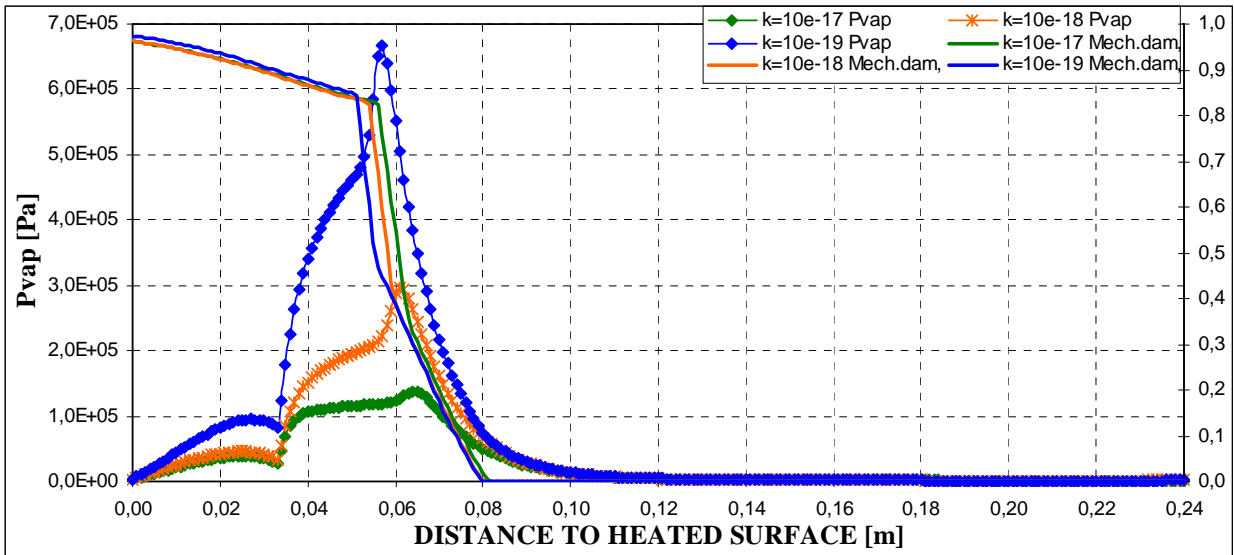


(b)

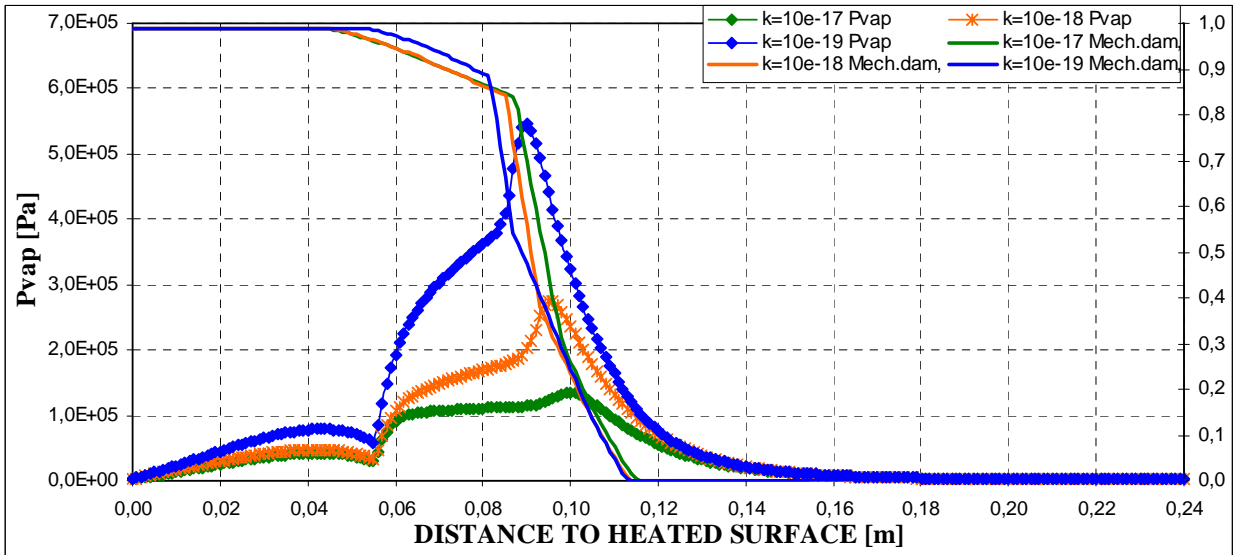


(c)

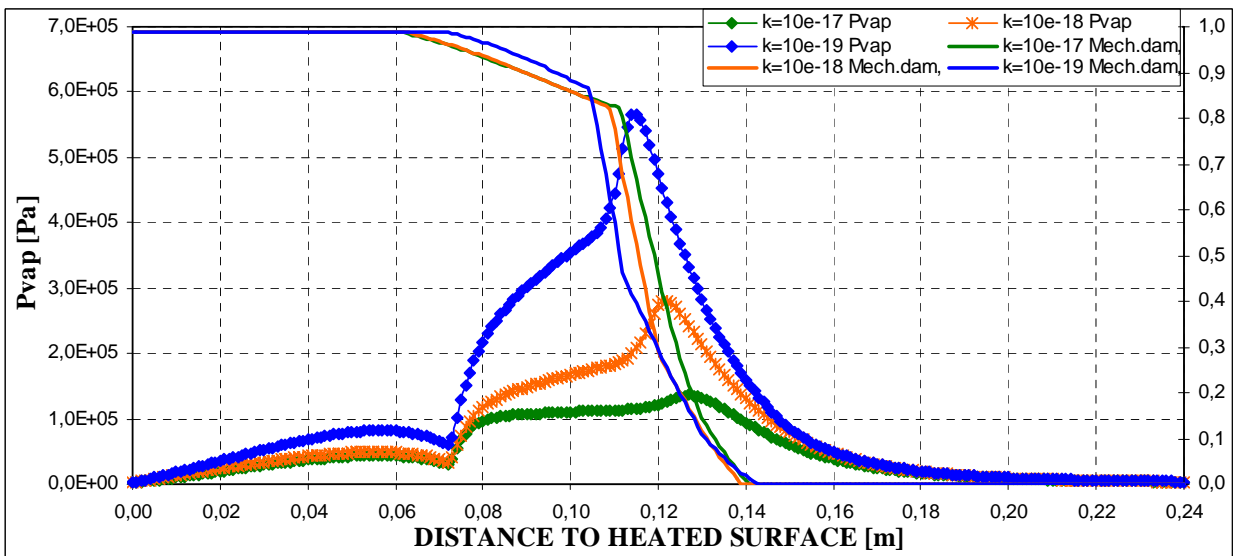
Figure 4-93. Mechanical damage and vapour pressure distribution for three values of intrinsic permeability ($10^{-17}, 10^{-18}, 10^{-19}$) in case of $s=60\%$, Thickness = 12 centimetres, PAR2 SLOW Heating curve, Material C90
(a) 1 hour; (b) 2 hours; (c) 3 hours



(a)

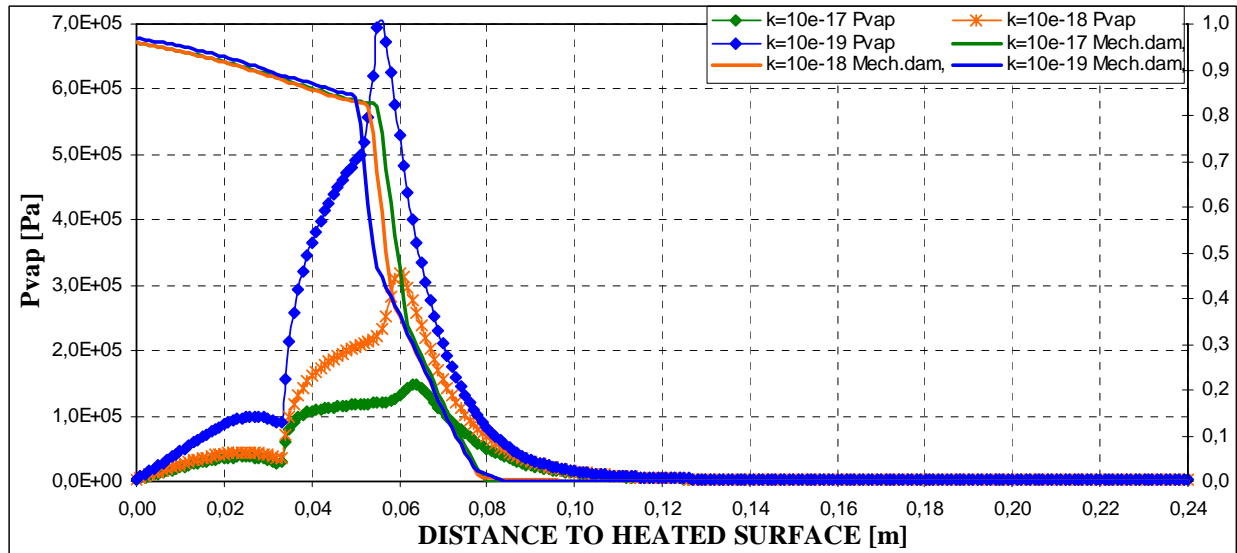


(b)

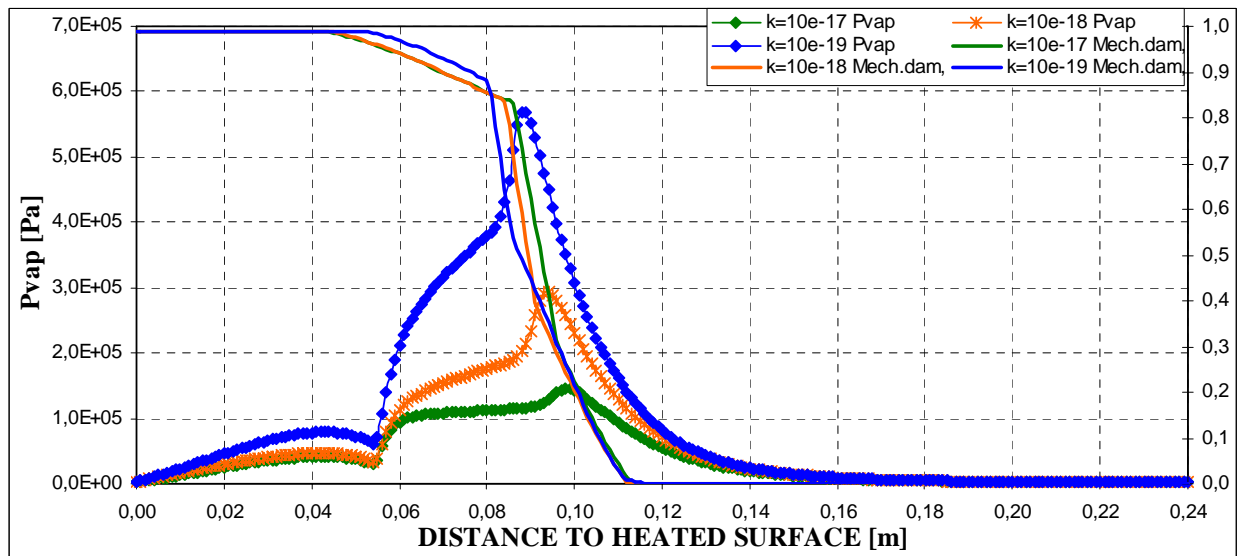


(c)

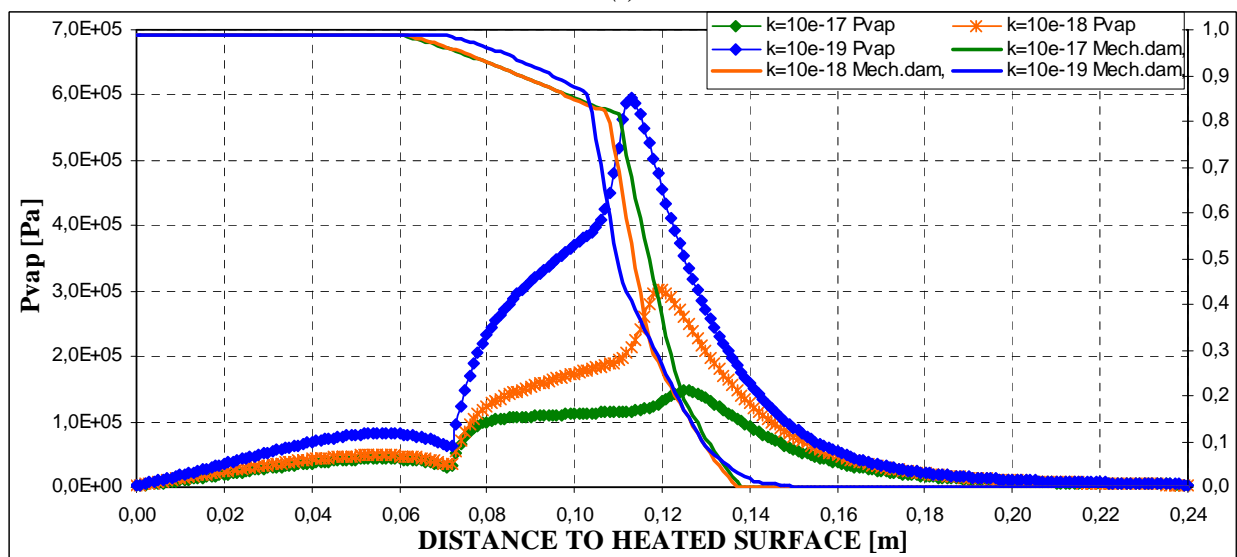
Figure 4-94. Mechanical damage and vapour pressure distribution for three values of intrinsic permeability ($10^{-17}, 10^{-18}, 10^{-19}$) in case of $s=40\%$, Thickness = 24 centimetres, PAR1 ISO Heating curve, Material C90
(a) 1 hour; (b) 2 hours; (c) 3 hours



(a)

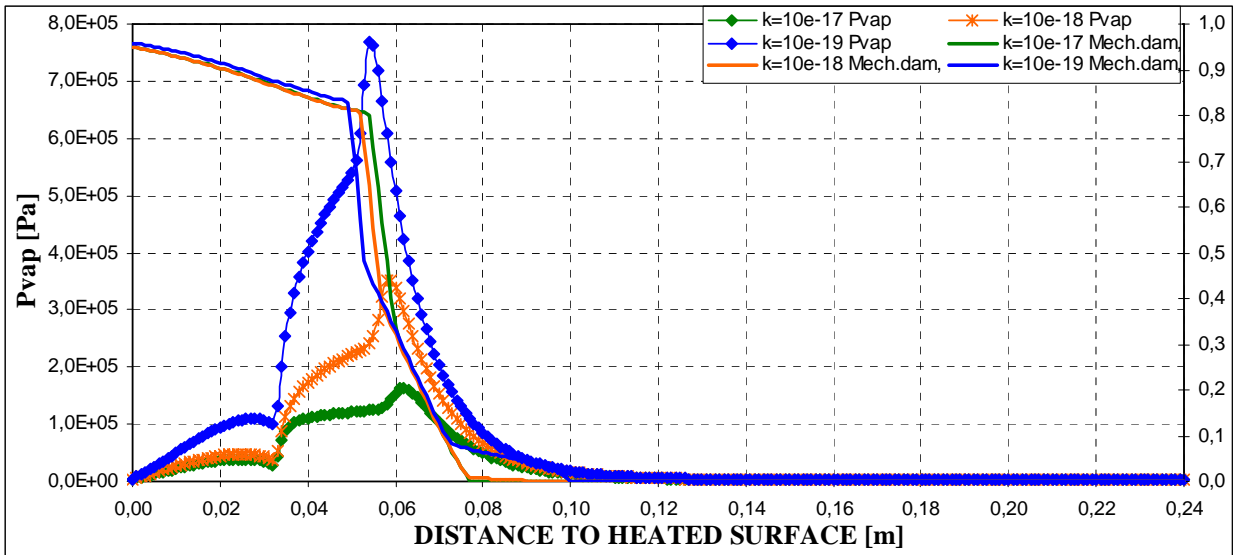


(b)

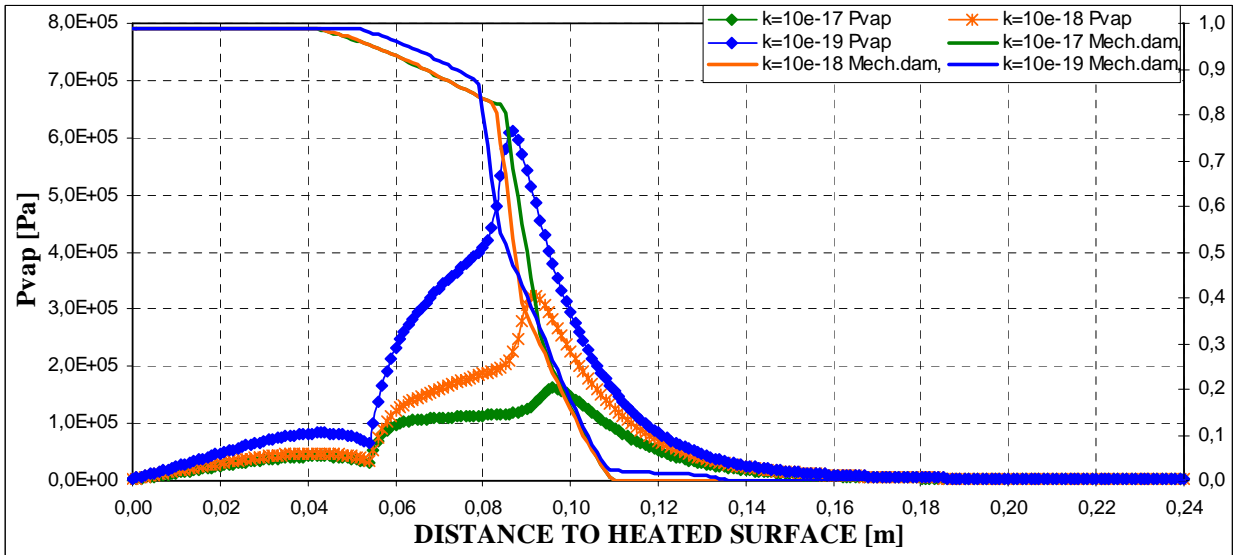


(c)

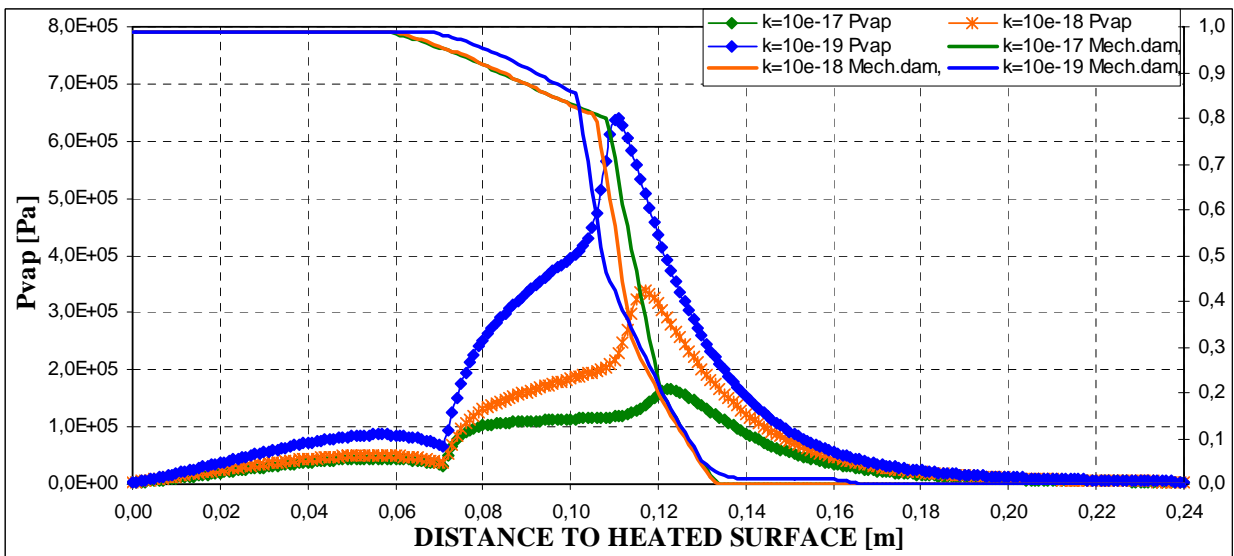
Figure 4-95. Mechanical damage and vapour pressure space distribution for three values of intrinsic permeability ($10^{-17}, 10^{-18}, 10^{-19}$) in case of $s=50\%$, Thickness = 24 centimetres, PAR1 ISO Heating curve, Material C90
(a) 1 hour; (b) 2 hours; (c) 3 hours



(a)

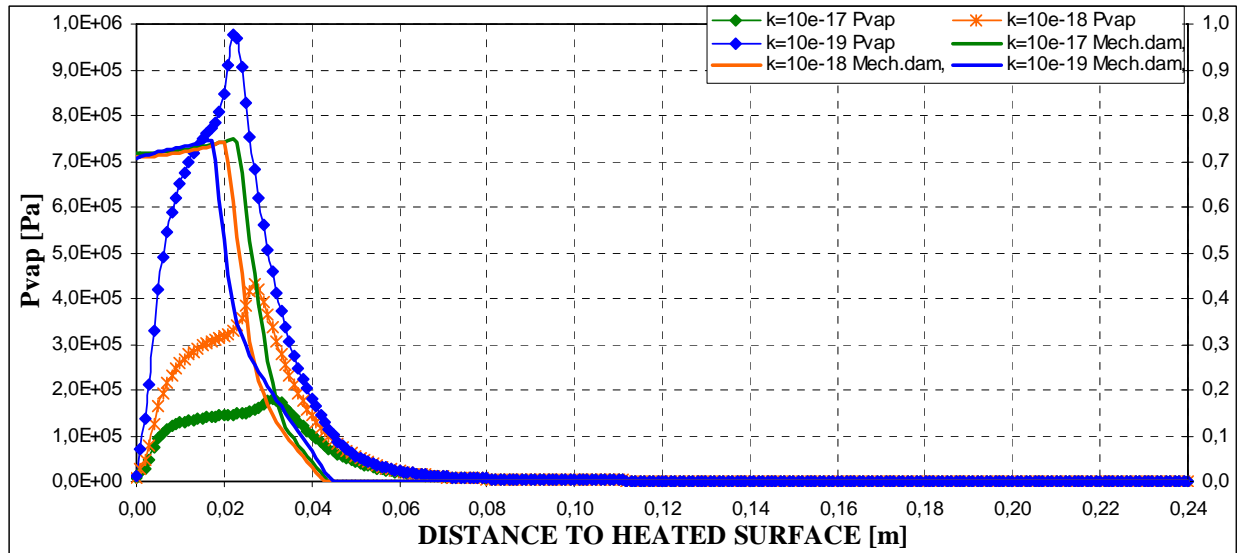


(b)

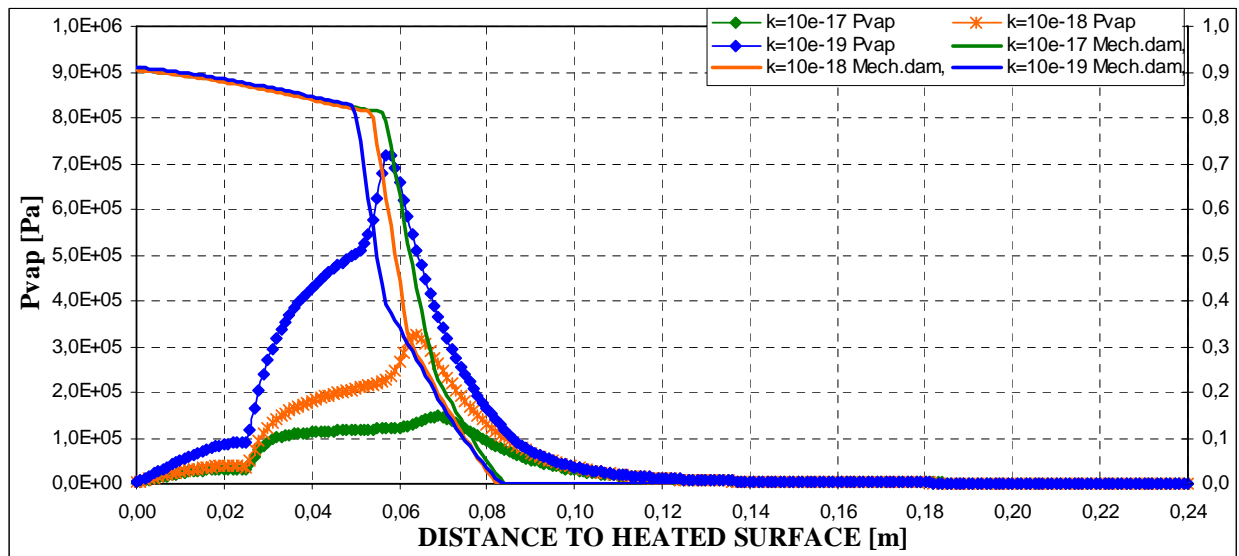


(c)

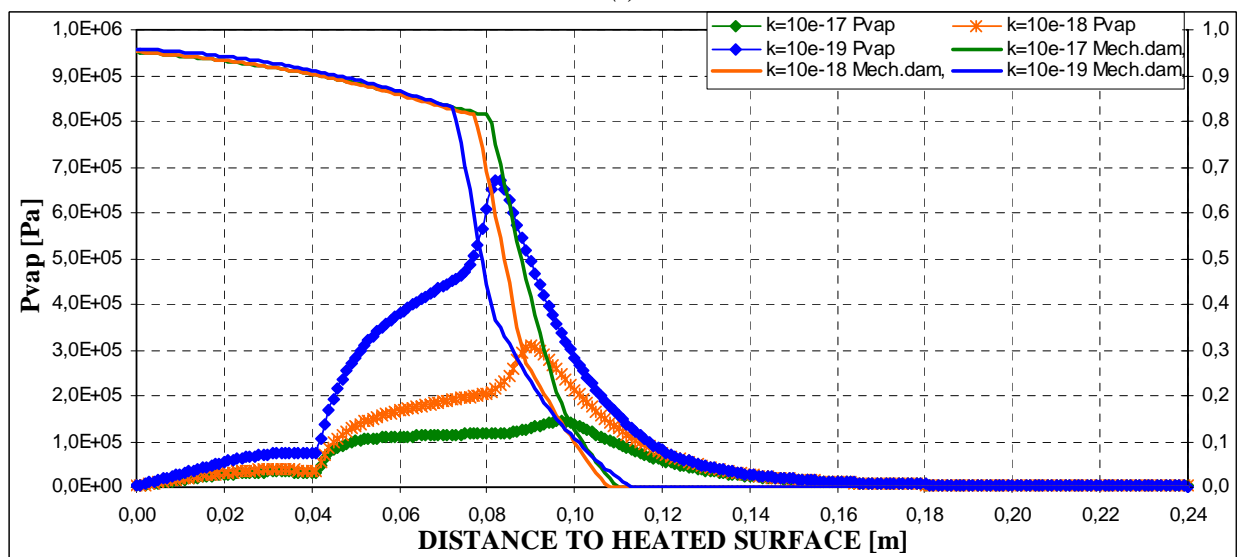
Figure 4-96. Mechanical damage and vapour pressure space distribution for three values of intrinsic permeability ($10^{-17}, 10^{-18}, 10^{-19}$) in case of $s=60\%$, Thickness = 24 centimetres, PAR1 ISO Heating curve, Material C90
(a) 1 hour; (b) 2 hours; (c) 3 hours



(a)

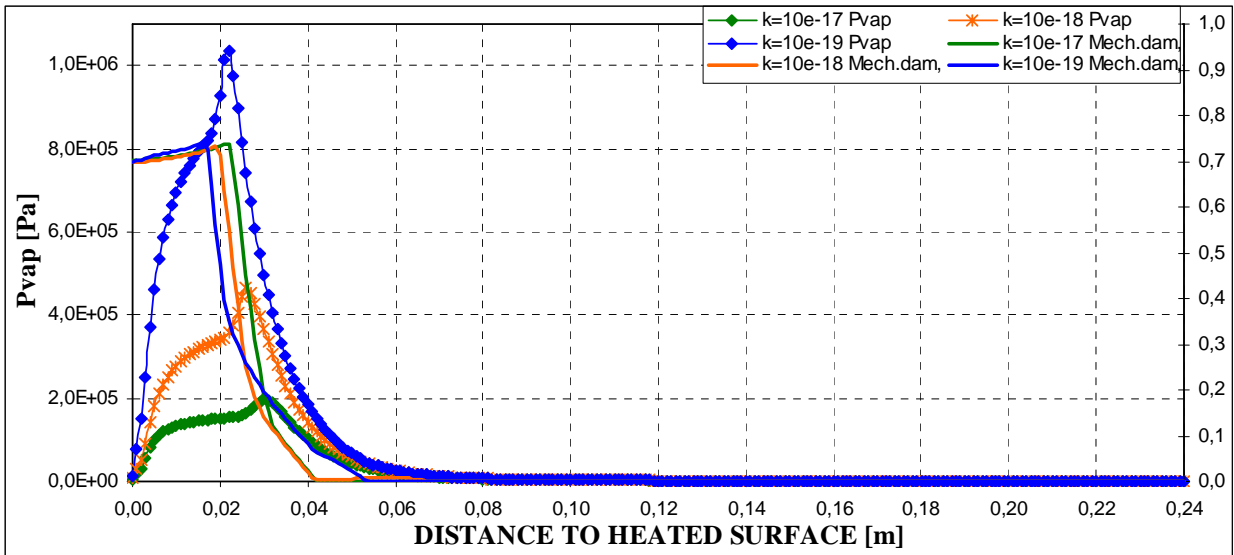


(b)

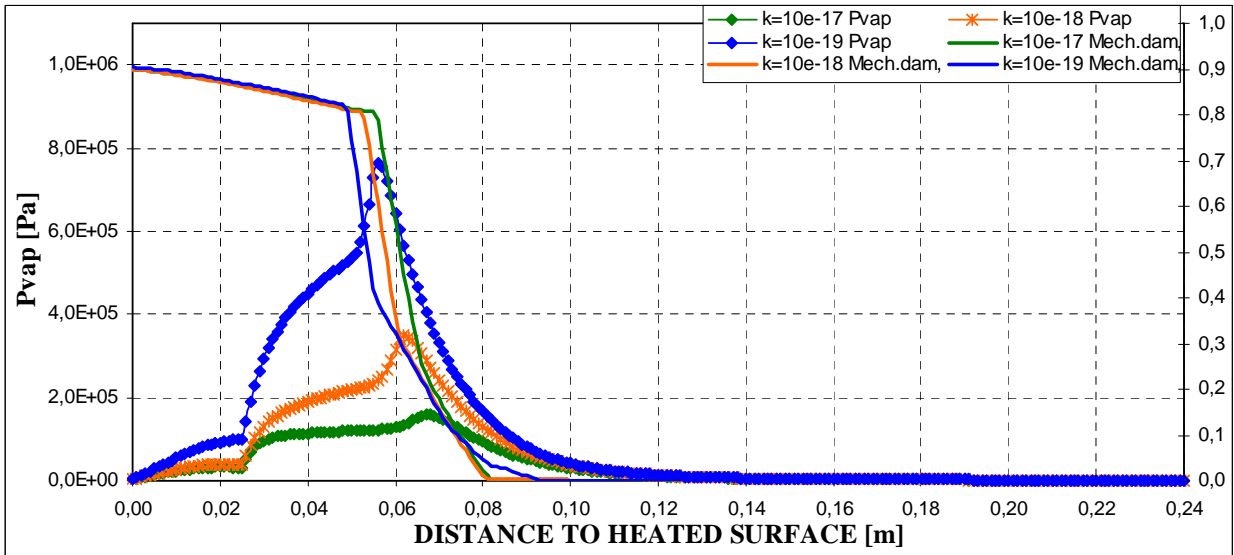


(c)

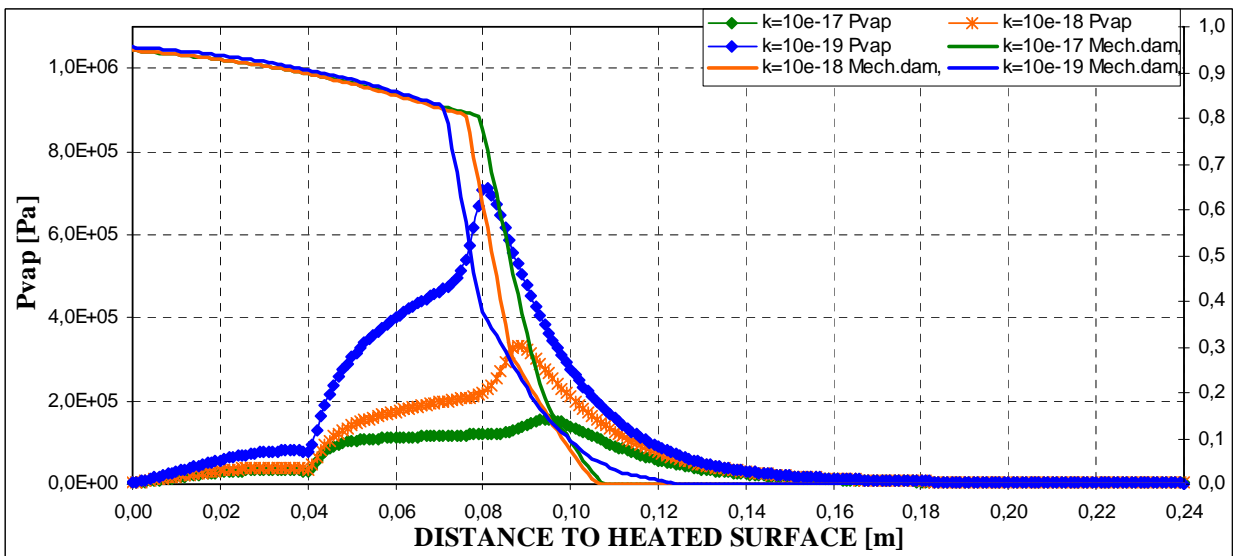
Figure 4-97. Mechanical damage and vapour pressure space distribution for three values of intrinsic permeability ($10^{-17}, 10^{-18}, 10^{-19}$) in case of $s=40\%$, Thickness = 24 centimetres, PAR2 SLOW Heating curve, Material C90
(a) 1 hour; (b) 2 hours; (c) 3 hours



(a)

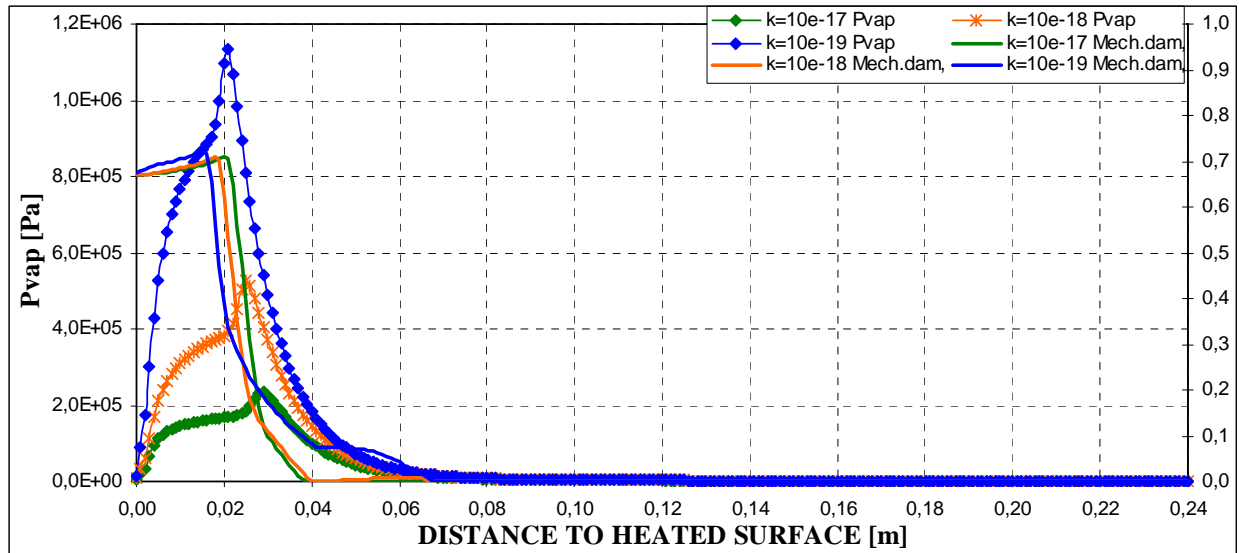


(b)

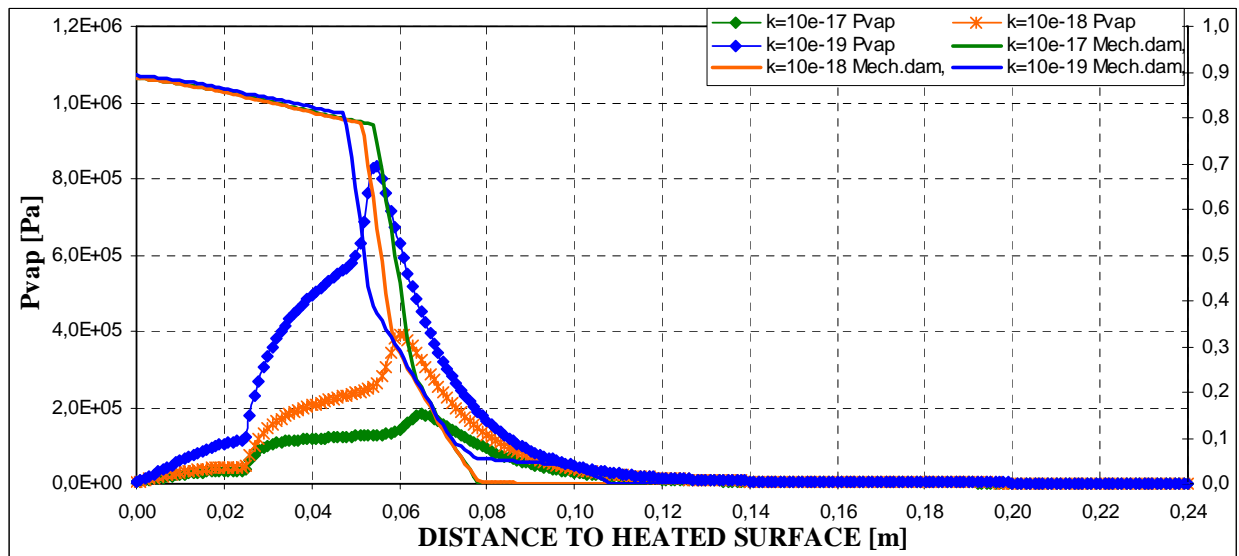


(c)

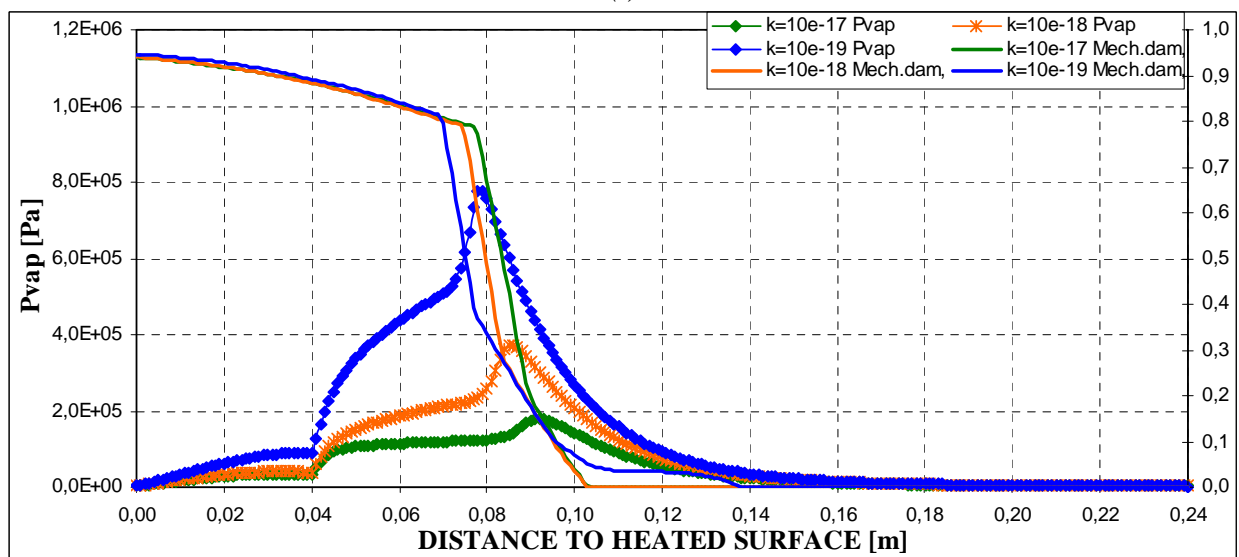
Figure 4-98. Mechanical damage and vapour pressure space distribution for three values of intrinsic permeability ($10^{-17}, 10^{-18}, 10^{-19}$) in case of $s=50\%$, Thickness = 24 centimetres, PAR2 SLOW Heating curve, Material C90
(a) 1 hour; (b) 2 hours; (c) 3 hours



(a)

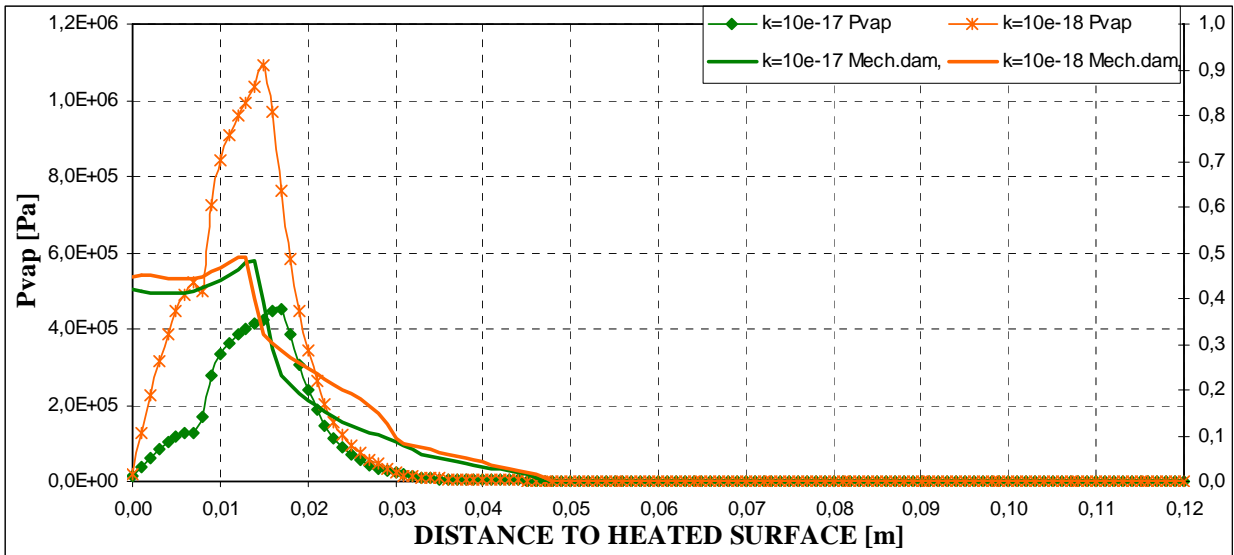


(b)

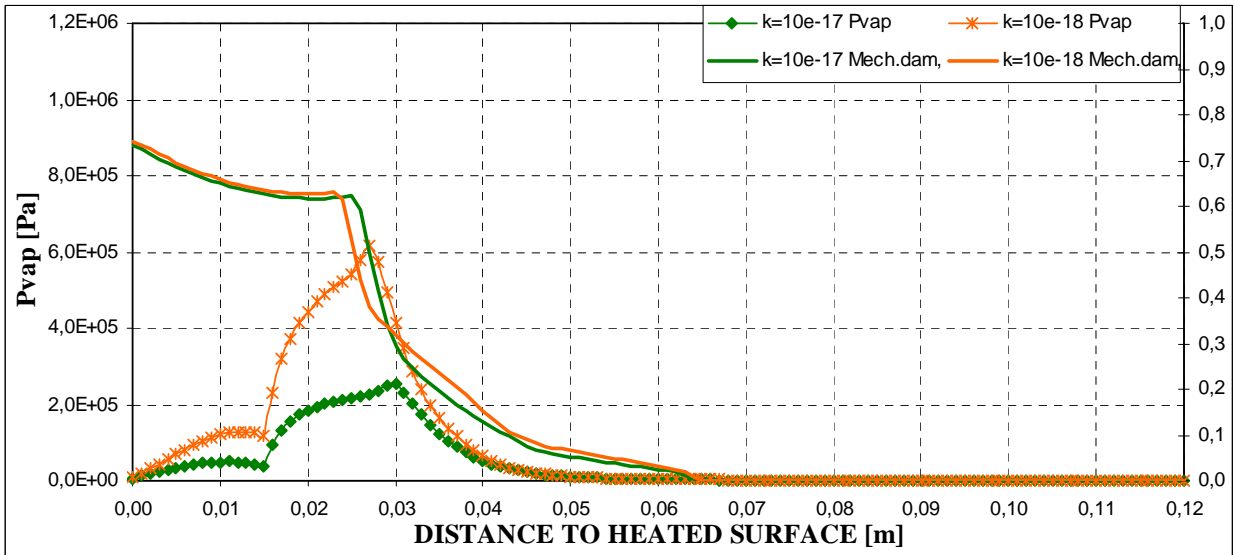


(c)

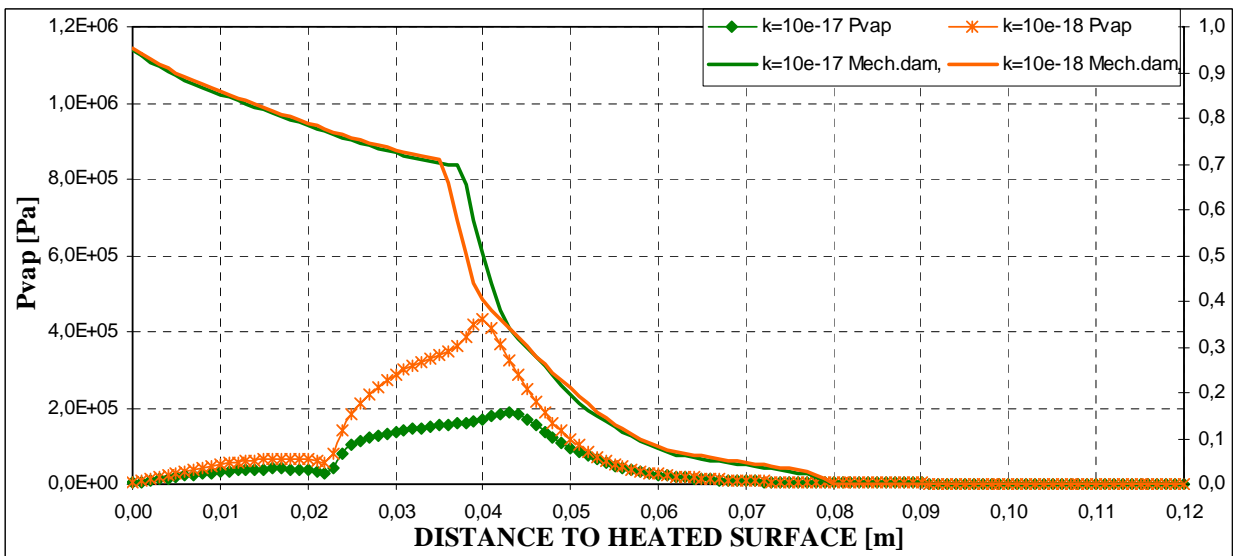
Figure 4-99. Mechanical damage and vapour pressure distribution for three values of intrinsic permeability ($10^{-17}, 10^{-18}, 10^{-19}$) in case of $s=60\%$, Thickness = 24 centimetres, PAR2 SLOW Heating curve, Material C90
(a) 1 hour; (b) 2 hours; (c) 3 hours



(a)

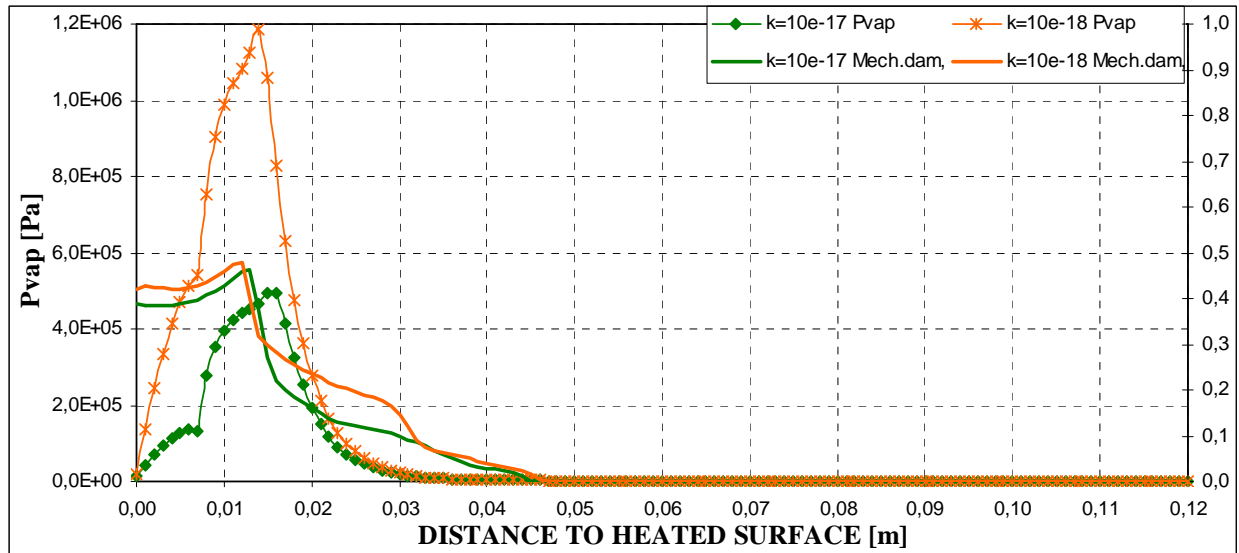


(b)

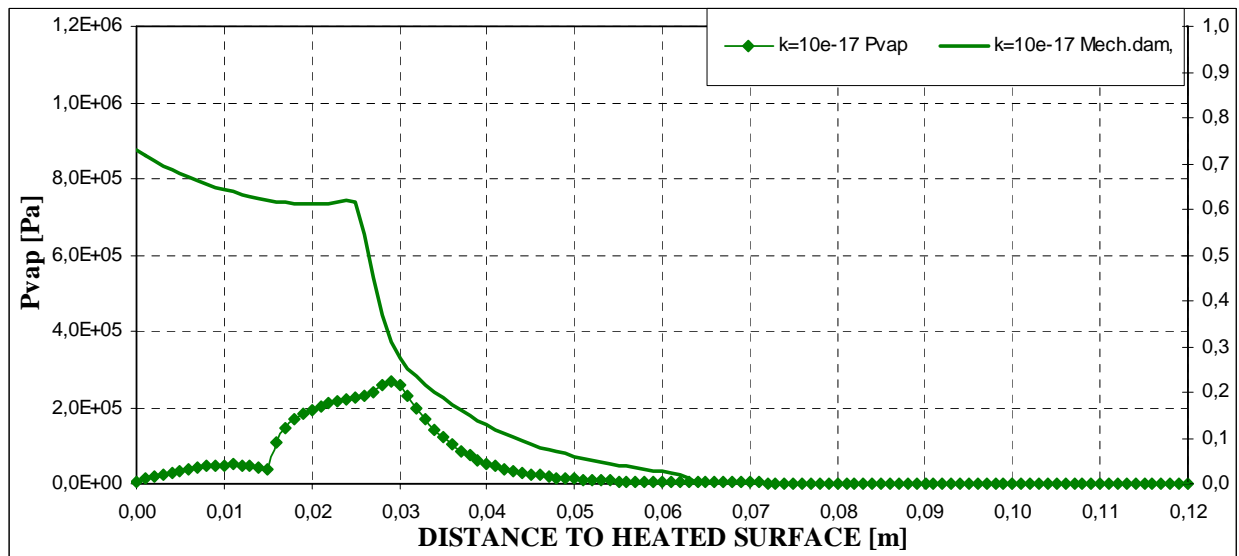


(c)

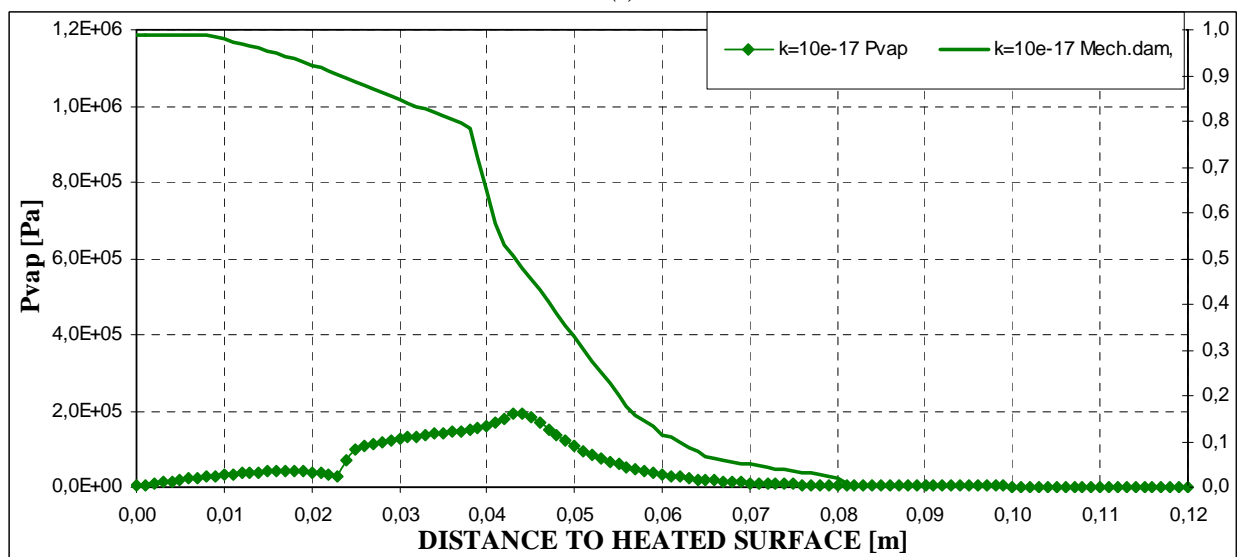
Figure 4-100. Mechanical damage and vapour pressure space distribution for two values of intrinsic permeability ($10^{-17}, 10^{-18}$) in case of $s=40\%$, Thickness = 12 centimetres, PAR3 HYDROCARBON Heating curve, Material C60
(a) 300 seconds; (b) 600 seconds; (c) 1.020 seconds



(a)

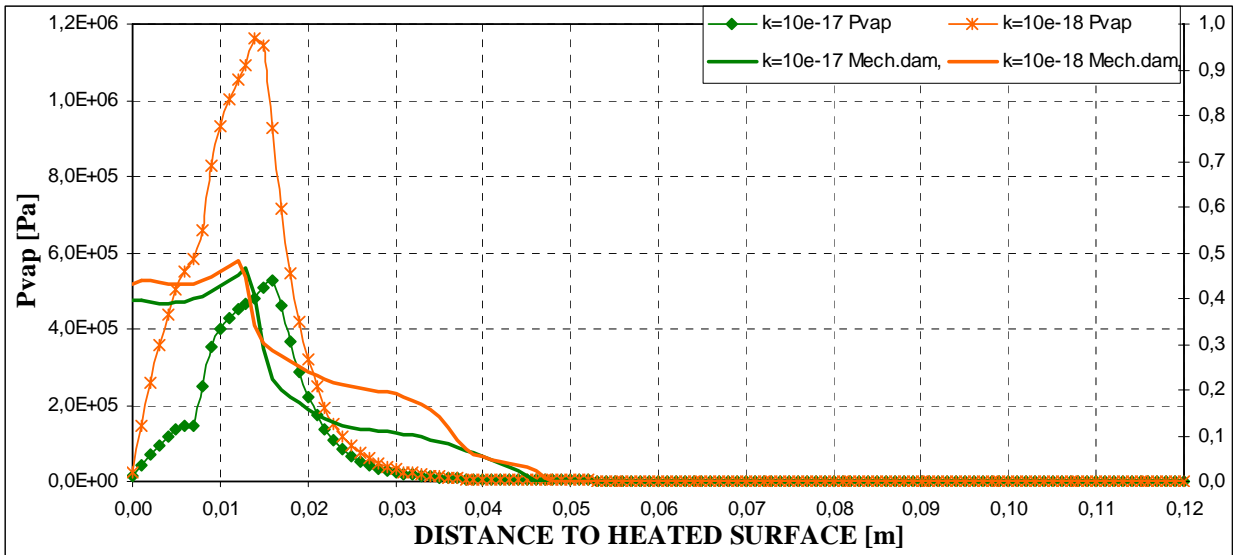


(b)

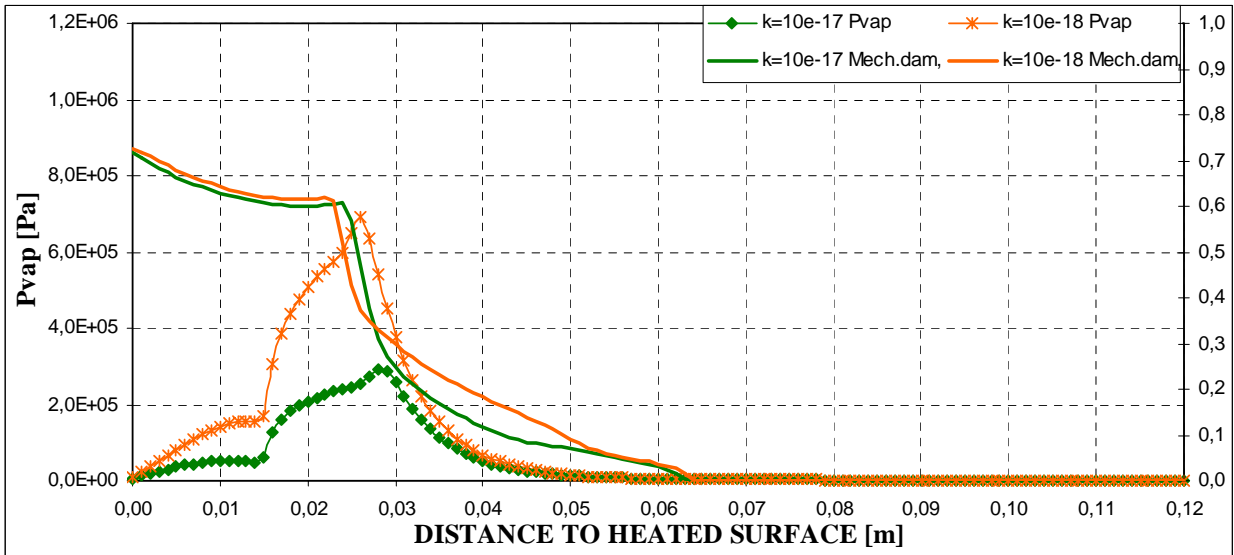


(c)

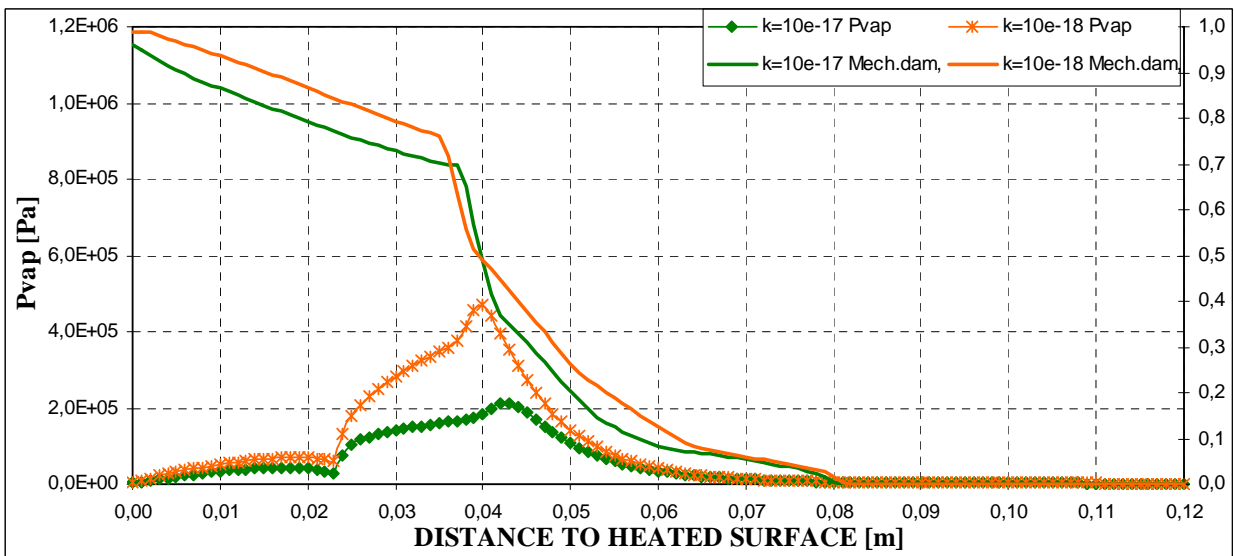
Figure 4-101. Mechanical damage and vapour pressure distribution for two values of intrinsic permeability (10^{-17} , 10^{-18}) in case of $s=50\%$, Thickness = 12 centimetres, PAR3 HYDROCARBON Heating curve, Material C60
(a) 285 seconds; (b) 600 seconds; (c) 1.065 seconds



(a)

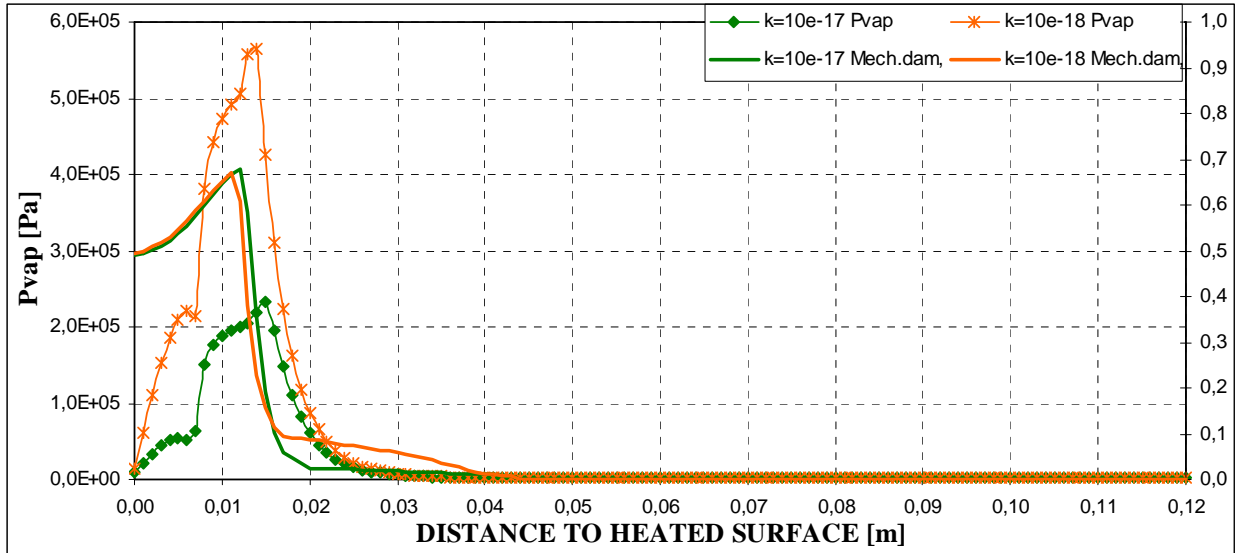


(b)

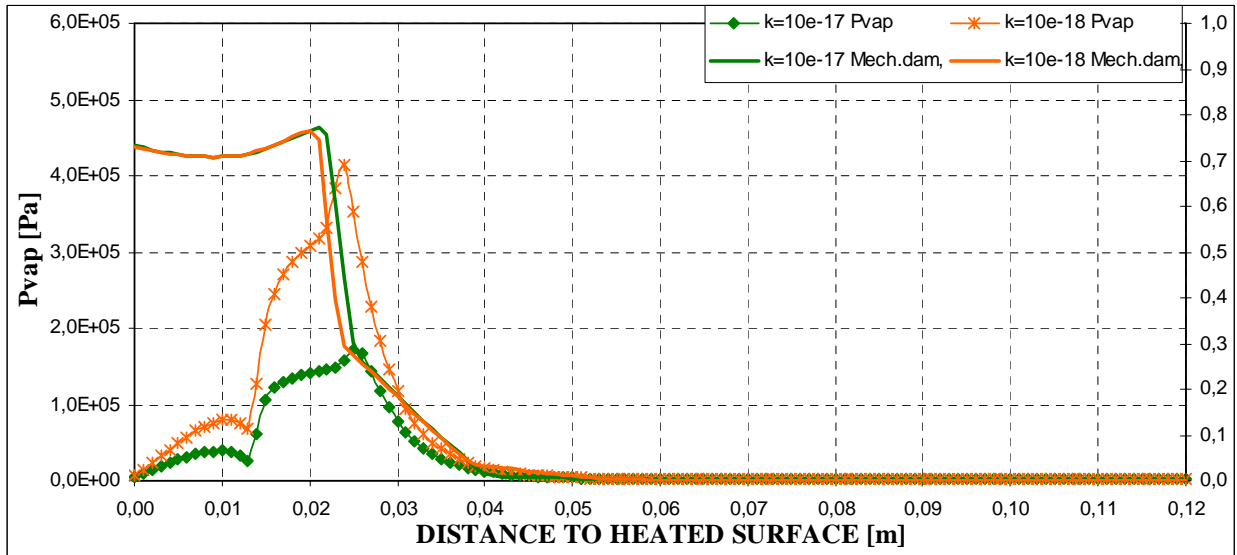


(c)

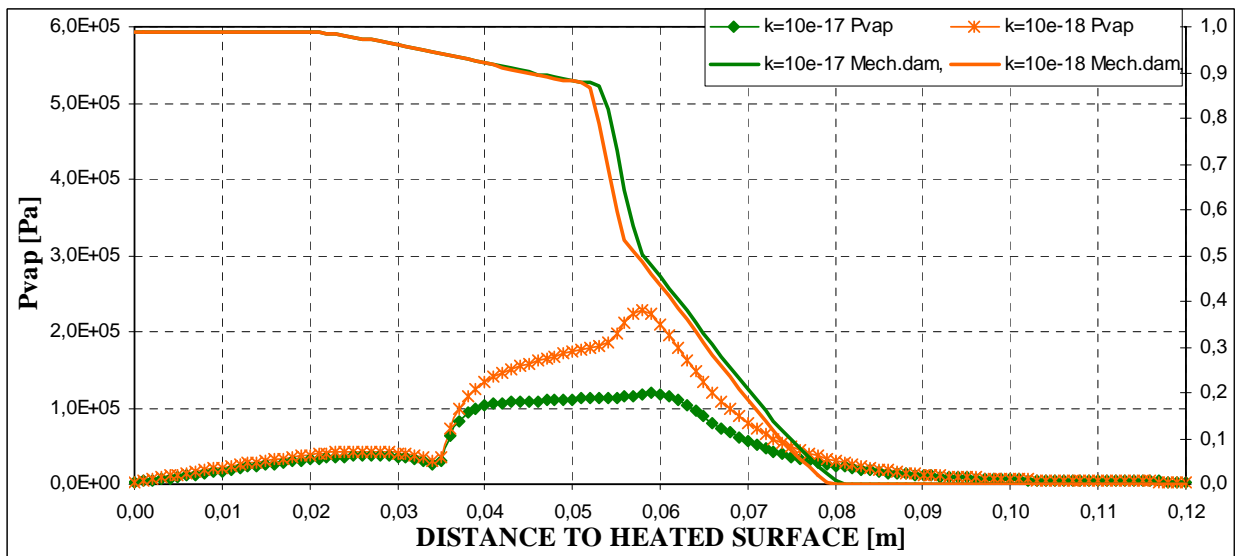
Figure 4-102. Mechanical damage and vapour pressure space distribution for two values of intrinsic permeability ($10^{-17}, 10^{-18}$) in case of $s=60\%$, Thickness = 12 centimetres, PAR3 HYDROCARBON Heating curve, Material C60
(a) 300 seconds; (b) 600 seconds; (c) 1.080 seconds



(a)

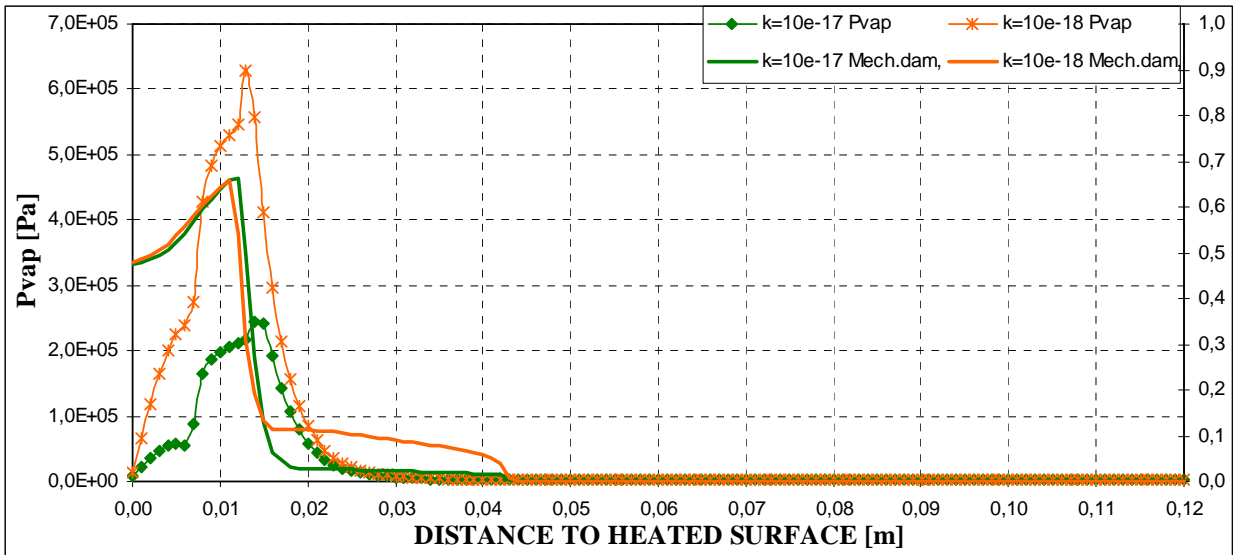


(b)

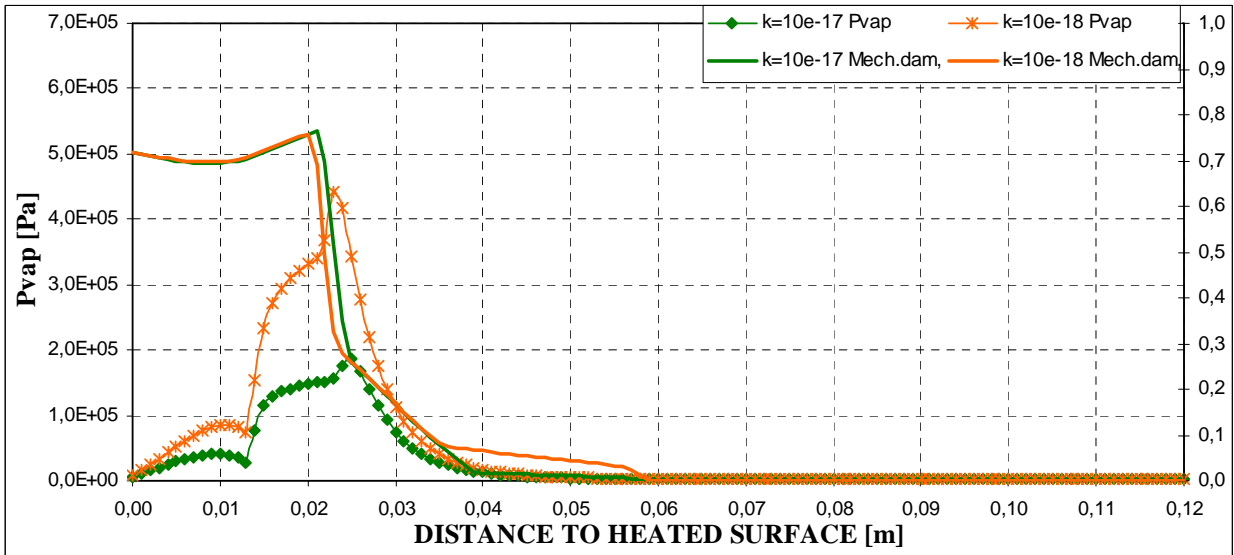


(c)

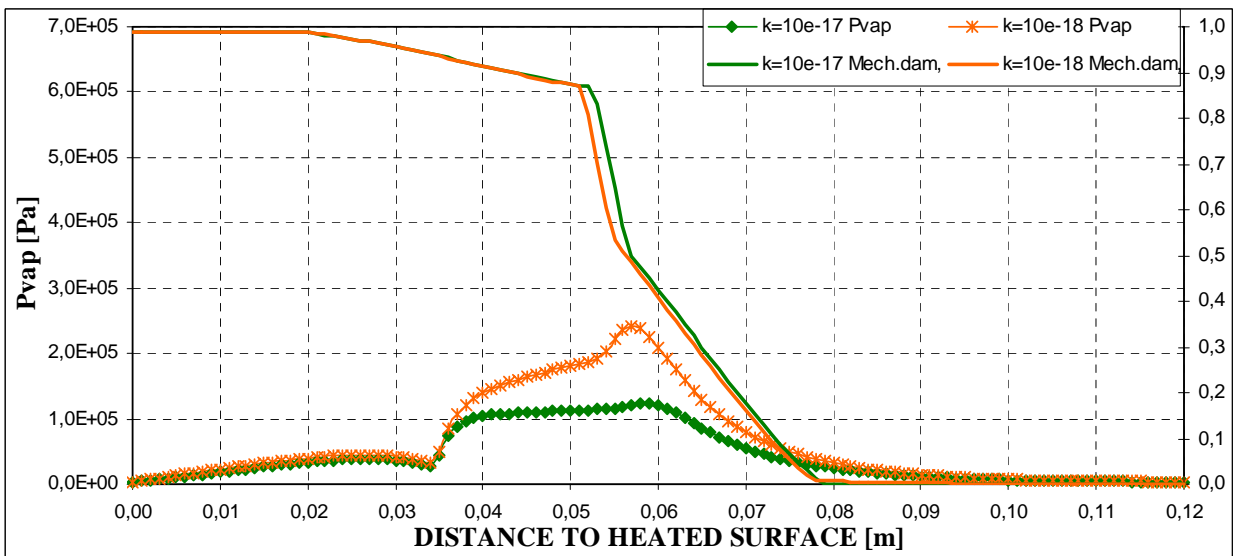
Figure 4-103. Mechanical damage and vapour pressure space distribution for two values of intrinsic permeability ($10^{-17}, 10^{-18}$) in case of $s=40\%$, Thickness = 12 centimetres, PAR3 HYDROCARBON Heating curve, Material C90
(a) 300 seconds; (b) 600 seconds; (c) 2.400 seconds



(a)

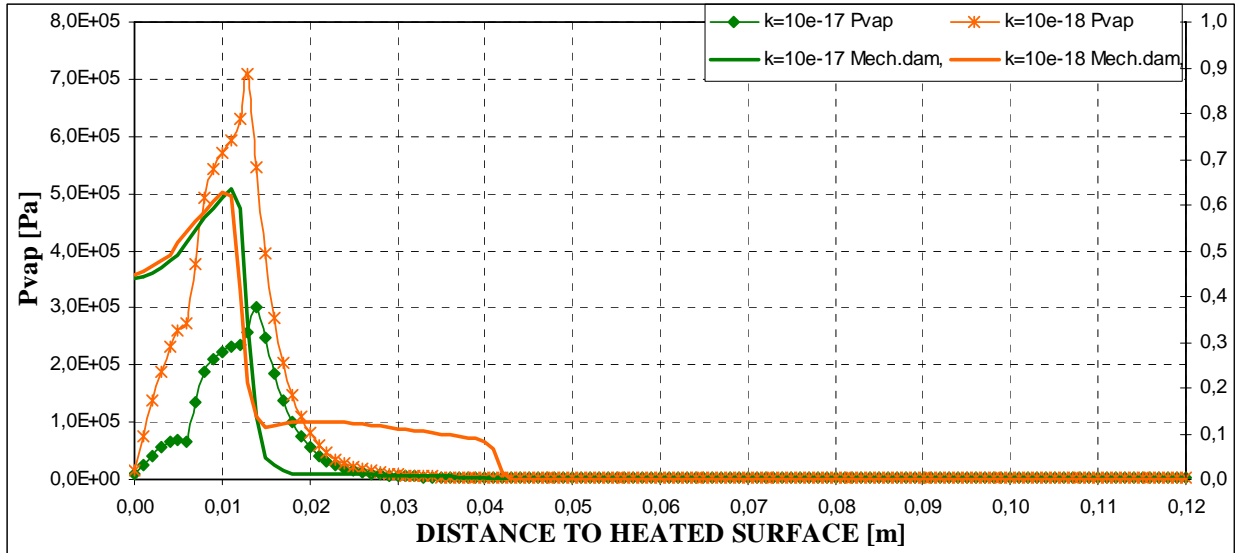


(b)

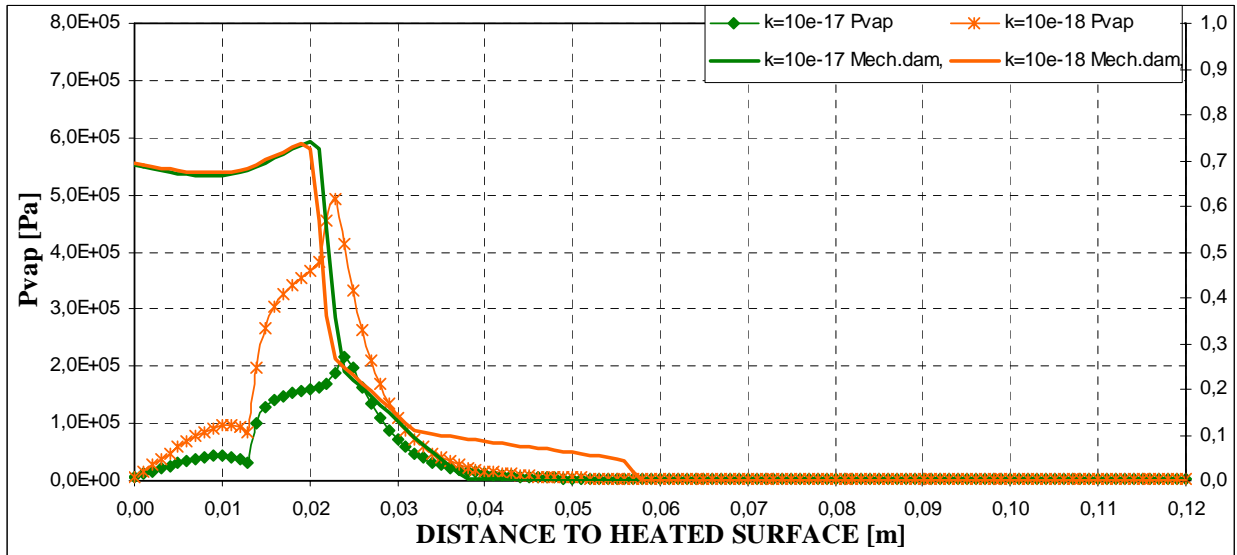


(c)

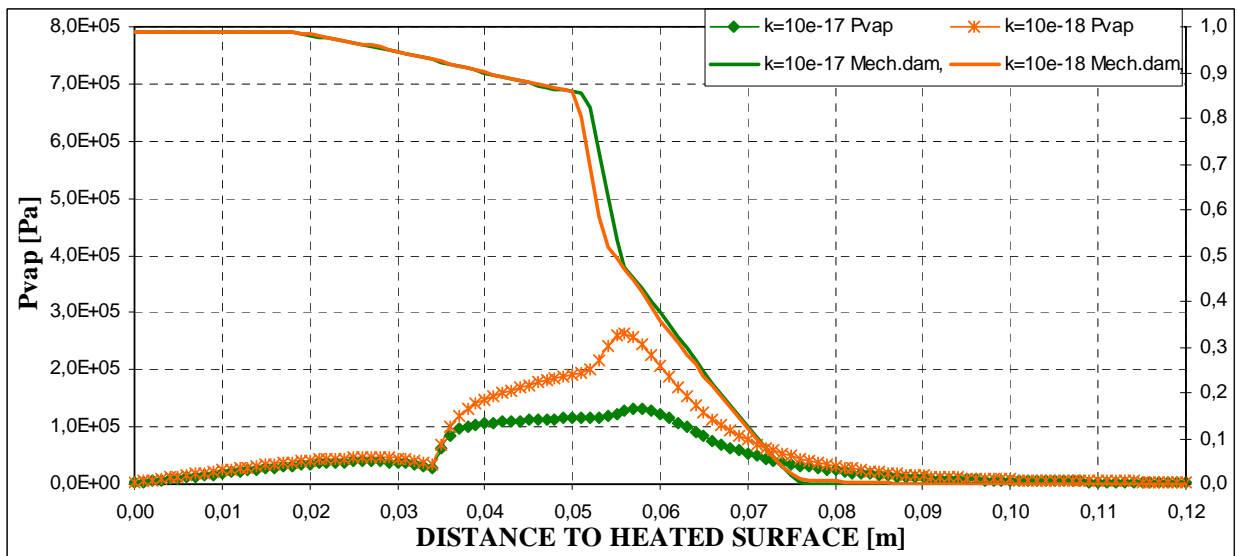
Figure 4-104. Mechanical damage and vapour pressure space distribution for two values of intrinsic permeability ($10^{-17}, 10^{-18}$) in case of $s=50\%$, Thickness = 12 centimetres, PAR3 HYDROCARBON Heating curve, Material C90 (a) 300 seconds; (b) 600 seconds; (c) 2.400 seconds



(a)



(b)



(c)

Figure 4-105. Mechanical damage and vapour pressure space distribution for two values of intrinsic permeability ($10^{-17}, 10^{-18}$) in case of $s=60\%$, Thickness = 12 centimetres, PAR3 HYDROCARBON Heating curve, Material C90
(a) 300 seconds; (b) 600 seconds; (c) 2.400 seconds

- Analogously, as Intrinsic Permeability increases the Mechanical Damage level at a certain depth decreases. At the inner layers, among 5 and 10 centimetres away from the heated surface, it is observed that the material is not completely cracked at the end of the simulation and that the final Mechanical Damage level also decreases as Intrinsic Permeability increases.

Comparing this set of results (cases 1 to 9, figures 4-75 to 4-77) with those obtained for other combinations of the heating profile and the material, the following conclusions may be excerpted:

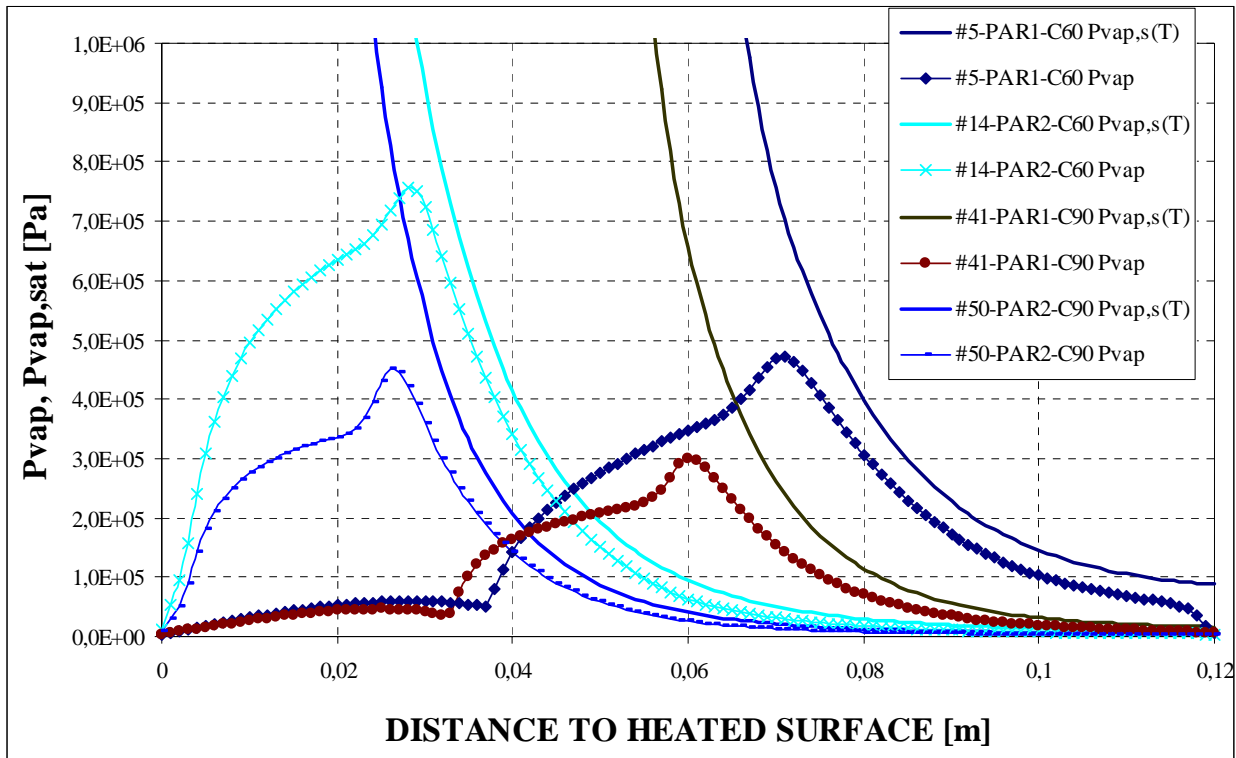


Figure 4-106. Vapour Pressure and Saturation Vapour Pressure space distributions at 3.600 seconds for an intrinsic permeability of 10^{-18} and an Initial Saturation Degree of $s=50\%$, considering: Thickness = 12 centimetres
 (a) #5-PAR1-ISO heating curve and C60 material (b) #14-PAR2-Slow heating curve and C60 material
 (c) #41-PAR1-ISO heating curve and C90 material (d) #50-PAR2-Slow heating curve and C90 material

As shown in figure 4-106, as it was expectable a slower heating curve leads to a maximum vapour pressure value much closer to the heated surface and with a higher value at any certain instant – 3.600 seconds in this graph –. In reference to the material influence, the change from C60 (H.S.C.) to C90 (U.H.S.C.) makes the maximum vapour pressure value arise closer to the heated surface while being lower, independently of the heating profile. Analogously happens at other stages of the heating process, as shown in figure 4-107 after 2 hours of simulation. At any instant, cases with C90 material show larger differences of vapour pressure values with respect to the saturation vapour pressure corresponding to the temperature at each depth than in case with C60 material. These differences increase with time due to the progressive drying of material.

If one compares the vapour pressure spatial distributions corresponding to the instant at which the heated surface temperature is 473 K, temperature above which thermal spalling is usually observed, it is again observed than in these conditions C90 material shows lower vapour pressure values (being its maximum closer to the surface). On the other hand, a slower heating profile leads to a much wider but lower distribution of vapour pressure values, mainly due to a characteristic higher absolute time that enables larger diffusion and capillary processes.

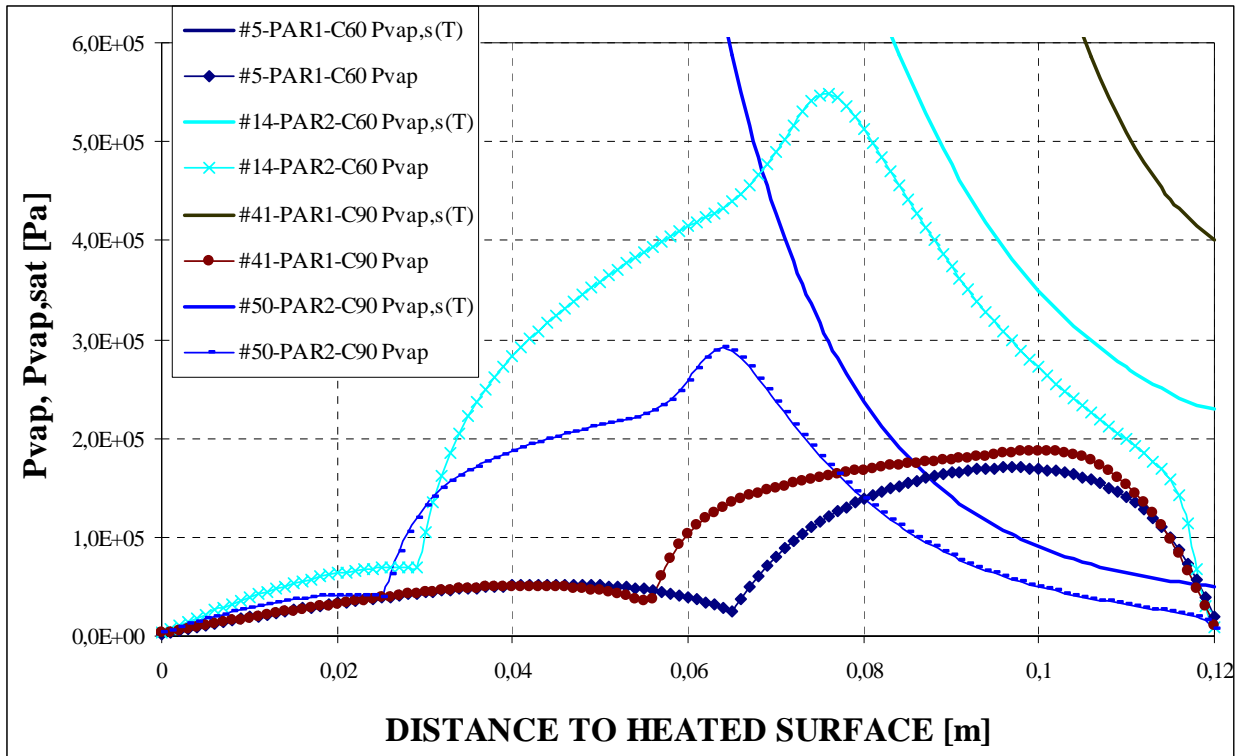


Figure 4-107. Vapour Pressure and Saturation Vapour Pressure space distributions at 7.200 seconds for an intrinsic permeability of 10^{-18} and an Initial Saturation Degree of $s=50\%$, considering: Thickness = 12 centimetres
 (a) #5-PAR1-ISO heating curve and C60 material (b) #14-PAR2-Slow heating curve and C60 material
 (c) #41-PAR1-ISO heating curve and C90 material (d) #50-PAR2-Slow heating curve and C90 material

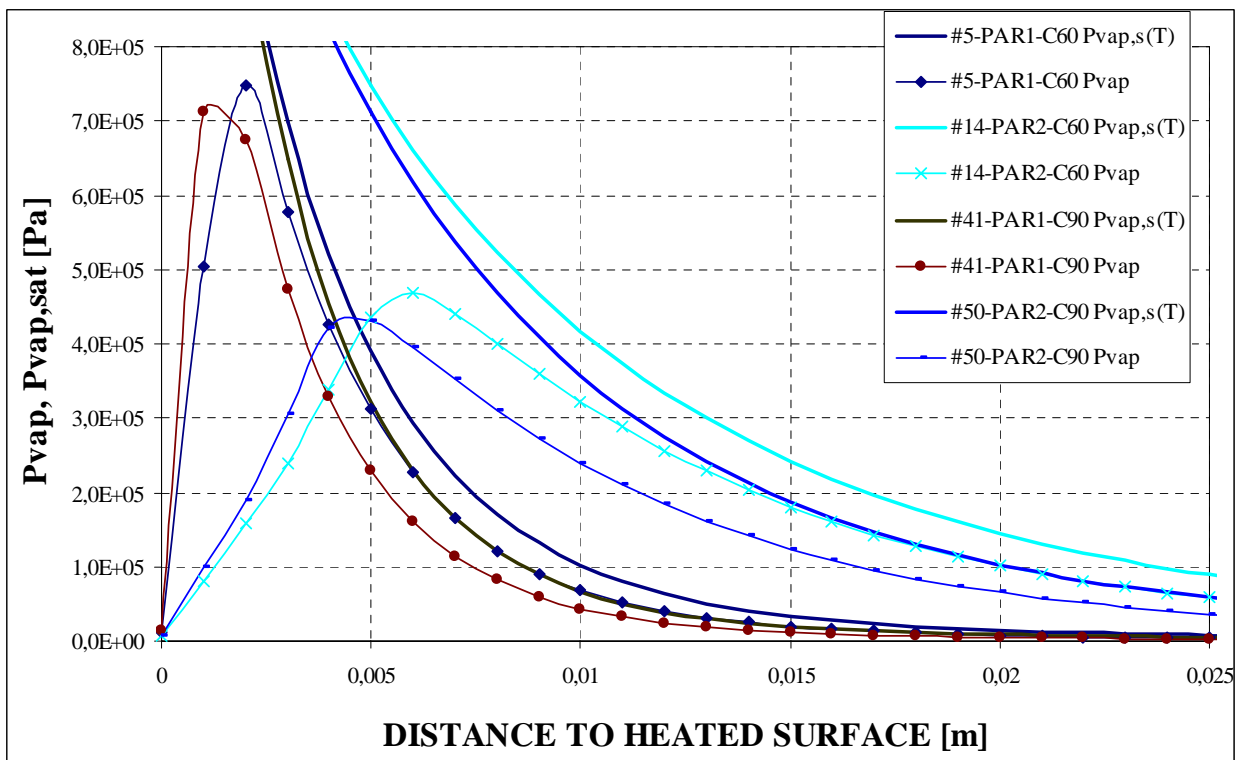


Figure 4-108. Vapour Pressure and Saturation Vapour Pressure space distributions at a heated surface temperature of 473 K, for an intrinsic permeability of 10^{-18} and an Initial Saturation Degree of $s=50\%$, considering: Thickness = 12 centimetres
 (a) #5-PAR1-ISO heating curve and C60 material (b) #14-PAR2-Slow heating curve and C60 material
 (c) #41-PAR1-ISO heating curve and C90 material (d) #50-PAR2-Slow heating curve and C90 material

Some more particular conclusions about the spatial distributions of the vapour pressure and the mechanical damage are the following:

The mechanical damage levels are lower when considering a Slow heating profile (see for example figures 4-78 to 4-80 compared against figures 4-75 to 4-77), being in these cases the depths at which the maximum value of the vapour pressure appears also lower (if the same absolute instant is compared).

In the cases featured by a thickness of 24 centimetres and an ISO heating profile (see figures 4-81 to 4-83) the spatial distribution of the vapour pressure and the mechanical damage are the same as for 12 centimetres during the initial heating stages. However, for higher absolute times – 7.200 and 10.800 seconds – these distributions are qualitatively different since there exist diffusion and capillary processes towards the non-heated surface which are not present in the cases of 12 centimetres, where certain vapour and liquid water fluxes are exchanged with the non-heated atmosphere, leading to a wider distribution of the vapour pressure distribution and varying the mechanical damage distribution beyond the first 12 centimetres (this fact does not affect significantly to the thermal spalling phenomena since, as it has been explained in the paragraph related to the spalling nomograms, they take place in layers located much closer to the heated surface).

Furthermore, for the case with a thickness of 50 centimetres (figure 4-87) the mechanical damage distribution does not show significant differences with that corresponding to a thickness of 24 centimetres but, on the contrary, the maximum value of the vapour pressure only reaches at any instant a 60% of the value corresponding both to the thicknesses of 12 and 24 centimetres.

4.5.7 Time evolution considerations on a sample case: #5-TH12K018RH50PAR1C60

Finally, a sample case – #5-TH12K018RH50PAR1C60 – has been selected to show the time evolution of the most relevant parameters with influence on thermal spalling phenomena, with the purpose of giving a graphical and intuitive description of the processes involved in its occurrence. The selected combination, #5-TH12K018RH50PAR1C60, stands for a case characterised by a *thickness*=12 cm, $k=10^{-18}$ m², $S_{init}=50\%$, *Parametric curve*=ISO Curve (Par1) and C60 material.

The figures showing the time evolution of these parameters are the following ones:

<i>Figure number</i>	<i>Parameter</i>	<i>Figure number</i>	<i>Parameter</i>
4-109	<i>Temperature [K]</i>	4-114	<i>Effective Stress xx [Pa]</i>
4-110	<i>Mechanical damage [-]</i>	4-115	<i>Effective Stress yy [Pa]</i>
4-111	<i>Gas Pressure [Pa]</i>	4-116	<i>Saturation [-]</i>
4-112	<i>Elastic Energy [J/m³]</i>	4-117	<i>Vapour Pressure [Pa]</i>
4-113	<i>Capillary Pressure [Pa]</i>	4-118	<i>Relative Humidity [-]</i>

Table 4-59. Figures showing the time evolution of parameters with influence on thermal spalling.

The surface of the concrete structural element considered herein is heated both by a convective flux (from the surrounding air of higher temperature) and by a radiation flux (direct from the flames and/or from other heated surfaces), what results in a gradual increase of the element temperature, starting from the surface zone [9] (see figure 4-109).

The temperature gradients appear, in part, because almost all moisture must evaporate in the temperature range of 100-200°C before a further temperature increase, what requires a considerable amount of energy. Due to moisture evaporation, the relative humidity in the surface zone (initially 50% for this case) decreases to a very low value, figure 4-118, and a sharp front, separating the moist and dry material, moves inwards. At this front intensive evaporation takes place, increasing considerably the vapour pressure (see figure 4-117).

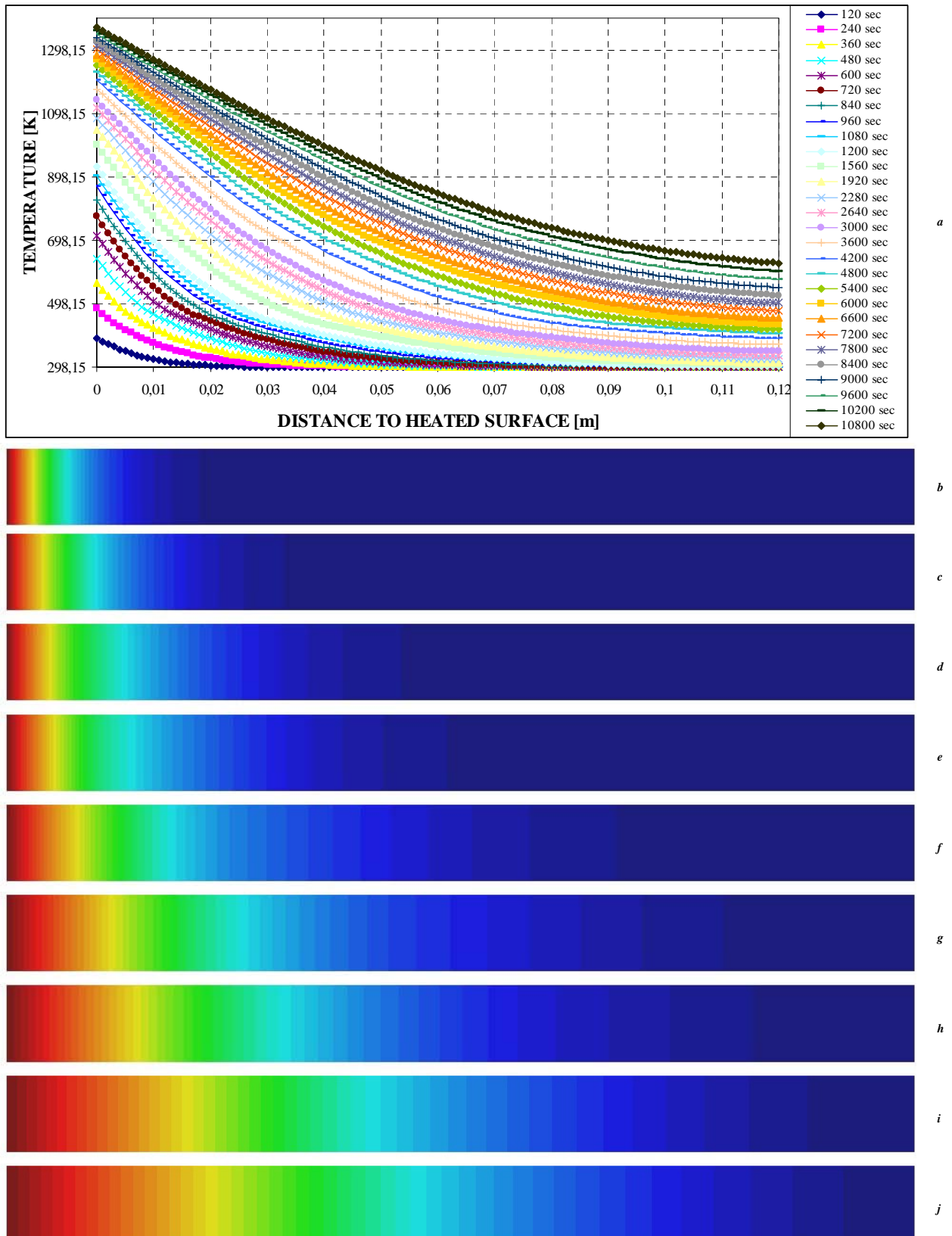


Figure 4-109. Temperature space distributions for a thickness of 12 centimetres, an intrinsic permeability of 10^{-18} m^2 , an Initial Saturation Degree of $s=50\%$, a PARI-ISO heating curve and a C60 material (#5-TH12K018RH50PAR1C60)
 (a) Graphical evolution; **Important Remark:** The following spatial distributions colours are scaled at each instant.
 (b) Spatial distribution at 120 seconds; (c) Spatial distribution at 240 seconds; (d) Spatial distribution at 480 seconds;
 (e) Spatial distribution at 600 seconds; (f) Spatial distribution at 1.200 seconds; (g) Spatial distribution at 2.400 seconds;
 (h) Spatial distribution at 3.600 seconds; (i) Spatial distribution at 7.200 seconds; (j) Spatial distribution at 10.800 seconds

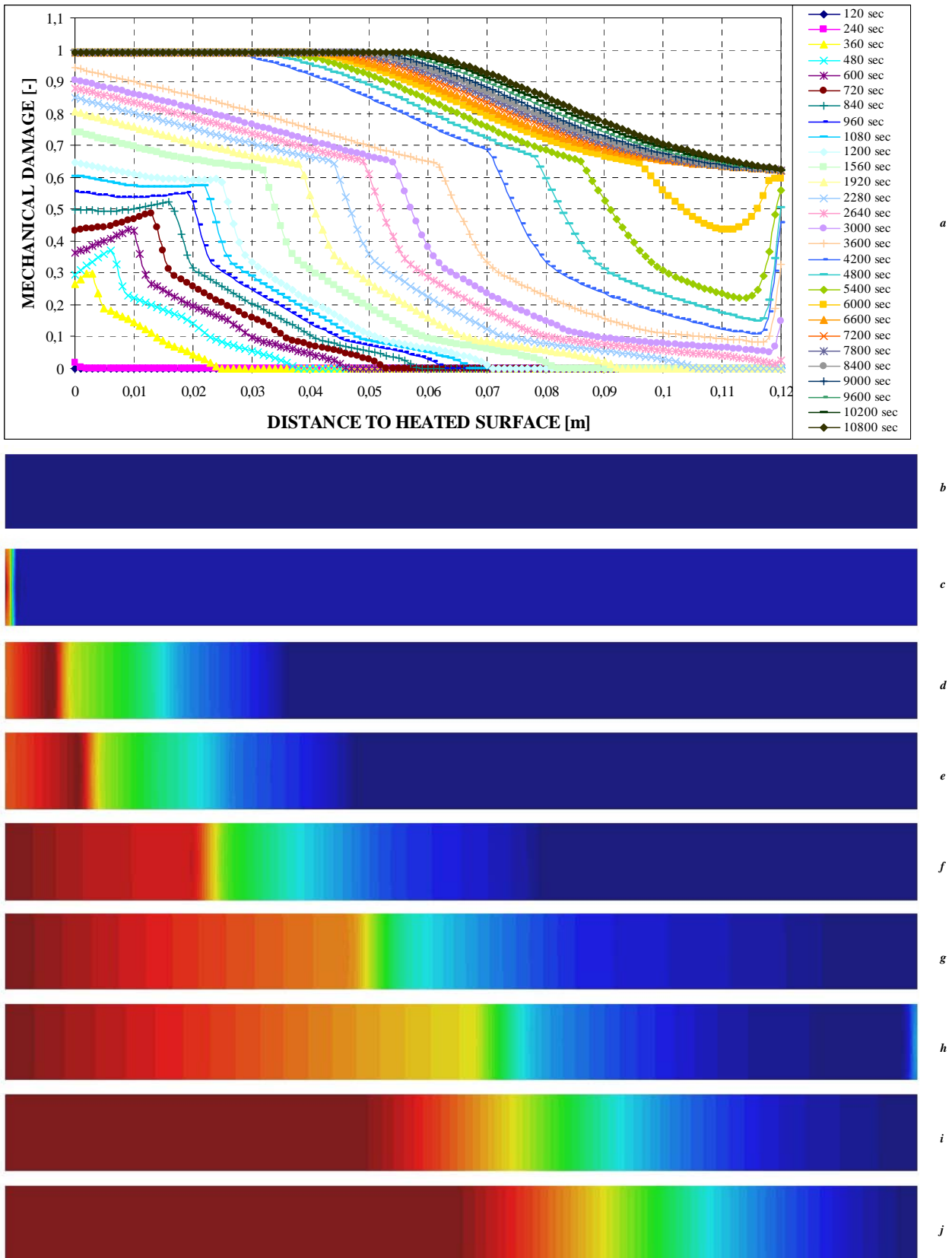


Figure 4-110. Mechanical damage space distributions for a thickness of 12 centimetres, an intrinsic permeability of 10^{-18} m^2 , an Initial Saturation Degree of $s=50\%$, a PAR1-ISO heating curve and a C60 material (#5-TH12K018RH50PAR1C60)
 (a) Graphical evolution; **Important Remark:** The following spatial distributions colours are scaled at each instant.
 (b) Spatial distribution at 120 seconds; (c) Spatial distribution at 240 seconds; (d) Spatial distribution at 480 seconds;
 (e) Spatial distribution at 600 seconds; (f) Spatial distribution at 1.200 seconds; (g) Spatial distribution at 2.400 seconds;
 (h) Spatial distribution at 3.600 seconds; (i) Spatial distribution at 7.200 seconds; (j) Spatial distribution at 10.800 seconds

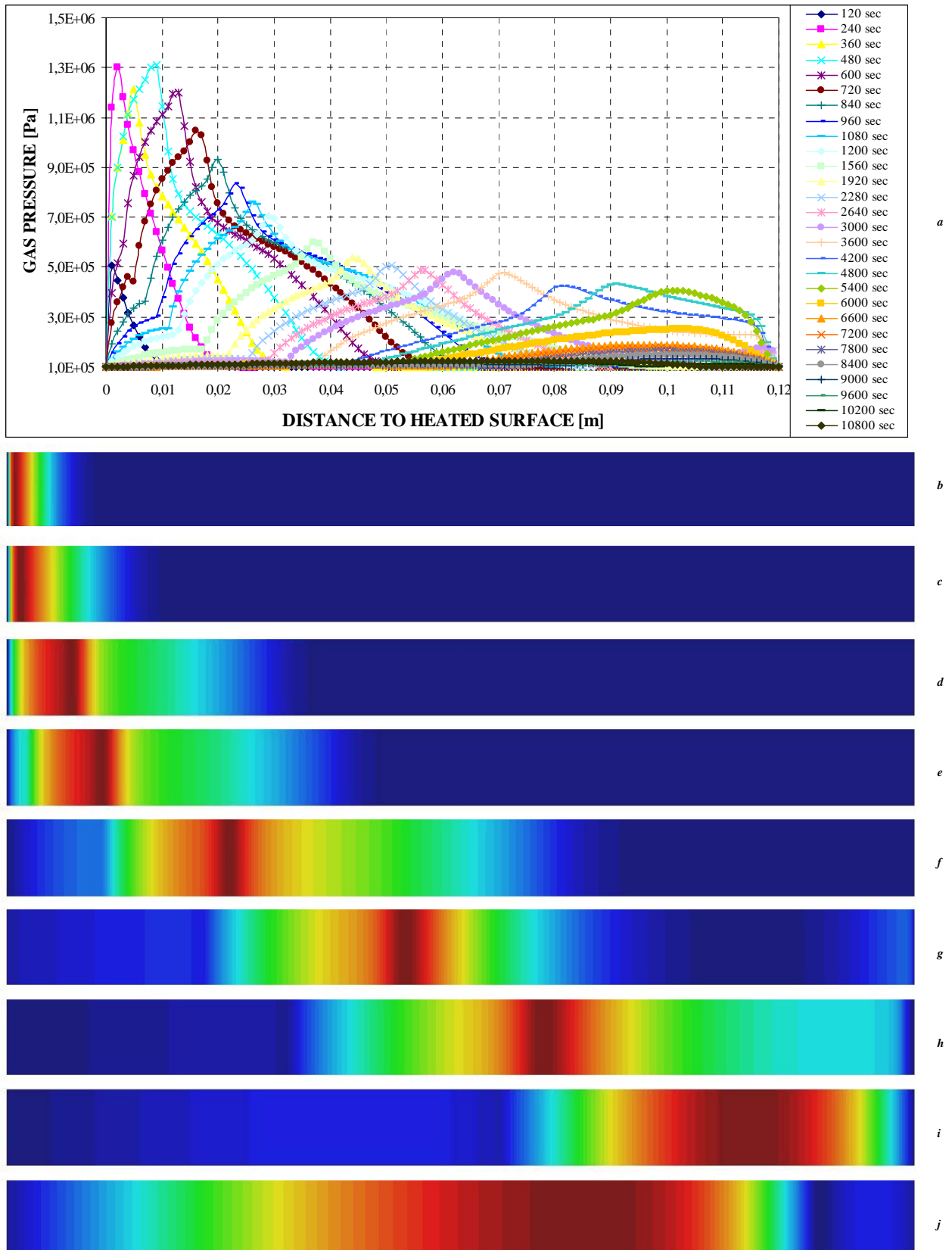


Figure 4-111. Gas pressure space distributions for a thickness of 12 centimetres, an intrinsic permeability of 10^{-18} m^2 , an Initial Saturation Degree of $s=50\%$, a PAR1-ISO heating curve and a C60 material (#5-TH12K018RH50PARIC60)
 (a) Graphical evolution; **Important Remark:** The following spatial distributions colours are scaled at each instant.
 (b) Spatial distribution at 120 seconds; (c) Spatial distribution at 240 seconds; (d) Spatial distribution at 480 seconds;
 (e) Spatial distribution at 600 seconds; (f) Spatial distribution at 1.200 seconds; (g) Spatial distribution at 2.400 seconds;
 (h) Spatial distribution at 3.600 seconds; (i) Spatial distribution at 7.200 seconds; (j) Spatial distribution at 10.800 seconds

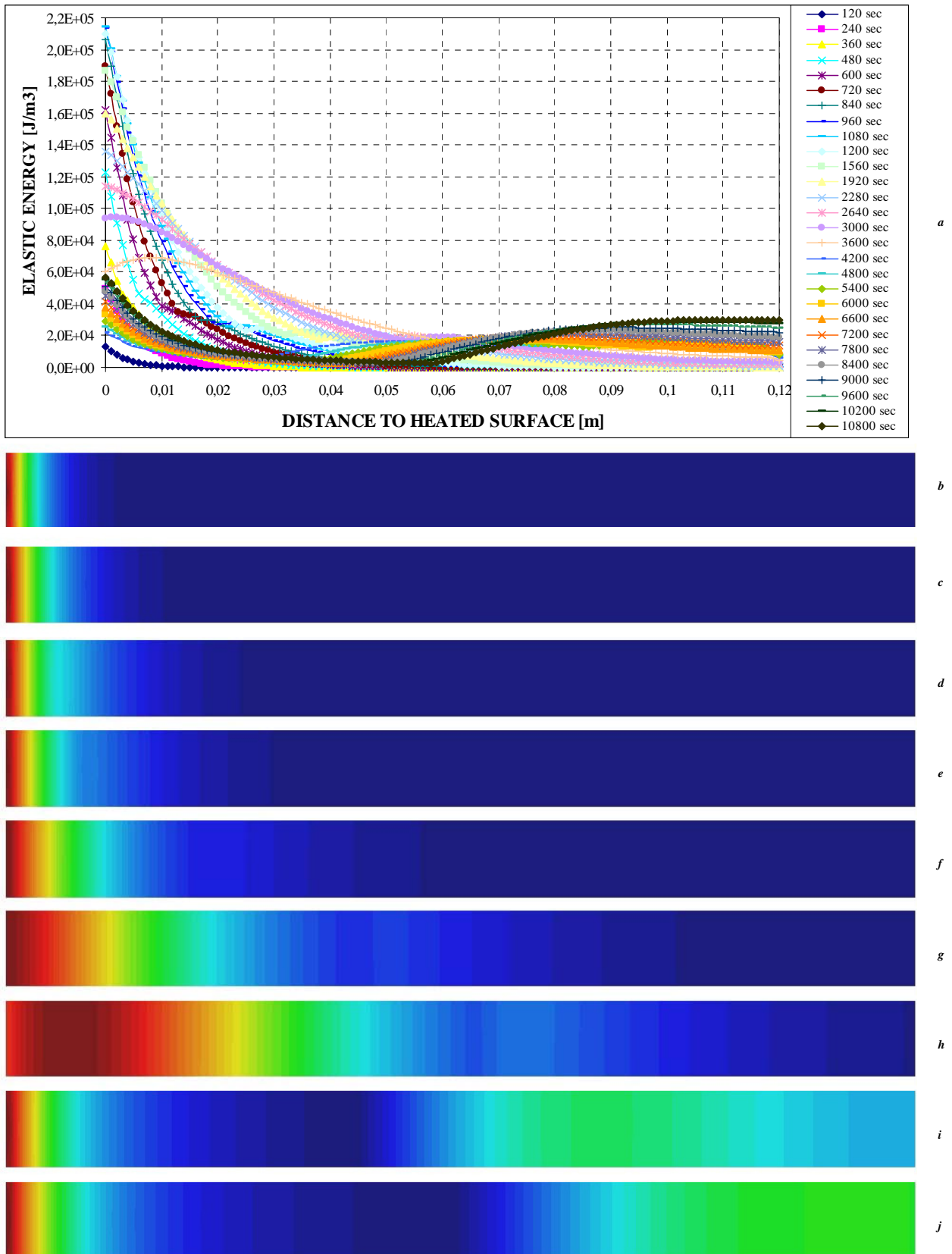


Figure 4-112. Elastic energy space distributions for a thickness of 12 centimetres, an intrinsic permeability of 10^{-18} m^2 , an Initial Saturation Degree of $s=50\%$, a PARI-ISO heating curve and a C60 material (#5-TH12K018RH50PARI C60)
 (a) Graphical evolution; **Important Remark:** The following spatial distributions colours are scaled at each instant.
 (b) Spatial distribution at 120 seconds; (c) Spatial distribution at 240 seconds; (d) Spatial distribution at 480 seconds;
 (e) Spatial distribution at 600 seconds; (f) Spatial distribution at 1.200 seconds; (g) Spatial distribution at 2.400 seconds;
 (h) Spatial distribution at 3.600 seconds; (i) Spatial distribution at 7.200 seconds; (j) Spatial distribution at 10.800 seconds

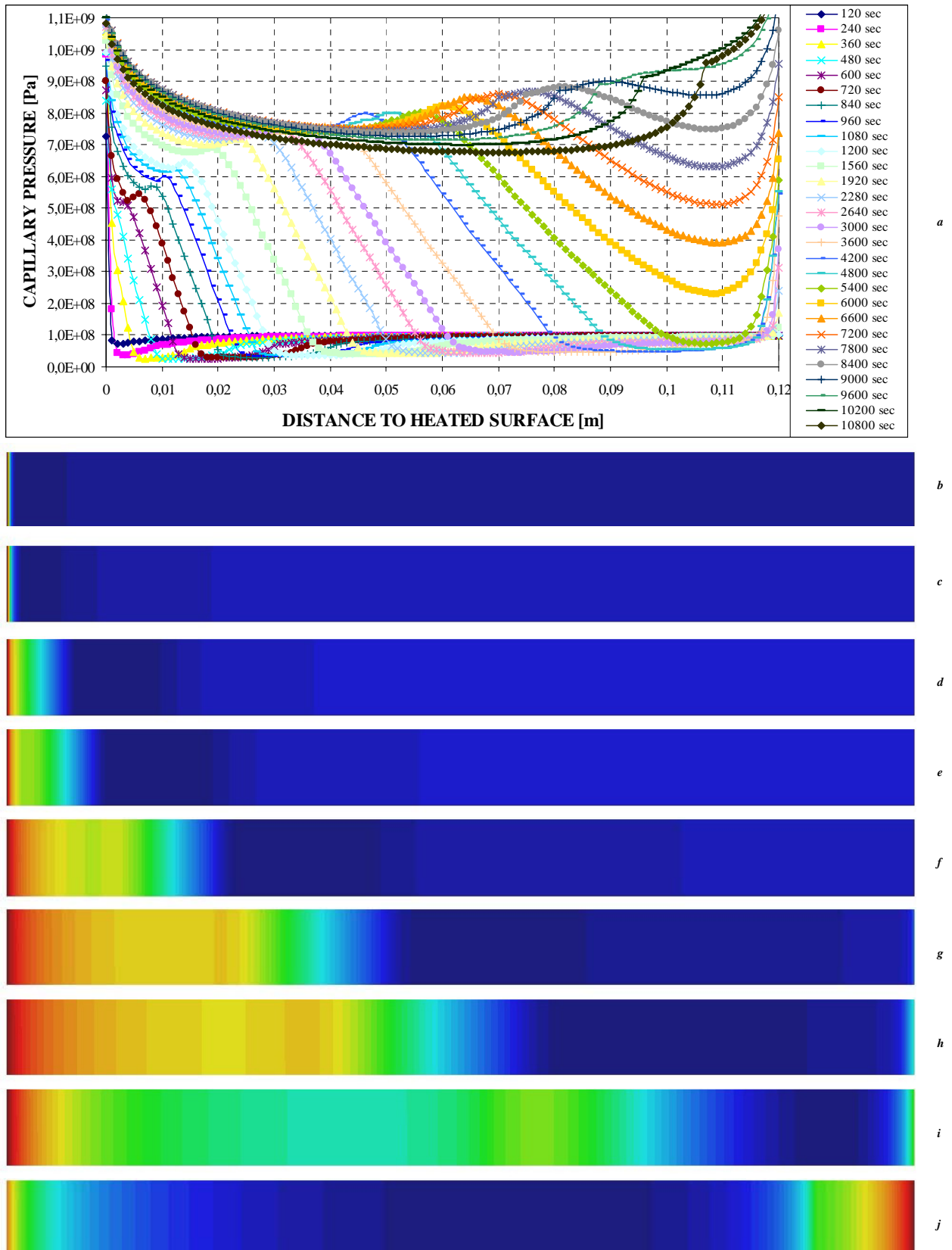


Figure 4-113. Capillary pressure space distributions for a thickness of 12 centimetres, an intrinsic permeability of 10^{-18} m^2 , an Initial Saturation Degree of $s=50\%$, a PARI-ISO heating curve and a C60 material (#5-TH12K018RH50PARIC60)
 (a) Graphical evolution; **Important Remark:** The following spatial distributions colours are scaled at each instant.
 (b) Spatial distribution at 120 seconds; (c) Spatial distribution at 240 seconds; (d) Spatial distribution at 480 seconds;
 (e) Spatial distribution at 600 seconds; (f) Spatial distribution at 1.200 seconds; (g) Spatial distribution at 2.400 seconds;
 (h) Spatial distribution at 3.600 seconds; (i) Spatial distribution at 7.200 seconds; (j) Spatial distribution at 10.800 seconds

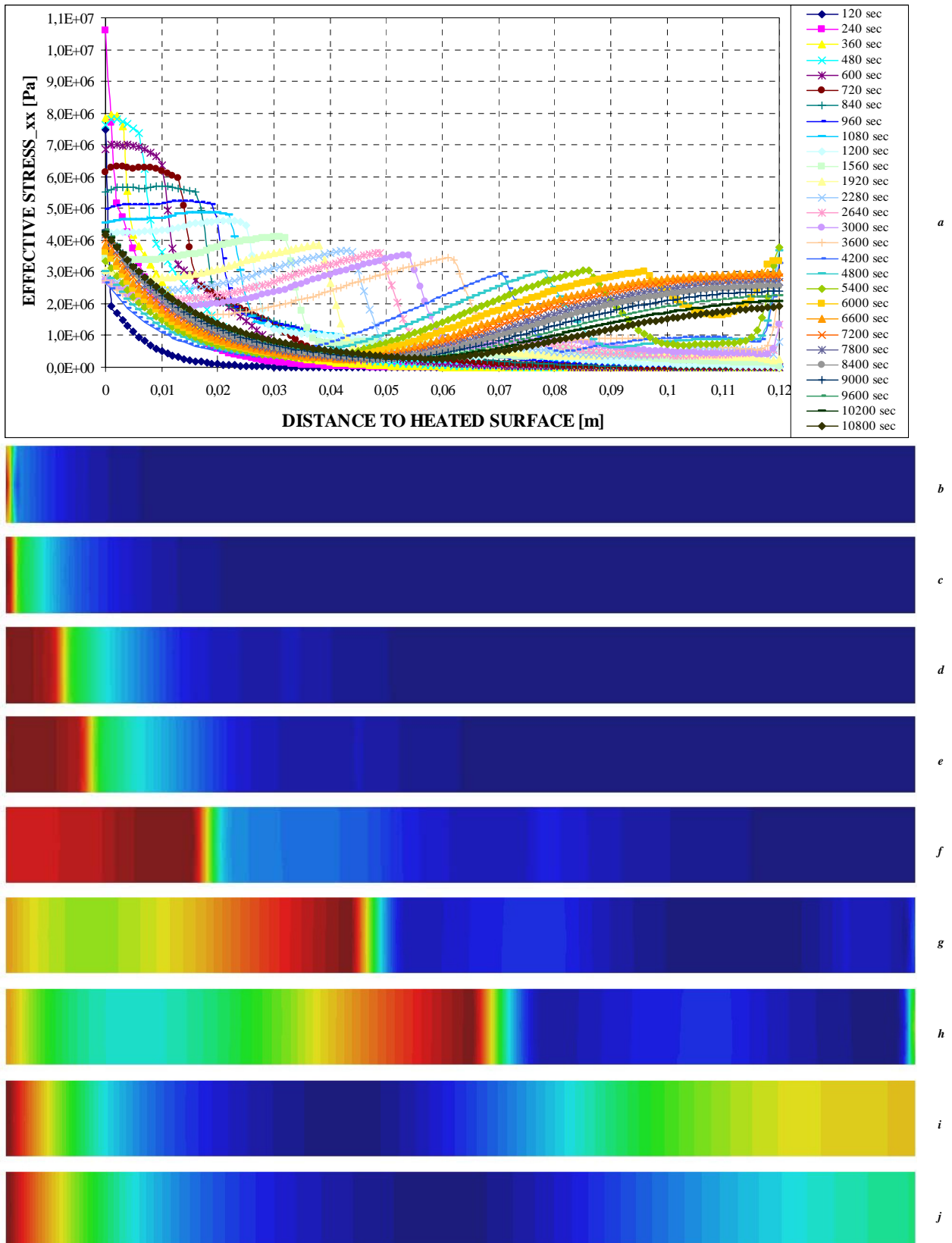


Figure 4-114. Stress σ_x (in longitudinal direction, perpendicular to heated surface) space distributions for a thickness of 12 cm, an intrinsic permeability of 10^{-18} m^2 , an Initial Saturation Degree of $s=50\%$, an ISO heating curve and a C60 material
 (a) Graphical evolution; **Important Remark:** The following spatial distributions colours are scaled at each instant.
 (b) Spatial distribution at 120 seconds; (c) Spatial distribution at 240 seconds; (d) Spatial distribution at 480 seconds;
 (e) Spatial distribution at 600 seconds; (f) Spatial distribution at 1.200 seconds; (g) Spatial distribution at 2.400 seconds;
 (h) Spatial distribution at 3.600 seconds; (i) Spatial distribution at 7.200 seconds; (j) Spatial distribution at 10.800 seconds

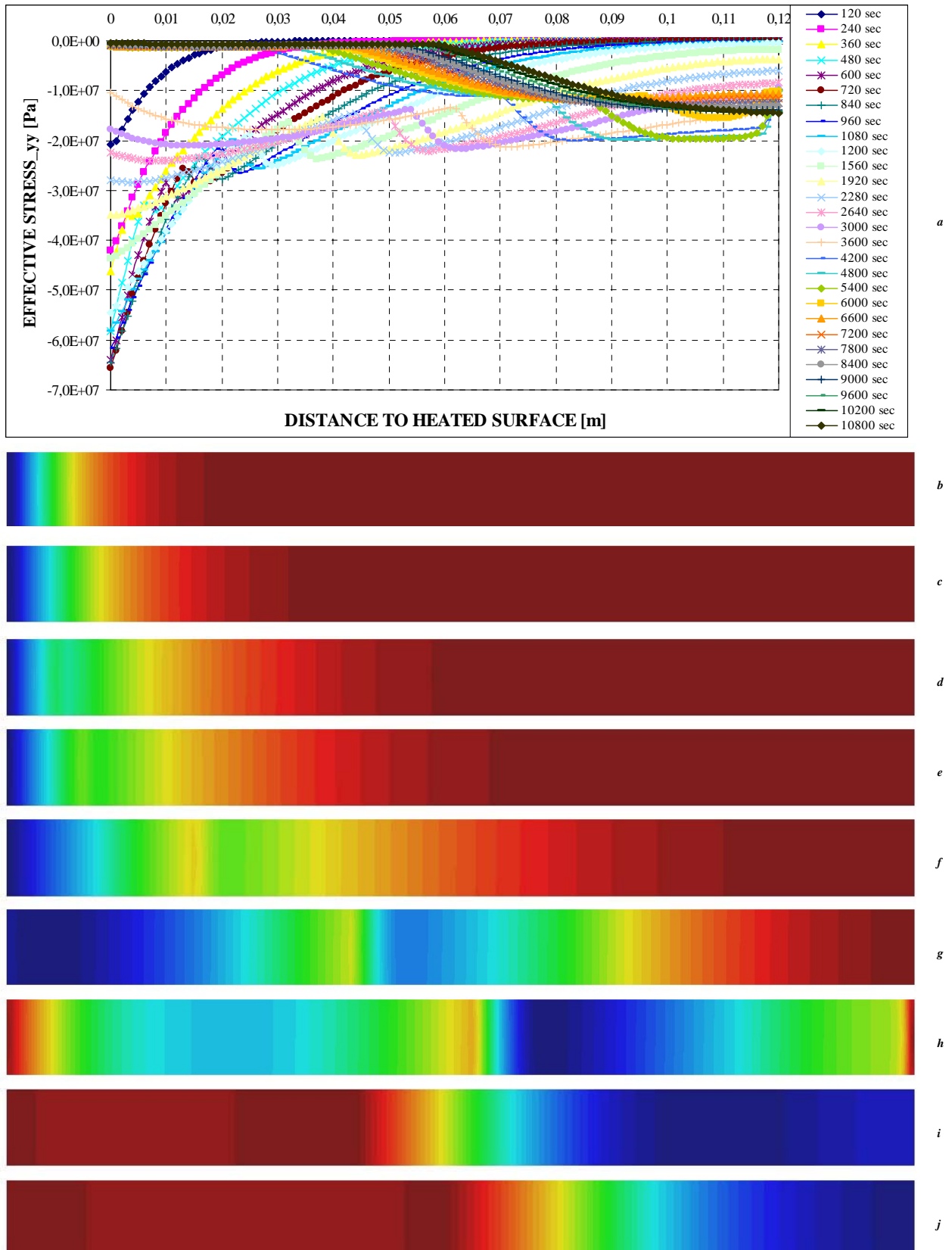


Figure 4-115. Stress σ_y (in the direction parallel to the heated surface) space distributions for a thickness of 12 centimetres, an intrinsic permeability of 10^{-18} m^2 , an Initial Saturation Degree of $s=50\%$, a PARI-ISO heating curve and a C60 material
 (a) Graphical evolution; **Important Remark:** The following spatial distributions colours are scaled at each instant.

(b) Spatial distribution at 120 seconds; (c) Spatial distribution at 240 seconds; (d) Spatial distribution at 480 seconds; (e) Spatial distribution at 600 seconds; (f) Spatial distribution at 1.200 seconds; (g) Spatial distribution at 2.400 seconds; (h) Spatial distribution at 3.600 seconds; (i) Spatial distribution at 7.200 seconds; (j) Spatial distribution at 10.800 seconds

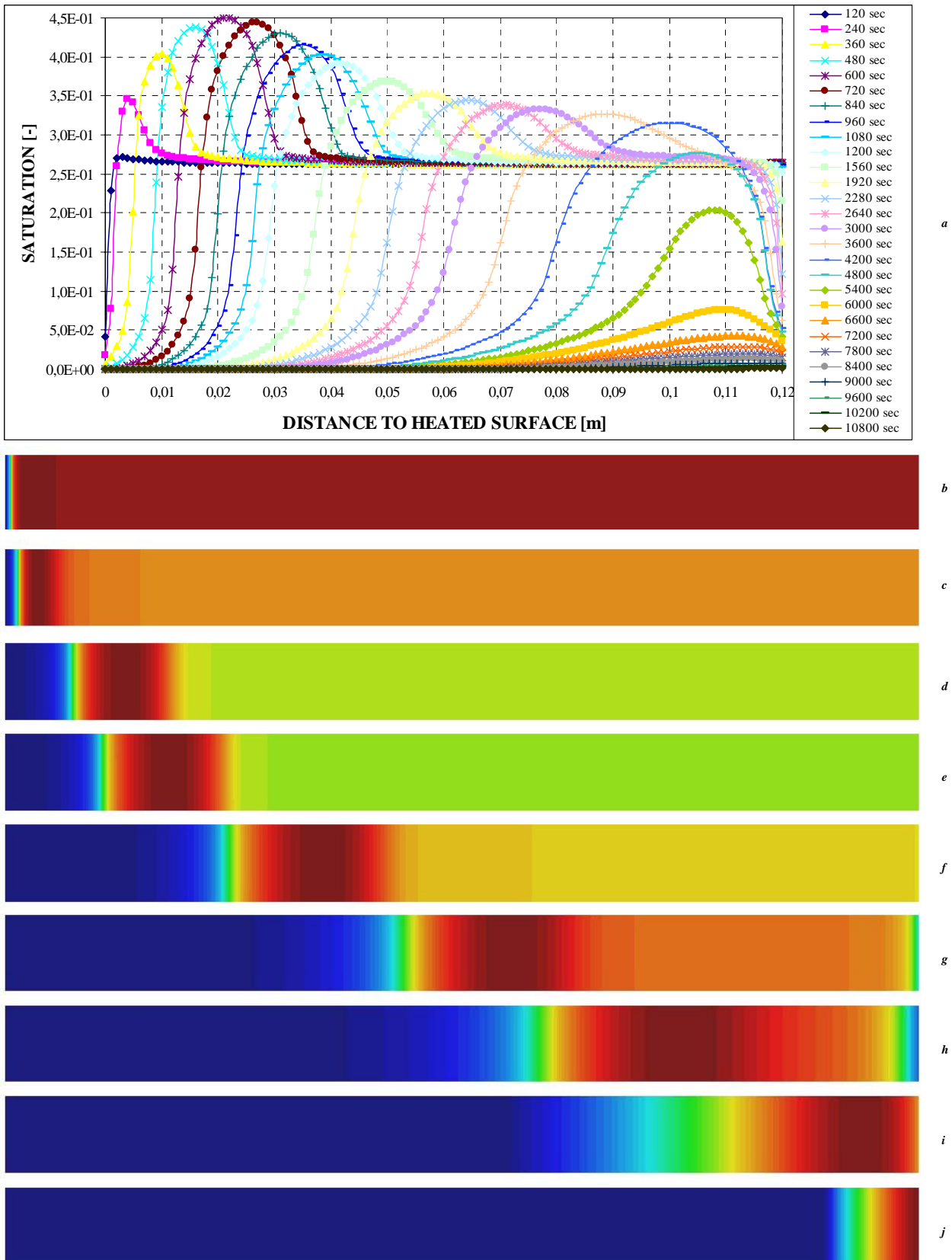


Figure 4-116. Saturation space distributions for a thickness of 12 centimetres, an intrinsic permeability of 10^{-18} m^2 , an Initial Saturation Degree of $s=50\%$, a PAR1-ISO heating curve and a C60 material (#5-TH12K018RH50PAR1C60)
 (a) Graphical evolution; **Important Remark:** The following spatial distributions colours are scaled at each instant.
 (b) Spatial distribution at 120 seconds; (c) Spatial distribution at 240 seconds; (d) Spatial distribution at 480 seconds;
 (e) Spatial distribution at 600 seconds; (f) Spatial distribution at 1.200 seconds; (g) Spatial distribution at 2.400 seconds;
 (h) Spatial distribution at 3.600 seconds; (i) Spatial distribution at 7.200 seconds; (j) Spatial distribution at 10.800 seconds

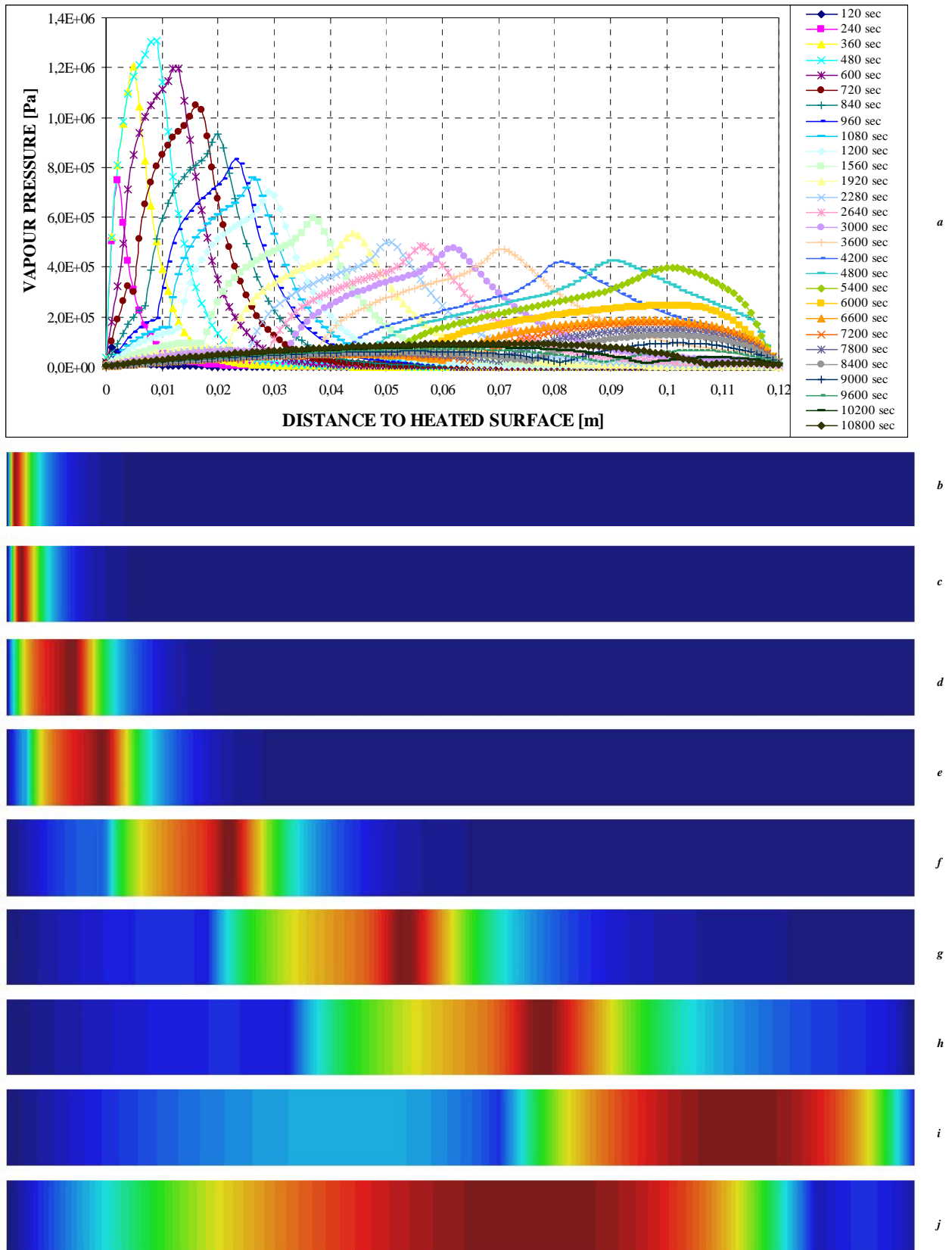


Figure 4-117. Vapour pressure space distributions for a thickness of 12 centimetres, an intrinsic permeability of 10^{-18} m^2 , an Initial Saturation Degree of $s=50\%$, a PARI-ISO heating curve and a C60 material (#5-TH12K018RH50PARIC60)
 (a) Graphical evolution; **Important Remark:** The following spatial distributions colours are scaled at each instant.
 (b) Spatial distribution at 120 seconds; (c) Spatial distribution at 240 seconds; (d) Spatial distribution at 480 seconds;
 (e) Spatial distribution at 600 seconds; (f) Spatial distribution at 1.200 seconds; (g) Spatial distribution at 2.400 seconds;
 (h) Spatial distribution at 3.600 seconds; (i) Spatial distribution at 7.200 seconds; (j) Spatial distribution at 10.800 seconds

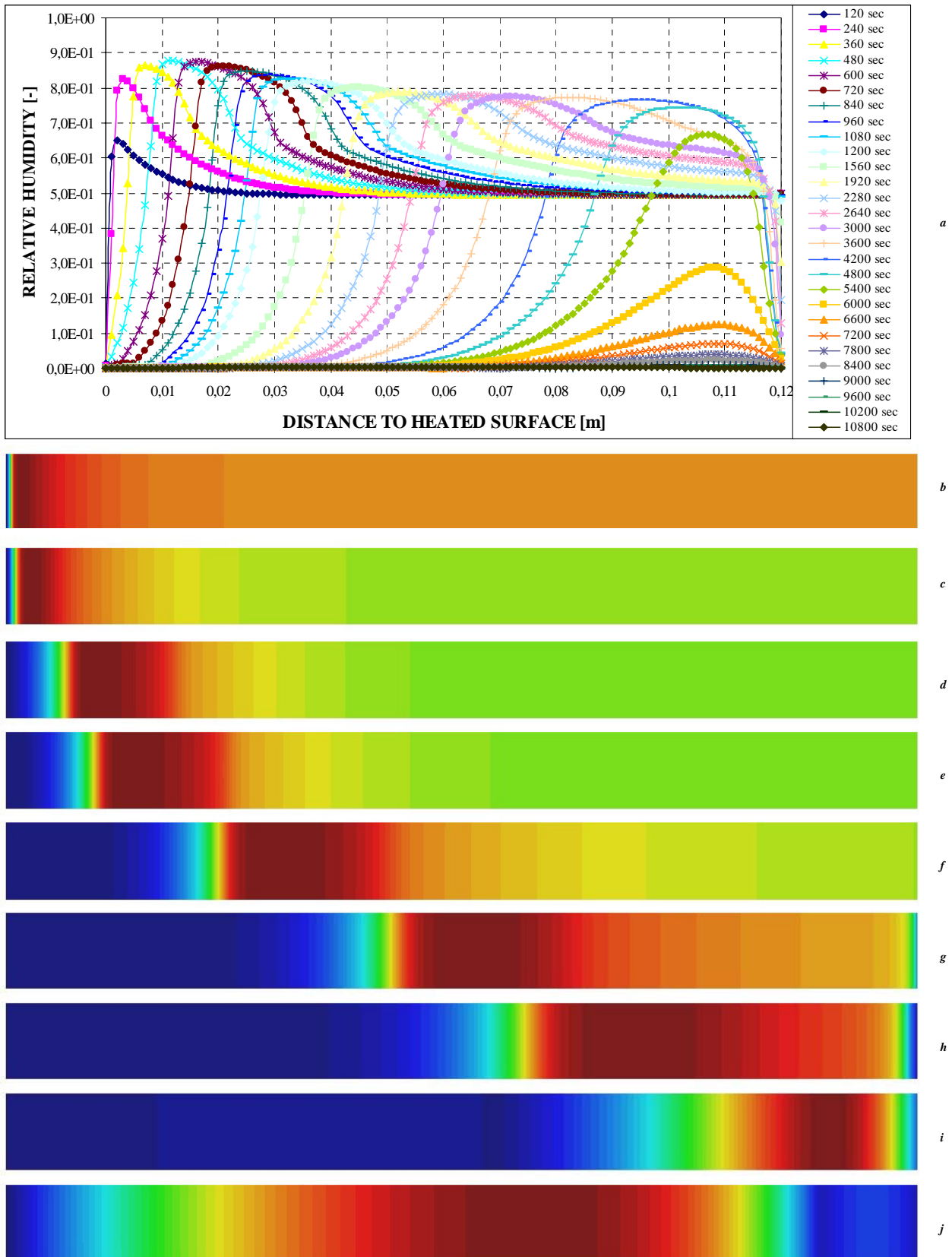


Figure 4-118. Relative humidity space distributions for a thickness of 12 centimetres, an intrinsic permeability of 10^{-18} m^2 , an Initial Saturation Degree of $s=50\%$, a PARI-ISO heating curve and a C60 material (#5-TH12K018RH50PARI C60)
 (a) Graphical evolution; **Important Remark:** The following spatial distributions colours are scaled at each instant.
 (b) Spatial distribution at 120 seconds; (c) Spatial distribution at 240 seconds; (d) Spatial distribution at 480 seconds;
 (e) Spatial distribution at 600 seconds; (f) Spatial distribution at 1.200 seconds; (g) Spatial distribution at 2.400 seconds;
 (h) Spatial distribution at 3.600 seconds; (i) Spatial distribution at 7.200 seconds; (j) Spatial distribution at 10.800 seconds

The maximum values of vapour and gas pressures (figures 4-117 and 4-111 respectively) increase initially and then they tend to decrease as the surface temperature increases and the front moves inwards. The maximum value of gas pressure usually coincides with the position where the temperature of approximately 200°C occurs. In the regions with lower temperature, below about 130°C, the gas pressure increase is caused mainly by a growth of the dry air pressure due to heating, achieving the maximum value of 0,25 – 0,4 MPa at the position with a temperature of about 100°C. In the regions with higher temperature, the effect of a rapid increase of vapour pressure due to heating and temperature-dependence of the saturation vapour pressure predominate. At temperatures 200-300 °C the gas in the material pores consists mainly of water vapour and the gradients of vapour pressure cause the vapour flow both towards the surface and inwards. The latter mass flow results in vapour condensation when the hot vapour inflows colder – internal layers of the concrete element – and in an increase of the relative humidity (see figure 4-118) above the initial value, often referred to as “moisture clog” or “saturation plug”. An additional increase of the liquid water volume in the material pores is due to the water thermal dilatation, which is particularly important above the temperature of about 160°C. A significant decrease of the gas permeability may be observed due to these effects, resulting in a decrease of the pore space available for the gas phase.

Increasing temperature causes the material dilatation of the aggregate which in part is due to concrete dehydration (products of the chemical reactions have greater volume than the initial volume of a concrete), in part due to material cracking and progressive crack opening, and finally due to “normal” thermal dilatation of the material skeleton. The concrete cracking during heating is caused by an incompatibility of thermal dilatation of the aggregate and the cement paste, resulting in high traction stresses in the Inter-Phase Transition Zones and development of local micro-cracks. Due to these cracks and chemical transformations of concrete (dehydration), the concrete strength properties and Young’s modulus degrade gradually, what can be expressed [9] in terms of the so-called thermo-chemical damage parameter.

A thermal dilatation of the external layers of a heated element is constrained by the core material which has visibly lower temperature (figure 4-109). This causes considerable macro-stresses in the external layers of the element, compression in the direction parallel to the heated surface (figure 4-115) and traction in the direction perpendicular to it (figure 4-114), as well as an accumulation of the elastic strain energy (figure 4-112). The tensile stresses may cause further development of cracks and fractures, parallel to the element surface, resulting in subsequent degradation of the material strength properties in the surface zone (figure 4-110). An additional, external compressive load parallel to the element surface can intensify the aforementioned phenomena. Due to cracking, stresses in the load bearing cross-section of the structural element, so-called “net stresses” in the sense of the damage theory, are increasing, what influences further material degradation.

Development of the cracks, both of thermo-chemical origin and the macro-stresses induced ones, causes a considerable increase of the material intrinsic permeability, and thereupon gas pressure decreases in the external layers where high temperatures are observed (see figure 4-117). The highest values of gas pressure usually correspond to the temperature 150-250 °C, and this is also the range where the so-called thermal spalling of concrete usually occurs (when elastic strain energy of constrained thermal dilatation, accumulated in the surface layer and then rapidly released after concrete fracture is considerable, the thermal spalling can be violent and explosive in nature, as it has been explained on paragraph 4.5.3.8. through the analysis of the velocities of the spalled-off pieces). On paragraph 4.5.3 it has already been analyzed in depth what is the contribution of these high values of pressure to the overall spalling phenomena and, hence, the relative importance to thermal spalling of the work performed by compressed gas against the contribution of the constrained elastic energy.

4.6 RESUME OF THE CONCLUSIONS OF THE CHAPTER

4.6.1 About the Time and Position of Main Fracture and the Sensitivity Analysis

1. As an starting point, it has been evaluated the sensitivity of the hygro-thermo-chemo-mechanical processes involved on the High-Strength concretes behaviour under a natural fire to some relevant parameters whose values may be chosen from a very early stage of High-Rise Buildings design or already known in case of existing High-Rise Buildings, such as the initial moisture content of concrete, its intrinsic permeability, the rate of temperature increase (fire intensity), the porosity, compressive strength, type of aggregate – and, in general, the whole set of hygro-thermo-chemical properties of concrete –, and the dimensions of the structural element.

2. Considering the physics of the phenomena involved in thermal spalling in heated concrete presented in previous paragraphs, it has resulted quite obvious that a high initial moisture content, a high heating rate, a low concrete porosity (hence also permeability), an additional compressive load parallel to the heated surface, and the use of aggregates with high thermal expansion are in general factors favouring Thermal Spalling. The following main particular conclusions have been reached from the works presented in this chapter (it must be remembered that the conclusions presented hereon are valid for the ranges of study of each parameter detailed on paragraph 4.3.2.):

2.1. The time and position of the main fracture of concrete elements heated during a natural fire in a High-Rise building – and hence the Thermal Spalling risk – have been determined (*paragraph 4.5.2.*), by means of the analysis of the evolution of a carefully selected Spalling Index, for a total amount of ninety one possible situations with different values of the Initial Saturation Degree, Intrinsic Permeability, Thickness of the structural concrete element, Heating profile and general definition of the Material.

2.1.1. For the High Strength Concrete considered – C60 – the worst case from the spalling point of view has clearly been the #82–TH12K019RH60PAR3C60 case, combining the lowest value of the intrinsic permeability at ambient temperature, the highest value of the initial saturation degree and the fastest heating profile (the Hydrocarbon Heating Curve). The same combinations have resulted to be the worst when considering each of the slower heating curves (ISO and Slow), both for C60 and C90 (Ultra High Strength Concrete) materials (combinations #27–TH24K019RH60PAR1C60 and #45–TH12K019RH60PAR1C90 respectively).

2.1.2. The position of main fracture in C90 material (U.H.S.C.) has been determined closer to the heated surface than in the C60 (H.S.C.) case. Furthermore, the selected Spalling Index values have resulted lower in C90 (U.H.S.C.) cases, mainly due to higher cracking and mechanical damage levels in C90 – which leads to lower gas pressure values – and to the lower restrained elastic energy in C90 (U.H.S.C.) cases derived from the already stated closeness of the main fracture to the heated surface in C90 (U.H.S.C.) cases.

2.1.3. About the influence of the heating profile: as the heating profile considered is faster and more severe (Slow → ISO → Hydrocarbon), independently of the material considered, the following trends arise for all the combinations of the Initial Saturation Degree and the Intrinsic Permeability:

2.1.3.1. The Is_4 Spalling Index values increase.

2.1.3.2. The number of combinations of the Initial Saturation Degree and the Intrinsic Permeability where Thermal Spalling occurs increases.

- 2.1.3.3. The time at which it is found the maximum risk of spalling (maximum value of the Is_4 spalling index) decreases.
- 2.1.3.4. The position of the main fracture is closer to the heated surface.
- 2.1.4. About the influence of the material is as follows: independently of the heating curve considered, the following trends arise for all the combinations of the Initial Saturation Degree and the Intrinsic Permeability:
- 2.1.4.1. The Is_4 Spalling Index values are higher for C60 (H.S.C.) than for C90 (U.H.S.C.).
- 2.1.4.2. The number of combinations of the Initial Saturation Degree and the Intrinsic Permeability where Thermal Spalling occurs is higher for C60 (H.S.C.) material.
- 2.1.4.3. The time at which it is found the maximum risk of spalling (maximum value of the Is_4 Spalling Index) is higher for C60 (H.S.C.) material (later in time), but as it is expectable from the situation detailed in last paragraphs – lower gas pressure and restrained elastic energy in the C90 (U.H.S.C.) cases – it will be less violent in type (see conclusions in paragraph 4.6.2) for C90 (U.H.S.C.) materials.
- 2.1.4.4. The position of the main fracture is closer to the heated surface for C90 (U.H.S.C.) material just in some cases (mainly for the Slow Heating curve). In the rest of cases, there are no significant differences between the position of the main fracture between C60 (H.S.C.) and C90 (U.H.S.C.).
- 2.1.4.5. There is a well-defined trend with the mechanical damage values, being significantly higher in the cases corresponding to C90 (U.H.S.C.) material.
- 2.1.5. The value of the intrinsic permeability and the heating profiles have shown a determinant role in the Thermal Spalling phenomena, independently of the initial saturation degree to which hygro-thermo-chemical-mechanical processes occurred during Thermal Spalling have presented much less sensitivity within the ranges considered. The sensitivity of results to the Intrinsic Permeability and the Heating Profile is higher on C60 material (H.S.C.) than in C90 material (U.H.S.C.).
- 2.2. The thickness of the structural element does not appear to be, in the range considered within this chapter, with any influence on Thermal Spalling processes since they arise close to the heated surface. However, it has an influence on the liquid and vapour water fluxes far from the heated surface, which could have a significant influence on the matters studied herein if an extremely slow or very long duration heating profile was considered – only in cases that would not be representative of natural fires in High-Rise buildings –.

4.6.2 About the Spalling Nomograms and the Energetic Analysis of Thermal Spalling

1. The data referred to in last paragraph, together with other relevant results concerning Thermal Spalling such as the available energy in each situation, have been represented on a set of eight charts in the initial saturation degree – intrinsic permeability domain, so it has been possible to define some dangerous regions with respect to the spalling occurrence (*paragraph 4.5.3*). These nomograms have shown, through a fast, graphical and intuitive methodology understandable for all of their expected users, the following conclusions common to all of them

(other particular conclusions for some of the nomograms can be read in paragraphs 4.5.3.1 to 4.5.3.8 but are out of the scope of this resume):

- 1.1. Most of the analyzed cases experiment Thermal Spalling – energetically viable – (at only 2-4 minutes from the start of the fire when considering the Hydrocarbon heating curve, 10 minutes from the start of the fire when considering the ISO heating curve and later on, at about 1 hour, for the slowest heating curve admitted by Eurocode regulation [18]), especially when considering C60 material (H.S.C.).
- 1.2. The worst combination of the Initial Saturation Degree and the Intrinsic Permeability, from the point of view of Thermal Spalling risk, is always featured by $S = 60\%$ and $k_0 = 10^{-19} \text{ m}^2$.
- 1.3. The best combination of the Initial Saturation Degree and the Intrinsic Permeability, from the point of view of Thermal Spalling risk, is always featured by $S = 40\%$ and $k_0 = 10^{-17} \text{ m}^2$.
- 1.4. It is observed a little sensitivity of the I_{s4} Spalling Index values to the Initial Saturation Degree. On the contrary, it is observed a very pronounced sensitivity of the I_{s4} spalling index values to the Intrinsic Permeability level – the larger increase of the I_{s4} spalling index value is found when changing the Intrinsic Permeability from $k_0 = 10^{-18} \text{ m}^2$ to $k_0 = 10^{-19} \text{ m}^2$, so this last value seems to be an upper limit for Intrinsic Permeability from the point of view of Thermal Spalling –.

2. It has also been analyzed the energetic viability of Thermal Spalling and, hence, of the spalling risk and its expectable type (either violent and explosive or slow in nature) in every possible set of conditions so both Designers and Fire Fighting Services have a valuable information in order to take decisions about design and about the expectable consequences of fire fighting actions from a really intuitive, graphical and immediate point of view.

Beyond this result, it has also been estimated the energetic contributions to Thermal Spalling occurrence of both the compressed gas and the constrained elastic energy since the relative importance of the build-up of high pore pressure closed to the heated concrete surface (as a result of rapid evaporation of the moisture) and the release of the stored energy (due to the thermal stresses resulting from high values of restrained strains caused by temperature gradients), had not been already established. The expectable type of spalling, either violent and explosive or slow in nature, in every possible set of conditions has been determined through the calculation of the velocity of the spalled-off pieces and the following conclusions have arisen:

- 2.1. About the influence of the heating profile: as the heating profile considered is faster and more severe (Slow → ISO → Hydrocarbon), independently of the material considered, the following trends arise for all the combinations of the Initial Saturation Degree and the Intrinsic Permeability:
 - 2.1.1. The average velocity of the spalled pieces increases.
 - 2.1.2. About the energetic analysis comparison, the following conclusions are only referred to heating curves ISO and Slow, since the lack of convergence of Hydrocarbon cases may lead to deceptive conclusions about this particular matter:
 - The relative contribution of the constrained elastic energy decreases as the heating profile increases its speed and severity. On the other hand, the relative contribution of the work done by compressed gas increases. This might be due to higher gas pressures arising with faster heating profiles.

- 2.2. About the influence of the material is as follows: independently of the heating curve considered, the following trends arise for all the combinations of the Initial Saturation Degree and the Intrinsic Permeability:
- 2.2.1. The average velocity of the spalled pieces is higher for C60 material (H.S.C.),
- 2.2.2. About the energetic analysis comparison, the following conclusions are only referred to heating curves ISO and Slow, since the lack of convergence of Hydrocarbon cases may lead to deceptive conclusions about this particular matter:
- The relative contribution of the constrained elastic energy is higher for the C90 material (U.H.S.C.) than for the C60 material (H.S.C.). This trend is more pronounced for high values of the Intrinsic Permeability (10^{-17} and 10^{-18} m²) than for 10^{-19} m².
- 2.3. About the relative energetic contribution of compressed gas and the constrained elastic energy to spalling occurrence, it is observed that:
- 2.3.1. For the highest levels of the Intrinsic Permeability, the main contributor is the constrained elastic energy ΔU .
- 2.3.2. For the lowest levels of the Intrinsic Permeability, the main contributor is the compressed gas W .
- 2.3.3. The Initial Saturation Degree does not affect significantly, within the considered range of values, to the relative energetic contribution of both factors.
- 2.4. The highest average velocity of the spalled-off pieces, among all of the cases analyzed, is case #82-TH12K019RH60PAR3C60 corresponding to the Hydrocarbon heating curve and C60 material (H.S.C.).
- 2.5. Referring only to cases with Slow and ISO Heating curves, the case with the highest average velocity of the spalled-off pieces is case #27-TH24K019RH60PAR1C60, corresponding to an Initial Saturation Degree at 60%, an Intrinsic Permeability value of 10^{-19} m², an ISO heating curve and C60 material. The mean velocity of the spalled-off pieces considering only the spalling cases not related to Hydrocarbon heating curve is 7,1 m/s and its median value is 4,8 m/s (considering zero values for the cases where spalling is not occurring).
- 2.6. The distribution of average velocities of spalled pieces evaluated for each combination indicates the existence of two peaks, lying with the range of $4,5 < v \leq 6,0$ m/s and of $7,5 < v \leq 9,0$ m/s. As it can be observed on figure 4-38 these results show good accordance with the experimental results obtained by [32] recording spalling events by means of a high-speed camera, giving insight into the size/shape and velocity of the spalled pieces.

4.6.3 About the Evolution of each Parameter affecting the Physics of Thermal Spalling Phenomena

1. Related to the temperature-evolution of the Gas and Vapour Pressures and the Total Damage, the following general conclusions have arisen (other particular conclusions for some of the comparisons developed can be read in paragraphs 4.5.4.1 to 4.5.4.6 but are out of the scope of this resume):

- 1.1. The maximum absolute gas pressure reached during the three hours of simulations is always found, for all of the depths considered, within the temperature range of 473 ± 50 K, being this the temperature at which spalling is usually observed. This fact suggests that despite the I_{s4} maximum values are achieved at higher temperatures, Thermal Spalling may be occurring before the instants corresponding to these maxima, as it was explained on table 4-43.
- 1.2. Gas pressure values corresponding both to its absolute maxima and to the instant where the I_{s4} Spalling Index reaches its maximum value at each case, at the position of the main fracture, range from the values exposed on next table:

<i>Material</i>	<i>Heating Profile</i>	<i>Range of Gas Pressure Absolute maximum [MPa]</i>	<i>Range of Gas Pressure Value at the instant of maximum I_{s4} at the main fracture position [MPa]</i>
C60 (H.S.C.)	Hydrocarbon	$1,2 \leq p^g \leq 5,7$ *	$0,2 \leq p^g \leq 4,4$ *
	ISO 834	$0,6 \leq p^g \leq 2,7$	$0,4 \leq p^g \leq 2,0$
	Parametric-Slow	$0,3 \leq p^g \leq 1,8$	$0,2 \leq p^g \leq 1,3$
C90 (U.H.S.C.)	Hydrocarbon	$0,9 \leq p^g \leq 4,8$ *	$0,4 \leq p^g \leq 2,1$ *
	ISO 834	$0,5 \leq p^g \leq 2,6$	$0,2 \leq p^g \leq 1,2$
	Parametric-Slow	$0,3 \leq p^g \leq 1,3$	$0,1 \leq p^g \leq 0,8$

Table 4-60. Gas Pressure values ranges for different types of Heating Profiles and materials.

***Remark:** Results corresponding to 12 centimetres cases, taking into account that some of the cases featuring Hydrocarbon heating curve have not converged during the three hours of simulation, so their corresponding gas pressure values may be even higher.

- 1.3. It is observed a slight increase of the maximum absolute gas and vapour pressures as the Initial Saturation Degree increases, but the temperature at which these maxima appear is not affected. This increase is higher when considering the Slow heating curve. The maximum absolute vapour pressure values matches in time with the maximum of gas pressure. The difference between gas and vapour pressure is, for the Hydrocarbon heating curve cases, much lower than in the case featured by a Slow heating curve.
- 1.4. On the contrary, it is clearly observed a pronounced sensitivity of both the maximum absolute gas pressure and the pressure corresponding to the maximum I_{s4} Spalling Index with the values of the Intrinsic Permeability, increasing all of these pressures as the latter decreases. The temperature at which these maxima are found decreases when increasing Intrinsic Permeability, so it can be easily concluded that low values of Intrinsic Permeability may lead to spalling phenomena more violent but not necessarily occurring earlier.
- 1.5. Analogously, as Intrinsic Permeability increases the Total Damage level at the temperatures showing both the maximum absolute gas pressure and the pressure corresponding to the maximum I_{s4} Spalling Index decrease – being this decrease slight at the cases featured by C90 material (U.H.S.C.). At the inner layers, among 5 and 10 centimetres away from the heated surface, it is observed that the material is not completely cracked at the end of the simulation and that the final Total Damage level also decreases as Intrinsic Permeability increases.
- 1.6. It is worthy to remark that the evolution curve of Total Damage at all of the depths considered present a singularity – in the form of a sudden reduction of its slope, reduction almost to zero in the cases featured by the Hydrocarbon heating curve – at

the temperatures where gas and vapour pressure maxima are reached. This fact suggests that the compressed gas contribution to material damaging is significant.

2. Related to the time-evolution of the Vapour Pressure and the Mechanical Damage distributions, the following general conclusions have arisen (other particular conclusions for some of the comparisons developed can be read in paragraphs 4.5.6 but are out of the scope of this resume):

2.1. For the set of cases adopted as a reference, featured by a 12 centimetres thick structural element of C60 material (H.S.C.) and with an ISO heating curve applied (cases 1 to 9), beyond what explained on previous paragraphs it is observed that:

2.1.1. The depth where the vapour pressure shows its maximum values increases with time up to an absolute heating time of 9.600 seconds, instant at which the maximum value (much lower than in the previous stages) moves towards the heated surface. The maximum absolute vapour pressure reached at each instant matches the gas pressure maximum (in depth and absolute time) and is always found within the temperature range of 473 ± 50 K, being this the temperature at which spalling is usually observed. This fact suggests that despite the I_{s4} maximum values are achieved at higher temperatures, within the range of 573 ± 25 K, spalling may be occurring before the instants corresponding to these maxima, as it was explained on table 4-43.

2.1.2. The regions where mechanical damage values are maxima at any certain instant are those most exposed to temperature rising (close to the heated surface). However, one must remember that a lower depth does not necessarily mean higher Total/Mechanical Damage levels at the same temperature.

2.1.3. It is observed a slight increase of the maximum value of the vapour pressure and a decrease of its corresponding depth as the Initial Saturation Degree increases. On the other hand, it is clearly observed a pronounced sensitivity of the maximum absolute vapour pressure with the values of the Intrinsic Permeability, increasing this pressure as the latter decreases. The depth at which these maxima are found increases with Intrinsic Permeability.

2.1.4. As Intrinsic Permeability increases the Mechanical Damage level at a certain depth decreases.

2.2. From the comparison of the set of cases adopted as a reference, against the rest of possible situations, it is observed that:

2.2.1. A slower heating curve leads to a maximum vapour pressure value much closer to the heated surface and with a higher value at any certain instant.

2.2.2. In reference to the material influence, the change from C60 (H.S.C.) to C90 (U.H.S.C.) makes the maximum vapour pressure value arise closer to the heated surface while being lower, independently of the heating profile. At any instant, cases with C90 material (U.H.S.C.) show larger differences of vapour pressure values with respect to the saturation vapour pressure corresponding to the temperature at each depth than in case with C60 material (H.S.C.). These differences increase with time due to the progressive drying of material.

2.2.3. If one compares the vapour pressure spatial distributions corresponding to the instant at which the heated surface temperature is 473 K, temperature above which thermal spalling is usually observed, it is again observed than in these conditions C90 material (U.H.S.C.) shows lower vapour pressure values (being

its maximum closer to the surface). On the other hand, a slower heating profile leads to a much wider but lower distribution of vapour pressure values, mainly due to a characteristic higher absolute time that enables larger diffusion and capillary processes.

2.2.4. The mechanical damage levels are lower when considering a Slow heating profile, being in these cases the depths at which the maximum value of the vapour pressure appears also lower (if the same absolute instant is compared).

2.2.5. In the cases featured by a thickness of 24 centimetres and an ISO heating profile the spatial distribution of the vapour pressure and the mechanical damage are the same as for 12 centimetres during the initial heating stages. However, for higher absolute times – 7.200 and 10.800 seconds – these distributions are qualitatively different since there exist diffusion and capillary processes towards the non-heated surface which are not present in the cases of 12 centimetres, where certain vapour and liquid water fluxes are exchanged with the non-heated atmosphere, leading to a wider distribution of the vapour pressure distribution and varying the mechanical damage distribution beyond the first 12 centimetres (this fact does not affect significantly to the Thermal Spalling phenomena since, as it has been explained in the paragraph related to the spalling nomograms, they take place in layers located much closer to the heated surface).

4.6.4 About extended tasks to go more deeply into Thermal Spalling Research

1. In this chapter it has been established as the time where Thermal Spalling will take place, that corresponding to the maximum value of the I_{s4} Spalling Index. However, as it has been explained during the work, there are instants before reaching this point at which Thermal Spalling would be energetically viable but with lower levels of damage – cracking –. Therefore, it is still needed to analyze what is the time-evolution of the energy available for Thermal Spalling combined with the determination of the lowest level of cracking needed for its occurrence – remember that a crack thickness of 0,5 millimetres is assumed in the energetic analyses included in this thesis –. The former analysis is worked out in Chapter 6 of this Thesis.

2. As it has been exposed, the Thermal Spalling phenomena derived from the calculations developed usually occur at quite superficial layers of the heated concrete element (less than 1 centimetre from the heated surface for ISO heating cases, less than 2 centimetres in Slow heating cases and less than 5 millimetres in Hydrocarbon heating cases). This fact means that, although the reinforcing concrete cover is reduced due to the spalled-off pieces, it is not directly exposed to fire. There is a need of studying what will happen after the first superficial pieces have spalled-off, being possible – but not corroborated – that Thermal Spalling phenomena accelerates as successive layers are progressively spalled-off until the reinforcement bars are reached and exposed directly to fire.

3. On the other hand, there is still a need for a mathematical model allowing analysing the hygro-thermal, chemical and deterioration processes in concrete structures at high temperature more precisely, and which will allow us to predict the thermal spalling phenomenon using purely ‘mechanical’ criteria, and not ‘heuristic’ ones, as the presented here. This should possibly take into account a stochastic nature of the phenomenon and its both local and global character. In some authors’ opinion [9], the latter could be considered, for example, by using a multi-scale type model, involving a micro-level for predicting physical properties of the concrete components (i.e. cement paste, Inter-phase Transition Zone and aggregate), a meso-level for analysis of their interactions (e.g. by means of fracture mechanics), and finally, a macro-scale for

evaluation of the whole structure performance at given ambient conditions. The model used in this chapter, after appropriate modifications, could be used for the macro-scale analysis.

4. Finally, an extension of all of these works – basically the development of Spalling Indexes correlated against experimental data – to cases with bidimensional fluxes of heat and mass are necessary to excerpt conclusions for certain structural elements such as square columns, where Corner Thermal Spalling is often the most dangerous type.

4.7 BIBLIOGRAPHY OF THE CHAPTER

Bibliography of the chapter

- [1] Brite Euram III BRPR-CT95-0065 HITECO, *Understanding and industrial application of High Performance Concrete in High Temperature Environment – Final report*, 1999.
- [2] G.W. Shorter, T.Z. Harmathy, *Moisture clog spalling*, Proc. Instit. Civil Engr. 20 (1965) 75-90.
- [3] H. Saito, *Explosive spalling of prestressed concrete in fire*, Internal Report No 22, Building Research Institute, Japan, 1965.
- [4] T.Z. Harmathy, *Effect of moisture on the fire endurance of building elements*, ASTM special technical publication 385, Philadelphia, 1965.
- [5] V.V. Zhukov, *Explosive failure of concrete during a fire* (in Russian). Translation No. DT 2124, Joint Fire Research Organization, Borehamwood, 1975.
- [6] P.J. Sullivan, A.A. Akhtaruzzaman, *Explosive spalling of concrete exposed to high temperature*, in: Proc. Of First International on Structural Mechanics in Reactor Technology, Berlin, 1971
- [7] R.J. Connelly, *The spalling of concrete in fires*, Ph.D. thesis, Aston University, 1995, pp. 294
- [8] N. Khoylou, *Modelling of moisture migration and spalling behaviour in non-uniformly heated concrete*, Ph.D. thesis, Imperial College, London, 1997, pp.1147.
- [9] D. Gawin, F. Pesavento, B.A. Schrefler, *Towards prediction of the thermal spalling risk through a multi-phase porous media model of concrete*, Comput. Methods Appl. Mech. Engrg. . 195 (2006) 5707-5729.
- [10] Z.P. Bazant, W. Thonguthai, *Pore pressure and drying of concrete at high temperature*, J. Engrg. Mech. ASCE 104 (1978) 1059-1079.
- [11] R. Felicetti, P. Gambarova, M.P. Natali Sora, G. Rosati, *Caratterizzazione mecánica di calcestruzzi ad alta ed altissima resistenza esposti ad alta temperatura*, Brite Euram III report, 1999.
- [12] K.D. Hertz, *Limits of spalling of fire-exposed-concrete*, Fire Safety Journal 38 (2003) pp. 103-116
- [13] J.G. Quintiere, *Principles of Fire Behaviour*, Book, Delmar Publishers, 1st edition 1998.
- [14] F. Pesavento, *Non linear modelling of concrete as multiphase porous material in high temperature conditions*, Ph.D. Thesis, Dipartimento di Costruzioni e Trasporti – Università degli Studi di Padova, 2000
- [15] M. Goyeneche, D.M. Bruneau, D. Lasseaux, *On a film flor model to describe free water transfer in a hygroscopic capillary porous médium during drying*, Transport in Porous Media, June 2000
- [16] Bungale S. Taranath, *Steel, Concrete & Composite design of tall buildings*, Book, Mc Graw Hill, 2nd edition 1998.
- [17] L.T. Phan, *High-Strength concrete at High Temperature – An overview*, Building Fire Research Laboratory Online Library, National Institute of Standards and Technology, Gaithersburg, 2002.
- [18] UNE-EN 1991-1-2, Eurocódigo 1: Acciones en estructuras. Parte 1-2: Acciones generales. Acciones en estructuras expuestas al fuego, Mayo 2004.
- [19] Preparation of concrete specimens CRC and C60.SF, 12-month Technical Report / Aalborg Pórtland, Brite Euram III, BE-1158 HITECO/1/AP/BA/970630.1/Vfin, June 1997.
- [20] U. Diederichs, *Mechanical behaviour of C60 Concrete at High Temperature*, Task 2.2, Mid Term Report, Brite Euram III – HITECO Programme, BE-95-1158, December 1997.
- [21] P. Kalifa, H. Sallée- CSTB, *Thermal properties, total water porosity and split failure strength*, Task 2.1, Annual Report 97, Brite Euram III – HITECO Programme, BE-95-1158, December 1997.
- [22] G.A. Khoury, *Mechanical Behaviour at High Temperature*, Task 2.2, Final Report, Brite Euram III – HITECO Programme, BE-95-1158, August 1999.
- [23] V. Baroghel-Bouny, M. Mainguy, T. Lassabatere, O. Coussy, *Characterization and identification of equilibrium and transfer moisture properties for ordinary and high-performance cementitious materials*, Cement and Concret Research 29, 1225-1238, 1999.
- [24] 12-monthly Progress report n° 2, Brite Euram III-HITECO Programme, 01/01/97 to 31/12/97.
- [25] U. Schneider, H.J. Herbst, *Permeabilitaet und Porositaet von Beton bei hohen Temperaturen* (in german), Deutscher Ausschuss fuer Stahlbeton, 403, 23-52, 1989.
- [26] C. Alonso, E. Gayo, C. Andrade, - CSIC, *Microstructural characterisation as a function of temperatura*, Task 2.3, Final Report, Brite Euram III – HITECO Programme, BE-95-1158.
- [27] T.Z. Harmathy, L.W. Allen, *Thermal properties of selected masonry unit concretes*, ACI Journal, February, 132-142, 1973.
- [28] U. Diederichs, *Mechanical behaviour of C90 concrete at high temperature*, Brite Euram III – HITECO Programme, BE-95-1158, Annual report 97-Task 2.2, December 1997.
- [29] K. Juvas, *Basic mechanical characterization*, 12-month technical report/Partek/PCD, Brite Euram III – HITECO Programme, December 1997.
- [30] U. Diederichs, U. Jumppanen, V. Fenttala, *Behaviour of high strength concrete at elevated temperatures*. Espoo 1989 : Helsinki University of technology, Departement of structural Engineering 1992, Report 92 p72.

- [31] D. Gawin, F. Pesavento, B.A. Schrefler, *Modelling of Hygro-Thermal Behaviour and Damage of Concrete at Temperature Above the Critical Point of Water*, Int. J. Numer. Anal. Meth. Geomech. 26 (2002) 537-562.
- [32] M. Zeiml, R. Lackner, *New insight into spalling of near-surface layers of concrete subjected to fire loading*, Int. Conf. on Computational Methods for Coupled Problems in Science and Engineering, Ibiza, 2007, pp 283-286.

Bibliography of the annexes

- [A.1] D. Gawin, F. Pesavento, B.A. Schrefler, *Towards prediction of the thermal spalling risk through a multi-phase porous media model of concrete*, Comput. Methods Appl. Mech. Engrg . 195 (2006) 5707-5729.
- [A.2] Brite Euram III BRPR-CT95-0065 HITECO, *Understanding and industrial application of High Performance Concrete in High Temperature Environment – Final report*, 1999.
- [A.3] R. Felicetti, P. Gambarova, M.P. Natali Sora, G. Rosati, *Caratterizzazione mecánica di calcestruzzi ad alta ed altissima resistenza esposti ad alta temperatura*, Brite Euram III report, 1999.
- [B.1] Brite Euram III BRPR-CT95-0065 HITECO, *Understanding and industrial application of High Performance Concrete in High Temperature Environment – Theoretical Manual*, April 2006.
- [B.2] Brite Euram III BRPR-CT95-0065 HITECO, *Understanding and industrial application of High Performance Concrete in High Temperature Environment – User Guide*, May 2006.

Appendix 4A. SPALLING INDEX EVOLUTION FOR EACH COMBINATION

Appendix 4B. INPUT FILES FOR THE HYGRO-THERMO-CHEMO-MECHANICAL CALCULATIONS

Appendix 4C. ACCEPTED PUBLICATIONS RELATED TO THIS CHAPTER

(See next pages)

*THIS PAGE IS INTENTIONALLY
LEFT BLANK*